Nuclear Safety
NEA/CSNI/R(2000)7
August 2000

OCDE

Flame Acceleration and Deflagration-to-Detonation Transition in Nuclear Safety

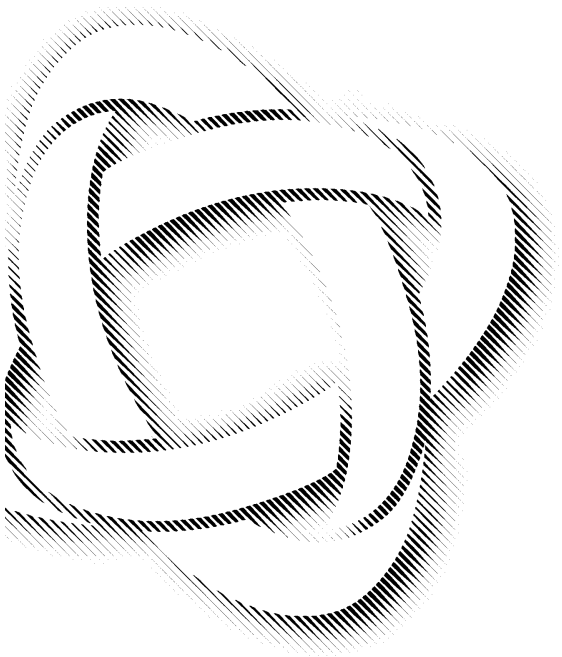

State-of-the Art Report
by a Group of Experts

OECD Nuclear Energy Agency
Le Seine Saint-Germain - 12, boulevard des Îles
F-92130 Issy-les-Moulineaux, France
Tél. +33 (0)1 45 24 82 00 - Fax +33 (0)1 45 24 11 10
Internet: http://www.nea.fr

AEN NEA

N U C L E A R • E N E R G Y • A G E N C Y

State-of-the-Art Report

On

Flame Acceleration

And

Deflagration-to-Detonation

Transition In

Nuclear Safety

W. Breitung
C. Chan
S. Dorofeev
A. Eder
B. Gelfand
M. Heitsch
R. Klein
A. Malliakos
E. Shepherd
E. Studer
P. Thibault

Additional copies of this CD
and of the paper report
can be obtained from

Dr. Jacques Royen
Deputy Head
Nuclear Safety Division
OECD Nuclear Energy Agency
Le Seine - Saint Germain
12 Boulevard des Iles
F-92130 Issy-les-Moulineaux
France
E-mail: jacques.royen@oecd.org

TABLE OF CONTENTS

continued.…

TABLE OF CONTENTS (continued)

continued . . .

TABLE OF CONTENTS (concluded)

FOREWORD

Flame acceleration (FA) and deflagration-to-detonation transition (DDT) are important phenomena in severe accidents because they can largely influence the maximum loads from hydrogen combustion sequences and the consequential structural damage. The ultimate goal in hydrogen mitigation is to design countermeasures that allow operators to avoid FA and DDT. In current nuclear power plants, the load-bearing capacity of the main internal structures is jeopardized by flame speeds in excess of about 100 m/s. New containment designs could, in principle, be constructed to carry higher dynamic loads, however, at the expense of additional costs. To judge the potential for fast flames and DDT, the causes and underlying processes have to be understood. Criteria may then be derived that can be used in three-dimensional numerical containment simulations, testing the effectiveness of hydrogen mitigation methods, to decide whether FA or even DDT is possible.

A review of Flame Acceleration (FA) and Deflagration-to-Detonation Transition (DDT) in Containment had been prepared for the NEA Committee on the Safety of Nuclear Installations (CSNI) as a State-of-the-Art Report (SOAR) in 1992 [reference NEA/CSNI/R(92)3]. Since the issuing of that report, several very significant new experimental and theoretical projects had been initiated and had started to bear fruit, in the United States, Japan, Germany, France, Canada, the Russian Federation, and under the auspices of the European Commission. After discussions held at the September 1996 meeting of CSNI's Principal Working Group on the Confinement of Accidental Radioactive Releases (PWG4), the Committee agreed that a new report should be initiated with the objective of compiling information from these programmes for the benefit of Member countries.

Dr. W. Breitung (Forschungszentrum Karlsruhe, FZK) agreed to take the lead in the preparation of the new State-of-the-Art Report. A small Writing Group was set up; its members are listed in Annexes 1 and 2.

The Writing Group met twice in 1998 and twice in 1999. Lead Authors were appointed for the various chapters of the report. The final version was endorsed by PWG4 in September 1999 and by CSNI in December 1999.

The CSNI expresses its gratitude to the various governments and organizations that made experimental and analytical data available for the preparation of the report as well as the resources—time, staff, competence, effort and money—devoted to this substantial piece of work. The role of the Lead Authors was essential in preparing the document; they also deserve all our gratitude. Special thanks are due to the FZK, in particular to Dr. W. Breitung, who—in addition to preparing chapters—led and co-ordinated the efforts and produced the final draft. Without their generous and vigorous support, their competence and hard work, the report would have taken a much longer time to produce and its quality would necessarily have been lower.

Thanks are due also to Ms. A. Soonawala who expertly edited the report, improving its readability and its layout.

EXECUTIVE SUMMARY

This report concerns the key issue of hydrogen combustion that may occur as a result of severe accidents in nuclear power plants, namely to predict which type of combustion will occur: a slow flame, a fast turbulent flame, or a detonation. This question is crucial because the combustion mode governs the amplitude and time scale of the containment pressure load.

Chapter 1 introduces the phenomena of flame acceleration (FA) and deflagration-to-detonation transition (DDT) with respect to the relevance of these processes in severe accidents, the basic physical phenomena that define the detonation limits involved in these processes, and options for control and mitigation of these processes.

Chapter 2 describes the basic elements of FA and DDT, which have been understood for many years. Both these phenomena are basically due to the intrinsic instability of flame surfaces. Depending on the mixture composition, the initial pressure and temperature conditions, the geometrical configuration and, most importantly, the physical size (or scale) of the reactive system, FA and detonation on-set may or may not occur What has been missing up until now are quantitative predictions of FA and DDT for given conditions.

Chapter 3 outlines the significant advances that have been made in this field during the last decade (1990-1999). Two criteria were derived from a large new experimental database. The first criterion predicts the potential for spontaneous FA to supersonic flame speeds. This criterion controls the formation of shocks that have sufficient strength to trigger a secondary local explosion. The second criterion governs the amplification and transmission of this local explosion to a stable detonation in the undisturbed mixture. For this step, the effective geometrical size of the reactive mixture must be greater than 7 times the detonation cell width of the average mixture composition. Both conditions, namely the critical flame velocity and the minimum scale requirement, are necessary for a complete DDT. The two criteria allow realistic assessments of the FA and DDT potential during an accident scenario. Rules and data for evaluation of the criteria in reactor containments are formulated.

An important property of these criteria is that they can be evaluated from the results of three dimensional (3D) computational fluid dynamics (CFD) distribution calculations, which provide all the necessary data for mixture composition and geometrical scales. Depending on these results, the criteria allow us to predict the fastest combustion regime possible, namely either slow deflagration, fast turbulent deflagration, or detonation. An approach on how to use the criteria within a lumped-parameter framework is described in Section 6.3.

Chapter 4 summarizes the state-of-the-art of the mathematical description of these 3 combustion regimes. It starts with modelling of non-reacting turbulent flames, putting major emphasis on Reynolds-averaged Navier-Stokes equations. Different types of closure approaches are discussed. An important practical issue for large-scale nuclear containments is the modelling of obstacles for which porosity models are described. Moreover, the key ideas for large eddy simulation are summarized.

For simulation of turbulent premixed combustion, three model categories are described, covering heuristic closures, flamelet models, and probability density function (PDF) approaches. The realistic representation of chemistry poses a major challenge to numerical modellers because of its wide range of inherent time scales. Chapter 4 presents heuristic models for the net effect of numerical reactions as well as for more sophisticated reduced chemistry models and the most recent developments, aiming at a systematic mathematical approach to chemistry reduction.

The particular numerical challenges posed to a numerical flow solver in the context of FA and DDT are discussed, and the current most-popular finite-difference and finite-volume approaches are presented. For numerical representation of the combustion front, essentially 2 alternatives exist: (a) detailed models for all relevant physical processes within the turbulent combustion zone, or (b) treatment of the reaction front as a discontinuous surface in space.

Chapter 5 gives examples for recent mathematical and numerical model developments and their validation by corresponding experiments. Moreover, the important question is addressed: which tool to choose for which task in practical applications. For many of the every day engineering tasks, it would be inefficient to employ the most advanced and complex modelling tools giving the currently best-possible answers. On the other hand, with increasing requirements on the precision of safety analysis, a demand for detailed and sophisticated modelling exists. Therefore, a good compromise seems to be the compilation of a hierarchy of models with increasing levels of detail, starting from coarse-grain zero-dimensional lumped-parameter models to high-resolution 3D tools. The choice of model then is primarily governed by the type of processes to be resolved and the required precision.

With respect to simulation of FA and DDT, first-level models neglecting momentum exchange have very restricted predictive value. The next level of computational complexity that allows representation of 3D global unsteady but statistically averaged flow fields provides estimates for the influence of momentum exchange and the effects from the other previously neglected terms in the Navier-Stokes equations. This level of modelling allows realistic assessments of potential structural loads that are due to high-speed combustion events. However, this kind of approach still misses events that are triggered by localized processes and can then develop into global combustion events. Examples are ignition by hot spots or detonation onset through gas-dynamic–reactive resonances. Reliable modelling of this kind of process requires an even more advanced modelling level that is able to resolve the smallest flow scales, e.g., by sophisticated dynamic mesh refinement.

Chapter 6 describes how the tested model approaches, outlined in Chapter 5, are currently applied to reactor containment analysis. Two different levels of model sophistication are currently applied. The first one is based on the mixture and geometry information available within conventional zero-dimensional lumped-parameter models. This fast and relatively easy analytical method is useful to screen a large number of different event sequences for the risk-dominating cases. However, this screening procedure requires well- experienced users who are familiar with the intrinsic uncertainties of lumped-parameter distribution calculations, in order not to miss critical accident sequences. The identified critical cases should then be investigated with the next higher level of model sophistication, using three-dimensional CFD tools.

The higher precision of CFD prediction with respect to FA and DDT potential comes first from the solved equations (3D, fully compressible Navier-Stokes equations, including momentum balance and a complete set of fluid dynamic terms); second, from the much finer spatial resolution (typically 1 m^3 versus 1000 m^3 with a lumped-parameter method); and third, from the correspondingly smaller numerical truncation errors and mixing effects. The given examples of full CFD distribution analysis with the corresponding evaluation of the FA and DDT criteria demonstrate that currently available CFD tools allow us to exam the relative merits of different mitigation schemes. For a given plant, mitigation system, accident scenario, and set of hydrogen-steam sources, the times and space regions with FA and DDT potential can be clearly identified. In case of unacceptable risk, the mitigation measure can be varied in order to reach a negligible threat for the containment integrity.

Chapter 7 summarizes the significant advances, outlined above, in the understanding of FA and DDT during this decade. In addition, the most important topics for future work on mechanistic calculations are described; these topics aim at a better definition of the initial conditions for FA and DDT (the

H_2-steam sources and the prediction of their distribution); a decreased conservatism in the currently applied FA and DDT criteria (inhomogeneous and vented mixtures); and improved numerical CFD simulation techniques for fast turbulent deflagration and detonations (advanced models, higher spatial resolution, massive parallel processing).

1. INTRODUCTION*

This introductory chapter looks at the phenomena of flame acceleration (FA) and deflagration-to-detonation transition (DDT) from four different perspectives:

- relevance of these processes for core-melt accidents,
- basic physical phenomena that define the detonation limits involved in these processes,
- options for control of FA and DDT, and
- hydrogen mitigation.

1.1 Relevance of FA and DDT in Severe Accidents.

The relevance of FA and DDT processes in postulated severe accidents arises from theoretical estimates and large-scale experiments. The assumption is that 100% of the fuel-cladding Zircaloy oxidizes (but not the other in-vessel Zr or steel structures) and that the generated hydrogen is homogeneously distributed in the available containment volume, thereby leading to dry hydrogen concentrations of between 12% and 21% in American plant designs [1.1]. For operating and future European pressurized-water reactor (PWR) designs with a large dry containment, the same assumptions lead to dry H_2 concentrations of between 17% and 20% [1.2]. Typical steam concentrations are from 20% to 70%, depending on the accident scenario. These conditions define the "global distribution" area shown in Figure 1.1-1.

Since nuclear power plant (NPP) containments are highly complex multi-compartment structures, H_2 gradients can generally develop in certain space and time intervals. The inhomogeneity of the hydrogen distribution mainly depends on details of the H_2 source (location, release rate), the containment design, and the efficiency of natural-convection processes. Three-dimensional distribution calculations for German 1300 MWe PWRs have often shown gas compositions in the "local distribution" area of Figure 1.1-1.

Hydrogen distribution under severe accident conditions was extensively investigated on full reactor scale in the HDR-E11 test series, using Helium gas as H_2 simulant [1.3]. Typical measured H_2 (He)-steam concentrations are included in Figure 1.1-1 for HDR tests simulating different accident sequences. A detailed state-of-the-art report (SOAR) on containment thermalhydraulics and hydrogen distribution has been published [1.4].

Figure 1.1-1 also depicts estimates for limits of flammability, FA, and DDT on a large scale. Comparison of these limits with the above described fields of possible gas compositions clearly shows that FA and DDT are relevant for severe accident studies. These fast combustion modes appear possible on local and even global scales, depending on details of the hydrogen source. It is also important to note that the steam concentration in the containment has a large effect on the combustion mode. The steam concentration is mainly governed by the balance between the steam release rate and the steam condensation rate, which, in turn, depends on the size and surface temperature of the internal containment structures.

*[1] Dr. W. Breitung is the lead author of Chapter 1

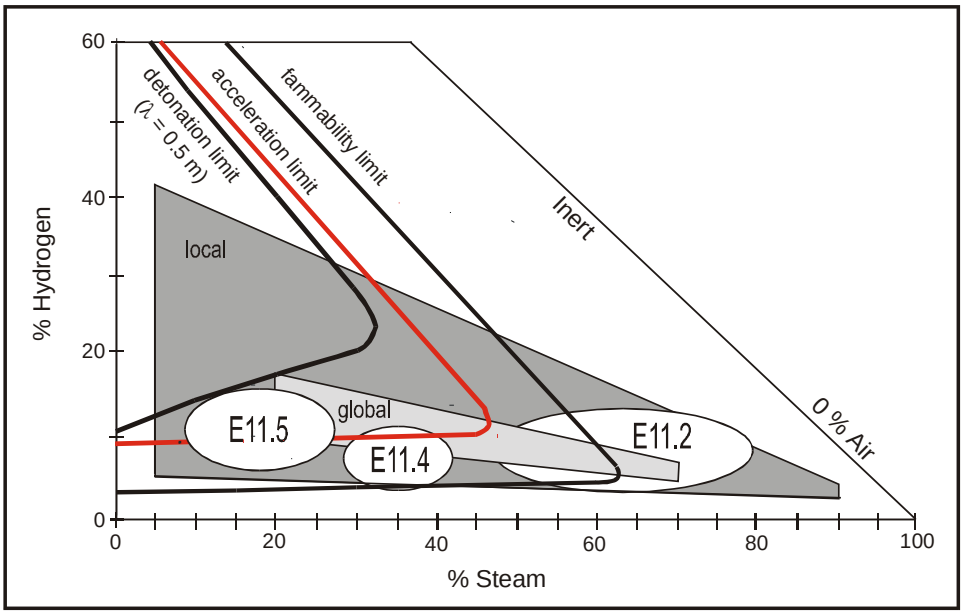

Fig.1.1-1.Theoretical estimates and large-scale HDR E-11 distribution tests demonstrate the possibility of FA and DDT processes in severe accidents

Relatively dry or wet containment atmospheres can develop in different accident sequences, as, for example,. demonstrated by the HDR distribution tests E11.5 and E11.2, respectively (Figure 1.1-1). Flame acceleration and DDT become a major concern in dry or medium-dry scenarios (tests E11.5, E11.4, Figure 1.1-1).

1.2 Basic Physical Processes

If severe accidents should lead to mixtures inside the detonation limits shown in Figure 1.1-1, two classes of detonation initiation can, in principle, be distinguished:

- direct strong initiation by an external energy source; and

- indirect initiation with a weak ignition, followed by a self-induced FA and DDT.

In the first case, the energy necessary to establish a self-sustaining stable detonation front wave system is provided by the external source, e.g., a spark or high explosive. In the second case, the initiation energy is provided by the combustible mixture itself. Different modes have been observed for the indirect detonation initiation; it can be induced, for example, by FA along tubes or channels, turbulent jets, and turbulence-generating fans.

In severe accident environments, the direct initiation by an external energy source seems less likely than the indirect mode because the necessary initiation energies are much greater than those for a weak ignition. The measured orders of magnitude for direct initiation in free clouds are 10 to 1000 kJ for H_2-air mixtures with equivalence ratios from 0.75 to 0.5 [1.5], whereas only millijoules are required to trigger a weak ignition in H_2-air mixtures. The only potential ignition source for a direct initiation may be a high-voltage spark or arc in a well-confined geometry. Many more possibilities exist for weak ignitions. It has been suspected that the spontaneous burn in the Three Mile Island (TMI) Unit 2 accident that led to the only significant containment load (3 bar), was initiated by a ringing telephone. The processes following a weak ignition in a sensible combustible mixture, which

is enclosed by a complicated 3D structure with internal flow obstacles, involve extremely complex interactions between turbulent flow and chemistry. From a global point of view, chemical energy is converted and concentrated to high mechanical energy densities, which, in turn, trigger large chemical reaction rates through high temperatures. The simulation of these processes generally requires computation of unsteady, turbulent, and compressible reactive flow problems in multi-dimensional geometries with high spatial resolution.

The significance of FA and DDT processes for reactor safety is due to the fact that these fast combustion modes can be extremely destructive. They have the highest damage potential for internal containment structures; for safety systems that are required for safe termination of the accident (sprays, recombiners); and for the outer containment shell that is the last barrier against the release of radioactivity into the environment.

The concern about the outer containment shell is not only connected to its function as the ultimate barrier, but the concern is also due to its complicated structural behaviour. All modern containment buildings are a complex composite of different structural elements, including an undisturbed shell, personal and material locks, and hatches of different sizes and design, as well as penetrations for electrical cables and pipes. This system has been qualified for a certain global and static design pressure, which is generally related to the maximum blowdown pressure from a break of the primary coolant line.

However, in a severe accident, which is not part of the licensing process, in existing plants FA and DDT may become possible. In this case, new containment load classes would arise, namely high local or even global dynamic loads. The structural behaviour of containment components under such dynamic pressure and impulse loads is complicated and difficult to evaluate. An effective way to protect the containment integrity even for the case of beyond-design accidents is therefore to control the hydrogen behaviour in such a way that the possibility of FA and DDT occurring is decreased or even excluded. It is clear that this improvement of public and environmental protection against the consequences of severe accidents requires a detailed understanding of FA and DDT.

1.3 Options for Control of FA and DDT

The strengthening of the containment barrier function for severe accident scenarios is realized in various countries by introducing hydrogen management systems. For existing plants, the goal is to significantly reduce the probability of containment failure in cases of degraded core accidents, whereas for future plants the goal is generally a hydrogen control system that prevents the occurrence of FA and DDT by design for a spectrum of representative accident scenarios.

The amount and rate of hydrogen generated in an accident varies for different reactor designs and accident scenarios. Large reactors have a proportionally greater mass of available zirconium, and, hence, a potentially large hydrogen source term. The CANDU design is exceptional in having a comparatively small initial hydrogen release term. The relatively small hydrogen release for the CANDU design is due to the distributed channel-type core surrounded by an additional heat sink provided by the moderator water, which effectively arrests severe-accident progression at the point of fuel-cladding oxidation, preventing the continued hydrogen releases associated with complete core-melt. Moreover, CANDU fuel cladding is relatively thin, for neutron economy purposes, resulting in a correspondingly small mass of hydrogen released in the short term from fuel-cladding oxidation. The net result is a total short-term hydrogen mass release of less than 100 kg for the CANDU 600 MW reactors, and up to 300 kg for the new CANDU 900 MW design. As a result, the initiating sequence

for hydrogen production (loss of cooling + loss of emergency core-cooling) in the CANDU reactor is included in the design basis of the plant.

For CANDU reactors, the strategy of hydrogen management is either to dilute or to remove the hydrogen in the containment atmosphere. Because of a limited hydrogen source term and a relatively large containment building, dilution of hydrogen with containment air is the most readily available means of dealing with a broad range of hydrogen releases. Besides relying on natural convection to mix the hydrogen with containment air, CANDU reactors also employ local air coolers, for steam removal, that promote forced convection circulation, provided electrical energy is available. A "well-mixed" containment atmosphere is not flammable. In situations when a flammable mixture is created in isolated regions inside the containment, a deliberate ignition system is employed as a second line of defence. For removal of hydrogen, CANDU reactors employ both igniters and catalytic recombiners for short- and long-term hydrogen control, respectively.

Hydrogen management in existing German 1300 MWe nuclear power plants is designed to cope with the potential in-vessel hydrogen production, which is typically about 500 kg. The first licensing applications for a system of catalytic recombiners were submitted in 1998; implementation of the recombiners is expected to start in 1999. Detailed distribution analyses of the recombiner concept with lumped-parameter codes and with a 3D computational fluid dynamics (CFD) code have shown the exclusion of significant containment loads from FA and DDT for the investigated accident scenarios. A large risk reduction will be obtained for beyond-design accidents with the proposed hydrogen control by a catalytic recombiner.

For the future EPR, which is a joint development of the German and French industry for a next-generation European plant design, the new safety goal is that even in case of a severe accident the radiological consequences must be essentially restricted to the plant itself and may not lead to large permanent relocation areas. This goal implies that containment integrity must be demonstrated for all possible hydrogen combustion loads. The joint recommendations of the French and German Advisory Committees (Groupe Permanent des Reacteurs and Reaktorsicherheitskommission) require that the plant has to be designed to cope with the maximum amount of hydrogen that could accumulate in the containment building during a low-pressure core-melt accident. More specifically, the Committees requested that the possibility of global detonations must be practically eliminated. Catalytic recombiners and igniters were recommended as possible components of a hydrogen control system. In order to exclude large-scale detonations and to demonstrate that the maximum possible combustion loads during representative severe accident sequences remain within the containment design capabilities, extensive 3D distribution and combustion calculations will be performed with different recombiner-igniter options. An important aspect of these analyses is to show that FA and DDT can be controlled. For future plant designs that try to shift the design-basis loads into the extremely unlikely region of severe accidents, the understanding of FA and DDT is of the utmost significance.

1.4 Hydrogen Mitigation

In the context of FA and DDT, the current SOAR appropriately addresses issue of controlling these fast combustion modes under severe accident conditions. We first summarize the general requirements for hydrogen mitigation systems and then give a brief discussion of the most important current technical options for hydrogen control in NPPs. An extended summary of this topic can be found in Reference [1.6].

1.4.1 General Requirements

As required for any other industrial installation, the requirements for a combustion and fire protection system in a nuclear containment must be carefully evaluated to provide the necessary basis for the technical specification.

The system must first of all fulfil the following acceptance criteria:

- There should be no adverse effects on normal operation, plant personnel, and plant response to severe accidents.

- The containment will be protected, and no new load mechanisms should appear (thermal loads, missiles).

- The safety systems for accident termination should remain unaffected.

With respect to the design of the mitigation system, the following requirements must be met:

- The mitigation system must perform the intended function with high reliability in all anticipated severe accident environments.

- The design of the mitigation system must be effective for a wide spectrum of accidents.

- The design of the mitigation system must be qualified for seismic design event.

- The mitigation system must have redundancy of components.

- The mitigation system must be fail-safe.

- The mitigation system must have clear activation criteria if it is an active system.

- The mitigation system of an existing plant must have the potential to be retrofitted.

- The mitigation system should be cost-effective to install, maintain, and test.

When technical components have been qualified with respect to these design requirements, the next step is to predict the outcome of a system of components for severe accident conditions and for full containment scale. The following analysis requirements exist:

- The system efficiency must be predicted for different bounding accident scenarios, e.g., the integral hydrogen removal rates of the system.

- A sensitivity analysis of the number and location of the components is needed to ensure adequate design and safety margins.

- The consequences of a random ignition for the mitigation system and for containment pressure loads must be understood.

- The verification of the theoretical tools and codes used for the scale-up and the prediction of component efficiency for the reactor case must be performed.

A large amount of work has been devoted in a number of countries to identify mitigation solutions that satisfy these stringent requirements. It turned out that conventional non-nuclear combustion and fire protection methods are not directly adaptable to severe accidents in NPPs. The problems are mainly related to the large scale of the containment, high-potential flame speeds (little time for system activation), high hydrogen release rates (kilograms per second of H_2), and incompatibility with other nuclear safety rules (fire prevention).

1.4.2 Hydrogen Mitigation Techniques

The following three load-reducing mitigation techniques have shown sufficient potential for application in existing and future PWR power plants:

- catalytic recombiners,
- spark igniters, and
- pre- and post-accident dilution.

1.4.2.1 Catalytic recombiners

Figure 1.4.2.1-1 shows as an example the catalytic recombiner developed by Siemens. Other designs were developed by Atomic Energy of Canada Limited (AECL) in Canada and Nuklear Ingenieur Service (NIS) in Germany. Hydrogen recombines with oxygen from air on Pt-containing catalytic surfaces. The heat of reaction produces a natural draft in the convection duct and establishes a stable self-feeding process of the gas at the lower entrance. The advantage of such a module is that it works passively and also in steam-inerted mixtures as long as the H_2 and O_2 concentrations are above approximately 1%. The disadvantage is the relatively low removal capacity per module (several grams per second of H_2), compared with typical release rates, which can reach 1 kg/s H_2 in large plants. This typical release rate clearly creates the possibility of local H_2 enrichments occurring during transient accident phases with high H_2 release rates.

Another currently unresolved issue is ignition of the hydrogen-air-steam mixture under certain overload conditions, which depend on the recombiner design and steam concentration. It is anticipated that new improved recombiner designs for H_2 concentrations above 10% will become available in the near future. Recombiner ignition should either be suppressed or become predictable, so that this effect could be taken into account in future containment analyses.

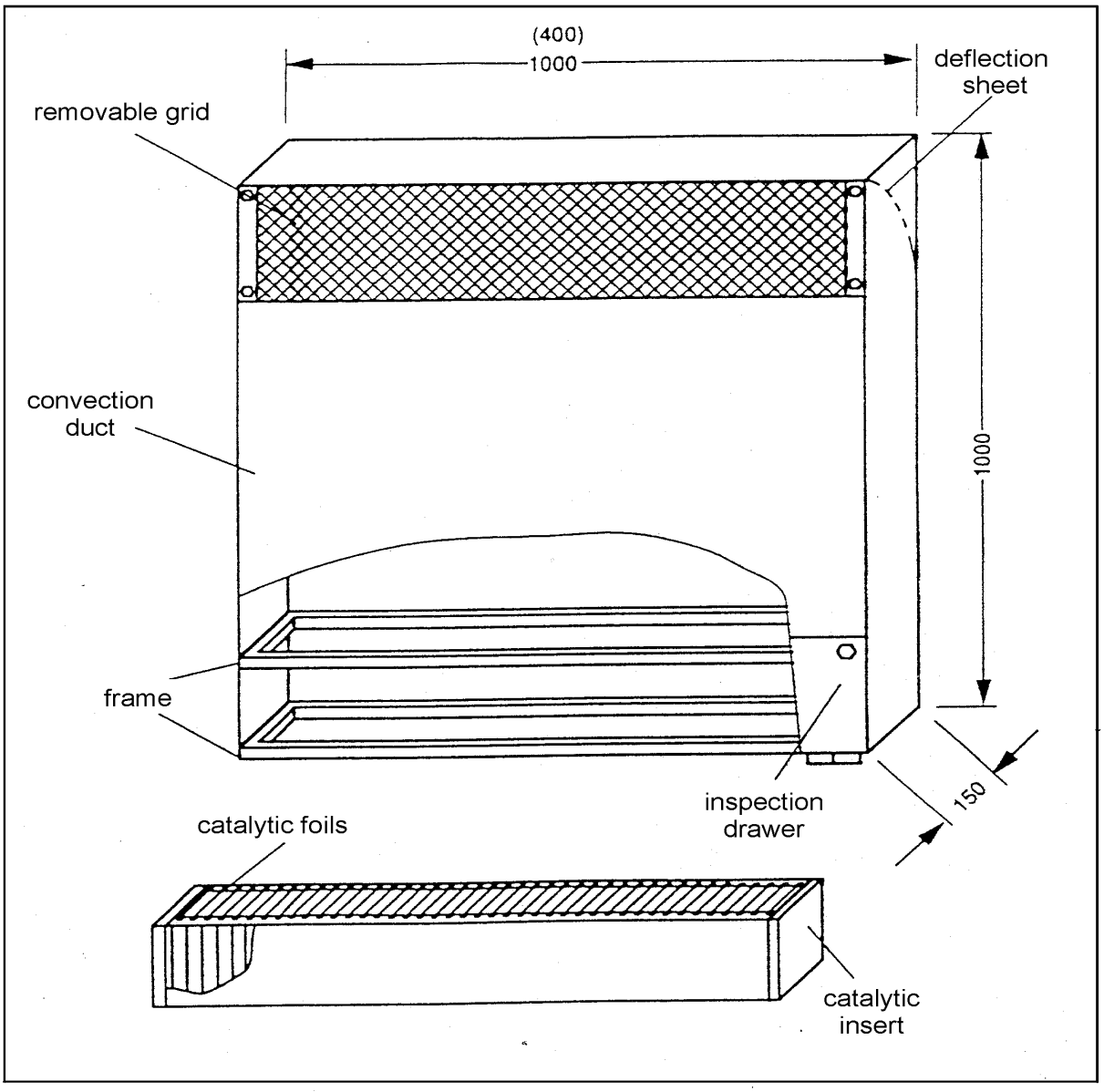

Figure.1. 4.2.1-1 Catalytic recombiner design of Siemens KWU

Recent investigations for German PWR plants using the 3D CFD program GASFLOW [1.7] have revealed a number of new results for recombiner efficiency on full plant scale:

- The removal rate of a recombiner depends only on the local H_2 concentration at the recombiner position, which, in turn, is largely determined by the global flow field in the containment. The natural draft of the recombiner itself can be neglected in most cases because the effected space region is limited to a distance of a few metres. A good resolution of the local H_2 concentration is necessary for a realistic calculation of the individual recombiner efficiency.

- In the investigated small-break (SB) and large-break loss-of coolant accidents (LBLOCA) scenarios, the recombiners did not provide a noticeable additional mixing effect because the small momentum of the recombiner exhaust gases is dissipated in the near environment, and the succeeding exhaust gas motion is buoyancy-dominated.

- In accident sequences leading to well-mixed conditions, a system of catalytic recombiners can be an effective safety-oriented mitigation approach, which acts within the first few hours after hydrogen release. (For example, in one of the investigated cases with about 50 recombiners and 530 kg H_2 total release, the integral H_2 removal rate was initially 180 kg/h H_2 and then decreased proportionally to the residual H_2 or O_2 concentration in the containment.)

Corresponding lumped-parameter analyses covering also the long-term evaluation of the containment atmosphere composition, pressure and temperature were performed with the RALOC code [1.8].

In summary, present recombiner designs fulfil the above-listed acceptance, design and analysis requirements almost completely. The principal drawback of current designs is the low recombination rate, related to the hydrogen sources expected during core degradation. An open point concerns the potential of mixture ignition under transient overloads during accident phases with high H_2 release rates.

Future recombiner designs should find the best compromise between the two apparently opposing requirements of high recombination rate and low ignition potential.

1.4.2.2 Igniters

The second important mitigation approach is deliberate ignition of flammable accident mixtures with igniters. The intention is to start a deflagration as early as possible before dangerous amounts of hydrogen have accumulated. Two types of devices have been developed, namely glow-plug and spark igniters. Glow-plug igniters require a continuous power supply, which may not be available in severe accident sequences. Siemens developed an autark battery-powered spark igniter, which is activated by temperature or pressure set points (Figure 1.4.2.2-1). This module operates passively and does not require operator action. The reliable function was shown for a wide range of severe accident conditions [1.9].

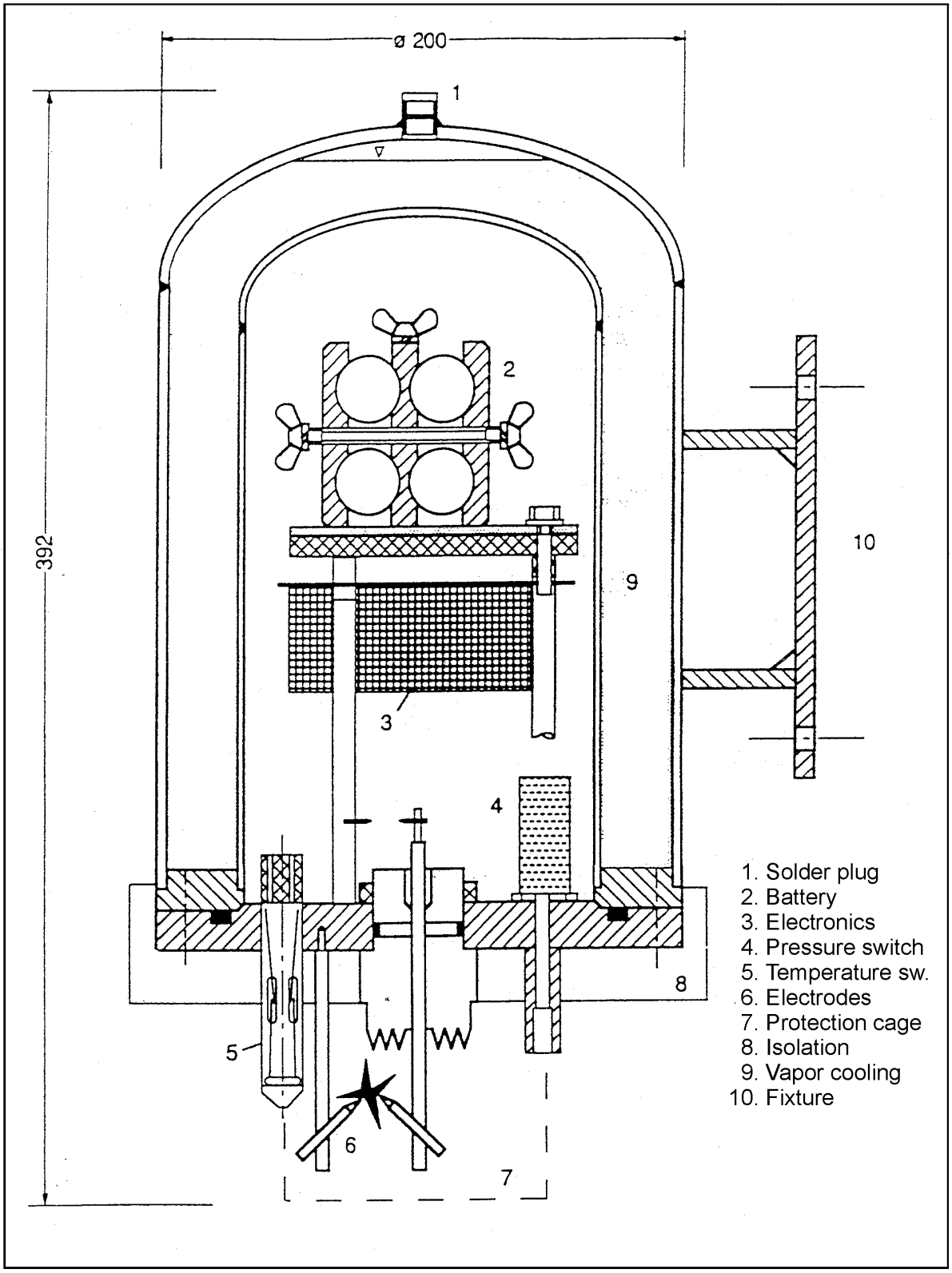

Figure 1.4.2.2-1 Autark spark igniter developed by Siemens WZB 89

The initial design used a spark interval of 10 s. Large-scale experiments with dynamic H_2 injection and spark ignition [1.10] have shown however, that a shorter spark interval would bring an additional safety margin. Ignition occurs only after the edge of the combustible gas cloud has arrived at the nearest igniter position, and the next spark is activated. The flame then travels back to the source location. A short spark interval would minimize the H_2 content of the cloud at first ignition.

The main question in the application of the igniter concept is its safety orientation. The use of igniters should reduce the overall risk to the containment and should not create new additional hazards such as a local detonation. A new methodology for safe igniter implementation in a 3D containment was recently developed and implemented into the GASFLOW code [1.11]. The method was applied to a bounding dry release scenario in a future PWR in which the steam from the core is condensed in a water pool. In the unmitigated case, significant DDT potential developed in the whole containment, including the possibility of global detonations. The analysis with igniters in different positions predicted deflagration or detonation in the break compartment, depending on the location of the igniter. Igniter positions were found that lead to early ignition, effective H_2 removal, and negligible pressure loads. This approach can be used to determine the number and position of igniters necessary to control different hydrogen-release scenarios in different plant designs.

In summary, the installation of an igniter system for H_2 mitigation requires careful analysis regarding the number and location of igniters to exclude local detonations. The theoretical understanding and the numerical tools are sufficiently developed and verified to allow conclusive predictions with sufficient safety margins. The principal drawback of igniters is that they are not effective under inert conditions, which can arise from high steam concentrations or local oxygen burnout.

1.4.2.3 *Pre- and post-accident dilution*

A third option for H_2 mitigation is dilution of the accident atmosphere with an incondensable gas to suppress energetic combustion regimes or even full inertization to suppress combustion completely. The inert gas (CO_2 or N_2) can, in principle, be added before or after initiation of a severe accident.

The most rigorous solution of course is complete permanent inertization of the containment atmosphere. General consensus is that this approach is acceptable for boiling-water reactor (BWR) plants; however, it violates the first acceptance criterion given above in the case of PWR plants, namely no adverse effect on normal operation. There are three main reasons for this difference:

- Meltdown of a BWR core would create much larger hydrogen masses because of the additional Zr shrouds; the resulting mixtures could be very reactive.

- BWR containments are much smaller, and hence easier to inert and de-inert for refuelling.

- All important safety and technical support systems are located outside of the BWR containment and can be easily checked during normal operation.

For many BWRs worldwide, permanent inertization has been chosen as the optimum hydrogen mitigation method. This approach appears very convincing for accidents that occur while the reactor is on-power, but accidents that occur during a shutdown state are not protected because of containment de-inertization during refuelling and maintenance.

For PWRs with large dry containments the options of partial or full inertization after initiation of a severe accident remain. Both approaches have been investigated experimentally and theoretically, e.g., [1.12, 1.13], using gaseous or liquid carbon dioxide.

With respect to the general acceptance, design, and analysis requirements for mitigation methods, the following aspects of post-accident dilution are important:

- It is an active method, which requires decision, actuation, and completion within a restricted time window to be effective (0.5 to 1 h),

- A complex system is required for technical realization (permanent storage of ≈100 tonnes of liquid or gaseous CO_2).

- The distribution and mixing of a CO_2 jet in a complex multi-room structure filled with lighter gases (air, steam) is a non-trivial process, requiring detailed CFD analysis; the result can strongly depend on time and location of the CO_2 injection [1.14].

- Addition of CO_2 may increase the pressure significantly, for example, for full inertization roughly 60 vol % of (steam + CO_2) are required.

- The addition of CO_2 leads to an overpressurized containment, even long after termination of the accident.

A good compromise with respect to the various requirements and safety aspects could be a fast truly homogeneous post-accident dilution technique with proven suppression of the fast combustion regimes, only marginal pressure increase, and reduced maintenance costs. However, the design of post-accident dilution (or inertization) methods is not a simple straightforward task because complex natural-convection processes between fluids of different densities in a multi-room structure determine the remaining combustion potential.

1.5 References

[1.1] J.W. Yang, Z. Musicki and S. Nimnual, Hydrogen Combustion Control and Value-Impact Analysis for PWR Dry Containments, NUREG/CR-5662, June 1991.

[1.2] J. Rohde, GRS, private communication, 1997.

[1.3] G. Katzenmeier, H.U. Hahn and T. Cron (eds.), HDR Sicherheitsprogramm, Abschlußbericht Phase III, Techn. Fachbericht [HDR –Safety Program, Final Report Phase III Technical Report] PHDR 115-94, March 1994.

[1.4] H. Karwat et al., State-of-Art-Report on Containment Thermalhydraulics and Hydrogen Distribution, CSNI Report NEA/CSNI/R(99)16, June 1999.

[1.5] M.P. Sherman and M. Berman, The Possibility of Local Detonations During Degraded-Core Accidents in the Bellefonte NPP Nuclear Technology, Vol. 81, 1988, 63.

[1.6] J. Royen, Closing Remarks, OECD/NEA/CSNI Workshop on the Implementation of Hydrogen Mitigation Techniques, Winnipeg, Manitoba, Canada, May 13-15, 1996, AECL Report, AECL-11762; CSNI Report, NEA/CSNI/R(96)8, March 1997.

[1.7] P. Royl, H. Rochholz, W. Breitung, J.R. Travis, G. Necker and A. Veser, GASFLOW-Analysen zur Wirksamkeit eines Rekombinatorkonzepts bei einem postulierten Surge-line LOCA im Kernkraftwerk Neckarwestheim-2 [GASFLOW Analysis Concerning the Efficiency of a Recombinator Concept in Case of a Postulated Surge-Line LOCA in the Power Plant Neckarwestheim-2], Report FZKA-6333, Forschungszentrum Karlsruhe, Germany, 1999.

[1.8] M. Tiltmann and J. Rohde, Wirksamkeit eines Systems katalytischer Rekombinatoren in Sicherheitsbehältern von DWR-Anlagen deutscher Bauart. [Efficiency of a System of Catalytic Recombiners in PWR Containments of German Type], GRS-A-2628, Gesellschaft für Anlagen-und Reaktorsicherheit (GRS) mbH, Cologne, 1998.

[1.9] R. Heck, G. Keller, K. Schmidt and H.J. Zimmer, Hydrogen Reduction Following Severe Accidents Using the Dual Recombiner-igniter Concept, Nuclear Engineering and Design, Vol. 157, 1995, 311.

[1.10] W. Breitung, S.B. Dorofeev and V.P. Sidorov, "Large Scale Hydrogen-air Combustion Experiments with Dynamic H_2-injection and Spark Ignition", Transact. of the 13th Int. Conf. on Structural Mechanics in Reactor Technology (SMiRT-13), Porto Allegre, Brazil, August 13–18, 1995, Vol. I, 199.

[1.11] W. Breitung, S.B. Dorofeev and J.R. Travis, A Mechanistic Approach to Safe Igniter Implementation for Hydrogen Mitigation, Proc. of the OECD/NEA/CSNI Workshop on the Implementation of Hydrogen Mitigation Techniques, Winnipeg, Manitoba, Canada, May 13–15, 1996, AECL Report, AECL-11762; CSNI Report, NEA/CSNI/R(96)8; March 1997, 199-218.

[1.12] B.A. Eckardt, Semi-passive PAD (Post-accident Dilution) System Combined with Recombiners or Igniters for e.g. Multiple-unit VVER, Proc. of the OECD/NEA(CSNI Workshop on the Implementation of Hydrogen Mitigation Techniques, Winnipeg, Manitoba, Canada, May 13–15, 1996, AECL Report, AECL-11762; CSNI Report, NEA/CSNI/R(96)8; March 1997, 331-359.

[1.13] H. Karwat and B. Stolze, The Inertisation of PWR Containments by Injection of Liquid Carbon Dioxide, AECL Report, AECL-11762; CSNI Report, NEA/CSNI/R(96)/8; March 1997, 315-330.

[1.14] P. Royl, J.R. Travis, E.A. Haytcher and H. Wilkening, Analysis of Mitigation Measures during Steam/Hydrogen Distribution in Nuclear Reactor Containments with the 3D Field Code GASFLOW", AECL Report, AECL-11762; CSNI Report, NEA/CSNI/R(96)8; March 1997, 129-141.

2. PROCESSES OF FA AND DDT*

2.1 Introduction

A freely expanding flame is intrinsically unstable. It has been demonstrated, both in laboratory-scale experiments [2.1-2.4] and large-scale experiments [2.5-2.8], that obstacles located along the path of an expanding flame can cause rapid flame acceleration. Qualitatively, the mechanism for this flame acceleration is well understood. Thermal expansion of the hot combustion products produces movement in the unburned gas. If obstacles are present, turbulence can be generated in the combustion-induced flow. Turbulence increases the local burning rate by increasing both the surface area of the flame and the transport of local mass and energy. An overall higher burning rate, in turn, produces a higher flow velocity in the unburned gas. This feedback loop results in a continuous acceleration of the propagating flame. Under appropriate conditions, this can lead to transition to detonation.

Turbulence induced by obstacles in the displacement flow does not always enhance the burning rate. Depending on the mixture sensitivity, high-intensity turbulence can lower the overall burning rate by excessive flame stretching and by rapid mixing of the burned products and the cold unburned mixture. If the temperature of the reaction zone is lowered to a level that can no longer sustain continuous propagation of the flame, a flame can be extinguished locally. The quenching by turbulence becomes more significant as the velocity of the unburned gas increases. For some insensitive mixtures, this can set a limit to the positive feedback mechanism and, in some cases, lead to the total extinction of the flame. Hence both the rate of flame acceleration and the eventual outcome (maximum flame speed attained) depend on the competing effects of turbulence on combustion.

This chapter summarizes some of the key findings since the publishing of the last state-of-the-art report on DDT in 1991. It should be noted that to give a comprehensive discussion of the phenomena on flame acceleration and DDT is beyond of the scope of this chapter. Only a brief overview of recent works is presented. Furthermore, this chapter only cites studies that are relevant to the nuclear industry.

To provide a proper perspective of the issue, this chapter describes in some detail the key mechanisms that are responsible for flame acceleration and transition to detonation. It outlines the various eventual outcomes of flame acceleration. It also summarizes some of the recent studies that have contributed to the current understanding of the phenomena. Finally, this chapter discusses the various possible responses of a structure that has been subjected to a pressure load resulting from an accelerated flame or a detonation wave.

2.2 Flame and Detonation Propagation Regimes

Depending on the fuel concentration and the flow geometry, flame acceleration may be expected to progress through a series of regimes, as depicted in Figure 2.2-1. For the case of mild ignition, the first phase involves a laminar flame that propagates at a velocity determined by the laminar burning velocity and the density ratio across the flame front. This phase of the flame propagation is very well understood, and data are available for a wide range of hydrogen-air mixtures. The laminar flame propagation regime is relatively short-lived and is soon replaced by a "wrinkled" flame regime. For

* Lead authors of Chapter 2 are Dr. Calvin Chan of AECL and Dr. Paul Thibault of Combustion Dynamics Ltd.

most accidental explosions, this regime can persist over relatively large flame propagation distances. For this reason, it is therefore far more important than the initial laminar regime. Because of the increase in flame area, the burning rate, and hence the flame propagation velocity for the wrinkled flame can be several times higher than for the laminar flame.

Because of turbulence generated by obstacles or boundary layers, the wrinkled flame eventually transforms into a turbulent flame brush. This change results in further flame acceleration because of the increase in surface area of the laminar flamelets inside the flame brush. For sufficiently high levels of turbulence, the flamelet structure may be destroyed and then replaced by a distributed reaction zone structure.

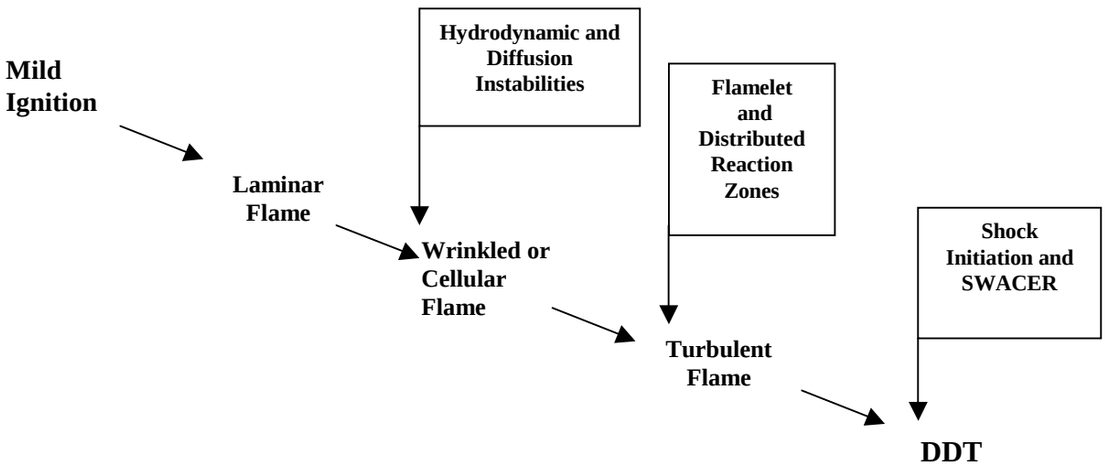

Figure 2.2-1 Regimes of flame propagation leading to DDT
(SWACER = shock wave amplification by coherent energy release)

The flame acceleration process can eventually lead to DDT through shock ignition or the SWACER amplification mechanism. For configurations involving repeated obstacles, the turbulent flame propagation regime is self-accelerating because of the feedback mechanism between the flame velocity and the level of turbulence ahead of the flame front. The final flame velocity produced by the turbulent flame acceleration process depends on a variety of parameters, including the mixture composition, the dimensions of the enclosure, and the size, shape, and distribution of the obstacles.

Figure 2.2-2 shows the flame trajectories for flame propagation in tubes filled with obstacles. Figure 2.2-3 shows the maximum flame speed achievable in tubes of various diameters. Various turbulent flame and detonation propagation regimes have been identified for hydrogen-air mixtures in obstacle-filled tubes. These regimes include

1. a quenching regime where the flame fails to propagate,

2. a subsonic regime where the flame is travelling at a speed that is slower than the sound speed of the combustion products,

3. a choked regime where the flame speed is comparable with the sound speed of the combustion products,

4. a quasi-detonation regime with a velocity between the sonic and Chapman-Jouguet (CJ) velocity,

5. a CJ detonation regime where the propagation velocity is equal to the CJ detonation velocity.

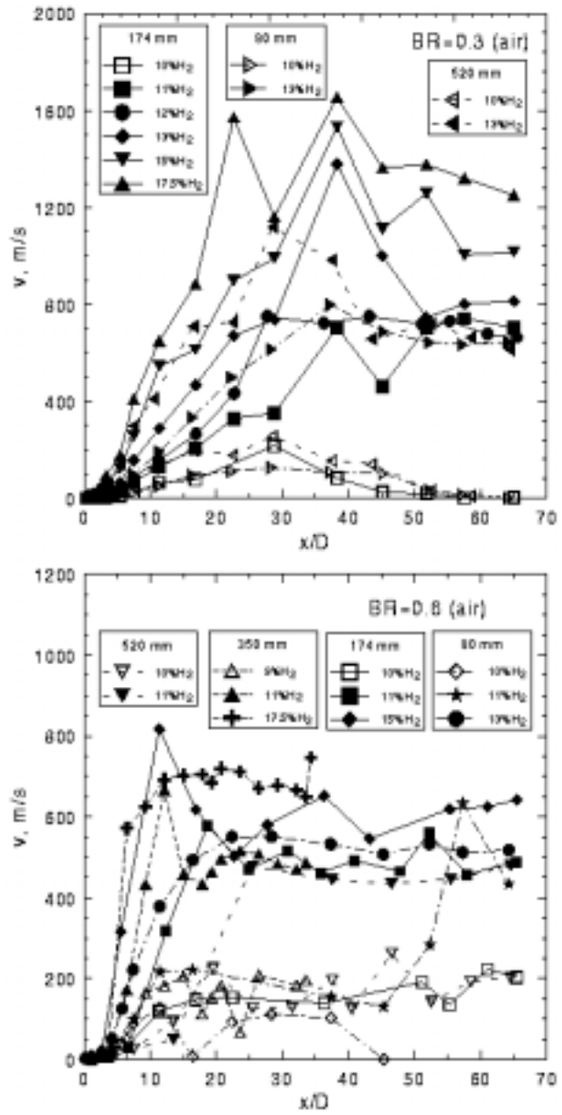

Figure 2.2-2. Visible speeds of turbulent flame propagation versus reduced distance along tubes (D - tube diameter) for lean hydrogen-air mixtures. Blockage Ratio (BR) = 0.3 (upper) and 0.6 (lower). Obstacle spacing is equal to D. Solid points - fast combustion regimes (choked flames and quasi-detonations), empty points - slow combustion regimes [2.9].

It should be noted that the above regimes are geometry-dependent for a given mixture. Consequently, the concentration range for each regime in Figure 2.2-3 may differ for circular tubes and rectangular channels.

2.2.1 Quenching Regime

For sufficiently large BRs (blocked area and total cross-sectional area) in which the pressure difference across the orifice plate can build up rapidly, the flame is observed first to accelerate and then to quench itself after propagating past a certain number of orifice plates. This regime is referred to as the "quenching regime". (Quenching means that the flame ultimately ceases to propagate.) In this regime, flame propagation can be considered as the successive explosion of a continuous sequence of combustion chambers interconnected by orifice plates. Ignition of the mixture in one chamber is achieved by the venting of the hot combustion products from the upstream chamber through the orifice. Quenching occurs when the hot turbulent jet of product gases fails to cause ignition in the downstream chamber because of the rapid entrainment and turbulent mixing of the cold unburned mixture with the hot product of the jet. As shown in Figure 2.2-3, for most hydrogen-air mixtures, the boundaries between the quenching regime and the other flame propagation regimes are very distinct.

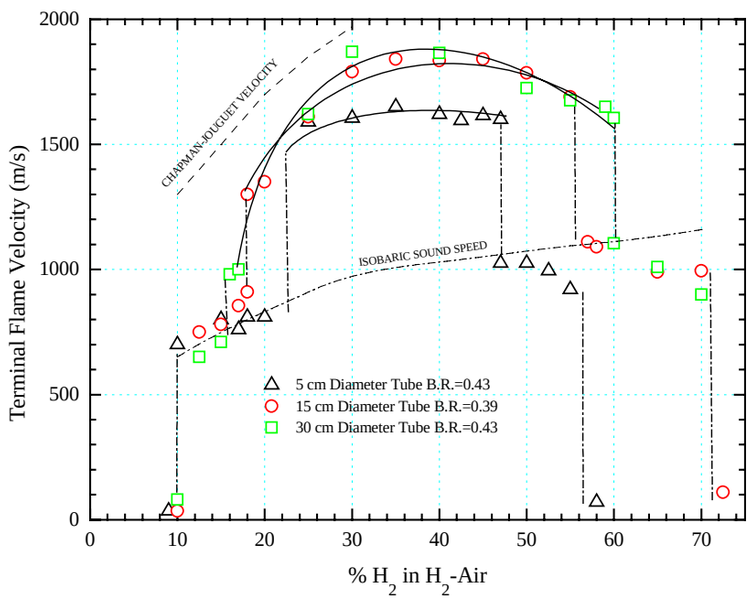

Figure 2.2-3. Maximum flame speeds for H_2-air mixtures in tubes of different sizes

2.2.2 Subsonic Flame Regime

Total quenching of hydrogen-air flames is not always possible. In this case, a quasi-steady flame with an average velocity range from a few tens of metres per second to a couple hundreds of metres per second is possible. This subsonic velocity is a result of a competition of the positive (enhancement)

and the negative (quenching) aspects of turbulence on combustion. Such a flame is highly unstable. A slight change in the boundary condition can cause the flame to quench totally or suddenly jump to another flame propagation regime. This instability is clearly shown in Figure 2.2-3.

2.2.3 Choking Regime

When the conditions for quenching are not met, the flame continuously accelerates to reach a final steady-state value. When this happens, flame propagation can be considered as a quasi-steady one-dimensional compressible flow in a pipe with friction and heat addition. This regime is referred to as the choking regime, where the combined effects of wall friction and heat addition control the final steady-state flame speed.

2.2.4 Quasi-detonation Regime

Since the flame speeds typically attained in the choking regime are of the order of 1000 m/s, a local explosion leading to an onset of detonation may occur. If the orifice diameter, d, is sufficiently large, a stable detonation wave can be formed. For detonation combustion, it is found that the detonation cell size, λ, provides an important characteristic length that can be used to determine the limit of detonation propagation. When d/λ exceeds a certain critical value, a successful transition from deflagration to detonation can occur. In the detonation regime, the propagation mechanism will be one of shock ignition and transverse wave motion corresponding to a normal detonation. The detonation velocity, however, can be significantly below that of the normal CJ value because of the severe momentum losses in the obstacle-filled tube. In previous studies of detonation propagation in very rough tubes by Shchelkin [2.10] and Guenoche and Manson [2.11], detonation velocities of less than 50% of the CJ value have been observed. Such sub-CJ steady-state detonation waves have been called quasi-detonation waves. As a result, this regime is referred to as the "quasi-detonation regime".

2.2.5 CJ Detonation Regime

To examine flame propagation in tubes of different sizes, similar experiments were performed with various hydrogen-air mixture in three different tubes. Results are summarized in Figure 2.2-3. The above propagation regimes are clearly visible. It is of interest to note that in a composition of near 24% H_2-air there occurs another transition within the detonation regime itself. In this case the transition is from the sub-CJ quasi-detonation regime discussed above to the CJ detonation regime. The cell size for the 24% H_2-air composition is about 2 cm. This gives a value of $d/\lambda = 13$, which is the condition at which the detonation propagation would be insensitive to the wall effects. That is to say, if the unobstructed area in a tube is sufficiently large, the propagation of a detonation wave is unaffected by the obstruction.

2.2.6 Criteria for the Various Propagation Regimes

As seen from Figure 2.2-3, an increase in the tube diameter results in an increase in the threshold concentrations for the transition between the various regimes. Various criteria have been proposed for these transitions. Requirements for fast and unstable flames may be expressed in terms of a criteria, described in Section 3.2.2, which is expressed in terms of the combustion expansion ratio, the flame thickness, and a geometric scale. For the quenching regime, the minimum blockage diameter depends on the sensitivity of the mixture and the pressure gradient across the blockage during the passage of the flame front [2.12, 2.13]. For the quasi-detonation and CJ regimes, the criteria are usually

expressed in terms of a characteristic dimension such as the blockage or tube diameter, and the detonation cell size. A general guideline is that quasi-detonations become possible when the blockage diameter is larger than the detonation cell size, λ, for the mixture. A CJ detonation, on the other hand, is possible when the unobstructed tube diameter is larger than approximately 13λ, which corresponds to the critical tube diameter discussed in Section 2.3.2. For a particular obstacle geometry, the limiting conditions for DDT may also be described in terms of a 7λ criteria, which is described in Section 3.2 of this report.

2.3 The Effect of Confinement on Flame and Detonation Propagation

The limiting conditions for DDT discussed in the previous section represent the best currently available estimates of the necessary conditions. For DDT to occur, a flame needs to accelerate to beyond a certain critical flame speed. This speed is usually close to the choking flame speed (i.e., approximately 600 m/s). As a result, to assess the likelihood of DDT, it is necessary to examine the conditions that can affect the FA process. Examples of such conditions are the obstacle configuration (spacing and blockage) and the level of confinement of the surrounding walls.

2.3.1 Effect of Confinement on Flame Propagation

The positive feedback between the flame propagation and turbulence generation in a channel is very sensitive to the level of confinement in the channel [2.14-2.17]. A decrease in confinement, using top-venting, for example, reduces the flow velocity ahead of the flame, thereby reducing the obstacle-induced turbulence.

Large-scale experiments, with H_2-air mixtures relevant for reactor safety were performed in the FLAME facility [2.17]. FLAME is a large rectangular channel 30.5 m long, 2.44 m high, and 1.83 m wide. It is closed on the ignition end and open on the far end. The presence of the obstacles tested greatly increased the flame speeds, overpressures, and tendency for DDT compared with similar tests without obstacles. Similarly, transverse venting reduced the flame speeds, overpressures, and the possibility of DDT.

Figure 2.3.1-1 shows the maximum equivalent planar flame speed as a function of hydrogen mole fraction for five series of tests, no top venting and no obstacles, 50% top venting and obstacles, and 13% top venting with no obstacles. Tests with no top venting are indicated with shaded squares; tests with 13% top venting are indicated with open triangles, and tests with 50% top venting are indicated with shaded circles. The tests with obstacles are distinguished from those without obstacles (dashed line instead of a solid line). For those tests in which DDT did occur, an upward pointing arrow from the maximum equivalent planar flame speed point indicates that the combustion accelerates and approaches detonation speeds.

The effect of the presence of obstacles is shown by the lower hydrogen concentration required to attain the same maximum equivalent flame speed or overpressure compared with a similar test without obstacles. With 50% top venting and no obstacles present, this speed would not have been attained even for a stoichiometric mixture. The inhibiting effect of large degrees of transverse venting on the flame speed and overpressures is evident. The complex behaviour of small degrees of transverse venting is observed in the 13% top venting test series. For lean mixtures below approximately 18% hydrogen mole fraction, the flame speeds are lower and overpressures comparable to those obtained in similar

tests without transverse venting. Above this hydrogen concentration, the flame speeds and overpressures are higher than in tests without transverse venting.

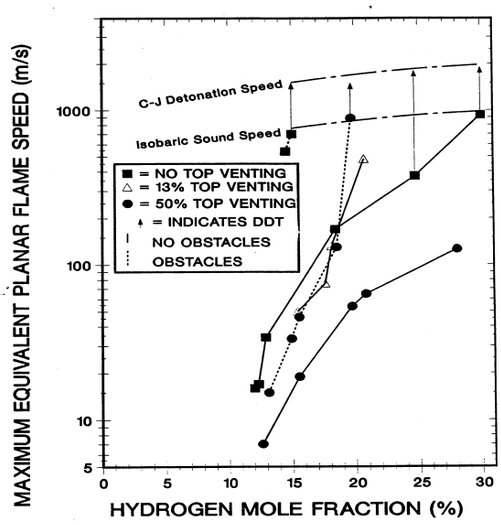

Figure 2.3.1-1 Combustion front velocity versus hydrogen mole fraction for hydrogen-air mixtures at 500 K and 0.1 MPa at the High-Temperature Combustion Facility at BNL. Open circles denote the average velocity over roughly the second half of the vessel and error bars represent the standard deviation in the measured velocity. Open squares denote the maximum flame velocity for slow deflagration.

2.3.2 Effect of Confinement on Detonation Propagation

As in the case of flames, detonations are also very sensitive to the level of confinement. A sudden removal of confinement at the end of a tube, for example, can result in detonation failure. The 'critical tube' diameter for which detonation failure occurs is determined by the sensitivity of the mixture, which is expressed in terms of the detonation cell size λ. For fuel-air mixtures with an irregular cellular structure, the critical diameter $D_c \cong 13\lambda$.

Figure 2.3.2-1 displays the detonation cell size data for a hydrogen-air mixture as a function of initial temperature [2.18, 2.19]. As seen from this figure for an initial temperature of 300 K, cell size measurements can vary by a factor of 2. This is due to differences in the interpretation and preparation of the smoke foils used to record the cellular structure.

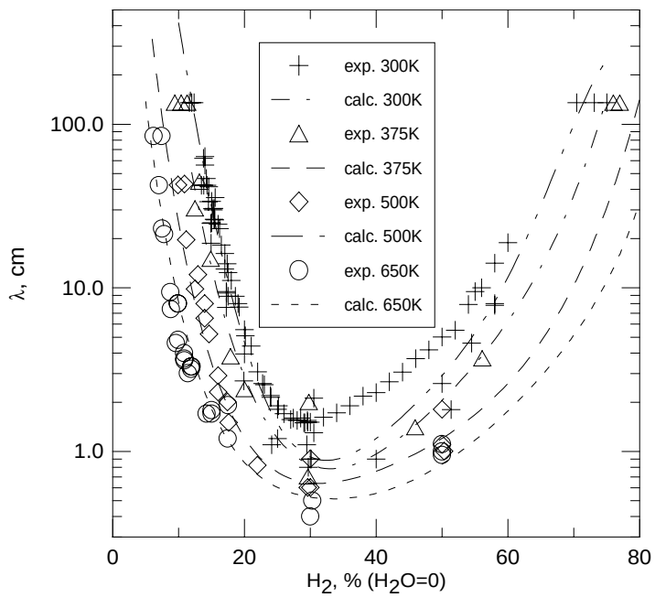

Figure 2.3.2-1 Detonation cell size for hydrogen-air mixture at different initial temperatures [2.18, 2.19]

2.4 Mechanisms Involved in FA

Although the various flame and detonation propagation regimes are relatively well established, the underlying mechanisms can be complex and, in some cases, poorly understood.

2.4.1 Laminar Flame and Flame-folding Regimes

The early stage of flame propagation involves a laminar flame regime followed by a wrinkled or cellular flame. The laminar flame velocity is determined by thermal and mass transport across the flame front and the heat released because of combustion. It can be predicted using readily available chemical kinetics codes. The more important wrinkled flame regime is controlled by a variety of diffusion and hydrodynamic instabilities that are much more difficult to model. The cellular flame propagation has been described by Markstein and Somers [2.20] and by Markstein [2.21] and theoretically analyzed by numerous authors, including Clavin and Williams [2.22], Joulin and Clavin [2.23], Pecle and Clavens [2.24]. The flame cell size typically varies between 0.5 cm and 3.5 cm and increases with the square of the burning velocity. Figure 2.4.1-1 displays typical flame structures as a function of the Lewis and Zel'dovich numbers [2.25]. A detailed view of the flame structure is also provided in Figure 2.4.1-2, which displays a laser-induced predissociation fluorescence (LIPF) image of a cellular flame front [2.26, 2.27]. From a modelling point of view, the flame-folding regime is usually addressed by adopting a flame surface enhancement factor that is derived from flame propagation experiments for a particular mixture composition.

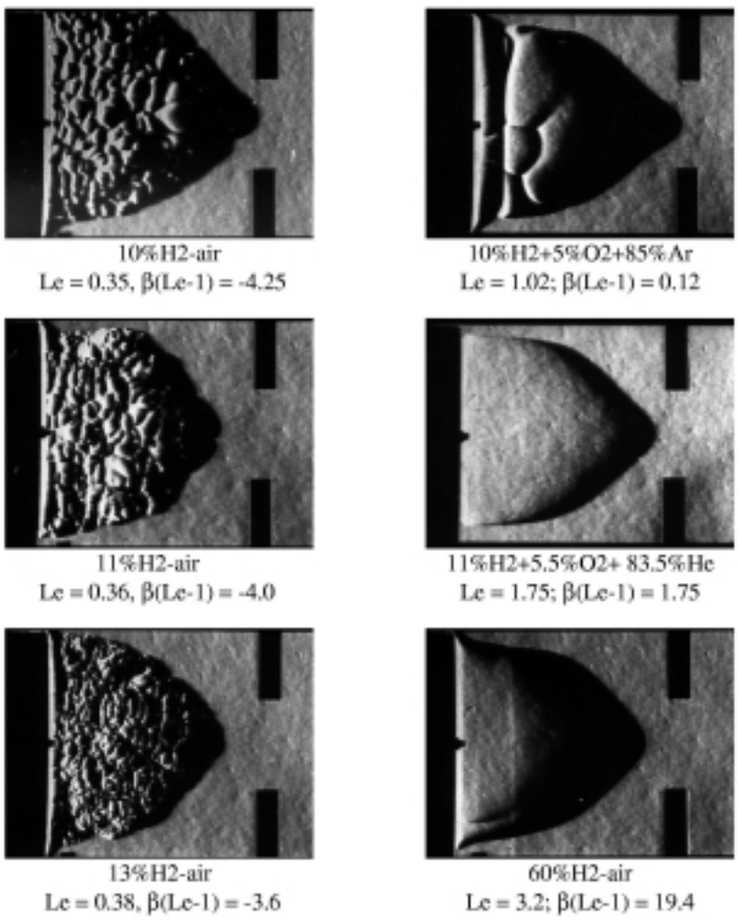

Figure 2.4.1-1 Effect of Lewis number on flame structure. Threshold for thermal-diffusion instability corresponds to $\beta(Le - 1) < -2$. $\beta = E_a(T_b-T_u)/T_b^2$ is Zel'dovich number, where E_a effective activation energy, T_u and T_b – unburned and burned gas temperatures [2.25].

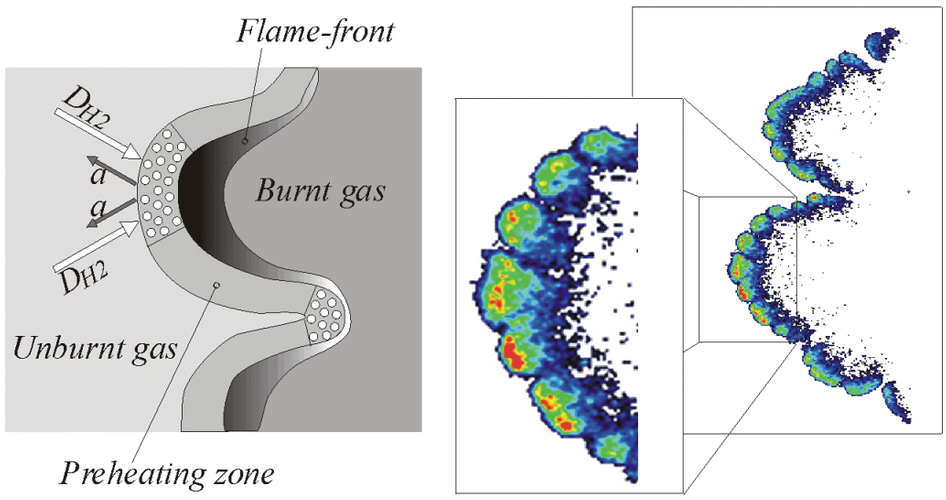

Figure 2.4.1-2 Schematic (left) illustrating competition between thermal diffusion, a, and hydrogen diffusion, $D_{H2,}$ in a lean hydrogen-air flame laser-induced predissociation fluorescence (LIPF) image (right) displaying reaction zone in cellular flame front [2.26, 2.27].

2.4.2 Turbulent Combustion and Acceleration

The wrinkled flame regime is soon followed by a turbulent flame regime when the flame encounters a wall or an obstacle. The mechanisms responsible for the turbulence include Kelvin-Helmholtz, or Rayleigh-Taylor instabilities, which are triggered when the flame is suddenly accelerated over an obstacle or through a vent [2.28]. In the case of a flame propagating over repeated obstacles, this is a self-accelerating process that is due to the feedback mechanism between the flame propagation and the flow velocity and turbulence generated ahead of the flame.

The structure of the turbulent flame brush depends greatly on the turbulence intensity and the characteristic time scales for combustion and turbulence. If the combustion time scale is smaller than the turbulent eddy turnover time, the flame brush may be modelled as consisting of a large number of distinct laminar "flamelets". On the other hand, if the combustion is slow compared with the eddy turnover time, the reaction zones inside the flame brush become distributed and require a different modelling approach. The Borghi diagram [2.29] provides a useful classification of turbulent combustion regimes based on non-dimensional numbers such as the Karlovitz and Damköhler numbers. Figure 2.4.2-1 displays a Borghi diagram with LIPF images of the flame structure for the various regimes [2.26]. As discussed in Chapter 4, the validity of theoretical models depends greatly on the Borghi diagram regime and the corresponding flame front structure.

2.4.3 Acoustic-flame and Shock-flame Interactions

Flame propagation in an enclosure generates acoustic waves that can interact with the flame front and promote flame acceleration though a variety of instability mechanisms. Such instabilities have been observed by Guenoche [2.30] and Leyer and Manson [2.31] for open-ended and closed tubes, by Kogarko and Ryzkor [2.31] for closed spherical chambers and by van Wingerden and Zeeuwen.

[2.33] and Tamanini and Chaffee. [2.34] for vented enclosures. For rich propane-air mixtures, van Wingerden and Zeeuwen observed that these instabilities can result in a peak pressure enhancement factor of 8, whereas Tamanini and Chaffee observed enhancement factors of 2 to 9 for stoichiometric methane-air and propane-air mixtures.

Flame acoustic instabilities have usually been associated with relatively slow flames in enclosures that are relatively free of obstacles. Such instabilities have been successfully eliminated by lining the enclosure walls with materials that can absorb acoustic waves. More recently, however, Shepherd and Lee [2.12] reported flame acceleration experiments in tubes with repeated obstacles, with and without an absorbing material on the tube wall. These experiments, performed with a hydrogen-oxygen mixture, indicate that the presence of an absorbing material reduces the final flame velocity from 1000 m/s to 100 m/s. These results would suggest that acoustic flame instabilities may in fact not be limited to slow flames in obstacle-free environments.

The exact nature of the acoustic-flame instabilities have been reviewed by Oran and Gardner [2.35] and have been modelled by Searby and Rochwerger [2.36], Joulin [2.37], Jackson et al. [2.38], and Kansa and Perlee [2.39]. These mechanisms include flame distortion caused by the flame-acoustic wave interaction, and wave amplification caused by the coherence between the acoustic wave and the exothermic energy release (Rayleigh criterion).

Finally, sufficient fast flames can produce a shock wave that can reflect off a wall and interact with the flame. As shown by Markstein and Somers [2.20], this can result in severe flame distortion which can induce flame acceleration and, in extreme cases, cause transition to detonation [2.40, 2.41].

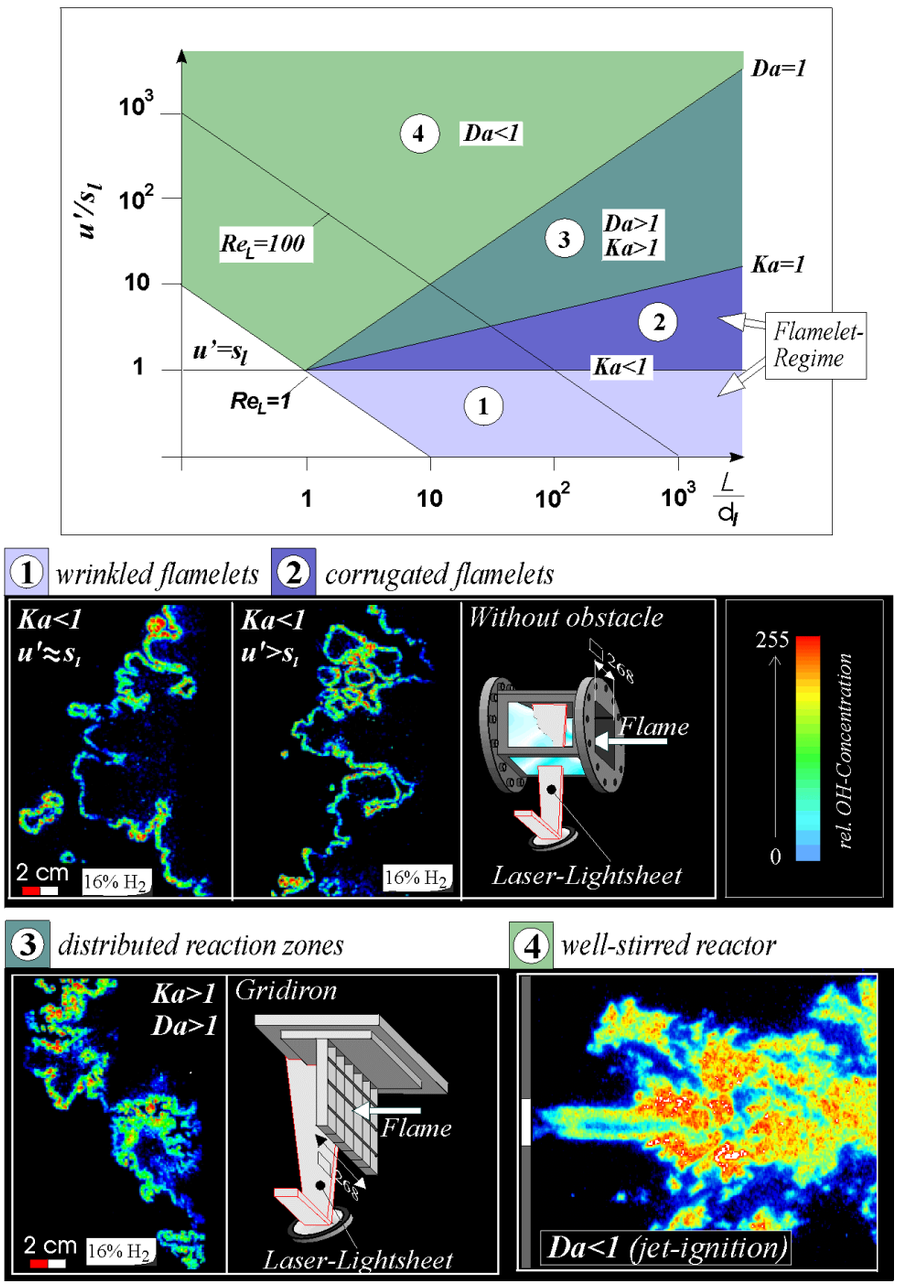

Figure 2.4.2-1 Borghi Diagram (top) categorizing the flame propagation regime in terms of the turbulence intensity, u', the laminar burning velocity, s_l, the integral length scale, L, the laminar flame thickness, d_l, the Damköhler number, Da , the Karlowitz number, Ka, and the turbulent Reynolds number, Re_L. LIPF images (bottom) of flame structure for the various regimes [2.29].

2.4.4 Global and Local Quenching

Flame quenching can occur for a wide spectrum of flame propagation regimes including laminar, wrinkled, and turbulent flames.

2.4.4.1 Quenching of laminar flames and flammability limits

Theoretically, a mixture is flammable, if a flame, regardless of how it was produced, continues propagating within the mixture. However, beyond a certain range of mixture composition, continued propagation of a reaction front is no longer possible because of heat losses to walls and low burned gas temperature. This composition limit is commonly known as the flammability limit. The measured limit can be affected by the size of the apparatus as well as the strength of the ignition source. Coward and Jones [2.42] suggested that tube diameters larger than 5 cm are needed to produce limits that are free of wall effects. They also found that a minimum tube length of 1.2 m is required to avoid the igniter effects. Using a 5-cm-diameter, 1.8-m-long tube, Kumar [2.43] measured the flammability limits for various hydrogen-air-steam mixtures at 100°C and 200°C. These results, summarized in Figure 2.4.4.1-1, show that steam can significantly reduce the range of the flammability. At an initial temperature of 100°C, a mixture is not flammable if it contains more than 63% of steam by volume. Results also show that increasing the gas temperature widens the flammability limits. It was observed that the flammability limits are greatly influenced by the buoyancy effects. The upward propagation limits (assisted by the buoyancy) are different from the downward propagation limits for hydrogen-lean mixtures. Results also show that there is a difference (~5 H_2 vol %) between the upward and the downward flammability limits. However, the difference for the upward and the downward limits is relatively small for hydrogen-rich mixtures. It was also observed that the lean flammability limits are not sensitive to the steam content, whereas the rich flammability limits are greatly affected by the steam content in the mixture. It should be noted that near-flammability-limit mixtures are not very reactive. These mixtures usually cannot support flame acceleration to supersonic velocities and DDT.

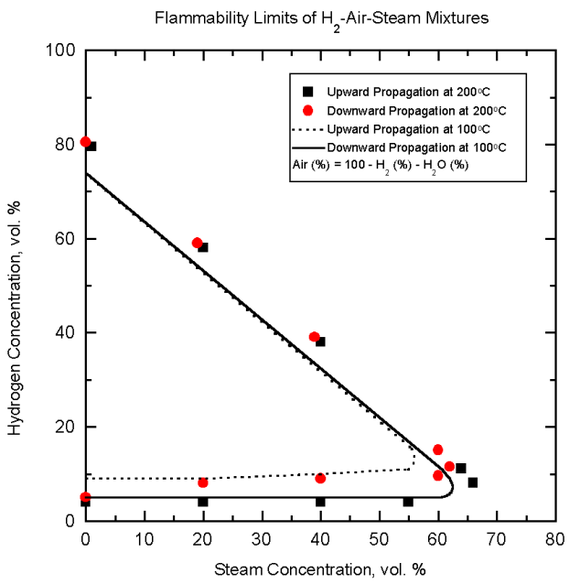

Figure 2.4.4.1-1 Flammability limits for hydrogen-air-steam mixtures [2.43]

2.4.4.2 Quenching of turbulent flames

The same turbulent mixing processes that produce flame acceleration can also result in local or global quenching. For turbulent flames that are in the flamelet regime, this quenching is due to excessive stretching of the laminar flamelets. For more turbulent flames, quenching can occur because of the mixing of cold unburned gas into the distributed reaction zones. The flame-quenching process has been investigated by various authors including Abdel-Gayed and Bradley [2.44], Ballal and Lefebvre [2.45], Checkel and Thomas [2.46], Chomiac [2.47], Phillips [2.48] and Larsen [2.49].

Local quenching is important to the flame acceleration process because it can lead to violent secondary explosions and DDT. Global quenching has been observed for lean flames propagating in tubes filled with obstacles [2.50, 2.51]. It has also been observed when a flame propagates through an orifice into an unconfined area [2.13]. In this case, the minimum quenching diameter increases with the magnitude of the pressure differential generated across the orifice before the arrival of the flame front.

2.4.5 Effects of Buoyancy

Buoyancy affects the early stages of flame propagation and is particularly important for large-scale explosions. These effects are considered to become significant when the Froude number, $Fr = \frac{u^2}{gL}$, is small. There are three potentially important effects of buoyancy. First, the gravitational effect lifts the flame, thereby modifying its path and often bringing it in contact with the top boundary, which can result in local cooling and quenching. Second, for mixtures between the flammability limits for upward and downward propagation, flame propagation may be limited to the top of a channel resulting in incomplete combustion in the bottom section. As can be seen from Figure 2.4.4.1-1, this is more likely to occur for lean hydrogen-air flames where the limits differ significantly for upward and downward propagation. Finally, upward acceleration can result in Rayleigh-Taylor instabilities that can promote acceleration.

2.5 Mechanisms Involved in DDT

2.5.1 Types of DDT Phenomena

Transition from deflagration to detonation can be observed in a wide variety of situations, including flame propagation in smooth tubes or channels [2.52, 2.53], flame acceleration caused by repeated obstacles [2.54-2.56], and jet ignition [2.57-2.60]. The processes leading to detonation can be classified into 2 categories:

1. detonation initiation resulting from shock reflection or shock focusing, and

2. transition to detonation caused by instabilities near the flame front or caused by flame interactions with a shock wave, another flame or a wall, or caused by the explosion of a previously quenched pocket of combustible gas.

The first category essentially involves a direct initiation process where the shock strength is sufficient to auto-ignite the gas and promote detonation. For accidental explosions where the shock is produced by an accelerating flame, this process becomes much more probable when the shock interacts with a

corner or a concave wall that can produce shock focusing. Shock initiation is an important mechanism in maintaining the propagation of quasi-detonations in a channel or a tube filled with obstacles [2.54-2.56]. It has also been found to be very efficient in promoting detonation for relatively slow flames propagating towards an orifice, a corner, or a concave wall [2.61-2.71].

The second category of DDT processes is considerably more complex because it involves a variety of instabilities and mixing processes. Detonation in smooth tubes can occur because of a variety of reasons including (a) DDT ahead of the turbulent flame brush, (b) DDT inside the flame brush, or (c) DDT resulting from the interaction between the flame front with a reflected shock wave. DDT can also occur in a flame jet because of a flame-vortex interaction that promotes a suitable temperature and concentration gradient for inducing DDT by means of the SWACER mechanism discussed in Section 2.5.2.

2.5.2 Underlying Mechanisms

Although DDT appears though a variety of seemingly unrelated phenomena, there is increasing evidence that these phenomena may be controlled by a single underlying mechanism. It has been suggested by Zel'dovich et al. [2.72-2.74] and Lee et al. [2.75] that induction time gradients associated with temperature and concentration gradients may be ultimately responsible for a wide range of detonation initiation observations. The mechanism proposed by these authors rests on the formation of an induction time gradient that can produce a spatial time sequence of energy release. This sequence can then produce a compression wave that is gradually amplified into a strong shock wave that can auto-ignite the mixture and produce DDT. This process of shock wave amplification by coherent energy release (SWACER) was used by Lee et al. [2.75] and Yoshikawa [2.76] to explain the shockless photo-initiation of gaseous detonations.

Numerous calculations have been presented in the literature to demonstrate the SWACER or Zel'dovich gradient process. These include the early studies by Zel'dovich et al. [2.72-2.74], Lee et al. [2.75], Yoshikawa [2.76] and those by Yoshikawa, Thibault and Hassam that were discussed in the review papers by Lee and Moen [2.77] and Shepherd and Lee [2.12]. More recent calculations have been performed by Clark [2.78], Frolov et al. [2.79], Dorofeev et al. [2.80-2.82], Gelfand et al. [2.83], Smijanovski and Klein [2.84], Khokhlov et al. [2.85, 2.86], and others [2.87-2.97]. These authors have established a strong theoretical foundation for the amplification process, and have demonstrated the role of the SWACER or Zel'dovich gradient mechanism for various DDT and direct initiation problems. One observation from these studies is that the minimum size of the pre-established gradient required for DDT is approximately 10 times the detonation cell size (see Section 3.2.3). There is also an optimal range of induction time gradients that can promote a shock amplification process that can lead to DDT [2.85, 2.96].

Because temperature and concentration gradients are formed by a wide variety of processes, the SWACER mechanism is believed to be an underlying mechanism for a wide variety of detonation phenomena including

1. direct detonation initiation that is due to the temperature gradient behind the leading shock,

2. detonation initiation that is due to shock focusing,

3. DDT in tubes that is caused by the temperature gradient in the boundary layer or between a fast flame and the leading shock,

4. DDT that is due to pre-compression at the end of a channel by a slow flame,

5. DDT in rough or obstacle-filled tubes,

6. jet initiation caused by temperature and concentration gradients in the flame/vortex structure, and

7. DDT in multi-phase systems resulting from the temperature relaxation caused by the particles.

In spite of the number of SWACER calculations that can be found in the literature, few of these can be directly and convincingly linked to a particular experimental result. This is particularly true for problems involving turbulent mixing for which calculations usually assume a spontaneous formation of a temperature or concentration gradient or both. The actual formation of such gradients involves a variety of turbulent mixing and combustion mechanisms. These mechanisms introduce additional instabilities that must be addressed by the calculations in order to be truly predictive. Such difficulties have recently been addressed by Khokhlov et al. [2.85, 2.86], who investigated the very difficult problem of DDT caused by shock-flame interaction. This type of DDT, which has been observed by Thomas et al. [2.41], involves a Meshov-Richmeyer instability, where the reflected shock interacts with the flame front. The severe flame distortion produced by this instability then produces Kelvin-Helmholtz instabilities, which increase the flame area and the rate of combustion. The very high resolution calculations of Khokhlov et al. [2.85, 2.86] have been able to resolve these instabilities and capture the DDT process that occurs inside a temperature gradient. These Navier-Stokes calculations remain limited in that they do not directly account for the fine-scale turbulent mixing. Nevertheless, they represent one of the most successful efforts so far to isolate the SWACER mechanism for a particular experimental DDT observation.

2.6 Recent Experimental Results

The above description of FA and DDT mechanisms has included recent experimental data obtained from various laboratories in Europe and in North America:

1. The large-scale deflagration experiments performed in the RUT facility [2.98]: These experiments, along with previous DDT experiments, contributed to the formulation of the 7λ criterion (Figure 2.6-1).

2. The experiments performed by Thomas et al. [2.41, 2.99] for DDT produced by the interaction of a reflected shock with a flame kernel: These experiments, along with the calculations of Khokhlov et al. [2.85, 2.86] have shed considerable light on the DDT phenomenon and the underlying SWACER mechanism (Figure 2.6-2).

3. The shock focusing experiments performed by Chan et al. [2.100] and Gelfand and Khomik. [2.101]: These experiments have demonstrated that a relatively weak shock can trigger DDT when concave reflecting surfaces are present in the enclosure (Figure 2.6-3),

4. The detailed LIPF experiments performed by the Technical University of Munich on flame propagation and jet ignition [2.103]. (Figure 2.6-4).

5. Experiments on DDT induced by a focused shock wave were performed in FZK for various focusing geometry: Three test series addressing three different DDT modes in a combustion tube (12 m long, 35 cm ID) were performed [2.102]. Detailed results from these experiments are presented in Appendix E.

6. Experiments were performed at BNL [2.110] in the High-Temperature Combustion Facility (HTCF) to study flame acceleration and DDT with and without venting at high initial temperatures (up to 650 K) (Figures 2.6-5 and 2.6-6). In these experiments, orifices with a blockage ratio of 0.43 (spaced 1 tube diameter apart) were used to induce and to promote flame acceleration. The central element of the HTCF is a 27-cm-inner-diameter and 21.3-m-long cylindrical test vessel designed for a maximum allowable working pressure of 10.0 MPa at 700 K.

2.7 Pressure Development and Structural Response

2.7.1 Pressures Associated with Flames, Detonations, and DDT

Flame acceleration in an enclosure produces pressures that, in some cases, may be high enough to threaten the survival of the enclosure or its substructures. The pressure developed inside the enclosure depends on

1. the size of the combustible gas region,

2. the concentration of the combustible gas, and

3. the size of the enclosure and the arrangement of the obstacles.

In the case of a uniform mixture inside the enclosure, and no heat losses, the peak pressure achieved in the enclosure can vary between the constant volume combustion pressure to the very high pressures associated with DDT. As indicated by Craven and Greig [2.104], the pressure produced by DDT depends on the flame propagation process prior to DDT. The worst-case scenario proposed by Craven and Greig involves the transition to detonation on a reflected shock produced by a fast flame. Calculations indicate that the peak pressure produced on the wall of an enclosure by such an event can be an order of magnitude higher than the detonation pressure for the mixture. The Craven and Greig scenario has been observed in the laboratory by Kogarko [2.105], Chan et al. [2.100] and Zhang et al. [2.106]. In the latter study, a peak reflected pressure of 250 atm was observed for a hydrocarbon-air mixture at an initial pressure of 1 atm.

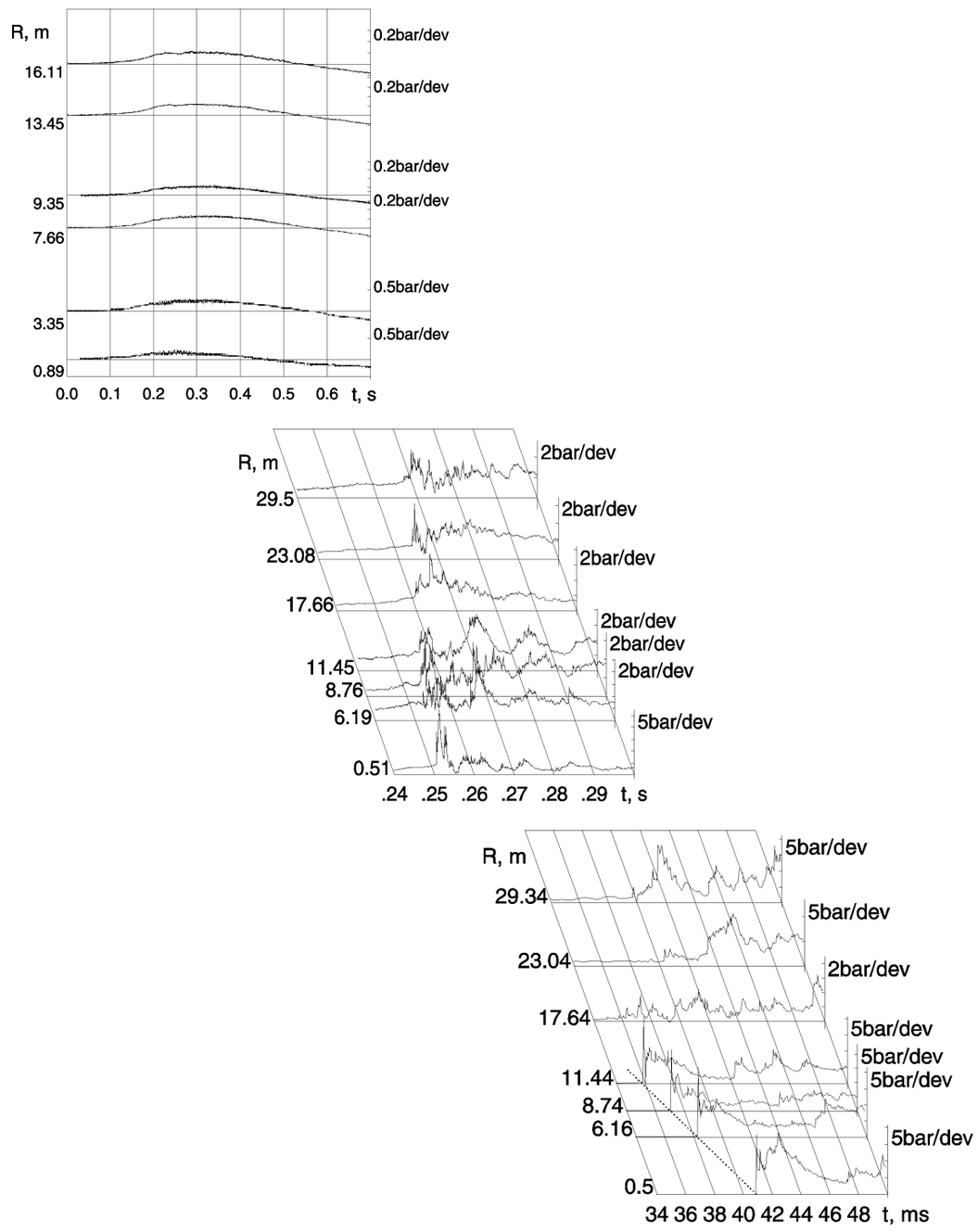

Figure 2.6-1 Pressure histories obtained in RUT Facility. Top: Slow deflagration, 8% H_2 in air. Middle: Fast turbulent deflagration, 19% H_2 in air. Bottom: DDT, 42% H_2 in air. Concentrations correspond to average values within the 310 m^3 vented enclosure.

It should be noted that the peak pressure alone is insufficient to determine the vulnerability of a structure. Pressure records associated with DDT or a stable detonation display a sharp pressure rise followed by a decay, which is relatively rapid for DDT. Slow and fast deflagrations, on the other hand, display a more gradual pressure rise and decay. The details of the pressure histories can be very important in assessing the response of a particular structure.

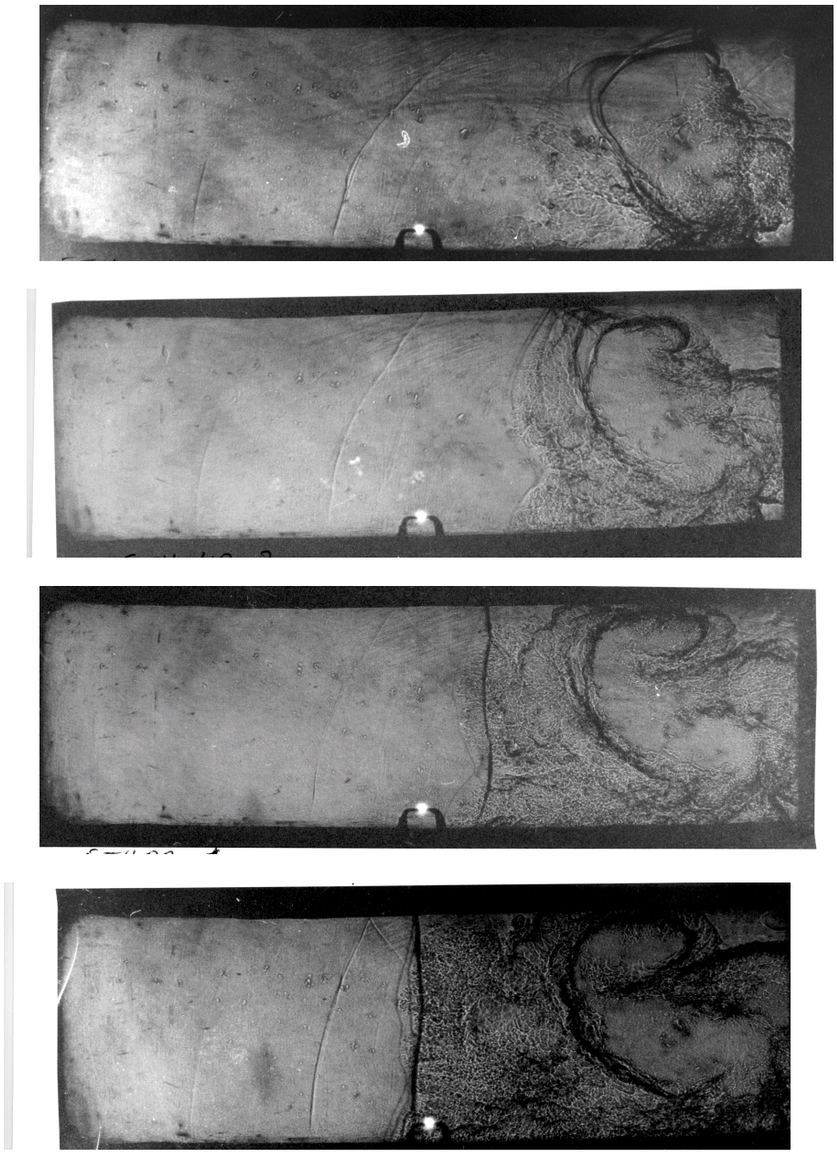

Figure 2.6-2 Schlieren images of DDT resulting from flame-shock interaction [2.99]

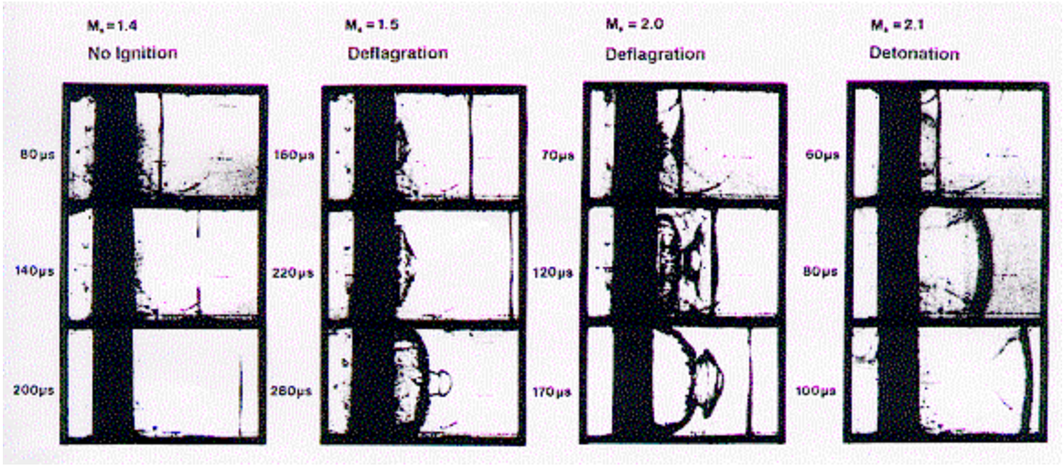

Figure 2.6-3 Schlieren photographs showing the outcomes resulting from a collision of a shock wave with a hemispherical cup (dia.= 3 cm) . (Chan et al. [2.100])

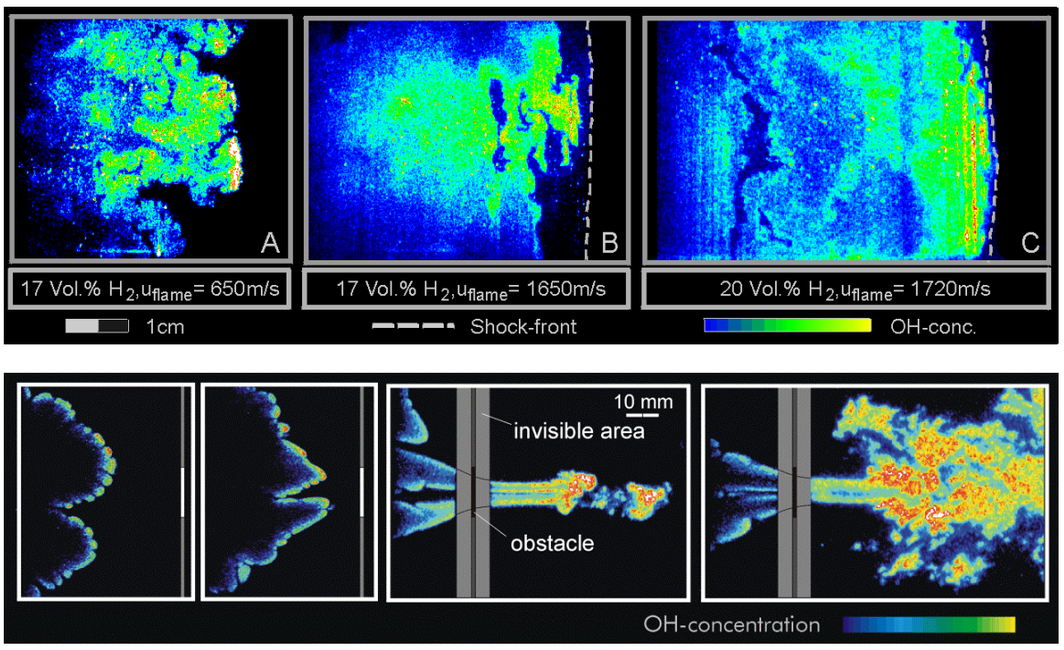

Figure 2.6-4 LIPF images from the Technical University of Munich. Top images of a fast propagating flame, a detonation for a mixture close to the detonation limit for the facility, and a fully developed detonation [2.26]. Bottom: Flame-jet ignition for a 12% hydrogen-air flame [2.27]. The combustion-regime behind the free jet of a direct ignition can be assigned to the well-stirred reactor regime in the Borghi diagram.

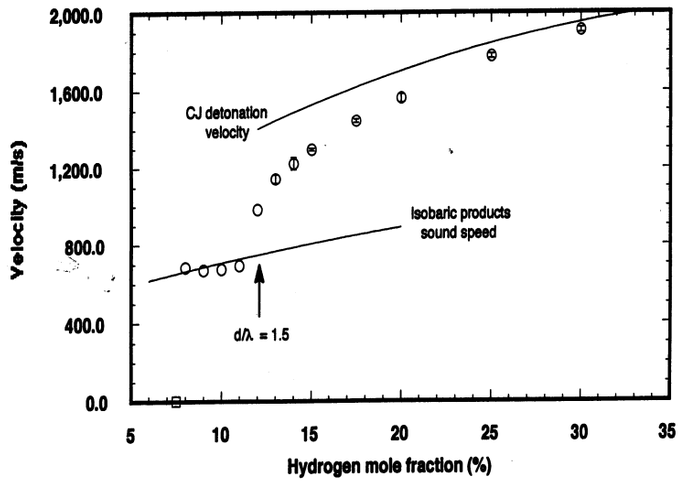

Figure 2.6-5 Combustion front velocity versus hydrogen mole fraction for hydrogen-air mixtures at 500 K and 0.1 MPa at the HTCF at BNL. Open circles denote the average velocity over roughly the second half of the vessel, and error bars represent the standard deviation in the measured velocity. Open squares denote the maximum flame velocity for slow deflagration.

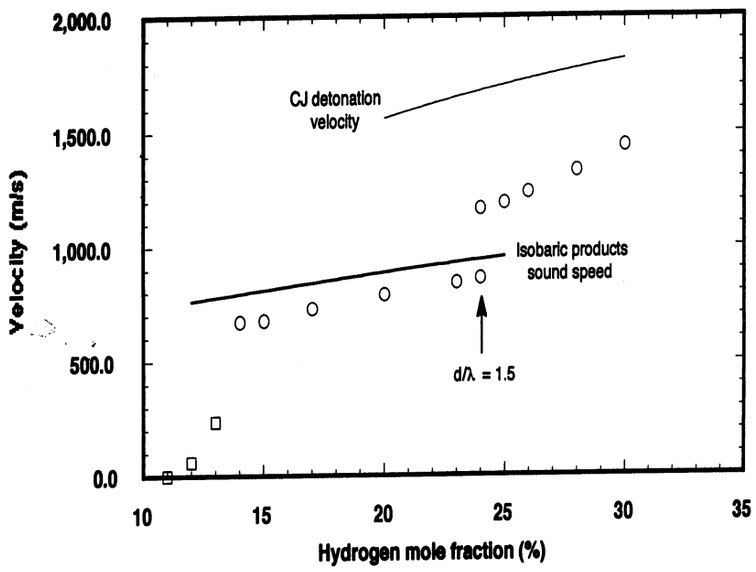

Figure 2.6-6 Combustion front velocity versus hydrogen mole fraction for hydrogen-air mixtures with 25% steam at 500 K and 0.1 MPa at the HTCF at BNL. Open circles denote the average velocity over roughly the second half of the vessel, and error bars represent the standard deviation in the measured velocity. Open squares denote the maximum flame velocity for slow deflagration.

2.7.2 Structural Response

Important factors affecting the response of a structure to a transient pressure loading include the peak pressure and the length of the rise and decay times compared to the characteristic response time of the structure.

Table 2.7.2-1 lists typical natural frequencies for various nuclear reactor components based on the work of Breitung et al. [2.107], and Breitung and Redlinger [2.108] and Studer and Petit [2.109]. Concrete containment building frequencies were obtained by Studer and Petit based on an eigen-frequency analysis for a typical PWR reactor. It can be seen that the frequency range that is of interest for nuclear reactors is approximately 5 to 500 Hz.

Breitung and Redlinger [2.108] performed a detailed 1-degree-of-freedom analysis for a set of representative time histories for scenarios involving slow flames, fast flames, stable detonations, and DDT. Figure 2.7.2-1 displays the frequency dependence of the effective static pressure ratio, P_{eff}, that would produce the same deflection as the transient loading. The frequency range in this figure corresponds to the range of natural frequencies for nuclear reactor components shown in Table 2.7.2-1. It can be seen from this figure that the stable detonation is the most severe combustion mode throughout this frequency range. In the range of 5 to 25 Hz, which is characteristic of the frequency response of concrete nuclear reactor containment buildings, the stable detonation and fast deflagrations display a similar response, whereas DDT and slow deflagrations exhibit a weaker response. This finding differs from that reported by Studer and Petit (Table 2.7.2-2), who observe significantly larger displacements for fast deflagrations with progressively lower responses for DDT and a stable detonation. These authors concluded that the fast deflagration is the most severe scenario for a concrete containment building. The different conclusions emerging from these 2 studies could be attributed to the different structural response models or to the different pressure histories used to characterize the various flame and detonation regimes. Assessment of the vulnerability of nuclear containment buildings and substructures will require more work in the analysis of experimental results and in the development of detailed models.

Table 2.7.2-1 Typical natural frequencies for various nuclear reactor components

Structure Type	Frequency (Hz)
Spherical Steel Containment (Bending Mode) [2.108]	6-12
Spherical Steel Containment (Membrane Mode) [2.108]	50
Concrete Containment [2.108]	5-8
Concrete Containment [2.109]	12-22
Stiff Reinforced Concrete Substructures [2.108]	<500
Technical Installations [2.108]	100-400

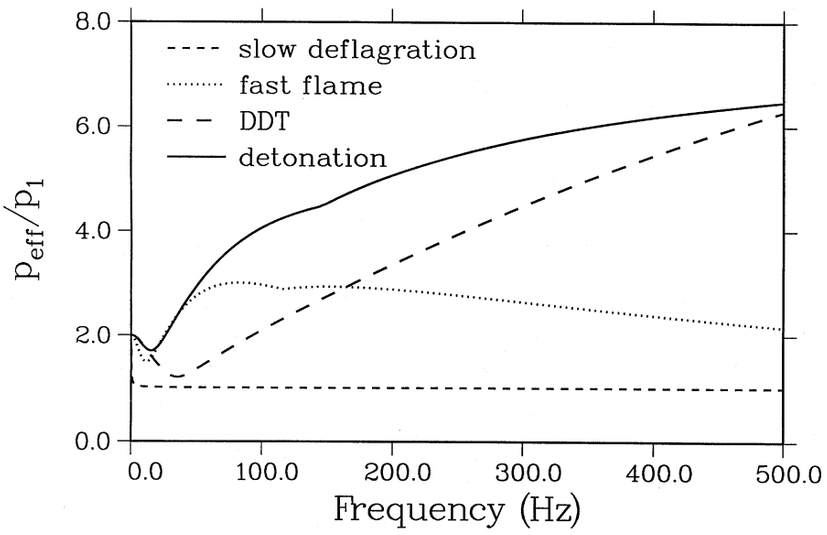

Figure 2.7.2-1 Normalized effective static pressure for a frequency range relevant to nuclear reactor applications [2.108]. Pressures are normalized relative to the long-term combustion pressure

Table 2.7.2-2. Containment wall displacements for the various combustion models and structural eigen frequencies [2.109]

Eigen Frequency (Hz)	Fast Deflagration (mm)	DDT (mm)	Stable Detonation (mm)
12.47	45	10	7.4
14.01	32	9.9	7.3
18.73	22	9.4	7.0
22.01	16	9.0	6.7

2.8 Summary

Flame acceleration and transition to detonation are complex phenomena. Within the scope of this chapter, it is impossible to review and discuss all the studies in the subject area. As a result, only some key studies relevant to the nuclear industry have been included. Nevertheless, the material presented in this chapter represents a snapshot of current understanding of the phenomena.

In Section 2.2, the regimes of various eventual outcomes of flame acceleration are discussed. These possible outcomes are well understood; they depend on the initial gas mixture composition and the boundary conditions such as walls and obstruction configurations. However, the rate at which these outcomes are reached is not well understood. As indicated in Section 2.3, the degree of confinement

of the gas mixture dominates the flame acceleration rate. It is not possible to estimate the flame acceleration rate for a given set of conditions. More work in this area is definitely needed to determine the effects of confinement on flame acceleration.

Sections 2.4 and 2.5 describe the mechanisms responsible for flame acceleration and transition to detonation. Qualitatively, these mechanisms are also well understood. However, the current understanding of the phenomena still cannot enable analysts to develop models that can predict flame acceleration and eventual transition to detonation (to be discussed in Chapter 4). Nevertheless, new findings have helped these analysts to refine their models and provide direction for future works.

Section 2.6 outlines some of the recent works in the area of FA and DDT. This work includes large-scale experiments in the RUT facility and detailed flame structure measurement using LIPF and schlieren photography. Only a brief discussion is given here. Readers should go to the cited references to get the details of these works. Section 2.7 discusses briefly the response of various structures subjected to a pressure load of an accelerated flame or a detonation wave. As mentioned in this section, the knowledge in this area is still at its infant state. More work is definitely needed in this area in order to estimate the structural response in any acceptable certainly.

Although FA and DDT are qualitatively understood, they remain a big challenge to scientists to develop models capable of predicting the dynamic process and the eventual consequence of these phenomena.

2.9 References

2.1 H.Gg Wagner, *Some Experiments about Flame Acceleration, Fuel-Air Explosions*, University of Waterloo Press, 1982, 77-99.

2.2 I.O. Moen, M. Donato, R. Knystautas and J.H.S. Lee, Flame Acceleration Due to Turbulence Produced by Obstacles, Combustion ands Flame, Vol. 39, 1980, 21-32.

2.3 J.H.S. Lee, R. Knystautas and C.K. Chan, Turbulent Flame Propagation in Obstacle-Filled Tubes, In 20th Symposium (International) on Combustion, The Combustion Institute, 1985, 1663-1672.

2.4 C.K. Chan, J.H.S. Lee, I.O. Moen and P. Thibault, Turbulent Flame Acceleration and Pressure Development in Tubes, In Proc. of the First Specialist Meeting (International) of the Combustion Institute, Bordeaux, France, 1981, 479-484.

2.5 B.H. Hjertager, K. Fuhre, S.J. Parker and J.R. Bakke, Flame Acceleration of Propane-Air in Large-Scale Obstacled Tube, Progress in Astronautics and Aeronautics, Vol. 94, AIAA, 1983, 504-522.

2.6 I.O. Moen, J.H.S. Lee, G.H. Hjertager, K. Fuhre and R.K. Eckhoff, Pressure Development due to Turbulent Flame Acceleration in Large-Scale Methane-Air Explosions, Combustion and Flame, Vol. 47, 1982, 31-52.

2.7 C.J.M. Van Wingerden and J.P. Zeeuwen, Investigation of the Explosion-Enhancing Properties of a Pipe-Rack-Like Obstacle Array, Progress in Astronautics and Aeronautics Vol.106, 1986, 53.

2.8 J.C. Cummings, J.R. Torczynski and W.B. Benedick, Flame Acceleration in Mixtures of Hydrogen and Air, Sandia National Laboratory Report, SAND-86-O173, 1987.

2.9 S.B. Dorofeev, private communication, 1999.

2.10 K.I. Shchelkin, Effect of Tube Surface Roughness on Origin and Propagation of Detonation in Gas, Journal of Experimental and Theoretical Physics (USSR), 10, 1940, 823-827.

2.11 H. Guenoche, and N. Manson, Influence des Conditions aux Limites sur la Propagation des Ondes de Choc et de Combustion, Rev. de l'Inst. Francais de Petrole, No. 2, 1949, 53-69.

2.12 J.E. Shepherd and J.H.S. Lee, On the Transition from Deflagration to Detonation, *Major Research Topics in Combustion*, Editors: M.Y. Hussaini, A. Kumar, R.G. Voit, Springer Verlag, Berlin, 1991.

2.13 P. Thibault, Y.K. Liu, C.K. Chan, J.H. Lee, R. Knystautas, C. Guirao, B. Hjertager and K. Fuhre, Transmission of an Explosion Through an Orifice. Proc. of the 19th Symposium (International) on Combustion, Haifa, Israel, 1982, 599-606.

2.14 C.K. Chan, I.O. Moen and J.H.S. Lee, Influence of Confinement on Flame Acceleration Due to Repeated Obstacles, Combustion and Flame 49, 1983, 27-39.

2.15 R.K. Kumar W.A. Dewit and D.R. Greig, Vented Explosion of Hydrogen/Air Mixtures in a Large Volume, Combustion Science and Technology 66, 1989, 251-266.

2.16 H. Pfortner, H. Schneider, W. Drenkhahn and C. Koch, Flame Acceleration and Build-Up in Partially Confined Clouds, Presented at the 9th International Colloquium on Dynamics of Explosions and Reactive Systems, Poitiers, France, 1983.

2.17 M.P. Sherman, S.R. Tieszen and W.B. Benedick, FLAME Facility: The Effect of Obstacles and Transverse Venting on Flame Acceleration and Transition to Detonation for Hydrogen/Air Mixtures at Large Scale, Sandia National Laboratories Report, NUREG/CR-5275 or SAND-85-1264, 1989.

2.18 G. Ciccarelli, T. Ginsberg, J. Boccio, C. Economos, K. Sato and M. Kinoshita, Detonation Cell Size Measurements and Predictions in Hydrogen-Air-Steam Mixtures at Elevated Temperatures, Combustion and Flame, Vol. 99. No. 2, 1994, 212-220.

2.19 M. Kaneshige, and J.E. Shepherd, Detonation Database, Report FM-97-8, GALCIT, Explosion Dynamics Laboratory, 1997.

2.20 G.H. Markstein and L.M. Somers, Cellular Flame Structure and Vibratory Flame Movement in N-Butane-Methane Mixtures, Fourth Symposium (International) on Combustion, Williams & Wilkins, 1964.

2.21 G.H. Markstein, *Nonsteady Flame Propagation*, Pargamon Press, Oxford, England, 1964.

2.22 P. Clavin and F.A. Williams, Effects of Molecular Diffusion and Thermal Expansion on the Structure and Dynamics of Premixed Flames in Turbulent Flows of Large Scale and Low Intensity, Journal of Fluid Mechanics, Vol. 116, 1981, 252-282.

2.23 G. Joulin and P. Clavin, Linear Stability Analysis of Nonadiabatic Flames: Diffusion Thermal Model, Combustion and Flame, Vol. 35, 1979, 139-153.

2.24 P. Pecle and P. Clavin, Influence of Hydrodynamics and Diffusion Upon the Stability of Laminar Premixed Flames, Journal of Fluid Mechanics, Vol. 124, 1982, 219-237.

2.25 M. Kuzenetsov, V. Alekseev, A. Bezmelnitsyn, W. Breitung, S. Dorofeev, I. Matsukov, A. Veser and Yu. Yankin, Effect of Obstacle Geometry on Behavior of Turbulent Flames, IAE-6137/3 FZKA-6328, 1999.

2.26 N. Ardey, Structure and Acceleration of Turbulent Hydrogen-Air-Flames Within Obstructed Confinements, PhD Thesis, Technical University of Munich, 1998.

2.27 M. Jordan, Ignition and Combustion of Premixed Turbulent Jets, PhD Thesis, Technical University of Munich, 1999.

2.28 T. Hirano, Behaviour of Propagating Premixed Flames, Hikita Memorial Lecture.

2.29 N. Peters, Laminar Flamelet Concepts in Turbulent Combustion, 21st Symposium (International) on Combustion, The Combustion Institute, Pittsburgh, 1986, 1231-1256.

2.30 H. Guenoche, Rev. Inst. Franc. Petrole, Vol. 4, 1949, 48.

2.31 J.C. Leyer and N. Manson, Development of Vibratory Flame Propagation in Short Closed Tubes and Vessels Thirteenth Symposium (International) on Combustion, The Combustion Institute, Pittsburgh, 1971, 551-557.

2.32 S.M. Kogarko, and D.L. Ryzhkov, Journal of Technology and Physics USSR, Vol. 31, 1961, 211.

2.33 C.J.M. Van Wingerden and J.P. Zeeuwen, On the Role of Acoustically Driven Flame Instabilities in Vented Gas Explosions and Elimination, Combustion and Flame, Vol. 51, 1983, 109-111.

2.34 F. Tamanini and J.L. Chaffee, Turbulent Vented Gas Explosions with and Without Acoustic Waves, Symposium (International) on Combustion, The Combustion Institute, Pittsburgh, 1992, 1845-1851.

2.35 E.S. Oran and J.H. Gardner, Chemical-Acoustic Interactions in Combustion Systems, Progress in Energy and Combustion Science, Vol. 11, 1985, 253-276.

2.36 G. Searby and D. Rochwerger, A Parametric Acoustic Instability in Flames, Journal of Fluid Mechanics, Vol. 231, 1991, 529-543.

2.37 G. Joulin, On the Response of Premixed Flames to Time Dependent Stretch and Curvature, Combustion Science and Technology, Vol. 97, 1994, 219.

2.38 T.L. Jackson, M.G. Macaraeg and M.Y. Hussaini, The Role of Acoustics in Flame/Vortex Interactions, Journal of Fluid Mechanics, Vol. 254, 1993, 259-603.

2.39 E. Kansa and H.E. Perlee, Constant-Volume Flame Propagation: Finite-Sound-Speed Theory, United States Department of the Interior, Bureau of Mines, Report of Investigations 8163, 1976.

2.40 T. Scarincini, J.H. Lee, G.O. Thomas, R. Brambrey and D.H. Edwards, Progress in Astronautics and Aeronautics, AIAA, Vol. 152, 1993, 3-24.

2.41 G.O. Thomas, C.J. Sands, R.J. Brambrey and S.A. Jones, Experimental Observations of the Onset of Turbulent Combustion Following Shock-Flame Interaction, Proceedings of the 16th International Colloquium on the Dynamics of Explosions and Reactive Systems, Cracow, 1997, 2-5.

2.42 H.F. Coward and G.W. Jones, Limits of Flammability of Gases and Vapors, U.S. Bureau of Mines Bulletin 503, 1953.

2.43 R.K. Kumar, Flammability Limits of Hydrogen-Oxygen-Diluent Systems: Horizontal Propagation Limits, AECL Report, WNRE-626, 1985.

2.44 R.G. Abdel-Gayed and D. Bradley, The Influence of Turbulence upon the Rate of Turbulent Burning, Proc. of the First Specialist Meeting on Fuel-Air Explosions, Montreal, Canada, 1981.

2.45 D.R. Ballal and A.H. Lefebvre, The Influence of Flow Parameters on Minimum Ignition Energy and Quenching Distance, 15th Symposium (International) on Combustion, The Combustion Institute, Pittsburgh, 1975, 1473.

2.46 M.D. Checkel and A. Thomas, Turbulent Combustion of Premixed Flames in Closed Vessels, Combustion and Flame, Vol. 96, 1994, 351-370.

2.47 J. Chomiac, Flame Development from an Ignition Kernel in Laminar and Turbulent Homogeneous Mixtures, 17th Symposium (International) on Combustion. The Combustion Institute, Pittsburgh, 1979, 25.

2.48 H. Phillips, The Save Gap Rivisited, Progress in Astronautics and Aeronautics, AIAA, Vol. 114, 1988, 77-96.

2.49 O. Larsen, A Study of Critical Dimensions of Holes for Transmission of Gas Explosions and Development and Testing of a Schlieren System for Studying Jets of Hot Combustion Products, Thesis for the degree of Cand. Scient., University of Bergen, Norway, 1998.

2.50 J.H. Lee, R. Knystautas and C.K. Chan, Turbulent Flame Propagation in Obstacle-Filled Tubes, 20th Symposium International) on Combustion, The Combustion Institute, 1985, 1663-1672.

2.51 R. Knystautas, J.H.S. Lee, O. Peraldi, and C.K. Chan, Transmission of a Flame from a Rough to a Smooth Wall Tube, Progress in Astronautics and Aeronautics, Vol. 106, 1986, 37-52.

2.52 B. Lewis and G. von Elbe, *Combustion Flames and Explosions of Gases*, 2nd Edition Academic Press, New York, 1961.

2.53 P.A. Urtiew and A.K. Oppenheim, Experimental Observations of Transition to Detonation in an Explosive Gas, Proc. of the Royal Society, Vol. A295, 1966, 13-28.

2.54 O. Peraldi, R. Knystautas and J.H. Lee, Criteria for Transition to Detonation in Tubes, 21st Symposium (International) on Combustion, The Combustion Institute, 1988, 1629.

2.55 C.K. Chan and D.R. Greig, The Structures of Fast Deflagrations and Quasi-Detonations", 22nd Symposium (International) on Combustion, The Combustion Institute, 1988, 1733-1739.

2.56 A. Teodorczyk, J.H.S. Lee and R. Knystautas, Propagation Mechanisms of Quasi-Detonations, 22nd Symposium (International) on Combustion, The Combustion Institute, 1988, 1723-1731.

2.57 F. Carnasciali, J.H. Lee, R. Knytautas and F. Fineschi, Turbulent Jet Initiation of Detonation", Combustion and Flame, Vol. 84, 1991, 170.

2.58 D.J. MacKay, S.B. Murray, I.O. Moen and P.A. Thibault, Flame-Jet Ignition of Large Fuel-Air Clouds, 22nd Symposium (International) on Combustion, The Combustion Institute, 1988, 1339-1353.

2.59 R. Knystautas, J.H. Lee, I. Moen and H.G. Wagner, Direct Initiation of Spherical Detonation by a Hot Turbulent Gas Jet, 17th Symposium (International) on Combustion, The Combustion Institute, Pittsburgh, 1979, 1235-1245.

2.60 M. Schildnecht, W. Geiger and M. Stock, Progress in Astronautics and Aeronautics, Vol. 94, 1985, 474-490.

2.61 A.A. Borisov, B.E. Gelfand, G.I. Skachkov et al., Selfignition of Gaseous Mixtures by Focusing of Reflected Shock Waves, Chimicheskaya Phisika, Vol. 7, No. 12, 1988, 1387.

2.62 A. Borisov, B. Gelfand, G. Skatchkov, et al., Ignition of Gaseous Combustible Mixtures in Focused Shock Waves, Current Topics in Shock Waves, Proc. of the 17th ISSW, AIP, N.Y., 1990, 696-701.

2.63 C.K. Chan, D. Lau, P.A. Thibault and J.D. Penrose, Ignition and Detonation Initiation by Shock Focussing, 17th International Symposium on Shock Waves and Shock Tubes, Lehigh University, Bethlehem, Pennsylvania, USA, July 17-21, 1989, AIP Proceedings 208, 1990, 161-166.

2.64 C.K. Chan, Initiation of Detonation Induced by a Focused Shock Wave, 15th International Colloquium on Explosion and Reactive Systems, 1994.

2.65 B.E. Gelfand, S.M. Frolov, S.P. Medvedev and S.A. Tsyganov, Three Cases of Shock Wave Focusing in a Two Phase Combustible Medium, Shock Waves, Proceedings, Sendai, Japan, 1991, Springer Verlag, Vol II, 1992, 837-842.

2.66 C.K. Chan, A. Guerrero and D. McCooeye, Shock Induced Transition to Detonation, Paper at 2nd Canadian and German Workshop, 1993.

2.67 O.V. Achasov, A.A. Labuda, O.G. Penzijakov and R.M. Pushkin, Shock Waves Initiation of Detonation in Semiclosed Cavity, Chimicheskaya Phisika, Vol. 12, No. 5, 1993, 714-716.

2.68 M. Rose, P. Roth and U. Uphoff, Ignition of Reactive Gas by Focusing of Shock Wave, Proc. of 16th ICDERS, Krakow, 1997, 554-556.

2.69 V.Yu. Gidaspov, I.A. Ivanov and I.A.,Krinlov, Numerical Modeling of Detonation in Focusing Channel, Mathem. Modeling, Vol. 4, No. 4, 1992, 85-88.

2.70 Detonation Ignition Characteristics of H_2-Air Mixtures Under Conditions of Shock Focusing, IChPh RAS @ INR FZK Research Report, 1993.

2.71 Complete Experimental Investigation of Shock Wave Focusing Phenomena in H_2 + Air Mixtures with Additives", IChPh RAS @ INR FZK Research Report, 1994.

2.72 Ya. B. Zel'dovich, V.B. Librovich, G.M. Makhviladze and G.I. Sivashinsky, On the Development of Detonation in a Non-Uniformly Preheated Gas, Astronautica Acta, Vol. 15, 1970, 313-321.

2.73 Ya. B. Zel'dovich, Regime Classification of an Exothermic Reaction with Non-Uniform Initial Conditions, Combustion and Flame, Vol. 39, 1990, 211-214.

2.74 Ya. B. Zel'dovich, B.E. Gelfand, S.A. Tsyganov, S.M. Frolov and A.N. Polenov, Concentration and Temperature Non-Uniformities (CTN) of Combustible Mixtures as a Reason of Pressure Generation, 11th Colloquium on Dynamics of Explosions and Reactive Systems (ICDERS), Warsaw, Vol. 89, 1988.

2.75 J.H.S. Lee, R. Knystautas and N. Yoshikawa, Photochemical Initiation and Gaseous Detonations, Acta Astronautica, Vol. 5, 1978, 971-972.

2.76 N. Yoshikawa, Coherent Shock Wave Amplification in Photo-Chemical Initiation of Gaseous Detonations, PhD Thesis, Department of Mechanical Engineering, McGill University, Montreal, Quebec, Canada, 1980.

2.77 J.H.S. Lee and I.O. Moen, The Mechanisms of Transition from Deflagration to Detonation in Vapor Cloud Explosions, Progress in Energy and Combustion Science, Vol. 6, 1980, 359-389.

2.78 J.F. Clark, Fast Flames, Waves and Detonations, Progress in Energy and Combustion Science, Vol. 15, 1989, 241-271.

2.79 S.M. Frolov, B.E. Gelfand and S.A. Tsygonov, Spontaneous Combustion Regimes, Soviet Journal of Explosion and Combustion Shock Waves, Vol. 28, No. 5, 1992, 132-27.

2.80 S.B. Dorofeev, A.A. Efimenko and A.S. Kochurko, Numerical Study of Detonation Self-Initiation Conditions, 15th ICDERS, Boulder, Colorado, 1995, 425-428.

2.81 S.B. Dorofeev, A.V. Bezmelnitsin and V.P. Sidorov, Transition to Detonation in Vented Hydrogen-Air Explosion, Combustion and Flame, Vol. 103(3), 1995, 243-246.

2.82 S.B. Dorofeev, A.S. Kochurko, A.A. Efimenko and B.B. Chaivanov, Evaluation of Hydrogen Explosion Hazard, Nuclear Engineering and Design, Vol. 148, No. 2, 1994, 305-310.

2.83 B.E. Gelfand, S.P., Medvedev, A.N. Polenov, S.V. Khomik and A.M. Bartenev, Basic Selfignition Regimes and Conditions for their Realization in Combustible Gas Mixtures, Combustion, Explosion and Shock Waves, Vol. 33, No. 2, 1997, 127-133.

2.84 V. Smijanovski and R. Klein, Flame Front Tracking via In-Cell Reconstruction, Proceedings of the 5th International Conference on Hyperbolic Systems, SUNY, Stony Brook, June 1994.

2.85 A.M. Khokhlov, S.E. Oran and J.C. Wheeler, A Theory of Deflagration-to-Detonation Transition in Unconfined Flames, Combustion and Flame, Vol 108, 1997, 503-517.

2.86 A.M. Khokhlov, E.S. Oran and G.O. Thomas, Numerical Simulation of Deflagration-to-Detonation Transition: The Role of Shock-Flame Interactions in Turbulent Flames, Combustion and Flame, in Press.

2.87 J.W. Dold, M. Short, J.F. Clark and N. Nikiforakis, Accumulating Sequence of Ignitions from a Propagating Pulse, Combustion and Flame, Vol. 100, 1995, 465-473.

2.88 M. Short and J.W. Dold, Corrections to Zel'dovich's <<Spontaneous Flame>> and the Onset of Detonation via Nonuniform Preheating, Dynamic Aspects of Explosion Phenomena (edited, by Kuhl A.L. et al.), Prog. In Astronautics and Aeronautics, AIAA, Vol. 154, 1993, 59-75.

2.89 A.M. Bartenev and B.E. Gelfand, Weak and Strong Ignition Within the Scope of Spontaneous Flame Concept, Twenty Fifth Symposium (International) on Combustion, The Combustion Institute, Pittsburgh, 1994, 61-64.

2.90 I. Sochet, M. Aminallah and J. Brossard, Detonability of Fuel-Oxygen and Fuel-Air Mixtures, International Journal of Shock Waves, Vol. 7, 1997, 163-174.

2.91 I. Sochet, A. Reboux and J. Brossard, Detonability of Spatially Non-Uniform Gasous Mixtures, 14th ICDERS Coimbra Portugal, Preprints II: E1.7.1-E1.7.10, 1993.

2.92 S.P. Medvedev, A.N. Polenov, S.V. Khomik and B.E. Gelfand, Initiation of Upstream-Directed Detonation Induced by the Venting of Gaseous Explosion, Twenty-Fifth

Symposium (International) on Combustion, The Combustion Institute, Pittsburgh, 1994, 73-78.

2.93 R. Blumental, K. Fieweger, K.H. Komp and G. Adomeit, Gas Dynamic Features of Self Ignition of Nondiluted Fuel/Air Mixtures at High Pressure, Combustion Science and Technology, Vol. 137, 1996, 113-114.

2.94 L. He and P. Clavin, Numerical and Analytical Studies of the Initiation of Combustion Wave by Hot Pockets, *Experimental, Modelling and Computation in Flow*, Turbulence and Combustion (ed. J. Desileri, J. Wiley), Vol. 1, 1996, 137-157.

2.95 U. Behrens, G. Langer, M. Stock and R. Wirkner, Deflagration-Detonation Transition in Hydrogen-Air-Steam Mixtures. Relevance in the Experimental Results for Real accidents Situations, Nuclear Engineering and Design, Vol. 130, 1991, 43-50.

2.96 Determination of Spontaneous Detonation (SWACER) and Flame Propagation Criteria in H_2 + Air Mixtures, Report IchP RAS @ INR FZK, 1994.

2.97 Investigation of Spontaneous Detonation Ignition Under Nonuniform Pressure and Temperature Conditions, Report IchP RAS @ INR FZK, 1993.

2.98 S.B. Dorofeev, V.P. Sidorov, M.S. Kuznetsov, I.D. Matsukov and V.I. Alekseev, Effect of Scale on the Onset of Detonations, Proc. of 17th International Colloquium on Dynamics of Explosion and Reactive Systems, Heidelberg, 1999.

2.99 G.O. Thomas, private communication 1999.

2.100 C.K. Chan and W.A. Dewit, DDT in End Gases, 27^{th} Symposium (International) on Combustion, Vol. 2, 1996, 2679.

2.101 B.E. Gelfand and S.V. Khomik, Investigation of Hydrogen + Air Fast Flame Propagation and DDT in Tube with Multidimensional Endplates, IChP RAS @INR FXK Report, 1998.

2.102 A. Veser, W. Breitung, G. Engel, G. Stern and A. Kotchourko, Deflagration-to-Detonation-Transition Experiments in Shock Tube and Obstacle Array Geometries, Report FZKA-6355, Research Center Karlsruhe, 1999.

2.103 A. Eder, C. Gerlach and F. Mayinger, Experimental Observation of Fast Deflagrations and Transition to Detonations in Hydrogen-Air Mixtures, submitted to the Symposium on Energy Engineering in the 21rst Century, Jan. 9-13, Hong Kong, 2000.

2.104 A.D Craven and D.R. Greig, The Development of Detonation OverPressures in Pipelines, Chem E Symposium Series 25, 1968, 41-50.

2.105 S.M. Kogarko, Investigation of the Pressure at the End of a Tube in Connection with Rapid Nonstationary Combustion, Soviet Physics – Technical Physics (ZhTF) 28:2041.

2.106 F. Zhang, P.A. Thibault and S. Murray, Transition from Deflagration to Detonation in Multi-Phase Slug, Combustion and Flame, Vol. 114, 1998, 13-24.

2.107 W. Breitung, S.B. Dorofeev, A.A. Efimenko, A.S. Kochurko, R. Redlinger and V.P. Sidorov, Large-Scale Experiments on Hydrogen-Air Detonation Loads and their Numerical Simulation, Proc. Int. Topl. Mtg. Advanced Reactor Safety, Pittsburgh, Pennsylvania, April 17-21, 1994, 733.

2.108 W. Breitung and R. Redlinger, A Model for Structural Response to Hydrogen Combustion Loads in Severe Accidents, Nuclear Technology, Vol. 111, 1995, 420- 425.

2.109 E. Studer and M. Petit, Use of RUT Large Scale Combustion Test Results for Reactor Applications, International Association for Structural Mechanics in Reactor Technology, 14th International Conference on Structural Mechanics in Reactor Technology, Lyon, France, 1997.

2.110 G. Ciccarelli, J.L. Boccio, T. Ginsberg, C. Finfrock, L. Gerlach, H. Tawaga and A. Malliakos, The Effect of Initial Temperature on Flame Acceleration and Deflagration-to-Detonation Transition Phenomenon, NUREG/CR-6509, May 1998.

3. CRITERIA FOR FA AND DDT LIMITS*

3.1 Introduction

The processes following weak ignition in a combustible mixture can result in generation of a variety of different combustion regimes ranging from slow flames to detonations. Different combustion regimes occur because of the intrinsic ability of combustion waves to accelerate and to undergo transition to detonation. Fast combustion modes that resulted from FA and DDT can be extremely destructive. Thus from the practical point of view, it is important to predict the type of combustion regimes that can be developed under certain initial and boundary conditions.

Detailed description of all processes following weak ignition in a combustible mixture is extremely difficult at present. This is due to complicated interactions of compressible flow, turbulence, and chemical reactions, which should be described at high spatial and temporal resolution. In this situation, much effort has been focused on development of criteria for FA and DDT. These criteria are aimed at description of initial and boundary conditions under which flame acceleration and DDT can be expected. An overview of criteria that can be used to evaluate possibility of FA and DDT is presented in this chapter.

3.2 Criteria for FA

3.2.1 Buoyancy Limits

3.2.1.1 Downward/upward flame propagation limits.

Buoyancy effects essentially limit the ability of flame acceleration for mixtures that are close to flammability limits. If ignition occurs in a mixture, which is in between upward and downward propagation limits (in hydrogen-air mixtures at normal initial conditions these are 4 vol % and 8 vol %), incomplete combustion is observed. Buoyancy lifts the flame ball upward as it expands, and hence only a fraction of the total volume of the mixture is burned. The turbulence is able to enhance the completeness of combustion, but no chance exists for effective flame acceleration under these conditions. Thus a comparison of the composition of the mixture with that for the download propagation limit gives an indication of the possibility of flame acceleration.

3.2.1.2 Froude number

Froude number *Fr* is a dimensionless parameter, which determines the influence of natural convection on flame shape and properties

$$Fr = v^2/2gR\ , \tag{3.1}$$

where v is visible flame speed, g is gravitational acceleration, and R is flame radius. The critical value of the Froude number is estimated to be $Fr^* = 0.11$ [3.1]. For $Fr < Fr^*$, buoyancy dominates the process of expansion of combustion products. Under these conditions, the most effective mechanism of flame acceleration (feedback between the flame flow produced and the flame itself) does not work. The critical Froude number may be used as a criterion for the possibility of flame acceleration.

---

* Dr. Sergei B. Dorofeev is the lead author for this chapter.

For laminar H_2-air flames of 1 m in radius, values of Froude number are 0.05 and 0.16 for mixtures of 9% and 10% H_2 in air, assuming $v = \sigma S_L$ (where σ is ratio of densities of reactants and products, and S_L is laminar flame speed). This gives a reasonable estimate that flames with H_2 concentration of less than 9.5% and $R > 1$ m should be significantly affected by buoyancy. It should be noted that estimates of the buoyancy effect that make use of Froude number are not as direct and easy as it seems. Such estimates are reliable only for small-enough flame kernels, which can be considered as laminar. In other cases, values of visible flame speed, v, are required, which depend on the actual combustion regime.

3.2.2 Effects of Mixture Reactivity and Scale (σ - Criterion)

Unlike the buoyancy-driven flames, deflagrations dominated by the product expansion provide favourable conditions for flame acceleration. If such a possibility exists, it is important to estimate whether the flame is able to accelerate under given conditions resulting in fast turbulent combustion regimes (such as 'sonic' or 'choked' flames) and, possibly, in the transition to detonation, or the flame acceleration is inefficient ending at a benign combustion and even flame quenching.

An important fundamental problem that should be solved to provide a foundation for such predictions is an adequate description of the mutual affect of scale and mixture properties on the resulting combustion mode. The influence of various factors, including scale, on the turbulent flame propagation and flame acceleration phenomenon was studied extensively (see e. g., [3.2-3.7]). Turbulent velocity correlations have been suggested in References [3.5 to 3.7] and in other studies, which include intrinsically the effect of scale. However, quantitative criteria for flame acceleration are difficult to formulate on the basis of these correlations because they require that a current level of turbulence to be known in all phases of the process.

A series of tests was recently conducted to systematically study the effects of scale and mixture properties on the behaviour of turbulent flames in obstructed areas [3.8, 3.9]. A set of dimensionless parameters was chosen that could influence the flame-flow-flame feedback in obstructed areas. These parameters are defined by the intrinsic length, time and velocity scales of the combustion processes, and by mixture properties:

$$L_T/\delta,\ \sigma,\ S_L/c_{sr},\ S_L/c_{sp},\ \gamma_r,\ Le, \text{ and } \beta, \tag{3.2}$$

where L_T is the integral length scale of turbulence, δ is the laminar flame thickness, σ is the ratio of densities of reactants and products (expansion ratio), S_L is the laminar flame speed, c_{sr} and c_{sp} are the sound speeds in reactants and products, γ_r is the specific heat ratio in reactants, Le is the Lewis number, $\beta = E_a(T_b - T_u)/(RT_b^2)$ is the Zeldovich number, E_a is the effective activation energy, T_u is the initial, and T_b is the maximum flame temperature.

In obstructed areas, the integral length scale of turbulence is defined mainly by geometrical configuration [3.10]. Other parameters in Equation (3.2) are defined by mixture properties. The parameters in Equation (3.2), thus, can be considered as those defining a priori a *potential* for flame acceleration.

The experiments described in References [3.8 and 3.9] were focused on the effect of these parameters. Three tubes (174, 350, and 520 mm id) and explosion channel (80 mm x 80 mm cross-section) were used in the tests. Different mixtures were chosen in order to provide (1) a wide range of the scaling parameters and (2) combinations with similar values of the parameters at different scales.

It was found that under certain conditions the flame accelerates effectively in explosion channels, resulting in fast supersonic (in a laboratory framework) regimes of propagation such as choked flames

and detonations. Another option was ineffective flame acceleration resulting in relatively slow, subsonic regimes of propagation. Some examples are presented in Figures. 3.2.2-1 to 3.2.2-3. For slow combustion regimes, the maximum speed of flame propagation appeared to increase with scale. Despite this effect, a very significant difference in the maximum propagation speeds and corresponding levels of overpressures was observed between slow and fast regimes for all scales. This significant difference allows us to define a criterion for flame acceleration that is based on the corresponding critical conditions in channels with obstacles.

Experimental results [3.8, 3.9] showed that parameters L/δ and σ were the most important ones among all the sets (3.2) in defining flame acceleration rate. At the same time, the type (slow or fast) of final regime of flame propagation at sufficiently large scale was found to depend mainly on the value of mixture expansion ratio σ. In view of this observation, it was suggested that all mixtures may be divided into "weak" and "strong". Flame acceleration and development of fast combustion regimes are possible in strong mixtures under favourable conditions at sufficiently large scale. Flame acceleration in weak mixtures is inefficient, even under favourable conditions. A criterion for flame acceleration was suggested in Reference [3.10] as a requirement of a large-enough value of σ:

$$\sigma > \sigma^*(\beta, Le) \,, \tag{3.3}$$

where σ^* is the critical value, which is expected to be function of β and Le.

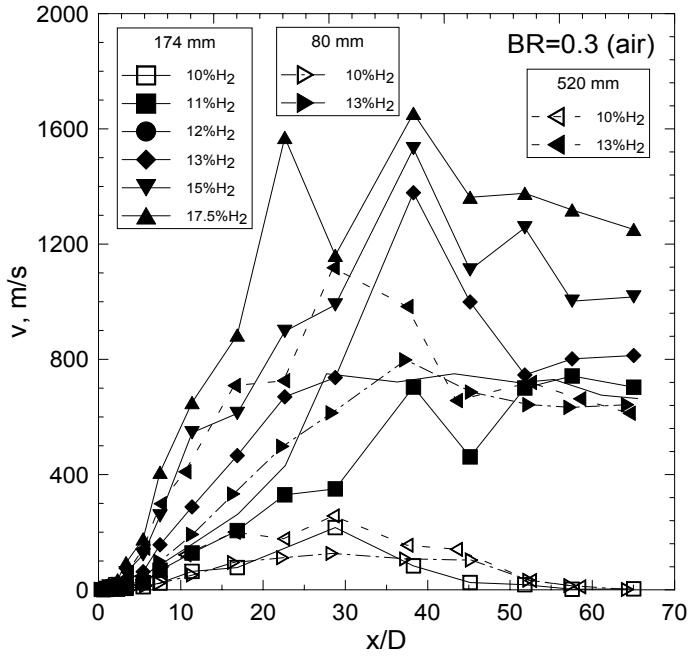

Figure 3.2.2-1 Visible speeds of flame propagation versus reduced distance along tubes (*D* - tube diameter) for lean hydrogen-air mixtures. Blockage ratio = 0.3; obstacle spacing is equal to *D*. Solid points represent fast combustion regimes (choked flames and quasi-detonations); empty points represent slow combustion regimes.

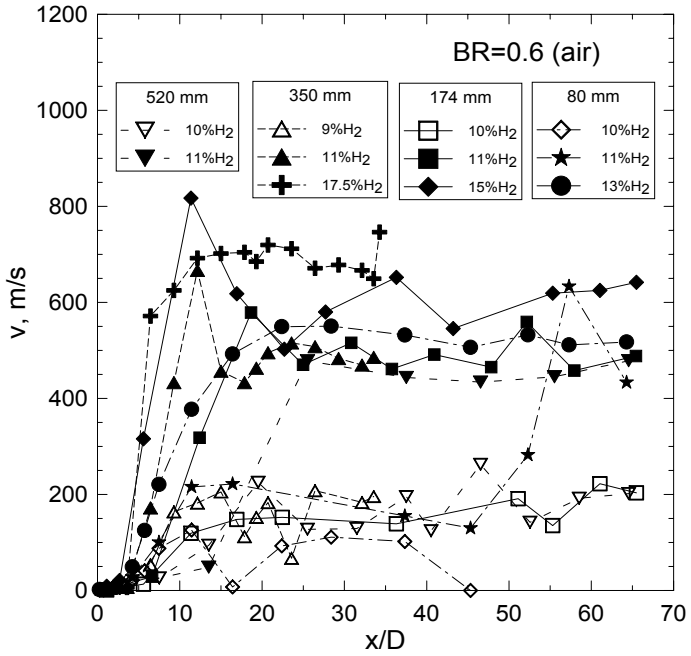

Figure 3.2.2-2 Visible speeds of flame propagation versus reduced distance along for lean hydrogen-air mixtures. Blockage ratio = 0.6. Solid points show fast combustion regimes (choked flames); empty points show slow combustion regimes.

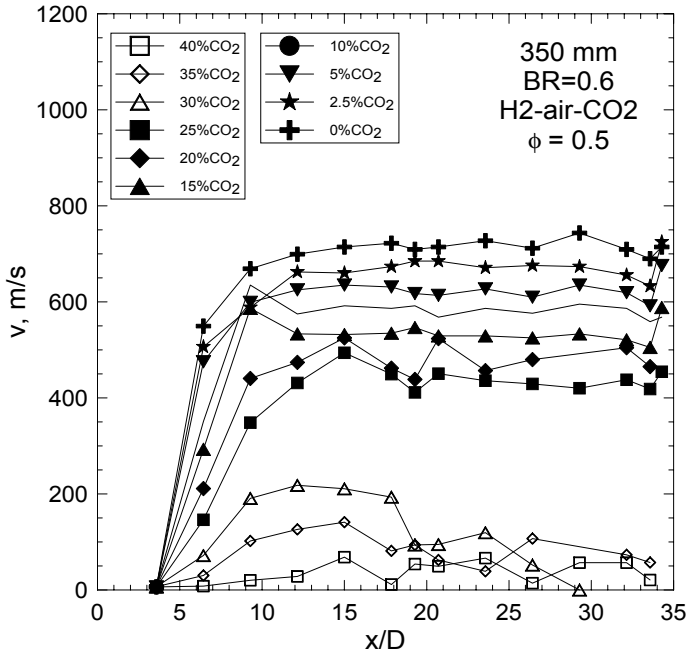

Figure 3.2.2-3 Visible speeds of flame propagation versus reduced distance along the tube for lean hydrogen-air mixtures (equivalence ratio $\phi = 0.5$) diluted with CO_2. Blockage ratio = 0.6. Solid points show fast combustion regimes (choked flames); empty points show slow combustion regimes.

3.2.3 Experimental Correlations for FA Criterion

A large amount of experimental data on turbulent flame acceleration is available at conditions representative of nuclear safety. In this section, these data are considered.

Experiments were conducted in the High-Temperature Combustion Facility (HTCF) facility at the Brookhaven National Laboratory (BNL) to study flame acceleration and DDT in hydrogen-air and hydrogen-air-steam mixtures with different hydrogen and steam concentrations. The experiments were performed without venting and with 5.1% venting at initial mixture temperatures up to 650K [3.11]. The HTCF is 21.3 m long and has an internal diameter of 27.3 cm. Periodic orifice plates were installed down the length of the entire detonation tube. The orifice plates have an outer diameter of 27.3 cm, an inner diameter of 20.6 cm, and a spacing of 1 tube diameter.

Experiments were conducted at the Sandia National Laboratories (SNL) with hydrogen-air-steam and hydrogen-air mixtures in the Heated Detonation Tube (HDT) to determine the region of benign combustion (between the flammability limits and the DDT limits) [3.12]. The HDT is 12 m long and has internal diameter of 43 cm. Obstacles were used with 30% blockage ratio annular rings, and alternate rings and disks of 60% blockage ratio. The initial conditions were 383 K and 1 or 3 atm pressure.

RUT facility tests were performed at Russian Research Centre “Kurchatov Institute” (RRC KI0 with hydrogen-air mixtures with and without steam dilution in a complex geometry [3.13, 3.14]. The first part of the facility was a channel of 2.5 x 2.3-m cross-section and 34.6 m long; the second part was a canyon of 6 x 2.5-m cross-section and 10.5 m long, and the third one was a channel of 2.5 x 2.3-m cross-section and 20 m long. Twelve concrete obstacles were placed along the first channel with a spacing of 2.5 m (blockage ratios were 0.3 and 0.6). Initial temperature in tests with steam was close to 375 K. Initial pressure in all the tests was 1 atm.

FLAME facility data were obtained at the Sandia National Laboratories in a study of FA and DDT of hydrogen-air mixtures [3.15]. FLAME is a large (30.5 m long) rectangular channel that has an interior width of 1.83 m and a height of 2.44 m. The blockage ratio was 0.0 (no obstacles) or 0.33 in the tests. Initial conditions were normal in these tests.

FZK experiments [3.9] were performed in a 35-cm-diameter, 12-m-long length with equidistant rings as obstacles (blockage ratio was 0.6 spacing was 35cm). Flame acceleration was studied in hydrogen-air mixtures and in hydrogen-oxygen (2:1) mixture, diluted with nitrogen, argon, helium and CO_2. Experiments were conducted under normal initial conditions.

CHANNEL, DRIVER, and TORPEDO experiments provided data on turbulent flame propagation regimes in obstructed areas at different scales [3.8, 3.9]. Blockage ratios ranged from 0.1 to 0.9. Distances between obstacles were equal to the transverse size of each tube for all these facilities. Mixture compositions were varied in the tests. Experiments were conducted under normal conditions. The CHANNEL facility is a tube with a square cross-section of 80 mm × 80 mm and 5.28-m length. Rectangular obstacles were mounted along upper and bottom plates. Different hydrogen-air mixtures and stoichiometric hydrogen-oxygen, diluted by argon or helium were used in these tests. The DRIVER facility is a detonation tube of 174 mm id and approximately 12-m length. Hydrogen-air mixtures and stoichiometric hydrogen-oxygen mixtures diluted with nitrogen, argon, or helium were used in this facility. The TORPEDO facility is a 520-mm tube of 30.3-m length. Hydrogen-air mixtures and stoichiometric hydrogen-oxygen, diluted by helium were used in these tests.

Results of the analyses [3.10] are presented in Figures 3.2.3-1 to 3.2.3-6. Data points are marked with labels given in Table 3.2.3-1. Black points correspond to fast combustion regimes, and light gray points to slow combustion regimes.

Table 3.2.3-1 Experimental data used in correlations for flame acceleration criterion

Data source	Label	Blockage ratio BR	Tube or channel size L, mm	Initial temperature T, K	Mixture type	Equivalence ratio ϕ
HTCF-BNL [3.11]	b1	0.43	273	300	H_2/air	<1
HTCF-BNL [3.11]	b2	0.43	273	500	H_2/air	<1
HTCF-BNL [3.11]	b3	0.43	273	650	H_2/air	<1
HTCF-BNL [3.11]	b4	0.43	273	400	H_2/air/H_2O	<1
HTCF-BNL [3.11]	b5	0.43	$_2$73	500	H_2/air/H_2O	<1
HTCF-BNL [3.11]	b6	0.43	273	650	H_2/air/H_2O	<1
CHANNEL-RRCKI [3.9]	c1	0.1	80	293	H_2/air	<1; >1
CHANNEL-RRCKI [3.9]	c2	0.3	80	293	H_2/air	<1; >1
CHANNEL-RRCKI [3.9]	c3	0.6	80	293	H_2/air	<1; >1
CHANNEL-RRCKI [3.9]	c4	0.9	80	293	H_2/air	<1; >1
CHANNEL-RRCKI [3.9]	c5	0.6	80	293	H_2/O_2/He	1
CHANNEL-RRCKI [3.9]	c6	0.6	80	293	H_2/O_2/Ar	1
DRIVER-RRCKI [3.9]	d1	0.09	174	293	H_2/air	<1; >1
DRIVER-RRCKI [3.9]	d2	0.3	174	293	H_2/air	<1; >1
DRIVER-RRCKI [3.9]	d3	0.6	174	293	H_2/air	<1; >1
DRIVER-RRCKI [3.9]	d4	0.9	174	293	H_2/air	<1; >1
DRIVER-RRCKI [3.9]	d5	0.09	174	293	$H_2/O_2/N_2$	1
DRIVER-RRCKI [3.9]	d6	0.3	174	293	$H_2/O_2/N_2$	1
DRIVER-RRCKI [3.9]	d7	0.6	174	293	$H_2/O_2/N_2$	1
DRIVER-RRCKI [3.9]	d8	0.9	174	293	$H_2/O_2/N_2$	1
DRIVER-RRCKI [3.9]	e1	0.09	174	293	H_2/O_2/He	1
DRIVER-RRCKI [3.9]	e2	0.3	174	293	H_2/O_2/He	1
DRIVER-RRCKI [3.9]	e3	0.6	174	293	H_2/O_2/He	1
DRIVER-RRCKI [3.9]	e5	0.09	174	293	H_2/O_2/Ar	1
DRIVER-RRCKI [3.9]	e6	0.3	174	293	H_2/O_2/Ar	1
DRIVER-RRCKI [3.9]	e7	0.6	174	293	H_2/O_2/Ar	1
FLAME-SNL [3.15]	f1	0.33	1830	293	H_2/air	<1
FLAME-SNL [3.15]	f2	0	1830	293	H_2/air	<1
FZK [3.9]	g1	0.6	350	293	H_2/air	<1; >1
FZK [3.9]	g2	0.6	350	293	$H_2/O_2/N_2$	1
FZK [3.9]	g3	0.6	350	293	H_2/O_2/He	1
FZK [3.9]	g4	0.6	350	293	H_2/O_2/Ar	1
FZK [3.9]	g5	0.6	350	293	$H_2/O_2/CO_2$	1
FZK [3.9]	g6	0.6	350	293	H_2/air/CO_2	.5
FZK [3.9]	g7	0.6	350	293	H_2/air/CO_2	1
FZK [3.9]	g8	0.6	350	293	H_2/air/CO_2	2
FZK [3.9]	g9	0.6	350	293	H_2/air/CO_2	4

continued . . .

Table 3.2.3-1 (concluded)

Data source	Label	Blockage ratio BR	Tube or channel size L, mm	Initial temperature T, K	Mixture type	Equivalence ratio ϕ
RUT-RRCKI [3.13]	r1	0.6	2250	293	H_2/air	<1
RUT-RRCKI [3.13]	r2	0.3	2250	293	H_2/air	<1
RUT-RRCKI [3.13]	r3	0	2250	293	H_2/air	<1
RUT-RRCKI [3.14]	r4	0.3	2250	375	H_2/air/H_2O	≤1
HDT-SNL [3.12]	s1	0.6	406	383	H_2/air	>1
HDT-SNL [3.12]	s2	0.3	406	383	H_2/air/H_2O	>1
TORPEDO-RRCKI [3.9]	t1	0.6	520	293	H_2/air	<1; >1
TORPEDO-RRCKI [3.9]	t2	0.6	520	293	H_2/O_2/He	1
TORPEDO-RRCKI [3.9]	t3	0.3	520	293	H_2/air	<1; >1
TORPEDO-RRCKI [3.9]	t4	0.1	520	293	H_2/air	<1; >1

The plot of σ-values versus initial temperature is shown in Figure 3.2.3-1. It is seen that the border between fast and slow flames in terms of σ goes down with initial temperature. In fact, such a behaviour should be expected. The mixtures are characterized by the intrinsic temperature scale - parameter *Ea/R*. In the dimensionless form, the rigorous parameter is the Zeldovich number $\beta = Ea(T_b - T_u)/RT_b^2$. Qualitatively, the influence of initial temperature on effectiveness of the flame acceleration is connected with the increase of the effect of local turbulent mixing on suppression of burning rate at high β-values. Such a general effect, however, is expected to be influenced by a local behaviour of a flame element that is stretched and curved by turbulent motions.

The Zeldovich number is known to play an important role in the stability of stretched flames in a combination with the Lewis number [3.16]. Normal burning rate of stretched flames U_n relative to burned mixture may be expressed by

$$U_n/U_L\text{-}1 = - Ma_b\, \delta/U_L\cdot(1/A\cdot dA/dt) \,, \tag{3.3}$$

where U_L is the laminar flame speed relative to burned mixture, A is the elementary area of the flame front, and Ma_b is the Markstein number defined relative to burned mixture.

The value of $1/A\cdot dA/dt$ represents the flame stretch, which in highly turbulent flow is due to turbulence. The value of the Markstein number, Ma_b, determines the effect of stretch on variations of local burning velocities. For two reactant mixtures with a single-step reaction the Ma_b is estimated as [3.16]:

$$Ma_b = \frac{\sigma}{\sigma-1}\left(\ln\sigma + \frac{\beta(Le-1)}{2(\sigma-1)}\right)\int_0^{\sigma-1}\frac{\ln(1+x)dx}{x} \,, \tag{3.4}$$

where x is dummy variable of integration. The combination $\beta(Le\text{-}1)$ defines the value and even the sign of Ma_b. At large negative values of $\beta(Le\text{-}1)$, $Ma_b < 0$ and the flame stretch results in a local increase of burning velocity. With $Ma_b > 0$, the flame stretch tends to decrease the burning velocity and can result in flame quench.

The combination $\beta(Le-1)$ is also the defining parameter for thermal-diffusion flame instability. The stability boundary corresponds to $\beta(Le-1) = -2$. Flames are stable with $\beta(Le-1) > -2$, and unstable with $\beta(Le-1) < -2$. These speculations show that parameter $\beta(Le-1)$ is expected to be important in correlations of experimental data.

Figure 3.2.3-2 shows combustion regimes in $(\sigma - \beta(Le-1))$ plot. The value $\beta(Le-1) = -2$ indeed appeared as a threshold value. With $\beta(Le-1) < -2$ the borderline between slow and fast combustion regimes changes with $\beta(Le-1)$ in the range $\sigma^* = 2 - 3.75$. With $\beta(Le-1) > -2$, which corresponds to thermal-diffusely stable flames, an abrupt change of limiting values of σ is observed. Values of σ ranges from 3.5 to 4.0 for $\beta(Le-1) > -2$. A similar picture is seen in the $(\sigma - Ma_b)$ plot presented in Figure 3.2.3-3. Threshold value here corresponds to $Ma_b = 0$.

Data of Figures 3.2.3-2 and 3.2.3-3 suggest that correlations with other parameters should be made separately for mixtures with $\beta(Le-1) < -2$ and with $\beta(Le-1) > -2$. For stable flames with $\beta(Le-1) > -2$, these correlations are presented in Figures 3.2.3-4 and 3.2.3-5. Critical σ-values for effective flame acceleration do not depend significantly on scale ratio L/δ (Figure 3.2.3-4 and on Zeldovich number β (Figure 3.2.3-5). For unstable flames with $\beta(Le-1) < -2$, critical σ-values can be considered to be a function of Zeldovich number β (Figure 3.2.3-6).

Experimental correlations presented in this section permit us to suggest the following necessary conditions for development of fast combustion regimes [3.10].

$$\sigma > (3.5 \div 4), \quad \text{for mixtures with } \beta(Le - 1) > -2 \; ; \tag{3.5}$$

$$\sigma > \sigma^*(\beta), \quad \text{for mixtures with } \beta(Le - 1) < -2 \; , \tag{3.6}$$

where the function $\sigma^*(\beta)$ is given by the correlation shown in Figure 3.2.3-6. These conditions are expressed in terms of mixture properties and give the possibility to divide mixtures into “strong” and “weak”, depending on their ability to support effective flame acceleration under favourable geometrical conditions.

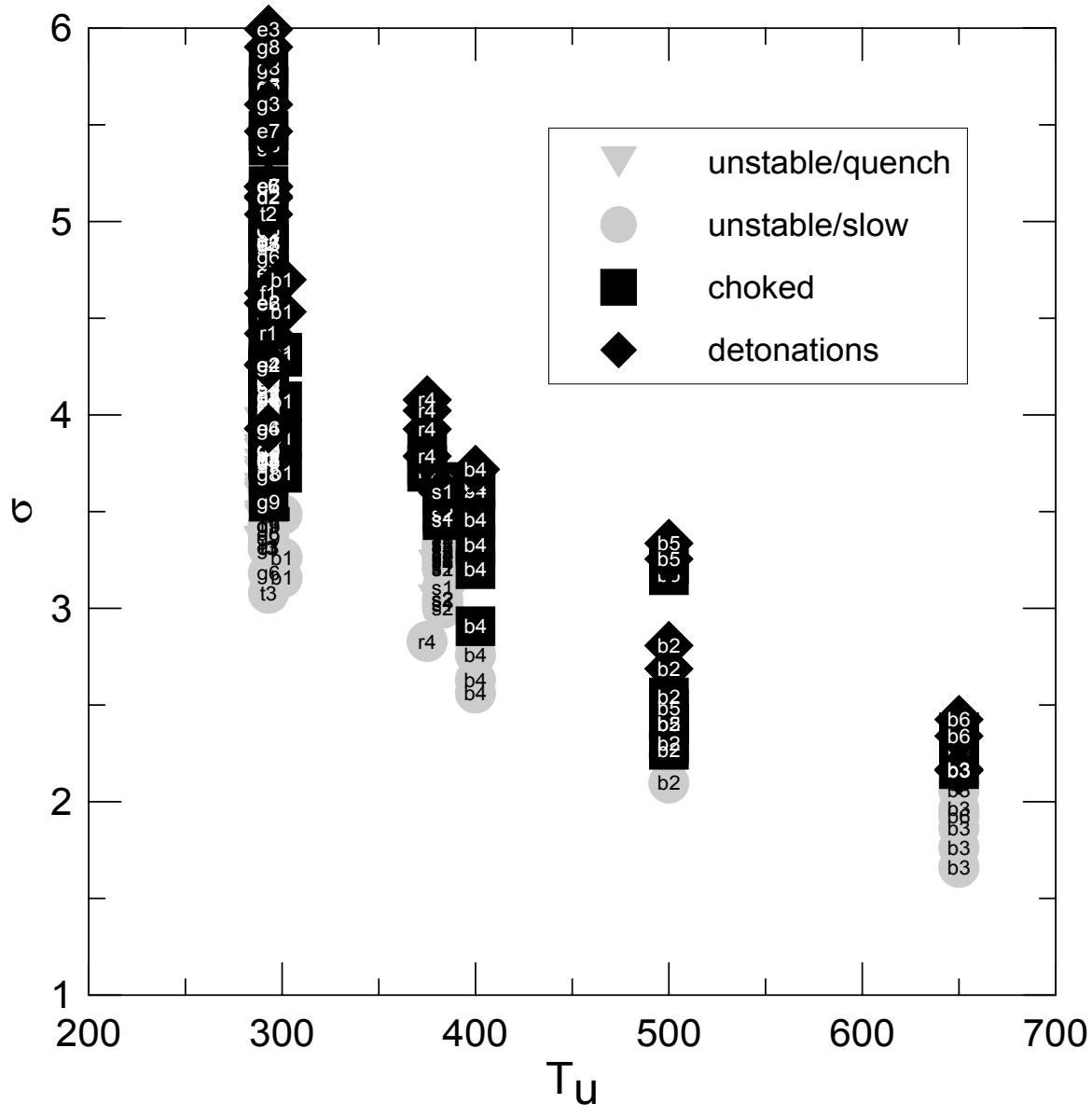

Figure 3.2.3-1 Resulting combustion regime as a function of expansion ratio σ and initial temperature T_u. Black points show fast combustion regimes, and gray points show slow combustion regimes.

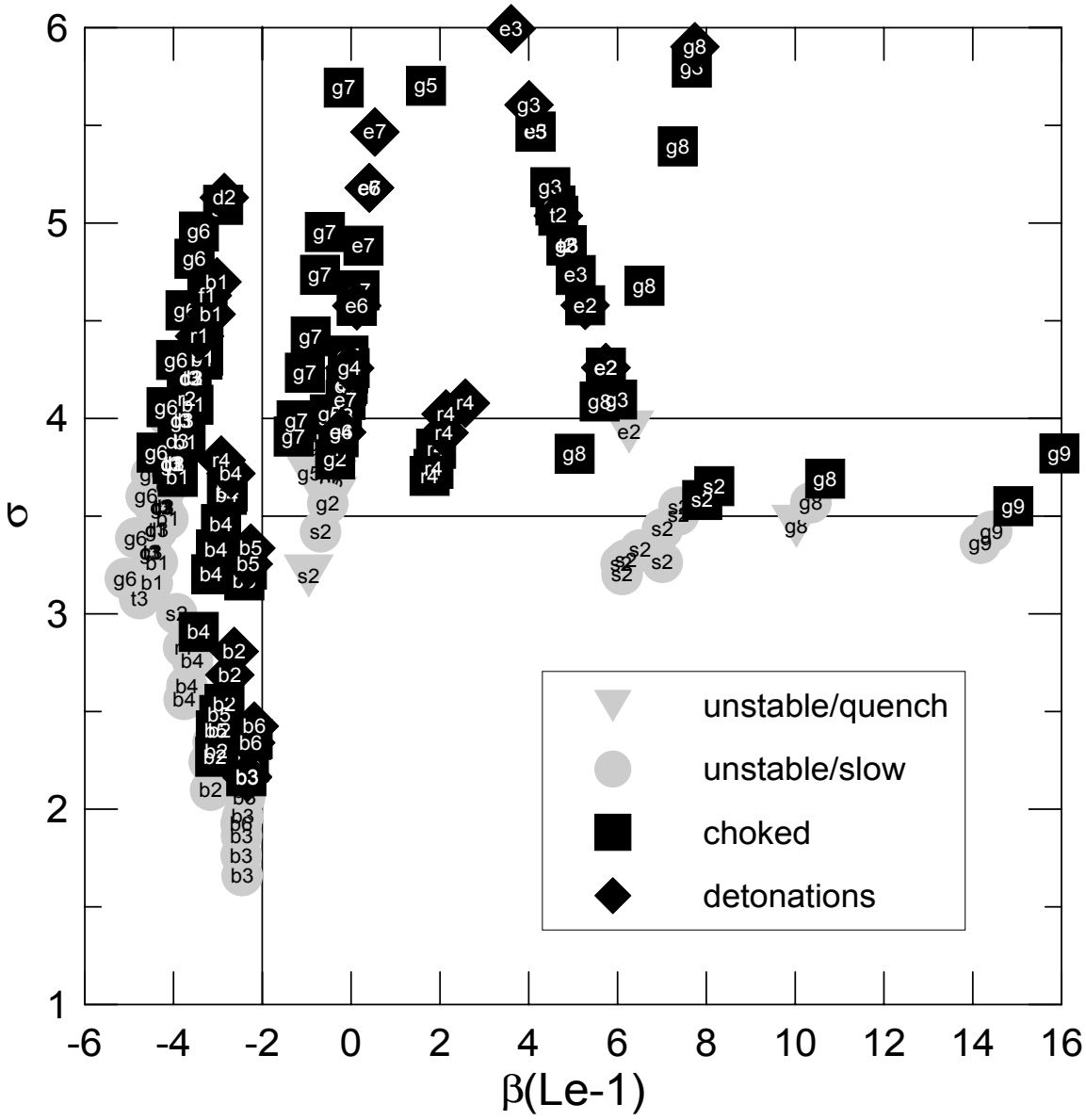

Figure 3.2.3-2 Resulting combustion regime as a function of expansion ratio σ and $\beta(Le - 1)$. Black points represent fast combustion regimes, and gray points represent slow combustion regimes.

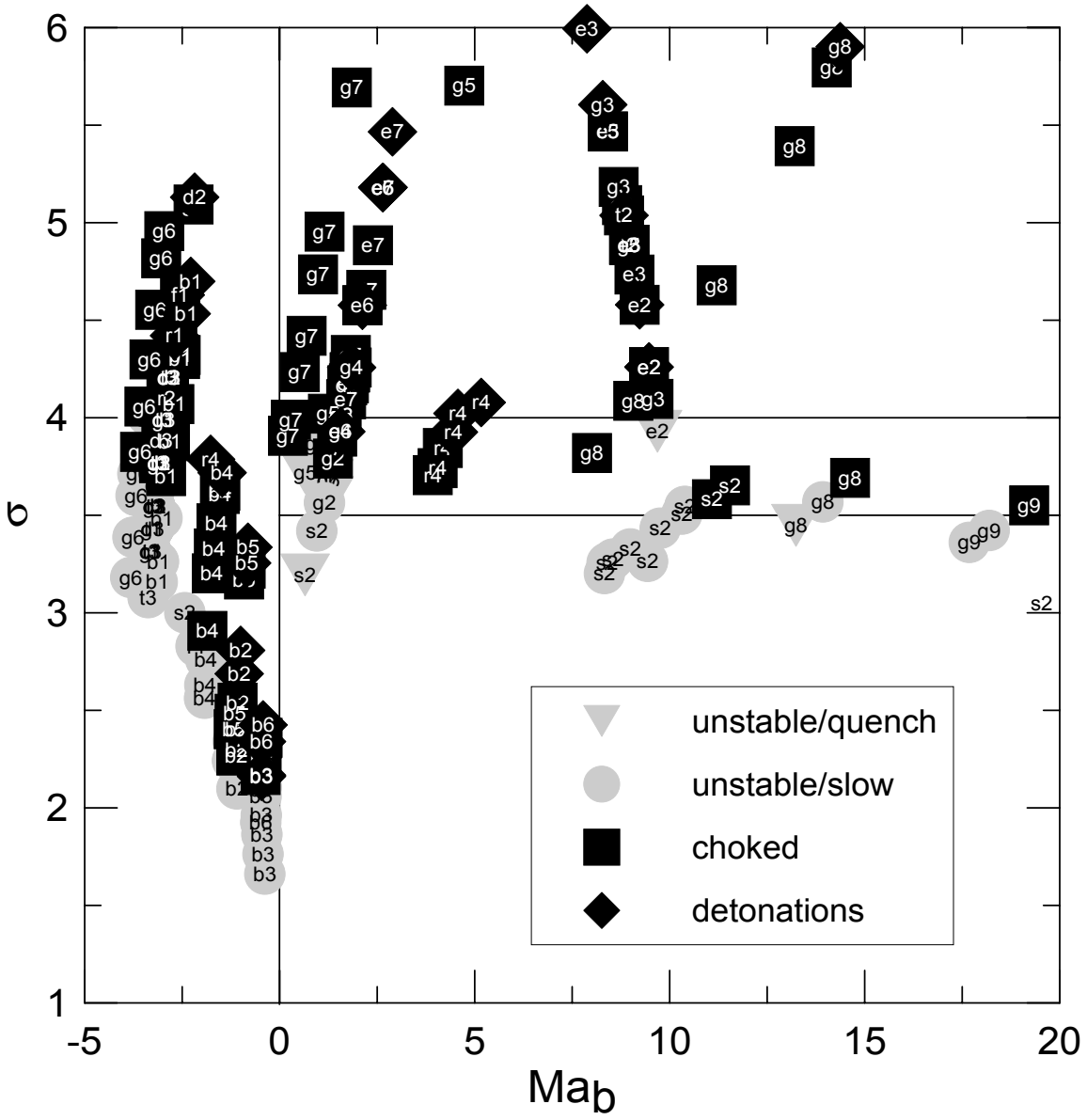

Figure 3.2.3-3 Resulting combustion regime as a function of expansion ratio σ and Ma_b. Black points represent fast combustion regimes, and gray points represent slow combustion regimes.

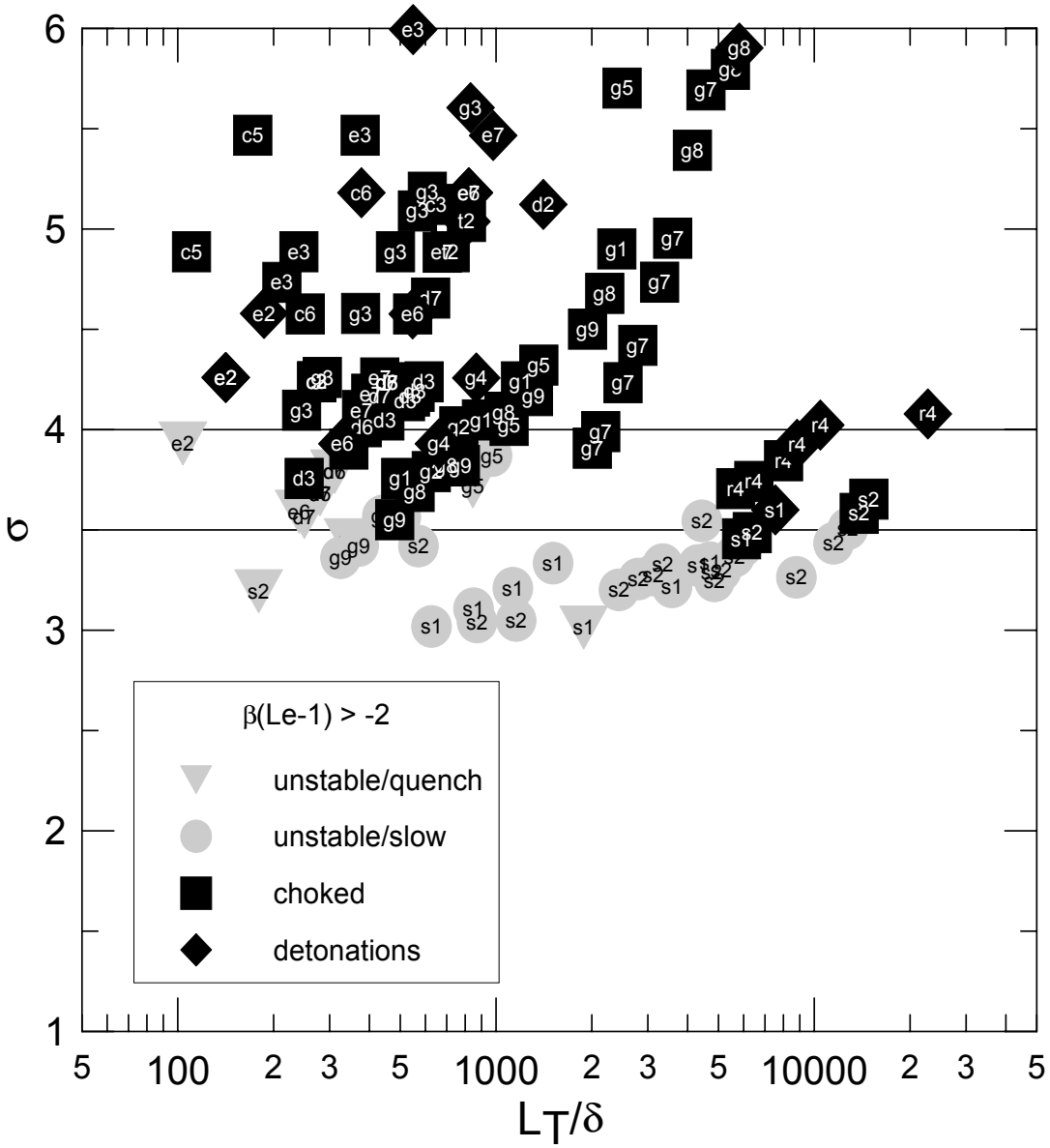

Figure 3.2.3-4 Resulting combustion regime as a function of expansion ratio σ and scale ratio L/δ for mixtures with $\beta(Le - 1) > -2$. Black points represent fast combustion regimes, and gray points represent slow combustion regimes.

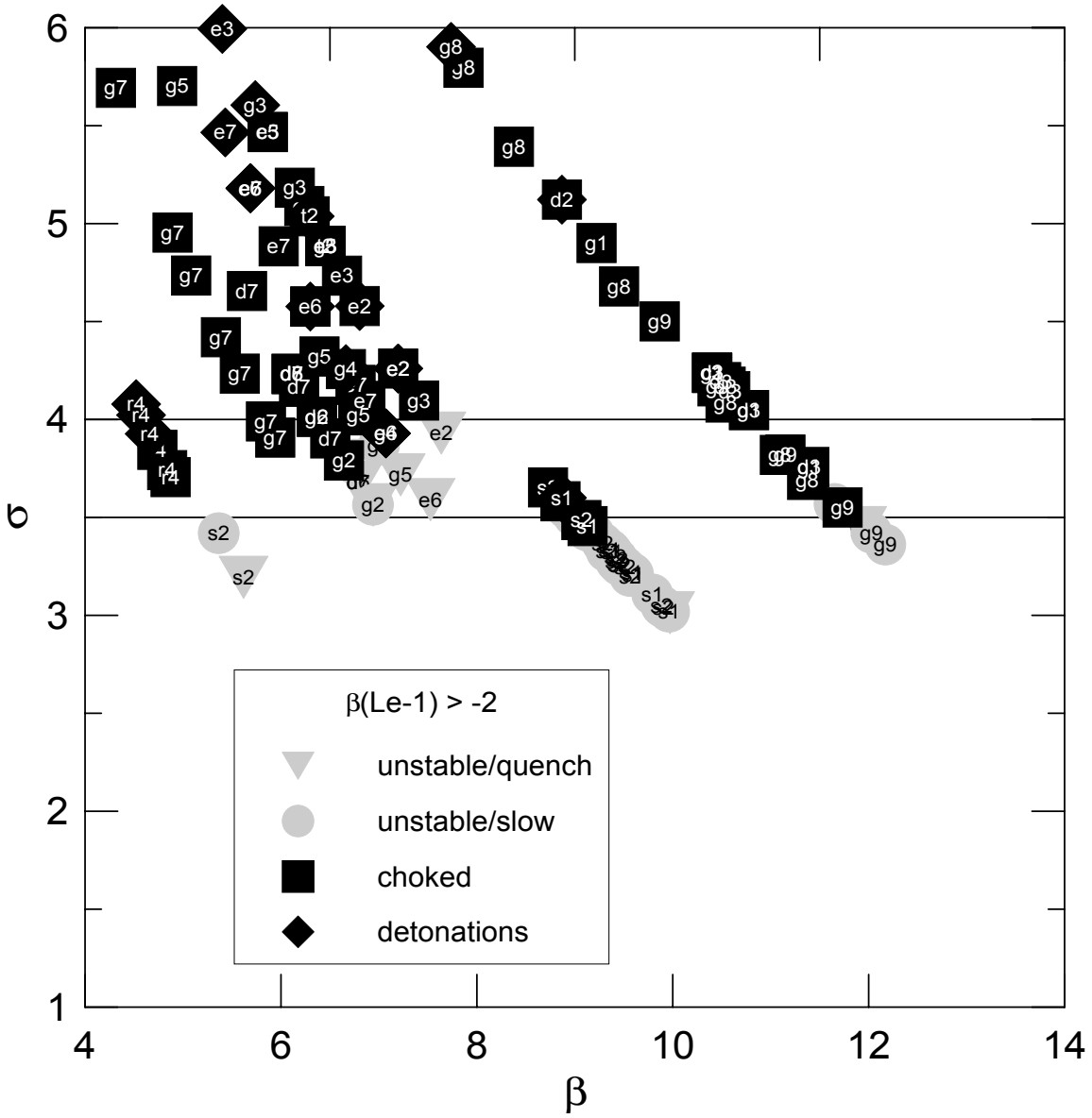

Figure 3.2.3-5 Resulting combustion regime as a function of expansion ratio σ and Zeldovich number β for mixtures with $\beta(Le - 1) > -2$. Black points represent fast combustion regimes. and gray points represent slow combustion regimes.

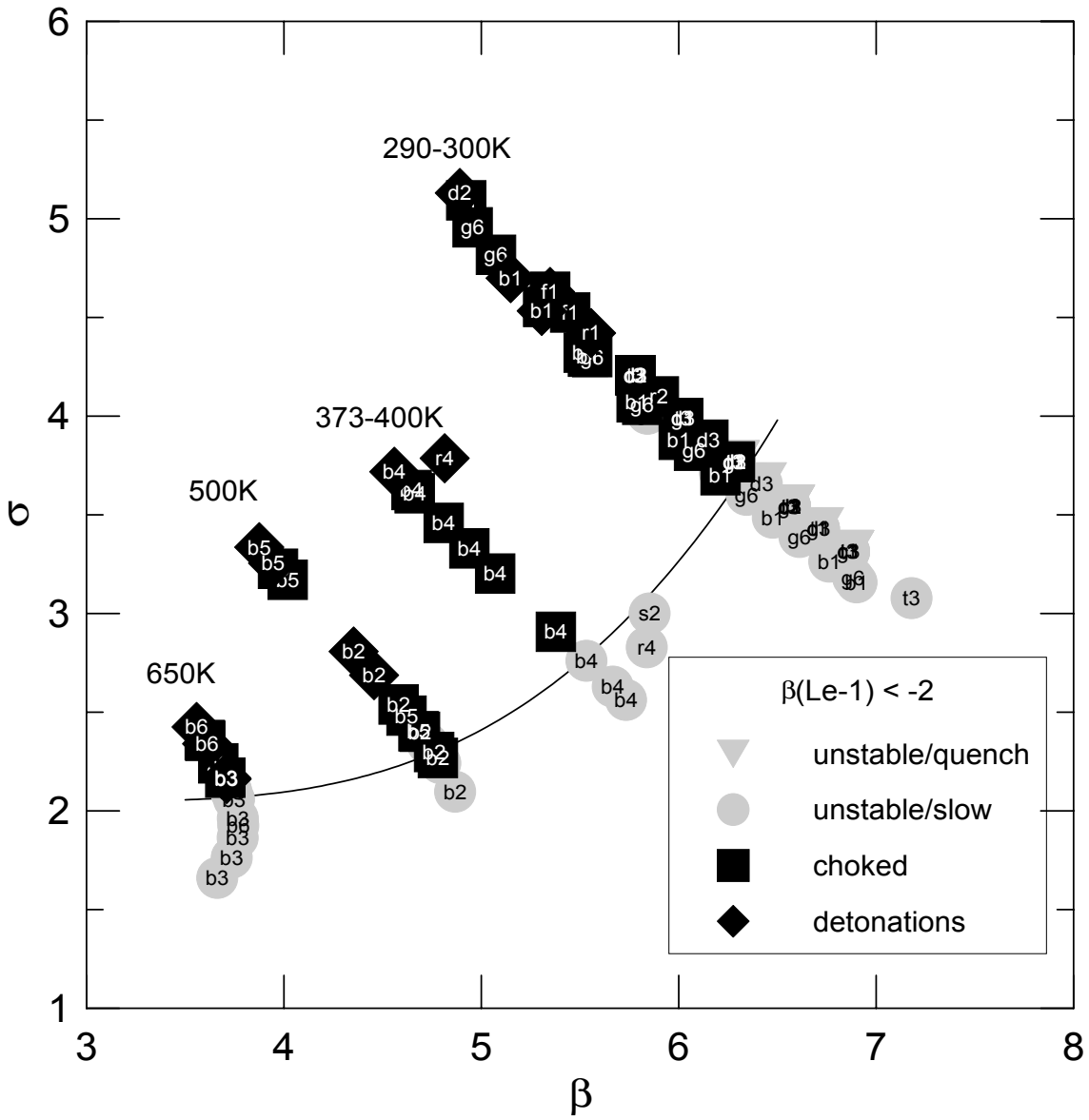

Figure 3.2.3-6 Resulting combustion regime as a function of expansion ratio σ and Zeldovich number β for mixtures with $\beta(Le - 1) < -2$. Black points represent fast combustion regimes, and gray points represent slow combustion regimes. Groups of points are marked with values of initial temperatures for hydrogen-air-steam mixtures.

3.2.4 Applications of σ - Criterion and Corresponding Uncertainties

To apply the criteria stated in Equations (3.5) and (3.6), values of β and *Le* are required for each particular mixture. First of all, the value of $\beta(Le-1)$ should be estimated. For mixtures typical of containment atmospheres (hydrogen-air-steam) such estimates [3.10] suggest that H_2-lean mixtures are characterized by $\beta(Le - 1) < -2$ and H_2-rich and stoichiometric ones by $\beta(Le - 1) > -2$. Mixtures close to stoichiometry on the lean side with equivalence ratio ϕ from 0.7 to 1.0 (depending on initial temperature and steam concentration) are at the border $\beta(Le - 1) = -2$.

Thus for H_2-rich and stoichiometric hydrogen-air-steam mixtures, the condition expressed in Equation (3.6) should be applied to estimate limits of effective flame acceleration. For H_2-lean hydrogen-air-steam mixtures, limits for effective flame acceleration are expected to depend on β, and, hence, on initial temperature.

To calculate β, the values of effective activation energy *Ea* and T_b in addition to T_u are required. Thermodynamic calculations provide data on T_b for each particular mixture (equilibrium temperature of combustion products at constant pressure). Effective activation energy *Ea* can be estimated from dependence of laminar flame speed on T_b. For lean hydrogen-air-steam mixtures, such estimates give an average value of $Ea/R \approx 9800$ K (for rich mixtures $Ea/R \approx 17700$ K) [3.10]. These estimates and a correlation shown in Figure 3.2.3-6 provide data for determination of flame acceleration limits in terms of mixture compositions.

There are some uncertainties connected with estimations of flame acceleration limits. First of all, it should be stressed once more that the criteria expressed in Equations (3.5) and (3.6) represent necessary but not sufficient conditions for effective flame acceleration. Other requirements should be met as well so that the flame propagation can result in formation of fast combustion regimes. The most important of them are the requirements of a large-enough scale (flame propagation distance) and favourable geometry (obstructions) for effective flame acceleration.

Another type of uncertainty is connected with a spread of critical σ-values. For rich mixtures, it is given by the range from 3.5 to 4.0 for σ*. It should also be noted that no experimental data are available for rich hydrogen-air-steam mixtures at $T_u > 383$ K. Additional experiments are required to evaluate the limit expressed in Equation (3.6) for rich mixtures at $T_u > 383$ K.

A considerable spread in limiting σ-values (3.5 ÷ 4.0) may be connected with an influence of additional parameters on effectiveness of flame acceleration. In particular, the laminar flame Mach number S_L/c_{sr} may play a role. An accurate estimation of the possible influence of this parameter is difficult because no reliable data on S_L are available for some of mixture compositions. In view of this, definition of critical conditions in terms of σ (even taking into account the spread of critical values) should be considered as more reliable because σ-values are only given by thermodynamic mixture properties.

For lean mixtures, the error of limiting σ-values (Figure 3.2.3-6) can be estimated as ±4%, which results, for example, in the σ*-range from 2.7 to 2.9 for $\beta \approx 5.5$ ($T_u \approx 400$ K). If hydrogen-air-steam mixtures are considered without additional components or dilution (e. g., CO_2, N_2, CO, etc.), the unavoidable uncertainty connected with determination of *Ea* (and, hence, β) can be eliminated by using limiting $\sigma^*(T_u)$-values from Figure 3.2.3-1 instead of those from Figure 3.2.3-6. In other cases, the critical condition in form of $\sigma^*(\beta)$ is preferable, and uncertainty in β-value should be taken into account.

A third type of uncertainty is connected with a border between stable and unstable flames $\beta(Le - 1) = -2$. The exact location of this border (in terms of the mixture composition under given initial conditions) is difficult to define because of inevitable errors in determination of *Le* and β. What is also unclear is how sharp the difference is in limiting conditions for mixtures that are close to this stability boundary. No experimental data are available for mixtures with $\beta(Le-1)$ from -2.2 to -1.3 in Figures 3.2.4-1 to -6. Additional analysis and, probably, experiments are necessary to clarify the critical conditions for mixtures with equivalence ratios ϕ in the range from 0.7 to 1.0.

Limits of flame acceleration for hydrogen-air-steam mixtures at T = 375 K and p = 1 atm and corresponding uncertainties are shown as an example in Figure 3.2.4-1. The limits are presented using hydrogen concentration in a dry mixture (H_2(dry) = H_2/(H_2+air), vol %) and steam concentration (vol %) as variables.

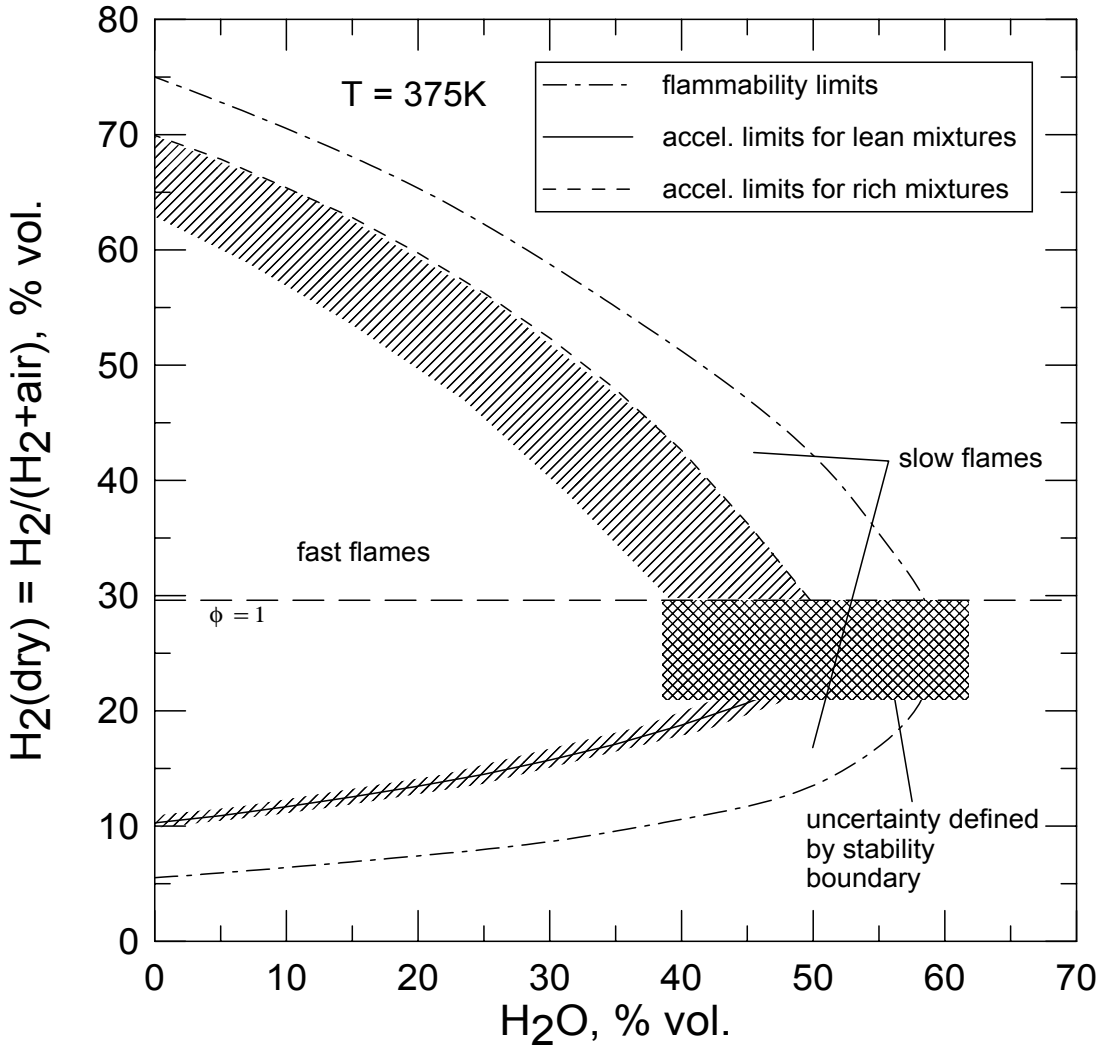

Figure 3.2.4-1 Limits of flame acceleration for hydrogen-air-steam mixtures at T = 375 K and p = 1 atm. Ranges of uncertainties are shown by shadow areas.

The uncertainties discussed above can be taken into account by using conservative estimates, that is, by using the minimum σ*-values for each set of initial conditions. Additional experiments and analysis can help in narrowing the range of uncertainties in application of the σ-criterion.

3.3 Necessary Criteria for DDT

Useful practical information can be obtained if one addresses separately different phases of DDT, namely the creation of conditions for DDT (Phase 1) and the onset of detonations (Phase 2). For each of these phases, the necessary conditions may be formulated, which provide a number of DDT criteria for practical applications. These criteria give necessary but not sufficient conditions. If some or all of them are satisfied, it does not mean that detonation should certainly be initiated. There are probably other requirements that should also be met. However, if one of the necessary criteria is not satisfied, detonation should not be expected. This important point gives simple estimates from a conservative side for accident analysis.

3.3.1 Detonability Limits

The detonability limits of a reactive mixture are the critical conditions for the propagation of self-sustained detonation. The critical conditions denote both the initial and boundary conditions of the explosive mixture. If a self-sustained detonation propagation is not possible, DDT cannot be expected. In this view, the detonability limits can be considered as a "first level" of DDT criteria.

A detailed discussion of detonability limits can be found in several reviews (see e. g., [3.17-3.19]). Here we will just mention some important values. The limit for stable detonation propagation in a cylindrical smooth-walled tube (limiting tube diameter) is estimated to be $D^* = \lambda/\pi$. For wide planar channels with height H much smaller than the width W, the channel width should accommodate at least one detonation cell for stable detonation propagation $W^* = \lambda$.

3.3.2 Criteria for Phase 1 of DDT

It is generally considered that processes of DDT can be divided into two main phases. Phase 1 involves a variety of processes that create conditions for the onset of detonations. Phase 2 is the actual process of detonation formation − the onset of detonations. A number of requirements have been found that are necessary to provide conditions for DDT (Phase 1 of the process).

3.3.2.1 Fast flame requirement

It was shown that turbulent flames should accelerate to result in 'choked' or 'sonic' combustion regime to produce conditions for the onset of detonations [3.19, 3.20]. Flame speeds in laboratory flame are close to isobaric sound speeds in combustion products (about 500 to 1000 m/s) in this combustion regime. The results obtained recently show that no DDT was observed; indeed, in some cases a flame did not accelerate to a nearly choking regime. The necessary criterion may be formulated that the flame should be accelerated to result in a fast, nearly choking, combustion regime to make DDT possible. Thus the σ criterion for flame acceleration described in Section 3.2 can also used as one of the necessary conditions for DDT.

3.3.2.2 Critical flame Mach numbers

Because different initial conditions − in terms of mixture composition, temperature, and pressure— are relevant for nuclear safety, the definition of critical flame speeds in absolute values cannot be satisfactory. The flame Mach number (flame speed normalized by sound speed in uncompressed mixture) represents a parameter that is more relevant for a variety of initial conditions. The Mach number of choked flames is about 2. Recently, a series of tests was conducted [3.21] to determine the critical values of flame Mach numbers for DDT in a variety of hydrogen-air steam mixtures. The minimum value of 1.5 was found for the most-sensitive mixture used in the tests [3.21].

3.3.2.3 Minimum shock Mach numbers

The requirement of the development of a relatively fast combustion regime prior to DDT is connected with the necessary creation of a local explosion somewhere in the flow that includes flame brush and a system of shocks ahead of the flame. The faster the flame, the stronger the shocks generated, and consequently the more effective is the turbulent mixing of products and reactants, thereby promoting initiation of a localized explosion. One of the important mechanisms (but not the only one) that causes localized explosions to occur is connected with shock reflections from obstacles. Although mild ignitions in reflections are the intrinsic feature of propagating fast deflagration waves, strong ignitions can lead to formation of detonation wavelets, which in certain conditions can result in fully developed detonations.

To provide initiation of localized explosion in reflections, the flame should be able to generate a shock wave with some critical Mach number. A number of tests were made [3.22, 3.23] to determine the critical shock Mach numbers that are capable of giving strong ignition in reflections. The composition of mixtures and the configuration of reflectors were varied. More recently, critical shock Mach number experiments were conducted at a larger scale (FZK tube, 350 mm id) [3.24] compared with studies described in References [3.22 and 3.23].

The following conclusions can be made, to summarize the results of critical Mach number experiments in hydrogen-containing mixtures:

1. Shock (blast) waves with Mach numbers $M < 1.2$ cannot cause the secondary ignition being reflected from focusing surfaces and obstacles.

2. Shock (blast) waves with $1.2 < M < 1.4$ can cause secondary ignition in reflections from focusing surfaces and obstacles, thus favouring escalation of the explosion.

3. Shock (blast) waves with $M > 1.4$ can cause initiation of detonations in the vicinity of reflecting surfaces.

4. Scale affects the possibility of the initiation of detonation in shock-wave reflections. Usually, the critical Mach numbers for initiation of local detonations decrease as the scale increases.

No model is currently available that is able to adequately describe the mutual influence of shock strength, mixture properties, and scale on possibility of detonation initiation in reflections. The experimental data on detonation initiation in shock-wave reflections should help to develop and verify detailed models of DDT phenomena.

3.3.3 *Criteria for Onset of Detonations*

3.3.3.1 Minimum tube diameter criterion ($d > \lambda$)

A detailed study of DDT in tubes was conducted at McGill University [3.19, 3.20]. Flame acceleration and transition to detonation were studied in tubes having an internal diameter of 5 to 30 cm, and with orifice plates installed inside the tubes. Blockage ratio (BR), fuel type, and mixture composition were variables in these experiments. Detonation cell size, λ, was used to characterize the sensitivity of the mixture to detonation initiation. This means that different mixtures were compared on the basis of the value of the cell size. It was found that, for an optimum blockage ratio of BR = 0.43, a size of the unobstructed passage, d, of more than 1λ is necessary for transition to detonation. This criterion can be used as the necessary condition for DDT in obstructed channels. However, it is only applicable for very long channels, having a length of more than 10 to 20 times their width.

Long channels with or without obstacles are not typical of the geometry of containment buildings. A chain of connected compartments could principally represent a similar geometry. However, even for long channels, the critical value of *d* appeared to depend on obstacle configuration (see Table 3.3.3-1). The critical ratio d/λ increases with a decrease of obstacle spacing and with an increase of blockage ratio, BR. DDT is easier to achieve for a smaller BR and for a greater distance between obstacles. Variations of critical d/λ can be quite large, ranging from 0.8 to 5.1. Despite the obvious limitations of the criterion for long channels ($d > \lambda$), it gives an important indication of the effect of geometrical scale on the transition to detonation. The detonation cell size, λ, increases with changes of the mixture composition below and above stoichiometry. Consequently, the larger the scale the wider is the composition range for DDT.

Table 3.3.3-1 Critical conditions for DDT in channels and tubes having different configuration of obstacles

BR	Channel width *W*, mm	Channel height *H*, mm	Unobstructed passage *d*, mm	Obstacle spacing, mm	Maximum λ for DDT, mm	d/λ	Reference
0.43	16	57	31.6	50.56	8.8	3.6	[3.25]
0.43	16	57	31.6	101.12	11.7	2.7	[3.25]
0.43	50*		37.4	50	31	1.2	[3.26]
0.43	150*		114	150	100	1.1	[3.26]
0.43	300*		226	300	190	1.2	[3.26]
0.45	61.8	55.4	30	32.1	13	2.3	[3.27]
0.45	61.8	55.4	30	64.2	20	1.5	[3.27]
0.45	61.8	55.4	30	128.4	36	0.8	[3.27]
0.3	350*		293	525	220	1.3	[3.9]
0.6	350*		220	350	44	5.1	[3.9]

*) Tube diameter

3.3.3.2 Minimum scale requirement for onset of detonations

A number of studies focused on the analysis of the processes involved in the second phase of DDT – the onset of detonations. It was assumed that necessary conditions for generation of localized explosion (Phase 1) are met, and the process of the actual formation of a detonation wave was studied. It was shown that several factors can influence the process of detonation formation. First, a local distribution of mixture properties (auto-ignition delay time) in a sensitized region should provide coupling of chemical and gas dynamic processes that result in the formation of an explosion wave [3.28-3.30]. Second, this wave should survive propagating from a sensitized to an unpertubed mixture [3.31-3.34]. Finally, the explosion wave should be adjusted for a chemical length scale of the ambient mixture. The latter, naturally, gives a measure for the minimum size of the sensitized region, which is necessary for the formation of detonation.

Numerical and analytical studies were conducted to determine the minimum size of the sensitized region [3.31-3.35]. Critical conditions for detonation formation in a locally sensitized mixture were studied. A sensitized region was modelled by temperature distributions [3.31-3.33], addition of a fast reactive component [3.31-3.33], and mixed products and reactants [3.34]. The problem of the propagation of an explosion wave through reactivity gradients was also studied analytically as a separate problem [3.35].

The main results of these studies are summarized here: the minimum size of a sensitized region is required for the onset of a detonation; this size depends on the properties of the mixture surrounding the sensitized region; and a characteristic length scale for this process is of the order of 10λ, in terms of detonation cell width, λ, of the unperturbed mixture. Some details of the detonation formation process may influence the minimum size for detonation onset. A decrease of the volumetric energy content in the sensitized region (e. g., for temperature non-uniformities), results in the minimum size increase. In the opposite case of the detonation onset in a locally pre-compressed region (e. g., for auto-ignition from shock reflections), detonation onset is facilitated. In cases of detonation formation as an expanding wave (e. g., spherical symmetry), the minimum size was found to be increased because of curvature effects. A combination of the above factors is typical for DDT events. It is hardly possible, thus, to define a universal criterion for the onset of detonations. However, an engineering estimate for practical applications has been suggested [3.13, 3.31-3.33], assuming that a detonation is developed initially as a planar wave, volumetric energy content is uniform, and typical fuel-air mixtures are considered. With these assumptions, the minimum macroscopic size of sensitized mixture for detonation onset was estimated to be about 7λ.

The results of numerical studies described above were obtained using some types of one-dimensional (1D) models for detonation formation in nonuniform mixtures. Obvious limitations of 1D models limit the reliability of their predictions, especially that of quantitative character. In view of this, it is important to mention some recent experimental results, which confirm, generally, the main conclusions of these calculations.

A series of experiments [3.36] was conducted to study critical conditions for propagation of explosion waves through reactivity gradients. Propagation of a detonation wave from a donor mixture through a gradient region to a less-reactive acceptor mixture was studied using hydrogen-air mixtures in a 174-mm tube. The length of the donor mixture, the width of the gradient region Δx, and the reactivity of acceptor mixture were varied in the tests. It was shown that a critical sensitivity gradient $(\Delta\lambda/\Delta x)^*$ ($\Delta\lambda$ is the difference in cell sizes between acceptor and donor mixtures) may be defined, which determines a possibility of detonation decay in the gradient region. Detonations decayed in the gradient region, in the cases of $(\Delta\lambda/\Delta x) > (\Delta\lambda/\Delta x)^*$. It was also found that the critical value of $(\Delta\lambda/\Delta x)^*$ depends significantly on the difference in energy densities of donor and acceptor mixtures. The more energetic the donor mixture was compared with the acceptor mixture, the sharper (greater ($\Delta\lambda/\Delta x)^*$) was the critical gradient for detonation decay. Extrapolation of the experimental results to the uniform energy density resulted in critical values of $(\Delta x/\Delta\lambda)^* \approx 10$. These experimental data, thus, appeared to be in accord, qualitatively, with the results of numerical calculations described earlier in this section. The critical values of the gradient for hydrogen-air mixtures appeared also to be in a reasonable quantitative agreement with the calculations.

Another aspect of the numerical and analytical predictions for the minimum size of a gradient region for detonation initiation concerns the effect of symmetry (initiation of spherical detonations). Recent results of turbulent jet initiation experiments [3.37] showed that the minimum requirement for initiation of spherical detonations by turbulent jet (in the absence of confining structure effects) may be expressed as $D_{jet} > 24\lambda$, where D_{jet} is the orifice size of the initiating jet. This is about 3 times as much as what should be expected for initiation of a planar wave (10λ) in accordance with results of numerical and analytical models.

These data support the results of theoretical analyses of main features of spontaneous onset of detonations in a sensitized mixture region. They show once more that some minimum size of the sensitized (or gradient) region is required for the onset of detonation. These results show, also, that the order of magnitude for the minimum size is about 10λ (λ corresponds to the surrounding mixture), and that this size can vary from several λ to several tenths of λ depending on particular conditions. In

such a situation, a detonation onset criterion, which is aimed at describing the effect of scale with an accuracy better than an order of magnitude, should be primarily based on appropriate experimental correlations.

In the discussion presented here, the detonation cell size was used as a measure of mixture sensitivity. This allows scaling of DDT conditions found for different mixtures and compositions. The cell size data themselves are available for conditions typical of severe accidents. The data and corresponding interpolation methods are described in Appendix D. It should be noted, however, that the cell size cannot be considered as a fundamental mixture property. Its application as a scaling parameter should be validated experimentally. Fortunately, for mixtures typical of containment atmospheres (H_2-air, H_2-air-H_2O, H_2-air-CO_2 at normal and elevated initial temperatures), the detonation cell size has shown to be a reliable scaling parameter [3.38-3.42]. Corresponding details are given in Section 3.3.4.

3.3.3.3 L/λ-correlation (7λ criterion)

In order to formulate a criterion for the onset of detonations that describes the effect of scale, a definition of a *characteristic geometrical size L* of an enclosure is necessary. The size *L* should give a measure of the possible macroscopic size of a sensitized mixture where detonations might originate and develop. A requirement for this size to be large enough compared with the detonation cell size of the mixture can form the necessary detonation onset criterion. Originally [3.13, 3.32, 3.42, 3.43], such a criterion was formulated as $L > 7\lambda$, where *L* was defined as a characteristic (average) size of a room filled with combustible mixture (or the size of a mixture cloud). Experimental data generally showed a good agreement with $L > 7\lambda$ criterion over a wide range of scales and mixture compositions.

Despite a general agreement of the $L > 7\lambda$ criterion with experimental data, definitions for the characteristic size *L* used in References [3.13, 3.32, 3.42, and 3.43] were not always unambiguous, especially for practical applications. It was more or less established that good correlations were observed for rooms (or mixture clouds) with relatively small aspect ratios, where the size *L* could be easily defined as a sort of average of the corresponding geometrical sizes. An appropriate and clear definition of *L* for chains of connected rooms (or tubes with obstacles) was not derived in References [3.13, 3.32, 3.42, and 3.43]. Practical analyses of containment buildings showed that a system of connected rooms requires a special attention as the most typical geometry. In addition, a large amount of new experimental data was obtained recently, especially for DDT in obstructed channels. All these factors indicated that an additional analysis of the L/λ-correlation is of interest for practical applications.

The L/λ-correlation was reconsidered in Reference 3.44, in terms of a system of connected rooms. It was assumed that a characteristic size L_1 for a single room is the average size from two maximum room sizes. Such a definition showed a good correlation in earlier analyses, and provides a certain conservatism for rooms with large aspect ratios. We need to notice that the results of correlations are not very sensitive to the definition of the characteristic size of a single room. The average size, or the cubic root from the room volume, gives very close results for available experimental data.

Thus for single room it was assumed that

$$L_1 = (S + H)/2 \,, \tag{3.7}$$

where *H* and *S* are room height and length respectively (which are greater than room width *W*). It was suggested that if room 1 is connected with room 2 through some opening, the characteristic size *L* of the system of rooms 1 and 2 is defined by

$$L = L_1 + \alpha L_2 \,, \tag{3.8}$$

where L_1 and L_2 are characteristic sizes of room 1 and 2 respectively, and α is a parameter that describes the size of the opening between rooms. A large database on DDT conditions in obstructed channels and tubes can be used to find an appropriate definition for the parameter α. For long channels with repeated obstacles (which can be considered as a chain of rooms, all with characteristic sizes equal to L_1) one can obtain instead of Equation (3.8) the following form:

$$L = L_1 + \alpha(L_1 + \alpha(L_1 + \ldots)) , \tag{3.9}$$

or

$$L = L_1 + \alpha L . \tag{3.10}$$

Thus characteristic size for the channel with obstacles appeared to be given by

$$L = L_1/(1-\alpha) . \tag{3.11}$$

A comparison with experimental data for DDT in channels and tubes was made assuming different definitions for α, namely, $\alpha = (d/D)^{1/2}$, $\alpha = d/D$, and $\alpha = (d/D)^2$, where d is unobstructed passage, and D is tube diameter (or channel height $D = H$). It was found that the best correlation was observed for α defined as

$$\alpha = d/D . \tag{3.12}$$

Such a definition (Equations (3.7), (3.11), and (3.12)) for the characteristic size L is qualitatively in accord with observations that detonation onset is facilitated in obstructed channels with increase of d/D (decrease of blockage ratio) and with increase of obstacle spacing. Indeed, for the same D, L increases with increase of S and d/D. Moreover, the critical ratio L/λ for DDT appeared to be nearly constant for different configurations of obstacles and close to 7, as was suggested in the earlier studies [3.13, 3.32, 3.42, 3.43].

The characteristic size L of obstructed channels has clear geometrical interpretation, especially for cases of $S = H$. This observation is illustrated by Figure 3.3.3.3-1.

It should be noted that the definition for L (Equation (3.11)) has a singularity for $\alpha = 1$. This singularity leads to large increase of L for α close to unity (small BR). Such a singularity can be easily avoided by limiting the range of application of Equation (3.11) for the cases with large-enough values of BR, for example, BR > 0.1. In cases BR ≤ 0.1, the system of connected rooms can be considered as a single room with L defined by Equation (3.7).

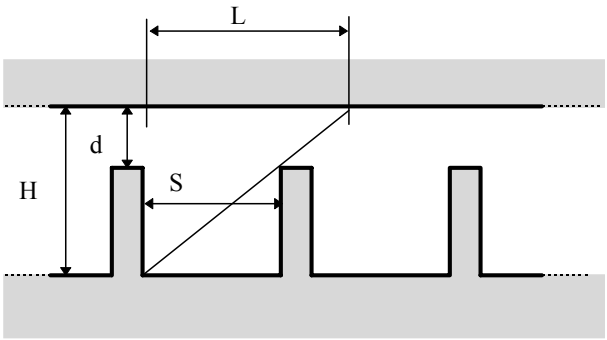

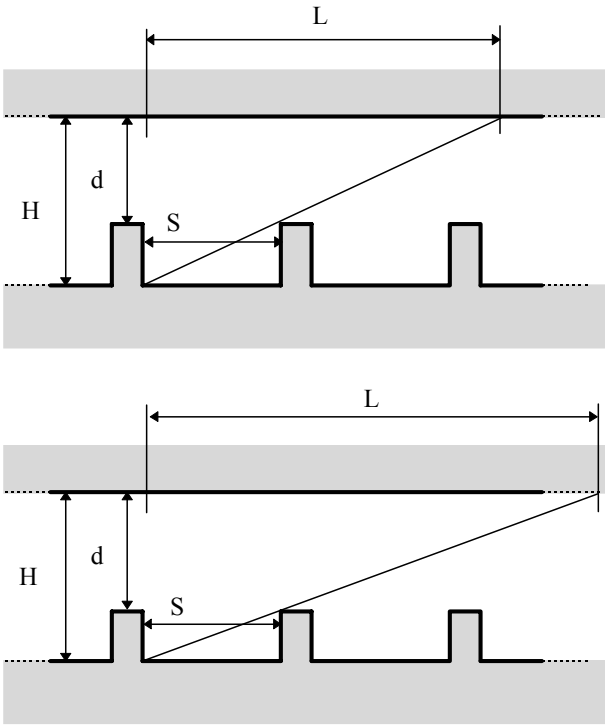

Figure 3.3.3.3-1 Graphical illustration of characteristic size L for channels with obstacles and its changes with blockage ratio.

3.3.3.4 Comparison of $d > \lambda$ and L/λ Criteria

Both the minimum tube diameter and the L/λ criteria are based on comparison of characteristic geometrical sizes of an enclosure with the characteristic chemical length scale λ of the mixture. Applications of these criteria are limited by reliability of λ as a scaling parameter for a particular range of mixtures and initial conditions. This aspect should be verified first against an appropriate set of experimental data. The difference between these criteria is due to different definitions of characteristic geometrical sizes. In the $d > \lambda$ criterion, the minimum transverse size of unobstructed passage in a channel is required for onset of detonation. In the L/λ criterion, the minimum distance for detonation formation is required. These requirements, thus, do not contradict each other and may be considered as complimentary. The first approach ($d > \lambda$) is applicable to long channels with obstacles. The second one (L/λ), principally, allows us to address a wider range of typical geometrical configurations should an appropriate correlation be obtained.

3.3.4 Experimental Correlations for Detonation Onset Criteria

A considerable database has been accumulated in literature on limiting conditions for DDT. This database includes the McGill University small-scale tests on DDT [3.25-3.27], experiments in the FLAME Facility [3.15], BNL tests [3.11] and Whiteshell Laboratories (AECL) data [3.21]. Recently, large-scale DDT experiments with hydrogen-air, hydrogen-air-steam, and hydrogen-air-CO_2 mixtures were conducted at Russian Research Centre 'Kurchatov Institute' [3.13, 3.14, 3.38-3.40, 3.44, 3.45] in the RUT facility. Experiments were also made in MINIRUT experimental apparatus at scale 1:50 of RUT facility [3.45, 3.46]. New data on DDT conditions were also obtained in obstructed channels with transverse sizes 80, 174, 350, 520 mm [3.8, 3.9] for a wide range of hydrogen mixtures.

In this section, the detonation onset criteria are examined by comparison with this set of experimental data on DDT conditions.

3.3.4.1 Cell size as scaling parameter

Reliability of detonation cell size as a scaling parameter for detonation onset conditions can be estimated without any reference to DDT criteria. For that, critical values of λ for the onset of detonations should be compared in similar geometrical configurations and for different mixtures and scales. For hydrogen-air mixtures at relatively small scales, this comparison has already been done in the database [3.25-3.27] that summarizes a series of DDT experiments in tubes. It was also shown by results of DDT tests at BNL [3.11] for hydrogen-air-steam mixtures at initial temperatures up to 650 K.

A comparison of the critical λ values may be made also for a large range of scales and geometrical configurations on the basis of the RUT and MINIRUT tests, including

- hydrogen-air, hydrogen-air-steam, hydrogen-air-CO_2 mixtures at large scale;

- two typical geometrical configurations (obstructed channel and room); and

- two 50 times different scales.

Data of Tables 3.3.4.1-1 and 3.3.4.1-2 and Figures 3.3.4.1-1 and 3.3.4.1-2 show that the critical values of λ are similar for different mixtures and initial conditions at the same scale and geometrical configurations. The ratio of the critical λ-values is indeed close to the ratio of scales for tests with similar geometry.

It may be concluded that for the range of scales, mixtures, and initial conditions tested, detonation cell sizes can be used as a reliable scaling parameter for characterization of the detonation onset conditions.

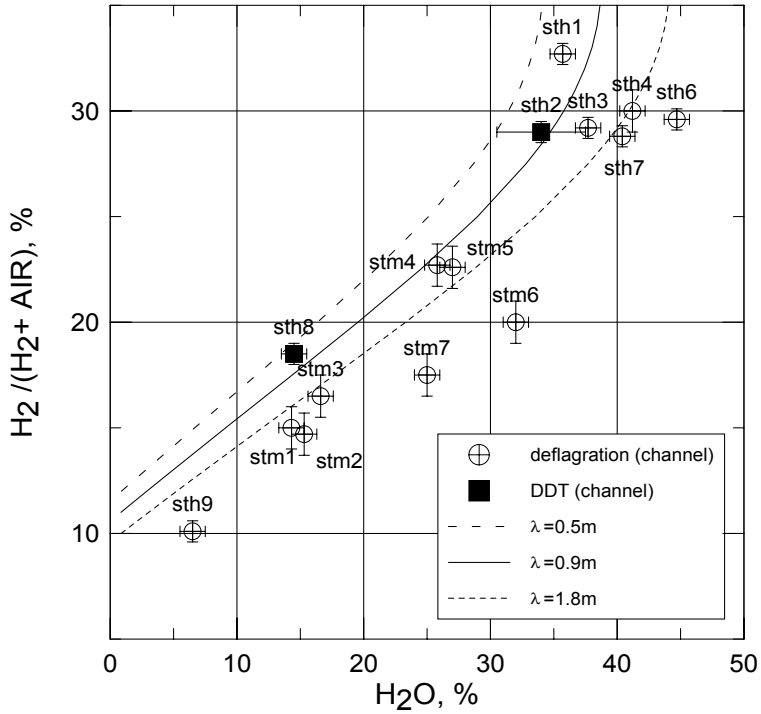

Figure 3.3.4.1-1 Combustion mode as a function of hydrogen (dry) and steam concentrations in an obstructed channel of the RUT Facility

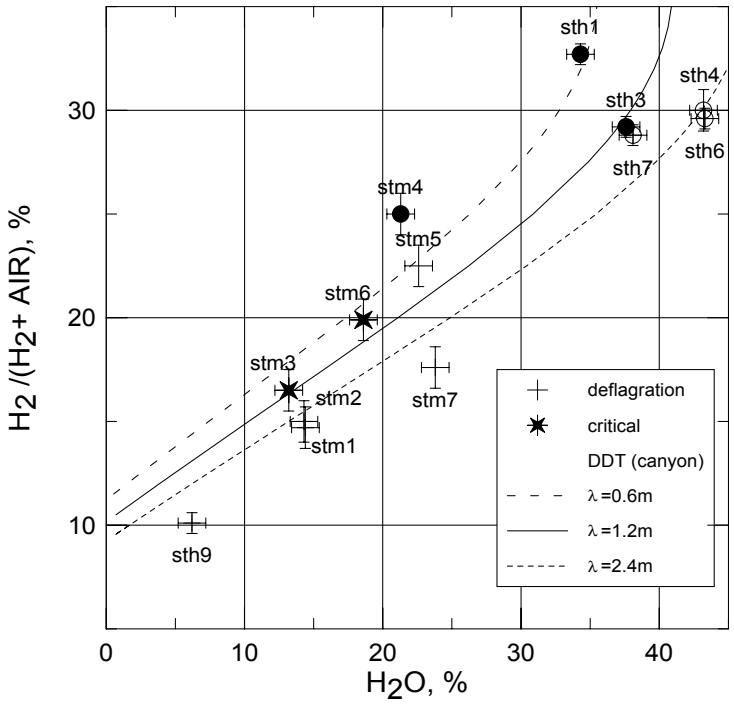

Figure 3.3.4.1-2 Combustion mode as a function of hydrogen (dry) and steam concentrations in a room (canyon) of the RUT Facility

Table 3.3.4.1-1 Critical values of λ for detonation onset at large scale (RUT facility)

Mixtures	Channel geometry	Room geometry
H_2/air at 285 K	-	≈1 m
H_2/air/H_2O at 375 K	≈ 0.9 m	≈1.2 m
H_2/air/CO_2 at 285 K	0.7 - 0.9 m	0.9 - 1.2 m

Table 3.3.4.1-2 Critical values of λ for detonation onset at two different scales and similar geometry

	RUT	MINIRUT (scale 1:50)	$\lambda_{RUT}/\lambda_{MINIRUT}$
	λ, mm		
Channel	900	18	50
Room	1200	21-25	48-57

3.3.4.2 L/λ-correlation (7λ criterion)

Characteristic geometrical sizes L and detonation cell widths of combustible mixtures are compared here for each particular case of deflagration and DDT. The characteristic sizes, L, were calculated for each case according to Equations (3.7), (3.8), (3.11), and (3.12). Detonation cell sizes were determined using data presented in Appendix D. Experimental data used for the L/λ-correlation are listed in Table 3.3.4.2-1

The summary of experimental results is presented in Figure 3.3.4.2-1. Data are marked with labels given in Table 3.3.4.2-1. Figure 3.3.4.2-1 shows combustion modes (DDT or deflagration) as a function of characteristic geometrical size L, and detonation cell width λ. A good correlation is observed for $L/\lambda \approx 7$ within the accuracy of the cell size data over a wide range of scales. The minimum ratio of $L/\lambda = 5.6$ for few cases of DDT can be found among the general borderline of $L/\lambda \approx 7$ in the correlation presented in Figure 3.3.4.2-1. This is just a 20% deviation, which is much smaller than inaccuracy of the cell size data.

It should be noted once more that such a correlation can be only considered as a necessary but not a sufficient condition for DDT. If 7λ criterion is not satisfied (over the 7λ line in Figure 3.3.4.2-1), detonation cannot be expected. In the opposite case (below the 7λ line in Figure 3.3.4.2-1), development of combustion process can result in both detonation and deflagration regimes. Data for channels with BR = 0.1 (d1 and t4 data labels) show an example that 7λ-criterion does not give a sufficient condition for DDT. Onset of detonations was observed in this case for ratios L/λ considerably higher than 7. Flame acceleration was inefficient with BR = 0.1, flames accelerated until the end of the channel, but did not reach a velocity high enough for DDT. For BR > 0.1, the necessary requirement for development of fast flames was satisfied, and DDT was observed in cases where the scale was large enough for onset of detonations ($L > 7\lambda$).

The data presented here show that quite a good L/λ-correlation can be obtained for a variety of different geometrical configurations. Probably, such a correlation can be further improved by using better definitions for characteristic size L. We need to note, however, that the accuracy of the cell size data for severe accident conditions is not as good as the agreement observed in Figure 3.3.4.2-1. As shown in Appendix D, average uncertainty in the cell size estimation is given by a factor of 1.5, and

the maximum one can be more than a factor of 2. This should be taken into account in practical applications of the 7λ-criterion.

Table 3.3.4.2-1 Experimental data used in L/λ-correlation for onset of detonations

Data source	Label	Blockage ratio BR	Tube or channel size D (H), mm	Initial temperature T, K	Mixture type	Equivalence ratio ϕ
AECL [3.21]	a1	0.31	280	373	H_2/air/H_2O	
HTCF-BNL [3.11]	b1	0.43	273	300	H_2/air	<1
HTCF-BNL [3.11]	b2	0.43	273	500	H_2/air	<1
HTCF-BNL [3.11]	b3	0.43	273	650	H_2/air	<1
HTCF-BNL [3.11]	b4	0.43	273	400	H_2/air/H_2O	<1
HTCF-BNL [3.11]	b5	0.43	273	500	H_2/air/H_2O	<1
HTCF-BNL [3.11]	b6	0.43	273	650	H_2/air/H_2O	<1
CHANNEL-RRCKI [3.9]	c1	0.1	80	293	H_2/air	<1; >1
CHANNEL-RRCKI [3.9]	c2	0.3	80	293	H_2/air	<1; >1
CHANNEL-RRCKI [3.9]	c3	0.6	80	293	H_2/air	<1; >1
DRIVER-RRCKI [3.9]	d1	0.09	174	293	H_2/air	<1; >1
DRIVER-RRCKI [3.9]	d2	0.3	174	293	H_2/air	<1; >1
DRIVER-RRCKI [3.9]	d3	0.6	174	293	H_2/air	<1; >1
DRIVER-RRCKI [3.9]	d4	0.9	174	293	H_2/air	<1
FLAME-SNL [3.15]	f1	0.33	1830	293	H_2/air	<1
mini-FLAME-SNL [3.47]	f3	0.33	150	293	H_2/air	<1
FZK [3.9]	g1	0.6	350	293	H_2/air	<1; >1
FZK [3.9]	g2	0.6	350	293	$H_2/O_2/N_2$	1
FZK [3.9]	g3	0.3	350	293	H_2/air	1
FZK [3.9]	g6	0.6	350	293	H_2/air/CO_2	.5
FZK [3.9]	g7	0.6	350	293	H_2/air/CO_2	1
FZK [3.9]	g8	0.6	350	293	H_2/air/CO_2	2
FZK [3.9]	g9	0.6	350	293	H_2/air/CO_2	4
McGill [3.25]	m1	0.44	16 x 57 x 50	293	H_2/air	<1
McGill [3.25]	m2	0.44	16 x 57 x 100	293	H_2/air	<1
McGill [3.26]	m3	0.43	50	293	H_2, CH-fuels/air	<1
McGill [3.26]	m4	0.43	150	293	H_2, CH-fuels/air	<1
McGill [3.26]	m5	0.43	300	293	H_2, CH-fuels/air	<1
McGill [3.27]	m6	0.44	65 x 52 x 32	293	H_2, CH-fuels/air	<1
McGill [3.27]	m7	0.44	65 x 52 x 64	293	H_2, CH-fuels/air	<1
McGill [3.27]	m8	0.44	65 x 52 x 128	293	H_2, CH-fuels/air	<1
RUT-RRCKI [3.13]	r1	0.6	2250	293	H_2/air	<1
RUT-RRCKI [3.13]	r2	0.3	2250	293	H_2/air	<1
RUT-RRCKI [3.13]	r3	room	10.5 x 6 x 2.3 m	293	H_2/air	<1
RUT-RRCKI [3.14]	r4	room	10.5 x 6 x 2.3 m	375	H_2/air/H_2O	≤1
RUT-RRCKI [3.14]	r5	0.3	2250	375	H_2/air/H_2O	≤1
RUT-RRCKI [3.40]	r6	0.3	2250	293	H_2/air/CO_2	<1
RUT-RRCKI [3.40]	r7	room	10.5 x 6 x 2.3 m	293	H_2/air/CO_2	<1
RUT-RRCKI [3.45]	ri	room	15 x 6 x 2.3 m	293	H_2 -injection	≤1

continued . . .

Table 3.3.4.2-1 (concluded)

Data source	Label	Blockage ratio BR	Tube or channel size D (H), mm	Initial temperature T, K	Mixture type	Equivalence ratio ϕ
HDT-SNL [3.12]	s1	0.6	406	383	H_2/air	>1
HDT-SNL [3.12]	s2	0.3	406	383	H_2/air/H_2O	>1
TORPEDO-RRCKI [3.9]	t1	0.6	520	293	H_2/air	<1; >1
TORPEDO-RRCKI [3.9]	t3	0.3	520	293	H_2/air	<1; >1
TORPEDO-RRCKI [3.9]	t4	0.1	520	293	H_2/air	<1; >1
mini-RUT-RRCKI [3.44]	v1	0.3	46	293	H_2/air	<1
mini-RUT-RRCKI [3.44]	v2	room	210 x 120 x 50	293	H_2/air	<1

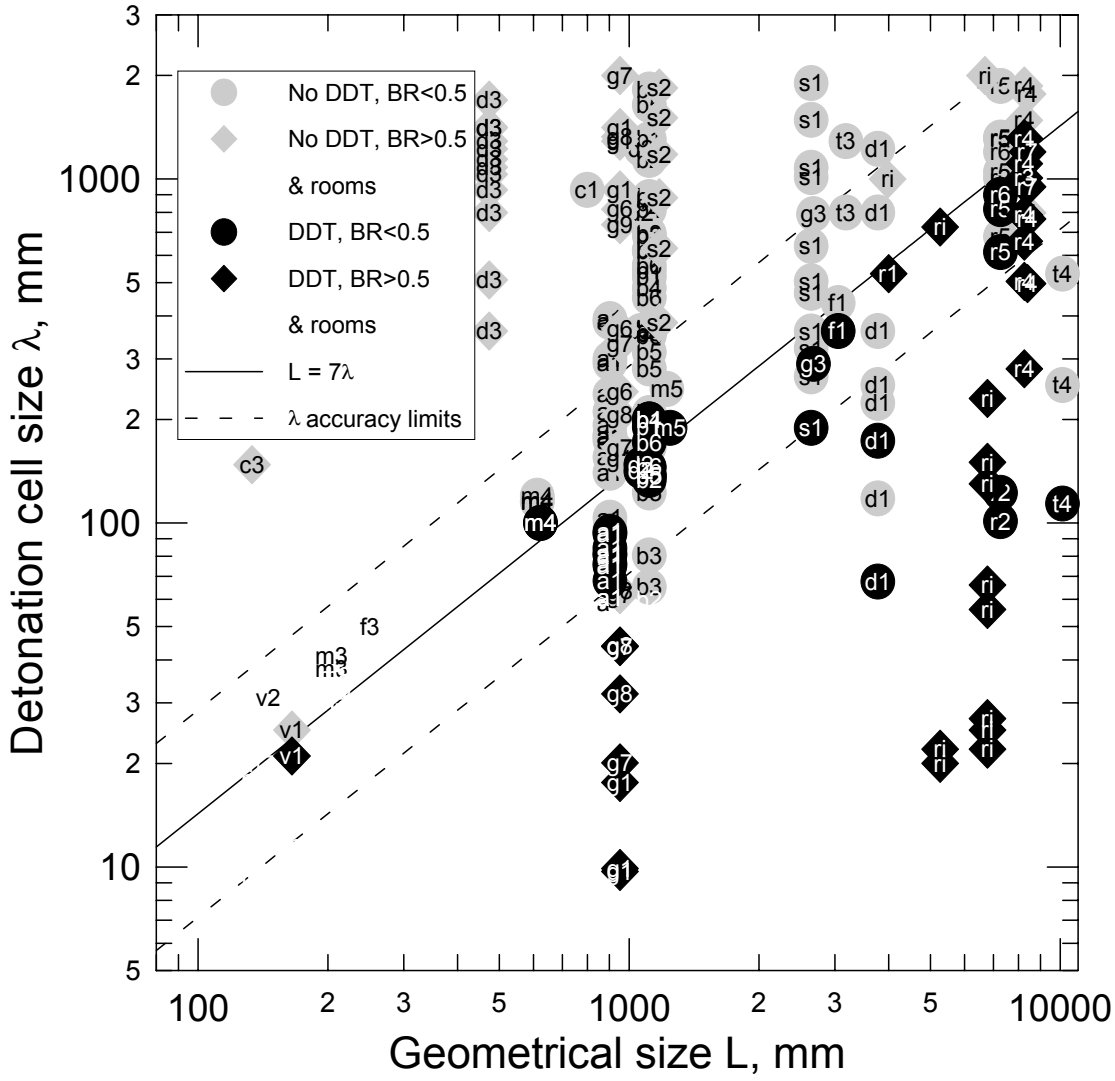

Figure 3.3.4.2-1 ***L/λ*-correlation for onset of detonations**

3.3.4.3 Correlations for turbulent jet initiation

The initiation of detonations by a turbulent jet of combustion products represents one type of DDT phenomena. This initiation mode can occur when combustion of a gaseous mixture in a confined chamber with a venting orifice results in the injection of combustion products' jet through the orifice into another mixture volume outside the chamber (see Figure 3.3.4.3-1). It was shown first by Knystautas et al. in 1979 [3.48] that such a jet is able to initiate detonation in the surrounding mixture in cases the jet gas velocity and the jet size are large enough. Since that time, a number of studies were conducted to determine critical conditions for turbulent jet initiation of detonation [3.37, 3.48-3.56]. Correlations of the jet orifice size d_0 and detonation cell size λ of the surrounding mixture were usually used to characterize the critical conditions. A considerable spread of the critical d_0/λ values from about 10 to more than 60 can be found in these studies.

It has been indicated in many studies [3.37, 3.49-3.51, 3.53-3.56] that the onset of detonation is usually induced or influenced by confining structures. A limited number of observations have been made that show direct initiation of detonation in the turbulent jet of combustion products [3.37, 3.51, 3.55, 3.56]. As suggested in Reference [3.37], the cases when initiation process is dominated by interaction with confining structures are rather cases of DDT but not true cases of the turbulent jet initiation. The turbulent jet plays a role of a strong ignition source, and detonation occurs at a later stage of combustion. The jet orifice size is not a single characteristic scale in these cases, and correlations in terms of d_0/λ are not appropriate to characterize the critical conditions.

To extract experimental data that correspond to true cases of turbulent jet initiation, one can consider the results of the tests under nearly unconfined conditions. These are tests where the combustible mixture was confined with only a thin plastic bag [3.37, 3.51, 3.54, 3.55] and tests where the size of the experimental chamber was large enough compared with the jet orifice size d_0 [3.55]. A correlation for critical conditions of the turbulent jet initiation, based on these data is presented in Figure 3.3.4.3-2. Figure 3.3.4.3-2 shows that minimum jet orifice size d_0 for onset of detonations in the jet can be estimated in the range from 14λ to 24λ.

As mentioned in Section 3.3.3, the minimum scale requirement for the onset of detonation in the spherical initiation mode is more severe than that in the planar case, and the difference can be described approximately by a factor of 3. If detonation onset is observed near the rigid wall or near the ground surface, it is possible to assume that an explosion wave develops initially as a planar wave. In the truly unconfined conditions (far from physical boundaries), only a spherical wave can be initially formed. This is the case for detonation formation directly in the turbulent jet. It may be suggested that the difference in experimental correlations $L/\lambda > 7$ and $d_0/\lambda > (14 \div 24)$ can be attributed mainly to the different (planar or spherical) initiation modes.

If one considers combustion processes in a system of connected rooms, the scenario of jet initiation is, principally, possible. An initiating jet can be formed in the connection between two compartments with the size d_0. Because d_0 is always smaller than the characteristic room size L, the requirement for direct initiation in the jet $d_0 > (14 \div 24)\lambda$ appears to be much less demanding than that for DDT ($L > 7\lambda$). In this situation, DDT should be considered as a more probable event. However, if condition $d_0 > (14 \div 24)\lambda$ is satisfied, there is a high probability that detonation will be initiated next to the connection. Such an estimate of DDT location can be important for safety analysis because very high local loads are typical of DDT events.

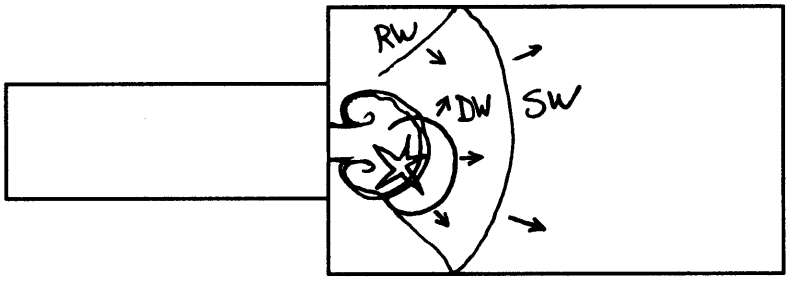

Figure 3.3.4.3-1 Schematic illustration of turbulent jet initiation of detonation. Jet of combustion products enters from the left chamber through an orifice to the right chamber. A detonation wave (DW) can be originated in the products and reactants mixing region.

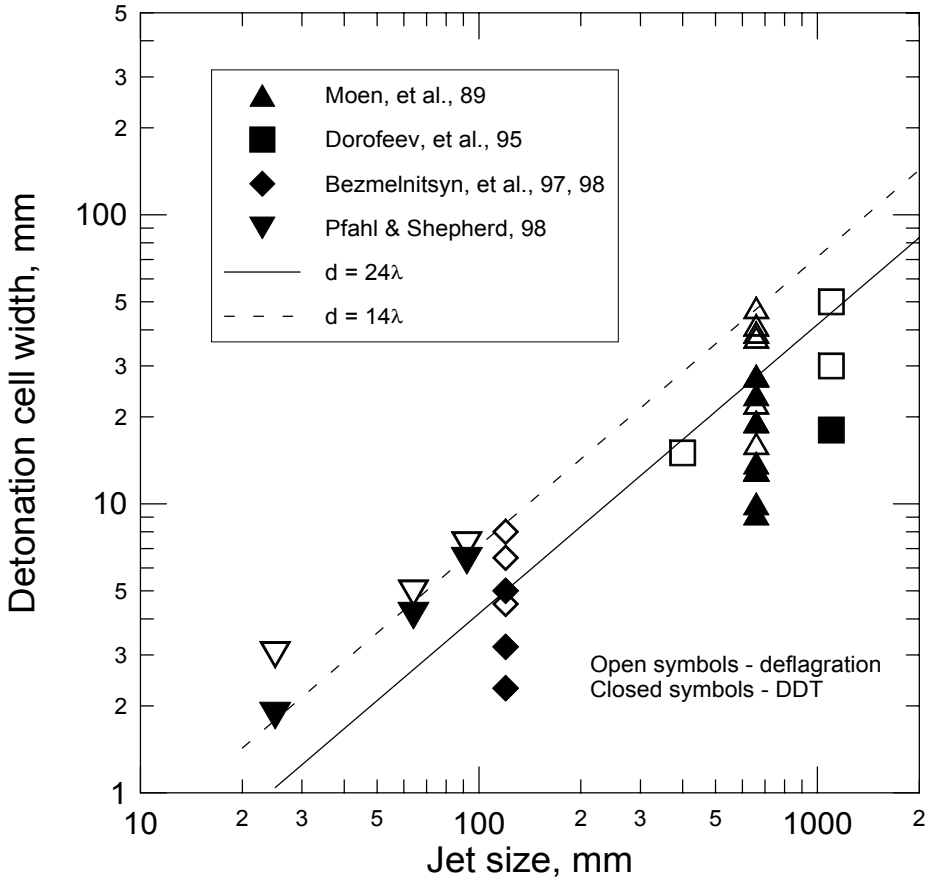

Figure 3.3.4.3-2 Correlation for initiation of spherical detonations by a turbulent jet of combustion products. Data are taken from References [3.37, 3.51, and 3.54-3.56].

3.3.5 Applications of DDT Criteria and Corresponding Uncertainties

First of all, we need to emphasize once more that all DDT criteria considered in this report may be used as necessary conditions only. They give a sign that DDT can principally be expected under certain conditions and scale. They do not show, however, that DDT will necessarily occur, if these criteria are satisfied. The most important point for practical application is that DDT should not be expected, if one of these criteria is not satisfied. The necessary DDT criteria, thus, are appropriate for conservative estimates of the possibility of DDT. The term "conservative" here means that an analysis based on necessary but not sufficient conditions is conservative since it can indicate a possibility that DDT can occur in some cases when DDT cannot actually occur because of factors that are not considered in the analysis. The level of such a conservatism can be reduced if several DDT criteria are used simultaneously. At the same time, it should be emphasized that these are empirical criteria. They are based on the currently available set of data, and it is possible that they will be revised in future as more information becomes available.

DDT criteria impose limitations on different phases and aspects of the combustion process. Among the criteria considered in this report, σ, d/λ, L/λ, and d_0/λ correlations are the most readily available for nuclear safety applications. Application and uncertainties of σ-criterion for flame acceleration were discussed in Section 3.2.4. Here, the detonation onset criteria will be discussed.

3.3.5.1 d/λ correlation (minimum tube diameter criterion)

Application of this criterion is appropriate for relatively long channels. In the case of rooms, or connected compartments with large blockage ratios, the d/λ-criterion can result in significantly overconservative estimates. Inaccuracy of the cell size data should be taken into account in practical applications.

3.3.5.2 L/λ correlation (7λ criterion)

This criterion was formulated in order to address different geometrical configurations typical of a containment building. For each compartment of a containment, a characteristic size L should be determined. In most cases of particular geometrical configurations, Equations (3.7) to (3.12) give a guideline for determination of L.

It should be noted, however, that actual geometry of a containment does not always permit a clear definition of L as it was used in Equations (3.7) to (3.12). Some necessary amendments are given below. In cases of some difficulties with determination of L, the general approach should be to use the maximum L value from a number of choices.

In a typical situation of a system of connected rooms, some rooms can be connected to several others. Characteristic size L of the room 1 connected to rooms 2 , . . , n can be calculated according to an extended version of Equation (3.8):

$$L = L_1 + \alpha_2 L_2 + \ldots + \alpha_n L_n , \tag{3.13}$$

where $\alpha_2, \ldots \alpha_n$ are parameters that describe sizes of connections between rooms. Such a way to account for neighbouring rooms is only important for large-enough open connections between rooms.

In some situations, parameter α cannot be defined directly as $\alpha = d/D$. Several possible ways to replace Equation (3.12) can be suggested:

$$\alpha = (L_1 s/V_1)^{1/2} ; \tag{3.14}$$

$$\alpha = (s/6/\Phi)^{1/2}, \qquad (3.15)$$

where s is the area of connection to a neighbouring room, V_1 is total volume of the room, and Φ is total area of all room walls, including open connections. Equations (3.14) and (3.15) are written using parameters that can be easily defined in a containment.

Inaccuracies of determination of L for some cases define the first type of uncertainty in application of L/λ correlation. The range of this uncertainty can be estimated using difference in L values calculated using different available options for each particular case. Generally, this is certainly lower by a factor of 2, which defines the accuracy of the cell size data.

A second type of uncertainty is defined by the accuracy of the cell size data. As shown in Appendix D, average uncertainty in the cell size estimation for nuclear safety applications is given by a factor of 1.5, and the maximum one can be more than a factor of 2. This inaccuracy should be taken into account by using a correction factor for λ values for L/λcorrelation. If λ is determined using interpolation methods presented in Appendix D, the cell size values reduced by a factor of 1.5 to 2 should be used in L/λ correlations. This is necessary because far interpolations and even extrapolations of the cell size data are unavoidable in applications. A possibility to use directly the cell size values can be considered on case-by-case basis if mixture compositions and initial conditions are close to the range of reliable experimental data (see Appendix D).

A third type of uncertainty is connected with applications of L/λ correlation for volumes with characteristic size exceeding 10 to 15 m (the range given is due to inaccuracy of λ). The problem is that no detonations were observed in experiments with a cell size of more than 2 m. This is the maximum reported λ-value, which was estimated in HDT Facility tests at the Sandia National Laboratories from spacing of a transverse wave for a single-spin detonation. Thus any extrapolation of the cell size values beyond $\lambda \approx 2$ m is questionable. It does not mean, however, that L/λ correlation is useless for large compartments with $L > 10$ to 15 m (e.g., dome part of a containment). Application of this correlation gives a conclusion that DDT is possible in such compartments for all mixtures with $\lambda < 2$m. Possibility of DDT in mixtures less sensitive than those with $\lambda \approx 2$m is uncertain.

In view of this uncertainty, it may be suggested that the possibility of effective flame acceleration should be the main interest for large compartments. Namely, σ-correlations can be applied. If effective flame acceleration is impossible (weak mixture), fast flames cannot be developed and DDT is impossible as well, disregarding the value of λ. In the opposite case, development of fast explosion regimes, including detonations, cannot be excluded.

3.3.5.3 d_0/λ-correlation (turbulent jet initiation)

As mentioned in the previous section, DDT in a given compartment is a much more probable event compared with the turbulent jet initiation. Thus, d/λ and L/λ should be used first. Critical conditions for turbulent jet initiation can be useful to identify locations where the onset of detonation can be expected.

3.3.5.4 Combination of σ- and L/λ-correlations

An example of the combined application of σ and L/λ correlations is presented in Figure 3.3.5.4-1 for hydrogen-air steam mixtures at 375 K and 1 atm initial pressure. Conservative estimates were used for limits of flame acceleration (the minimum σ*-values). The DDT border is shown as λ = 2 m curve. This means that inside this border, DDT is possible in rooms with $L > 7*2/1.5 \approx 10$ m. It should be emphasized that DDT limits depend on scale, whereas flame acceleration limits (σ criterion) do not.

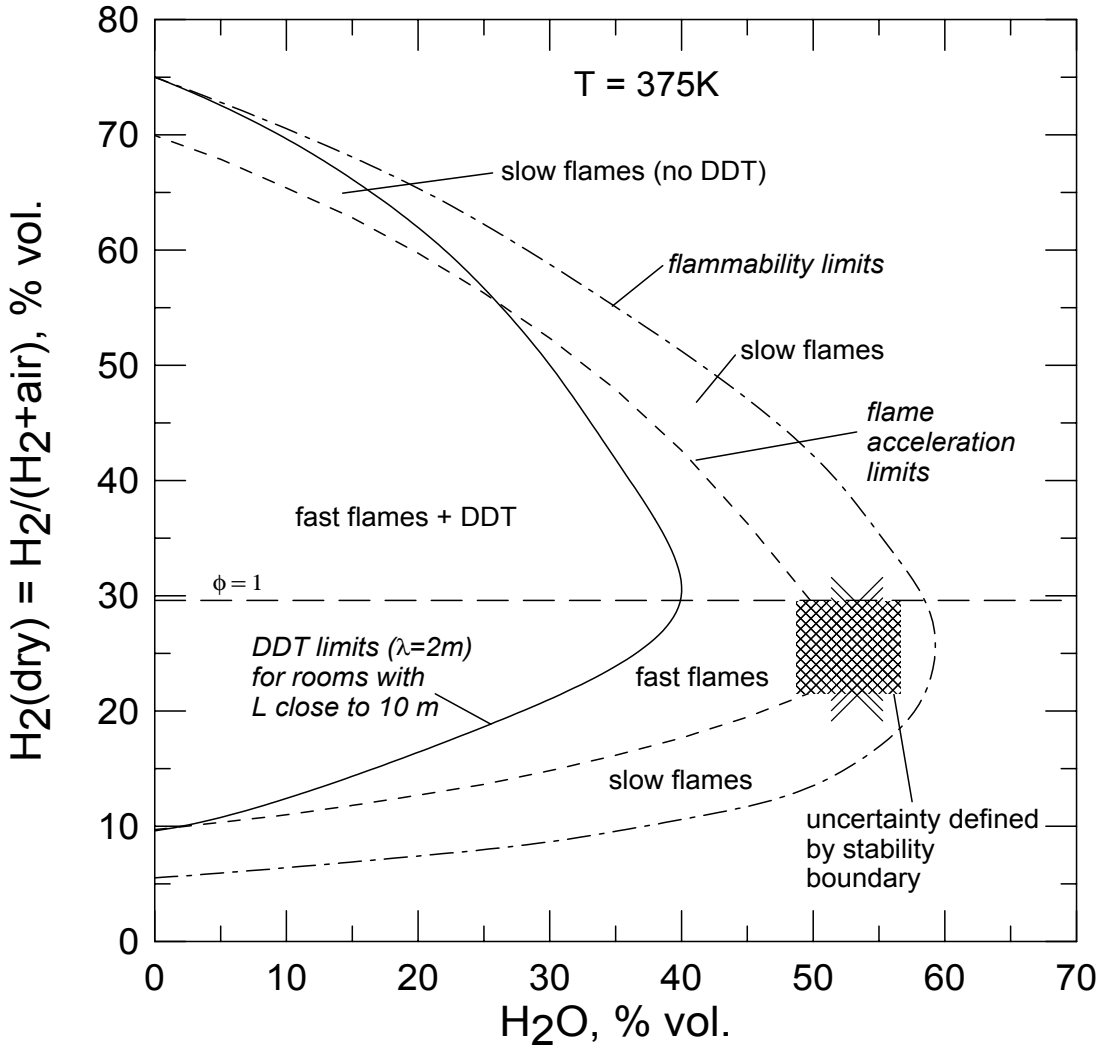

Figure 3.3.5.4-1 Limits and possible regimes of combustion for hydrogen-air-steam mixtures at T = 375 K and p = 1 atm

3.3.5.5 Application of L/λ correlation in non-uniform mixtures

Concentration gradients can be expected in a containment as a result of the processes of hydrogen injection and mixing. In the case that a concentration gradient exists in a compartment or combustible cloud, it is difficult to directly apply the criteria for detonation onset that are based on detonation cell size λ. It is necessary, at least, to define what λ value from the range defined by the concentration distribution should be used as the representative chemical length scale.

The most conservative assumption is to use the minimum λ, which corresponds to the most-sensitive mixture composition. At the same time, it is a highest probability that a detonation is originated in the most-sensitive part of the mixture (minimum cell size). To classify a detonation as a global event for the given compartment or cloud, the detonation should be transmitted then to the less-sensitive part. This possibility, as explained in Section 3.3.3, depends mainly on the value of λ in the insensitive part of mixture surrounding the detonation origin.

To resolve this conflict an approximation can be suggested that some average cell size should be compared with characteristic size L of the compartment (cloud) to estimate wheter a detonation is possible as a global event. Because of non-linear behaviour of the cell size function on concentration (see Appendix D), λ of average composition $<C>$ is usually smaller than the average cell size $<\lambda>$. Thus the use of $\lambda(<C>)$ gives more conservative estimates for L/λ criterion. In many cases, the average composition is the only information available from distribution calculations (e. g., from lumped-parameter codes).

It should be emphasized that the use of $\lambda(<C>)$ for L/λ criterion gives only a global estimate. If L appears to be less than $7\lambda(<C>)$, it does not mean that detonation cannot be expected locally, somewhere inside the compartment (cloud), where mixture is more sensitive. To make more detailed estimations, information on composition distribution is required.

If such information is available, one can consider the following logical scheme. Assuming that detonation is formed already inside a small volume with a characteristic size X_1 with a sensitive composition C_1, one can test whether the detonation survives propagation to the distance X_2 with less-sensitive composition C_2. A schematic of such a problem for planar case, which will be considered first, is shown in Figure 3.3.5.5-1

According to the results [3.35], the possibility of detonation transition to location X_2 is defined dominantly by the length of the gradient $L \approx X_2$, and the value of cell size at location X_2: $L > A\lambda(C_2)$. Factor A depends on the energy density difference between mixtures C_1 and C_2. For constant energy density it is close to 7 used in the L/λ correlation. If this difference is described through CJ detonation velocities D_1 and D_2, experimental data for lean hydrogen air mixtures [3.36] suggest that

$$\log(A) \propto \cdot D_1^2/D_2^2 , \tag{3.16}$$

If one assumes for simplicity that C_1 and C_2 represent concentrations of a limiting component, then $D_1^2/D_2^2 \approx C_1/C_2$. According to Equation (3.16), for a given C_2, $\log(L)$ decreases linearly with C_1 as shown in Figure 3.3.5.5-1. Point C in Figure 3.3.5.5-1 corresponds to the critical value of L_C for detonation formation at location X_2.

Point E in Figure 3.3.5.5-1 gives an estimation of critical L from the cell size of the least-sensitive mixture ($L_E = 7\lambda(C_2)$), without taking into account the energy density difference (underconservative estimate). Point A corresponds to the critical L_A defined by the minimum λ ($L_A = 7\lambda(C_1)$) and gives an

overconservative estimate. Point A should be always lower than point C since the minimum L_A defined by this point is a fraction of L_C value for point C.

Point B is defined as $L_B = 7\lambda(<C>)$. If the function $log(\lambda) = f(C)$ is concave, what is generally true for hydrogen-air-steam mixtures, point B is lower than C, giving a conservative estimate for L/λ correlation. The same is not always true for point D ($L_D = 7(<\lambda>)$). Thus the above consideration gives an explanation of why the use of $\lambda(<C>)$ for L/λ correlation should give a conservative estimate.

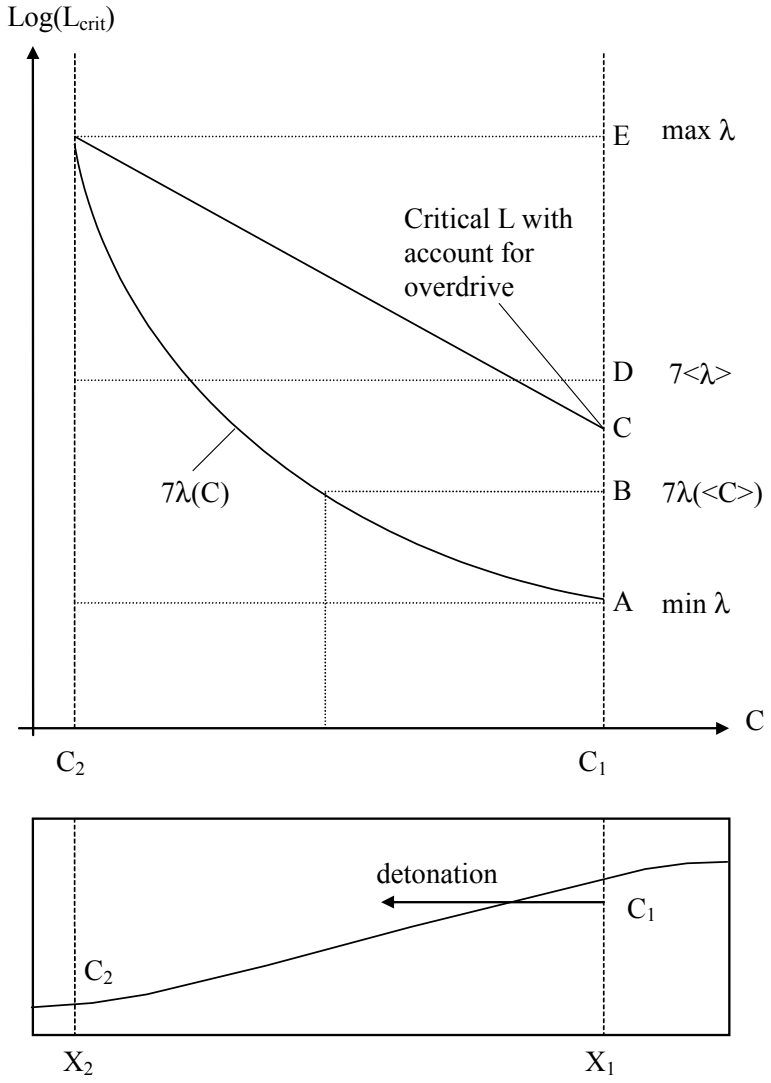

Figure 3.3.5.5-1 Schematic illustration of different options to estimate minimum cloud size (critical gradient) for the possibility of detonation in a location X_2 in that cloud.

In the non-planar cases of detonation wave formation, the above speculations can be also applicable, but factor A is expected to be greater than 7, as mentioned in Section 3.2.3.2. This value gives an additional conservatism in applications of the criterion $L > 7(<\lambda>)$.

Thus two possible approximate solutions can be suggested for application of L/λ correlation for non-uniform cases. The first one makes use of the characteristic size L of a compartment (mixture cloud) and the cell size of the average composition. The criterion $L > 7\lambda(<C>)$ should give an estimate of the possibility of global detonations in the compartment. If detailed distribution of components is unknown and significant gradients can be expected, the possibility of local detonations in a part of the compartment (cloud) cannot be estimated with this criterion.

This approach was applied in large-scale experiments on dynamic hydrogen injection and ignition in the RUT Facility [3.45] and showed good results. Corresponding data (labelled "ri") are shown in Figure 3.3.4.2-1.

The second solution implies that concentration distribution is known. One can start from the cloud boundary with determination of $L\ (\approx V^{1/3})$ and $<\lambda>$, and test the criterion $L/\lambda(<C>)$ for the cloud. If it is not satisfied, a more sensitive part of the cloud can be enveloped, new values of L and $\lambda(<C>)$ can be determined, and the criterion can be tested again. This procedure can be repeated going into smaller and more sensitive cloud parts. If at a certain stage the 7λ criterion appears to be satisfied, this means that detonation is principally possible, locally, inside this part of the mixture. Such a procedure that gives indications of the possibility of local detonations should be considered, thus, as more conservative compared with the first solution.

It should be noted that these solutions for non-uniform mixtures can be applied only as estimates. Although they are based on the DDT correlations for uniform cases and on experimental data on detonation behaviour in non-uniform mixtures (lean hydrogen-air at normal initial temperature and pressure), no direct experiments are available to verify them in detail.

3.4 Summary

An overview of criteria for FA and DDT has been presented in this chapter. These criteria address one of the important practical problems, namely, what type of combustion might be expected: slow flames, fast flames, or detonations. It was shown that boundaries separating various flame regimes depend not only on the composition of the mixture, but also on thermodynamic state, geometrical configuration, and on the physical size or scale of an enclosure.

It is important to note that only a number of empirical necessary conditions for FA and DDT have been formulated up to the present. They are based on the currently available set of data, and are the subject of ongoing research.

One of these conditions states that FA is only possible in mixtures having large-enough expansion ratio $\sigma > \sigma^*$ (see details in Section 3.2). The requirement of large-enough σ is the necessary but not a sufficient condition for development of fast combustion regimes. A sufficiently long flame path and/or favourable geometrical configuration promoting flame folding and stretching should be present in order that the flame can actually accelerate to high velocities. If the flame has accelerated to velocities of about the speed of sound in combustion products, the conditions for spontaneous formation of detonation can be reached.

The second important set of the necessary conditions states that detonation may only occur if the physical size L the compartment containing mixture is sufficiently large compared to the chemical length scale that characterizes the sensitivity of the mixture. The usual choice of the chemical length

scale is the detonation cell size λ. The necessary criteria for DDT described in Section 3.3 are expressed in a form of $L > \alpha\lambda$. The value of the constant α depends on the particular geometrical configuration and on the definition of the characteristic geometrical size L (see details in Section 3.3).

Combined application of FA and DDT criteria enable a more refined evaluation of possible combustion regimes than was previously possible for severe accidents in nuclear power plants. At the same time there are uncertainties, which are described in Sections 3.2.4 and 3.3.4. These uncertainties should be taken into account in practical applications of the criteria for FA and DDT.

3.5 References

3.1. V. S. Babkin, A. Ya. Vykhristuk, V. N. Krivulin, et al., *Archivum Combustionis,* Vol. 4, No 4, 1984, 321.

3.2. I. O. Moen, J. H. S. Lee, B. H. Hjertager, K. Fuhre and R. K. Eckhov, Pressure Development due to Turbulent Flame Acceleration in Large-Scale Methane-Air Explosions, *Combustion and Flame*, Vol. 47, 1982, 31-52.

3.3. I. O. Moen, M. Donato, R. Knystautas, J. H. S. Lee and H. Gr. Wagner, In: *AIAA Progress in Astronautics and Aeronautics*, Vol. 75, 1981, 31.

3.4. B. H. Hjertager, M. Bjørkhaug and K. Fuhre, Gas Explosion Experiments in 1:33 and 1:5 Scale Offshore Separator and Compressor Modules using Stoichiometric Homogeneous Fuel/Air Clouds, *Journal of Loss Prevention in Processes Industries*, Vol. 1, 1988, 197-205.

3.5. C. A. Catlin and D. M. Johnson, Experimental Scaling of the Flame Acceleration Phase of an Explosion by Changing Fuel Gas Reactivity, *Combustion and Flame*, Vol. 88, 1992, 15-27.

3.6. R. G. Abdel-Gayed and D. Bradley, Criteria for Turbulent Propagation Limits of Premixed Flames, *Combustion and Flame*, Vol. 62, 1985, 61-68.

3.7. R. G. Abdel-Gayed, D. Bradley, M. H. Hamid and M. Lawes, Lewis Number Effects on Turbulent Burning Velocity, *20th Symposium International on Combustion*. The Combustion Institute, Pittsburgh, 1984, 505-512.

3.8. S. B. Dorofeev, M. S. Kuznetsov, V. I. Alekseev, A. A. Efimenko, A. V. Bezmelnitsyn, Yu. G. Yankin and W. Breitung, Effect of Scale and Mixture Properties on Behavior of Turbulent Flames in Obstructed Areas, Preprint IAE-6127/3, RRC "Kurchatov Institute" Report FZKA-6268, Forschungszentrum Karlsruhe, 1999.

3.9. M. S. Kuznetsov, V. I. Alekseev, A. V. Bezmelnitsyn, W. Breitung, S. B. Dorofeev, I. D. Matsukov, A Veser and Yu. G. Yankin, Effect of Obstacle Geometry on Behavior of Turbulent Flames. Preprint IAE-6137/3, RRC "Kurchatov Institute", Report FZKA-6328, Forschungszentrum Karlsruhe, 1999.

3.10. S. B. Dorofeev, M. S. Kuznetsov, V. I. Alekseev, A. A. Efimenko and W. Breitung, Evaluation of Limits for Effective Flame Acceleration in Hydrogen Mixtures. Preprint IAE-6150/3, RRC "Kurchatov Institute" Report FZKA-6349, Forschungszentrum Karlsruhe, 1999.

3.11. G. Ciccarelly, J. Boccio, T. Ginsberg, C. Finfrock, L. Gerlach, H. Tagava and A. Malliakos, The Effect of Initial Temperature on Flame Acceleration and Deflagration-to-Detonation Transition Phenomenon, NUREG/CR-6509, BNL-NUREG-52515, 1998.

3.12. M. P. Sherman, M. Berman and R. F. Beyer, Experimental Investigation of Pressure and Blockage Effects on Combustion Limits in H_2-air-steam Mixtures, Sandia National Laboratories Report No. SAND91-0252, 1993.

3.13. S. B. Dorofeev, V. P. Sidorov, A. E. Dvoinishnikov and W. Breitung, Deflagration to Detonation transition in Large Confined Volume of Lean Hydrogen-Air Mixtures, *Combustion and Flame* Vol. 104, 1996, 95–110.

3.14. S. B. Dorofeev, V. P. Sidorov, A. E. Dvoinishnikov, A. Denkevits, A. Efimenko and A. Lelyakin, Large Scale Hydrogen-Air-Steam DDT Experiments in the RUT Facility. Test Series 1996. Report RRC KI 80-05/16, RRC "Kurchatov Institute", 1997.

3.15. M. S. Sherman, S. Tieszen, and W. Benedick, The Effect of Obstacles and Transverse Venting on Flame Acceleration and Transition to Detonation for Hydrogen-Air Mixtures at Large Scale, NUREG/CR-5275, SAND 85-1264, 1989.

3.16. P. Clavin, Dynamic Behavior of Premixed Flame Fronts in Laminar and Turbulent Flows, *Progress in Energy and Combustion Sciences*, Vol. 11, 1985, 1-59.

3.17. J. E. Shepherd and J. H. S. Lee, On the Transition from Deflagration to Detonation. In:: Major Research Topics of Combustion, M. Y. Hussaini, A. Kumar, R. G. Voit Eds. Springer Verlag, Berlin, 1991.

3.18. M. Berman, A Critical Review of Recent Large-Scale Experiments on Hydrogen-Air Detonations, *Nuclear Science and Engineering*, Vol. 93, 1986, 321-347.

3.19. C. M. Guirao, R. Knystautas and J. H. S. Lee, A Summary of Hydrogen-Air Detonations for Reactor Safety, Report NUREG/CR-4961, Sandia National Laboratories/McGill University, 1989.

3.20. O. Peraldi, R. Knystautas and J. H. S. Lee, Criteria for Transition to Detonation in Tubes, *21st Symposium International on Combustion,* The Combustion Institute, Pittsburgh, PA, 1986, 1629-1637.

3.21. C. K. Chan and W. A. Dewit, Deflagration to Detonation Transition in End Gases, *26th International Symposium on Combustion*, The Combustion Institute, Pittsburgh, PA, 1996, 2679-2684.

3.22. C. K. Chan, Collision of a Shock Wave with Obstacle in a Combustible Mixture, *Combustion and Flame* 100, 1995, 341-348.

3.23. B. E. Gelfand, O. E. Popov, S. P. Medvedev, S. V. Khomok, A. Yu. Kusharin and G. L. Agafonov, Selfignition of Hydrogen-oxygen Mixtures at High Pressure, In: CD-ROM *Proceedings of 21th International Symposium on Shock Waves*, paper 2400, 1997.

3.24. B. Gelfand, S. Khomik, S. Medvedev, A. Polenov, A. Bartenev, W. Breitung and A. Veser, A. Investigation of Hydrogen-air Fast Flame Propagation and DDT in Tube with Multidimensional Endplates *Proceedings of the Colloquium on Gas, Vapor, Hybrid and Fuel-Air Explosions*, Schaumburg, IL, USA, 21-25 September, 1998, 434-455.

3.25. A. Teodorczyk, J. H. S. Lee, R. Knystautas, Photographic Studies of the Structure and Propagation Mechanisms of Quasi-Detonations in a Rough Tube, In: *AIAA Progress in Astroanautics and Aeronautics*, Vol. 133, 1990, 233-240.

3.26. J. H. Lee, R. Knystautas and C. K. Chan, Turbulent Flame Propagation in Obstacle-filled Tubes, *20th Symposium International on Combustion.* The Combustion Institute, Pittsburgh, PA, 1984, 1663-1672.

3.27. A. Teodorczyc, J. H. S. Lee and R. Knystautas, Propagation Mechanisms of Quasi-detonations, *22nd Symposium International on Combustion.* The Combustion Institute, Pittsburgh, PA, 1988, 1723-1731.

3.28. Ya. B. Zel'dovich, B. E. Gelfand, S. A. Tsyganov, S. M. Frolov and A. N. Polenov, Concentration and Temperature Non-Uniformities (CTN) of Combustible Mixtures as a Reason of Pressure Generation, In: *AIAA Progress in Astronautics and Aeronautics* (A. L. Kuhl, Ed.), Vol. 114, 1988, 99-123.

3.29. M. Short and J. W. Dold, Corrections to Zel'dovich's Spontaneous Flame and the Onset of Detonation via Nonuniform Preheating, In: AIAA *Progress in Astronautics and Aeronautics* (A. L. Kuhl, Ed.), Vol. 154, 1993, 59-74.

3.30. J. W. Dold, M. Short, J. F. Clarke and N. Nikiforakis, Accumulating Sequence of Ignitions from a Propagating Pulse, *Combustion and Flame*, Vol. 100, 1995, 475-473.

3.31. S. B. Dorofeev, A. S. Kochurko and B. B. Chaivanov, Detonation Onset Conditions in Spatially Nonuniform Combustible Mixtures, *Sixteenth Symposium (International) on Loss Prevention and Safety Promotion in the Processes Industries,* Oslo, Vol. 4, 1989, 22-1 - 22-19.

3.32. S. B. Dorofeev, A. A. Efimenko, A. S. Kochurko and B. B. Chaivanov, Evaluation of the Hydrogen Explosions Hazard, *Nuclear Engineering and Design,* Vol. 148, 1994, 305-316.

3.33. S. B. Dorofeev, A. A. Efimenko and A. S. Kochurko, Numerical Study of Detonation Self-initiation Conditions, *Proceedings of 15th International Colloquium on Dynamics of Explosions and Reactive Systems*, Boulder, Colorado, 1995, 425-428.

3.34. A. M. Khokhlov, E. S. Oran and J. C. Wheeler, A Theory of DDT in Unconfined Flames, *Combustion and Flame,* Vol. 108, 1997, 503-517.

3.35. S. I. Kryuchkov, S. B. Dorofeev and A. A. Efimenko, Critical Conditions for Detonation Propagation through Mixture with Decreasing Reaction Rate, *26th International Symposium on Combustion*, The Combustion Institute, Pittsburgh, 1996, 2965-2972.

3.36. M. S. Kuznetsov, V. I. Alekseev, S. B. Dorofeev, I. D. Matsukov and J. L. Boccio, Detonation Propagation, Decay, and Reinitiation in Nonuniform Gaseous Mixtures, *27th Symposium International on Combustion*. The Combustion Institute, Pittsburgh, 1998, 2241-2247.

3.37. A. V. Bezmelnitsyn, S. B. Dorofeev and Yu. G. Yankin, Direct Comparison of Detonation Initiation by Turbulent Jet under Confined and Unconfined Conditions, *Proceedings of 16th International Colloquium on Dynamics of Explosions and Reactive Systems*, Cracow, Poland, 1997, 222-225.

3.38. V. P. Sidorov and S. B. Dorofeev, Large-Scale Experiments and Scaling of DDT Conditions in Hydrogen-Air-Steam Mixtures - an Overview, *Proceedings of the Workshop on Severe Accident Research in Japan* (SARJ-97) JAERI-Conf 98-009, 1998, 162-182.

3.39. V. P. Sidorov and S. B. Dorofeev, Influence of Initial Temperature, Dilution and Scale on DDT Conditions in Hydrogen-air mixtures, *Arhivum Combustionis*, Vol. 18, No 1-4, 1998, 87-103.

3.40. V. P. Sidorov, M. S. Kuznetsov, I. D. Matsukov, V. I. Alekseev, A. V. Denkevits and S. B. Dorofeev, Large Scale DDT and Detonation Transmission Experiments with Hydrogen Containing Mixtures in the RUT Facility. Test Series 1998. Report RRC "Kurchatov Institute" RRC KI 80-05/17, April 1999.

3.41. S. B. Dorofeev, Effect of Scale on the Onset of Detonations, *Proceedings of 7th International Conference on Numerical Combustion.* York, UK, 1998, 24-25.

3.42. S. B. Dorofeev, V. P. Sidorov, W. Breitung and A. S. Kotchourko, Large-scale Combustion Tests in the RUT Facility: Experimental Study, Numerical Simulations and Analysis on Turbulent Deflagrations and DDT, *Transactions of 14th International Conference on Structural Mechanics in Reactor Technology,* Lyon, France, Vol. 10, 1997, 275-283.

3.43. S. B. Dorofeev, Turbulent Combustion and DDT Events as an Upper Bound for Hydrogen Mitigation Techniques, OECD/NEA/CSNI Workshop on the Implementation of Hydrogen Mitigation Techniques, Winnipeg, Manitoba, Canada, 1996, AECL-11762, NEA/CSNI/R(96)8, 415-433.

3.44. S. B. Dorofeev, V. P. Sidorov, M. S. Kuznetsov, I. D. Matsukov and V. I. Alekseev, Effect of Scale on the Onset of Detonations, In: *CDROM Proceedings of 17th International Colloquium on Dynamics of Explosions and Reactive Systems*, Heidelberg, Germany, 1999, ISBN 3-932217-01-2.

3.45. I. D. Matsukov, M. S. Kuznetsov, V. I. Alekseev and S. B. Dorofeev, Photographic Study of Transition from Fast Deflagrations to Detonations, *22nd International Symposium on Shock Waves*, London, UK, 1999, 370-375.

3.46. S. B. Dorofeev, V. P. Sidorov and W. Breitung, Explosions Resulted from Accidental Release and Ignition of Hydrogen at Dynamic Conditions, *Pre-prints of the 2nd International Specialist Meeting on Fuel-Air Explosions*, Bergen, Norway, 1996, 3.36-3.48.

3.47. M. P. Sherman, S. R. Tieszen and W. B. Benedick, Sandia National Laboratories Report No. SAND89-0859, 1989.

3.48. R. Knystautas, J. H. Lee, I. O. Moen and H. G. Wagner, Direct Initiation of Spherical Detonation by a Hot Turbulent Gas Jet, *17th Symposium International on Combustion*, The Combustion Institute, Pittsburgh, PA, 1979, 1235-1242.

3.49. M. Schildknecht, W. Geiger and M. Stock, Flame Propagation an Pressure Buildup in a Free Gas-Air mixture Due to Jet Ignition, In *AIAA Progress in Astronautics and Aeronautics* (A.L. Kuhl, Ed.), Vol. 94, 1985, 474-490.

3.50. I. O. Moen, D. Bjerketvedt, A. Jenssen and P. A. Thibault, Transition to Detonation in a Large Fuel-Air Cloud, *Combustion and Flame* Vol. 61, 1985, 285-291.

3.51. I. O. Moen, D. Bjerketvedt, T. Engenbretsen and A. Jenssen, Transition to Detonation in a Flame Jet, *Combustion and Flame* Vol. 75, 1989, 297-308.

3.52. F. Carnasciali, J. H. S. Lee, R. Knystautas and F. Fineschi, Turbulent Jet Initiation of Detonation, *Combustion and Flame* Vol. 84, 1991, 170-180.

3.53. S. B. Dorofeev, A. V. Bezmelnitsyn, V. P. Sidorov, Yu. G. Yankin and I. D. Matsukov, Turbulent Jet Initiation of Detonation in Hydrogen-Air Mixtures, Proc. *14th International Colloquium on Dynamics of Explosions and Reactive Systems*, University of Coimbra, Coimbra, Vol. 2, 1993, D2.4.1-D2.4.10.

3.54. S. B. Dorofeev, V. P. Sidorov, A. E. Dvoinishnikov and A. V. Bezmelnitsyn, Transition to Detonation in Large Confined and Unconfined Fuel-air Clouds, *Proceedings of 15th Int. Colloquium on the Dynamics of Explosions and Reactive Systems*, Boulder, CO, 1995, 421-425.

3.55. A. V. Bezmelnitsyn, Experimental Study of Conditions for Detonation Initiation by a Jet of Combustion Products. Ph.D. dissertation, RRC "Kurchatov Institute", Moscow, 1998.

3.56. U. J. Pfahl and J. E. Shepherd, Jet Initiation of Deflagration and Detonation in Stoichiometric H_2-O_2-N_2 Mixtures, GALCIT Report FM 99-1. California Institute of Technology, Pasadena, CA USA, 1988.

4. DETAILED MODELLING OF FA AND DDT*

4.1 Introduction

4.1.1 On the Notion of "State of the Art": Research versus Applications

The "state of the art" in numerical turbulent combustion modelling is a notion that strongly depends on individual interpretation. As in many fields of science and engineering, there is a considerable gap between the "state of the art in research" and the "state of the art in applications". A rough estimate of the time delay for a theory to grow from the research to the application level is about 10 years! Even though this report addresses the end user more than the researcher, we will attempt to strike a balance by including relevant information on ongoing research efforts in order to provide an impression where the research community currently sees a need for improvements.

4.1.2 Building Blocks of a Numerical Turbulent Combustion Model

There are two primary constituents to a numerical turbulent combustion model:

1. the abstract mathematical turbulent combustion model, and
2. its numerical implementation.

An abstract mathematical model for turbulent combustion must include submodels for [4.1]

1a. turbulent non-reacting variable density flows,

1b. the influence of turbulence on combustion, and

1c. the influence of combustion on the turbulent flow.

Obviously, all these ingredients must be properly represented numerically, leading to a demand for associated numerical discretizations.

4.1.3 Outline of this Chapter

Each section in this chapter will begin by stating the key problems addressed and will introduce some basic concepts needed to follow the subsequent explanations.

The numerical modelling of turbulent combustion depends heavily on the underlying flow model. Thus Section 4.2 first describes current approaches to the modelling of non-reacting turbulent flows. The major emphasis will be on models based on the Reynolds-averaged Navier-Stokes equations. Both simplified gradient transport closures as well as more advanced Reynolds stress models will be discussed. An important practical issue for large-scale applications in nuclear reactor containments, oil platforms, and

* Professor Dr.-Ing. Rupert Klein
is the lead author for Chapter 4.

other systems with similar geometric complexity is the modelling of subgrid-scale obstacles such as pipes, metal grids, armatures etc.. Related subgrid-scale "porosity models" have been designed in the context of oil platform safety analysis. They will be covered in a separate Subsection. The concluding Subsection summarizes the key ideas of large eddy simulation (LES).

Section 4.3 describes 3 categories of turbulent combustion models. There are heuristic closures, which aim at covering the major transition from kinetics-determined to turbulent-mixing-determined reaction progress. The more sophisticated "flamelet" models include detailed information about the underlying physical mechanisms in the turbulence-determined regime of combustion. The third category is most appropriate in the well-stirred reactor regime, in which turbulent mixing is extremely intense and chemical kinetics controls the reaction progress. Most appropriate for this regime are methods based on the probability density function (PDF) approach. The concluding Subsection summarizes LES ideas in the context of turbulent combustion. Each of the modelling approaches will be discussed with reference to the list of necessary submodels (1a – 1c) given in Section 4.1.2.

Even for the simple hydrogen-oxygen reaction system, there are on the order of 15 chemical species and 40 elementary chemical kinetic reactions. Realistic hydrocarbon chemistry or the reaction kinetics of polluted hydrogen-air-steam systems require the solution of even larger reaction kinetic systems. Besides the sheer size of the resulting equation system, realistic chemistry represents a substantial challenge to numerical modellers because of its wide range of inherent time scales and because of the fact that many of the rapid degrees of freedom are stiff relaxation processes. Section 4.4 first discusses the problems related to fast time scales and stiff reactions in more detail. Summaries of more or less heuristic models for the net effects of chemical reactions as well as more sophisticated reduced chemical models follow (see also the related Subsection on computational chemistry reduction in Section 4.5)

Section 4.5 first gives an account of the particular numerical challenges posed to a numerical flow solver in the context of FA and DDT. In the light of these issues, we will then discuss the current most popular finite-difference and finite-volume numerical methods. The relevant Subsection ends with a summary of open issues and pointers to current research in this area, including applications of finite-element techniques.

The numerical representation of turbulent premixed combustion events requires a priori decisions regarding the resolution of the combustion front. The alternatives are (i) to include detailed models of all relevant physical processes within the turbulent combustion region or (ii) to consider the reaction front as a surface of discontinuity separating burnt from unburnt gases. The former ansatz requires higher numerical resolution and more sophisticated and detailled modelling; the latter compromises on details but provides better control of what is and what is not modelled because it restricts modelling to a few well-defined submodules. The turbulent combustion models introduced in Section 4.3 are reconsidered and evaluated regarding the numerical requirements necessary for their implementation. The Section ends with an explanation of recent developments aiming at a systematic, mathematically sound and purely numerical/algorithmic approach to chemistry reduction. These methods, when applicable, largely free the user of acquiring detailed first-hand experience with the chemical kinetics at hand.

Section 4.6 summarizes some of the key issues raised in this chapter.

4.2 Turbulent Flow Models

4.2.1 The Necessity of Turbulence Closure

High Reynolds number (low friction) flows are characterized by the fact that flow instabilities can occur at a broad range of length scales. The largest scale is limited in size only by the overall system dimensions, whereas the smallest possible length scale of instability is associated with viscous damping. Following Kolmogorov's scaling arguments [4.2, 4.3] the ratio of the largest "integral scale of turbulence" to the smallest "Kolmogorov length" is of the order $O(\mathrm{Re}^{3/4})$. Suppose that, as a rough estimate, one needed about 10 grid points to accurately resolve a smooth flow structure with a given numerical method. Then, a three-dimensional numerical simulation that resolves all the details of a fully developed turbulent flow will require on the order of $10 \times \mathrm{Re}^{9/4}$ grid points. Current computer capacities allow computational grids with about 10^7 grid cells, so that Reynolds numbers of $\mathrm{Re} \approx 1000$ are close to the limit of what can be dealt with today.

Given the characteristic viscosities, densities and flow velocities in practical gas-phase combustion systems, a Reynolds number $\mathrm{Re} \sim 1000$ is associated with domain sizes on the order of a few centimetres or less! Correlating, on the other hand, the aforementioned Reynolds number dependence of the required numerical degrees of freedom with the fact that realistic Reynolds numbers in large-scale systems are of the order of $\mathrm{Re} > 10^7$, we conclude that fully resolved numerical turbulence simulations will stay out of reach for quite some time to come. As a result, the net effects of the fine scales of turbulence on the large resolved ones need to be modelled.

Practically all numerical turbulent flow models rely on Reynolds' idea [4.4] of separating the statistical means of the flow variables from their fluctuations ((LES) will be addressed shortly). One is interested in computing the former, while the effects of the latter should be modelled. This separation is formally done by suitable averaging procedures, which can be spatial, temporal, or formal ensemble averages. Reynolds originally considered constant density incompressible flows. His "Reynolds averaging" procedure implies splitting the velocity field into mean and fluctuations according to

$$\boldsymbol{v} = \overline{\boldsymbol{v}} + \boldsymbol{v}' \,, \tag{4.2.1}$$

where the averaging procedure $\overline{\{\,\cdot\,\}}$ implies that

$$\overline{\boldsymbol{v}'} \equiv 0 \,. \tag{4.2.2}$$

For compressible variable density flows, averaging the velocity field turns out to be inconvenient, [4.5]. More appropriate is the density-weighted "Favre-average":

$$\boldsymbol{v} = \tilde{\boldsymbol{v}} + \boldsymbol{v}'' \,, \tag{4.2.3}$$

where

$$\overline{\rho}\tilde{\boldsymbol{v}} = \overline{\rho \boldsymbol{v}} \tag{4.2.4}$$

by definition, and ρ is the fluid density. A simple characterization of Favre-averaging states that one averages *densities* of physical quantities rather than the specific quantities, i.e., rather than "quantities per unit mass".

Consider, for example, the conservation laws for mass, momentum, and energy of an inert ideal gas

$$\begin{array}{rcrcrcl} (\rho)_t & + & \nabla\cdot(\rho\boldsymbol{v}) & & & = & 0 \\ (\rho\boldsymbol{v})_t & + & \nabla\cdot(\rho\boldsymbol{v}\circ\boldsymbol{v}+\nabla p) & + & \nabla\cdot\boldsymbol{\tau} & = & 0 \\ (\rho e)_t & + & \nabla\cdot(\boldsymbol{v}\,[\rho e+p]) & + & \nabla\cdot(\boldsymbol{j}_T+\boldsymbol{\tau}\cdot\boldsymbol{v}) & = & 0\,. \end{array} \tag{4.2.5}$$

Here $\rho, \boldsymbol{v}, p, e$ are the mass density, fluid flow velocity, pressure, and total energy per unit mass, respectively, and $\boldsymbol{\tau}, \boldsymbol{j}_T$ denote the molecular transport of momentum and heat, respectively. These transport terms and the pressure are related to the mass, momentum, energy and species densities ρ, $\rho\boldsymbol{v}$, ρe through the caloric equation of state

$$\rho e = \frac{p}{\gamma-1} + \frac{1}{2}\rho\boldsymbol{v}^2 \tag{4.2.6}$$

and the transport models

$$\begin{array}{rcl} \boldsymbol{\tau} & = & -\mu\left(\nabla\boldsymbol{v}+(\nabla\boldsymbol{v})^T\right)-\eta\,(\nabla\cdot\boldsymbol{v})\,\mathbf{1} \\ \boldsymbol{j}_T & = & -\kappa\,\nabla T\,. \end{array} \tag{4.2.7}$$

The temperature T is related to pressure and density through the thermal equation of state

$$T = \frac{p}{\rho R}\,. \tag{4.2.8}$$

The quantities $\gamma, R, \mu, \eta, \kappa$ are the isentropic exponent, the ideal gas constant, the shear and bulk viscosities and the heat conductivity, respectively. All of them are assumed constant here because we wish to elucidate some principles of turbulence modelling rather than providing a detailed tutorial for direct application. The reader should consult fundamental text books on combustion such as Reference [4.6] for a comprehensive summary of the fundamental governing equations, including more complex equations of state and sophisticated molecular transport schemes.

The key problem of turbulence modelling arises from averaging the non-linear terms in Equation (4.2.5). For instance, the averaged non-linear momentum flux reads

$$\overline{\rho\boldsymbol{v}\circ\boldsymbol{v}} = \overline{\rho}\,\tilde{\boldsymbol{v}}\circ\tilde{\boldsymbol{v}} + \overline{\rho\,\boldsymbol{v}''\circ\boldsymbol{v}''}\,. \tag{4.2.9}$$

The correlation between the velocity fluctuations in the turbulent stress tensor

$$\boldsymbol{\tau}_\tau = \overline{\rho\,\boldsymbol{v}''\circ\boldsymbol{v}''} \tag{4.2.10}$$

cannot generally be expressed analytically as a function of the mean field variables such as $\tilde{\boldsymbol{v}}$. Therefore, the goal pursued when averaging the equations—namely to derive a system of equations for the mean quantities only—has not been achieved. To obtain a closed system (with a sufficient number of equations for all the unknowns), one introduces closure approximations that replace the unknown correlations with explicit functions or functionals of the mean quantities. There is no rigorous theory yet that would provide a rigid guideline for the construction of such a closure. Therefore, a number of more or less heuristic closure approximations have been developed in recent years.

4.2.2 Algebraic, One- and Two-equation Models

The common feature of this class of closures is that practically all of them rely on a gradient diffusion approximation for the turbulent transport terms (such as the second one in Equation (4.2.9)). An analogy between the net transport induced by turbulent velocity fluctuations and the molecular transport that is due to thermal fluctuations of molecules is invoked. For monatomic gases, the gradient expressions for the viscous stress tensor and heat flux from Equation (4.2.7) can be derived rigorously. For the analogous turbulent fluxes one postulates

$$\boldsymbol{\tau}_\tau = -\mu_\tau \left(\nabla\tilde{\boldsymbol{v}} + (\nabla\tilde{\boldsymbol{v}})^T\right) - \eta_\tau \left(\nabla\cdot\tilde{\boldsymbol{v}}\right) \mathbf{1} + \frac{2}{3}\overline{\rho}k\,\mathbf{1} \tag{4.2.11}$$

where

$$\overline{\rho}k = \frac{1}{2}\overline{\rho\boldsymbol{v}''\cdot\boldsymbol{v}''} \tag{4.2.12}$$

is the average kinetic energy of turbulent fluctuations per unit volume, and μ_τ, η_τ are suitable modelled effective turbulent transport coefficients. For consistency with the definition of the turbulent stress tensor from Equation (4.2.10) and of the turbulent kinetic energy from Equation (4.2.12), one must require that $\eta_\tau = -\frac{2}{3}\mu_\tau$. Given the gradient diffusion ansatz, the next issue is the determination of the effective transport coefficients such as μ_τ.

Algebraic turbulence models. These models proceed by invoking Prandtl's mixing length hypothesis. The idea is that compact packets of turbulent fluid traverse a characteristic length ℓ_{mix} relative to the mean flow, thereby carrying fluctuations of energy, momentum etc. to other fluid regions. Obviously, statistical velocity fluctuations will then lead to a net transport of energy and momentum whose intensity is strongly influenced by (i) the mixing length and (ii) the amplitude of the fluctuations carried by the fluid packets. Assuming that a typical mass element should carry fluctuations that correspond to the difference in the mean flow quantities across the mixing length, one characterizes the fluctuations of any quantity ϕ by $\ell_{\text{mix}}|\nabla\tilde{\phi}|$.

With these intuitive considerations, a typical algebraic approximation to the turbulent viscosity reads, [4.5, 4.7],

$$\mu_\tau = \overline{\rho}\,\ell_{\text{mix}}^2|\tilde{\boldsymbol{\omega}}| \tag{4.2.13}$$

where

$$\tilde{\boldsymbol{\omega}} = \nabla\times\tilde{\boldsymbol{v}} \tag{4.2.14}$$

is the mean vorticity vector. (Alternative linear expressions involving the mean velocity gradients may replace $|\boldsymbol{\omega}|$ in other algebraic turbulence models.)

The remaining task is the modelling of the mixing length, for which we will give an example that is valid for constant density incompressible flows: Elaborate algebraic closure models take into account the experimental observation that typical turbulent boundary layers exhibit a two- or more-layer structure. Within the immediate vicinity of bounding walls, turbulent fluctuation displacements increase roughly in proportion with the distance y from the wall. Outside this inner region, the amplitudes saturate or may even decay. The inner region, called the logarithmic sublayer, leads to expressions such as [4.5, 4.7]

$$\ell_{\text{mix}} = k\,y\,\left[1 - e^{-y^+/y_A}\right] \tag{4.2.15}$$

with y_A a function of the mean flow conditions near the wall, but independent of the wall distance y. For the outer region Reference [4.7] proposes

$$\mu_\tau = \alpha C_{cp} F_{\text{wake}} F_{\text{Kleb}}(y; y_{\max}/C_{\text{Kleb}}) \tag{4.2.16}$$

with the Klebanov function

$$F_{\mathrm{Kleb}}(y;\delta) = \left[1 - 5.5\left(\frac{y}{\delta}\right)^6\right]^{-1} \tag{4.2.17}$$

and

$$\begin{aligned} F_{\mathrm{wake}}(y;\delta) &= \min\left[y_{\max}F_{\max}, C_{\mathrm{wk}}y_{\max}U_{\mathrm{dif}}^2/F_{\max}\right] \\ F_{\max} &= \frac{1}{\kappa}\left[\max_y(\ell_{\mathrm{mix}}|\boldsymbol{\omega}|)\right] . \end{aligned} \tag{4.2.18}$$

Moreover, U_{dif} is the maximum mean velocity difference across a boundary layer, a wake or a jet flow, $y_{\max}$ is the distance from a wall or symmetry line at which $\ell_{\mathrm{mix}}|\boldsymbol{\omega}|$ attains its maximum, and $\kappa, \alpha, C_{\mathrm{cp}}, C_{\mathrm{Kleb}}, C_{\mathrm{wk}}$ are modelling constants that must be fitted to experimental data sets.

The key message here is not the detailed structure of this sample closure model. It should rather be noticed that all the features of the shear stress model have been generated in a heuristic, empirical way. They are not derived from first principles, and thus cannot be considered as general turbulent flow closures. The structure of these models reflects very detailed experimental observations and with proper choices of all model constants many experimental findings. However, as noted in Reference [4.5], one such set-up can be expected to operate with sufficient accuracy only for applications whose flows fall within a range of similar flows that were used to establish both the model structure and the values of all free constants.

It is also important that most algebraic models have been designed to represent wall-bounded or free shear flows or both, but that they are not designed and well tested for more general multi-dimensional flow situations. As a consequence, flow computations based on algebraic turbulence models that deal with very general initial and boundary data may yield utterly incorrect results—unless tuned to the specific kind of application.

One- and two-equation models. These models also start from the Reynolds- or Favre-averaged equations, but incorporate more fundamental principles in constructing closure approximations. These models also employ a gradient flux approximation, so that the increased sophistication relative to algebraic closures manifests itself through the modelling of the effective transport coefficients.

One key observation is that the intensity of the velocity fluctuations—or in other words, the turbulent kinetic energy—should critically influence the net turbulent transport. Thus if one were able to obtain—e.g., a characteristic length ℓ_τ or time scale t_τ of turbulence—then dimensional arguments would automatically lead to $\nu_\tau = \mu_\tau/\overline{\rho} \sim \ell_\tau\sqrt{k} \sim kt_\tau$.

This observation is crucial, because an *exact* equation for the turbulent kinetic energy can be derived. Wilcox [4.5] provides a derivation of the turbulent kinetic energy equation in the context of variable density flows

$$\begin{aligned} \bar{\rho}\frac{\partial k}{\partial t} + \bar{\rho}\tilde{\boldsymbol{v}}\cdot\nabla k &= \bar{\rho}\,\boldsymbol{\tau}_\tau : \nabla\tilde{\boldsymbol{v}} - \overline{\rho\,\boldsymbol{\tau}:\nabla\boldsymbol{v}''} + \nabla\cdot\left\{\overline{\rho\,\boldsymbol{\tau}\cdot\boldsymbol{v}''} - \overline{\rho\,\boldsymbol{v}''\frac{\boldsymbol{v}''^2}{2}} - \overline{p'\boldsymbol{v}''}\right\} \\ &\quad -\overline{\boldsymbol{v}''}\cdot\nabla\bar{p} + \overline{p'\nabla\cdot\boldsymbol{v}''} . \end{aligned} \tag{4.2.19}$$

With such an equation at least part of the closure model can be based on exact information, even though a number of terms within that equation representing fluctuation correlations must again be modelled.

One- and two-equation models now differ in how they obtain the second missing dimensional characteristic scale ℓ_τ or t_τ. One-equation models proceed in a similar fashion as the algebraic models discussed earlier [4.5]: The mixing length is assessed through an algebraic formula. Experience shows that this formula generally needs to incorporate explicitly some specific reference to the flow configuration considered. Thus a one-equation model is not closed in the sense that it would consist of a given set of *universal* partial differential equations whose solutions are determined by supplementing initial and boundary conditions. In contrast, the model equations themselves are changed from one set of such input data to another through adjustments of the mixing length and the associated variations of the turbulent transport coefficients.

Two-equation models introduce an additional transport equation for the missing quantity. There are models that directly model a characteristic turbulent mixing length ℓ, the product $k\ell$ or the inverse ω of a characteristic turbulence time scale, (see References [4.3,4.8 to 4.12] and related references in Reference [4.5]). These lead to "k-ℓ", "k-$k\ell$", "k-ω"–models, all of which aim at improvements of generality over the aforementioned algebraic and one-equation models.

The most popular approach, however, is the k-ϵ–model [4.13]. The approach may be motivated by the desire to model one of the unclosed terms in the turbulent kinetic energy equation, namely

$$\bar{\rho}\tilde{\epsilon} = \overline{\rho\,\boldsymbol{\tau} : \nabla \boldsymbol{v}''}\,. \tag{4.2.20}$$

This term describes the molecular level dissipation of turbulent kinetic energy. Besides being one of the unclosed terms from Equation (4.2.19), the turbulent dissipation also plays a key role in Kolmogorov's fundamental paper on scaling laws of turbulence [4.2]. In that paper, Kolomogorov postulates a self-similar energy cascade, defined by (i) energy input on the largest scales of turbulence, (ii) transformation through a cascade of smaller and smaller flow structures through non-linear inertia effects, and (iii) the ultimate dissipation of this energy at the smallest scale, which is called the "Kolmogorov scale". The existence of such a cascade with a rate of energy transfer between scales that is independent of scale itself has considerable consequences which Kolmogorov explored by means of dimensional analysis. The turbulent dissipation—or the turbulent kinetic energy transfer rate—being such a fundamental quantity, it is tempting to include it directly in a turbulence model, thereby introducing a model variable that captures some of the essence of the energy cascade.

Unfortunately, the turbulent kinetic energy dissipation rate from Equation (4.2.20) satisfies a tremendously complex governing equation with unclosed terms that are very hard to measure or assess accurately by other means. As a consequence, modelling has been guided by scaling and dimensional arguments. Modelled equations have been introduced that are *completely heuristic* but composed of all ingredients that formally appear in the exact equation (see Reference [4.5]). These key ingredients are convection by the mean flow, turbulent transport, molecular transport, production, and dissipation.

The k-ϵ / k-ω approaches have first been established for constant density incompressible flows but were extended later to variable density incompressible and (weakly) compressible flows in References [4.14 to 4.16]. These extensions are far from trivial. New equations describing the mass and energy balances must be introduced, and a number of new turbulence effects arise that lead to new unclosed terms [4.5]:

- turbulent heat fluxes,
- dilatation-induced dissipation of kinetic energy ($\nabla\cdot\boldsymbol{v} \neq 0$!),

- pressure-diffusion and pressure-dilatation correlations, and
- pressure work from velocity fluctuations.

A detailed description of how these effects are incorporated into existing turbulence models is beyond the scope of the present report. It may suffice here to say that modelling in the framework of two-equation models remains, based on judicious scaling and dimensional arguments.

4.2.2.1 Summary and qualifications

Two-equation turbulence models should be considered the current "state of the art in applications". These models are found in all major commercial flow simulation codes. The simpler algebraic and one-equation models still have their merits when used in applications that they have been especially tuned to. In these situations they provide results comparable in quality to two-equation models, albeit at the cost of a much narrower range of applicability of a given set-up of all model coefficients and constants.

There are a number of qualifications to be made that are, unfortunately, often disregarded in engineering applications. Algebraic, one- and two-equation models have been developed originally for specific flow situations, such as shear and boundary layers. They are not well suited without special tuning to more complex flows with recirculation zones, flow detachments etc.. This is of particular importance for real-life applications in fire and explosion safety. The relevant flows and flow geometries are hardly ever within the domain of applicability of these relatively simple turbulent flow models. Thus any results generated with these models must be considered with considerable scepticism! This $does\ not$ imply that k-ϵ- or k-ω-based models cannot be applied, but it $does$ imply that one should expect considerable fine tuning of these models to be necessary from one application to another. To overcome these pitfalls, two major research and development directions have emerged over the years.

- *Reynolds stress models* go beyond two-equation models in that they relax the gradient transport approximation for turbulent fluxes such as those of Equation (4.2.11) and instead introduce new dynamic equations for the turbulent fluxes themselves. This adds flexibility in incorporating new physical effects and allows us to construct models that are applicable over a much wider range of physical situations without fine-tuning, at the cost of increased model complexity.
- *Large eddy simulation* models stay with simpler modelling of small-scale effects, but they run at much higher numerical resolution. Therefore, these models generate part of the turbulent energy cascade all by themselves and aim at using the gained information to improve the description of the unresolved scales. With this approach, the underlying models remain simple and are expected to be even simpler than the more sophisticated two-equation models, but much higher demands on computing power arise.

Common to both Reynolds stress and large eddy simulation models is the possibility of a much-improved description of turbulent transport in turbulent premixed flames. This issue will be discussed in more detail in connection with turbulent flame-flow coupling in a later section.

Reynolds stress models and LES for inert flows are discussed next.

4.2.3 Reynolds Stress Models

Instead of assuming a specific form of the relation between mean flow quantities and turbulent transport, Reynolds stress models compute the transport terms themselves from modelled transport equations. Thus in three space dimensions six equations for quantities $\overline{\rho u_i'' u_j''}$ are added to the mass, momentum and energy balances. (Because of the symmetry of the Reynolds stress tensor, it is not necessary to calculate all the nine stress components independently.) Generally, this approach adds flexibility to incorporate new physical effects and allows us to construct models with a much wider range of applicability without fine tuning.

The stress transport equations are derived, more or less straightforwardly, by manipulating the original equations. Thus one first subtracts the averaged momentum equation from the original one in order to obtain an equation for the averaged momentum $\overline{\rho \boldsymbol{v}''}$. Tensorial multiplication by $\boldsymbol{v}''$ and subsequent averaging leads to equations of the form

$$\overline{\boldsymbol{v}'' \circ \frac{\partial \rho \boldsymbol{v}''}{\partial t}} + ... = ... \tag{4.2.21}$$

In a similar fashion, one derives from the non-conservative from of the momentum equation the counterpart

$$\overline{\rho \boldsymbol{v}'' \circ \frac{\partial \boldsymbol{v}''}{\partial t}} + ... = ... \tag{4.2.22}$$

Addition of these 2 equations yields the desired transport equation for the Reynolds stresses. Wilcox [4.5] provides the following compact formulation of these equations for the case of constant density, incompressible flows, which we cite here for illustration of the modelling issues involved:

$$\frac{\partial \boldsymbol{\tau}_\tau}{\partial t} + \bar{\boldsymbol{v}} \cdot \nabla \boldsymbol{\tau}_\tau = -\boldsymbol{\tau}_\tau \cdot \nabla \bar{\boldsymbol{v}} - (\boldsymbol{\tau}_\tau \cdot \nabla \bar{\boldsymbol{v}})^t + \boldsymbol{\epsilon} - \boldsymbol{\Pi} + \nabla \cdot (\nu \nabla \boldsymbol{\tau}_\tau + \boldsymbol{C}) \tag{4.2.23}$$

where

$$\boldsymbol{\Pi} = \overline{\frac{p'}{\rho} (\nabla \boldsymbol{v}' + (\nabla \boldsymbol{v}')^t)} \tag{4.2.24}$$

$$\boldsymbol{\epsilon} = 2\overline{\nu (\nabla \boldsymbol{v}')^t \cdot \nabla \boldsymbol{v}'} \tag{4.2.25}$$

$$\rho \nabla \cdot \boldsymbol{C} = \rho \overline{\boldsymbol{v}' \circ \boldsymbol{v}' (\nabla \cdot \boldsymbol{v}')} + \nabla (\overline{p' \boldsymbol{v}'}) + \left(\nabla (\overline{p' \boldsymbol{v}'}) \right)^t . \tag{4.2.26}$$

The key advantages of including a stress transport model are that certain effects that are lost in the more simplified algebraic, one- and two-equation models are now included and provide for the desired enhanced capabilities and more general applicability. These include

- effects of flow history;
- convection, production and body force effects which—under appropriate closure—allow the inclusion of streamline curvature, system rotation, and stratification effects at least qualitatively [4.5]; and
- unequal normal stresses, allowing proper adjustment under sudden non-isotropic changes of strain rates.

On the other hand, this ansatz changes not only the number of equations to be solved, but also modifies the mathematical character of the equation system: Molecular transport in the original Navier-Stokes equations figures as a second derivative damping term changing the equation type from hyperbolic (elliptic/hyperbolic) for the inviscid case to parabolic (elliptic/parabolic) for viscous unsteady compressible (incompressible) flows. In the Reynolds stress equations, the turbulent transport terms are now unknown variables themselves, and thus the character of the original balance equations remains unchanged, whereas the equation type is now determined by the Reynolds stress equations. Their type, in turn, depends on the closure approximations introduced for all triple correlations. The change of the equation type obviously has consequences for the choice of appropriate numerical techniques, and a general recipe is hard to provide because of this dependence on modelling assumptions.

Notice also, that closure requires determination of $\boldsymbol{\Pi}, \boldsymbol{\epsilon}, \boldsymbol{C}$. The most popular Reynolds stress models (see e.g., [4.17]) introduce explicit closures for the pressure strain and triple correlations covered by $\boldsymbol{\Pi}, \boldsymbol{C}$, but keep an additional dynamic equation for the dissipation tensor $\boldsymbol{\epsilon}$. Thus one introduces, e.g.,

$$\boldsymbol{\epsilon} = \epsilon \left(\frac{2}{3}\mathbf{1} + 2 f_s \boldsymbol{B} \right) \tag{4.2.27}$$

where $\boldsymbol{B}$ is the Reynolds stress anisotropy tensor

$$\boldsymbol{B} = \frac{1}{2\,k} \left(\boldsymbol{\tau}_\tau - \frac{2}{3}\,k\,\mathbf{1} \right) , \tag{4.2.28}$$

k is the turbulent kinetic energy

$$k = \frac{1}{2}\,\mathrm{tr}(\boldsymbol{\tau}_\tau) \tag{4.2.29}$$

and f_s is a Reynolds number dependent weight function

$$f_s = \left(1 + \frac{1}{10} Re_t \right)^{-1} . \tag{4.2.30}$$

Then, in order to obtain the full dissipation tensor, $\boldsymbol{\epsilon}$, one needs to model the time evolution of its trace ϵ from Equation (4.2.27). This is done by including either a dissipation evolution equation as in a k-ϵ model (see [4.17,4.18] and many other references in Reference [4.5]) or by modelling the evolution of a characteristic turbulence time scale $t_t \sim \omega^{-1}$ through an ω-equation [4.19, 4.20].

4.2.3.1 Summary and qualifications

Reynolds stress transport models do succeed in overcoming many of the shortcomings of the simpler models discussed in the last subsection. There are a number of well-documented Reynolds stress models in the literature and their performance on various flow configurations has been extensively tested by comparison with experimental data. Flows with streamline curvature, boundary layers with strong pressure gradients, rotating flows, and boundary layer flows with separation have been modelled with much higher accuracy than has been possible with algebraic, one- or two-equation models [4.5].

These improvements are obtained at the cost of considerably increased model complexity involving equation systems whose structure differs substantially from that of the Navier-Stokes equations. This last fact should be considered as one of the major obstacles to a more widespread application of Reynolds stress transport models in everyday engineering investigations: Navier-Stokes solvers are more or less readily available and are straightforwardly extendable to algebraic, one- and two-equation turbulence modelling. Incorporation of Reynolds stress models requires dramatically more intense efforts.

In the context of combustion simulations, we will see later on that Reynolds stress transport models provide a very natural framework for sophisticated flame-flow coupling schemes. The importance of this aspect should not be underestimated and will be discussed in detail in Section 4.3.4.2.

We should not leave unmentioned the recent development of an intermediate complexity turbulence closure by Oberlack [4.21 to 4.23]. Oberlack observes that one of the major shortcomings of algebraic, one- and two-equation models is their inherent assumption of local isotropy of turbulent transport. He reconsiders Rotta's [4.24] original derivations of multi-point statistics of turbulent flows and essentially derives an anisotropic version of a k-ℓ model. The key advantage of this approach is that the model structure remains comparable to that of a k-ϵ or k-ω model, while the above-mentioned shortcomings regarding isotropy assumptions are removed! The model is still awaiting wider application but should be kept in mind as a promising compromise between algebraic, one- and two-equation models on the one hand and full-fledged Reynolds stress models on the other.

4.2.4 Large Eddy Simulation (LES)

4.2.4.1 The key ideas of LES

An important aspect of all the Reynolds averaged flow models from Sections 4.2.2, 4.2.3 is that they model *all* turbulent fluctuation scales while only the gross flow features are computed explicitly. As a consequence, $none$ of the small-scale turbulent fluctuations are computed in a dynamical fashion, and the turbulence statistics are completely unaccessible. No information on the inherently unsteady nature of turbulence is provided by these models. This observation is particularly disturbing if one aims at an improved understanding of these unsteady fluctuations or, as in combustion, is interested in the interactions between small-scale turbulent fluctuations and the aero-thermochemistry. (See also Section 4.3.1.)

There is an additional aspect of Reynolds-averaged models that is relevant to the subsequent discussions of LES: In practically all real-life applications the largest turbulent fluctuations (on the integral scale of turbulence) are inhomogeneous and non-isotropic. Thus much of the advanced theory of turbulence, which is based to a large extent on just these assumptions of homogeneity and isotropy, is—strictly speaking—not applicable. This obviously complicates the task of modelling considerably.

Both these problems are addressed by LES as follows: One begins by noting that—according to the widely accepted Kolmogorov theory—turbulence is characterized by an energy cascade from large to ever-smaller scales. Energy is fed into a turbulent system at the largest scales comparable to the characteristic system dimensions. It is re-distributed through non-linear instabilities to a hierarchy of smaller and smaller flow structures. Ultimately, it is dissipated at the Kolmogorov dissipation scale. As more and more non-linear energy transfers take place, one intuitively assumes that the emerging small scales are less and less influenced by the detailed larger scale flow patterns that they originate from. One expects the smaller scales to nearly satisfy the restrictive assumptions of homogeneity and isotropy, thereby allowing simplified modelling procedures.

Large eddy simulation thus operates with numerical resolutions that allow one to represent a sufficient range of scales so that (i) most of the kinetic energy of the turbulent fluctuations is captured and that (ii) the smallest resolved scales are considerably smaller than the integral scale of turbulence. Obviously, one still cannot completely resolve all the flow features down to the Kolmogorov dissipation scale, and some kind of "subgrid modelling" is still required.

Common to all LES models is the concept of "filtering". The space, time, or ensemble averaging of standard Reynolds-averaged models is replaced by spatial filtering procedures that only in the simplest case are actual spatial averages with a fixed averaging domain size. More generally, an LES filter is of the form

$$\overline{\boldsymbol{v}}(\boldsymbol{x},t) = \iiint G(\boldsymbol{x}-\boldsymbol{\xi};\Delta)\boldsymbol{v}(\boldsymbol{\xi},t)\,d^3\boldsymbol{\xi} \tag{4.2.31}$$

with a filter function $G(\boldsymbol{r};\Delta)$ satisfying the conditions

$$G \geq 0\,, \qquad G(\boldsymbol{r};\Delta) \to 0 \qquad \text{as} \qquad \frac{|\boldsymbol{r}|}{\Delta} \to \infty \tag{4.2.32}$$

and the normalization

$$\iiint G(\boldsymbol{r};\Delta)\,d^3\boldsymbol{r} = 1\,. \tag{4.2.33}$$

The filtered flow quantities such as $\overline{\boldsymbol{v}}$ in Equation (4.2.31) are the primary unknowns in an LES model. One of the first choices in constructing a LES model is to choose such a filter. Simple algebraic space averaging, corresponding to a box filter, filtering in Fourier space, Gaussian filter weights in physical space, and a host of alternatives have been proposed [4.5, 4.25]. The common point is that any filter introduces a characteristic length Δ, which defines the smallest resolved scale and thus separates computed from modelled flow structures.

Given a filter definition one can proceed to derive new governing equations for the filtered quantities by applying the filter to the original unfiltered equations. For example, for incompressible constant density flow, the divergence constraint and momentum equation read

$$\nabla\cdot\overline{\boldsymbol{v}} = 0 \tag{4.2.34}$$

and

$$\frac{\partial\overline{\boldsymbol{v}}}{\partial t} + \nabla\cdot(\overline{\boldsymbol{v}\circ\boldsymbol{v}}) + \frac{1}{\rho}\nabla\overline{p} - \nu\nabla^2\overline{\boldsymbol{v}} = 0\,. \tag{4.2.35}$$

The challenge in LES modelling becomes clear when the filtered non-linear convection term is decomposed as

$$\overline{\boldsymbol{v}\circ\boldsymbol{v}} = \overline{\boldsymbol{v}}\circ\overline{\boldsymbol{v}} + \boldsymbol{L} + \boldsymbol{C} + \boldsymbol{R} \tag{4.2.36}$$

where

$$\begin{aligned} \boldsymbol{L} &= \overline{\overline{\boldsymbol{v}}\circ\overline{\boldsymbol{v}}} - \overline{\boldsymbol{v}}\circ\overline{\boldsymbol{v}} \\ \boldsymbol{C} &= \overline{\overline{\boldsymbol{v}}\circ\boldsymbol{v}'} + \overline{\boldsymbol{v}'\circ\overline{\boldsymbol{v}}} \\ \boldsymbol{R} &= \overline{\boldsymbol{v}'\circ\boldsymbol{v}'} \end{aligned} \tag{4.2.37}$$

are subgrid-scale non-linear flux contributions that require modelling. These terms are dubbed the "Leonard stress", the "cross-term stress", and the "subgrid-scale (SGS) Reynolds stress", respectively.

Notice that, depending on the choice of filter, one may have

$$\overline{\overline{\boldsymbol{v}}} \neq \overline{\boldsymbol{v}}\,, \tag{4.2.38}$$

which is in contrast to standard Reynolds averaging and implies that the cross-term stresses are generally non-zero. This non-standard behaviour of LES filtering can also have a non-negligible influence on subgrid-scale modelling.

Two major modelling approaches have emerged over the past decade: Explicit subgrid-scale models, the origin of which go back to Smagorinsky's fundamental work, [4.26], and the more recent dynamic LES models following a seminal paper by Germano et al. [4.27], (see also the reviews in References [4.28 to 4.31]).

4.2.4.2 Explicit subgrid-scale models

An important presumption of this kind of model is a *directed* energy cascade, in which energy as well as information are transferred from large to small scales. Under these conditions it would be irrelevant at which scale precisely the cascade is truncated. It would be sufficient to capture and dissipate the transferred flux of energy at some scale that is small enough to guarantee that there is negligible dynamic "backscatter" from this smallest resolved scale back up to the larger dynamic flow structures.

Models using an explicit small-scale viscosity build on this concept and essentially assign the smallest resolved numerical grid scale to be the dissipation scale Δ. In the simplest case, an effective mixing length eddy viscosity is introduced [4.26] that has the smallest mesh size as the effective mixing length. Since the fundamental problem of representing the net effect of small scales that are *not* resolvable on the given numerical mesh remains the same as in Reynolds-averaged models, one can go to any sophistication in modelling the subgrid-scale effects. Thus while the above-mentioned Smagorinsky methodology corresponds to an algebraic turbulence model, a one-equation subgrid-scale model has been proposed by Lilly [4.32], a second-order closure by Deardorff [4.33], and novel non-linear stress-strain relations by Bardina et al. [4.34]. The reader should consult the above-mentioned reviews and the original papers referenced therein for more detail.

4.2.4.3 Dynamic subgrid-scale models

Germano et al. [4.27] went one step further in exploring the cascade idea for subgrid-scale modelling. They observed that according to standard concepts, the cascade is directed from the large to the small scales and that at the small-scale end of the spectrum the dynamics is close to self-similar. Under these conditions, an LES that resolves a considerable part of the cascade already features a suitable representation of small-scale dynamics. All that is needed to close the subgrid-scale problem is to extrapolate the computed grid-based results in a suitable fashion to the unresolved scales.

Under this premise, one should expect that the subgrid-scales act on the smallest resolved scales in a fashion that is completely analogous—except for suitable rescaling—to the action from the smallest resolved scales to the next larger ones. This latter action is accessible within the data produced in the LES computation, so that the remaining task is to find the appropriate extrapolation and re-scaling rules.

Invoking a mixing length hypothesis for subgrid-scale turbulent fluxes, the subgrid-scale stress tensor is written as

$$\boldsymbol{\tau}_{\mathrm{SGS}} = 2\,\mu_{\mathrm{SGS}}\overline{\boldsymbol{S}} - \frac{2}{3}\mu_{\mathrm{SGS}}(\nabla\cdot\overline{\boldsymbol{v}})\,\mathbf{1} \tag{4.2.39}$$

where

$$\overline{\boldsymbol{S}} = \frac{1}{2}\left(\nabla\overline{\boldsymbol{v}} + (\nabla\overline{\boldsymbol{v}})^t\right) \tag{4.2.40}$$

and where the subgrid-scale viscosity is defined as

$$\mu_{\mathrm{SGS}} = C_s\,\rho\,\Delta^2\,|\overline{\boldsymbol{S}}|\,. \tag{4.2.41}$$

This very simple approach leaves one with a single open modelling coefficient C_s that remains to be determined. The crucial new idea in dynamic modelling now is to not assign this coefficient in advance but to adjust it in a suitable fashion *dynamically* from the computed data.

It is assumed that the smallest resolved scale acts on the next larger scales in the same fashion as the unresolved scales should influence the smallest resolved scales. If that is so, the unknown coefficient C_s should be computable from resolved data only. Thus Germano et al. [4.27] introduce a second filter in addition to the original subgrid-scale filter, whose filter scale $\hat{\Delta}$ is larger than Δ. Next the $\hat{\Delta}$ filter is applied to the Δ filtered equations and it is required that the new field $\hat{\overline{\boldsymbol{v}}}$ satisfies an equation analogous to that for the $\overline{\boldsymbol{v}}$-field. Considering the combined convective and subgrid-scale viscosity terms (for constant density incompressible flows as an example) one obtains

$$\widehat{\overline{\boldsymbol{v}} \circ \overline{\boldsymbol{v}}} - 2\,C_s\Big(\Delta^2\,\widehat{|\overline{\boldsymbol{S}}|\overline{\boldsymbol{S}}}\Big) = \hat{\overline{\boldsymbol{v}}} \circ \hat{\overline{\boldsymbol{v}}} - 2\,C_s\,\hat{\Delta}^2\,|\hat{\overline{\boldsymbol{S}}}|\hat{\overline{\boldsymbol{S}}} \tag{4.2.42}$$

or, equivalently,

$$2\,C_s\,\Delta^2\,\boldsymbol{M} = \boldsymbol{L} \tag{4.2.43}$$

with the obvious definitions

$$\begin{aligned} \boldsymbol{L} &= \widehat{\overline{\boldsymbol{v}} \circ \overline{\boldsymbol{v}}} - \hat{\overline{\boldsymbol{v}}} \circ \hat{\overline{\boldsymbol{v}}} \\ \boldsymbol{M} &= \widehat{|\overline{\boldsymbol{S}}|\overline{\boldsymbol{S}}} - \frac{\hat{\Delta}^2}{\Delta^2}\,|\hat{\overline{\boldsymbol{S}}}|\hat{\overline{\boldsymbol{S}}}\,. \end{aligned} \tag{4.2.44}$$

A single equation for C_s is now extracted by contracting that equation with $\boldsymbol{M}$ and averaging the result over at least the larger filter scale $\hat{\Delta}$. Let this average be denoted by angular brackets, then

$$C_s\,\Delta^2 = \frac{\langle \boldsymbol{L} : \boldsymbol{M} \rangle}{2\,\langle \boldsymbol{M} : \boldsymbol{M} \rangle}\,. \tag{4.2.45}$$

Some conceptual problems with spatially isotropic and temporally instantaneous averages for $\langle\cdot\rangle$ have been removed by Meneveau et al. [4.35] by introducing averages along particle paths. This approach introduces an improved flow history dependence and properly accounts for strong anisotropy that may develop, e.g., in separation flows, flows over obstacles etc.. For an implementation, see Reference [4.36].

Dynamic subgrid-scale modelling has the crucial advantage that the model viscosity properly responds to local flow structures. As can be seen from the above derivation, subgrid-scale viscosity is introduced only when the Tensor $\boldsymbol{L}$ detects considerable differences between the net convective non-linear flux on the Δ-scale and the non-linear flux from the $\hat{\Delta}$-filtered velocities. If there is no small-scale activity underneath the $\hat{\Delta}$-scale, then subgrid dissipation is not invoked.

In an interesting fashion, dynamic subgrid viscosities of the Germano type respond not only to the computed flow data but also, in an intricate fashion, to the numerical method used. When a more dissipative numerical scheme is employed, the numerical dissipation automatically suppresses some of the small scale dynamics. As a consequence, the the tensor $\boldsymbol{L}$ will sense less activity than it would under a non-dissipative numerical scheme. In this fashion, the dependence of the sum-total of numerical and subgrid-model dissipation will be diminished. (Obviously, this kind of model will not and should not introduce negative viscosities under normal conditions, so that overly dissipative numerics *will* have a negative effect in smooth flow regions! The dynamic subgrid model thus does not relieve one from the demand to use high-accuracy numerical methods in general.)

4.2.4.4 Summary and qualifications

Large eddy simulation is an alternative to Reynolds-averaged turbulence modelling. It requires much higher numerical resolution and therefore is not yet applicable to very large-scale systems. To provide a scale, we cite Haworth [4.37] who predicts that LES will be routinely applicable for internal combustion engine simulations (lengths scales of order 10 cm) within the coming years. On the other hand, successful LES provides insight into the dynamics of turbulence that Reynolds-averaged flow simulations cannot offer. Since the upper range of length scales is resolved numerically, much of the non-linear chaotic dynamics of turbulence is represented and can be compared with experimental measurements. Moreover, integral-scale flow statistics can be evaluated and probabilities of selected events can be extracted. This could be of primary importance for combustion modelling as will be elucidated in a later section on LES in combustion.

The original hope that the principal tasks of modelling would be simplified has been fulfilled in the sense that, for example, high-resolution LES allows proper resolution of near-wall flows without specialized wall interaction models. The dynamic extension of the very simple Smagorinsky one-coefficient model has already brought considerable progress and success. It should be kept in mind, however, that the dynamic adjustment idea of Germano et al. can be transferred also to intrinsically more complex models (with many more free coefficients) as has been pointed out by Jimenez [4.38].

Despite this "success story" of LES , Reynolds-averaged modelling will not be replaced completely in the near future for the following reasons:

- For large-scale systems, reliable LES with sufficient resolution will be computationally too demanding for years to come.
- The detailed flow dynamics information provided by LES is simply not of interest in many applications where global statistical mean values are all that is needed.
- Large eddy simulation models are far from being fully established and proven for the tremendous range of engineering fluid mechanical applications. In particular, proper LES approaches for flows that involve additional physics, such as multiple fluid phases, strong gravitational stratification or the aero-thermochemistry of combustion are still in their infancy. For some of these systems it is, for example, not at all clear that there is a well-defined cascade, so that the LES methodology itself may become questionable.

4.2.5 Subgrid-scale Porosity Models

Many practical applications involve very complex geometries with a wide variety of obstacles such as tubes and grids. Since such obstacles may be much smaller than the enclosure, it is often prohibitively expensive to resolve each obstacle.

This problem can be addressed by implementing a sub-grid model for obstacles that are smaller than the computational grid. Subgrid models have been developed to address the flow resistance, heat transfer, turbulence generation, and the enhanced combustion resulting from the subgrid obstacles. The flow resistance is introduced as a source term in the momentum Equation $(4.2.5)_2$ after it has been averaged

and closed though a suitable turbulence model. The momentum source term can be written as

$$S_v = -\frac{\alpha}{d} C_d \frac{1}{2} \rho |\boldsymbol{v}| \boldsymbol{v} \tag{4.2.46}$$

where d is the characteristic dimension of the obstacle; C_d is the drag coefficient; and the constant, α, is a friction factor that depends on the shape of the obstacle, the number of obstacles per unit volume and the spatial arrangement of the obstacles. The above approach has been used extensively in the modelling of explosions on off-shore platforms [4.39]. The drag coefficient may be assumed to be constant for a particular obstacle shape or may vary with the Reynolds number and the Mach number of the gas flow over the obstacle. Similarly, the subgrid heat transfer can be modelled by including a heat loss term [4.40, 4.41] in the energy equation. For a dense obstacle array, the density ρ in Equation $(4.2.5)_2$ should be multiplied by a porosity factor, ϕ, which corresponds to the volume fraction occupied by the gas.

Subgrid obstacles can produce turbulence that, as discussed in the following section, can greatly increase the rate of combustion. The turbulence produced by subgrid obstacles can be modelled by adding an appropriate source term in the equation for the turbulent kinetic energy, k, discussed in Section 4.2.2. One approach is to assume that the turbulent kinetic energy produced by the obstacles is a constant fraction, C_k, of the energy loss associated with momentum loss caused by drag [4.39]. Another approach is to use a one-parameter turbulence model for a particular geometry. Sha et al. [4.40] have used this approach to model multi-phase heat transfer in tube bundles. Finally, the turbulent length scale, ℓ, required by many combustion models, is usually expressed as a fraction of a characteristic length scale, such as the size of the obstacle or the spacing between obstacles. Benchmark tests, performed for a steady flow though a finite length (5 m) of obstacles [4.39], indicate that subgrid obstacle models can provide an accurate solution inside the obstacle array. However, a grid size approaching that of the obstacles can be required to resolve the strong gradient in the turbulent flow properties immediately downstream of the obstacles.

4.3 Turbulent Combustion Models

4.3.1 Regimes of Turbulent Premixed Combustion

A coarse estimation of how a turbulent flow field and premixed combustion may interact can be generated by comparing their respective characteristic length and time scales. As a basis for the subsequent discussions, we list the major relevant scales and provide brief explanations of their physical meaning:

Scales and characteristics of fully developed turbulence:

k	Turbulent kinetic energy	Kinetic energy per unit mass of turbulent velocity fluctuations.
ϵ	Energy dissipation rate	According to Kolmogorov's theory, [4.2,4.3], the dissipation rate is characteristic for both the actual rate of molecular energy dissipation at the Kolmogorov scale and the energy transfer rate through the cascade between ℓ and ℓ_K.
ℓ	Integral scale	Largest identifiable scale of turbulent fluctuations.

$u' \sim \sqrt{2k}$	Fluctuation velocity	Characteristic magnitude of turbulent velocity fluctuations; observed at the integral scale.
$\tau \sim \dfrac{\ell}{u'}$	Integral time scale	Also called "eddy turnover time".
$\mathrm{Re}_t \sim \dfrac{u'\ell}{\nu}$	Turbulent Reynolds number	Notice this Reynolds number is based on turbulent fluctuation length and velocity scales, but *not* with the scales of the overall flow field. Reynolds numbers based on system dimensions and mean flow velocities may be orders of magnitude greater than Re_t
$\ell_{\mathrm{Kol}} \sim \left(\dfrac{\nu^3}{\epsilon}\right)^{\frac{1}{4}} \sim \ell\,\mathrm{Re}_t^{-\frac{3}{4}}$	Kolmogorov scale	Smallest identifiable scale of turbulent fluctuations. At the Kolmogorov scale, the fluctuation energy that has cascaded down from the integral scale is dissipated.
$\tau_{\mathrm{Kol}} \sim \left(\dfrac{\nu}{\epsilon}\right)^{\frac{1}{2}} \sim \tau\,\mathrm{Re}_t^{-\frac{1}{2}}$	Kolmogorov time scale	Characteristic time of motion of the smallest turbulent eddies; also inverse of a characteristic strain rate at the Kolmogorov scale.
$u_{\mathrm{Kol}} \sim \dfrac{\ell_{\mathrm{Kol}}}{\tau_{\mathrm{Kol}}} \sim u'\mathrm{Re}_t^{-\frac{1}{4}}$	Kolmogorov velocity scale	Velocity fluctuation at the Kolmogorov scale.

Scales and characteristics of aero-thermochemistry:

s_L	laminar flame speed	Characteristic propagation velocity of a laminar flame *relative to the unburnt gas*.
ℓ_F	laminar flame thickness	Characteristic thickness of a laminar flame *including* the preheat and reaction zones.
ℓ_R	laminar reaction zone thickness	Characteristic thickness of the reaction zone within a laminar flame.
$t_F \sim \frac{\ell_F}{s_L}$	Flame passage time scale	Time a laminar flame needs to pass over its own structure.

t_Q	Quenching time scale	Inverse of a typical strain rate sufficient to quench the reaction zone of a laminar flame. t_Q may also be considered as a characteristic chemical reaction time scale.

Relevant characteristic non-dimensional numbers:

$\mathrm{Re}_t \sim \dfrac{u'\ell}{\nu}$	Turbulent Reynolds number	See above
$\mathrm{Da} \sim \dfrac{\tau}{t_F}$	Damköhler number	Indicates whether chemistry is fast $(\mathrm{Da} \gg 1)$ or slow $(\mathrm{Da} \ll 1)$ relative to the integral scale turbulence dynamics.
$\mathrm{Ka} \sim \dfrac{t_F}{\tau_{\mathrm{Kol}}}$	Karlovitz number	Indicates at which point $(\mathrm{Ka} \approx 1)$ the smallest turbulent eddies penetrate into the laminar flamelet preheat zones.
$\mathrm{K} \sim \dfrac{t_F}{\tau_{\mathrm{Kol}}}$	Karlovitz Stretch Factor	Indicates at which point $(\mathrm{K} \approx 1)$ the turbulence correlation time becomes comparable with the laminar flamelet passage time ℓ_F/s_L.
$\mathrm{Kq} \sim \dfrac{t_Q}{\tau_{\mathrm{Kol}}}$	Quench-Karlovitz number	Indicates at which point $(\mathrm{Kq} \approx 1)$ the smallest turbulent eddies quench the quasi-laminar thin reaction zones.

As we follow Peters [4.42, 4.43] closely, we consider the Borghi-Diagram displayed in Figure 4.3.1-1. There are two extreme regimes. The "the well-stirred reactor regime" is characterized by limitingly slow chemistry, whereas in the "eddy breakup regime" there is infinitely fast chemistry and infinitely slow molecular transport. Notice that the conceptually possible regime of infinitely fast chemistry at finite molecular transport efficiency is not of interest for applications because this regime would correspond with infinitely fast laminar flame propagation as shown in Reference [4.44].

Well-stirred reactor regime. Here the chemistry is so slow compared to the turbulent motions that all chemical species are always locally well mixed and chemical reactions proceed essentially at a kinetics-dominated rate. Modelling in this regime will proceed by separating the processes of mixing and reaction: Turbulent mixing and convection generate statistical distributions of the aero-thermochemical scalar variables (species mass fractions, enthalpy, temperature) and chemistry progresses according to the appropriate chemical kinetic scheme in a quasi-homogeneous fashion. Because of the typical strong non-linearity of realistic chemical reaction mechanisms, modelling must generally take into account that the mean kinetic reaction rates are *not* equal to the reaction rate functions evaluated with the mean scalars. Only under extreme conditions will scalar fluctuations be sufficiently damped to allow straightforward evaluation of chemical rates with the mean values of the relevant scalars. To capture the influence of scalar fluctuations on the mean rates under more general circumstances, the most appropriate

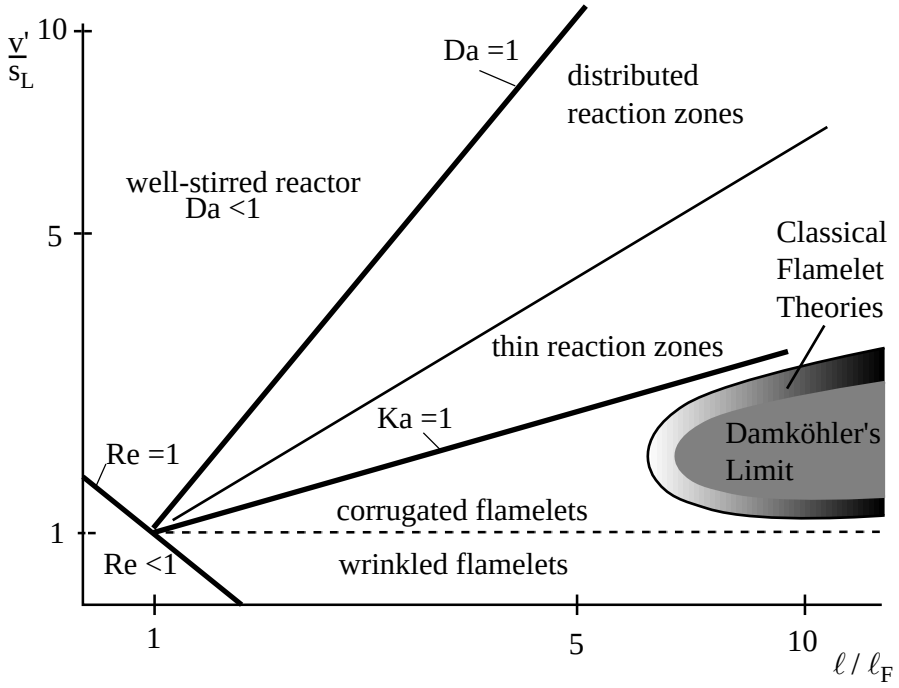

Figure 4.3.1-1: The Borghi diagram for regimes of turbulent premixed combustion

approaches include a joint probability density function (PDF) for the reactive scalars. Mean reaction rates are then evaluated by averaging the chemical rates with respect to this probability distribution. These PDF-methods are discussed in Section 4.3.7.

Eddy breakup regime. This is the opposite limit of infinitely fast chemistry and infinitely slow molecular transport. The label "eddy breakup" implies that as soon as a turbulent eddy mixes reactive gases that have suitable thermodynamic states these are burnt instantaneously. This picture of "mixed is burnt" is most appropriate for non-premixed combustion where in fact the fuel and oxidizer species can react only when brought together by molecular-level mixing. Turbulence greatly enhances this mixing process by multiple folding of the fuel-oxidizer separation layer and increasing the scalar gradients responsible for driving the molecular level diffusive fluxes. For premixed combustion, the "mixed is burnt" picture is less intuitive as fuel and oxidizer species are by definition already premixed. However, the cold reactants are unable to burn under most realistic conditions since the highly non-linear chemistry is frozen at ambient temperatures. Thus for the reaction front to progress, it is necessary that the unburnt gases be prepared for reaction on the molecular level by getting into close contact with the hot and radical-loaded burnt gases. Here, turbulent mixing comes in by multiple folding of the separation layer between unburnt and burnt gases, which is nothing but a locally one-dimensional laminar flame. Under these conditions, the turbulent flame folding determines the net reactant consumption, and the mean chemical rates are proportional to the inverse of the turbulent integral time scale τ. Modelling in the eddy breakup regime is discussed in Section 4.3.3.

Most realistic combustion systems do not satisfy the drastically simplifying assumptions underlying the two limit regimes described above. A hierarchy of increasingly complex models has been developed in recent years to cope with the fact that turbulence and chemistry generally interact on a wide range of length and time scales, depending on the specific application.

Laminar flamelet regime. This regime is similar to the eddy breakup limit in that reaction takes place within narrow, quasi-laminar flame zones. The key difference is that turbulence is not sufficiently intense to override the inherent laminar flame dynamics. On the one hand, the geometrical distortion of the flame surfaces (which may be multiple connected) is governed by both turbulent transport and laminar flame propagation dynamics. The latter includes the relative motion between flame and unburnt gases and laminar flame instabilities [4.1, 4.45]. On the other hand, the flame progression speed is perturbed by flame stretch, flame curvature, and unsteady thermodynamic conditions in the vicinity of the flame. The most important task of modelling in the flamelet regime is a proper description of the flame surface area increase, while higher-order corrections are induced by perturbations of the laminar flame structure [4.46, 4.47]. One may distinguish the "wrinkled flamelet" and "corrugated flamelet" regimes, depending on whether the inherent laminar flame dynamics or turbulent convection dominates the evolution of the flame surface.

Thin reaction zone regime. With increasing turbulence intensity, the smallest turbulent eddies decrease in size until their extension becomes comparable to the laminar flame thickness. Peters [4.43] introduces the "thin reaction zone regime" in which the laminar flame structure is disrupted by turbulent mixing, while the generally much thinner quasi-laminar reaction zones still survive. Thus the pre-conditioning process that brings the unburnt gas to thermodynamic-chemical conditions at which reaction commences is modified by turbulence, while the ultimate progress of reactions still proceeds in a locally quasi-laminar fashion. In this regime, the net rate of fuel consumption is influenced at a comparable level by both the effective reaction surface area and the turbulence-dominated pre-conditioning process. Consistent models appropriate for this regime are being introduced into numerical modelling only as this report is being compiled.

Distributed reaction zone regime. At even higher turbulence intensities, the turbulence-induced strain on the reaction zones becomes sufficient to quench them at least locally. Thus because of the intermittency of turbulence, thin reaction zone combustion and well-stirred reactor regions begin to co-exist. Currently, there are no models that would appropriately interpolate across this threshold. The most promising ansatz in this direction appears to be extended PDF methods that would properly account for the intimate coupling between reaction and molecular transport in the flamelet and thin reaction zone regimes, while keeping the option of modelling the turbulence-dominated well-stirred reactor regime.

4.3.2 Modelling Strategies: Distributed Reaction versus Reaction Fronts

Two principally different approaches to modelling the progress of turbulent premixed combustion must be distinguished. The most popular approach describes turbulent combustion by an equation system that is as close in structure to the original reactive Navier Stokes equations as possible. In this set-up the key modelled quantities are the mean volumetric reaction rates (for a characteristic reaction progress variable) and the net turbulent transport within the effective turbulent "flame brush". The interaction between mean reaction and turbulent transport then yields the overall reactant consumption rate [4.48 to 4.52].

The alternative approach considers a turbulent premixed flame as an effective reacting discontinuity. Here, the detailed internal processes within the flame brush are not resolved, but the overall reaction progress is described as being a net turbulent flame speed s_T, in analogy with the laminar burning velocity s_L, [4.53, 4.54].

Although the former approach has the advantage of incorporating detailed models of all the sub-processes within the flame brush, its disadvantage is that it actually *must* incorporate these detailed models in order

to properly function at all. The only modelled quantities for the second approach are the turbulent burning velocity s_T and suitable jump conditions for the turbulence quantities across the flame, which cannot be derived straightforwardly from the conservation principles. Its disadvantage is that there are highly unsteady combustion regimes where the internal turbulent flame structure is far from quasi-steady and the notion of a turbulent burning velocity becomes questionable in the first place.

The importance of a proper interaction between turbulent transport and net chemical reaction progress in a resolved flame brush cannot be overestimated. As pointed out, e.g., by Chorin [4.55] and by Teng et al. [4.56], the net propagation speed of deflagration wave (i.e., of a "flame") with respect to the unburnt gases depends on the detailed internal flame structure. This is in contrast to shock or detonation waves, whose propagation speed is determined solely by initial and boundary data of the flow problem (see also Section 4.5.4 below). As a consequence, the first modelling strategy described above must always incorporate proper submodels for both the mean reaction rates and the turbulent transport processes. Neglect of one of these ingredients will provoke utterly wrong results!

4.3.3 Eddy breakup and extensions

Eddy breakup models are typically formulated according the the first modelling strategy described in Section 4.3.2. It should be noted, however, that the eddy breakup limit corresponds, under the propagating flame front modelling paradigm, to Damköhler's [4.57] classical turbulent flame speed prediction,

$$s_T \sim u' \; . \tag{4.3.1}$$

High-speed combustion simulations for the large-scale RUT facility using this modelling approach have been reported in References [4.53, 4.58].

4.3.3.1 Mean reaction rate modelling

As discussed above, in this regime turbulent mixing dominates the net reactant consumption. Thus the characteristic consumption rate is proportional to the inverse of the turbulence integral time scale τ. In addition, it is known that reactions are frozen in the cold unburnt and that they cease when all the reactants are consumed. Introducing a suitably defined reaction progress variable $\tilde{c}$, with $\tilde{c} = 0$ in the unburnt gas and $c = 1$ in the burnt, the mean reaction progress is modelled as

$$\frac{\partial \bar{\rho}\tilde{c}}{\partial t} + \nabla\cdot(\bar{\rho}\tilde{c}\tilde{\boldsymbol{v}}) = \nabla\cdot(\mu_\tau \nabla\tilde{c}) + \bar{\rho}\tilde{\omega} \tag{4.3.2}$$

where

$$\tilde{\omega} = \frac{1}{\tau_{\mathrm{EBU}}}\,\tilde{c}(1-\tilde{c}) \; . \tag{4.3.3}$$

In actual numerical implementations, the determination of the turbulent characteristic time scale depends on the underlying flow turbulence model. For the most-often-used one- and two equation models—which provide a characteristic turbulent kinetic energy k and either a turbulent mixing length ℓ, a turbulent energy dissipation ϵ, or a turbulent dissipation rate ω_τ—the turbulence time scale is modelled as

$$\frac{1}{\tau_{\mathrm{EBU}}} = \frac{1}{\tau} = \sim \left(\frac{k}{\ell^2}\right)^{\frac{1}{2}} \sim \frac{\epsilon}{k} \sim \omega_\tau \; . \tag{4.3.4}$$

Obviously, this modelling strategy completely neglects chemical kinetic influences. As a consequence, these models systematically overpredict the chemical energy conversion when either chemical reactions

have not yet been ignited at all or when the well-stirred reactor regime with kinetics-dominated reaction is approached. A heuristic correction [4.51, 4.52] that, with appropriate tuning, considerably improves eddy breakup predictions simply replaces the turbulence dictated $1/\tau_{\mathrm{EBU}} = 1/\tau$ from Equation (4.3.4) with

$$\frac{1}{\tau_{\mathrm{EBU}}} = \min\left(\frac{1}{\tau}, \frac{1}{t_{\mathrm{ch}}}\right) , \tag{4.3.5}$$

where $1/t_{\mathrm{ch}}$ is a suitable estimate of the relevant slowest chemical time scale that is controlling the reaction progress. This can be either an ignition delay time for unreacted gases undergoing an auto-ignition process, or it may be a laminar flamelet quenching time scale when the transition between the eddy breakup and well-stirred reactor regimes is to be modelled in a heuristic fashion.

4.3.3.2 Turbulent transport within the flame brush

Eddy breakup models and their extensions as formulated originally in References [4.48, 4.51, 4.52, 4.59, 4.60] typically focus on the mean reaction rate model as described above. The fact, discussed in Section 4.3.2, that there must be a suitably balanced approach taking into account also the turbulent transport processes is normally neglected. The available standard turbulent transport models applied in the burnt and unburnt gases are simply transferred to the flame brush region as well.

Notice, however, that the Bray, Moss, Libby (BML) model [4.49, 4.50], which specifically addresses the issue of turbulent transport in the flamelet regime, is applicable in the eddy breakup limit as well. Thus a very sophisticated turbulent transport scheme, suited for combination with an eddy breakup approach is available in the literature. For more details on the BML model, see Section 4.3.4.2.

4.3.3.3 Summary and qualifications

Eddy breakup modelling provides a crude first approach to turbulent combustion simulations when the primary interest is in (i) worst-case estimates for high-intensity turbulence and (ii) details of the flame acceleration history from ignition to high-speed combustion are irrelevant. Heuristic extensions of EBU models to include characteristic time scales of chemistry lack a systematic derivation from first principles and should be considered as ad hoc "fixes". With suitable fine tuning of the detailed chemical time scale models, one might obtain reasonable agreement with experimental data and obtain limited predictive capabilities within the range of conditions that was used in fine tuning the models.

Much more sophisticated modelling is required to obtain true predictive capabilities both for flame acceleration and the kinetics-dominated high-turbulence intensity regime responsible for potential transition to detonation.

4.3.4 Flamelet Models

The key goals behind flamelet modelling are to incorporate effects of (i) fast but finite reaction rates, (ii) the inherent quasi-laminar flame dynamics, and (iii) the intimate coupling between chemical reactions and molecular transport that arises when rapid chemistry enforces very thin flame structures. Recent work by Peters [4.43] has revealed that in the true flamelet regime, where quasi-laminar flame structures including preheat and reaction zones actually persist, the effects of finite rate chemistry appear as perturbations only. The dominant effect to be accounted for is the inherent flamelet dynamics, including various forms of flame instability, [4.1], and the competition between self-induced flame motion and turbulent convection.

4.3.4.1 *Mean reaction rate modelling*

We distinguish again between the two principal modelling strategies from Section 4.3.2.

Flame fronts and turbulent burning velocities. Much of the flamelet modelling literature ([4.45, 4.61] and references in [4.1]) focus on deriving effective turbulent burning velocities s_T, which could readily be incorporated in numerical flame front tracking schemes [4.53, 4.54]. Given a mean laminar flamelet burning velocity $\overline{s_L}$, averaged along the flamelet surface(s), the key problem is to assess the net flame area increase that is due to the influence of turbulent convection. The net turbulent burning velocity is then expressed as

$$s_T = \frac{A}{\overline{\overline{A_{\text{eff}}}}}\,\overline{s_L}\,, \tag{4.3.6}$$

where A_{eff} denotes the net flame area of an averaged turbulent flame surface that is centred within the flame brush region, while A is the total laminar flamelet surface area for the same section of the turbulent flame brush.

The laminar and turbulent flame surface dynamics are conveniently described by a level set procedure. The flame surface is defined as the zero level set of a scalar function $G(\boldsymbol{x}, t)$ satisfying the G-equation

$$\frac{\partial G}{\partial t} + (\boldsymbol{v} + s\boldsymbol{n}) \cdot \nabla G = 0 \quad \text{on} \quad G(\boldsymbol{x}, t) = 0 \tag{4.3.7}$$

and some constraint away from the flame front, such as, [4.62],

$$|\nabla G| = 1 \quad \text{for} \quad G(\boldsymbol{x}, t) \neq 0\,. \tag{4.3.8}$$

Various different approaches towards assessing the area ratio in Equation (4.3.6) have been proposed. Fractal surface ideas have been introduced, e.g., in Reference [4.63]. Assuming the flame surface to be a fractal with dimension D one obtains expressions of the type

$$\frac{A}{\overline{\overline{A_{\text{eff}}}}} = \left(\frac{\ell}{\ell_{\min}}\right)^{D-1} \tag{4.3.9}$$

where D is the fractal dimension of the flamelet surface and $\ell_{\min}$ is the shortest characteristic length of flamelet corrugations. At the time there had been intense discussions as to whether this minimum length scale would correspond to the Kolmogorov length of the unburnt gas turbulent flow or whether this length was determined by a balance of turbulent flame advection and flame propagation relative to the unburnt. The latter approach naturally introduces the Gibson length ℓ_{G}. It is the characteristic length that is defined as the very fluctuation length scale within the turbulent energy spectrum at which the turbulent fluctuation velocity matches the laminar burning velocity [4.42]. A brief dimensional analysis based on the Kolmogorov scalings leads to

$$\frac{\ell}{\ell_{\text{G}}} = \left(\frac{u'}{s_L}\right)^3\,. \tag{4.3.10}$$

Re-normalization group procedures applied to the level set formulation from Equation (4.3.7) for the laminar flame surface motion are suggested in Reference [4.61], leading essentially to the Damköhler limit in Equation (4.3.1). Another corroboration of this result is provided by Peters [4.45], who suggests closure of the level set equation along the lines of more standard turbulence closure procedures.

As mentioned, most of these models end up reproducing Damköhler's law from Equation (4.3.1) in the limit of large turbulence intensity $u'/s_L \gg 1$ and providing some kind of interpolation down to small turbulence intensities $u'/s_L \ll 1$, in which case $s_T \sim s_L$. The net burning velocity law in these cases would read

$$\frac{s_T}{s_L} = 1 + \left(\frac{u'}{s_L}\right)^n \tag{4.3.11}$$

with some power n close to unity.

These earlier attempts have concentrated, in fact, on the limit of large turbulence intensity hoping to derive the experimentally observed sublinear growth of s_T with u' (the bending effect) solely from the flame surface dynamics under turbulence. It has only recently been clarified that this bending effect arises—most likely—not from flame surface dynamics but from a transition into the thin reaction zone regime (see Section 4.3.5).

The more important range of turbulence intensities, where $u'/s_L = O(1)$ has been largely neglected as pointed out by Bray [4.1]. Consequently, it is in this regime where new modelling ideas incorporating the inherent stability features of laminar flames are needed. Unfortunately, this regime is of primary importance for flame acceleration in the early stages after initiation of a laminar flame kernel.

Resolved flame brushes and mean reaction rates. The alternative modelling strategy has been pursued for the flamelet regime since the first introduction of the Bray-Moss-Libby model (BML), [4.49, 4.50]. Even though, these authors focus most of their attention on the proper modelling of turbulent transport in the flame brush, their principal approach follows the resolved flame brush strategy and thus they do propose closure approximations for the mean reaction rates. One major result in this context is a more systematic derivation of the eddy breakup formulae from Equations (4.3.3), (4.3.4) in the limit of high turbulence intensity. For moderate turbulence intensities, their mean reaction rate modelling is similar to more recent approaches based on "flame surface area densities", as described next.

An approach that is based on effective continuum equations for turbulent combustion in the flamelet regime (in the sense of homogenization) must provide net distributed source terms per unit volume in the finite-volume framework or per unit mass in a primitive variable formulation. A relation between these effective distributed source terms and the singular surface based sources on the flamelet microscale must be provided. This is done by introducing the "surface area density" Σ, i.e., the flamelet surface area per unit volume. The burnt gas production rate per unit volume $\tilde{\omega}$ from Equation (4.3.2) would then read

$$\tilde{\omega} = \overline{s_L}\,\Sigma\,, \tag{4.3.12}$$

and the key task of modelling is to obtain the surface area density $\Sigma(\boldsymbol{x}, t)$.

The flamelet surface evolves because of (i) convection by the unburnt gas velocity $\boldsymbol{v}_u$ immediately in front of the flamelet and the self-induced motion of the surface in its normal direction at speed s_L. Given $\boldsymbol{v}_u$ and s_L, an exact flame surface area evolution equation can be derived [4.64, 4.65]. Two alternative formulations have been proposed that are mathematically equivalent, but lend themselves to different modelling strategies:

As an example, we provide here the propagative formulation, [4.46],

$$\frac{\partial \Sigma}{\partial t} + \nabla\cdot\left(\langle \boldsymbol{v}_u + s_L \boldsymbol{n}\rangle_s\,\Sigma\right) = \langle \nabla\cdot\boldsymbol{v}_u - (\boldsymbol{n}\circ\boldsymbol{n}) : \nabla\boldsymbol{v}_u\rangle_s\,\Sigma + \langle s_L\kappa\rangle_s\,\Sigma \tag{4.3.13}$$

where $\boldsymbol{n}$ is the local flamelet surface normal, $\kappa = \nabla \cdot \boldsymbol{n}$ is the mean flamelet curvature, and $\langle \cdot \rangle_s$ denotes conditional averaging along the flamelet surface. The respective terms in this equation describe (i) the temporal accumulation of flame surface area, (ii) mean transport by the combined action of unburnt gas flow, and self-induced motion, (iii) surface stretching by the unburnt gas flow and (iv) surface stretching because of the self-induced motion of the curved flamelet surface.

The alternative "reaction-diffusion formulation" contains terms that directly correspond to those in Equation (4.3.13), but these are cast into a form that more resembles a standard reaction-diffusion equation as implied by its name. It is a matter of modelling strategies and numerical techniques, as to which of the formulations is actually used.

Obviously, most of the terms in these flame surface area density equations are not known exactly in a turbulent flow, so that the resulting equation needs closure [4.66 to 4.70]. Vervisch and Veynante, [4.46] provide an excellent summary of various modelling approaches as well as their numerical and experimental validation in References [4.71] and [4.72], respectively. Various aspects of observations from direct numerical simulations and experiments are well reproduced by the modelled flame surface area equations.

Unfortunately, the key ingredients of inherent flamelet stability, which become important under moderate turbulence intensities are not yet considered in these models [4.1].

4.3.4.2 Turbulent transport within the flame brush

It is remarkable that there is only one serious strain of work, originally authored by Bray et al. [4.49] and Bray et al. [4.50], that aims at a systematic assessment of combustion-induced modifications of turbulent transport. This is particularly disturbing in light of the outstanding importance of the effective transport for the net combustion rates, (see Sections 4.3.2 and 4.5.4).

Bray et al. [4.49, 4.50], and Bray and Peters [4.47] start off by observing that in the flamelet regime the probability of actually landing within a flamelet is extremely low, even within the turbulent flame brush. (See also References [4.1, 4.73].) The reason is that—by definition of the regime—preheating and combustion are concentrated within asymptotically thin layers that occupy only a small amount of space. Based on this observation, they conclude that the probability density of a characteristic reaction progress variable c, say, must be of the form

$$P(c; \boldsymbol{x}, t) = \alpha(\boldsymbol{x}, t)\, \delta(c) + \beta(\boldsymbol{x}, t)\, \delta(1 - c) + \gamma(\boldsymbol{x}, t)\, f(c; \boldsymbol{x}, t) \tag{4.3.14}$$

where $\delta(\cdot)$ is the Dirac-delta distribution, $f(c; \boldsymbol{x}, t)$ is an order $O(1)$ function, whose detailed form is not specified, and where the coefficients α, β, γ satisfy the *crucial* estimates

$$\alpha, \beta = O(1) \qquad \text{but} \qquad \gamma \ll 1\,. \tag{4.3.15}$$

The progress variable varies from $c = 0$ in the unburnt gas to $c = 1$ in the burnt, so that $\alpha(\boldsymbol{x}, t), \beta(\boldsymbol{x}, t)$ correspond to the probabilities of finding unburnt and burnt gas conditions, respectively.

After introduction of conditional averages $\overline{\cdot}^u, \overline{\cdot}^b$ with respect to unburnt and burnt conditions and heavily using the fact that $\gamma \ll 1$, the authors arrive at asymptotic formulae for the turbulent transport terms such as $\widetilde{\boldsymbol{v}'' c''}$ in the Favre-averaged turbulent transport equation for the reaction progress variable or $\widetilde{\boldsymbol{v}'' \circ \boldsymbol{v}''}$ in the momentum equations

$$\widetilde{\boldsymbol{v}'' c''} = \tilde{c}\,(1 - \tilde{c})\,(\overline{\boldsymbol{v}}^b - \overline{\boldsymbol{v}}^u) \tag{4.3.16}$$

and

$$\widetilde{\boldsymbol{v}'' \circ \boldsymbol{v}''} = (1-\tilde{c})\,\overline{\boldsymbol{v}' \circ \boldsymbol{v}'}^{u} + \tilde{c}\,\overline{\boldsymbol{v}' \circ \boldsymbol{v}'}^{b} + \tilde{c}\,(1-\tilde{c})\,(\overline{\boldsymbol{v}}^{b} - \overline{\boldsymbol{v}}^{u}) \circ (\overline{\boldsymbol{v}}^{b} - \overline{\boldsymbol{v}}^{u})\;. \tag{4.3.17}$$

It should be noted that in a natural way, this theory suggests the introduction of Reynolds stress models, as the primary quantities appearing here are the Reynolds stresses themselves. One does *not* obtain any formulae justifying a gradient transport approximation.

In fact, an interesting observation concerns the counter gradient transport. (cf. [4.72]). In a regime of not too intense turbulence, one may expect that the conditional mean velocities $\overline{\boldsymbol{v}}^{u}$ and $\overline{\boldsymbol{v}}^{b}$ will differ by the thermal expansion induced within the turbulent flame brush, i.e.,

$$\overline{\boldsymbol{n}} \cdot (\overline{\boldsymbol{v}}^{b} - \overline{\boldsymbol{v}}^{u}) \approx -s_T\,(\frac{\rho_u}{\rho_b} - 1) < 0\;, \tag{4.3.18}$$

where $\overline{\boldsymbol{n}}$ is the mean flame front normal pointing towards the unburnt gases. From the sign of this expression, we conclude that the net turbulent scalar transport of c will be directed towards the *burnt* gases. On the other hand, $c = 1$ in the burnt and $c = 0$ in the unburnt gases, so that a standard gradient transport approximation would yield

$$\overline{\boldsymbol{n}} \cdot (-D_t \nabla \tilde{c}) > 0 \tag{4.3.19}$$

so that the standard approximation would predict transport towards the *unburnt* gases. This somewhat surprising result is neglected in practically all turbulent combustion models that are not derivatives of the Bray, Moss, and Libby approach!

Veynante et al. [4.74] have closely analyzed direct numerical simulations by Rutland and Trouvé [4.75] and Trouvé et al. [4.76], which are set up in different regimes of turbulence intensity and surprisingly imply contradictory conclusions about the presence or not of countergradient transport. Veynante et al. conclude (see also [4.46]) that *both* numerical simulation results are nevertheless compatible with the BML formalism explained above: It turns out that the underlying presumption leading to the sign in Equation (4.3.18), namely that the *conditional* mean velocities within the flame brush satisfy an overall estimate based on the total thermal gas expansion, becomes less and less accurate as the turbulence intensity increases. For high turbulence intensities, turbulent mixing dominates the expansion-induced separation of burnt and unburnt gases and the net scalar transport changes sign.

Thus one may conclude that less-sophisticated modelling approaches based on standard gradient transport approximations throughout the combustion region will yield reasonable results for high-speed flames. But, as observed previously, the regime of low-to-moderate intensity turbulence, which is most crucial for the initial stages of flame acceleration, is not properly represented by such simplified schemes.

4.3.4.3 Statistical evaluation through presumed PDFs

The flamelet ansatz introduces strong statistical correlations between various flow variables and transport fluxes. The knowledge that molecular diffusion always occurs in conjunction with chemical reaction simplifies statistical evaluations considerably. Given a characteristic coordinate c that resolves the flamelet structures (such as a normalized reaction progress variable), chemical reaction source terms, diffusive fluxes, species concentrations etc. can all be expressed explicitly in terms of c and a few additional parameters $\boldsymbol{\chi}$ characterizing the flamelet structure (such as an outer strain or the flamelet surface curvature). Statistical averages of any such quantity $Q(c)$, say, can then be obtained if a probability density for c and the flamelet parameters is available:

$$\overline{Q}(\boldsymbol{x}, t) = \int\!\!\int Q(c)\, P(c; \boldsymbol{\chi}; \boldsymbol{x}, t)\, dc\, d\boldsymbol{\chi}\;. \tag{4.3.20}$$

Now we will see in Section 4.3.7 below that a full-fledged model describing the time evolution of such a PDF is extremely complex and that its introduction at the level of flamelet models would destroy their appealing simplicity.

The standard compromise here is to introduce presumed PDFs. One a priori assumes that the PDF will have shapes close to a certain class of representative functions that have few free parameters. Thus given those parameters, the PDF is known. Next, one derives governing equations for those free parameters, solves these (or their closed counterparts) numerically, and uses the obtained fields of parameters to locally define the presumed PDF.

The typical "β-PDF", [4.46, 4.77], has two free parameters, which can be related uniquely to mean and standard deviation of the distribution. Under these conditions it is sufficient to obtain appropriate estimates of the mean and of the fluctuations in order to determine the probability distribution. In the "presumed PDF approaches" one introduces, in fact, in addition to a transport equation for the turbulent mean of c an additional model equation for the standard deviation. These equations can formally be derived rigorously, but the resulting terms generally need closure. In summary, a presumed PDF model requires one additional equation for the turbulent scalar fluctuations, while avoiding the complexities of a full PDF transport equation.

Presumed PDF models are very popular in the context of flamelet, thin reaction zone, and the various conditional moment closure approaches.

4.3.4.4 Summary and qualifications

Flamelet models provide a systematic methodology, based on first principles, to address turbulent combustion modelling in a regime that covers the eddy breakup limit. Combustion is still concentrated in narrow fronts, but the length, time, and velocity scales of thin flame dynamics begin to non-trivially interact with the flow turbulence. Following recent arguments by Peters [4.43], the interaction of the self-induced flame geometry evolution—including flame instabilities—with turbulent convection is the most important aspect in the flamelet regime.

Promising and successful models for the mean volumetric chemical reaction progress, for effective turbulent flame speeds as well as for the modifications of turbulent transport by combustion have been proposed and widely tested. A host of flamelet models cater to various different numerical simulation strategies, such as reaction-turbulent diffusion type of modelling or flame front tracking approaches (see Section 4.5).

Unfortunately, most of the modelling efforts have been focused on the regime of high-intensity turbulence where turbulent motions dominate over the intrinsic flamelet dynamics. As previously stated, this is not the regime where flamelet models are most suitable [4.43]. As a consequence, the regime of low-to-moderate intensity turbulence, which is most important for the early stages of flame acceleration, is still in its modelling infancy.

The intimate interplay between reaction progress and turbulent transport that is crucial for the establishment of overall combustion rates has widely been neglected, except in the seminal work by Bray, Moss, Libby and their co-workers. It is of outmost importance that further developments of the flamelet theory for the low-to-moderate turbulenc intensity regime will include proper turbulent transport models from the start.

4.3.5 Thin Reaction Zones

As turbulence levels increase, one moves up vertically in the Borghi diagram from Figure 4.3.1-1 and approaches the line $\mathrm{Ka} = 1$. At this point the smallest fluid mechanical eddies (on the Kolmogorov scale) are comparable in size to the laminar flame preheat zone thickness, and these eddies will begin to non-trivially distort the laminar flamelet structures. Recent observations from direct numerical simulations by Poinsot et al. [4.78] indicate that this does not immediately imply a breakdown of all determinstic structures and the transition to the regime of truly distributed reactions. Rather, they continue to observe very strong correlations between reactions and molecular transport for Karlovitz numbers much higher than $\mathrm{Ka} = 1$.

Peters [4.43] independently argues that one must distinguish a complete laminar flame from its reaction zone. A laminar flame alway includes a reaction zone, but thin reaction zones may well exist without a flamelet's quasi-oned-imensional, quasi-steady preheat zones. In fact, since the reaction zones of laminar flames are typically thinner by an order of magnitude than the preheat-reaction zone complex of a laminar flamelet, one may expect thin reaction zones to exist up to much higher Karlovitz numbers than are necessary to disrupt the preheat zones.

Peters [4.43] proposes a new theory for turbulent premixed combustion that includes this new ansatz of "thin reaction zones" and unifies it with the classical flamelet ansatz. Implementations of this theory are current work in progress, so that no details will be given here. It may suffice to mention the probably most important result of this theory, namely a consistent explanation of the "bending effect" in turbulent premixed combustion: It is found experimentally that effective turbulent burning velocities do not follow Damköhler's limit of $s_T \sim u'$ for large turbulence intensities. One rather finds a sublinear growth and even a decay of the effective flame speed for very intense turbulence. The "classical" flamelet ansatz, which accounts for combustion in only quasi-laminar, quasi-one-dimensional flamelets, does not predict this bending. Rather, as pointed out earlier, the limit of classical flamelet theories for large turbulence intensities *should* be the Damköhler law, which in turn is equivalent to the eddy breakup limit.

The new theory in Reference [4.43] includes the effect of intense stirring within the preheat zone in front of the "thin reaction zones". Multi-dimensional turbulent fluctuations are accounted for when modelling the fluxes of species and heat into and out of the reaction zones. A formulation, based on the the G-equation or level set approach is developed that successfully unifies earlier flamelet theories and the new theory for the thin reaction zone regime. Limit considerations for quasi-stationary turbulent flames also lead to a new and unified effective turbulent burning velocity law.

4.3.6 Conditional Moment Closures

The ansatz of "conditional moment closure" was first introduced by Bilger [4.79]. Noticing that the typical fast chemistry of combustion reactions induces strong statistical correlations between reaction, diffusion, and convection, he proposed to systematically build combustion closure models by introducing statistical moments that are conditioned on selected characteristic reaction variables. Thus, for example, a vector of mean reaction rates is expressed as

$$\overline{\dot{\omega}} = \int_0^1 P(c)\, dc \tag{4.3.21}$$

where

$$\langle \boldsymbol{\omega} | c \rangle = \int_\xi \boldsymbol{\omega}(\xi, c) P(\xi|c)\, d\xi \tag{4.3.22}$$

is the conditional average of the reaction rate vector for a given value of the reaction progress variable. The variable ξ represents other quantities that the local reaction rate may depend on, such as temperature, other species concentrations etc..

The advantage of this approach is the following: If strong correlations between reaction rates and a structure variable such as c exist, and if these correlations capture the strongest fluctuations of the variable to be averaged, then modelling is greatly simplified: Conditional averages as in Equation (4.3.22), e.g., be approximated by simple evaluation at the mean state (conditioned on c) and all the statistics is covered by the probability density $P(c)$ in Equation (4.3.21).

This ansatz automatically captures the classical flamelet theories for premixed as well as non-premixed combustion and this author is convinced that it also describes the essence of the new theory of "thin reaction zones" formally. However, one should be aware that the formulae in Equations (4.3.21), (4.3.22) are mere formal representations that, all by themselves, do not yet represent a turbulent combustion closure. In order to actually evaluate these formulae, one must introduce concrete specifications regarding $P(c)$ and regarding the evaluation of Equation (4.3.22).

Thus specific closure models for the detailled distributions of, say, $\boldsymbol{\omega}$ with respect to the key progress variable c are to be invoked. It is at this point, where the formal framework of conditional moments must be backed by physical insight. Obvious candidates for the physical closure are flamelet models for premixed and non-premixed combustion, or one my borrow from the new thin reaction zone theory in Reference [4.43]. A wealth of publications is available that covers various modelling approaches as well as comparisons with experimental observations (see e.g., [4.80 to 4.82, 4.82] or [4.1]).

4.3.7 Statistical Modelling Based on a PDF Evolution Equation

Flamelet, thin reaction zone and conditional moment closure models all try to explore the fact that under many realistic conditions chemistry is fast and imposes strong correlations between those variables that describe the chemical reactions. This presumption, however, becomes inapplicable when Damköhler numbers decrease to order $O(1)$ or smaller. In this case, chemistry will generally still be stiff and fast enough to leave local traces in the form of strong fluctuations, but it is no longer strong enough to dominate the evolving flow structures. In this situation, a more general approach is needed that does not rely on a priori knowledge about statistical correlations.

4.3.7.1 The general PDF ansatz

Pope [4.83] has laid the foundation for a turbulent combustion modelling strategy that differs significantly from the other approaches described earlier. From the start, he assumes an inherently statistical nature of turbulent combustion and introduces a joint PDF—in the most general case involving all reactive and thermodynamic scalars as well as the flow velocities. The idea then is to model the temporal evolution of this probability density, say $P(\boldsymbol{Y}, p, T, \boldsymbol{v}; \boldsymbol{x}, t)$, and to obtain the measurable statistical means and correlations by integrating suitable moments of the PDF.

An involved derivation leads to the following exact PDF evolution equation [4.83]

$$\frac{\partial P}{\partial t} + \boldsymbol{v} \cdot \nabla_{\boldsymbol{x}} P + \boldsymbol{\omega}(T, p, \boldsymbol{Y}) \cdot \nabla_{\boldsymbol{Y}} P = \mathrm{MolecularTransport} \tag{4.3.23}$$

The first term denotes accumulation of probabilities, the second denotes transport in physical space by

the (fluctuating) velocities, the third describes deformation of the PDF because of chemical reactions, and the term on the left-hand side is responsible for the effect of molecular scale mixing (heat conduction, diffusion, etc) on the PDF.

Notably, the chemical reaction term is *closed*; that is, since all the arguments of $\boldsymbol{\omega}$ in Equation (4.3.23) are *in*dependent variables for the PDF, the "convection velocity" in the space of the reactive scalars is an explicit function that depends on the arguments of, but not on the PDF itself. This observation is absolutely crucical and is the reason for the considerable attractiveness of PDF models. While in other turbulent combustion closures one goes to great lengths in constructing expressions for the mean chemical reaction rates, one gets the analogue in PDF equations for free!

Even more striking, but less used in practice, is the fact that the convective term $\boldsymbol{v} \cdot \nabla_{\boldsymbol{x}} P(\boldsymbol{Y}, p, T, \boldsymbol{v}; \boldsymbol{x}, t)$ is also *closed*! The velocity, too, is an independent variable for the PDF, and hence the vector $\boldsymbol{v}$ in this expression is a known quantity. Hence the only term to be modelled is the microscopic molecular transport term on the right-hand side of Equation (4.3.23). To be clear, the convective transport term includes turbulent convection. Thus a full-fledged PDF-model that includes the velocity components as independent variables does not require a turbulence closure in the standard sense. Only those effects taking place at the very smallest scales on the level of molecular transport do require modelling.

As astounding and attactive as this property of joint PDF models might be at a first glance, it is not explored in many applied modelling systems. The reasons are that this kind of formulation does not fit into any of the more standard flow simulation frameworks, where the standard momentum balances are discretized and solved computationally. In addition, PDF implementations are computationally extremely demanding, simply because of the high dimensionality of the problem posed: The space of independent variables for the PDF comprises three space coordinates, time, three velocity coordinates, and as many additional independent scalars as there are independent chemical concentrations. Solving a partial differential equation in more than six-dimensional spaces by standard techniques is utterly unfeasible given the expected computational capacities for the coming decade. A compromise that saves at least the advantage on closed reaction terms will be summarized shortly.

The only contribution in Equation (4.3.23) that does require closure is the term on the right-hand side, which is induced by molecular transport. As molecular transport fluxes are driven by gradients of the relevant species, an exact and consistent PDF model description would require multi-point statistics [4.83]. This is generally avoided because it would increase the computational costs even further. Thus a number of mixing models have been developed in recent years that attempt to approximate the mixing term by known terms that only involve the one-point PDF, (see [4.83]).

4.3.7.2 Reduction of complexity by turbulence closure

Most flow simulation and combustion codes that are readily available (commercially or as research codes) rely on discrete integration of the balance equations of mass, momentum, and energy in addition to a set of species transport and reaction equations. Generally, modelling systems are developed "bottom up" by first implementing a flow solver and then adding the effects of chemistry with increasing complexity. To save considerable computational capacities and to avoid the effort of new code implementations of major dimension, a compromise is often introduced to simplify the PDF Equation (4.3.23)—albeit at the cost of greater uncertainty or imprecision. The idea is to consider the joint PDF for the reactive scalars and thermodynamic variables $P(\boldsymbol{Y}, p, T; \boldsymbol{x}, t)$ only. In this case, the convective term in Equation (4.3.23) can no longer be expressed explicitly in terms of the arguments of the PDF, but must be modelled. In

the most popular approach, which couples the PDF evolution to a standard flow turbulence model, one replaces the velocity $\boldsymbol{v}$ by its turbulent mean $\overline{\boldsymbol{v}}$ and fluctuations $\boldsymbol{v}''$, so that the PDF convection term becomes

$$\boldsymbol{v} \cdot \nabla_{\boldsymbol{x}} P = \overline{\boldsymbol{v}} \cdot \nabla_{\boldsymbol{x}} P + \overline{\boldsymbol{v}'' \cdot \nabla P} \,. \tag{4.3.24}$$

Given a mean velocity field $\overline{\boldsymbol{v}}$, computed by a standard turbulent flow model, the first term is closed. The second term denotes the statistical mean overall velocities of transport deviating from the mean motion. This turbulent transport term requires closure and again a number of closure models have been proposed (see e.g., [4.83,4.84]). This present simplification of the PDF modelling approach does not affect the key advantage of a closed reaction progress term as described above. Yet it allows a much easier embedding of the reaction modelling strategy in existing computational fluid dynamics (CFD) codes.

4.3.7.3 Regime of applicability and extended models

In assessing the regime of applicability of PDF models, one realizes that the key advantage of a closed reaction term is at the same time a limiting factor in applications: The tight statistical correlation between chemical activity and molecular transport, as observed above for flamelets and in the thin reaction zone regime, is by construction neglected in the PDF ansatz. The closures of the molecular mixing and turbulent transport terms are uncorrelated with the reaction progress in most PDF models, whereas in these quasi-deterministic regimes of combustion they are absolutely crucial and, in fact, are the fundamental basis of turbulent combustion modelling. As a consequence, without further modification, the regimes of applicability of PDF and flamelet or thin reaction zone models are disjoint.

Since most practical engineering applications belong to the flamelet regime, various efforts have been undertaken to extend the regime of applicability of PDF models. Anand and Pope [4.85] split the molecular transport term into 2 contributions. One corresponds to uncorrelated mixing of fluid away from chemically active zones, whereas the other incorporates the quasi-deterministic nature of reaction fronts in the flamelet and thin reaction zone regimes. Alternatives have been proposed, but a convincing unified framework for bridging the gap between flamelet and PDF models is still pending.

4.3.7.4 Monte Carlo simulation

As mentioned above, the dimensionality of the argument space of a PDF for combustion applications is large. In particular, it increases with the number of chemical species to be traced and, in realistic systems, can easily reach eight or more dimensions. Traditional discrete solution methods for partial differential equations lead to an exponential growth of computational requirements with the number of argument space dimensions, and hence quickly to unfeasible conditions.

A solution to this problem comes from Monte Carlo simulation. The PDF is implicitly represented by a cloud of quasi-Lagrangian particles in state space. A large set of state vectors is initialized, and the probability to find a state within a given subcell of the state space is set equal to the number of discrete particles within that cell divided by the total number of particles available. The time evolution of the PDF according to the evolution Equation (4.3.23) is mimicked by letting the particle states evolve in time in a suitable fashion. Pope [4.83] discusses how suitable actions on the particle states lead to an associated evolution of the discrete distribution that correspond in the limit of large particle numbers to the differential operators in the PDF equation.

It turns out that the computational effort of a Monte Carlo method grows *linearly* with the number of dimensions of the state space, so that PDF-based simulations become feasible for systems that are larger

than systems with the most simplified one- or two-step chemical models.

The closure models from References [4.83, 4.84] for molecular mixing and turbulent transport are also formulated as actions on particle states rather than state space (integro-) differential operators.

4.3.8 Large Eddy Simulation

Large eddy simulation for combustion problems is becoming increasingly popular for the same reasons explained in the context of LES for non-reacting flows. Considerable complications arise, however, because combustion processes considerably affect the turbulent flow structures. The general idea of dynamically computing all fluctuations on the largest turbulent scales, while modelling only those phenomena whose scale falls below the grid resolution is kept. However, major uncertainties remain as to what is the appropriate mathematical description of a turbulent flame on the smallest resolved scale. Vervisch and Veynante [4.46] list at least three different approaches that are currently pursued by various research groups:

1. *Artificially thickened flame fronts* [4.86]. Here, a modification of effective transport coefficients and reaction rate coefficients is introduced that artificially thickens the laminar flame structure so that it can be resolved on the given computational mesh, but in such a manner that a given effective flame speed is maintained. Combustion is then treated on the resolved scales as if it were laminar. The effective flame speed is the key quantity to be "subgrid modelled", because it is responsible for the increase of net combustion rates over the laminar case. A consistent dynamic subgrid-scale model is not yet available.

2. *G-equation or level set approaches* [4.87, 4.88]. Here the flame is treated at the resolved scale as a reactive discontinuity, and again the key quantity to be modelled is the effective turbulent burning velocity for that scale. This approach appears most consistent with dynamic subgrid-scale models, because there is a direct link between the quantity to be modelled and what is actually computed on the grid: The effective turbulent burning velocity is essentially proportional to the turbulent flame area increase that is due to subgrid-scale wrinkling and corrugation. The flame front wrinkling on the scales larger than the resolved ones is actually simulated by the level set approach and can be extracted by Germano-type filtering techniques. Hence a dynamic subgrid-scale model appears as a natural candidate. Despite these conceptually appealing properties, a successful closed formulation is still work in progress. Notice also that this approach requires a numerical flame front tracking method, which is considerably more complex than the standard reactive Navier-Stokes solver (see Section 4.5.5 below).

3. *Resolved flame structure in combination with flame surface area density modelling* [4.89]. Conceptually, this approach combines the advantages of the easier-to-implement resolved flame structure numerics with the flamelet idea of connecting turbulent flame speeds with effective flame surface areas. Explicit subgrid-scale closures can be tranferred from Reynolds-averaged turbulent combustion models. A conceptual difficulty arises for dynamic subgrid-scale modelling of the Germano type, because the key quantity to be extracted by filtering—namely the flame surface wrinkling—is not readily available on the smallest resolved scales. As the flame structure is represented by, say, five grid points one would have to go up to length scales of tens of grid points in each space direction to actually "see" the flame front wrinkling. That basically destroys the appeal of dynamic subgrid-scale modelling.

Large eddy simulation for combustion applications is gaining momentum in research at an increasing rate, but it cannot be considered "state of the art" by any means at this stage.

4.3.9 Reynolds' Averaging, LES, and PDFs in the Context of DDT

We include some principal considerations regarding the interpretation of results produced by the various modelling approaches described in this section. The key question that is addressed here is the following:

- What can and what cannot be concluded from any given simulation based on a Reynolds-averaged, LES or PDF simulation?

Two extremes elucidate the point: In the first example, we consider a non-reactive incompressible, constant density steady flow over a flat plate. In this case, a Reynolds-averaged computation will yield a steady-state (turbulent mean) velocity profile without visible fluctuations in the computed data. Even though all fluctuations are averaged out by definition, the mean velocity distribution may well be expected to be close to the velocities that one would measure in an experiment. In a typical situation, turbulent fluctuations may be expected to amount to about 10% of the local mean velocities. Thus the computation yields good insight into what would go on in an actual experiment.

A large eddy simulation would, even for steady-state mean flows, never approach a steady state. Persistent instabilities would provide for sustained fluctuations. Because of the chaotic nature of turbulence, one may not expect, however, to compute fluctuations that can—by time of occurance and location—be measured in an experiment. All one may expect from LES is to obtain an impression of the magitude of the fluctuations and hints at the local fluidmechanical mechanisms that are responsible for sustaining the fluctuations. Nevertheless, a single LES would exhibit many features that could directly be measured in an associated experiment, including mean values (upon time averaging), fluctuation levels, and their correlations.

The situation can change dramatically for a simulation of DDT in a mixture that is close to the DDT threshold. Depending on stochastic details of the initial and boundary conditions, the exact location and time of detonation birth will be highly irreproducible. Under suitable circumstances, DDT might even be suppressed. Thus within the ensemble of possible flows for a given set-up, there are subclasses that drastically differ from one another, with a range from "no combustion at all" to "detonation".

Assume for a moment that existing turbulence closures for Reynolds-averaged models would be appropriate in this case at all. Then, the resulting fields from a Reynolds-averaged model computation must be interpreted with great care, nevertheless. How close would the computed fields be to *any* single experimental observation? The answer is not at all! These averaged computations would loose their guiding role in "assessing what could happen" completely, and they take on a role of "exhibiting what a large number of nearly equal experimental runs would do to the mean"! It is clear that an experimental verification and validation of such a model would have to include a large number of measurements, and it remains unclear whether the computed results would be of any value to the design engineer.

For LES, the situation is more subtle. Depending on the nature of the "trigger" that is responsible for establishing the various different paths of evolution, an LES may or may not be interpretable as "close to direct experimental observation". If it is subgrid processes that trigger changes of the evolution path, then the same qualifications given for Reynolds-averaged modelling above hold also for LES. If, however, the

relevant processes occur on the resolved scales, then LES would be able to map out the different possible solution classes and yield representative results for each of them.

Provided again that subgrid models are suitable for the task, PDF models are most generally applicable, and there is little uncertainty regarding the interpretation of results. If the ensemble of possible solutions is made up of largely differing subclasses, then a computed PDF should therefore exhibit peaks or clusters. Interestingly, one cannot, from the standard one-point PDF, reconstruct the solution classes, though. Assume, for example, that the PDF shows bimodal distributions of the reaction progress variable in two different corners of a room in which combustion has taken place. Then, one cannot decide which combinations of

- no burn at all
- corner 1 burnt, corner 2 unburnt
- corner 1 unburnt, corner 2 burnt
- full burnout

are really achieved and are defining the possible sub-classes of solutions. The reason is that a one-point PDF does not allow one to assess spatial correlations!

4.4 Chemical Kinetics in Turbulent Combustion

For most practical purposes, the progress of chemical reactions is much less complex than one might expect on the basis of the overwhelming complexity of detailed chemical kinetic systems. A wide range of approximate modelling techniques has been developed in recent years. Their common goal is to filter from detailed kinetics only the minimal information needed to describe a given phenomenon of interest while discarding any complexity that is of minor importance. Depending on the phenomenon considered, the resulting simplified chemical model will generally be of varying complexity.

If, for example, only the auto-ignition delay of a reactive mixture is of interest, but not the subsequent details of the chemical energy conversion processes, then one can generally capture the essence with a single-step reaction model. A counter-example comes, for example, from automotive engine design. In addition to the dynamics of laminar flamelets, including their quenching limits, one is interested in pollutant formation levels during turbulent combustion. Accurate descriptions of all the relevant subprocesses require quite sophisticated kinetic models, even though considerable simplifications relative to detailed elementary kinetics are still possible, (see [4.90, 4.91]).

Pollutant formation processes should be of minor importance for the present topic of FA and DDT. However, the kinetics of auto-ignition, flamelet propagation, flamelet quenching etc. are of primary interest and require careful consideration.

4.4.1 Simplified Closures for Time Scale Transitions

In the context of the "regimes of premixed turbulent combustion" we have seen in Section 4.3.1 that transitions from chemistry-dominated to turbulence-dominated combustion must be expected. Chemical

kinetics becomes rate-limiting when turbulent mixing is so intense that reactions proceed locally in a quasi-homogeneous environment. In that case, reaction progress can well be modelled by straightforward chemical kinetics evaluated at the turbulent mean state. As turbulence intensities decrease, chemistry will become more intermittent and the mean reaction rates will diverge considerably from "chemical kinetics at the mean state". Yet, turbulent mixing will still be sufficiently intense to inhibit the formation of coherent structures with correlated chemical kinetic and transport sub-structures. This is the standard regime for applications of PDF methods. Chemical kinetics may be described in this regime by "reaction of individual Monte Carlo particles". No tight coupling to molecular transport is to be expected.

As turbulence intensities decrease further, one will observe the establishment of strong correlations of reaction and molecular transport, indicating the transition into the "thin reaction zone" and "flamelet" regimes.

In a coarse, leading order model for fast turbulent combustion, one may want to include only the two extreme cases of (i) infinitely fast chemistry plus high intensity turbulence and (ii) infinitely high turbulence intensity. As discussed earlier, these extremes correspond to the eddy breakup and to the well-stirred reactor regime, respectively. A typical flame acceleration process would start in the eddy breakup regime and, as the self-induced turbulence intensity increases, would transition to the well-stirred reactor type of combustion.

Kochurko et al. [4.51] and Breitung et al. [4.52] use a simple modification of the eddy breakup strategy in order to capture the essence of that transition. The mean reaction rate for an energy carrying progress variable is written as

$$\overline{\omega} = \frac{1}{\tau}\,\tilde{c}\,(1-\tilde{c})\;, \tag{4.4.1}$$

with a dynamic adjustment of the reaction time scale τ. For a given gas mixture with species mass fractions $\boldsymbol{Y}$, the auto-ignition delay time $t_{IGN}(\boldsymbol{Y})$ can be computed from detailed chemical kinetics and stored in either a table or in the form of an interpolation formula. A standard compressible k-ϵ model provides the integral time scale of turbulence as $\tau_t = k/\epsilon$. Now the reaction rate time scale τ from Equation (4.4.1) is simply determined as

$$\frac{1}{\tau} = \min\left(\frac{1}{t_{IGN}}, \frac{1}{\tau_t}\right)\;. \tag{4.4.2}$$

Obviously, any additional information on the important sub-processes that are available from theory or through heuristic arguments can be incorporated in such a simplified approach. One may, for example, consider the characteristic quenching time scale of laminar flamelets as the critical chemical time with which to compare the turbulent integral scale.

Practical implementations [4.51, 4.52] show that this approach does allow one to capture the qualitative behaviour of combustion in the limit of high turbulence intensity. Yet, a satisfactory formulation that would cover a wide range of mixture compositions, initial conditions etc. without fine tuning seems unachievable.

4.4.2 Semi-heuristic Reduced Chemical Kinetics

A more systematic approach is "standard reduced chemical kinetics" based on steady-state and partial equilibrium assumptions. The key ideas can be formulated by considering the system of ordinary differential equations for n_{spec} chemical species represented by their mass fractions $\boldsymbol{Y} = \{Y_i\}_{i=1}^{n_{\mathrm{spec}}}$. The

system

$$\frac{dY_i}{dt} = \sum_{r=1}^{n_{\rm reac}} (a_i^{r,+}\,\omega_r^+(\boldsymbol{Y}) - a_i^{r,-}\,\omega_r^-(\boldsymbol{Y}) \qquad\qquad (i = 1, n_{\rm spec}) \tag{4.4.3}$$

represents a detailed chemical kinetic scheme with $n_{\rm reac}$ reactions.

A **partial equilibrium** assumption states that for one of the elementary reactions the forward and backward rates are in an approximate balance. Thus

$$\frac{\mid \omega_r^+(\boldsymbol{Y}) - \omega_r^-(\boldsymbol{Y}) \mid}{\max\left(\mid \omega_r^+(\boldsymbol{Y}) \mid, \mid \omega_r^-(\boldsymbol{Y}) \mid\right)} \ll 1\,. \tag{4.4.4}$$

In this case, one obtains at leading order an approximate *algebraic* relation between the vector components of $\boldsymbol{Y}$ of the form

$$\omega_r^+(\boldsymbol{Y}) - \omega_r^-(\boldsymbol{Y}) = 0\,. \tag{4.4.5}$$

In favour of this algebraic constraint, one of the species mass fractions can be eliminated from the system of unknowns, and the associated evolution equation can be discarded.

In a similar fashion, the presence of chemical radicals gives rise to *steady-state approximations*. Assume that the consumption reactions for some species k are extremely fast in comparison with their production, i.e., that the species is extremely reactive. In that case, the concentration of that species in the mixture will always remain very small of order $\epsilon \ll 1$, say. In that case, one may conclude that $Y_k = \epsilon y_k$ and

$$\frac{dY_k}{dt} = \epsilon \frac{dy_k}{dt} = O(\epsilon) \ll 1 \tag{4.4.6}$$

provided the kinetic scheme does not allow for high frequency oscillations with characteristic time scale of order $O(\epsilon)$. Under that condition, Equation (4.4.6) gives rise to the algebraic constraint

$$\sum_{r=1}^{n_{\rm reac}} (a_k^{r,+}\,\omega_r^+(\boldsymbol{Y}) - a_k^{r,-}\,\omega_r^-(\boldsymbol{Y}) = 0\,. \tag{4.4.7}$$

Since the combinations of the rate expressions $a_k^{r,+}\,\omega_r^+(\boldsymbol{Y})$ typically contain the mass fraction Y_k, this equation may be used to express this variable as an algebraic function of the other mass fractions. The ordinary differential equation (ODE) governing its temporal evolution can then be discarded.

The combination of partial equilibrium and steady-state assumptions allows one to considerably reduce the complexity of detailled kinetic mechanisms. The result can be cast in the form of a new net reaction mechanism that is in the standard form $\mathrm{reactants} \leftrightarrow \mathrm{products}$, yet with much more complex effective rate expressions. In fact, the reaction rate expressions for these net reaction steps correspond exactly to the original detailled kinetic scheme. The only difference is that the mass fractions of all species whose dynamic evolution equations have been eliminated by steady-state and partial equilibrium assumptions are now expressed as algebraic functions of the remaining species.

The advantage of this approach over purely computational procedures, as described in Section 4.5.7 below, is that the net result is still in the form of an effective reaction mechanism familiar in chemistry. The resulting explicit formulae, allow further use of the reduced scheme in analytical studies of, say ignition delay times or laminar flame structures for the given reactive mixture [4.92, 4.93]. Another potential application is in Monte Carlo simulations of turbulent combustion based on the PDF methodology (see

Section 4.3.7 below), where the computational requirements for integrating the chemical history of many Monte Carlo realizations can be reduced.

Notice, however, that the reduction of the number of governing kinetic equations does not automatically lead to many orders of magnitude in computational savings. The algebraic constraints from steady-state and partial equilibrium assumptions induce additional complications in the numerical integration that are far from trivial [4.94, 4.95].

4.5 Numerical Reactive Flow Solvers

4.5.1 Governing Equations, Non-dimensionalization and General Discussion

To consistently discuss the numerical problems and their solutions that are specific to premixed combustion, some basic theoretical facts need to be summarized. As a basis, we will need a relevant mathematical description of reactive flows. The full governing equations of gas-phase combustion with as little approximation as is currently possible can be found in comprehensive textbooks on combustion theory, such as Reference [4.6]. Here we shall consider a simplified system only, so that the essential lines of thought can be worked out in a straightforward manner.

The simplified system to be discussed here consists, first of all, of the conservation equations for mass, momentum, and energy

$$\begin{array}{rcrcrcl} (\rho)_t & + & \nabla\cdot(\rho\boldsymbol{v}) & & & = & 0 \\ (\rho\boldsymbol{v})_t & + & \nabla\cdot(\rho\boldsymbol{v}\circ\boldsymbol{v}+\nabla p) & + & \nabla\cdot\boldsymbol{\tau} & = & 0 \\ (\rho e)_t & + & \nabla\cdot(\boldsymbol{v}\,[\rho e+p]) & + & \nabla\cdot\left(\boldsymbol{j}_T+\boldsymbol{\tau}\cdot\boldsymbol{v}+\sum_{i=1}^{n_{\mathrm{spec}}}(\Delta H)_i\,\boldsymbol{j}_i\right) & = & 0. \end{array} \tag{4.5.1}$$

Here $\rho, \boldsymbol{v}, p, e$ are the mass density, fluid flow velocity, pressure, and total energy per unit mass, respectively, and $\boldsymbol{\tau}, \boldsymbol{j}_T, \boldsymbol{j}_i$ denote the molecular transport of momentum, heat, and of the mass of the ith species, respectively. These transport terms and the pressure are related to the mass, momentum, energy, and species densities $\rho, \rho\boldsymbol{v}, \rho e, \rho Y_i$ through the caloric equation of state

$$\rho e = \frac{p}{\gamma-1} + \frac{1}{2}\rho\boldsymbol{v}^2 + \sum_{i=1}^{n_{\mathrm{spec}}}(\Delta H)_i\,\rho Y_i \tag{4.5.2}$$

and the transport models

$$\begin{array}{rcl} \boldsymbol{\tau} & = & -\mu\left(\nabla\boldsymbol{v}+(\nabla\boldsymbol{v})^T\right)-\eta\,(\nabla\cdot\boldsymbol{v})\,\mathbf{1} \\ \boldsymbol{j}_T & = & -\kappa\,\nabla T \\ \boldsymbol{j}_i & = & -\rho D_i\,\nabla Y_i. \end{array} \tag{4.5.3}$$

The temperature T is related to pressure and density via the thermal equation of state

$$T = \frac{p}{\rho R}\,. \tag{4.5.4}$$

The quantities $\gamma, R, \mu, \eta, \kappa, D_i, (\Delta H)_i$ are the isentropic exponent, the ideal gas constant, the shear and bulk viscosities, the heat conductivity, the species diffusivities and the species' formation enthalpies, respectively. All of them are assumed constant throughout this text.

The chemical species mass fractions Y_i satisfy the inhomogeneous balance laws

$$(\rho Y_i)_t + \nabla\cdot(\rho Y_i \boldsymbol{v}) + \nabla\cdot\boldsymbol{j}_i = \rho\omega_i \qquad (i = 1 \ldots n_{\text{spec}}) \tag{4.5.5}$$

where $\omega_i = \omega_i(p, \rho, Y_i)$ is the net production rate of species i per unit mass of the gas mixture.

When n_{spec} actually denotes the total number of chemical species in the system, then the sum of all equations in Equation (4.5.5) leads back to the mass conservation equation in Equation $(4.5.1)_1$ and yields a constraint for the rate expressions

$$\sum_{i=1}^{n_{\text{spec}}} \rho\omega_i = 0\,. \tag{4.5.6}$$

In this case, the mass conservation equation or one of the species balances is redundant. This overdetermination is overcome here by dropping one of the species balance equations while keeping the total mass balance.

4.5.1.1 Non-dimensionalization and scaling

Key features of these governing equations can be discussed conveniently after transformation to a new set of dependent and independent variables that is adapted to the reactive flow problems at hand. Reference quantities are chosen for non-dimensionalization that guarantee that the new non-dimensional variables are generally of order $O(1)$, while order of magnitude scalings appear in suitable non-dimensional characteristic numbers. We chose reference values $(\rho_{\text{ref}}, p_{\text{ref}}, u_{\text{ref}})$ for density, pressure and velocity, $(t_{\text{ref}}, \ell_{\text{ref}})$ for the time and space coordinates, (ω_{ref}) for chemical reaction rates and $(\mu_{\text{ref}}, \kappa_{\text{ref}}, D_{\text{ref}}, R_{\text{ref}}, (\Delta H)_{\text{ref}})$ for the parameters in the constitutive equations. Next, we define the new dependent and independent variables,

$$\rho' = \frac{\rho}{\rho_{\text{ref}}}, \quad p' = \frac{p}{p_{\text{ref}}}, \quad \boldsymbol{v}' = \frac{\boldsymbol{v}}{u_{\text{ref}}}, \quad T' = \frac{T}{p_{\text{ref}}/(\rho_{\text{ref}} R_{\text{ref}})}, \quad e' = \frac{e}{p_{\text{ref}}/\rho_{\text{ref}}} \tag{4.5.7}$$

and

$$\boldsymbol{x}' = \frac{\boldsymbol{x}}{\ell_{\text{ref}}}, \quad t' = \frac{t}{t_{\text{ref}}}\,. \tag{4.5.8}$$

The governing equations are then transformed into their scaled, non-dimensional analogues:

Conservation Laws:

$$\begin{aligned}
&\frac{1}{\text{Sr}}(\rho)_t &&+ \nabla\cdot(\rho\boldsymbol{v}) && && &&= 0\\
&\frac{1}{\text{Sr}}(\rho\boldsymbol{v})_t &&+ \nabla\cdot(\rho\boldsymbol{v}\circ\boldsymbol{v} + \frac{1}{M^2}\nabla p) &&+ \frac{1}{\text{Re}}\nabla\cdot\boldsymbol{\tau} && &&= 0\\
&\frac{1}{\text{Sr}}(\rho e)_t &&+ \nabla\cdot(\boldsymbol{v}[\rho e + p]) &&+ \frac{1}{\text{Re}}\nabla\cdot\left(\frac{1}{\text{Pr}}\boldsymbol{j}_T + M^2\,\boldsymbol{\tau}\cdot\boldsymbol{v} + \frac{Q}{\text{Sc}}\sum_{i=1}^{n_{\text{spec}}}\delta h_i\,\boldsymbol{j}_i\right) &&= 0.
\end{aligned} \tag{4.5.9}$$

Species Balances:

$$\frac{1}{\text{Sr}}(\rho Y_i)_t + \nabla\cdot(\rho Y_i\boldsymbol{v}) = -\frac{1}{\text{ReSc}}\nabla\cdot\boldsymbol{j}_i + \text{Da}\,\rho\omega_i \qquad (i = 1 \ldots n_{\text{spec}}) \tag{4.5.10}$$

Caloric Equation of State:

$$\rho e \;=\; \frac{p}{\gamma-1} + M^2\,\frac{1}{2}\rho \boldsymbol{v}^2 + Q\,\sum_{i=1}^{n_{\rm spec}} \delta h_i\,\rho Y_i \tag{4.5.11}$$

Thermal Equation of State:

$$T = \frac{p}{\rho}\,. \tag{4.5.12}$$

Transport Models:

$$\begin{aligned} \boldsymbol{\tau} &= -\mu'\left(\nabla\boldsymbol{v} + (\nabla\boldsymbol{v})^T\right) - \eta'\,(\nabla\cdot\boldsymbol{v})\,\mathbf{1} \\ \boldsymbol{j}_T &= -\kappa'\nabla T \\ \boldsymbol{j}_i &= -D_i'\,\nabla Y_i. \end{aligned} \tag{4.5.13}$$

Notice that in Equation (4.5.9) and Equation (4.5.11) we have introduced the scaled reaction enthalpies

$$\delta h_i = \frac{(\Delta H)_i}{(\Delta H)_{\rm ref}}\,, \tag{4.5.14}$$

and that $\mu' = \mu/\mu_{\rm ref}, \kappa' = \kappa/\kappa_{\rm ref}$ etc. in Equation (4.5.13) could all be set to unity in case of constant molecular transport coefficients.

The procedure of scaling the equations has led to a set of seven characteristic numbers:

Abbreviation	**Definition**	**Name**
Sr	$t_{\rm ref}u_{\rm ref}/\ell_{\rm ref}$	Strouhal number
M	$u_{\rm ref}/\sqrt{p_{\rm ref}/\rho_{\rm ref}}$	Mach number
Re	$\rho_{\rm ref}u_{\rm ref}\ell_{\rm ref}/\mu_{\rm ref}$	Reynolds number
Pr	$\mu_{\rm ref}/(\kappa_{\rm ref}/R_{\rm ref})$	Prandtl number
Sc	$\mu_{\rm ref}/\rho_{\rm ref}D_{\rm ref}$	Schmidt number
Da	$\omega_{\rm ref}\ell_{\rm ref}/u_{\rm ref}$	Damköhler number
Q	$(\Delta H)_{\rm ref}/(p_{\rm ref}/\rho_{\rm ref})$	Heat Release Parameter

(4.5.15)

There are several important observations regarding the structure of solutions of the full governing equations that emerge immediately from the exercise of non-dimensionalization and scaling:

1. **The low Mach number singularity**
   Obviously, as the Mach number M vanishes, the pressure gradient term in the momentum equation becomes singular.The mathematical nature of this singularity will be discussed in more detail below. Here, we merely emphasize that the low Mach number limit is of considerable importance during the initial stages of flame acceleration processes because it governs most of the inherent instabilities of laminar flames and flamelets at low-to-moderate turbulence intensities.

2. **The deflagration limit**
   A distinguished limit of large Damköhler numbers $\mathrm{Da} \gg 1$ and inefficient molecular transport $\mathrm{Re} \gg 1$ reveals the mathematical structure of laminar deflagrations (see [4.44, 4.56, 4.96] and Section 4.5.4 below). The mathematical structure of that limit carries over to turbulent combustion processes also, with drastic consequences for suitable reactive flow numerical methods.

3. **Stiff and fast chemistry singularities**
   The limit of large Damköhler numbers is not only relevant for the establishment of well-defined reaction fronts (flames). When chemical reactions that do not considerably contribute to the net chemical energy conversion are associated with large Damköhler numbers, they may nevertheless be of outmost importance when they involve chemical radicals. In that case, numerical challenges arise because minute concentrations of extremely reactive species must be computed on the basis of governing equations with extremely large rates. This leads to the typical numerical problem of "cancellation of significant digits" in finite computer arithmetic. Further computational issues associated with this limit will be discussed in Section 4.5.7.

4.5.2 The Low Mach Number Problem

In most real-life applications, such as spark-ignition engine combustion (no knock), industrial and household burners, flame acceleration in explosion processes etc., combustion-driven velocities are small compared with the speed of sound. This fact has profound consequences for both the mathematical behaviour of solutions to the governing equations from Section 4.5.1 and their numerical approximate solutions. Physically, in the limit of arbitrarily slow flow (or infinitely fast sound propagation) the elasticity of the gas with respect to bulk compression becomes negligible and soundwave propagation becomes unnoticeable. Mathematically, as the Mach number M from Equation (4.5.15) tends to zero, the pressure gradient contribution in the momentum equations Equation $(4.5.9)_2$ becomes singular. In order to explore the consequences of this singularity we consider a formal asymptotic analysis, closely following References [4.44, 4.97] and [4.98].

4.5.2.1 Asymptotic analysis

A systematic derivation of the governing equations for zero Mach number combustion has been given by Majda and Sethian [4.44]. The formulation adopted below, which explicitly focuses on the conservation equations for mass, momentum and energy, has been introduced in Reference [4.97] in conjunction with a multiple length-scale, single time-scale analysis.

In recounting their results we restrict our discussion to the case of an ideal gas mixture with a simple one-step reaction $F \rightarrow P$, where the fuel F is turned into the product species P. The chemical energy conversion rate then is $Q\,\rho\omega_F$ where Q quantifies the specific reaction enthalpy of the fuel species and $\rho\omega_F$ its production density. Under these conditions we need to describe the time evolution of only the fuel mass fraction Y_F using a single transport equation of the type described in Equation (4.5.10).

The asymptotic solution ansatz

$$\begin{aligned} p &= p_0(\boldsymbol{x},t) + Mp_1(\boldsymbol{x},t) + M^2 p_2(\boldsymbol{x},t) + o(M^2), \\ \boldsymbol{v} &= \boldsymbol{v}_0(\boldsymbol{x},t) + M\boldsymbol{v}_1(\boldsymbol{x},t) + o(M), \\ \rho &= \rho_0(\boldsymbol{x},t) + M\rho_1(\boldsymbol{x},t) + o(M), \\ Y_F &= Y_{F,0}(\boldsymbol{x},t) + MY_{F,1}(\boldsymbol{x},t) + o(M) \end{aligned} \tag{4.5.16}$$

is introduced into the dimensionless governing Equations (4.5.9) to (4.5.10). Following standard procedures of asymptotic analysis, one obtains a hierarchy of equations for the various expansion functions $p_i, \boldsymbol{v}_i, \rho_i, Y_{F,i}$ by collecting all terms multiplied by equal powers of the Mach number M and separately equating these to zero. The momentum equations to orders M^{-2} und M^{-1} become

$$\nabla p_0(\boldsymbol{x},t) = 0\,, \quad \nabla p_1(\boldsymbol{x},t) = 0\,. \tag{4.5.17}$$

One concludes that p_0 and p_1 depend on time only in this regime of length and time scales, so that

$$p_0 \equiv P_0(t) \qquad \text{and} \qquad p_1 \equiv P_1(t)\,. \tag{4.5.18}$$

The continuity and energy equations at leading order are then

$$\partial\rho_0/\partial t + \nabla\cdot(\rho_0\boldsymbol{v}_0) = 0 \tag{4.5.19}$$

$$\frac{1}{\gamma-1} d\,P_0/dt + \nabla\cdot(H_0\boldsymbol{v}_0) = \Big(\frac{1}{\mathrm{Pe}}\nabla\cdot(\lambda\nabla T_0) + \mathrm{Da}\,Q\,\rho\omega_F\Big)\,. \tag{4.5.20}$$

where

$$H_0(t) = \frac{\gamma}{\gamma-1}\,P_0(t)\,. \tag{4.5.21}$$

To arrive at Equation (4.5.20), one inserts the expansion Equation (4.5.16) into the energy conservation law Equation $(4.5.9)_3$, takes into account that the kinetic energy is by a factor of M^2 smaller than the thermal energy for $M \ll 1$ according to Equation (4.5.11) and uses the gradient condition from Equation (4.5.17) to pull the pressure out of the energy flux divergence expression. The contribution of the viscous forces to the energy budget, represented by the term $\nabla\cdot(\frac{M^2}{\mathrm{Re}}\,\boldsymbol{\tau}\cdot\boldsymbol{v})$, will appear first in the energy equation at order $O(M^2)$.

The momentum equation at order M^0 reads

$$\partial\rho_0\boldsymbol{v}_0/\partial t + \nabla\cdot(\rho_0\boldsymbol{v}_0\circ\boldsymbol{v}_0) + \nabla p_2 = -\frac{1}{\mathrm{Re}}\nabla\cdot\boldsymbol{\tau}_0\,. \tag{4.5.22}$$

Notice the change in structure of these equations: The pressure evolution equation does *not* determine the pressure variable p_2 appearing in the momentum equation! The appropriate interpretation, corresponding directly to the theory of incompressible flows, is that the equation for P_0 from Equation (4.5.20) is a divergence constraint for the leading order energy flux, i.e.,

$$\nabla\cdot(H_0(t)\,\boldsymbol{v}_0) = -\left[\frac{1}{\gamma-1} d\,P_0/dt - \Big(\frac{1}{\mathrm{Pe}}\nabla\cdot(\lambda\nabla T_0) + \mathrm{Da}\,Q\rho\omega_F\Big)\right] \tag{4.5.23}$$

and that the second-order pressure p_2 is responsible for guaranteeing that constraint to be observed. A useful and more familiar interpretation of this equation results from using explicitly that $H_0(t) = \gamma P_0(t)/(\gamma - 1)$ is a function of time only and deriving a

velocity divergence constraint

$$\nabla\cdot\boldsymbol{v}_0 = -\frac{1}{\gamma P_0}\left[d\,P_0/dt - (\gamma-1)\Big(\frac{1}{\mathrm{Pe}}\nabla\cdot(\lambda\nabla T_0) + \mathrm{Da}\,Q\rho\omega_F\Big)\right]. \tag{4.5.24}$$

We observe that the velocity divergence is driven by chemical energy conversion and energy transport effects: Chemical heat release, heat conduction, and global pressure changes conspire to induce a divergence field for the velocity. As a direct consequence, we derive from the mass continuity Equation (4.5.19) an equation that describes the temporal evolution of the density along particle paths

$$\frac{D\rho}{Dt} := \frac{\partial\rho}{\partial t} + \boldsymbol{v}\cdot\nabla\rho = -\rho\nabla\cdot\boldsymbol{v}\,. \tag{4.5.25}$$

To summarize, the energy conversion and transport processes drive the divergence of the energy flux, which is related to the velocity divergence. The latter, in turn, leads to compression or expansion of individual mass elements and thus to density variations of individual particles.

The original interpretation of Equation (4.5.23) as an energy flux divergence constraint proves to be useful in the construction of energy-conserving finite-volume methods, (see [4.98, 4.99]).

Equations (4.5.19) to (4.5.22) form a closed system, provided the temporal evolution of the leading-order pressure P_0 is known and the state dependence of the reaction rate $\rho\omega_F$ is given. For combustion under atmospheric conditions P_0 equals the atmospheric ambient pressure and is constant in time. For combustion in a closed chamber, we explore the fact that P_0 is homogeneous in space, integrate Equation (4.5.24) over the total flow domain, use Gauß' theorem to replace the divergence integrals with boundary integrals and obtain a global pressure evolution equation:

$$d\,P_0/dt = \frac{1}{\Omega}\left[-\oint_{\partial V}\left(\gamma P_0\boldsymbol{v} - \frac{\gamma-1}{\mathrm{Pe}}\,\lambda\nabla T_0\right)\cdot\boldsymbol{n}\,d\sigma + \mathrm{Da}\int_V(\gamma-1)Q\rho\omega_F\,dV\right] \tag{4.5.26}$$

where $\boldsymbol{n}$ is the outward pointing unit normal at the boundary, and $\Omega = \int_V dV$ is the total volume of the domain of integration V. Given appropriate velocity and thermal boundary conditions all changes of the background pressure are thus related to the overall chemical energy conversion within the domain.

The structure of the above equations is similar to that of incompressible, non-reactive flow in that there is convection, diffusion, and an explicit velocity divergence constraint. Thus appropriate extensions of incompressible flow solvers should, in principle, be able to handle zero Mach number reactive flows as well. See References [4.100 to 4.103] for reviews of typical developments based on this approach.

For a discussion of further aspects of low Mach number asymptotics, including the influence of high-frequency and long-wavelength acoustic perturbations, see References [4.97, 4.104].

4.5.2.2 Numerical consequences of the asymptotics

The most dramatic consequence of the asymptotic results is the pressure decomposition. Both the leading-order spatially homogeneous part $P_0(t)$ and the $O(M^2)$-perturbation $p_2(\boldsymbol{x}, t)$ enter the leading-order

system of equations in a non-trivial fashion. The leading order pressure P_0 determines the velocity divergence through the limit form of the energy Equation (4.5.24), but does not appear in the momentum equation at all. In contrast, the second-order pressure $p_2(\boldsymbol{x}, t)$ is energetically negligible, but yields the sole pressure gradient effect in the momentum equation.

This splitting of the pressure is dramatic because a numerical method designed to integrate the original unscaled equations Equation (4.5.1) to Equation (4.5.5) must *necessarily* fail when applied to very low Mach number combustion problems, unless special care is taken to introduce an appropriate separation and re-scaling of the pressure mean and its fluctuations.

To be more precise, consider a smooth low Mach number flow on a domain of characteristic size ℓ. The total pressure variation within the flow domain will be $M^2\,\delta p_2$, where $\delta p_2 = O(1)$ as $M \to 0$. Assume that the flow domain is discretized by n grid points across the length of ℓ so that the grid spacing is $\Delta x = \ell/n$. A second-order discrete representation of the derivative $\partial p/\partial x$ on a carthesian grid with constant spacing in the x-direction would read

$$\frac{\partial\, p}{\partial x} = \frac{p_{i+1,j} - p_{i-1,j}}{2\Delta x} + O((\Delta x)^2)\,. \tag{4.5.27}$$

Obviously, forming a discrete gradient requires that pressure differences be taken between neighbouring grid-cells. These pressure differences will be the smaller, the smaller (i) the Mach number M and (ii) the grid spacing, since we consider a smooth flow. We wish to assess how small a Mach number and how fine a numerical resolution we can afford without having to account for the usual loss of significant digits upon differencing large but almost equal numbers:

In the low Mach number limit, the pressure in the vicinity of the centre cell i can be expressed as

$$p(x) = p_i + M^2(x - x_i)\frac{\partial p_2}{\partial x} + O(M^2(\Delta x)^2) \tag{4.5.28}$$

In a typical situation the pressures p_{i-1}, p_{i+1} would thus scale as

$$p_{i-1} = p_i - M^2\,\Delta x\,p_2'\,, \quad p_{i+1} = p_i + M^2\,\Delta x\,p_2'\,, \qquad \Big(p_2' = O(1) \quad \text{as} \quad M, \Delta x \to 0\Big)\,. \tag{4.5.29}$$

Just to give an example, we let $p_i = 1.0$, $p_2' = 1.0$ and insert the exact results from this equation into the discrete differentiation formula from Equation (4.5.27). We evaluate the discrete gradient using a sequence of Mach numbers $M = 10^{-2}...10^{-4}$ and resolutions $\Delta x = 10^{-1}...10^{-3}$ and compare the numerical round-off error with the truncation error estimate $(\Delta x)^2$ for both single- and double-precision arithmetics. The results are given in Table 4.5.2.2- 1.

$$\frac{\mathrm{err}_{\mathrm{single}}}{(\boldsymbol{\Delta x})^{\mathbf{2}}}$$

There are a number of immediate conclusions to be drawn from the results in this table:

1. Single precision computations of pressure gradients will fail already at $M = 10^{-2}$.
2. Double precision evaluations begin to seriously deteriorate for $M < 10^{-3}$.

Table 4.5.2.2- 1: Round-off versus truncation errors for a single evaluation of $\partial p/\partial x$

$\Delta x/\ell$	M	$\left(\frac{p_{i+1}-p_{i-1}}{2M^2\Delta x}\right)_{ex.}$	$\frac{err_{single}}{(\Delta x)^2}$	$\frac{err_{double}}{(\Delta x)^2}$
0.1	10^{-2}	1.111	$2.12 \cdot 10^{-1}$	$1.72 \cdot 10^{-10}$
	10^{-3}	$''$	7.29	$7.98 \cdot 10^{-8}$
	10^{-4}	$''$	$1.0 \cdot 10^{2}$	$3.72 \cdot 10^{-6}$
0.01	10^{-2}	1.111	$7.23 \cdot 10^{2}$	$1.72 \cdot 10^{-8}$
	10^{-3}	$''$	$1.0 \cdot 10^{4}$	$2.80 \cdot 10^{-5}$
	10^{-4}	$''$	$1.0 \cdot 10^{4}$	$1.63 \cdot 10^{-3}$
0.001	10^{-2}	1.111	$7.29 \cdot 10^{4}$	$7.98 \cdot 10^{-4}$
	10^{-3}	$''$	$1.0 \cdot 10^{6}$	$3.72 \cdot 10^{-2}$
	10^{-4}	$''$	$1.0 \cdot 10^{6}$	0.16

3. There is a general loss of precision with increasing resolution of a fixed pressure distribution, which is aggravated by the low Mach number effect. Thus in contrast to intuition, increasing the numerical resolution may worsen the low Mach problem rather than providing improvements!

The first item is particularly alarming in the context of some current day commercial flow simulation codes, because these often have a user-defined option allowing one to run single-precision calculations in order to save computational capacities. Obviously, such an option should be supplemented with an automatic "low Mach number warning" or it should be automatically linked with special pressure scaling procedures that are suited to separate mean pressures from $O(M^2)$ pressure fluctuations.

For further reading on the round-off error problem for low Mach number computations see Sesterhenn et al. [4.105].

4.5.3 Compressible and Low Mach Number Flow Solvers

4.5.3.1 Compressible flow solvers

The numerical technology for simulating fully compressible flows has advanced to quite a mature state over the past two decades. Numerous textbooks and fundamental texts elucidate the basic ideas, [4.106], the advanced analysis, [4.107 to 4.110], and practical applications in combustion [4.111]. The references cited include finite-volume as well as finite-element approaches. Here, we summarize only the key difficulties associated with compressible flow simulation and sketch some numerical approaches to overcome them.

Weak solutions of non-linear hyperbolic equation systems. The key challenge some 25 years ago in the context of compressible flow simulation was to accurately handle non-linear propagating hyperbolic waves and to specifically allow for the formation of discontinous solutions. The obvious example and major motivation came from blast waves and shock-tube experiments, where one regularly observes the shock waves, i.e., discontinous travelling wave solutions to the compressible flow equations. Two critical features of such weak solutions had to be addressed: The first results from the fact that shock waves travel at speeds that are determined by the constraints of mass, momentum, and energy conservation. In particular, shock speeds cannot be extracted from an analysis of the governing differential equations, which have various equivalent formulations, only one of which respects automatically the above-mentioned conservation laws. The second difficulty is associated with the tendency of then-standard numerical discretizations to invoke spurious oscillations next to steep gradients (the Gibbs-phenomenon). Such oscillations are particularly critical in the context of reactive flow simulations because they may interact with highly non-linear chemical kinetic models to produce utterly false numerical predictions.

The first issue, obtaining the correct weak solutions, was essentially resolved by Lax and Wendroff, [4.112]. The authors proved that IF a numerical method converges AND is in conservation form, THEN it converges to weak solutions of the underlying conservation laws. This result determined much of the further developments, in that major research went into the design of numerical methods that automatically conserve mass, momentum, and energy by construction: Cell averages of these conserved quantities are updated solely by balancing fluxes across grid-cell interfaces. As a consequence, mass, momentum, and energy can only be distributed among the numerical grid-cells but cannot "get lost". It should be emphasized, though, that deviations from conservation mainly affect simulations for situations with strong shocks (order $O(1)$ pressure changes across). Weakly compressible flows, in which non-linear wave propagation essentially follows the theory of characteristics, can be simulated quite well with non-conservative, high-accuracy methods. Some of the extensions of incompressible flow solvers to the compressible regime take advantage of this fact, albeit compromising on the ability to compute strong shocks, [4.109, 4.110, 4.113 to 4.115]. (Note that the last two references include descriptions of finite-element techniques applied to compressible flow simulation.)

Regarding the second issue, avoiding spurious oscillations, two major strategies have been developed, both being essentially successful:

- non-linear artificial dissipation and
- non-linear upwind techniques.

The most successful representative of the first group is the the "flux corrected transport" (FCT) family of schemes. The underlying idea is to combine a quite dissipative first-order accurate numerical method that completely damps oscillations with a scheme of higher accuracy that, however, may allow the development of oscillations. A non-linear correction scheme is developed which, depending on local solution features, forces a transition from the high-accuracy scheme to the more dissipative one. These corrections are added only where necessary, so that the overall accuracy is that of the sophisticated scheme in regions of smooth solution, while the damping capabilities of the dissipative scheme are explored next to discontinuities. Fourth- and higher-order accurate versions of these FCT schemes have been proposed and are being used for combustion simulations [4.111, 4.116].

The second group of schemes, using non-linear upwind techniques, was pioneered by Godunov, see e.g., [4.106, 4.117]. A key observation is that the "damping" that occurs near shocks in gas dynamics

is really restricted to the extremely thin shock transition region, which is of a thickness comparable to merely a few mean free paths of the gas considered. Hence standard second- or higher-order dissipation is not taking place and cannot be responsible for the piecewise smooth, non-oscillatory solution behaviour close to physical shocks. In fact, a close analysis, based on the theory of characteristics, shows that oscillations are controlled by the directed transport of information along characteristics (in one space dimension), which are terminated when reaching a shock front and whose information is then dissipated. Godunov suggested a numerical approach that would automatically incorporate this non-linear selection of information transport, thereby avoiding the need for artificial viscosity terms. He proposed to compute the fluxes across grid cell interfaces in a numerical scheme in conservation form by exactly solving local "Riemann problems" (essentially equivalent to the standard shock tube problem, but with generalized initial states), which use the non-linear wave nature of the underlying system to resolve the jumps of state quantities between adjacent grid-cells. This basic structure proposed by Godunov has been taken up and developed further in various directions, the most established ones being higher-order extensions (the essentially non-oscillatory (ENO) version of the approach achieves the same formal accuracies as the corresponding FCT schemes), and simplifications that replace the originally required exact Riemann solution at grid-cell interfaces by approximate ones. The latter are easier to generalize to systems with non-trivial equations of state and are generally more efficient. For further details, the reader may want to consult the cited text books.

Detonation capturing. The mathematical nature of detonation waves, considered as reacting shock waves, is very similar to that of ordinary gas dynamic shocks. Therefore, one expects that the numerical schemes in the conservation form mentioned in the last paragraphs should be able to also "capture" detonation waves. In fact, the basic argument stating that conservative numerical schemes should produce the correct weak solutions if they converge can also be applied to detonations. As a consequence, there is a multitude of applications of FCT schemes or Godunov-type methods to problems of detonation physics, (see the past Combustion Symposia, the Shock Wave Symposia or the ICDERS conferences). There is one caveat, though, which may lead to surprising unphysical effects if naively overlooked [4.118]. In the limit of very rapid chemistry, equivalent to under-resolved representation of the detonation reaction zone, numerical schemes in conservation form can develop numerical solutions that appear to be very reasonable on the surface but are in fact completely false. The origin is an undesired non-linear interaction between the numerical dissipation resulting from averaging over grid-cells from one time step to the next and the highly non-linear combustion chemistry. This interaction can lead to artifical one-grid-cell-per-time step solutions that correspond to a weak detonation, followed by an ordinary inert shock rather than to a single strong detonation wave. This problem has been addressed in various ways, partly heuristic, partly theoretically founded, in Reference [4.111] and References [4.118 to 4.121].

4.5.3.2 Low Mach number flow solvers

Here, we summarize briefly two numerical approaches for low Mach number flows, which are being or becoming increasingly popular in the field of numerical combustion:

1. SIMPLE-type algorithms following ideas of Patankar [4.103] and
2. Projection-type methods, which borrow from Chorin [4.122 to 4.124].

These methods are finite-difference and finite-volume schemes. Finite-element methods will not be addressed in this section owing to lack of space and my personal experience in using these. The reader is referred to References [4.109, 4.125, 4.126], and [4.110] for further reading.

4.5.3.3 SIMPLE-type methods

The "semi-implicit method for pressure-linked equations" (SIMPLE) was originally designed for simulations of constant density incompressible flows [4.103]. It has later been extended to variable density incompressible and to moderately compressible flows, [4.127 to 4.129]. To explain the underlying strategy, we consider the simplest case of constant density ($\rho \equiv 1$) incompressible inviscid flows first: Thus we wish to solve

$$\frac{\partial \boldsymbol{v}}{\partial t} + \boldsymbol{v} \cdot \nabla \boldsymbol{v} + \nabla p_2 =: \frac{\partial \boldsymbol{v}}{\partial t} + \boldsymbol{C}[\boldsymbol{v}] + \nabla p_2 = 0 \tag{4.5.30}$$

with the divergence constraint

$$\nabla \cdot \boldsymbol{v} = 0\,. \tag{4.5.31}$$

The approach relies on an iteration scheme whose final result is the pressure field p_2, needed to update the velocity field from time level t^n to the next level t^{n+1} in such a way that the new field $\boldsymbol{v}^{n+1}$ satisfies the divergence constraint from Equation (4.5.31). Suppose that an estimated pressure field $p_2^{n,0}$ is available, which could be the pressure field from the last time step as indicated by the notation, but does not have to be. Suppose further that an implicit discretization for the velocity evolution equation is adopted

$$\frac{\boldsymbol{v}^{n+1} - \boldsymbol{v}^n}{\Delta t} + \left[\tilde{\boldsymbol{C}}_i[\boldsymbol{v}^{n+1}] + \tilde{\boldsymbol{C}}_e[\boldsymbol{v}^n]\right] + \tilde{\nabla} p_2^{n+\frac{1}{2}} = 0\,, \tag{4.5.32}$$

with $\tilde{\boldsymbol{C}}_e[\cdot], \tilde{\boldsymbol{C}}_i[\cdot]$ as explicit and implicit contributions to the discretization of the non-linear convection operator $\boldsymbol{C}[\boldsymbol{v}] = \boldsymbol{v} \cdot \nabla \boldsymbol{v}$, respectively (see [4.128, 4.129] for examples) and $\tilde{\nabla}$ a discrete approximation of the gradient operator. For convenience, we rewrite Equation (4.5.32) as

$$\tilde{\boldsymbol{A}}_i[\boldsymbol{v}^{n+1}] = \tilde{\boldsymbol{A}}_e[\boldsymbol{v}^n] - \tilde{\nabla} p_2^{n+\frac{1}{2}}\,. \tag{4.5.33}$$

where

$$\begin{aligned} \tilde{\boldsymbol{A}}_i[\cdot] &= \tfrac{1}{\Delta t}\left[\mathbf{1} + \Delta t\, \tilde{\boldsymbol{C}}_i\right][\cdot] \\ \tilde{\boldsymbol{A}}_e[\cdot] &= \tfrac{1}{\Delta t}\left[\mathbf{1} - \Delta t\, \tilde{\boldsymbol{C}}_e\right][\cdot] \end{aligned} \tag{4.5.34}$$

The SIMPLE method adopts a linear implicit formulation, so that $\tilde{\boldsymbol{A}}_i[\cdot]$ is in fact a linear operator, and then solves Equation (4.5.33) iteratively according to the following sequence:

Start:

$$\begin{aligned} \tilde{\nabla} p_2^{n+\frac{1}{2},0} &= \tilde{\nabla} p_2^{n,0} \\ \tilde{\boldsymbol{A}}_i[\boldsymbol{v}^{n+1,0}] &= \tilde{\boldsymbol{A}}_e[\boldsymbol{v}^n] - \tilde{\nabla} p_2^{n+\frac{1}{2},0} \end{aligned} \tag{4.5.35}$$

Iterative Correction:

$$\begin{aligned} p_2^{n+\frac{1}{2},\nu+1} &= p_2^{n+\frac{1}{2},\nu} + \delta p_2^{\nu} \\ \boldsymbol{v}^{n+1,\nu+1} &= \boldsymbol{v}^{n+1,\nu} + \delta \boldsymbol{v}^{\nu} \end{aligned} \tag{4.5.36}$$

Correction Equations:

$$\begin{aligned} \tilde{\boldsymbol{A}}_i[\delta\boldsymbol{v}^\nu] + \tilde{\nabla}\delta p_2^\nu &= 0 \\ \tilde{\nabla}\cdot\left(\boldsymbol{v}^{n+1,\nu} - \tilde{\boldsymbol{A}}_i^{-1}\left[\tilde{\nabla}\delta p_2^\nu\right]\right) &= 0\,. \end{aligned} \tag{4.5.37}$$

The last equation is the appropriate reformulation of the divergence constraint

$$\tilde{\nabla}\cdot\left(\boldsymbol{v}^{n+1,\nu} + \delta\boldsymbol{v}^\nu\right) = 0 \tag{4.5.38}$$

as an elliptic pressure correction equation. If the linearization of $\tilde{\boldsymbol{A}}_i$ yields a diagonal matrix, then the pressure correction equation is of Poisson type.

For combustion applications, one is interested in variable density flows (the hot burnt gas is typically expanded relative to the unburnt by a factor of 2 to 6) and often also in compressibility effects. Thus one has to consider the full compressible flow equations rather than the idealized case of an incompressible constant density fluid as discussed above.

The SIMPLE method has been extended to compressible flows by Karki and Patankar [4.127] (homentropic flow) and to the more general case of variable entropy compressible flows by Rhie [4.128] and Shyy [4.129]. The idea in all of these approaches is to replace the strict divergence constraint from Equation (4.5.31) by the continuity Equation $(4.5.9)_1$ and to introduce a thermodynamic coupling between pressure and density.

A simple argument shows that this is not yet sufficient to obtain an approximation to the full compressible flow equations: As in the incompressible case we have three momentum equations. The continuity equation now replaces the divergence constraint and is, thus, responsible for determining the pressure field. However, besides the pressure we have a new variable, the density, but no equation for it so far. If one opts to strictly couple pressure and density by a given function, $\rho = \rho(p)$, then this severly constrains the possible thermochemical processes. Combustion changes the entropy of the reacting mass elements and with it the pressure-density relation. Therefore, one more equation needs to be supplemented!

A natural choice that has been adopted frequently in combustion is to explicitly compute the time evolution of temperature T or of the internal energy. For an ideal gas one has

$$T = \frac{p}{\rho R} \qquad\qquad \rho = \frac{p}{RT} \tag{4.5.39}$$

and therefore

$$\frac{\partial\rho}{\partial t} = \frac{1}{RT}\frac{\partial p}{\partial t} - \frac{p}{RT^2}\frac{\partial T}{\partial t}\,. \tag{4.5.40}$$

Here the temperature time derivative must be obtained from a temperature evolution equation, to be derived from energy conservation. Notice that the "gas constant" R is generally not really constant in a reacting flow, but that it depends on the instantaneous local gas composition. In that case an additional term involving $\frac{\partial R}{\partial t}$ must be included in Equation (4.5.40). Variations of R must be computed using the results from the species balances Equation (4.5.10).

A possible extension of the SIMPLE approach now solves an approximate explicit equation for temperature and species, so that $\frac{\partial T}{\partial t}$, $\frac{\partial R}{\partial t}$ are known, and then discretizes the continuity equation as a pressure

correction system. The incompressible flow divergence constraint Equation (4.5.38) is first replaced with an equation of the form

$$\frac{\rho^{n+1,\nu}+\delta\rho^{\nu}-\rho^{n}}{\Delta t}+\nabla\cdot\left(\rho^{n+1,\nu}\boldsymbol{v}^{n+1,\nu}+\delta\rho^{\nu}\boldsymbol{v}^{n+1,\nu}+\rho^{n+1,\nu}\delta\boldsymbol{v}^{\nu}+\delta\rho^{\nu-1}\delta\boldsymbol{v}^{\nu-1}\right)=0\,, \quad (4.5.41)$$

where we have used an implicit first-order discretization for simplicity. The goal is to iterate on this equation based on the updating rules

$$\begin{aligned}\rho^{n+1,\nu+1} &= \rho^{n+1,\nu}+\delta\rho^{\nu}\\ \boldsymbol{v}^{n+1,\nu+1} &= \boldsymbol{v}^{n+1,\nu}+\delta\boldsymbol{v}^{\nu}\end{aligned} \quad (4.5.42)$$

and suitable relations between a pressure correction field δp_2^{ν} and the perturbations $\delta\rho^{\nu}, \delta\boldsymbol{v}^{\nu}$

$$\begin{aligned}\delta\rho^{\nu} &= C(\rho,P_0;M)\;\delta p_2^{\nu}\\ \delta\boldsymbol{v}^{\nu} &= -\tilde{\boldsymbol{A}}_i^{-1}\left[\tilde{\nabla}\delta p_2^{\nu}\right].\end{aligned} \quad (4.5.43)$$

Here $C(\rho,P_0;M)$ is an approximate derivative $\partial\rho/\partial p_2$ evaluated in an explicit fashion at either the old time level or at the last iteration level. In practice one uses an isentropic or an isothermal relation for $C(\rho,P_0;M)$. We notice that this choice is not crucial for the whole procedure because ultimately one iterates until the corrections $\delta\rho^{\nu}, \delta\boldsymbol{v}^{\nu}, \delta p_2^{\nu}$ become negligible and the continuity equation is solved to the desired accuracy. The choice of $C(\rho,P_0;M)$ merely influences the path of the iteration in state space, but not—if it converges—the final result. The velocity correction is analogous to the original version from Equation (4.5.37).

Importantly, the coefficient $C(\rho,P_0;M)$ describes the response of the density to perturbations of p_2, not to the full pressure p, so that

$$C(\rho,P_0;M)=\frac{\partial p}{\partial p_2}\left(\frac{\partial\rho}{\partial p}\right)_{\mathrm{S,T}}=M^2c_{\mathrm{S,T}}^{-2}\,, \quad (4.5.44)$$

where $c_{\mathrm{S,T}}$ is the isentropic or isothermal speed of sound. Thus as the Mach number vanishes, the limit of incompressibility is approached automatically in the sense that the response of the density to the pressure p_2 vanishes.

The perturbed continuity iteration Equation (4.5.41) includes a non-linear term $\nabla\cdot(\delta\rho\,\delta\boldsymbol{v})$. This term is lagged behind in the iteration cycle and is evaluated explicitly at $\nu-1$ so as to render the pressure correction equation a linear system. Here is the form of the pressure correction equation when the operator $\tilde{A}_i$ is diagonal with entries $1/\rho$

$$C\,\delta p_2^{\nu}+\Delta t\nabla\cdot\left(C\,\delta p_2^{\nu}\,\boldsymbol{v}^{\nu}-\nabla\delta p_2^{\nu}\right)=RHS\,. \quad (4.5.45)$$

The right-hand side includes all the terms treated explicitly or stemming from the old time or last iteration level.

An important observation is that the above equation involves a true *Laplacian* for δp_2^{ν} as the elliptic part of the operator. This is in contrast to many other schemes for variable density low Mach number flows, which end up with an elliptic pressure operator of the form $\nabla\cdot(\frac{1}{\rho}\nabla(\cdot))$. If the density is strongly

varying, then the numerical inversion of this latter operator is much more expensive than inverting a true Laplacian, for which special extremely fast schemes have been developed. This observation has been explored extensively in the construction of an efficient numerical scheme for reactive flows, sprays etc. by Haldenwang et al. [4.130].

To complete the picture, we should notice, however, that the formulation described above relies on an explicit estimate for density variations induced by entropy advection along particle paths. These effects must be included in the initial guess $\rho^{n+1,0}$. Otherwise, the assumptions built into the coefficient $C(\rho, P_0; M)$ would dominate the density variations. Currently, there seems to be no numerical technique that would manage to (i) rely on a pressure (correction) equation involving a true Laplacian and (ii) conserve total energy at the same time (see also [4.98]).

Related approaches are the pressure implicit second order (PISO) scheme [4.101, 4.131], which is currently used quite successfully for combustion simulations, [4.132, 4.133], and the method proposed by Geratz et al. [4.114] and Roller et al. [4.115].

4.5.3.4 Projection-type methods

The key idea of projection schemes can best be described by considering constant density incompressible inviscid flows. The governing equations are obtained from those derived in Section 4.5.2.1 by assuming zero heat release, $Q \equiv 0$, and constant density, $\rho \equiv 1$, by passing to the limit of infinite Reynolds and Peclet numbers, $(\mathrm{Re}, \mathrm{Pe} \to \infty)$ and then considering the zero Mach number limit, $M \equiv 0$. The continuity equation in that case becomes redundant, the momentum equation reduces to

$$\frac{\partial \boldsymbol{v}}{\partial t} + \boldsymbol{v} \cdot \nabla \boldsymbol{v} + \nabla p_2 = 0 \tag{4.5.46}$$

and the leading-order energy equation yields the homogeneous velocity divergence constraint

$$\nabla \cdot \boldsymbol{v} = 0\,. \tag{4.5.47}$$

Notice that $\nabla \cdot (\boldsymbol{v} \circ \boldsymbol{v}) \equiv \boldsymbol{v} \cdot \nabla \boldsymbol{v}$ when $\nabla \cdot \boldsymbol{v} \equiv 0$!

A projection scheme consists of 2 steps. Step 1 accounts for non-linear convection, $\boldsymbol{v} \cdot \nabla \boldsymbol{v}$, in an explicit fashion by solving the truncated system

$$\frac{\partial \boldsymbol{v}}{\partial t} + \boldsymbol{v} \cdot \nabla \boldsymbol{v} = 0 \tag{4.5.48}$$

over one time step. Given the velocity field $\boldsymbol{v}^n$ at time t^n, the first step provides a mapping

$$\boldsymbol{v}^* = \boldsymbol{v}^n - \Delta t \, (\boldsymbol{v} \cdot \nabla \boldsymbol{v})^n \tag{4.5.49}$$

with a suitable numerical approximation of the convection terms. There is no guarantee that $\boldsymbol{v}^*$ will satisfy the divergence condition from Equation (4.5.47), and so the second step consists of "projecting" this intermediate velocity field back onto the space of divergence-free fields:

$$\boldsymbol{v}^{n+1} = \boldsymbol{v}^* - \nabla \phi\,, \tag{4.5.50}$$

with ϕ adjusted so as to let $\boldsymbol{v}^{n+1}$ comply with the divergence constraint, i.e.,

$$\nabla^2 \phi = \nabla \cdot \boldsymbol{v}^*\,. \tag{4.5.51}$$

That the correction to $\boldsymbol{v}^*$ should be in the form of a gradient field becomes intuitively clear from a comparison of the original momentum Equation (4.5.46) and the truncated one from the first projection step Equation (4.5.48). It was the pressure gradient field that was left out in formulating the first step of the scheme. More elaborate explanations and justifications, based on the Helmholtz-Hodge decomposition of general vector fields, are given in the original references [4.122 to 4.124] and in related subsequent publications [4.134 to 4.138]. The reader may also want to consult Reference [4.126] for detailed discussions of some difficulties and pitfalls associated with this approach.

Major efforts have recently been spent to extend this approach by introducing higher-order approximations, dynamic adaptive grid refinement (see [4.139]) and by allowing variable densities (while still keeping the zero divergence constraint!), [4.134, 4.138]. Further extensions are aimed at the representation of low Mach number reacting flows [4.135, 4.140].

4.5.4 The Mathematics of Deflagrations

Chemical reactions are typically very fast once they are ignited. As a consequence, the available fuel is quickly burned and reactions typically are concentrated in narrow regions. In fact, the characteristic thickness of a laminar premixed flame front is of the order of fractions of a millimetre. A systematic derivation, showing how fast reaction (large Damköhler number $\mathrm{Da} \gg 1$), and inefficient molecular transport (large Reynolds and Peclet numbers $\mathrm{Re}, \mathrm{Pe} \gg 1$) conspire to lead to thin combustion fronts with finite propagation speeds is given in Reference [4.44].

Numerical methods must cope with these constraints of thin fronts and slow flows. One approach to the thin front problem is dynamic grid refinement, by which one concentrates the numerical spatial resolution dynamically within the flame region. An alternative is front tracking. This approach considers a flame front as a reactive discontinuity converting unburnt to burnt gases. In this fashion, one avoids the stringent resolution requirements associated with a detailed representation of the internal flame structure as well as the technical compications associated with dynamic gridding. On the other hand, the required numerical techniques themselves become more complex because in addition the standard flow solver, the time evolution of the flame geometry and its coupling to the flow field must be represented appropriately. Thus one has to balance complexity that is due to data arrangement, data structures etc. from dynamic grid refinement versus the additional complications implied by front tracking and front flow coupling.

Some important implications for both approaches can be extracted from a general analysis of the mathematical nature of such reactive discontinuities. One central question concerns the mechanisms that determine the front propagation velocity. Obviously, these mechanisms must be represented accurately in a numerical scheme, be it of the "front tracking" or of the "dynamically adaptive" type. The next subsection collects a few mathematical derivations that provide some insight into this question and suggest a number of conclustions regarding appropriate numerical methods.

4.5.4.1 Mathematical features of deflagrations and other discontinuities

For simplicity, we restrict much of the subsequent discussion to a single space dimension. The key observations will not depend on this limitation.

Jump conditions. Consider one-dimensional travelling wave solutions in an unbounded domain of the scaled governing equations from Equations (4.5.9) to (4.5.14). Any variable $\phi(\boldsymbol{x}, t)$ would be described

by

$$\phi(\boldsymbol{x},t) = \tilde{\phi}(x - Dt)\,, \tag{4.5.52}$$

where it is assumed that the wave travels in the x-direction at velocity D. Inserting this ansatz in the governing equations we obtain

$$\begin{aligned}
-D\frac{d}{d\xi}(\rho) \quad &+ \quad \frac{d}{d\xi}(\rho u) \qquad\qquad\quad &= \quad 0 \\
-D\frac{d}{d\xi}(\rho u) \quad &+ \quad \frac{d}{d\xi}(\rho u^2 + \frac{1}{M^2}\,p) \quad &= \quad -\frac{d}{d\xi}\left(\frac{1}{\mathrm{Re}}\tau_{x,x}\right) \\
-D\frac{d}{d\xi}(\rho e) \quad &+ \quad \frac{d}{d\xi}(u[\rho e + p]) \quad &= \quad -\frac{d}{d\xi}\left(\frac{1}{\mathrm{Pe}}j_{T,x} + \frac{M^2}{\mathrm{Re}}\tau_{x,x}u + \frac{Q}{\mathrm{ReSc}}\sum_{i=1}^{n_{\mathrm{spec}}}\delta h_i\, j_{i,x}\right).
\end{aligned} \tag{4.5.53}$$

from the conservation laws and

$$-D\frac{d}{d\xi}(\rho Y_i) + \frac{d}{d\xi}(\rho Y_i u) = -\frac{d}{d\xi}\left(\frac{1}{\mathrm{ReSc}}\,j_{i,x}\right) + \mathrm{Da}\rho\omega_i \qquad (i = 1\ldots n_{\mathrm{spec}}) \tag{4.5.54}$$

from the species balances. Here $\xi = x - Dt$ and $\tau_{x,x}, j_{T,x}, j_{i,x}$ are the x-components of the x-stress component, the heat conduction energy flux and the ith species diffusion fluxes, respectively.

Next, we integrate in ξ assuming that constant burnt gas and unburnt gas conditions $(\rho, u, p, Y_i)_b$ and $(\rho, u, p, Y_i)_u$ are attained as $\xi \to -\infty$ and $\xi \to \infty$, respectively. Under these assumptions, the diffusive fluxes and the heat conduction terms vanish as $|\xi| \to \infty$ because they are proportional to gradients of the dependent variables. Integration of Equation (4.5.53) yields

$$\begin{aligned}
-D[\![\rho]\!] \quad &+ \quad [\![\rho u]\!] \qquad\qquad &= \quad 0 \\
-D[\![\rho u]\!] \quad &+ \quad [\![\rho u^2 + \tfrac{1}{M^2}\,p]\!] \quad &= \quad 0 \\
-D[\![\rho e]\!] \quad &+ \quad [\![u(\rho e + p)]\!] \quad &= \quad 0.
\end{aligned} \tag{4.5.55}$$

These are the standard Rankine-Hugoniot jump condtions for gas dynamic discontinuities.

Since we assume that at large distances two constant states of burnt and unburnt should be attained, we must require that the chemical reaction rates vanish at both ends:

$$\boldsymbol{\omega}(T_u, p_u, \boldsymbol{Y}_u) = \boldsymbol{\omega}(T_b, p_b, \boldsymbol{Y}_b) = 0 \tag{4.5.56}$$

where

$$\boldsymbol{Y} = \{Y_j\}_{j=1}^{n_{\mathrm{spec}}} \qquad \text{and} \qquad \boldsymbol{\omega} = \{\omega_j\}_{j=1}^{n_{\mathrm{spec}}}\,. \tag{4.5.57}$$

In the unburnt gas this constraint is normally satisfied automatically because the reactions are frozen at low temperatures. Therefore, as in real-life applications, the unburnt gas composition can be chosen more or less arbitrarily. For the burnt gas one obtains a non-trivial constraint because temperatures will generally be high enough to allow chemical reactions to be active. Thus one may read the second equality in Equation (4.5.56) as algebraic constraints for the equilibrium species mass fractions $\boldsymbol{Y}^{\mathrm{eq}}(T_b, p_b, \boldsymbol{Y}_u)$:

$$\boldsymbol{\omega}\left(T_b, p_b, \boldsymbol{Y}^{\mathrm{eq}}(T_b, p_b, \boldsymbol{Y}_u)\right) = 0\,. \tag{4.5.58}$$

The dependence of $\boldsymbol{Y}^{\rm eq}(T_b, p_b, \boldsymbol{Y}_u)$ on $\boldsymbol{Y}_u$ results from the constraint that their detailed *atomic* compositions must be the same. After all, chemistry is nothing but a re-arrangement of atoms between molecules. The appropriate mathematical description is

$$\sum_{j=1}^{n_{\rm spec}} \nu_i^j \, \frac{1}{\mathcal{M}_j} \, (Y_{j,b} - Y_{j,u}) = 0 \qquad (i = 1 \ldots n_{\rm atoms}) \,, \tag{4.5.59}$$

where ν_i^j is the number of atoms of type i in a molecule of species j, and $\mathcal{M}_j$ is the molecular weight of species j.

Characteristic analysis of the inviscid, inert flow equations. We turn next to the question in which way a reactive discontinuity influences its surrounding flow field and in which way it must respond, in turn, to input from outside. Since in most practical applications the Reynolds and Peclet numbers are very large, important insight can be gained by analyzing the inviscid flow equations. Moreover, we are interested here in the behaviour of the flow *surrounding* a reactive front, so that we may restrict our discussion to the case of a reactive discontinuity embedded between the masses of non-reactive burnt and unburnt gases.

Thus we consider the conservation equations

$$\begin{array}{rcrcl} (\rho)_t & + & (\rho u)_x & = & 0 \\ (\rho u)_t & + & (\rho u^2 + \frac{1}{M^2}\, p)_x & = & 0 \\ (\rho e)_t & + & (u[\rho e + p])_x & = & 0. \end{array} \tag{4.5.60}$$

with

$$(\rho e) = \frac{p}{\gamma - 1} + \frac{M^2}{2} \rho u^2 \,. \tag{4.5.61}$$

Applying the chain rule of differentiation repeatedly and forming a number of linear combinations one may transform these equations to the quasi-linear form

$$\begin{array}{rcrcrcl} \rho_t & + & u\,\rho_x & + & \rho\, u_x & = & 0 \\ u_t & + & u\, u_x & + & \frac{1}{M^2}\frac{1}{\rho}\, p_x & = & 0 \\ p_t & + & u\, p_x & + & \gamma p\, u_x & = & 0. \end{array} \tag{4.5.62}$$

(In fact, the chain rule immediately yields Equation $(4.5.62)_1$, subtraction of [$u \times$ Equation $(4.5.60)_1$] from Equation $(4.5.60)_2$ yields Equation $(4.5.62)_2$ and subtraction of [$u \times$ Equation $(4.5.60)_2$] from Equation $(4.5.60)_3$ yields Equation $(4.5.62)_3$.)

Now subtraction of [$(\gamma p/\rho) \times$ Equation $(4.5.62)_1$] from Equation $(4.5.62)_3$ yields the first compatibility condition of the theory of characteristics:

$$(p_t + u p_x) - c^2 \, (\rho_t + u \rho_x) = 0 \tag{4.5.63}$$

where

$$c = \sqrt{\frac{\gamma p}{\rho}} \tag{4.5.64}$$

is the scaled speed of sound. Similarly, by adding and subtracting [$(M\,\rho c) \times$ Equation $(4.5.62)_2$] to / from Equation $(4.5.62)_3$ one obtains the compatibility conditions

$$\begin{array}{rcrcl} \left(p_t + (u + \frac{1}{M} c)\, p_x\right) & + & M\,\rho c\, \left(u_t + (u + \frac{1}{M} c)\, u_x\right) & = & 0 \\ \left(p_t + (u - \frac{1}{M} c)\, p_x\right) & - & M\,\rho c\, \left(u_t + (u - \frac{1}{M} c)\, u_x\right) & = & 0\,. \end{array} \tag{4.5.65}$$

The operators

$$\left(\frac{\partial}{\partial t}\right)_{\rm pp} = \frac{\partial}{\partial t} + u\,\frac{\partial}{\partial x} \qquad \text{and} \qquad \left(\frac{\partial}{\partial t}\right)^{\pm}_{\rm ac} = \frac{\partial}{\partial t} + (u \pm \tfrac{1}{M}c)\,\frac{\partial}{\partial x} \tag{4.5.66}$$

are "directional derivatives", describing time derivatives as seen by observers "pp" and "ac" moving with velocities u and $u \pm \frac{1}{M}c$, respectively. The observer motions $x_{\rm pp}(t)$ and $x^{\pm}_{\rm ac}(t)$ thus obey the evolution equations

$$\frac{dx_{\rm pp}}{dt} = u \qquad \text{and} \qquad \frac{dx^{\pm}_{\rm ac}}{dt} = u \pm \tfrac{1}{M}c\,. \tag{4.5.67}$$

In other words, $(\partial/\partial t)_{\rm pp}$ indicates temporal variations seen along a particle path, whereas $(\partial/\partial t)^{\pm}_{\rm ac}$ denotes time derivatives seen by an observer moving with an acoustic signal.

The three compatibility conditions from Equations (4.5.63) and (4.5.65) contain the same information as the original conservation laws (Equation (4.5.60)) or the primitive formulation (Equation (4.5.62)) as long as all required derivatives exist. The key advantage of this "characteristic formulation" is that it explicitly shows how information is transported in time. We will use this insight now to discuss the mathematical features of gas dynamic discontinuities. We consider Figure 4.5.4.1- 1 and ask, what information is

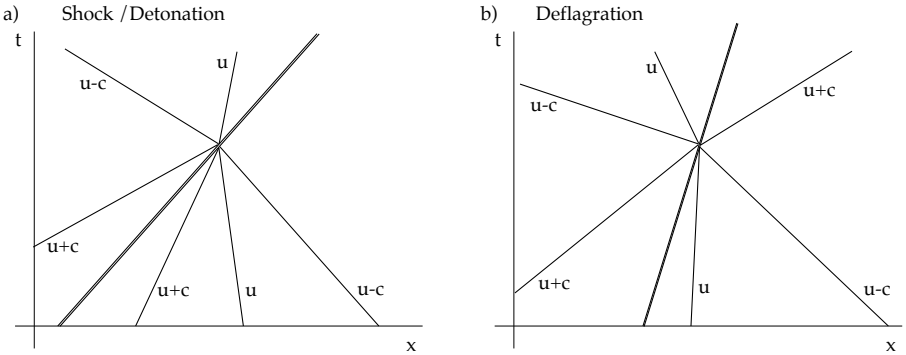

Figure 4.5.4.1- 1: Characteristic diagrams for shocks and detonations (a) and deflagrations (b)

available at any given time to determine the 2 states immediately in front of and behind a discontinuity together with its front propagation speed: For the species mass fractions we have $n_{\rm spec}$ equations from Equations (4.5.56) and (4.5.59), allowing us to determine the burnt gas composition, once the unburnt composition and the burnt gas pressure and temperature (or density) are known. (For a non-reactive front, such as a shock wave these reduce to the condition that the species mass fractions do not change across the front.)

Differentiating the fluxes $\rho Y_i u$ in the species transport equations (Equation (4.5.10)) and neglecting the right-hand-side expressions, one finds compatibility conditions for the species mass fractions in the unburnt gas,

$$\boldsymbol{Y}_t + u\,\boldsymbol{Y}_x = 0\,. \tag{4.5.68}$$

These equations state that the species mass fractions do not change along particle paths outside the reaction front. Based on this, one finds the unburnt gas composition in front of a discontinuity at any time t as follows: Track the particle path $dx_{pp}/dt = u$, which arrives at the front at time t, backwards in time until you reach the initial time $t = 0$. The composition found at that location is the same as the unburnt gas composition near the front at the later instance t (cf. Figure 4.5.4.1- 1).

Thus we only need to check whether there is a sufficient number of equations to determine pressures, densities, and velocities in the burnt and unburnt, (p_b, ρ_b, u_b) and (p_u, ρ_u, u_u), plus the front propagation speed D. These are altogether 7 unknowns.

Consider Figure 4.5.4.1- 1a, which shows the sketch of a propagating shock or detonation wave. The number of characteristic curves that *arrive* at the discontinuity from earlier times is 4. Adding the 3 jump conditions from Equation (4.5.55), we have 7 equations for the 7 unknowns. These turn out to be independent equations, and thus the burnt and unburnt states plus the propagation speed D are completely determined just through the equations of motion, the species transport equations outside the front, the Hugoniot jump conditions, and suitable initial or boundary data or both.

The situation is different for deflagrations as can be seen in Figure 4.5.4.1- 1b. The forward acoustic signal $dx^+_{ac}/dt = u + \frac{1}{M}c$ *emerges from* the discontinuity rather than *arriving at it*. Thus the associated compatibility conditions can only be used in determining the further evolution but not to connect the current states near the front to the given initial (and boundary) conditions. One determining equation for (p_b, ρ_b, u_b), (p_u, ρ_u, u_u) and D is missing! The missing relation is a burning velocity eigenvalue, providing an explicit functional relation between the pre- and post-front states and the propagation speed D. The burning rate law is typically given as

$$D = u_u + s(p_u, \rho_u, \boldsymbol{Y}_u) \tag{4.5.69}$$

with some explicit function $s(p, \rho, \boldsymbol{Y})$.

That a flame speed law must be provided in order to uniquely determine the propagation of a deflagration wave has a deeper physical reason than just the "number counting game" pursued above. Shock waves as well as detonations are governed by inviscid gas dynamics only. Chemical reactions in detonations are triggered by shock wave compression, and their exremely high, supersonic propagation speed renders the effects of molecular transport irrelevant. Once a shock has sufficiently compressed the gas, temperatures are high enough to lead to auto-ignition, and the reaction heat release sets in. The rate of fuel consumption is determined completely by this compression-ignition-reaction sequence that involves only inviscid gas dynamics.

This is in contrast to the physics of deflagrations. Here, the hot burnt gases preheat the unburnt gas right in front of the flame through heat conduction (or radiation or both) and chemical radicals diffuse out of the reaction zone into the unburnt gas region. Once this process of preheating and chemical preconditioning has lead to sufficient reactivity, combustion takes place and the front propagates. The whole process hinges on heat conduction and species diffusion, both of which are not represented in the characteristic analysis of the inviscid flow equations given above. We conclude that

The detailed processes within the flame structure crucially influence the flame propagation.

Consequences for numerical simulations of turbulent deflagrations. The importance of this simple statement for any attempt at numerical simulation of deflagration waves cannot be overestimated! Let us distinguish two very different alternative approaches:

1. detailed modelling of the inner flame structure, and
2. flame front tracking.

By the first approach one implements numerical representations of both the overall reaction and turbulent transport sub-mechanisms that are active within the flame region. As we have seen above, it is the detailed interplay between reaction rates and transport processes that is responsible for establishing the net unburnt gas mass consumption rate. As a consequence, equal emphasis must be given to either of these subprocesses. In other words, an excellent mean reaction rate model is useless unless combined with an equally sophisticated turbulent effective transport scheme because errors in the latter could completely falsify the overall combustion rates, regardless of the quality of the former. In addition, the "full-resolution approach" requires sufficient spatial and temporal numerical resolution of the flame region in order to achieve the desired accuracy in representing the reaction-transport interplay.

Flame front tracking approaches avoid the necessity of modelling the complex phenomena within a "flame brush". They represent a deflagration as a reactive discontinuity and obtain a closed equation system by supplying an explicit burning rate law as a function of the unburnt gas thermodynamic, composition, and turbulence state. The advantages of this approach over detailled modelling are (i) that it explicitly controls the net mass burning rate without relying on subtle interactions between submodels of net turbulent reaction rates and effective turbulent transport and (ii) that it allows much coarser spatial and temporal resolution. Its disadvantage is that one must supply effective turbulent flame speed functions, which can be derived from scratch only in particular regimes of turbulent combustion. Front tracking has one more advantage in the context of implementing experimental knowledge in a numerical simulation system: Measuring effective turbulent burning velocities experimentally is much easier than distinguishing detailed subprocesses within a flame brush by localized measurements.

We conclude that both approaches have their merits and preferred ranges of applications: In practical engineering applications, the front tracking approach is advantageous because (i) it has only a single modelled quantity, the turbulent burning velocity; and (ii) there is no need to resolve spatial scales on the order of the turbulent flame thickness. In contrast, detailled modelling of the turbulent suubprocesses within a flame brush is the more fundamental approach, by which one can, potentially, represent all the underlying physics leading to the establishment of the overall combustion rate. However, this approach is meaningful only if *all* the relevant subprocesses are properly modelled and resolved.

A flame front tracking scheme that allows the inclusion of a quasi-one-dimensional dynamic internal flame structure model is work in progress.

4.5.5 Numerical Representation of Deflagration Waves

4.5.5.1 Resolved turbulent flame structures

The advantages of an approach that relies on detailled numerical resolution of the internal structure of a deflagration are that

- All important physical sub-mechanisms within a turbulent flame zone as well as their interactions can be incorporated.
- The mathematical structure of the most popular turbulent combustion models is similar to a combination of standard non-reactive turbulent flow models and the laminar reactive Navier-Stokes equations. Thus available reactive flow solvers can be employed more or less "out of the box" for turbulent combustion simulations.

The disadvantages are that

- A detailed representation of the turbulent flame brush structure leads to minimum spatial resolution requirements that can become overwhelming for large-scale, industrial-size systems. This issue may enforce the use of dynamically adaptive grids, with all the added complexity.
- Advantage 2, above, holds only when the turbulent combustion model excludes certain non-standard effects, such as counter-gradient turbulent transport [4.49, 4.50]. If such effects are expected to be important, adequate numerical techniques must be implemented.

Unfortunately, a considerable number of physical effects that are expected to be important during the early stages of turbulent flame acceleration have been identified and are not properly represented by standard models. Bray lists the following, (see [4.1] and the extensive list of references therein):

- the modification of large-scale turbulent transport by heat release including the phenomenon of counter-gradient transport;
- the sensitivity of turbulent transport to pressure gradients.
- the generation of turbulence because of heat release;
- the modification of small-scale mixing, as characterized by viscous and scalar disspation, because of heat release;
- the modification of pressure-velocity fluctuation correlations in the second moment evolution equations as a result of heat release; and
- the introduction into the mean flow equations of additional characteristic length and time scales linked to laminar flame instabilities.

It is estimated that the importance of all these effects should decrease with increasing turbulence intensity and that it should become negligible as $u'/s_L \rightarrow \infty$. Thus successful simulations of high-speed turbulent combustion should be (and are) possible without inclusion of these effects. Yet, as stated earlier, accurate predictions of the transitional phase of flame acceleration require more sophisticated models and appropriate numerical techniques.

For example, implementations of the Bray-Moss-Libby model in the context of a consistent second-order closure are reported in Reference [4.141]. However, it is stated in Reference [4.1] that these authors did need to deviate from the original BML model in the closure of the second-order moment equations in order to overcome numerical difficulties arising from the non-standard structure of the BML model.

Given that there is no widespread agreement regarding the proper mathematical structure of a model that would incorporate all the effects mentioned above, little general advice can be given regarding the numerical techniques that should be employed or developed in order to cope with the arising complexities.

4.5.5.2 Flame front tracking

As mentioned above, flame front tracking requires the numerical representation of the flame geometry and its evolution *and* of the coupling between front and surrounding flow via the Rankine-Hugoniot conditions (Equation (4.5.55)).

*The level set or **G**-equation approach.* As discussed above, premixed flames propagate relative to the unburnt gas at the local burning velocity s. For a two-dimensional setting, the situation is sketched in Figure 4.5.5.2- 1. The propagation of points on a flame surface is determined by the superposition of convection by the unburnt gas flow and this self-propagation in the direction normal to the front

$$d\,\boldsymbol{x}_f/dt = \boldsymbol{v}_u + s\boldsymbol{n} = \boldsymbol{D}. \tag{4.5.70}$$

Here $\boldsymbol{n}$ is a unit normal vector on the front pointing towards the unburnt gas region. The level set or G-equation approach introduces a scalar field $G(\boldsymbol{x}, t)$ whose iso-surfaces

$$G(\boldsymbol{x}, t) = G_0 \tag{4.5.71}$$

are identified with flame fronts. Then

$$\boldsymbol{n} = -\left.\frac{\nabla G}{|\nabla G|}\right|_{G=G_0}. \tag{4.5.72}$$

The choice of G_0 is arbitrary but fixed for a single combustion event. The flame surface(s) $G = G_0$ naturally decompose the flow domain into unburnt gas ($G < G_0$) and burnt gas regions ($G > G_0$). Differentiating Equation (4.5.71) with respect to time and using Equation (4.5.70) one finds

$$\frac{\partial G}{\partial t} + \frac{d\boldsymbol{x}_f}{dt}\cdot\nabla G = \frac{\partial G}{\partial t} + \boldsymbol{D}\cdot\nabla G = 0\,, \tag{4.5.73}$$

the G-equation.

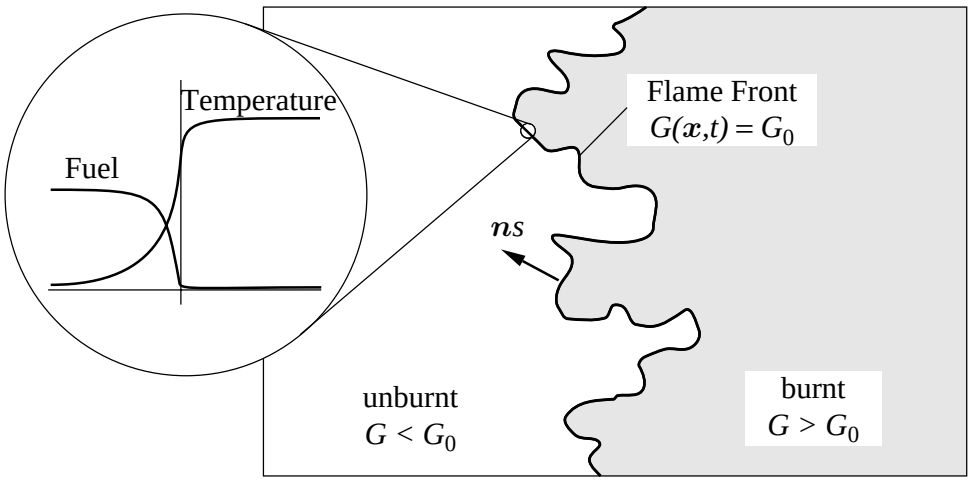

Figure 4.5.5.2- 1: Schematic representation of premixed flame front propagation

The key physical ingredients of the level set approach are the burning velocity law determining s as a function of thermo-chemical and flow conditions and some local features of the flame geometry. It is important to notice that s is defined as the relative velocity between points on the front and the unburnt

gas immediately *in front* of it. The relative velocity s_b between the burnt gas and the front differs from s because of the thermal gas expansion within the flame front and the associated jump of the normal velocity. Because of mass conservation the mass flux density normal to the front does not change across the discontinuity and the burnt gas relative speed is easily computed as

$$\rho s = (\rho s)_b = \rho_u s \quad \Rightarrow \quad s_b = \frac{\rho_u}{\rho_b} s \,. \tag{4.5.74}$$

Although both the flow velocity and the relative speed between flow field and front change across the flame, their sum, namely the vector $\boldsymbol{D}$ appearing in Equation (4.5.73), does not! This observation will be important in the subsequent construction of a numerical method.

Figure 4.5.5.2- 2 shows the temporal evolution of an initially sinusoidally distorted front according to Equation (4.5.73), with $s \equiv const.$ and with the unburnt gas at rest. The front motion then follows Huygens' principle, and one quickly observes the formation of sharp cusps on the front. Laminar flame theory, [4.96, 4.142], as well as modern theories of turbulent premixed combustion, [4.45, 4.77], yield modified, curvature dependent burning velocity laws of the type

$$s = s^0 - s^0 \mathcal{L} \kappa + \mathcal{L} \boldsymbol{n} \cdot \nabla \boldsymbol{v} \cdot \boldsymbol{n} \quad \text{where} \quad \kappa = \nabla \cdot \boldsymbol{n} \tag{4.5.75}$$

is the mean front curvature. The second and third terms describe the net effect of the (turbulent) diffusive processes (second term) and by outer straining of the flame by the surrounding flow field (third term). In detail, s^0 is the burning velocity of a plain, unstrained flame, $\mathcal{L}$ is an effective Markstein length, and κ is the local mean front curvature. As indicated in Figure 4.5.5.2- 2 the curvature is defined to be positive

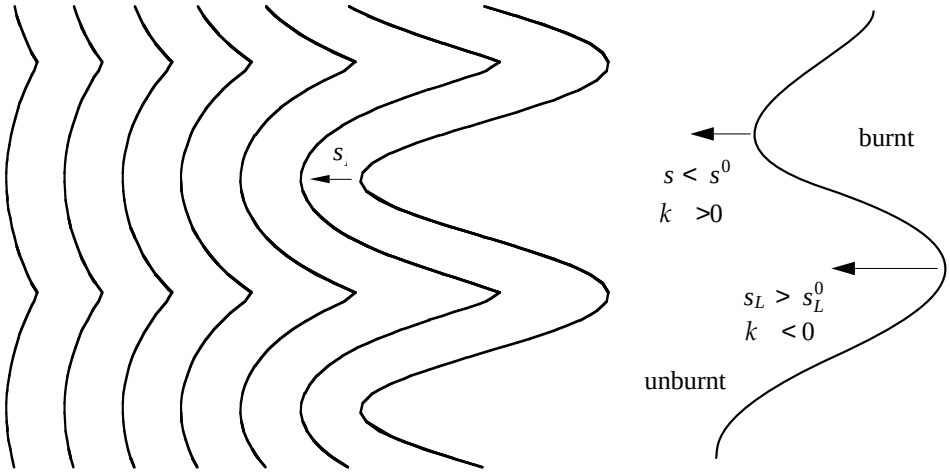

Figure 4.5.5.2- 2: Flame propagation according to Equation (4.5.73) for constant burning velocity s; schematic for the influence of curvature

when the front is convex with respect to the unburnt gas and vice versa. For positive Markstein numbers the curvature term thus prohibits the formation of sharp cusps on the flame front.

Determination of level sets away from the tracked front. There is one important issue that needs to be accounted for when dealing with "real" flames within which substantial chemical heat is released. The propagation Equation (4.5.73) is valid at the flame front only, since only at the front is the burning velocity s properly defined. Thus one needs to introduce additional constraints determining the time evolution of the scalar G away from the tracked interface. One option, proposed in Reference [4.62], is

to require the level set scalar to be a signed distance function away from the front. This is equivalent to requiring that

$$|\nabla G| = 1 \tag{4.5.76}$$

and the additional requirement that G be negative in the unburnt and positive in the burnt gas region. For a related numerical technique to enforce the distance function property, see Section 4.5.5.2.

Flame-flow coupling. Having adopted the level set approach to describe the evolution of the flame front geometry, one must next describe the mutual interactions between the tracked front and the surrounding flow. From Equation (4.5.70) and Equation (4.5.73) it is clear how the unburnt gas flow affects the flame motion: The flame propagation velocity consists of (i) passive advection by the unburnt gas velocity and (ii) of self-propagation induced by combustion. The unburnt gas conditions influence this latter part through explicit burning velocity laws as described in Section 4.5.4.

The front, in turn, influences the surrounding flow by enforcing the flame discontinuity jump conditions (Equation (4.5.55)) for the flow variables at the flame location $G(\boldsymbol{x}, t) = G_0$. Various methods have been developed in recent years to realize this coupling in the context of finite-volume methods, [4.53, 4.54, 4.99, 4.143 to 4.146]. These schemes mainly differ in their degree of complexity and detail and in their applicability to compressible and incompressible flows.

Chern and Colella [4.143], Bourlioux and Majda [4.144], and LeVeque and Shyue [4.145] consider compressible flows and treat the moving front surface as part of their time dependent numerical grid. For each of the subcells generated when a front intersects a grid-cell of the underlying computational mesh a complete conservative flux update is performed. The CFL-type time-step restrictions associated with updating small subcells are overcome by distributing excess accumulations of the conserved quantities among the neighbouring grid-cells. The schemes differ in how this is done in detail, but they all follow this common pattern.

The method described in Reference [4.53], which is also designed for compressible flows, compromises on the former schemes in that only *complete grid-cells* are updated by flux balances. The flame-generated subcells are used only in an "in-cell reconstruction step", which recovers burnt and unburnt gas conditions from the cell averages using a suitable set of recovery equations (see the appendix). The consequence is that, while the scheme *does* conserve mass, momentum, and energy between grid-cells and globally, it is *not* conservative with respect to these subcells. The method therefore does not automatically conserve mass, momentum, and energy between the pre- and post-front regions. For flame fronts, this just amounts to numerical truncation errors affecting the net burning rate and is not critical. However, in tracking a passive non-reactive fluid interface, such as the surface of a water droplet in air, this scheme would not conserve the droplet mass. An associated improvement is work in progress [4.98].

Terhoeven [4.146] and Klein [4.99], to our knowledge, are the first to propose a flame front tracking scheme for zero Mach number flows in the finite-volume context (see, however, also [4.147]). The key ideas are the same as those in Reference [4.53], but there are important modifications that become indispensable in the limit of small and zero Mach numbers. The key difficulty has been discussed earlier in Section 4.5.2. The second-order pressure p_2 in a low Mach number pressure expansion is responsible for flow accelerations. Within the flame discontinuity there is an order $O(1)$ density change and an associated flow acceleration. This can be accomplished only through a pressure discontinuity. The consequence is that the second-order pressure must satisfy a Poisson equation with a singular source term that ensures the appropriate pressure jump across the flame surface. For more detail the reader may wish

to consult the original references.

Fedkiw et al. [4.54] again consider compressibe flows, but go one step further in simplifying the approach. By compromising on conservation also for the complete "mixed cells", they are able to design a numerical method that is very attractive because of its simplicity and nearly dimension-independent formulation.

A sample result obtained using the capturing/tracking hybrid scheme from Reference [4.53] is described in Figs. 4.5.5.2- 3 and 4.5.5.2- 4. The RUT test h11 has been reproduced using a two-dimensional approximation, a standard $k-\epsilon$ turbulence model, and Damköhler's law to represent the effective turbulent burning velocity as

$$s_T = s_L + u' \qquad \text{where} \qquad u' = \sqrt{2k} \tag{4.5.77}$$

with k from the $k-\epsilon$ model data in the unburnt gas immediately in front of the flame. The coloured density contours show the propagation of the sharp flame surface in time, and the second figure shows a comparison of space-time diagrams of the flame tip location as taken from experiment and computation. It turns out that the initial phase is slightly misrepresented, in that the computed flame acceleration is too slow. Yet as soon as the first obstacle is reached, the experimental and computed flame locations agree convincingly well.

4.5.6 Numerical Issues of Stiff and Fast Chemistry

A typical chemical species balance equation reads

$$\frac{\partial \rho Y_i}{\partial t} + \nabla\cdot(\rho Y_i \boldsymbol{v}) + \nabla\cdot(\boldsymbol{j}_i) = -\rho \sum_{k=1}^{n_{\text{reac}}} a_i^k \omega_k(\boldsymbol{Y}, p, T)\,. \tag{4.5.78}$$

Here $\omega_k(\boldsymbol{Y}, p, T)$ is the reaction rate of the kth chemical reaction, and a_i^k is the stoichiometric coefficient of species i in the kth reaction. The standard form of the kth elementary reaction may read

$$\sum_{j=1}^{n_{\text{spec}}} a_j^{k,-} X^j \leftrightarrow \sum_{j=1}^{n_{\text{spec}}} a_j^{k,+} X^j \tag{4.5.79}$$

and then

$$a_j^k = a_j^{k,+} - a_j^{k,-}\,. \tag{4.5.80}$$

The classical Arrhenius law of mass action expressions for the reaction rate ω_k reads

$$\omega_k(\boldsymbol{Y}, p, T) = K_k^+ \, e^{-T_k^+/T} \prod_{j=1}^{n_{\text{spec}}} Y_j^{a_j^{k,+}} - K_k^- \, e^{-T_k^-/T} \prod_{j=1}^{n_{\text{spec}}} Y_j^{a_j^{k,-}} \tag{4.5.81}$$

The problems of "stiff, fast and complex" chemistry arise, because typically one has

$$K_k^+,\ K_k^-,\ n_{\text{spec}},\ n_{\text{reac}},\ \frac{T_k^+}{T_\infty},\ \frac{T_k^-}{T_\infty} \gg 1 \tag{4.5.82}$$

where T_∞ is a characteristic temperature in the system.

Although the requirements resulting from large numbers of species and reactions are more or less obvious (heavy computer time and memory demands), the issues of stiffness and rapidity of chemical reactions deserve an explanation.

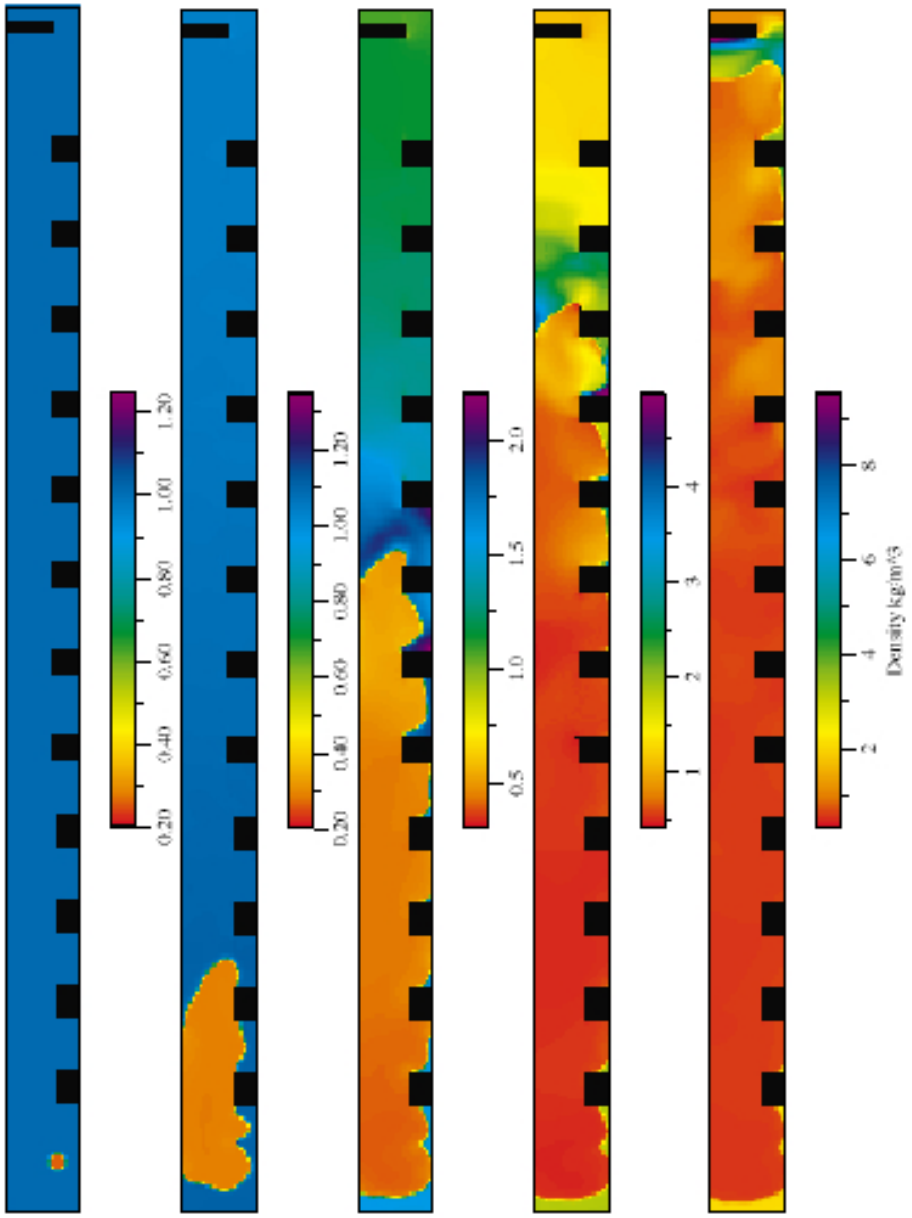

Figure 4.5.5.2- 3: Sequence of density contours as computed in a two-dimensional model for RUT test h11 using the flame front capturing/tracking hybrid scheme from Reference [4.53]

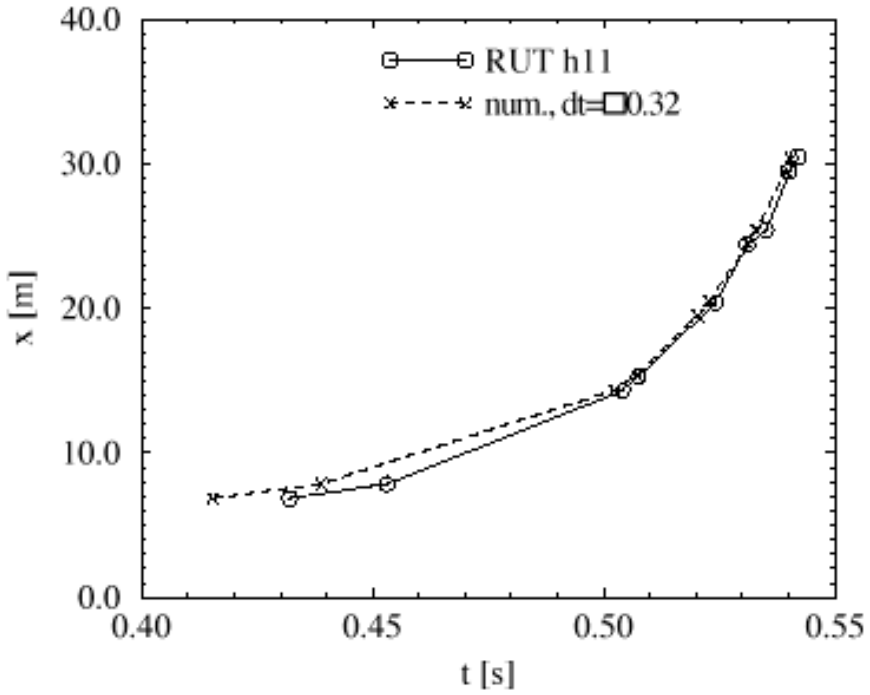

Figure 4.5.5.2- 4: Comparison of the time history of flame propagation in the test case from Figure 4.5.5.2- 3

4.5.6.1 Stiffness

For stiff reations, one or both of the reaction rate coefficients $K_k^{\pm} \exp(-T_k^{\pm}/T)$ is very large, much larger—in fact—than the inverse of a typical characteristic time of flow field evolution and of the actual time scale of reaction progress. As a consequence, the kth reaction must be in an approximate balance, with $|\omega_k| \ll K_k^{\pm} \exp(-T_k^{\pm}/T)$. Suppose now, that numerical approximation errors induce a perturbation of one of the species mass fractions $\delta Y_i \ll Y_i$. The resulting perturbation of the reaction rate is

$$\delta\omega_k = \left(K_k^+ \, e^{-T_k^+/T} \prod_{j \neq i} Y_j^{a_j^{k,+}} - K_k^- \, e^{-T_k^-/T} \prod_{j \neq i} Y_j^{a_j^{k,-}} \right) \delta Y_i \, . \tag{4.5.83}$$

One immediately finds that

$$\frac{\delta\omega_k}{\omega_k} \gg \frac{\delta Y_i}{Y_i} \tag{4.5.84}$$

indicating that minute errors in the species mass fractions induce large fluctuations of the reaction rates. Obviously, when the rate coefficients are sufficiently large, such perturbations lead to chemical kinetic responses with time scales that are orders of magnitude shorter than the actual characteristic chemical time scale of the exact solution. Extremely robust numerical integration schemes must be employed to handle this kind of situation without undue unstable numerical response.

However, even a robust, non-oscillatory numerical treatment is insufficient when the chemical species involved play a crucial role for the overall reaction progress. This is the case, for example, for chemical radicals such as the Hydrogen atom. These species are responsible for opening the reaction paths that

produce the major heat release in typical combustion systems. At the same time, they are extremely reactive, so that their consumption kinetics is extremely fast—in contrast to their production, which is typically much slower. The result is that radicals are consumed immediately whenever they are produced and that their mass fractions always remain very small. Since, on the other hand, they induce the primary breakup of the fuel species, it is adamant that their minute concentrations be computed very accurately. Hence robustness and accuracy are of equal importance and dynamically adaptive numerical techniques and error control must be invoked. The subtle numerical problems associated with stiff relaxation processes are discussed extensively in textbooks on the matter, such as Reference [4.148]. Most of these texts address systems of ordinary differential equations.

Obviously, the problem is aggravated when reaction processes in multi-dimensional flows are to be computed. We emphasize that the simple coupling of highly accurate stiff ODE solvers with standard multi-dimensional flow solvers through the popular operator splitting technique from Reference [4.149], will not automatically lead to a satisfactory solution. The sophisticated error control in the stiff ODE solvers will not indicate the additional errors induced by operator splitting between fluid mechanics and chemistry. Hence even though that approach will allow the construction of robust numerical methods, accuracy can be utterly corrupted.

We also emphasize that temporal and spatial adaptivity alone is insufficient when it is not combined with sophisticated refinement indicators that are based on fully multi-dimensional error control. Unfortunately, rigorously supported error estimators for large Reynolds number compressible and zero Mach number flows are work in progress at this time even for non-reactive flows [4.107, 4.108]!

4.5.6.2 Fast Chemistry

The physics associated with rapid heat release is distinguished here from the issues of stiff chemistry, even though they are closely related in that both are associated with short, chemistry-induced time scales. By the label "fast chemistry" we denote a situation where the actual time scale of chemical heat release whenever it occurs is much shorter than the characteristic time scales of the surrounding flow. Because of the tight coupling of chemical reaction progress and fluid mechanics through total energy conservation, fast chemical reactions are in all practical situations associated with the establishment of thin combustion zones. This statement holds for benign low Mach number diffusion flames (as on candles) as well as for the most violent combustion events, detonation waves. The combustion zones can be either thin laminar or quasi-laminar flames on the smallest scales or complete turbulent flame brushes when the overall length scale of the considered flow is sufficiently large. The latter is true, for example, for large-scale industrial devices.

In numerical simulations one is faced with the options of either developing sophisticated adaptive numerical techniques that allow one to resolve in detail the thin reaction fronts or to develop combined models and numerical schemes that handle these fronts as infinitily thin reactive surfaces. The former approach requires accurate modelling and numerical representation of all aero-thermodynamic processes that interact within the combustion zone. The advantage of that approach is, obviously, that each of these submechanisms can be accounted for and its effect assessed. The disadvavage is that in fact all the subprocesses *must* be represented properly to obtain acceptably accurate answers, (see also Section 4.5.4). The latter approach requires an accurate representation of the coupling between the reaction front and the surrounding flow and an equally accurate representation of the response of the reaction zone to fluid mechanical perturbations in the vicinity. The advantage of this approach is that it allows much coarser numerical resolution than the former and that it has fewer mechanisms to be modelled and computed,

such as flame speeds and effective jump conditions. The disadvantage is that effects on the length and time scale of the internal combustion zone structure are lost. (Compromises between both approaches are work that is in progress.)

Unless in a direct numerical simulation (DNS) of the compressible reactive Navier-Stokes equations all length and time scales are resolved, the effects of chemical kinetics enter in both approaches through suitable subgrid-scale turbulent combustion models. Notice that with the expected computational capacities for the next decade one cannot expect to resolve by DNS realistic scale turbulence combustion processes relevant to industrial safety problems. Hence the issue of an accurate integration of chemical species transport equations with detailed chemistry, as discussed in the previous subsection, becomes irrelevant. In fact, the turbulent combustion submodels most often have little in common with detailed chemical kinetics (see Section 4.3), so that the numerical algorithmic requirements are very different.

4.5.7 Computational Chemistry Reduction

The issues of stiffness and the overwhelming complexity of detailed chemical kinetics has fostered widespread interest in "reduced chemical kinetics" for decades [4.6, 4.90, 4.91]. Explicit analytical approaches that are based on asymptotic limit considerations have been discussed in Section 4.4.2 above. Here, we summarize a number of alternative techniques that are enjoying increasing popularity because of the fact that they are largely algorithmic and reduce the demand for chemical kinetics expertise that comes with the more traditional explicit reduction strategies.

4.5.7.1 Crucial observations

Consider a system of ordinary differential equations that might describe chemical reactions in a homogenous gaseous system,

$$\frac{d\boldsymbol{Y}}{dt} = \boldsymbol{R}(\boldsymbol{Y})\,. \tag{4.5.85}$$

The shortest time scales inherent in such a system can be assessed, on the one hand, by the inverse of the largest component of the rate vector $\boldsymbol{R} = \{R_i\}_{i=1}^n$, that is,

$$\tau_0 = \min_i \left(|R_i(\boldsymbol{Y})|\right)\,. \tag{4.5.86}$$

The crucial characteristic of stiff reaction systems, however, lies in the fact explained above, that there are hidden time scales much shorter than those visible in the actual evolution of the system and characterized by Equation (4.5.86). These inherent time scales can be assessed by considering the following transformations: The rate of change of the reaction rate vector $\boldsymbol{R}$ itself is governed by

$$\frac{d\boldsymbol{R}}{dt} = \left(\frac{\partial \boldsymbol{R}}{\partial \boldsymbol{Y}}\right)^T \cdot \frac{d\boldsymbol{Y}}{dt} = \boldsymbol{J}^T \cdot \boldsymbol{R}\,, \tag{4.5.87}$$

where $\boldsymbol{J} = \{J_{i,j}\}_{i,j=1}^n = \{\partial R_i/\partial Y_j\}_{i,j=1}^n$ is the Jacobian of the rate vector. A straightforward perturbation analysis shows that the same equation is also satisfied by perturbations $\delta\boldsymbol{Y}$ of the solution $\boldsymbol{Y}(t)$, that is,

$$\frac{d\delta\boldsymbol{Y}}{dt} = \left(\frac{\partial \boldsymbol{R}}{\partial \boldsymbol{Y}}\right)^T \cdot \delta\boldsymbol{Y} = \boldsymbol{J}^T \cdot \delta\boldsymbol{Y}\,. \tag{4.5.88}$$

Consider next an eigenvalue decomposition of the Jacobian $\boldsymbol{J}$ of the form

$$\boldsymbol{J} = \sum_{j=1}^{n} \lambda_j \boldsymbol{r}_j \circ \boldsymbol{\ell}^j \,, \tag{4.5.89}$$

where λ_j is the jth eigenvalue of the Jacobian, and $\boldsymbol{r}_j, \boldsymbol{\ell}^j$ are the associated right and left eigenvectors, respectively. (To streamline the discussion we do not address complications that may arise for incomplete sets of eigenvectors, multiple eigenvalues etc.)

Let the eigenvalues be ordered in an increasing sequence, so that

$$\lambda_1 < \lambda_2 < \ldots < \lambda_{j_0} < 0 < \lambda_{j_0+1} < \ldots < \lambda_n \tag{4.5.90}$$

Typical stiff behaviour arises when the first few eigenvalues are very large by modulus, that is, when

$$|\lambda_1|, |\lambda_2| < \ldots \gg 1 \,. \tag{4.5.91}$$

A decomposition of $\delta\boldsymbol{Y}$ with respect to the eigenvectors $\boldsymbol{r}_j$ according to

$$\delta\boldsymbol{Y} = \sum_{j=1}^{n} \phi^j(t) \boldsymbol{r}_j \tag{4.5.92}$$

with the $\boldsymbol{r}_j$ essentially frozen on the short relaxation time scales associated with λ_j yields

$$\frac{d\phi_j}{dt} = -\lambda_j \phi_j(t) \,. \tag{4.5.93}$$

This equation indicates, in an asymptotic sense for large $|\lambda_j|$, a rapid exponential decay of the solution component in the direction of the jth right eigenvector.

These relaxing degrees of freedom are unimportant because they will always merely drive the solution back onto submanifolds in state space where the related degree of freedom is relaxed out. This will be the case when ever the reaction vector $\boldsymbol{R}$ does not excite these fast relaxing modes; that is, when $\boldsymbol{R}$ has no component in the direction of the "fast" $\boldsymbol{r}_j$. This requirement can be cast into an algebraic constraint for the "slow" submanifolds in the space of $\boldsymbol{Y}$:

$$\boldsymbol{\ell}^j(\boldsymbol{Y}) \cdot \boldsymbol{R}(\boldsymbol{Y}) = 0 \qquad \text{for all } j \text{ satisfying } \lambda_j < 0 \text{ and } |\lambda_j| \gg 1 \,. \tag{4.5.94}$$

4.5.7.2 ILDMs – Intrinsic lower-dimensional manifolds

The idea in Reference [4.150] is to a priori constrain the state vector $\boldsymbol{Y}$ to submanifolds defined by Equation (4.5.94) or similar modified algebraic constraints. Since these algebraic relations depend only on the chemical rate funtion, they can be determined *before* an actual computation is started to solve the dynamical system (Equation (4.5.85)). The manifolds are actually tabulated and the chemistry is then treated in a computation by means of lookup tables rather than by actually solving the full ODE system. The approach has been validated extensively in References [4.150 to 4.152] and was shown to yield results that cover those from standard reduced chemical kinetics as discussed in Section 4.4.2. On the other hand, it can generate automatically different relevant subsystems that may emerge in different regimes of state space and that would require separately derived standard reduced schemes if one were to follow the explicit asymptotics-based approach.

A prominent example relevant to the present applications is the transition from auto-ignition to flame propagation chemistry. Auto-ignition mechanisms must include the details of radical production and thermal buildup, whereas the radicals in a propagating flame are supplied via molecular transport from the reaction zone. This elucidates that there can be crucial differences in the details of the effective reaction paths, depending on how the reaction system is coupled into a flow field.

A caveat is associated with the embedding of chemical reactions in a flow field. In this case, the governing equations for the species mass concentrations are not ordinary differential equations as in Equation (4.5.85), but full multi-dimensional transport equations

$$\frac{\partial \rho \boldsymbol{Y}}{\partial t} + \nabla\cdot(\rho \boldsymbol{Y} \boldsymbol{v}) + \nabla\cdot(\boldsymbol{j}) = \rho \boldsymbol{R}(\boldsymbol{Y}, p, T)\,. \tag{4.5.95}$$

Not only is this equation equipped with the transport terms resulting from convection and diffusion, but one also must include in $\boldsymbol{R}$ the dependence on two thermodynamic background variables, such as pressure and temperature. Although the key idea behind the ILDM approach is still valid, namely that one may expect the mass fraction vector to evolve in the immediate vicinity of the ILDMs, deviations occur because of these additional terms and they must be accounted for.

The conceptual problems to be overcome are that (i) the manifolds now depend on the thermodynamic backgound state and can thus vary with time and that (ii) the transport terms $\nabla\cdot(\rho \boldsymbol{Y} \boldsymbol{v}) + \nabla\cdot(\boldsymbol{j})$ will generally have components in the direction of the fast eigenvectors of $\boldsymbol{J}$. Even though strong efforts at overcoming these issues are on their way, application of the ILDM approach in dynamic reactive flow computations based on the standard conservation equations is by far not standard today. The approach has found considerably more resonance in the context of Monte Carlo PDF methods for turbulent combustion. As discussed in Section 4.3.7, the PDF is represented in a Monte Carlo simulation approximately by an ensemble of particles that undergo their individual histories. Part of that particle history, which is typically represented numerically by operator splitting, is the reaction progress according to an ODE as in Equation (4.5.85). In this case, one can take full advantage of the ILDM approach.

It should be mentioned that much of the development efforts for ILDM methods have gone into a quite technical issue that has little to do with the underlying fundamental and quite intriguing ideas: Organizing computationally efficient tabulation and lookup table procedures has proven to be more of an obstacle in the implementations that was probably expected originally. It turns out that quite sophisticated numerical techniques need to be invoked to really benefit from the advantages that the ILDM approach formally promises to offer.

4.5.7.3 CSP – Computational singular perturbations

The CSP approach [4.153, 4.154] aims at an algorithmic realization of concepts of asymptotic analysis. The key issues in simplifying complex chemical kinetics are

- to appropriately select relevant fast and slow time scales,
- to identify the characteristic dynamics associated with the fast scales, and
- to then pass to a limit where all the fast modes are relaxed and the overall evolution is governed by the slower time scales of interest only.

Consider again the evolution equation for the n-dimensional reaction rate vector $\boldsymbol{R}$ from Equation (4.5.87). Generally, one may turn this vector equation into a set of coupled scalar amplitude equations by decomposing $\boldsymbol{R}$ w.r.t. some basis $\{\boldsymbol{a}_i\}_{i=1}^n$:

$$\boldsymbol{R}(t) = \sum_{i=1}^{n} f^i(t)\, \boldsymbol{a}_i(t)\,. \tag{4.5.96}$$

For future reference, we introduce the dual basis $\{\boldsymbol{b}^i\}_{i=1}^n$ by

$$\boldsymbol{b}^i \cdot \boldsymbol{a}_j = \delta^i_j\,. \tag{4.5.97}$$

We left-multiply Equation (4.5.87) by $\boldsymbol{b}^i$ to obtain

$$\frac{df^i}{dt} + \sum_{j=1}^{n} f^j \left(\boldsymbol{b}^i \cdot \frac{d\boldsymbol{a}_j}{dt}\right) = \sum_{j=1}^{n} f^j \left(\boldsymbol{b}^i \cdot \boldsymbol{J} \cdot \boldsymbol{a}_j\right)\,. \tag{4.5.98}$$

In a more compact notation we have

$$\frac{df^i}{dt} = \sum_{j=1}^{n} f^j\, \Lambda^i_j\,, \tag{4.5.99}$$

where

$$\Lambda^i_j(t) = \boldsymbol{b}^i(t) \cdot \left(-\frac{d\boldsymbol{a}_j}{dt} + \boldsymbol{J}(t) \cdot \boldsymbol{a}_j(t)\right)\,. \tag{4.5.100}$$

If the considered system was linear, one could diagonalize the matrix $\{\Lambda^i_j\}$ and then solve n decoupled linear first-order equations exactly. The largest eigenvalues of the matrix (by modulus) would indicate the "fast modes", and the associated solution components would decay most rapidly if these eigenvalues were negative.

Chemical kinetics equations are generally highly non-linear and such an exact decoupling will not occur. However, one may seek to achieve at least an approximate decoupling of fast and slow motions in state space by choosing basis vectors $\{\boldsymbol{a}_i\}_{i=1}^n$ that lead to an approximately block-diagonal structure of $\{\Lambda^i_j\}$. An algorithmic procedure is proposed in References [4.153,4.154] that allows an iterative improvement of the underlying basis in state space in that the coupling between fast and slow subspaces decreases as ϵ^j, where ϵ is the time scale separation between the "current active time scale" (the fastest of the slow modes) and the slowest of the fast modes and j is the iteration index.

The CSP approach is intriguing in that it allows one, but does not require, to construct a simplified limit system with fewer degrees of freedom similar to the ILDM system. One can as well use the subdivision in state space into fast and slow modes in order to resolve numerically all the scales, but to apply specialized numerical techniques to the fast and slow subdynamics.

4.6 Summary

This chapter has compiled the state of the art in both the modelling and numerical simulation of FA and the transition to detonation. Summaries have been provided of main-stream and advanced models for flow turbulence, turbulent combustion, and for the efficient representation of chemical kinetics. Numerical methods for flow field simulations have been discussed with an emphasis on the present topic of FA and DDT.

4.6.1 Industry-level Modelling versus Current State of Research

In discussing computational modelling, one must distinguish between the needs of everyday engineering and scientific efforts at exploring the fundamental processes of a given phenomenon. Typically, engineering assessments require mainly an upper limit of potential loads, which then serve as the basis for the design of safety measures. Unfortunately, when dealing with combustion in large-scale systems and with a wide range of possible scenarios regarding gas composition and distribution, the potential upper load limits are subject to considerable statistical variation. As a consequence, simplified assessment tools can lead to either unacceptable conservatism or unacceptable uncertainties. Hence the demand for improved insight into the fundamental mechanisms of FA and DDT and the efforts at developing detailed numerical prediction tools as described in this chapter. (Simplified models of reduced complexity that can be used in routine engineering applications will be discussed in the next chapter.)

4.6.2 Adequate Levels of Modelling Detail and Numerical Resolution

Because of the complexity of the phenomena involved in FA and DDT, such as flow turbulence, chemical kinetic effects, multiple length scales, flame-acoustic interactions etc., various levels of modelling detail must be distinguished.

At the coarsest level, there are the lumped-parameter models, to be discussed shortly, which decompose a system into a finite, relatively small number of compartments. Conservation of mass and energy is formulated for these systems of interconnected subvolumes, and overall estimates of global pressures and average temperatures are obtained. Naturally, these models do not resolve the underlying reacting flow fields. In other words, the balance of momentum is not considered in detail. Also, it is not possible—except through qualitative parametrizations—to incorporate the effects of local events that may lead to sizeable global effects.

The interaction between energy and momentum becomes important for high-speed combustion, such as high-speed turbulent deflagrations and detonations. Here, a large percentage of the combustion energy release is converted to kinetic energy. It has been shown, for example, in Reference [4.155] that the resulting pressure pulses may lead to effective pressure loads that by far excede those expected from quasi-static (lumped-parameter) estimates. The next level of computational and modelling complexity thus involves simulation tools that allow the representation of global unsteady but statistically averaged flow fields and large-scale pressure waves. These simulation tools typically rely on coarse-grained computational meshes with grid sizes comparable to the integral scales of turbulence. Such codes are able to provide estimates for the influence of momentum exchanges and, in particular, allow a much improved assessment of potential structural loads that are due to high-speed combustion events.

These statistically averaged models include mean combustion rate models that are suitable to describe a well-established and relatively stable reaction progress. They also do allow the modelling of bulk effects of chemical kinetics, such as transitions between different regimes of turbulent combustion depending on whether chemical time scales are much shorter, comparable to, or longer than the characteristic time scales of turbulence. However, this kind of approach still misses out on those events that are triggered by localized processes but then develop into global combustion events. Unfortunately, some of the most dangerous mechanisms of deflagration-to-detonation transition are of that type: Local sequential or hot spot ignition may trigger the onset of detonation through gas-dynamic-reactive resonances, but the triggering event itself is a highly stochastic, localized, and rare event. Reliable modelling of this kind of process is not possible on the basis of standard statistical models of turbulence and turbulent combustion.

One rather needs sophisticated dynamic mesh refinement and models suitable to represent the smallest flow scales. A promising compromise between fully resolved DNS based on the reactive Navier-Stokes equations and statistical turbulence models is large eddy simulation.

Table 4.6.2-1 summarizes the orders of magnitude of the smallest length scales to be resolved in a typical nuclear reactor safety application under these different modelling paradigms.

Table 4.6.2-1: Rough estimate of resolution requirements as a function of modelling detail

Model Class	Smallest Scale	Resolved Processes
Lumped-Parameter Models	> 1 m	Large-scale-averaged (quasi-) thermodynamic balances
Statistical Turbulence Models	$0.1 \ldots 1$ m	Averaged flow quantities, *including* momentum balances *excluding* localized, rare events
Large Eddy Simulation (LES)	$0.01 \ldots 0.1$ m	Non-linear unsteady motions, *including* large-scale turbulence *excluding* disspation scales combustion scales localized, rare events
Direct Numerical Simulation (DNS)	$10^{-5} \ldots 10^{-2}$ m	All processes and full range of scales of underlying continuum model

4.6.2.1 Under-resolved computations

The estimates in Table 4.6.2-1 demonstrate that the interplay of various physical mechanisms typically occurs over a range of characteristic length (and time) scales. The non-linearity of the underlying governing equations dictates that processes occuring on different scales interact in a non-negligible fashion. As a consequence, any numerical computation that does not resolve all the length scales described by its model equations is generally bound to produce uncontrolled errors because it neglects the interactions on and with the small, unresolved scales. In particular, a DNS based on the reactive Navier-Stokes equations cannot be expected to correctly represent the evolution of a combustion process if the smallest flow and chemical reaction scales are not properly resolved. (As a rule of thumb, the grid Reynolds number, $\mathrm{Re}_{\mathrm{gr}} = u_{\mathrm{ref}}\Delta/\nu$, with Δ the computational grid size, should be or order unity or less.

Computations that do not satisfy this kind of criterion might, under special circumstances regarding initial and boundary data, yield valuable insight. But they should be interpreted with extreme care and should not be accepted as DNS in the original sense of the term.

4.6.3 Reproducibility and Predictability

The interpretation of the results of computational modelling must take into account the statistical nature of the processes modelled. It may be found found, for example, from the experiments to be reported in Chapter 5 that some experimental set-ups and combustible mixtures lead to very reproducible high-speed combustion events, whereas more marginal mixtures and only slightly obstacle-loaded configurations tend to produce large fluctuations in terms of the resulting overall flow fields. Importantly, there is, at

best, a weak correlation between the violence of an event and its marginality.

As one tries to narrow down the boundaries of existence of detonation and high-speed deflagration one must deal with increasingly marginal mixtures. Predictive modelling then requires a drastically increased amount of detail as well as the recognition of the very different statistical nature of turbulent combustion in these regimes. Among, say, 100 benign cases of combustion there may still be a few cases where transition to detonation occurs and effective structural loads are an order of magnitude larger than the average ones. We are not aware of a reliable modelling approach that would allow incorporation of such rare but important events and would still be comparable in complexity with standard statistical models of turbulence and turbulent combustion. Hence there is a demand for sophisticated DNS and LES tools.

4.6.4 Complex Geometries and Scaling

There is currently a principal difficulty in the context of model validation that is related to the scaling issues discussed in Section 4.5.1.1. None of the existing subgrid-scale turbulence closures is rigorously derived from first principles, i.e., from the original governing equations. One may thus expect that the similarity laws associated with the non-dimensional characteristic quantities, such as the Reynolds, Peclet, Mach, Froude, and Damköhler numbers will generally not be perfectly satisfied by the resulting effective models. As a consequence, one finds that application of one and the same model to geometrically similar but differently sized systems requires adjustment of a number of free modelling parameters. This is a highly non-negligible issue in nuclear reactor safety, because there are only very experimental set-ups of a geometrical size comparable to a real reactor containment.

The upscaling or downscaling of computational results therefore must be considered an unresolved question to this date. The availability of experimental results for geometrically exactly similar, but resized set-ups would be of outmost value for model validation.

There is another more subtle issue related to this same problem area: One typical and important way of validating a numerical flow solver is to perform convergence studies with respect to grid refinement. One considers one and the same physical situation and increases the numerical resolution (= decreases the mesh size) in a sequence of computations. Ideally, the results obtained should converge to the same limiting fields at a rate that depends on the order of accuracy of the numerical discretizations employed. Consider now a full-fledged simulation of a nuclear reactor containment. Such a simulation will typically include subgrid-scale models for small-scale obstacles and solid structures, as described in Section 4.2.5. Now, upon grid refinement the size of the smallest resolvable obstacle decreases in proportion with the mesh size. As a consequence, the underlying continuum problem that one is trying to solve changes, and the notion of "convergence" must be reconsidered.

In fact, there are at least two principally different interpretations of convergence:

- Convergence in a practical sense would postulate that the subgrid-scale models be applied only to the unresolved scales on any given grid. A convergence criterion would then require that the results of a fine-mesh computation, when restricted to the former coarse-grid, yield the same grid cell averages as did the coarse grid computations. Notice, however, that under this strategy more and more of the small-scale geometrical features of obstacles becomes resolved on the grid—the smallest resolved features corresponding to a fixed number of grid cells. Numerical truncation errors on the small-scale level will then not decrease with grid refinement and convergence in the

sense of numerical analysis is not achieved.

- A sound convergence study in the sense of numerical analysis would, in contrast, fix the continuum problem to be solved and then study the solution behaviour as the grid is refined. In particular, it would be decided once and for all of the compared computations which obstacles would be resolved and which ones be represented only by subgrid-scale models. This classification would not change with grid refinement. This latter approach is somewhat counter-intuititive and not widely used, but it is the only approach allowing one to verify that numerical truncation errors diminish with grid refinement.

4.7 References

[4.1] K. N. C. Bray, Challenges in Turbulent Combustion. In *Introduction to Turbulent Combustion*. (L. Vervisch, D. Veynante and D. Olivari, (editors)). The von Karman Institute, Rhode St. Genése, Belgium, 1999.

[4.2] A.N. Kolmogorov, Local Structure of Turbulence in Incompressible Viscous Fluids for Very Large Reynolds Number. Dol. Akad. Nauk SSSR, Vol. 30, 1941, 299–303.

[4.3] A.N. Kolmogorov, Equations of Turbulent Motion of an Incompressible Fluid. Izvestia Academy of Sciences, USSR; Physics, Vol. 6, 1942, 56–58.

[4.4] O. Reynolds, On the Dynamical Theory of Incompressible Viscous Fluids and the Determination of the Criterion. Philosophical Transactions of the Royal Society of London, Vol. A186, 1895, 123 ff.

[4.5] D. C. Wilcox, *Turbulence Modelling for CFD.* DCW Industries, Inc., La Canada, CA, second edition, 1998.

[4.6] F. A. Williams, *Combustion Theory.* Addison-Wesley Publishing Company, Menlo Park, CA, USA, second edition, 1985.

[4.7] B. S. Baldwin and H. Lomax, Thin-Layer Approximation and Algebraic Model for Separated Turbulent Flows. AIAA paper, 78-257, 1978.

[4.8] P. G. Saffman, A Model for Inhomogeneous Turbulent Flow. Proceedings of the Royal Society of London, Vol. A317, 1970, 417–433.

[4.9] B. E. Launder and D. B. Spalding, *Mathematical Models of Turbulence.* Academic Press, New York, NY, USA, 1972.

[4.10] C. G. Speziale, R. Abid and Anderson E. C., A Critical Evaluation of Turbulence Models for Near-Wall Turbulence. AIAA paper, 90-1481, 1990.

[4.11] B. R. Smith, The k-$k\ell$ Turbulence and Wall Layer Model for Compressible Flows. AIAA paper, 90-1483, 1990.

[4.12] B. R. Smith, A Near Wall Model for the k-ℓ Two Equation Turbulence Model. AIAA paper, 94-2386, 1994.

[4.13] W. P. Jones and B. E. Launder, The Prediction of Laminarization with a Two-Equation Model of Turbulence. International Journal for Heat and Mass Transfer, Vol. 15, 1972, 301–314.

[4.14] O. Zeman, Dilatational Dissipation: The Concept and Application in Modelling Compressible Mixing Layers. Physics of Fluids, Vol. A 2, 1990, 178–188.

[4.15] S. Sarkar, The Pressure-Dilatation Correlation in Compressible Flows. Physics of Fluids, Vol. A 4, 1992, 2674–2682.

[4.16] D. C. Wilcox, Dilatational Dissipation Corrections for Advanced Turbulence Models. AIAA Journal, Vol. 30, 1992, 2639–2646.

[4.17] B. E. Launder, G. J. Reece and W. Rodi, Progress in the Development of a Reynolds Stress Closure. Journal of Fluid Mechanics, Vol. 68, 1975, 537–566.

[4.18] B. E. Launder, (editor), *5th Biennial Colloquium on Computational Fluid Dynamics*. Manchester Insitute of Science and Technology, Manchester, UK, 1992.

[4.19] D. C. Wilcox and M. W. Rubesin, Progress in Turbulence Modelling for Complex Flow Fields Including Effects of Compressibility. NASA Tech. Rep., Vol. TP-1517, 1980.

[4.20] D. C. Wilcox, Multiscale Model for Turbulent Flows. AIAA Journal, Vol. 26, 1988, 1311–1320.

[4.21] M. Oberlack, Closure of the Dissipation Tensor and the Pressure–Strain Tensor Based on the Two-Point Correlation Equation. In *Turbulent Shear Flows 9*. (F. Durst, N. Kasagi, B. E. Launder, F. W. Schmidt, K. Suzuki and J. H. Whitelaw, (editors)). Springer, 1993.

[4.22] M. Oberlack and N. Peters, Closure of the Two-Point Correlation Equation in Physical Space as a Basis for Reynolds Stress Models. In *Near-Wall Turbulent Flows*. (R. M. C. So, C. G. Speziale and B. E. Launder, (editors)). Elsevier, 1993.

[4.23] M. Oberlack, Non-Isotropic Dissipation in Non-Homogeneous Turbulence. Journal of Fluid Mechanics, Vol. 350, 1997, 351–374.

[4.24] J. C. Rotta, *Turbulente Strömungen [Turbulent Flows]*. Teubner, Stuttgart, 1972.

[4.25] J. H. Ferziger, Large Eddy Simulations of Turbulent Flows. AIAA paper, 78-347, 1978.

[4.26] J. Smagorinsky, General Circulation Experiments with the Primitive Equations I: The Basic Experiment. Monthly Weather Review, Vol. 91, 1963, 99–164.

[4.27] M. Germano, U. Piomelli, P. Moin and W. Cabot, A Dynamic Subgrid Scale Large Eddy Viscosity Model. Physics of Fluids, Vol. A3, 1991, 1760 ff.

[4.28] J. H. Ferziger, Recent Advances in Large Eddy Simulation. In *Engineering Turbulence Modelling and Experiments 3*. (W. Rodi and G. Begeles, (editors)). Elsevier, New York, 1996, 163 ff.

[4.29] M. Lesieur and O. Metais, New Trends in Large Eddy Simulations of Turbulence. Annual Review of Fluid Mechanics, Vol. 28, 1996, 45 ff.

[4.30] W. Rodi, Comparison of LES and RANS Calculations of the Flow Around Bluff Bodies. Journal of Wind Engineering and Industrial Aerodynamics, Vol. 69-71, 1997, 55–75.

[4.31] W. Rodi, Large Eddy Simulation of the Flow Around Bluff Bodies – State of the Art. International Journal of the Japan Society of Mechanical Engineering, Vol. B41(2), 1998, 432–454.

[4.32] D. K. Lilly, On the Application of Eddy Viscosity Concept in the Intertial Subrange of Turbulence. National Center for Atmospheric Research, Boulder, CO, USA, Manuscript 123, 1966.

[4.33] J. W. Deardorff, The Use of Subgrid Turbulent Transport in a Three-Dimensional Model of Atmospheric Turbulence. ASME Journal of Fluids Engineering, Vol. 95, 1973, 429–438.

[4.34] J. Bardina, J. H. Ferziger and W. C. Reynolds, Improved Turbulence Models Based on Large Eddy Simulation of Homogeneous Incompressible Turbulent Flows. Stanford University, Department of Engineering Report TF-19, 1983.

[4.35] C. Meneveau, T. S. Lund and W. Cabot, A Lagrangian Dynamic Subgrid Scale Model of Turbulence. Journal of Fluid Mechanics, Vol. 319, 1996, 353–385.

[4.36] D. C. Haworth and K. Jansen, Large Eddy Simulation on Unstructured Deforming Meshes: Towards Reciprocating IC Engines. Computers and Fluids, Vol. to appear, 1999.

[4.37] D. C. Haworth, Turbulent Combustion Modelling and Applicatoins. In *Introduction to Turbulent Combustion*. (L. Vervisch, D. Veynante and D. Olivari, (editors)). The von Karman Institute, Rhode St. Genése, Belgium, 1999.

[4.38] J. Jimenez, On Why Dynamics Subgrid Scale Models Work. CTR Annual Research Briefs, Stanford University, Center for Turbulence Research, 1995.

[4.39] N. R. Popat, C. A. Catlin, B. J. Arntzen, R. P. Lindstedt, B. H. Hjertager, T. Solberg, O. Saeter and H. Van den Berg, Investigations to Improve and Assess the Accuracy of Computational Fluid Dynamic Based Explosion Models. Journal of Hazardous Materials, Vol. 45, 1996, 1–25.

[4.40] W. T. Sha, C. I. Yang, T. T. Kao and S. M. Cho, Multidimensional Numerical Modeling of Heat Exchangers. Journal of Heat Transfer, Vol. 104, 1982, 417–425.

[4.41] S. V. Patankar and D. B. Spalding, A Calculation Procedure for the Transient and Steady Behaviour of Shell-and-Tube Heat Exchangers. In *Heat Exchangers: Design and Theory Source Book*. (N.H Afgan and E.V. Schlunder, (editors)). McGraw-Hill, 1974, 155–176.

[4.42] N. Peters, Laminar Flamelet Concepts in Turbulent Combustion. In *21st Symposium (International) on Combustion*. The Combustion Institute, Pittsburgh, PA, USA, 1986, 1231–1250.

[4.43] N. Peters, The Turbulent Burning Velocity for Large Scale and Small Scale Turbulence. Journal of Fluid Mechanics, Vol. 384, 1999, 107–132.

[4.44] A. Majda and J. Sethian, The Derivation and Numerical Solution of the Equations for Zero Mach Number Combustion. Combustion Science and Technology, Vol. 42, 1985, 185–205.

[4.45] N. Peters, A Spectral Closure for Premixed Turbulent Combustion in the Flamelet Regime. Journal of Fluid Mechanics, Vol. 242, 1992, 611–629.

[4.46] L. Vervisch and D. Veynante, Turbulent Combustion Modelling. In *Introduction to Turbulent Combustion*. (L. Vervisch, D. Veynante and D. Olivari, (editors)). The von Karman Institute, Rhode St. Genése, Belgium, 1999.

[4.47] K. N. C. Bray and N. Peters, Laminar Flamelets in Turbulent Flames. In *Turbulent Reacting Flows*. (F. A. Williams and P. A. Libby, (editors)). Academic Press, London, 1994, 63–113.

[4.48] B. H. Hjertager, Simulation of Transient Compressible Turbulent Reactive Flows. Combustion Science and Technology, Vol. 27, 1982, 159 ff.

[4.49] K. N. C. Bray, J. Moss and P. A. Libby, Turbulent Transport in Premixed Turbulent Flames. In *Convective Transport and Instability Phenomena*. (J. Zierep and H. Oertel, (editors)). University of Karlsruhe, Karlsruhe, Germany, 1982.

[4.50] K. N. C. Bray, M. Champion and P. A. Libby, The Interaction between Turbulence and Chemistry in Premixed Turbulent Flames. In *Turbulent Reacting Flows*. (R. Borghi and S. Murphy, (editors)), Lecture Notes in Engineering, Vol. 40. Springer, Heidelberg, 1989.

[4.51] A. Kotchourko, W. Breitung, A. Veser and S. Dorofeev, Tube Experiments and Numerical Simulation on Tuburlent Hydrogen-Air Combuston. In *21st International Symposium on Shockwaves*, Australia, July 1997.

[4.52] W. Breitung, A. Kotchourko, A. Veser and W. Scholtyssek, Reactive Flow Simulation in Complex 3D Geometries using the COM3D Code. In *Severe Accident Research*, Japan. Nov., 1998.

[4.53] V. Smiljanovski, V. Moser and R. Klein, A Capturing-Tracking Hybrid Scheme for Deflagration Discontinuities. Journal of Combustion Theory and Modelling, Vol. 2(1), 1997, 183–215.

[4.54] R. P. Fedkiw, T. Aslam and S. Xu, The Ghost Fluid Method for Deflagration and Detonation Discontinuities. Journal of Computational Physics, Vol. xx, 1999, to appear.

[4.55] A. J. Chorin, Flame Advection and Propagation Algorithms. Journal of Computational Physics, Vol. 35, 1980, 1–11.

[4.56] Z. H. Teng, A. J. Chorin and T. P. Liu, Riemann Problems for Reacting Gas, with Application to Transition. SIAM Journal of Applied Mathematics, Vol. 42(5), 1982.

[4.57] G. Damköhler, Der Einfluss der Turbulenz auf die Flammengeschwindigkeit in Gasgemischen [The Influence of Turbulence on Flame Velocities in Gas Mixtures]. Zeitschrift für Elektochemie und angewandte Physikalische Chemie, Vol. 46, 1940, 601–626.
See also NACA Technical Memorandum 1112, 1947.

[4.58] V. Moser, *Simulation der Explosion magerer Wasserstoff-Luft-Gemische in großskaligen Geometrien [Explosion Simulation for Lean Hydrogen-Air Mixtures in Large Scale Geometries]*. PhD thesis, RWTH Aachen, 1997.

[4.59] D. Spalding, Mixing and Chemical Reaction in Steady Confined Turbulent Flames. In *13th Symposium (International) on Combustion*. The Combustion Institute, Pittsburgh, PA, USA, 1971, 649–657.

[4.60] B. F. Magnussen and B. H. Hjertager, On Mathematical Modelling of Turbulent Combustion with Special Emphasis on Soot Formation and Combustion. In *16th Symposium (International) on Combustion*. The Combustion Institute, Pittsburgh, PA, USA, 1976, 719–729.

[4.61] V. Yakhot, Propagation Velocity of Premixed Turbulent Flames. Combustion Science and Technology, Vol. 60, 1988, 191–214.

[4.62] M. Sussman, P. Smereka and S. Osher, A Level Set Approach for Computing Solutions to Incompressible Two-Phase Flow. Journal of Computational Physics, Vol. 114, 1994, 146–159.

[4.63] F. Gouldin, An Application of Fractals to Modelling Premixed Turbulent Flames. Combustion and Flame, Vol. 68, 1987, 249 ff.

[4.64] L. Vervisch, E. Bidaux, K. N. C. Bray and W. Kollmann, Surface Density Functions in Premixed Turbulent Combustion Modeling; Similarities Between the Probability Density Function and Flame Surface Density Approaches. Physics of Fluids, Vol. A 7, 1995, 2496–2503.

[4.65] L. Vervisch W. Kollmann and K. N. C. Bray, Dynamics of Iso-Concentration Surfaces in Premixed Turbulent Flames. 10th Symposium on Turbulent Shear Flows, Vol. 10, 1995.

[4.66] R. S. Cant, S. Pope and K. N. C. Bray, Modelling of Flamelet Surface to Volume Ratio in Turbulent Premixed Combustion. In *23th Symposium (International) on Combustion.* The Combustion Institute, Pittsburgh, PA, USA, 1990, 809–815.

[4.67] S. Candel and T. Poinsot, Flame Stretch and the Balance Equation for the Flame Area. Combustion Science and Technology, Vol. 70, 1990, 1–15.

[4.68] C. Meneveau and T. Poinsot, Stretching and Quenching of Flamelets in Premixed Turbulent Combustion. Combustion and Flame, Vol. 86, 1991, 311–332.

[4.69] W. Cheng and J. Diringer, Numerical Modelling of SI-Engine Combustion with a Flame Sheet Model. SAE paper 910268, 1991.

[4.70] T. Mantel and R. Borghi, A New Model of Premixed Wrinkled Flame Propagation Based on a Scalar Dissipation Equation. Combustion and Flame, Vol. 96, 1994, 443 ff.

[4.71] A. Trouvé and T. Poinsot, The Evolution Equation for the Flame Surface Density. Journal of Fluid Mechanics, Vol. 278, 1994, 1–31.

[4.72] D. Veynante, J. Piana, J. Duclos and C. Martel, Experimental Analysis of a Flame Surface Density Model for Premixed Turbulent Combustion. In *26th Symposium (International) on Combustion.* The Combustion Institute, Pittsburgh, PA, USA, 1996, 413–420.

[4.73] K. N. C. Bray, The Challenge of Turbulent Combustion. In *26th Symposium (International) on Combustion.* The Combustion Institute, Pittsburgh, PA, USA, 1996, 413–420.

[4.74] D. Veynante, A. Trouvé, K. N. C. Bray and T. Mantel, Gradient and Countergradient Scalar Transport in Turbulent Premixed Flames. Journal of Fluid Mechanics, Vol. 332, 1997, 263–293.

[4.75] C. J. Rutland and A. Trouvé, Direct Simulations of Premixed Turbulent Flames with Non-unity Lewis Numbers. Combustion and Flame, Vol. 94, 1993, 41–57.

[4.76] A. Trouvé, D. Veynante, K. N. C. Bray and T. Mantel, The Coupling Between Flame Surface Dynamics and Species Mass Conservation in Premixed Turbulent Combustion. In *Summer Program of the Center of Turbulence Research.* (P. Moin, J. H. Ferziger and W. C. Reynolds, (editors)). Center for Turbulence Research, Stanford University, Stanford, CA, USA, 1994.

[4.77] P. A. Libby and F.A. Williams, *Turbulent Reacting Flows.* Academic Press, London, UK, 1994.

[4.78] T. Poinsot, T. Echekki and M. Mungal, A Study of the Laminar Flame Tip and Implications for Premixed Turbulent Combustion. Combustion Science and Technology, Vol. 81, 1994, 45 ff.

[4.79] R. W. Bilger, The Structure of Turbulent Non-Premixed Flames. In *22nd Symposium (International) on Combustion.* The Combustion Institute, Pittsburgh, PA, USA, 1988.

[4.80] R. W. Bilger, Turbulent Diffusion Flames. Annual Review of Fluid Mechanics, Vol. 21, 1989, 101–135.

[4.81] R. W. Bilger, Conditional Moment Closure for Turbulent Reacting Flows. Physics of Fluids, Vol. 5, 1993, 327–334.

[4.82] R. W. Bilger and N. Peters, Comment and Reply on the "Assessment of Combustion and Submodels for Turbulent Nonpremixed Hydrocarbon Flames" by N. Swaminathan and R. W. Bilger. Combustion and Flame, Vol. 116, 1999, 677 ff.

[4.83] S. B. Pope, PDF Method for Turblent Reacting Flows. Progress in Energy and Combustion Science, Vol. 11, 1985, 119–195.

[4.84] C. Dopazo, Recent Developments in pdf Methods. In *Turbulent Reacting Flows*. (P. A. Libby and F. A. Williams, (editors)). Academic Press, London, 1994, 375–474.

[4.85] M. S. Anand and S. B. Pope, Calculations of Premixed Turbulent Flames by pdf Methods. Combustion and Flame, Vol. 67, 1987, 127ff.

[4.86] T. Butler and P. O'Rourke, A Numerical Method for Two-Dimensional Unsteady Reacting Flows. In *16th Symposium (International) on Combustion*. The Combustion Institute, Pittsburgh, PA, USA, 1977, 103–1515.

[4.87] A. Bourlioux, V. Moser and R. Klein, Large Eddy Simulation of Turbulent Premixed Flames Using a Capturing/Tracking Hybrid Approach. presented at 6th Intl. Conf. on Numerical Combustion, New Orleans, Louisiana, USA, 1996.

[4.88] S. Menon, Large Eddy Simulation of Combustion Instabilities. presented at 6th Intl. Conf. on Numerical Combustion, New Orleans, Louisiana, USA, 1996.

[4.89] M. Boger, D. Veynante and A. Trouvé, Direct Numerical Simulation Analysis of Flame Surface Density Concept for Large Eddy Simulation of Turbulent Premixed Combustion. In *27th Symposium (International) on Combustion*. The Combustion Institute, Pittsburgh, PA, USA, 1998.

[4.90] N. Peters, Systematic Reduction of Flame Kinetics: Principles and Details. In *Progress in Aeronautics and Astronautics*. (J. R. Bowen, N. Manson, A. K. Oppenheim and R. I. Soloukhin, (editors)). AIAA, 1988, 67–86.

[4.91] N. Peters and B. Rogg, *Reduced Kinetic Mechanisms for Applications in Combustion Systems*. Lecture Notes in Physics, Vol. 15. Springer Verlag, Heidelberg, 1993.

[4.92] H. Pitsch, N. Peters and K. Seshadri, Numerical and Asymptotic Studies of the Structure of Premixed Iso-Octane Flames. In *26th Symposium (International) on Combustion*. The Combustion Institute, Pittsburgh, PA, USA, 1996, 763–771.

[4.93] N. Peters and F. A. Williams, Asymptotic Structure of Stoichiometric Methane-Air Flames. Combustion and Flame, Vol. 68, 1987, 185–207.

[4.94] L. R. Petzold, A Description of DASSL: A Differential-Algebraic System Solver. In *Scientific Computing*. (R. S. Stepleman, (editor)). North-Holland, Amsterdam, New York, 1982, 65–68.

[4.95] K. E. Brenan, S. L. Campbell and L. R. Petzold, *Numerical Solution of Initial-Value Problems in Differential-Algebraic Equations*. North-Holland, Amsterdam, New York, 1989.

[4.96] M. Matalon and B. J. Matkowsky, Flames as Gasdynamic Discontinuities. Journal of Fluid Mechanics, Vol. 124, 1982, 239–259.

[4.97] R. Klein, Semi-Implicit Extension of a Godunov-Type Scheme Based on Low Mach Number Asymptotics I: One-Dimensional Flow. Journal of Computational Physics, Vol. 121, 1995, 213–237.

[4.98] Th. Schneider, N. Botta, R. Klein and K. J. Geratz, Extension of Finite Volume Compressible Flow Solvers to Multi-Dimensional, Variable Density Zero Mach Number Flows. Journal of Computational Physics, Vol. 155, 1999, 248–286.

[4.99] R. Klein, Numerics in Combustion. In *Introduction to Turbulent Combustion*. (L. Vervisch, D. Veynante and D. Olivari, (editors)). The von Karman Institute, Rhode St. Genése, Belgium, 1999.

[4.100] C. A. J. Fletcher, *Computational Techniques for Fluid-Dynamics—Fundamental and General Techniques*, Vol. 2. Springer Verlag, New York, 1988.

[4.101] R. I. Issa, Solution of the Implicitly Discretised Fluid Flow Equations by Operator-Splitting. Journal of Computational Physics, Vol. 62, 1986, 40–65.

[4.102] J. Kim and P. Moin, Application of a Fractional Step Method to Incompressible Navier-Stokes Equations. Journal of Computational Physics, Vol. 59, 1985, 308–323.

[4.103] S. V. Patankar, *Numerical Heat Transfer and Fluid Flow.* Hemisphere Publishing Corporation, 1980.

[4.104] R. Klein and N. Peters, Cumulative Effects of Weak Pressure Waves During the Induction Period of a Thermal Explosion in a Closed Cylinder. Journal of Fluid Mechanics, Vol. 187, 1988, 197–230.

[4.105] J. Sesterhenn, B. Müller and H. Thomann, Computation of Compressible Low Mach Number Flow. Computational Fluid Dynamics, Vol. 2, 1992, 829–833.

[4.106] R. J. LeVeque, *Numerical Methods for Conservation Laws.* Birkhäuser Verlag, Zürich, Schweiz, 1992. IBSN 0-521-43009-7.

[4.107] D. Kröner, (editor), *Numerical Schemes for Conservation Laws.* Wiley and Teubner, Stuttgart, Leipzig, 1996.

[4.108] D. Kröner, M. Ohlberger and C. Rhode, (editors), *An Introduction to Recent Developments in Theory and Numerics for Conservation Laws.* Lecture Notes in Computional Science and Engineering, Vol. 5. Springer, Berlin, Heidelberg, New York, 1998.

[4.109] T. J. R. Hughes, Multiscale Phenomena: Green's Functions, the Dirichlet-to-Neumann Formulation, Subgrid Scale Models, Bubbles and the Origins of Stabilized Methods. Computer Methods in Applied Mechanics and Engineering, Vol. l27, 1995, 387–401.

[4.110] R. Löhner, K. Morgan, J. Peraire and M. Vahdati, Finite Element Flux Corrected Transport (FEM-FCT) for the Euler and Navier-Stokes Equations. International Journal for Numerical Methods in Fluids, Vol. 7, 1997, 1093–1109.

[4.111] E.S. Oran and J.P. Boris, *Numerical Simulation of Reactive Flow.* Elsevier Science Publ., New York, 1987.

[4.112] P. D. Lax and B. Wendroff, Systems of Conservation Laws. Communications in Pure and Applied Mathematics, Vol. 13, 1960, 568–582.

[4.113] H. Bijl and P. A. Wesseling, Unified Method for Computing Incompressible and Compressible Flows in Boundary-Fitted Coordinates. Journal of Computational Physics, Vol. 141, 1998, 153–173.

[4.114] K.J. Geratz, R. Klein, C.-D. Munz and S. Roller, Multiple Pressure Variable (MPV) Approach for Low Mach Number Flows Based on Asymptotic Analysis. In *Flow Simulation with High-Performance Computers II. DFG Priority Research Programme Results*. (E. H. Hirschel, (editor)), Notes on Numerical Fluid Mechanics, Vol. 53. Vieweg Verlag, Braunschweig, 1996.

[4.115] S. Roller, C.-D. Munz, K.J. Geratz and R. Klein, The Extension of Incompressible Flow Solvers to the Weakly Compressible Regime. Theoretical and Numerical Fluid Dynamics, 1999, submitted for publication.

[4.116] D. N. Williams, L. Bauwens and Elaine S. Oran, Detailed Structure and Propagation of Three-Dimensional Detonations. In *26th Symposium (International) on Combustion*. The Combustion Institute, Pittsburgh, PA, USA, 1996, 649–657.

[4.117] B. Einfeldt, On Godunov-Type Methods for Gas Dynamics. SIAM Journal of Numerical Analysis, Vol. 25, 1988, 294–318.

[4.118] P. Colella, A. Majda and V. Roytburd, Theoretical and Numerical Structure for Reacting Shock Waves. SIAM Journal of Scientific and Statistical Computing, Vol. 7, 1986, 1059–1080.

[4.119] R. B. Pember, Numerical Methods for Hyperbolic Conservation Laws with Stiff Relaxation I. Spurious Solutions. SIAM Journal of Applied Mathematics, Vol. 53, 1993, 1293–1330.

[4.120] R.J. LeVeque and H.C. Yee, A Study of Numerical Methods for Hyperbolic Conservation Laws with Stiff Source Terms. Journal of Computational Physics, Vol. 86, 1990, 187–210.

[4.121] A. C. Berkenbosch, R. Kaaschieter and R. Klein, Detonation Capturing for Stiff Combustion Chemistry. Combustion Theory and Modelling, Vol. 2, 1998.

[4.122] A. J. Chorin, A Numerical Method for Solving Incompressible Viscous Flow Problems. Journal of Computational Physics, Vol. 2, 1967, 12–26.

[4.123] A. J. Chorin, Numerical Solution of the Navier-Stokes Equations. Mathematics of Computation, Vol. 22, 1968, 745–762.

[4.124] A. J. Chorin, On the Convergence of Discrete Approximations to the Navier-Stokes Equations. Mathematics of Computation, Vol. 23, 1969, 341–353.

[4.125] J. Lang, Adaptive Incompressible Flow Computations with Linearly Implicit Time Discretization and Stabilized Finite Elements. In *Computational Fluid Dynamics '98*. (K.D. Papailiou, D. Tsahalis, J. Periaux, C. Hirsch and M. Pandolfi, (editors)), John Wiley & Sons, New York. 1998.

[4.126] R. Rannacher, On Chorin's Projection Method for the Incompressible Navier-Stokes Equations. In *The Navier-Stokes Equations II—Theory and Numerical Methods*. (J. G. Heywood, (editor)), Vol. number 1530 in *Lecture Notes in Mathematics*. Springer Verlag, Berlin, 1992, 167–183.

[4.127] K. C. Karki and S. V. Patankar, Pressure Based Calculation Procedure for Viscous Flows at all Speeds in Arbitrary Configurations. AIAA Journal, Vol. 27, 1989, 1167–1174.

[4.128] C. M. Rhie, Pressure-Based Navier-Stokes Solver Using the Multigrid Method. AIAA Journal, Vol. 27, 1989, 1017–1018.

[4.129] W. Shyy, Elements of Pressure-Based Computational Algorithms for Complex Fluid Flow and Heat Transfer. Advances in Heat Transfer, Vol. 24, 1994, 191–275.

[4.130] P. Haldenwang, J. Daou, B. Denet and C. Nicoli, Low Mach Number Combustion Modelling for Droplet and Spray. presented at 5th Intl. Conference on Numerical Combustion, SIAM, York, UK, March 30 - April 1, 1998, 1998.

[4.131] R. I. Issa, A. D. Gosman and A. D. Watkins, The Computation of Compressible and Incompressible Recirculating Rlows by a Non-Iterative Implicit Scheme. Journal of Computational Physics, Vol. 62, 1986, 66–82.

[4.132] R. S. Cant and K. N. C. Bray, A Theoretical Model of Premixed Turbulent Combustion in Closed Vessels. Combustion and Flame, Vol. 76, 1989, 243–263.

[4.133] R. S. Cant and K. N. C. Bray, Strained Laminar Flamelet Calculation of Premixed Turbulent Combustion in a Closed Vessel. In *22nd Symposium (International) on Combustion*. The Combustion Institute, Pittsburgh, PA, USA, 1988, 791–799.

[4.134] J. B. Bell and D. L. Marcus, A Second-Order Projection Method for Variable-Density Flows. Journal of Computational Physics, Vol. 101, 1992, 334–348.

[4.135] M. Lai, J. B. Bell and P. Colella, A Projection Method for Combustion in the Zero Mach Number Limit. AIAA paper, 93-3369, 1993.

[4.136] J. van Kan, A Second-Order Accurate Pressure-Correction Scheme for Viscous incompressible flow. SIAM Journal of Scientific and Statistical Computing, Vol. 7, 1986, 870–891.

[4.137] P. M. Gresho, R. L. Sani and M. Engelman, *Incompressible Flow and the Finite Element Method*. John Wiley & Sons, New York, 1991.

[4.138] A.S. Almgren, J.B. Bell, P. Colella, L.H. Howell and M.L. Welcome, A Conservative Adaptive Projection Method for the Variable Density Incompressible Navier-Stokes Equations. LBNL Preprint, Vol. 39075 UC-405, 1996.

[4.139] M. J. Berger and P. Colella, Local Adaptive Mesh Refinement for Shock Hydrodynamics. Journal of Computational Physics, Vol. 82, 1989, 67–84.

[4.140] R. B. Pember, P. Colella, L. H. Howell, A. S. Almgren, J. B. Bell, K. C. Kaufman, W. A. Fiveland and J. P. Jessee, The Modeling of a Laboratory Natural Gas-Fired Furnace with a Higher-Order Projection Method for Unsteady Combustion. LBNL Preprint, Vol. LBNL-38800, 1996.

[4.141] P. Bailly and M. Champion, Counter-Gradient Diffusion in a Confined Turbulent Premixed Flame. Physics of Fluids, Vol. 9, 1997, 766–775.

[4.142] P. Clavin, Dynamic Behavior of Premixed Flame Fronts in Laminar and Turbulent Flows. Progress in Energy and Combustion Science, Vol. 11, 1985, 1–59.

[4.143] I. Chern and P. Colella, A Conservative Front Tracking Method for Hyperbolic Conservation Laws. UCRL-97200, Lawrence Livermore National Laboratory, 1987.

[4.144] A. Bourlioux and A. J. Majda, Theoretical and Numerical Structure for Two-Dimensional Unstable Detonations. Combustion and Flame, Vol. 90, 1992, 211–229.

[4.145] R. J. LeVeque and K.-M. Shyue, Two-Dimensional Front Tracking Based on High Resolution Wave Propagation Methods. Journal of Computational Physics, Vol. 123, 1996, 35–368.

[4.146] P. Terhoeven, *Ein numerisches Verfahren zur Berechnung von Flammenfronten bei kleiner Mach-Zahl [A Numerical Method for Flame Front Tracking at Low Mach Numbers]*. PhD thesis, RWTH Aachen, 1998.

[4.147] B. T. Helenbrook, L. Martinelli and C. K. Law, A Numerical Method for Solving Incompressible Flow Problems with a Surface of Discontinuity. Journal of Computational Physics, Vol. 148, 1999, 366–396.

[4.148] P. Deuflhard and A. Hohmann, *Numerical Analysis. A First Course in Scientific Computation.* W. de Gruyter, Berlin, New York, 1995.

[4.149] G. Strang, On the Construction and Comparison of Difference Schemes. SIAM Journal of Numerical Analysis, 1968, 506–517.

[4.150] U. Maas and S. B. Pope, Simplifying Chemical Kinetics: Intrinsic Lower Dimensional Manifolds in Composition Space. Combustion and Flame, Vol. 88, 1992, 239–264.

[4.151] U. Maas and S. B. Pope, Implementation of Simplified Chemical Kinetics Based on Intrinsic Low-Dimensional Manifolds. In *24th Symposium (International) on Combustion.* The Combustion Institute, Pittsburgh, PA, USA, 1992, 103–112.

[4.152] U. Maas and S. B. Pope, Laminar Flame Calculations Using Simplified Chemical Kinetics Based on Intrinsic Low-Dimensional Manifolds. In *25th Symposium (International) on Combustion.* The Combustion Institute, Pittsburgh, PA, USA, 1994, 1349–1359.

[4.153] S. H. Lam and D. A. Goussis, The CSP Method for Simplifying Kinetics. International Journal of Chemical Kinetics, Vol. 26, 1994, 461–486.

[4.154] H. S. Lam, Reduced Chemistry Modeling and Sensitivity Analysis. In *Aerothermochemistry for Hypersonic Technology 1994-1995*. (D. Olivari, (editor)). The von Karman Institute, Rhode St. Genése, Belgium, 1995.

[4.155] W. Breitung and R. Redlinger, Containment Pressure Loads from Hydrogen Combustion in Unmitigated Severe Accidents. Nuclear Technology, Vol. 111(3), 1995, 395–419.

5. EXPERIMENTS AND MODEL VALIDATION*

5.1 Introduction

In order to apply the models presented in the previous chapter, effort has to be put on the validation of the developed numerical tools. The final objective for all tools developed in this context is to estimate the danger potential that can arise after a hypothetical release of hydrogen into the containment atmosphere of a NPP. Therefore, the results of numerical simulations need to be comapared with basic experiments.

The first part of this chapter describes the test facilities that were used to investigate various combustion phenomena. Although the experimental results, presented in this chapter, are not detailed enough to be used as input data for independent numerical simulations, they are intended to give code developers a comprehensive overview of what kind of experiments were performed in various test facilities. In particular, shock-induced ignition and transition to detonation, accelerating flames in obstacle arrays, and turbulent combustion in complex and large-scale geometries are addressed.

The second part of this chapter deals with the state of simulating hydrogen combustion phenomena as they are currently applied. A comparison of the state of the art in the application versus the state of the art of what is theoretically possible as shown in Chapter 4 shows that there is still a wide gap between the two. This is mainly related to the lack of sufficient computing memory and run time. Nevertheless, with increasing concerns regarding the system safety, the demand for more detailed and sophisticated modelling increases as well. However, for most of the everyday engineering tasks, it would be ineffective and unnecessary to employ the most-advanced and most-complex modelling tools. A compromise is to compile a hierarchy of models with an increasing level of detail, starting from coarse-grained lumped-parameter codes up to combustion modelling in Reynolds-averaged Navier-Stokes (RNS) field codes. The latter are concerned with computer resources, the most common method of simulating turbulent combustion today.

The examples of code validation presented in the second part of this chapter show the potential of a specific combustion model implemented in a certain type of code. An exemplary list of selected codes – classified into the categories lumped parameter, hybrid CFD-lumped-parameter, and CFD-Codes – is shown.

* Andreas Eder is the lead author for Chapter 5.

5.2 Experiments for Code Validation

5.2.1 Shock Reflections and Focusing *

5.2.1.1 Preliminary remarks

The problem of shock (or blast) waves reflections and focusing in combustible media is one of the key problems of DDT phenomena. Up to now, a representative review of main experimental and theoretical results (e.g., [5.1 – 5.17]) in this field does not exist.

5.2.1.2 Experimental set-up and description of the reflectors used

3D reflectors. The experiments on shock focusing near 3D reflecting endplates were conducted in a horizontally placed laboratory shock tube. A general scheme of the experimental set-up in [5.3, 5.4, 5.12 – 5.14] is shown in Figure 5.2.1.2-1. The low-pressure chamber (LPC) had a circular cross-section diameter of $D = 54$ mm and the high-pressure chamber (HPC) was 50 mm in diameter. The lengths of LPC and HPC were 1 m and 0.5 m respectively. The initial pressure in LPC, p_1, was varied in the range 0.8 to 6 bar. The maximum pressure in HPC reached $p_4 = 100$ bar. Helium, nitrogen, and argon were used as driver gases. Initially, the HPC was separated from the LPC by a hermetically mounted bursting membrane. Six reflectors of various shapes were available in the experiments. The end part of the LPC was properly designed to allow easy replacement of the reflector, including the installation of the plane-surface end flange. The photographs and charts of the reflectors used are presented in Appendix C in Figures. C.3.1(a-e).

These 3D surfaces can be described as follows: two cones with a length/diameter ratios $L/D = 1.5$ and 0.5 respectively (Figures C.3.1 a,b); two parabolic reflectors with length/diameter ratios $L/D = 1.5$ and 0.5 respectively (Figures. C.3.1 c,d); pyramid with 90° angles between the top ridges and ratio of the height L to the diameter D of base-inscribed circle being 0.7 (Figure C.3.1e). The same experimental procedure for 3D spherical reflectors was used in Reference [5.8], but in that work, the cross-section of spherical cavity (F) was only part of the full channel cross-section as in the scheme shown in Figure C.3.1.f.

2D reflectors. The tests on shock focusing near 2D reflecting end plates were realized in laboratory shock tubes with a rectangular cross-section [5.3,5.4,5.12,5.13,5.15]. The geometry of used 2D reflectors and the scheme for the arrangement of pressure and radiation gauges are shown in Figure 5.2.1.2-2. The displacement of 2D reflectors was the same that used in Reference [5.6] and [5.8]. As shown in Figure C.3.2 the reflecting wedge did not fully cover the channel cross-section. The exhaustive information about main initial parameters in different series of experimental research is presented in Table 5.2.1.2-1. The table contains information about the type of gaseous mixture, volume concentration of H_2 (% H_2), type of reflectors used, size of the cross-section of the test channel S_t, range of initial pressure p_0, length of reflector L_r, content of nitrogen in the mixture, volume concentration of steam (% H_2O), initial temperature T_0, and ratio of reflector-covered area (F) to the cross-section of the test channel F/S_t.

* Contributed by Professor B. E. Gelfand

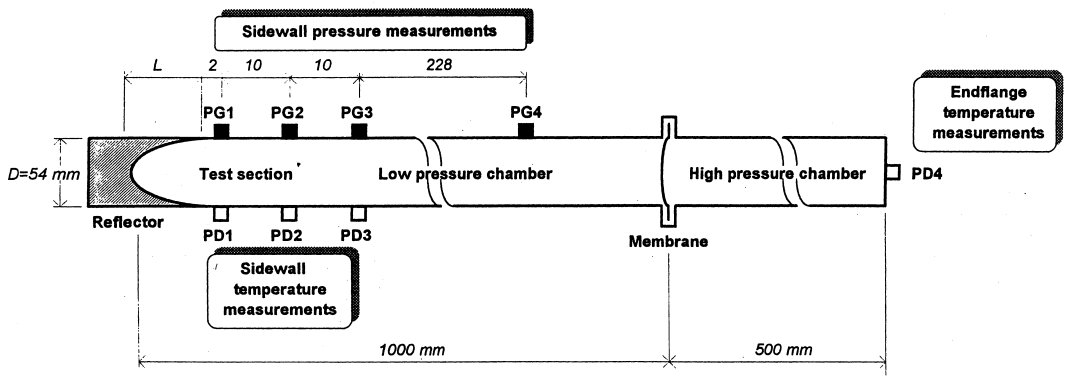

Figure 5.2.1.2-1 Scheme of the shock tube and the arrangement of the pressure and temperature measurement systems

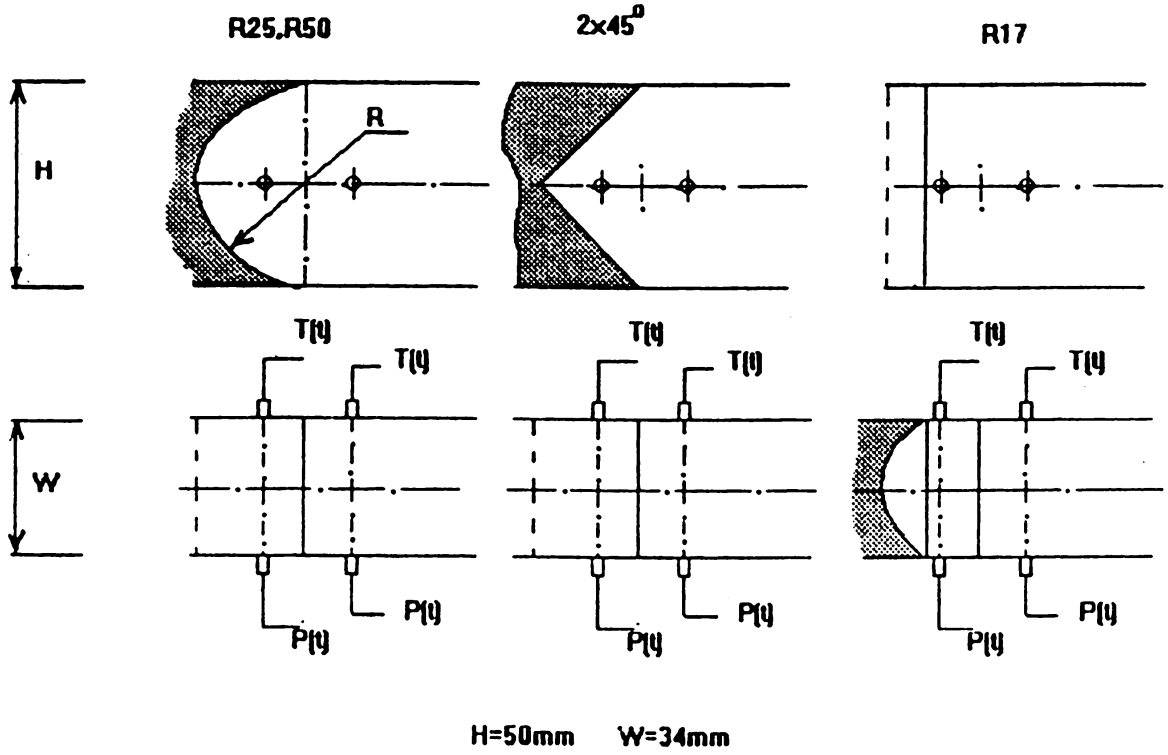

Figure 5.2.1.2-2 The main 2D reflectors and the scheme for the arrangement of pressure and radiation gauges

Table 5.2.1.2-1 Main initial parameters of shock focusing research

Mix	$\%H_2$	Refl.	S_t [mm^2]	P_0 [bar]	L [mm]	N_2/O_2	$\%H_2O$	T_0 [K]	F/S_t	[ref]
$2H_2 + O_2$	66%	wedge $15°$,$30°$,$45°$	90×90	0.05 - 0.2	12.7 - 60	0	0	293	$< 100\%$	[5.6]
H_2 + Air	15% - 60%	cylinders / radii $17, 25, 50$ mm, $45°$ wedge angle	34×50	1.0 - 3.0	$L = R$ $R = 36$ mm	3.76	0	293	$< 100\%$	[5.12, 5.13, 5.15]
H_2 + Air	15% - 60%	sphere: $R = 27$ mm cone: $R = 27$ mm parabola: $R = 27$ mm pyramid	$\pi \times 54^2/4$	1.0 - 3.0	$L/D = 1.0$ $L/D = 0.5, 1.0$ $L/D = 0.7$	3.76	0	293	$< 100\%$	[5.13]
H_2 + Air $2H_2 + O_2$	15% - 60% 66%	cylinders / radii $15, 22, 24$ mm	90×90	0.04 - 0.14	L= R	2.0 - 7.0	0% - 30%	293 - 393	9% - 28%	[5.8]
$2H_2 + O_2$	66%	sphere: $R = 35.7$ mm cylinder: $R = 22.5$ mm	$\pi \times 78^2/4$ 45×40	0.1 - 0.5	$L = 78$ mm $L = R$	0	0	293	83% 100%	[5.9]

5.2.1.3 Shock wave intensity, self-ignition regimes, mixture composition, and reflector type

A strong dependence was found experimentally between mixture composition and the type of reflectors installed near the end plates of the ignition-test shock tubes and the resulting shock wave intensity corresponding to different self-ignition regimes. Here, we discuss some important related observations.

3D reflectors One can plot the experimental dependence of Mach numbers corresponding to different self-ignition regimes in the mixture composition for each reflector used. A conical reflector $L/D = 1.5$ was chosen as a basis for the comparison. The dependence corresponding to this reflector is shown in Figure 5.2.1.3-1. A no-ignition region is shown below the curve 1. Curve 2 corresponds to the start of the self-ignition, which results not necessarily in flame front formation and propagation. Nevertheless, region A between curves 1 and 2 is potentially hazardous. Only the detonation-like strong ignition regimes take place in region C above the curve 3. Region B between curves 2 and 3 is responsible for mild ignition. As the ignition model approaches curve 3, it becomes transient and, finally, strong. These curves are U-shaped. Region B is extended when the hydrogen concentration approaches the limits. This is important for hazard assessments. Also, it is to be noted that stoichiometric mixtures are ignited at the reflection of shock perturbations propagating with a Mach number of about $M_{\min} = 1.1$. Therefore, a flame front moving with a velocity 330 m/s generates pressure disturbances that correspond to this shock wave intensity. These disturbances, being reflected from the obstacles, can cause secondary ignition, thus favouring the escalation of explosion.

Now let us consider the parabolic reflector with the same ratio $L/D = 1.5$. These data are presented in Appendix C, Figure C.3.3a. The results of conical and parabolic reflectors $(L/D = 1.5)$ are similar to each other except that for a parabolic reflector, the transition to strong ignition takes place at higher Mach numbers. Data for 3 reflectors with $L/D < 1$ are shown in Figure C.3.3 (b-d) of Appendix C. The incident shock wave Mach numbers at which self-ignition takes place are higher than those for the reflectors described above. This effect is more pronounced for near-limit mixtures. When the L/D ratio of the conical reflector changes from 1.5 to 0.5 (mixture with 15% H_2), the transient mode is replaced by the mild one at $M_{\min} = 2.13$, and, the strong regime changes to transient at $M_{\min} = 2.29$. Note that the

range of Mach numbers $M = 0.9$ to 1.0 is typical for the mild ignition regimes for near-limit mixtures ($M = M_{\rm tr} - M_+$), where $M_{\rm tr}$ and M_+ are respectively the Mach number corresponding to the transient regime of self-ignition and to the appearance of the self-ignition). This range is narrower for the 2D reflectors and is equal to $M_{\rm min} = 0.2$ to 0.5. Another specific feature of the ignition at the reflectors with $L/D < 1$ is the expansion of the domain of the mild ignition for stoichiometric mixture. For example, the strong mode occurs at $M_{\rm min} = 1.9$ for the pyramid, whereas the cone $L/D = 1.5$ requires $M_{\rm min} = 1.39$. The experiments performed confirm the conclusion [5.8] about the independence of critical shock wave intensity (i.e., Mach number) on the initial pressure in the range of 1 to 5 bar. The same results were obtained in tests conducted with a spherical reflector and described in Reference [5.8]. The domains of main explosion regimes are presented in Figure 5.2.1.3-2 for stoichiometric H_2 + O_2 mixture in the range of initial pressure $p_0 = (0.3$ to $14)$ kPa. Figure 5.2.1.3-3 demonstrates the dependence of low boundary of detonation domain for H_2 + air on mixture composition at elevated initial temperature. Figure 5.2.1.3-4 confirms the weak influence of initial pressure on the value of minimal Mach numbers for shock wave triggering detonation by focusing of the shock wave. Figures 5.2.1.3-5 and 5.2.1.3-6 represent the inhibition of self-ignition near spherical reflectors with additives of nitrogen or steam in a gaseous mixture.

2D reflectors. The tests performed allow us to present the dependence of the critical Mach numbers upon mixture composition and also for 2D reflectors. The typical dependence is presented in Figure 5.2.1.3-7 for a cylindrical reflector with radius of curvature $R = 17$ mm. No ignition occurs in the region below line 1. Zone A between lines 1 and 2 corresponds to the spotty ignition regime. Zone C above line 3 is responsible for the detonation explosive regime. In region B, between curves 2 and 3, transition regimes were observed. All 13 curves have a U-shaped form that is responsible for a known dependence of critical ignition and detonation parameters upon the mixture composition. A similar dependence was obtained for cylindrical reflectors with $R = 25$ mm, $R = 50$ mm, and for dihedral corner reflector 2, 4, 5 (see Figures C.3.4 a-c in Appendix C). The comparison of results for plane shock focusing at 3D (hemispherical) and 2D (cylindrical) reflectors is shown in Figure 5.2.1.3-8. As stated earlier, line 13 divides zones A, B, C for reflector $R = 17$ mm. Lines 1, 2, 3 demonstrate a significant decrease of critical Mach numbers at which the spotty and transition ignition regimes take place in the case of 3D reflectors. To summarize, the following observations are made from the results of these tests:

1. Shock or blast wave focusing, [5.18], inside 2D or 3D cavities essentially extends the range of parameters of pressure waves that can trigger explosion phenomena in H_2 + air mixtures.
2. The critical conditions for self-ignition in H_2 + air mixtures are determined for the wide nomenclature of focusing cavities. Three-dimensional cavities with conical and parabolic geometry are the most efficient for self-ignition in H_2 + air mixtures.
3. The dependence of critical Mach numbers responsible for self-ignition and the transition between ignition modes on the mixture composition have a characteristic U-shape.
4. Initial pressures in a range 0.1 to 5 bar do not affect the critical Mach number.

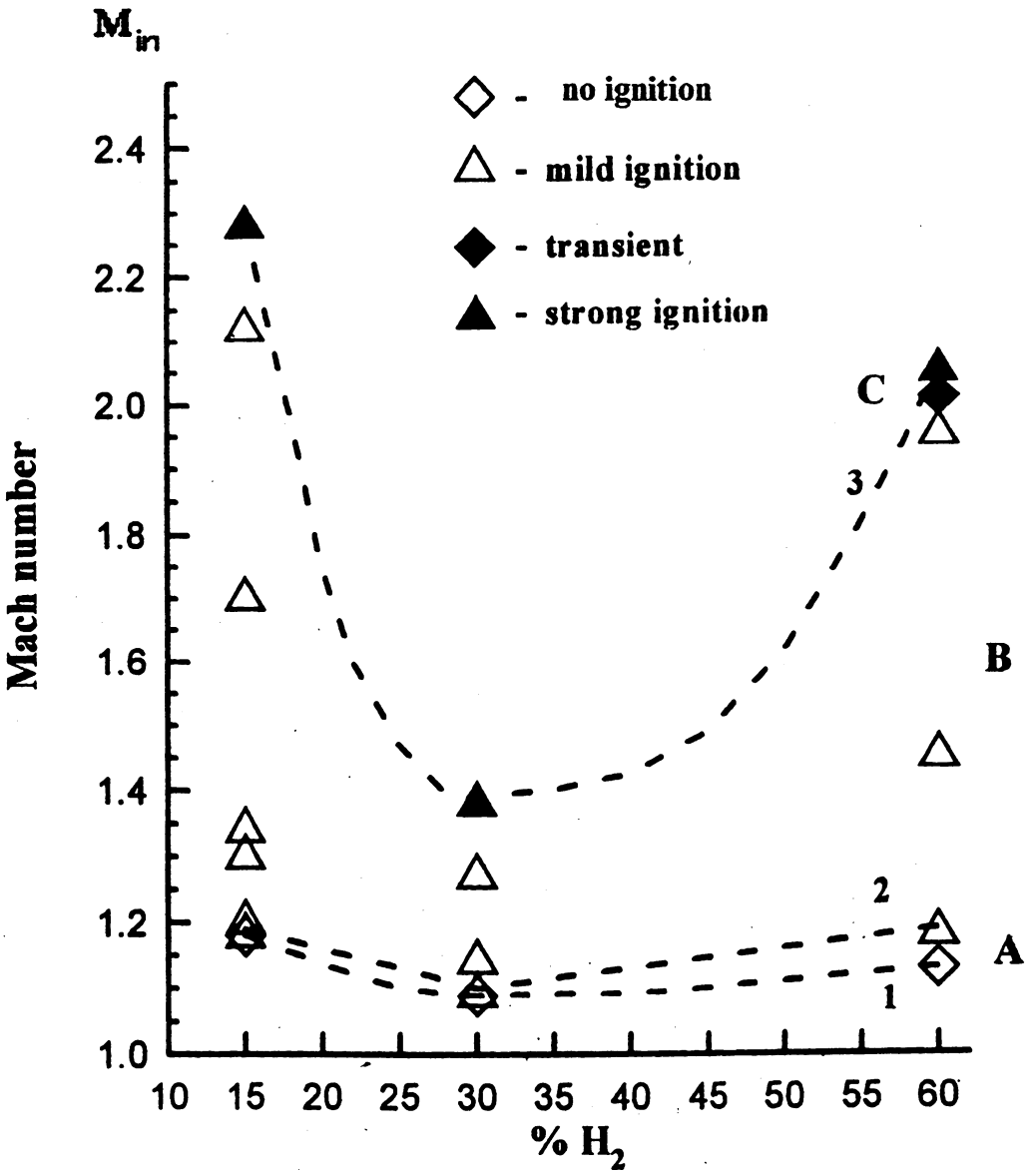

Figure 5.2.1.3-1 The incident shock Mach numbers corresponding with various modes of self-ignition versus hydrogen-air mixture composition. Reflector Cone $L/D = 1.5$. Curve 1 shows no ignition; curve 2 shows mild ignition with hot spot formation; curve 3 shows strong ignition; A shows the danger zone, where there is a possibility of ignition in the hot spots type; B shows the region of the mild-to-strong transient ignition; and C shows strong ignition zone.

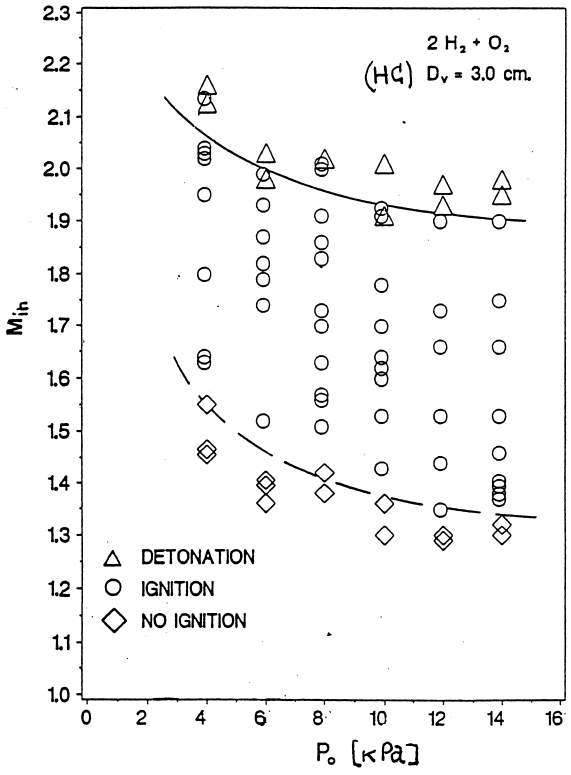

Figure 5.2.1.3-2 The influence of pressure on main self-ignition regimes near hemispherical reflector in $2H_2 + O_2$ mixture

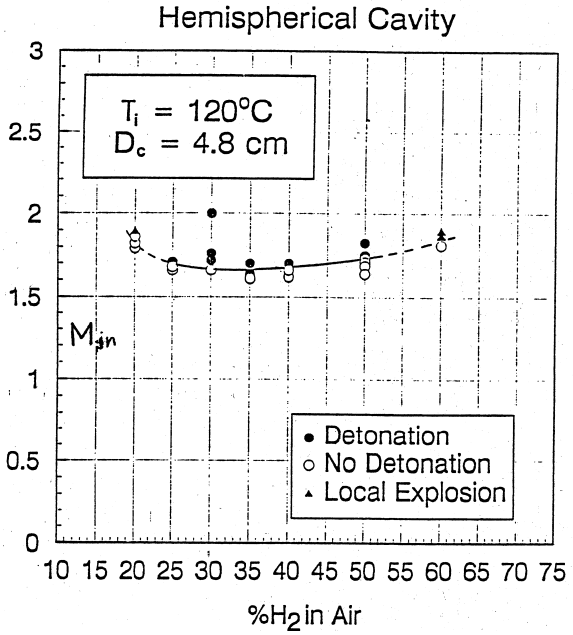

Figure 5.2.1.3-3 The influence of mixture composition on self-ignition near 3D reflector

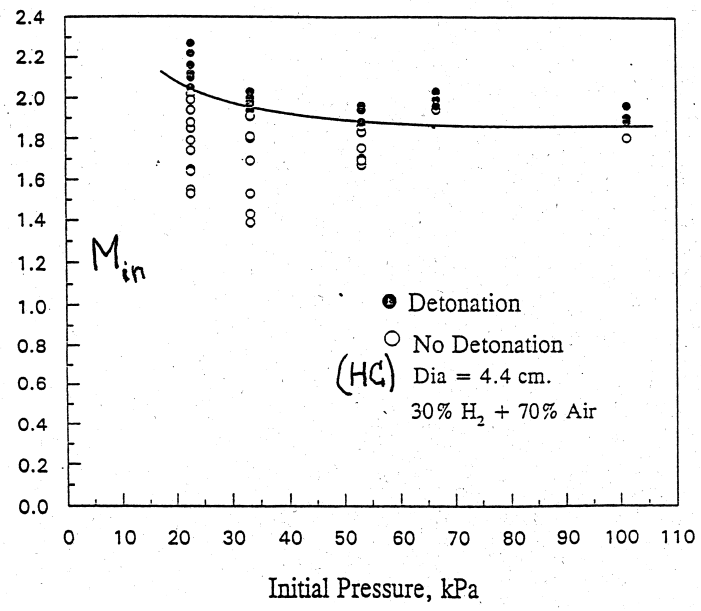

Figure 5.2.1.3-4 The influence of pressure on detonation domain boundary in 30% H_2 + 70% air mixture

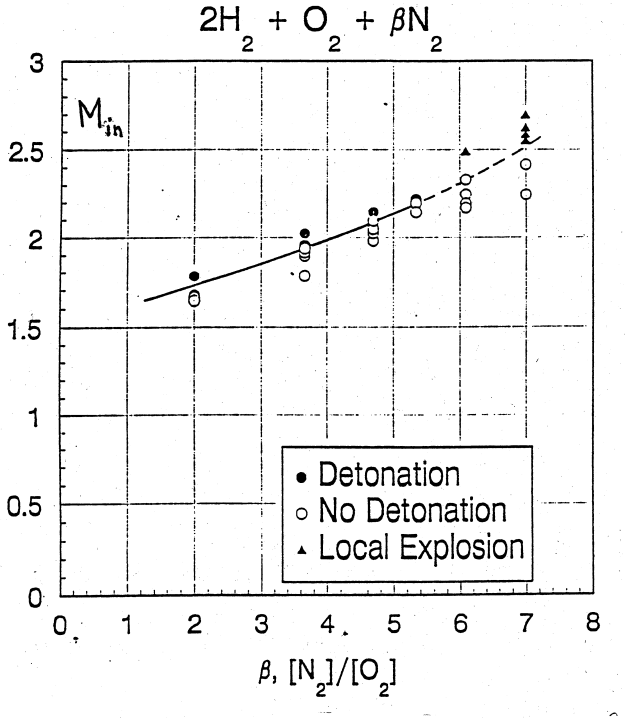

Figure 5.2.1.3-5 The influence of N_2/O_2 ratio on detonation domain boundary

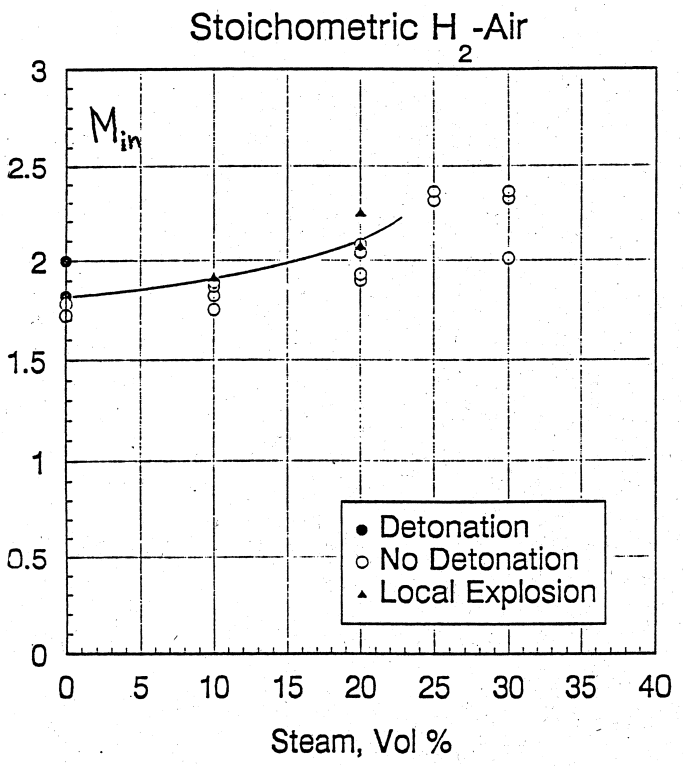

Figure 5.2.1.3-6 The influence of steam additive on detonation domain boundary

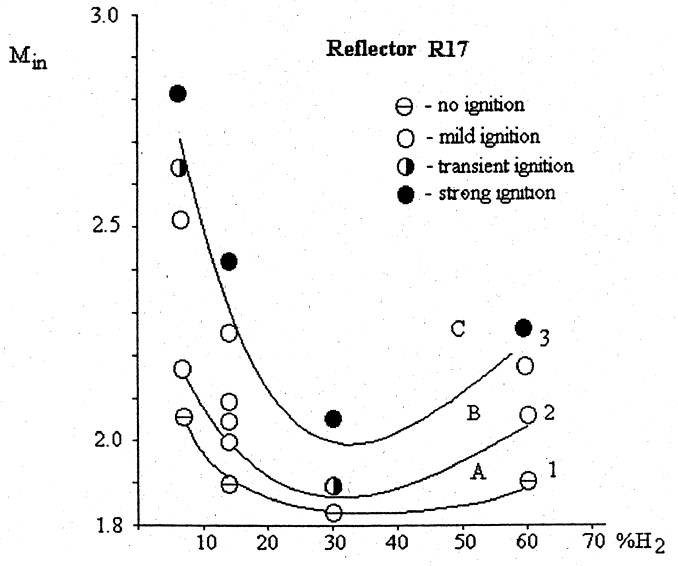

Figure 5.2.1.3-7 The critical incident shock Mach number versus the H_2-air mixture composition, spherical reflector R17. The regions A, B, and C and the curves 1, 2, and 3 correspond to Figure 5.2.1.3-8 for reflector R27.

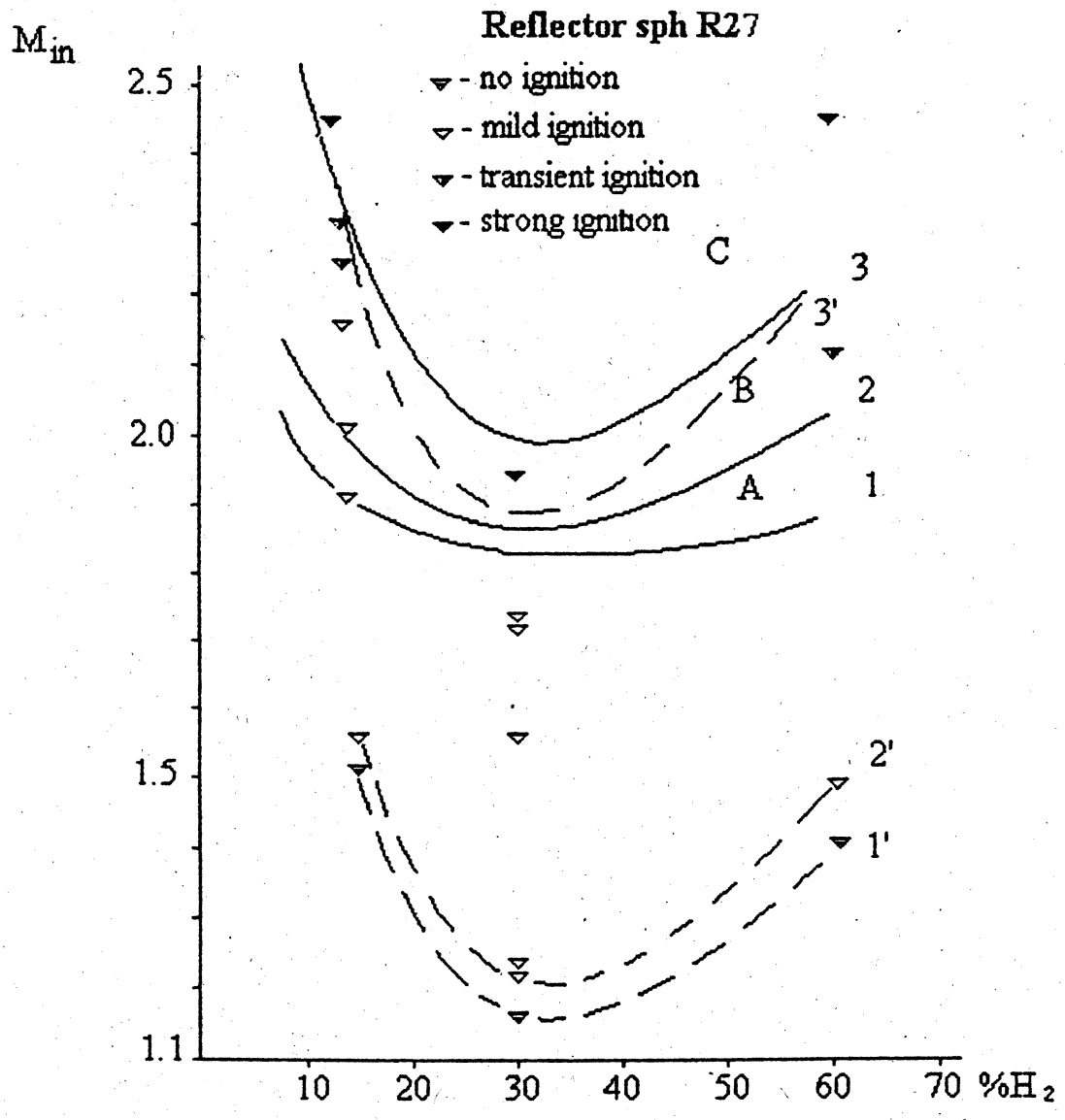

Figure 5.2.1.3-8 The critical incident shock Mach number versus the H_2-air mixture composition, spherical reflector R27. The regions A, B, and C and the curves 1, 2, and 3 correspond to Figure 5.2.1.3-7 for reflector R17.

5.2.1.4 Preliminary calculations of pressure and temperature time histories during shock wave focusing

The probability of self-ignition and the type of the subsequent mode of combustion in a reactive mixture depend on the change of temperature and pressure in space and time. From preliminary computations described in References [5.4,5.6,5.9 – 5.11,5.16,5.17], it follows that focusing of shock waves in a cavity causes fast changes of temperature and pressure in time, which are not typical of normal reflection at a flat surface. The sizes of the "hotest" zones, together with fields of pressure and temperature inside them, become larger after a series of complex interactions between reflected and attached wave structures. Thus the history of explosion regime depends on a ratio of characteristic times both linear gas dynamic scales and chemical processes. In particular, the time at which increased temperature τ will occur in a local zone corresponds to a certain extent with the characteristic time of a chemical reaction θ.

At $\tau < \theta$ ignition will not occur.

At $\tau > \theta$ ignition takes place in a local zone of the size δ.

At small δ the transition from deflagration to detonation is unlikely. Then the outcome of the development of explosion processes because of focusing of shock waves depends on the linear sizes of the focusing cavities. Another aspect of applying a numerical modelling technique to a problem under consideration is an investigation of complex wave dynamics during the self-ignition process under focusing conditions. It allows one to predict the "points of interest", i.e., positions of probes where the flow reveals specific features, and therefore, significantly facilitates the experimental method. With this aim, a special computer code was elaborated. The code uses a set of 2D Euler gas dynamics equations of conservation, coupled with a detailed scheme of chemical reactions between hydrogen and air. The Lax-Wendroff solution method was used, together with the flux-corrected transport (FCT)-algorithm for shock capturing. The chemical part of the solution was computed using the CHEMKIN package. To resolve the peculiarities of a flow near reflection surfaces, a special procedure of grid refinement was used. The code was verified by results of experimental findings shown above, and known theoretical and experimental data on the subject done by other authors.

An example of the preliminary calculation results is presented in Figures 5.2.1.4-1 and 5.2.1.4-2. The case considered is a computer visualization of an initiation of a combustion regime. Figure 5.2.1.4-1 presents a computer shadow-graph of the combustion process (i.e., modulus of density gradients), and Figure 5.2.1.4-2 shows pressure spatial distributions for inert and reactive cases (lower and upper parts of the pictures), respectively. The case considered has the following initial conditions: $p_0 = 0.0263$ MPa, $T_0 = 293$ K, initial shock Mach number $M = 2.0$. The mixture used was 15 % H_2 + 85 % air (reactive case) and 15 % H_2 + 85 % N_2 (inert case). Frames are presented after each 10 μs. Spatial sizes are shown in centimetres. The first four frames are the same both for inert and reactive cases. It is especially evident from Figure 5.2.1.4-2 that ignition takes place in the time interval between the fourth and fifth frames. After that, a fast combustion mode starts to propagate in the direction opposite to the gas flow. The temperature at the front is about 2400 K, and the temperature in the combustion products is steady at about 2000 K. The following specific features of the process could be noted:

1. A combustion wave accelerates fast (in 25 mm) after the primary explosion occurs. Further propagation proceeds at approximately the same radial speed.

2. The pressure distribution at the front is very non-uniform. Along the reflector boundaries, at the

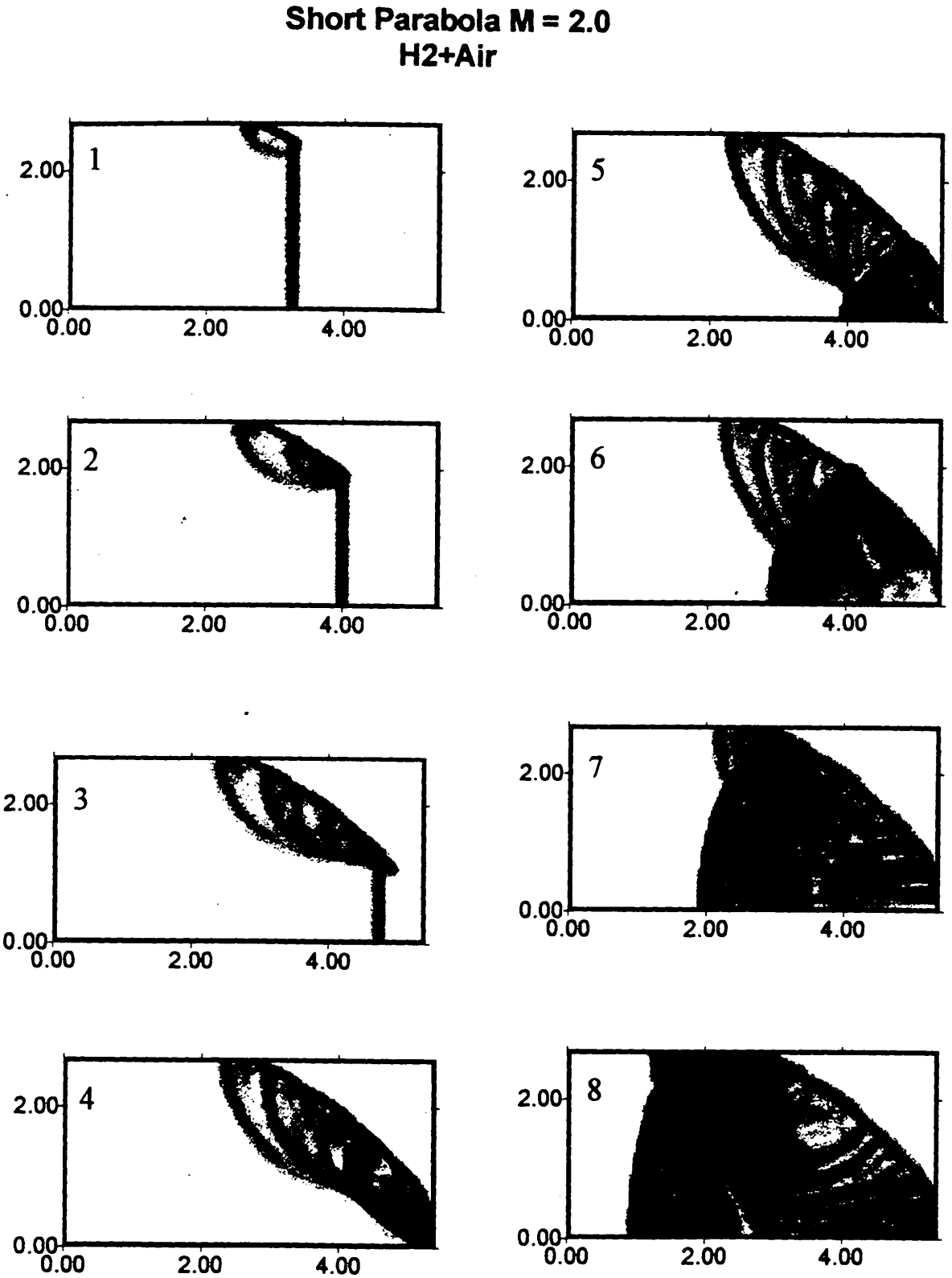

Figure 5.2.1.4-1 Combustion simulation of shock focusing

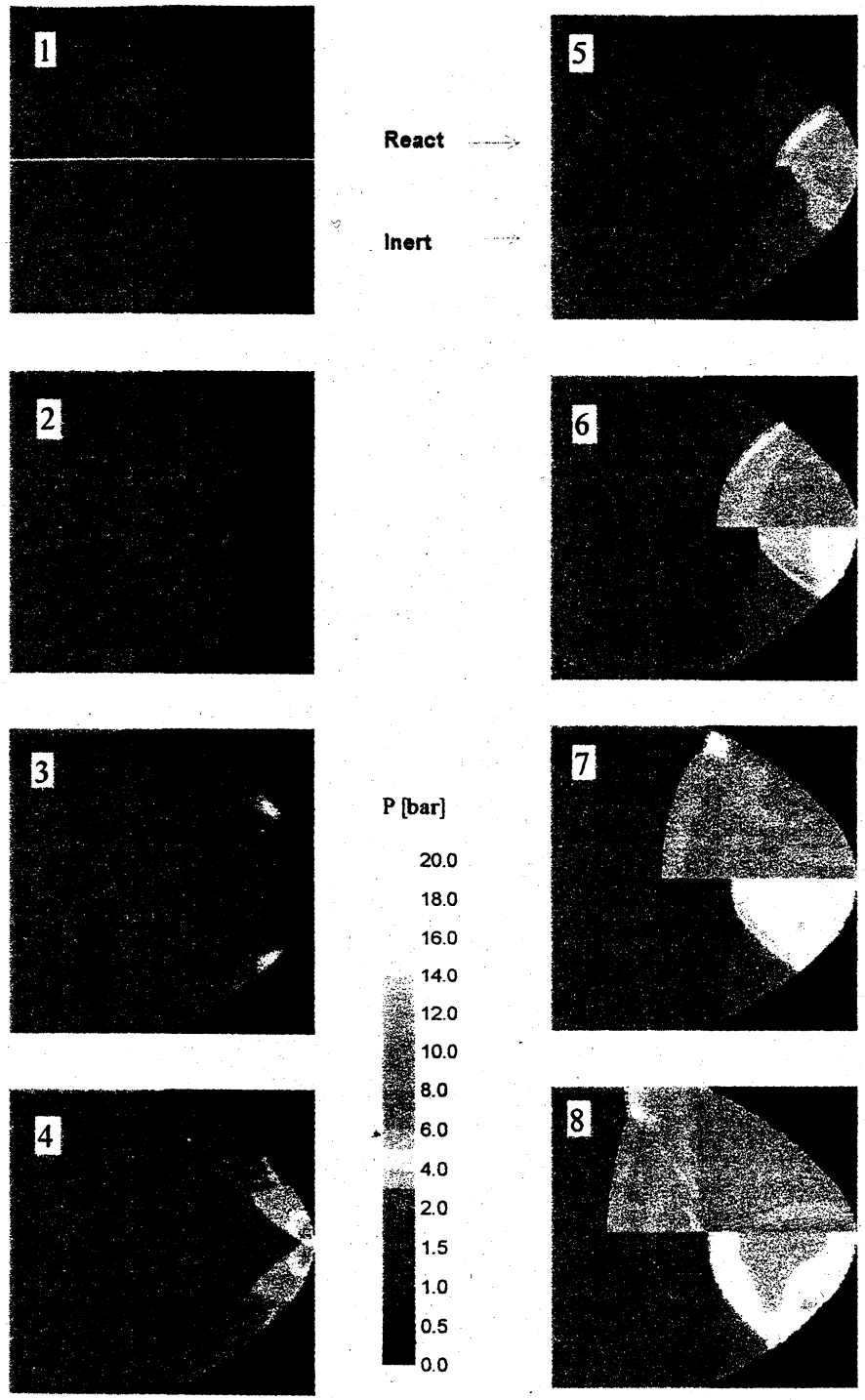

Figure 5.2.1.4-2 Pressure distribution

point where the reflection of incident shock wave changes its mode from a Mach number to a regular number, a sharp pressure rise is detected. Thus at the time that the combustion front leaves the reflection cavity (7th frame), the region with maximal pressure is located at the borders of the reflector.

3. At the same time (7th frame) behind the flame front in the combustion products, a secondary shock wave reaches its axis of symmetry (see Figure 5.2.1.4-1). This wave is formed at the point where the reflection mode changes.

Thus the combustion wave that leaves the reflection cavity has a noticeable non-uniform spatial structure. Evidently, at later times, depending on the size of a channel and the reactivity of the mixture, the wave can be transformed into a detonation with cellular structure.

5.2.1.5 Investigation of H_2 + air flame propagation and DDT in a channel with multi-dimensional end plates

As a logical final stage of separate research on shock waves focusing phenomena and fast deflagration in the congested area, a set of combined tests was performed in a cylindrical tube channel (filled by H_2-air) with a partially obstructed part and a multi-dimensional end plate. Three main regimes of loading from explosive combustion of H_2 - air mixtures near the obstructed space were distinguished on the basis of tests performed [5.14]:

First Regime: At a hydrogen concentration in air of 20% by volume, a non-decaying quasi-steady complex (QC) is emitted from the congested space. This complex consists of the pressure wave (SW1), followed by a combustion zone (FF1). The speeds of SW1 and FF1 are close to each other. The reflection of the QC at the end wall causes a reflected wave (RW) to appear in the combustion products, and the loading process does not depend on the reflector type.

Second Regime: At hydrogen concentrations in air in the range of 15% to 20% by volume, a decoupling complex, consisting of a shock wave (SW2) + decelerating delaying flame front (FF2), is emitted from a congested part of the channel. The reflection of SW2 results in reflected shock wave RSW moving in the unburned mixture ahead of flame front FF2. The reflection of SW2 at the flat end wall is not accompanied by additional self-ignition phenomena. Instead of that the reflection at the concave reflector gives the rise to secondary explosion waves (SEWs) or DDT from exothermic centres created by focusing SW2 inside the non-flat reflector. Other variants of the mentioned complex focusing briefly near an elliptical end plate are described without detailed analysis is described in Reference [5.19].

Third Regime: At hydrogen concentrations in air below 10% to 11% by volume, the speed of the deflagration front (FFi) inside a congested space is sufficient only for supporting a weak compression wave before the flame front in the congested part and a fan of acoustic waves ahead of the decelerating flame (FF3) in free space. The reflection of these waves at any type of reflector does not lead to the significant effect on the overall pressure increase during combustion in a channel.

5.2.1.6 Common conclusions

1. The shock (blast) wave-type disturbances with Mach numbers of $M < 1.2$ being reflected from focusing surfaces and the obstacles cannot cause secondary ignition.
2. The shock (blast) wave-type disturbances with Mach numbers of $1.2 < M \leq 1.4$ being reflected from the obstacles and concave surfaces can cause secondary ignition, thus favouring the escalation of explosion.
3. The shock (blast) wave-type disturbances with a Mach number of $M > 1.4$ being reflected from the obstacles can cause the detonation initiation in the vicinity of reflecting surfaces.

5.2.1.7 Experimental verification of reaction kinetic models relevant to self-ignition phenomena

The transition from deflagration to detonation of the hydrogen-air system and the hydrogen-water (steam, fog)-air system depends on the physico-chemical properties of an explosive mixture, the characteristics of the ignition process, and the interaction of ensuing deflagration waves with the environment. Critical for failure of the containment will be the pressure and time history and the resulting effective structural load. Recent investigations of the H_2-air (or O_2) self-ignition [5.20 – 5.26] have shown that the measured ignition delay times are partially in contradiction with the calculated data obtained with the established kinetic mechanism. Up to now, it has been assumed that the kinetic mechanism of the hydrogen-air system is one of the best-known reaction schemes [5.27 – 5.31]. However, the experimental results from References [5.20 – 5.22] and [5.32 – 5.34] show that in the region of "low" temperatures and also in the region of practically interesting high-pressure deviations of calculated and measured ignition delay times of more than 2 orders of magnitude occur. Figure 5.2.1.7-1 shows the typical example of the dependence of the ignition delay time τ_i on pressure p for different calculations and experiments in the form of a diagram $\tau_i = f(p)$ at a fixed level of temperature $T = \text{const.}$ ($T = 1000$ K for Figure 5.2.1.7-1).

There seems to be good agreement between theory and experiment for $p < 3$ bar, whereas for higher pressure, the devations are unacceptable. Figure 5.2.1.7-2 indicates a similar behaviour for the standard dependence of ignition delay times $\tau_i = f(T)$ at $p = \text{const.}$. The τ_i-values predicted for $T < 1100$ K are up to 10 times longer than those that were experimentally observed. The same results were obtained by comparison of calculated and measured values of τ_i taken behind oblique shock waves in stoichiometric H_2-air mixtures [5.30, 5.35].

The same features are typical for $H_2 - O_2$ mixtures. Figure 5.2.1.7-3 compares calculated and measured values of τ_i [5.20, 5.24] as a function $\tau_i = f(p)$ for several fixed levels of temperature in range $800 \text{ K} < T < 1200$ K. The figure also shows some experimental points representing $\tau_i = f(p, T)$. Numbers at the data points specify the temperature at which the corresponding τ_i values were measured. The summary of these results, including recent data from Reference [5.29] is as follows:

- At $T \approx 700 \text{ K} - 800$ K, the measured τ_i value differs from calculated values by a factor of $O(10^3)$.
- At $T \approx 800 \text{ K} - 900$ K, the difference amounts to a factor of $O(10^2)$.
- At $T \approx 900 \text{ K} - 1000$ K, the difference is more than tenfold.
- At $T > 1100$ K, the calculated dependence $\tau_i = f(p, T)$ agrees satisfactorily with the measured results.

The comparison of the calculated and measured dependence of $\tau_i = f(p,T)$ shows that available kinetic schemes fail to give a correct prediction for reactivity of H_2-air and H_2-O_2 mixtures in definite p/T ranges even when the latest recommended rate constants from, say, Reference [5.36] are used for the elementary reactions. For the DDT process, this observation is of greatest importance because it demonstrates the evidence for substantially higher reactivity of H_2-N_2-O_2 mixtures at "low" temperature, ranging from 800 K to 1000 K at pressures $p \geq$ 1MPa.

A further decisive influence is exerted by the high water vapour content present in the reactor containment under conditions of failure. Self-ignition of this H_2-air-steam mixture deviates from that of the H_2-air system. The calculated ratio $\tau_i(H_2O)/\tau_i = f(p,T,x_{H_2O})$ at fixed levels of temperature $T = 860\,K$, $T = 1000$ K, $and\, T = 1100$ K is presented in Figure 5.2.1.7-4. The time delay $\tau_i(H_2O)$ applies to "humid" H_2-air systems. Some reasonable experimental data from Reference [5.37] are given in Figure 5.2.1.7-4. A dotted line indicates a temperature $T \approx 860$ K and $x_{H_2O} = 0.07 \pm 0.03$. Again, as for "dry" mixtures, the theoretical predictions deviate significantly from the experimental data. Theory predicts an inhibition of self-ignition by addition of steam at a lower pressure than that used in the experiments.

Another important influence upon the physico-chemical processes in hydrogen oxidation is exerted by additives of NO_x, CO and CO_2, which may be formed during reactor accidents. The NO_x may be produced by the projected spark-ignition systems, and carbon-oxides will occur subseqent to oxidation of hydrocarbon compounds and concrete. The experimentally observed decrease of the τ_i value for small amounts of NO_x additives, 0.5% to 1%, can be predicted quite well for low-pressure self-ignition regime at $p < 10$ bar as is shown in Figure 5.2.1.7-5. Accordingly, it is found experimentally, [5.23, 5.33], that small (less than 1% by volume) additives of NO_2 to the lean H_2-air mixture reduce the lower detonation limit from 15.5% H_2 to 13% H_2 (in a tube of 41 mm diameter). Additives of CO did not change the value of τ_i, but transformed the type of self-ignition from mild to strong, [5.33], and promoted DDT behind the reflected shock wave. Additives of CO_2 inhibit the self-ignition not only by increasing the τ_i value but also by the transformation of strong self-ignition regime to mild regime, [5.34]. The dynamics of self-ignition phenomena was practically the same in shock waves with constant pressure and temperature and in blast waves with decreasing pressure and temperature, [5.32].

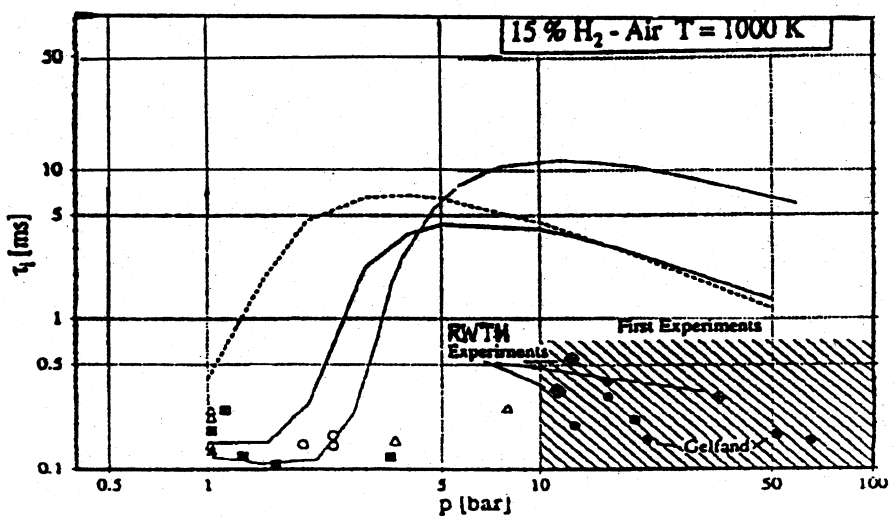

Figure 5.2.1.7-1 Ignition delay time $\tau_i = \tau_i(p)$, $T = 1000$ K (calculations and different experimental data)

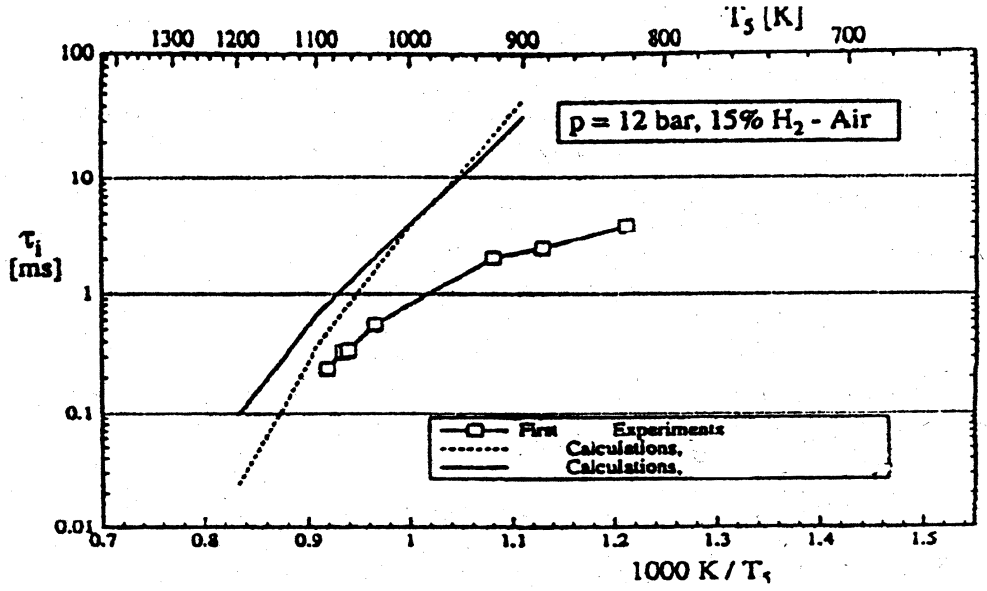

Figure 5.2.1.7-2 Ignition delay time $\tau_i = \tau_i(T)$, $p = 12$ bar (calculations and different experimental data)

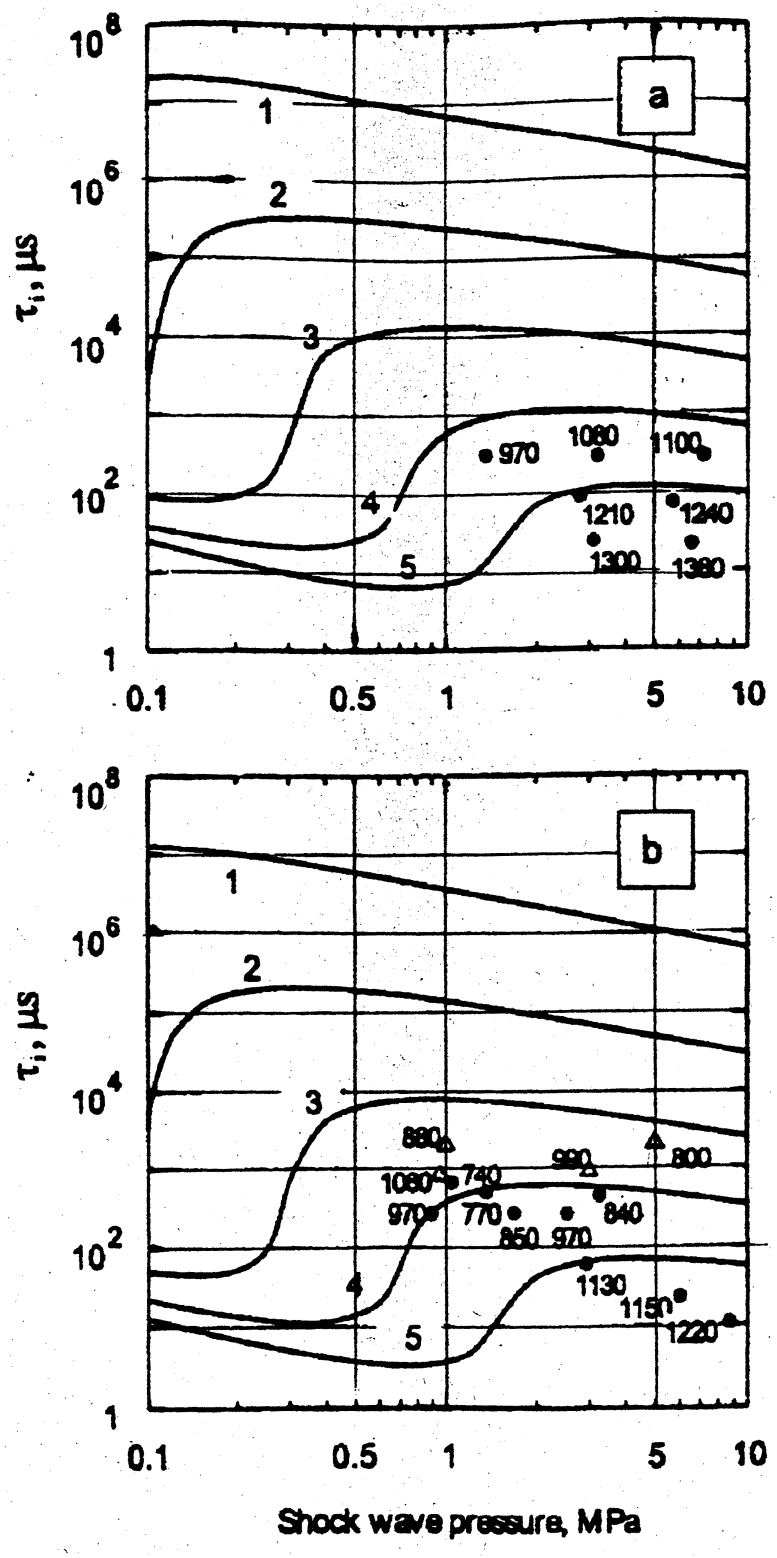

Figure 5.2.1.7-3 Comparison of measured with calculated ignition delays for (a) $0.05H_2 + 0.95O_2$ **and (b)** $0.15H_2 + 0.85O_2$ **mixtures as functions of pressure at temperartures (1)** 800 **K, (2)** 900 **K, (3)** 1000 **K, (4)** 1100 **K, and (5)** 1200 **K**

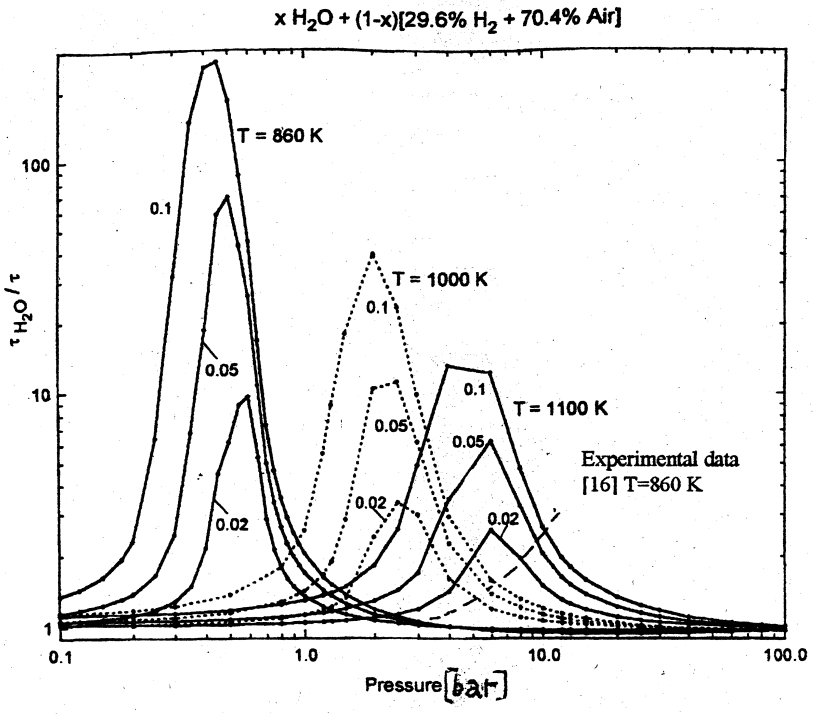

Figure 5.2.1.7-4 Influence of steam on self-ignition time delay of stoichiometric H_2-air mixtures

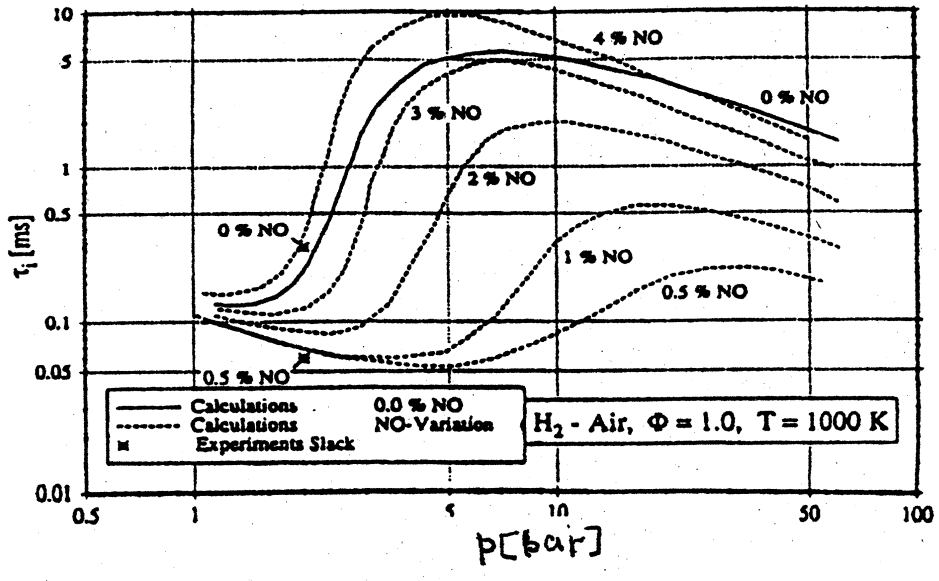

Figure 5.2.1.7-5 Ignition delay time $\tau_i = \tau_i(p)$, $T = 1000$ K; calculations were performed by RWTH Aachen and by [5.14] in comparison to experiments by Slack

5.2.1.8 *Volumetric oxidation and operating temperature limit experiments*

If a combustible mixture temperature is sufficiently high, the mixture may ignite without an external ignition source. Even at temperatures below the "auto-ignition temperature", chemical reactions occur that would tend to change the mixture composition with time. In Reference [5.38] preliminary experiments were conducted to determine the maximum vessel temperature that would result in the test mixture being injected into a heated vessel without burning. A stoichiometric H_2-air mixture at an initial pressure of 0.1 MPa was used for these experiments since it is the most sensitive mixture and thus would yield the lowest temperature limit. The results suggest that no "significant" chemical reaction occurred at $T \approx 588$ K. At $T = 700$ K, burning was observed in all cases, independent of mixture fill time. The experimental results were compared with corresponding calculated "reaction time" using CHEMKIN, a chemical kinetic code [5.39]. The measured time for ignition of the mixture upon injection was significanly shorter (about 1000 times) than the reaction times predicted by the CHEMKIN code. This indicates that either wall effects, which are not modelled in the CHEMKIN calculation, play an important role in the ignition of a mixture [5.20] or the constants used in the chemical kinetic equations are not accurate at the initial pressure and temperature conditions of the experiment as described in Reference [5.39].

5.2.2 Flame Propagation in Obstructed Areas[*]

5.2.2.1 *High-speed deflagration of gaseous mixtures*

Usually, shock waves are generated if the combustion velocities in hydrogen-air mixtures exceed $S > 100$ m/s. However, it is a well-known fact that in any mixture of gaseous fuel and air, the normal flame velocity u_n and visible flame velocity $u_v = \sigma u_n$ are well below 100 m/s. Here $\sigma = \rho_u/\rho_b$ is the expansion ratio, ρ_u is the density of the unburned mixture, and ρ_b is the density of combustion products. The investigations in References [5.40 – 5.51] showed that velocities $S > 100$ m/s in hydrogen-air mixtures can be achieved if forced turbulence of gaseous flow in an obstructed channel is used. The high speed of flame propagation is associated with the increase of the surface burning because of turbulence at obstacles. The kinetic differences in chemical processes in the case of combustion in obstructed channels are not significant.

To study the effect of obstacles on gaseous combustion various systems were used: separate perforated screens, a set of rods, spirals, and a system of screens with orifices. The obstacles were placed in a channel with diameters up to 2.5 m and in volumes with cylindrical symmetry. A set of tests was done in a series of concentric perforated spheres. The simplest types of obstructed channels are tubes with repeated steps or obstacles, or rough tubes. These constructions were used for the investigations of accelerating or quasi-stationary regimes of combustion with velocities $S > a$, where a is the speed of sound in the unburnt mixture, in tubes with diameters $d = 50 - 300$ mm and lengths $L = 3 - 12$ m. The appearance of pressure waves capable of causing self-ignition [5.40 – 5.51], expands the range of dangerous situations and requires special investigations.

5.2.2.2 *Main results of studies of explosion regimes*

To select the method of investigation and determine the range of initial conditions for possible future research, it is necessary to analyze the main results from previous studies on combustion regimes of hydrogen-air mixtures in (fully or partially) obstructed volumes. Unfortunately, up to now most of the

[*] Contributed by Professor B. E. Gelfand

Table 5.2.2.2-1 Initial experimental conditions from References [5.40 – 5.55]

P_0[bar]	T_0 [K]	%H_2	%H_2 =	%CO_2	%N_2	L_Ξ	L_{obs}	BR	δ [mm]	s [mm]	s/δ	L_{obs}/s	Obst.Type	[ref]
1	293	10 – 45		0 – 15	0 – 15	9	3	0.28 – 0.6	50 150 300	50 150 300	1 1 1	60 20 10	spiral rings	[5.42]
1	293 – 353	10 – 75	6 – 40			6	3	0.29 – 0.7	66.6	35 60 81 120 140 242 325 490	0.52 0.9 1.2 1.8 2.1 3.6 4.87 7.35	85 50 37 25 21 12 9 6	rings	[5.44] [5.45] [5.46]
1	293 – 353	10 – 62	0 – 30			6.4	6.4	0.3	280	280	1	23	buffles	[5.52]
1	293 – 400	12 – 20	0 – 30			5.7	5.7	0.1 – 0.28	1500	1100 550 275	0.73 0.36 0.18	5 10 21	cylindr. tubes	[5.48] [5.49]
1	293	10 – 25				2	0.9 – 1.35	0.5 – 0.71	54	50 – 480	0.93 – 0.89	12 24	rings	[5.50]
1	293	10 – 25				12	6	0.6	350	500	1.43	12	rings	[5.50]
1	293	9.8 – 12.5				34.6	34.6	0.3 – 0.6	2300 • 2500	2500 5000 •		12 6 •	concr. blocks	[5.51]
1	300 – 650	10 – 30	9 – 25			21.3	21.3	0.43	270	270	1	78	rings	[5.43] [5.54] [5.55]

data cited were from Reference [5.42]. Table 5.2.2.2-1 presents the data on the initial conditions in the investigations [5.40 – 5.51] on fast combustion regimes in hydrogen-air mixtures for a wider spectrum of tests.

The following information about combustible mixture properties is helpful for further discussion:

- normal flame velocity - u_n
- sound velocity in unburned mixture - a
- expansion ratio after burning - σ

Figure 5.2.2.2-1 presents the dependence of the above-mentioned parameters on the hydrogen volume content in air [5.46]. The values u_n and σ characterize the ability of the reaction. The sound speed a is a reference value for propagation regime classification in obstructed channels through the expression S/a.

The measurements in Reference [5.42] showed that the main parameter responsible for flame propagation velocity is the composition of the mixture. Figures 5.2.2.2-2 and 5.2.2.2-3 show the dependence of flame velocity in hydrogen-air mixtures in a channel containing obstructed and smooth parts. The obstructed part has blockage ratios of $BR = 0.4 \text{ to } 0.6$. The volume fraction of hydrogen was varied in a range $10\% \text{ to } 30\%$, but for practical applications the data with hydrogen content $10\% \text{ to } 20\%$ are especially important. No detonation was obtained for mixtures with hydrogen volume fractions of $< 12\%$, but at a length of $\approx 1\text{m}$, the acceleration of a flame up to a quasi-steady value of $S \approx 700\text{m/s}$ was detected; i.e. $S/a > 1$.

Subsonic regimes of fast deflagrations were pointed out in mixtures with hydrogen volume fraction of 10% to 30% in air. Figure 5.2.2.2-4 gives an overview of the measured levels of maximum flame velocities in obstructed channels with different types of obstacles (Schelkin spiral, a system of perforated screens with step $s = \delta$ in tube with diameter $\delta = 50\text{mm}$). At $s/\delta = 1$ and hydrogen volume fraction of $< 20\%$ neither the type of obstacles, nor the level of obstruction influence the explosion process. Further investigations showed that the diameter of the channel has also only a small effect on the combustion if the holding blockage ratio (BR) and the ratio s/δ are kept constant.

The studies in References [5.40,5.41,5.47] revealed the influence of the obstacle step height on the change of flame velocity. Figure 5.2.2.2-5 summarizes the results of experiments from References [5.44 – 5.47] for the mixture with hydrogen volume content of 16% and 24% in a channel with $BR = 0.69$. At $s/\delta < 1.8$ and hydrogen volume fraction of $< 16\%$, the distance between obstacles influences the flame velocity very slightly. Note that the effect of s/δ parameter on the maximal flame velocity in a channel at $10 > s/D > 3$. A summary of the effect of parameter s/δ is presented in Figure 5.2.2.2-6. Using various spacings between obstacles, one can change the type of explosion process. Figure 5.2.2.2-5(a,b) also presents the effect of a single diaphragm on the flame velocity. The diaphragm is placed at a distance of $100\ \text{mm}$ from the source of ignition in mixtures containing 16% and 24% hydrogen. Horizontal lines in Figure 5.2.2.2-5(a,b) represent the sound velocities in an unburned mixture. The change of explosion dynamics of a stoichiometric mixture diluted by a water-steam mixture in an obstructed channel [5.47] is shown in Figure 5.2.2.2-7. Dilution by more than 30% (vol) steam results in a drastic deceleration of the flame down to subsonic values at the exit of the obstructed part. In Reference [5.47] contradictory data are presented about the influence of initial temperature on fast flame propagation in a congested channel. Beauvais et al. [5.47] concluded that an increase of the initial temperature of a given mixture can have enhancing or damping effect on turbulent flame acceleration, depending on the geometrical boundary conditions. The length of the obstacle field in these experiments was likely insufficient to fully investigate the DDT phenomenon at elevated temperatures [5.53, 5.54]. The detonation run-up distance was found to decrease with increasing hydrogen mole fraction and with decreasing initial temperature.

All experimental results, obtained in a laboratory-scale facility, were confirmed by large-scale tests [5.48, 5.49, 5.51]. Quite recent results of large-scale tests are presented in Reference [5.49]. Flame acceleration tests were performed over a range of hydrogen-air-steam mixtures, obstacle spacing, blockage ratios, and igniter locations in a 1.5-m-diameter, 5.7-m-high cylindrical vessel (volume $\approx 10\ \text{m}^3$) . It was found that the flame speed increased as the hydrogen concentration increased, but decreased as the steam content increased. For accelerating flames, the flame speed rapidly increased with distance, reached a peak value, and then rapidly decreased. The peak flame speed was attained at approximately midheight. Of the diluents tested, steam was more effective than CO_2, and CO_2 was more effective than nitrogen in suppressing flame acceleration. The initial pressure had no significant effect on the flame speed. An increase in the obstacle spacing in range $0.18 < s/\delta < 0.73$ was found to decrease the peak flame speed nearly linearly. In small-scale tests [5.44, 5.45, 5.47], flame speeds did not depend on the spacing of obstacles in the range $s/\delta < 1$. Experiments performed with blockage ratios $0.1 < BR < 0.28$ indicated that peak flame speed increased as the obstacle BR increased. The direction of flame propagation did not have a significant effect on the peak flame speed.

The main result of observations in References [5.40 – 5.51] is a proof of the possibility of fast combustion regimes in obstructed channels. These regimes are accompanied by the generation of pressure waves, overtaking combustion waves. Thus the problem should be considered in the framework of unsteady interactions within a complex pressure wave-fast deflagration front system.

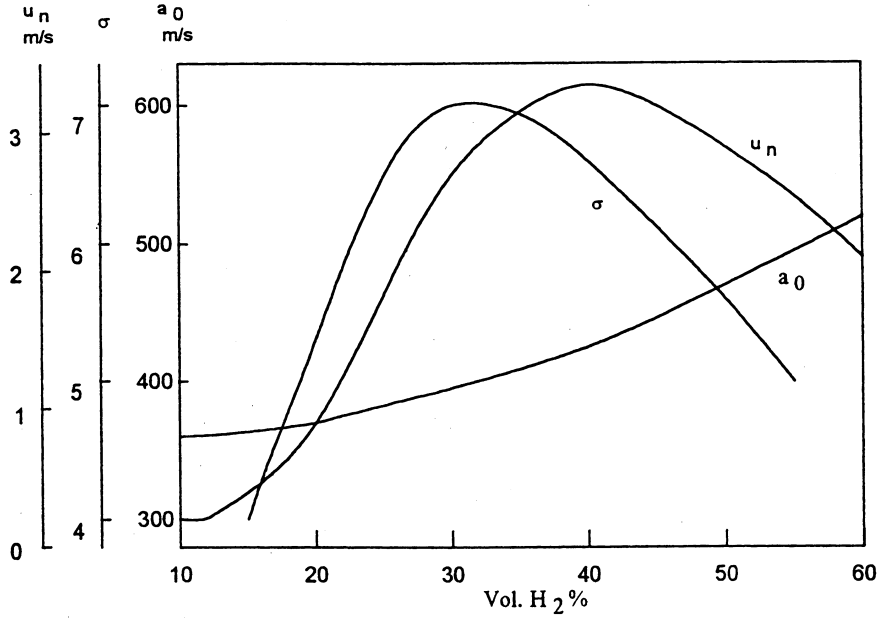

Figure 5.2.2.2-1 Normal burning velocity, speed of sound and expansion ratio of hydrogen-air mixtures

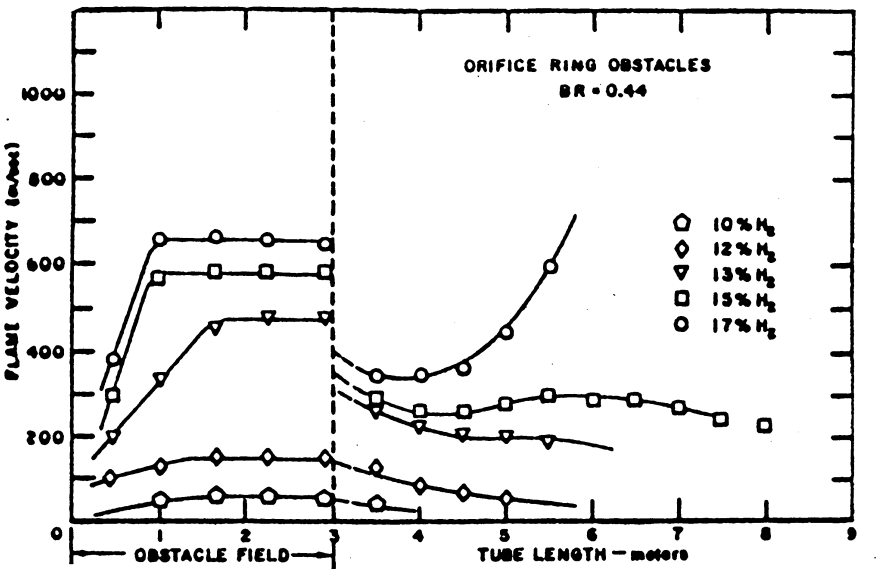

Figure 5.2.2.2-2 Variation of flame velocity along the flame tube for the orifice ring obstacles with a blockage ratio of $BR = 0.44$

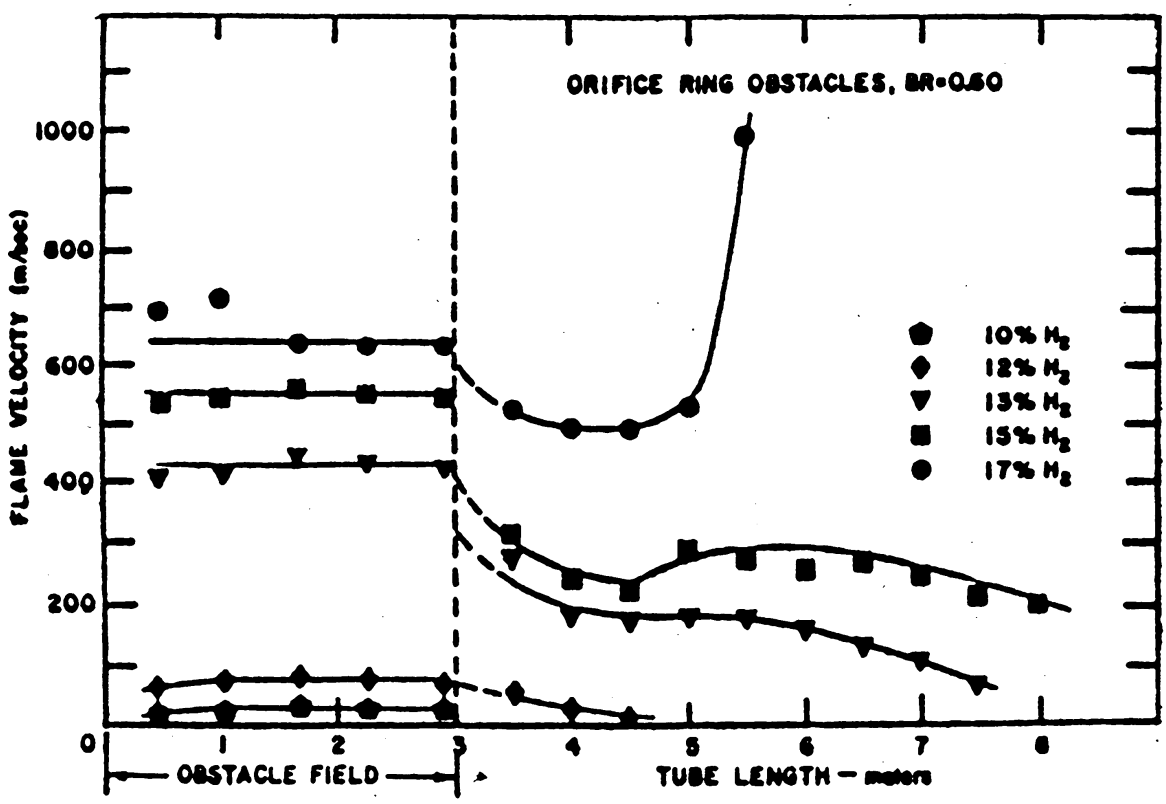

Figure 5.2.2.2-3 Variation of flame velocity along the flame tube for the orifice ring obstacles with a blockage ratio of $BR = 0.60$

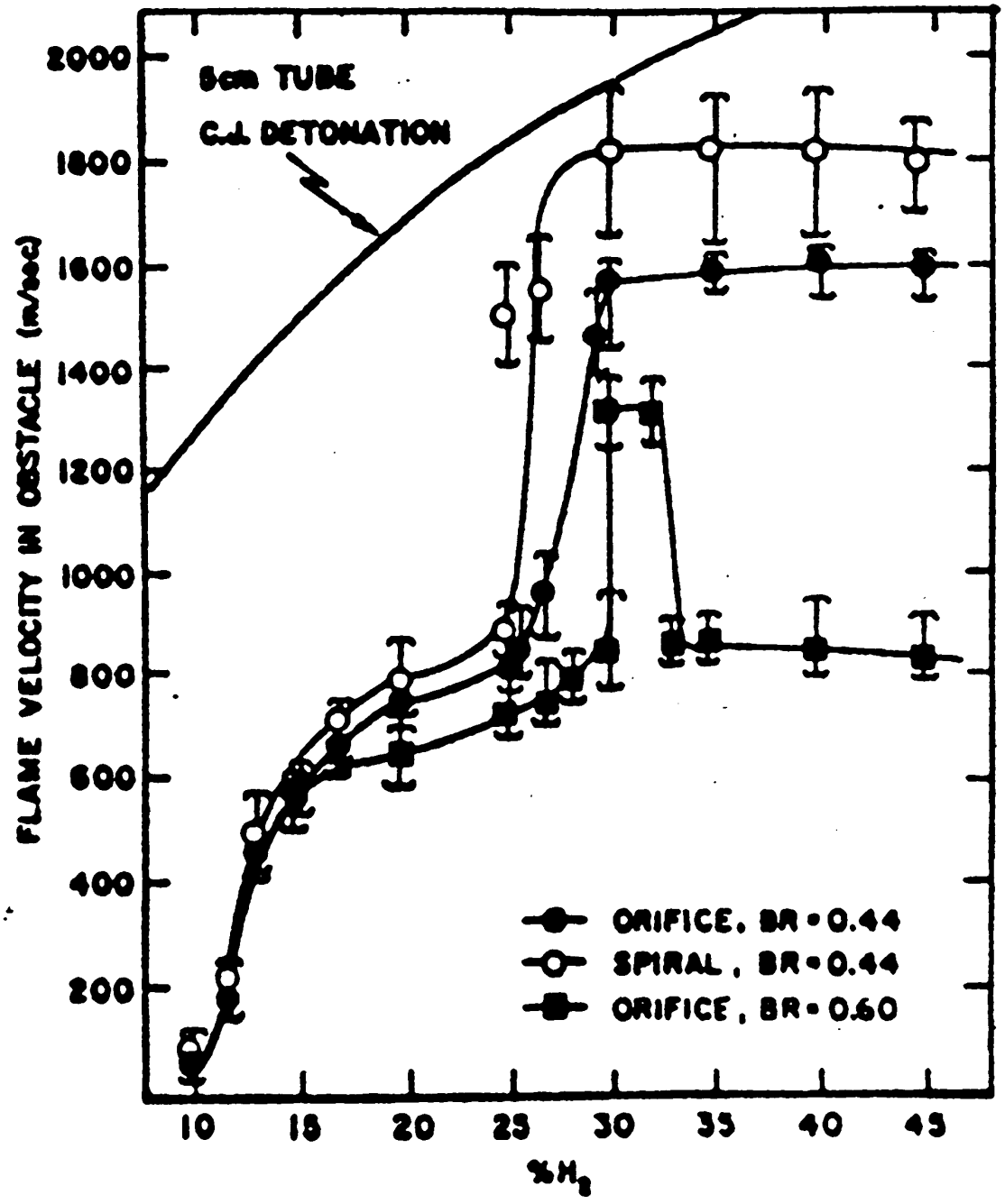

Figure 5.2.2.2-4 Variation of maximum steady-state flame velocity with composition of the H_2-air mixture

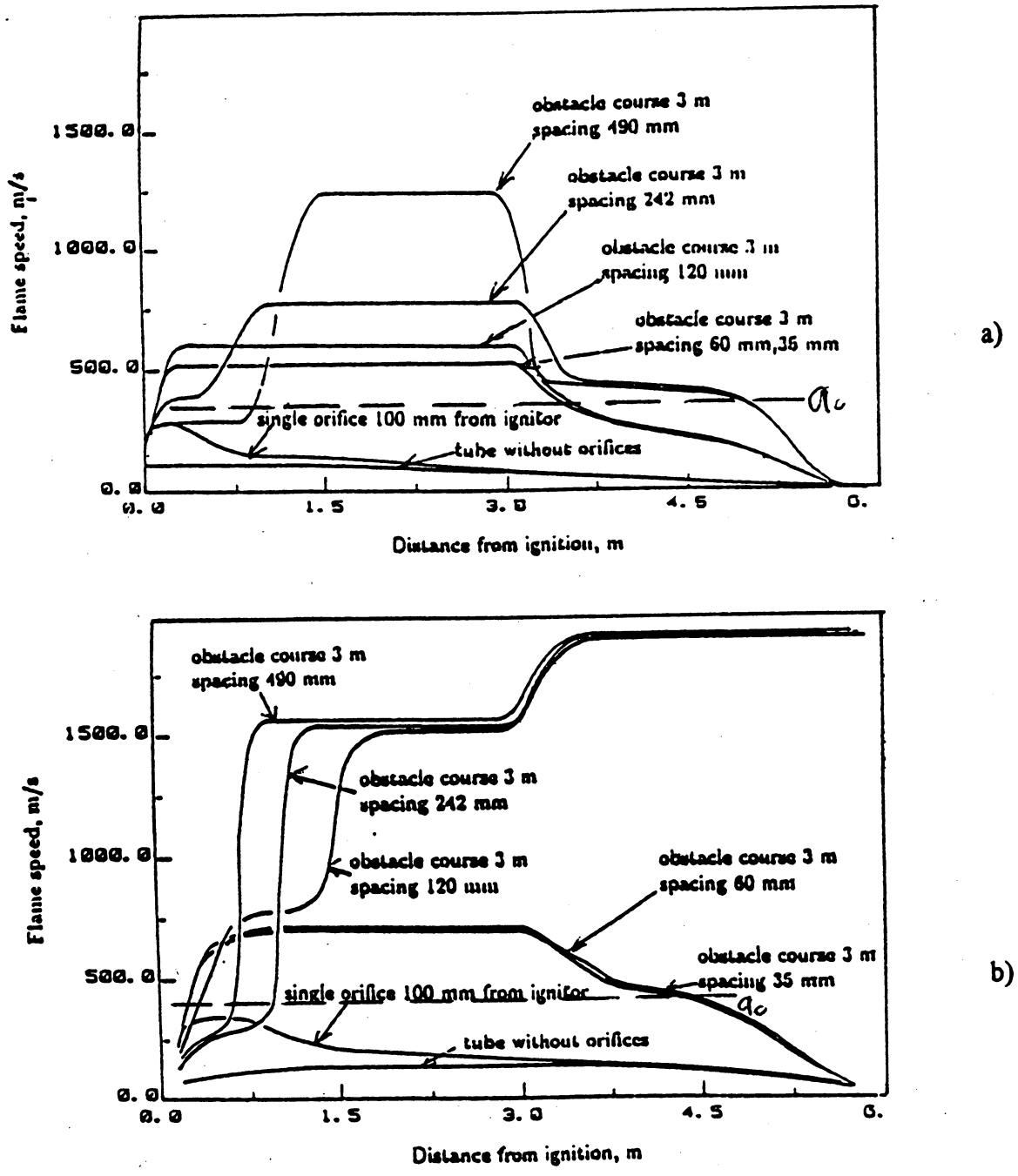

Figure 5.2.2.2-5 Flame profiles in the explosion tube for hydrogen-air mixtures. (a) $16\%H_2$**, (b)** $24\%H_2$**,** $BR = 0.7$

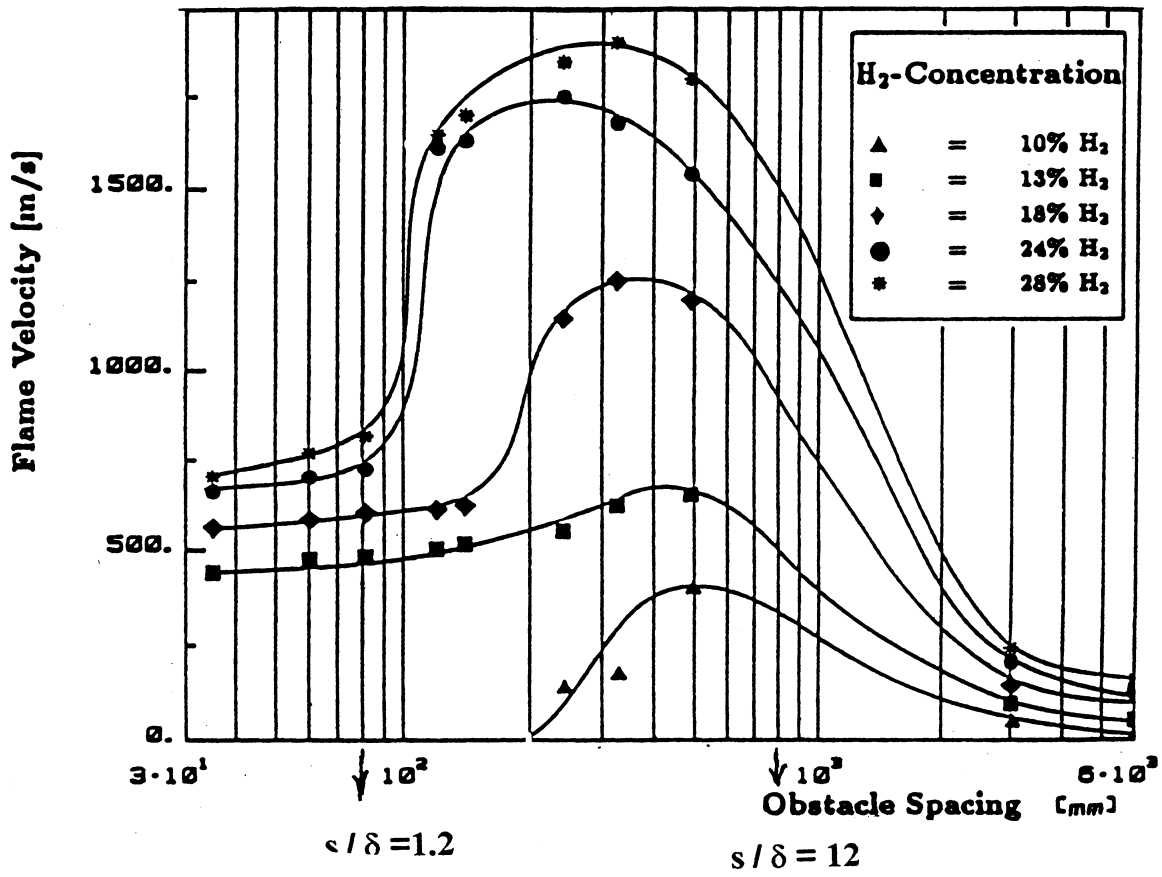

Figure 5.2.2.2-6 Maximum flame velocity as a function of obstacle spacing

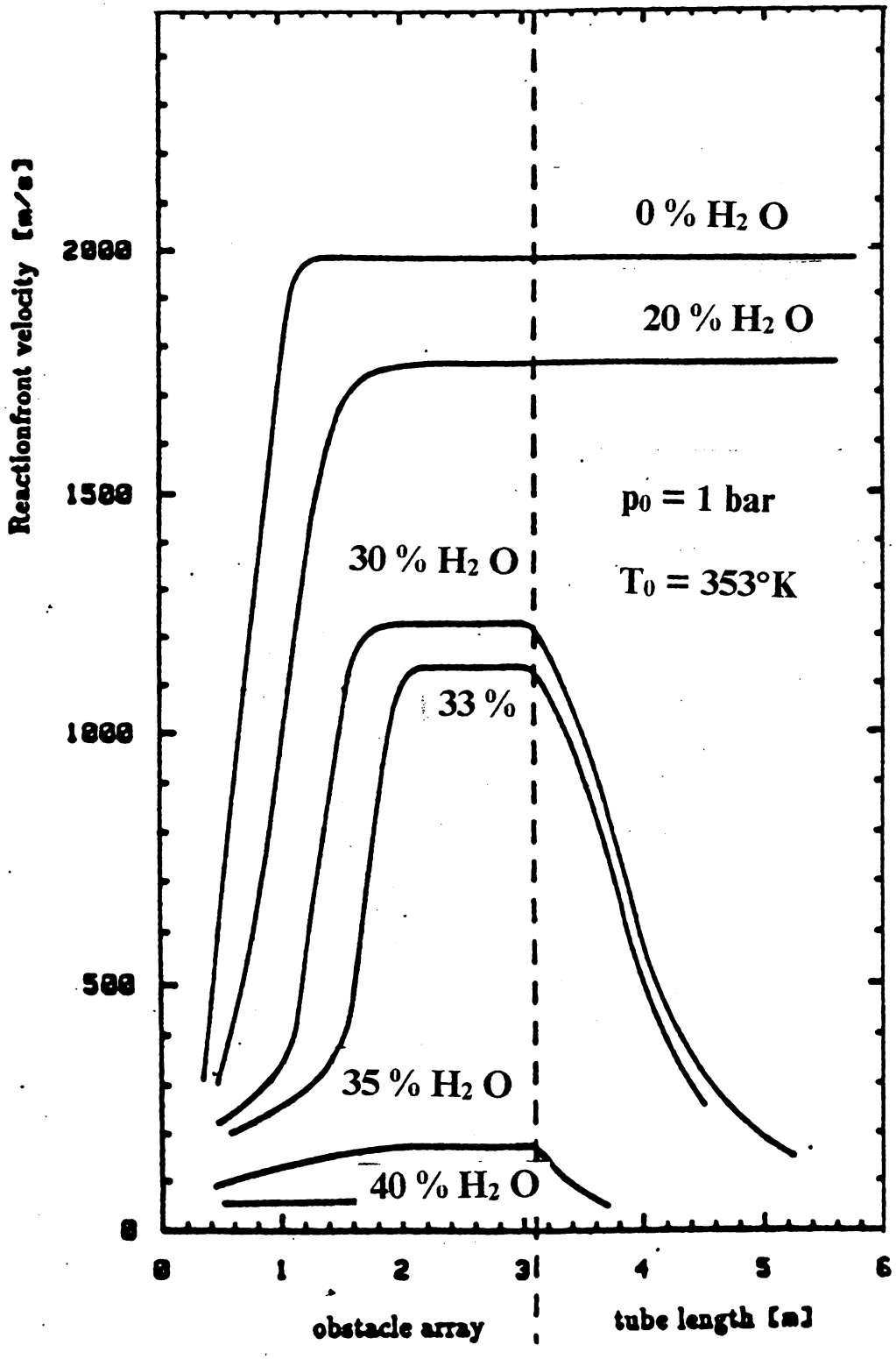

Figure 5.2.2.2-7 Variation of flame velocity along the partially obstructed tube

5.2.2.3 Influence of venting on flame propagation in obstacle-laden channels *

Experiments were performed at the Brookhaven National Laboratory (BNL) in the High-Temperature Combustion Facility (HTCF) to study the influence of venting on the propagation of deflagration . The experiments were jointly funded by the United States Nuclear Regulatory Commission (USNRC) and the Japanese Nuclear Power Engineering Corporation, which is sponsored by the Ministry of International Trade and Industry (MITI). The HTCF detonation tube, which can be heated up to a maximum temperature of 700 K with a temperature uniformly of $\pm 14K$, is 21.3 m long and is constructed from sections of stainless steel with an internal diameter of 273 mm. (see Figure 5.2.2.3-1). The test gases are mixed in a chamber fed with two pipes: one flowing air at room temperature and on the other a heated mixture of hydrogen and steam. The desired mixture composition is achieved by varying the individual constituent flow rates via choked venturis.

In the experiments investigating the DDT phenomenon, a flame is ignited and it subsequently accelerates as a result of turbulence generated in the induced flow ahead of it. For certain mixtures, this FA could lead to the initiation of a detonation wave. In order to promote flame acceleration, periodic orifice plates are installed down the length of the entire detonation tube. The orifice plates have an outer diameter of 273 mm (equivalent to the inner diameter of the tube), an inner diameter of 206 mm ($BR = 0.43$), and have a spacing of one tube diameter. A standard automobile diesel engine glow plug is used to ignite the test mixture at one end of the tube.

For venting experiments, the main modification of the detonation vessel was the addition of four vent sections that were inserted between non-vented pipe sections. Figure 5.2.2.3-2 shows a photograph of the detonation tube equipped with vent sections, and Figure 5.2.2.3-3 shows a schematic sketch of a vent section. These vent section consist of two standard pipe-crosses butt-welded together, with each pipe-cross having the same inner diameter as the detonation tube. The total vent area per vent section is thus 4 times the detonation tube cross-section area (5.1% of the total vessel surface). The vent openings are initially closed by vent covers that are dislodged when the vessel pressure increases as a result of combustion. The welded pipe-crosses are matted to the straight pipe sections using compatible flanges. The length of a vent section is 1.52 m, which is exactly half the length of a standard HTCF straight pipe section. In order to maintain the same total vessel-length-to-diameter ratio (e.g., 78) as the vessel without the vent sections, two of the straight sections are not utilized in the present experiments. In this way, five straight sections are not utilized in the present experiments, and five straight pipe sections are separated from each other by one of the four vent sections.

The parameters that most influence the FA process are the mixture composition, which includes the hydrogen concentration and the steam dilution, and the mixture's initial temperature. The hydrogen concentration was varied from a minimum where benign flames were produced to a maximum where vent covers were dislodged from their tethers. The initial temperature was varied between 300 K and 650 K, and the initial pressure was 0.1 MPa for all tests. In general, for the test apparatus configuration studied, venting reduced the likelihood of DDT at all initial temperatures tested. Flame propagation in the vented tube geometry consists of an initial FA phase followed by a quasi-steady-state phase where the combustion front velocity oscillates about a mean. The various flame propagation regimes have been classified as (1) slow deflagrations, (2) choking, and (3) detonation.

Slow deflagrations. The flame propagation in these various regimes is qualitatively similar to that observed in the test without venting, except for local perturbations induced by the vent sections. In the

* Contributed by Dr. A. Malliakos

slow deflagration regime, the flame accelerates to a maximum velocity of $100 \text{ to } 200 \text{ m/s}$ around the first vent section and then for the remainder of the tube decelerates to a velocity on the order of metres per second. No significant pressure is generated in this propagation regime.

Choking regime. In the choking regime, flame acceleration is followed by an oscillatory propagation mode where the flame accelerates in the tube section and decelerates across the vent section. The mean flame velocity during the oscillatory propagation is just under the speed of sound in the burnt products. The structure of the combustion front consists of a turbulent flame preceded by a weak precursor shock wave and a stronger leading shock wave. The leading shock wave is generated as a result of the coalescing of compression waves generated ahead of the turbulent flame. This leading shock wave has a typical pressure rise just under the adiabatic isochoric complete combustion (AICC) pressure. The weak wave is generated by decoupling of the leading shock wave and the flame during their passage through the vent section. Therefore, the weak precursor wave is a product of the leading shock wave after it emerges from the vent section.

Detonation regime. In the detonation propagation regime, which exists for particularly sensitive mixtures, a detonation wave is initiated at some point during FA. In all the cases tested, the detonation wave failed before the end of the vessel as a result of wave diffraction in the vent section. However, one would expect that if the mixture cell size is small enough, a detonation wave could propagate through the entire vessel unimpeded by the orifice plates at the venting.

The influence of venting on the combustion phenomenon could be measured by the magnitude of change in the choking and the DDT limits from tests without venting to tests with venting. The choking limit, which is in effect the minimum hydrogen composition where significant FA takes place, increased for all initial temperatures and steam dilution in the experiments with venting. The DDT limit, which in this case is defined as the minimum hydrogen composition where a detonation is observed, was equally affected by venting. For example, for hydrogen-air mixtures at 500 K, the DDT limits increased from 12% hydrogen with no venting to 15% hydrogen with venting. The study without venting had shown that for hydrogen-air mixtures at 500 K, the DDT limit criterion was $d/\lambda = 1$. In the present study with venting, for hydrogen-air mixtures at 500 K, the DDT limit is $d/\lambda = 5.5$.

Table 5.2.2.3-1 Choking and DDT limits for hydrogen-air mixtures

Temp (K)	Choking Limit		DDT Limit			
	No Venting	Venting	No Venting		Venting	
	Hydrogen [vol %]	Hydrogen [vol %]	Hydrogen [vol %]	d/λ [–]	Hydrogen [vol %]	d/λ [–]
300	11	12	15	1.0	N.A.	
500	8	11	12	1.5	15	5.5
650	11	13	11	5.5	13	11.9

Table 5.2.2.3-1 shows the choking and DDT limits for hydrogen-air mixtures for test with and without venting. Table 5.2.2.3-2 shows the same limits for hydrogen-air-steam mixtures for tests with and without venting. Figures 5.2.2.3-4 and 5.2.2.3-5 show a comparison of the combustion front velocity versus distance for a 10% and a 15% hydrogen-air mixture at 500 K with and without venting respectively.

Table 5.2.2.3-2 Choking and DDT limits for hydrogen-air-steam mixtures

Temp (K)	Choking Limit			DDT Limit			
	H_2O [vol %]	No Venting	Venting	No Venting		Venting	
		Hydrogen [vol %]	Hydrogen [vol %]	Hydrogen [vol %]	d/λ [–]	Hydrogen [vol %]	d/λ [–]
400	10	12	12	18	0.7	N.A.	
500	25	14	15	24	1.5	N.A.	
650	25	16	18	19	0.8	23	5.7

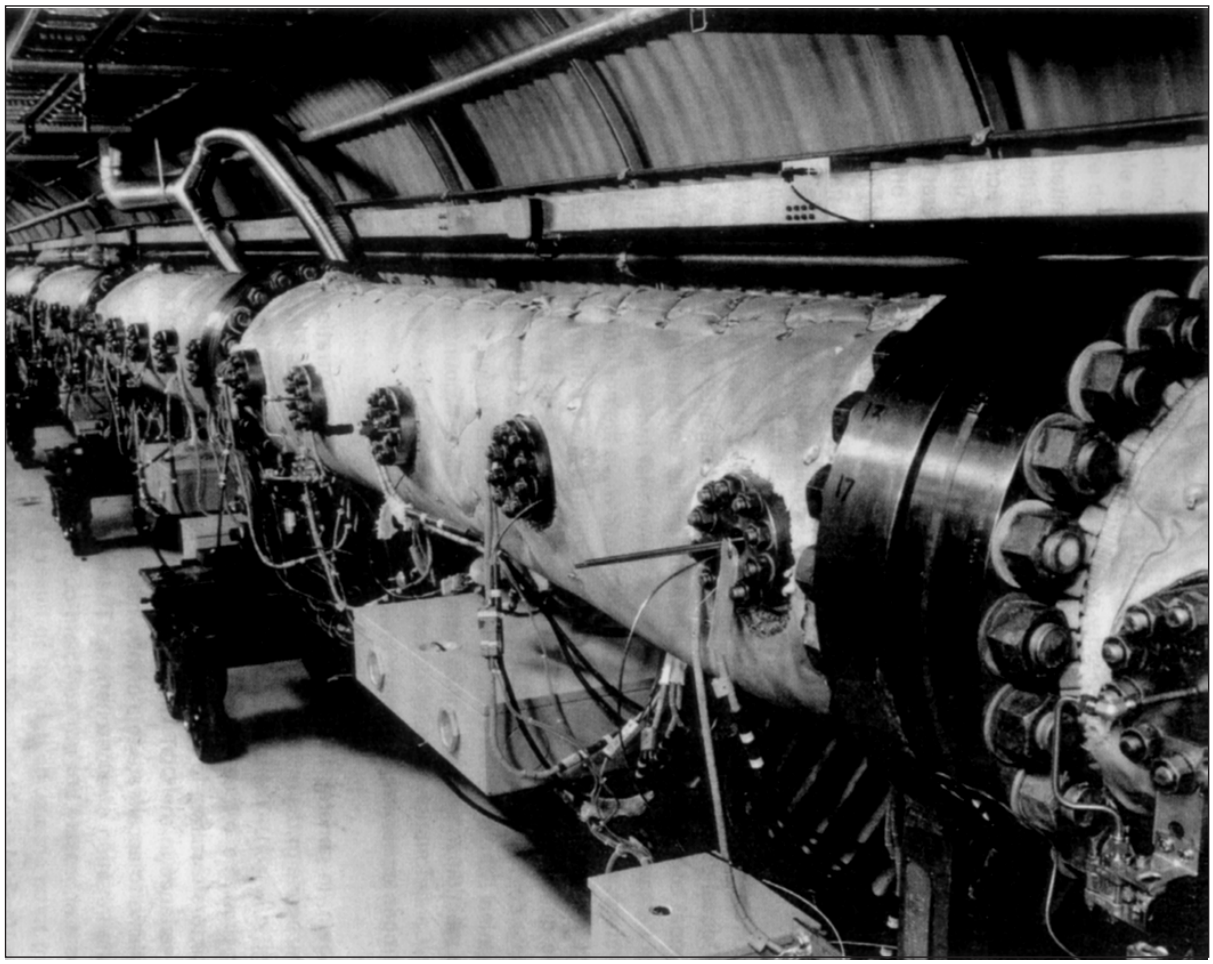

Figure 5.2.2.3-1 Photograph of the HTCF detonation tube located inside the 3.05-m tunnel

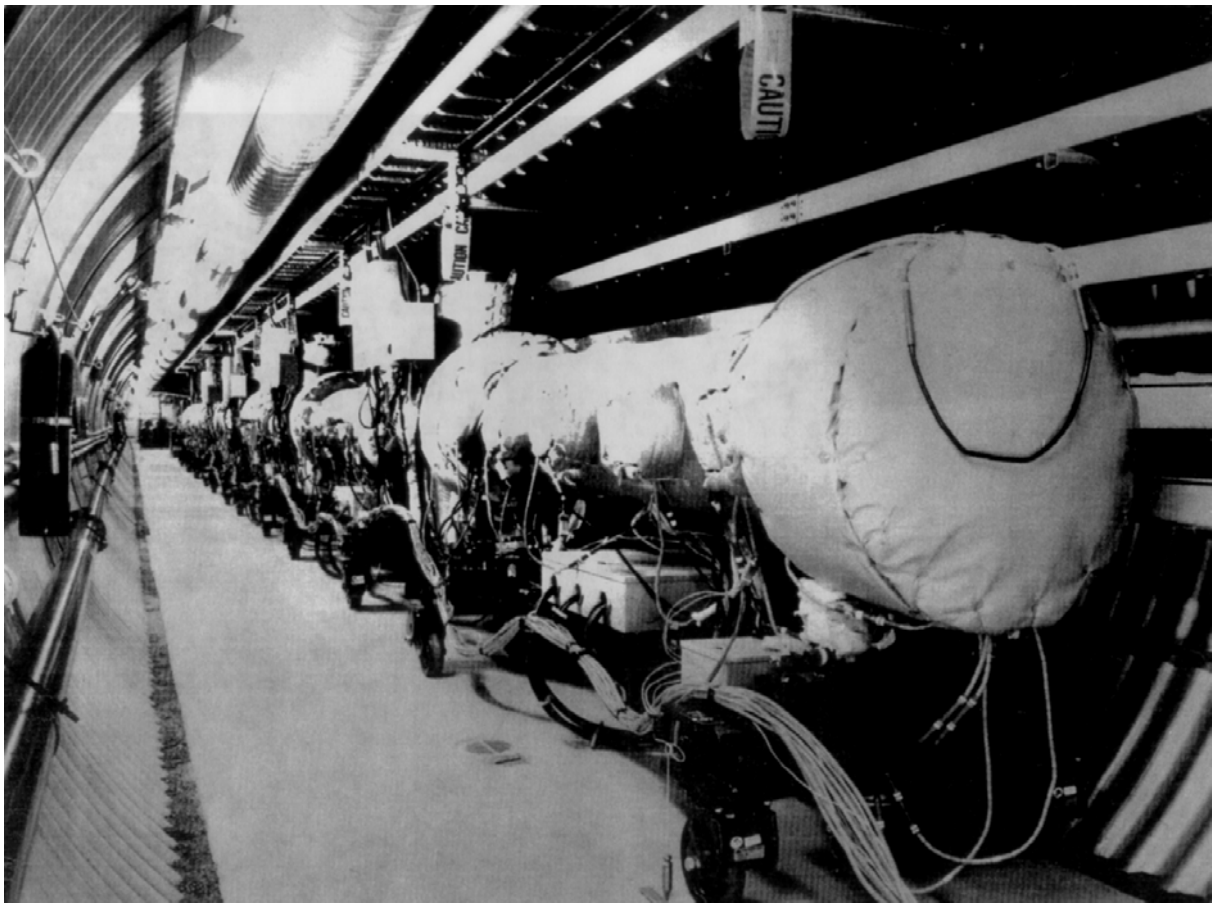

Figure 5.2.2.3-2 Photograph of the HTCF detonation tube equipped with vent sections

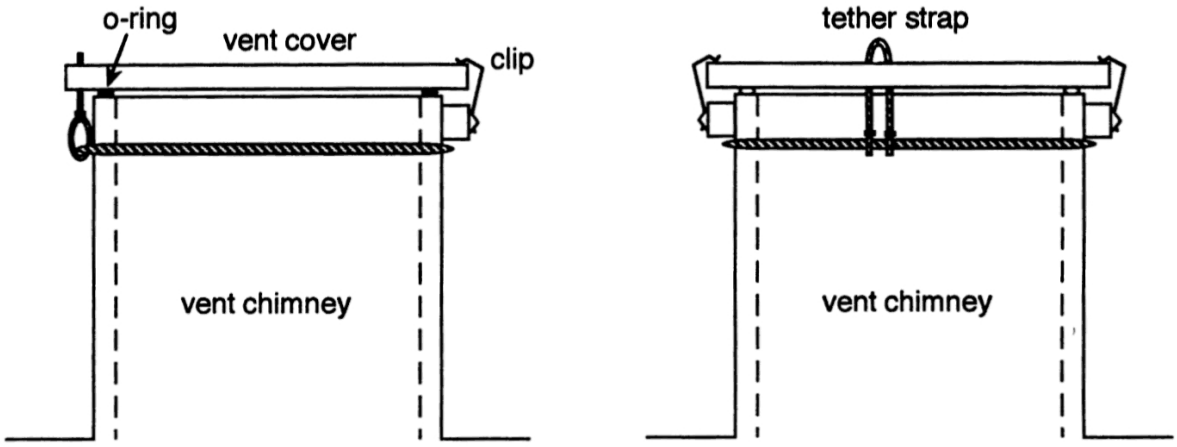

Figure 5.2.2.3-3 Schematic of vent cover tether strap and clip assembly, HTCF Facility

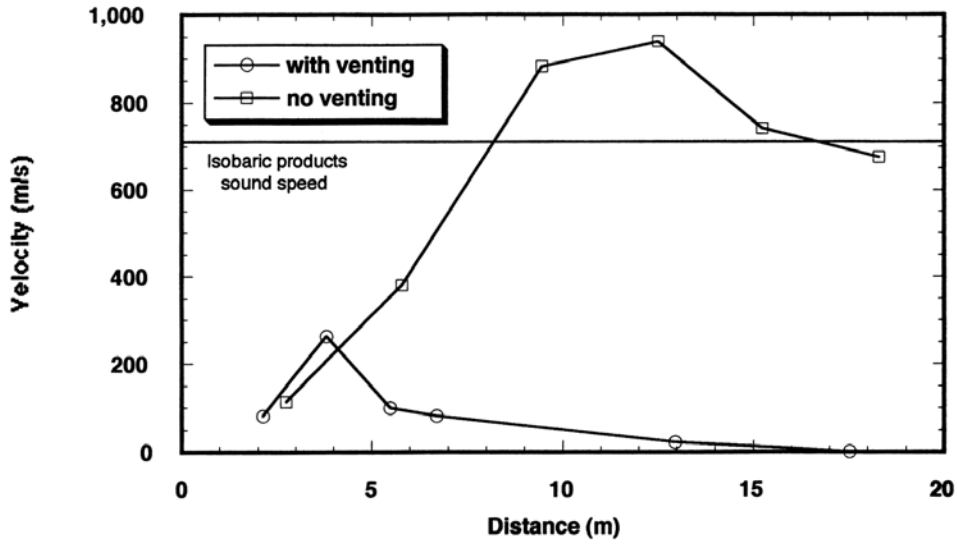

Figure 5.2.2.3-4 Comparison of the combustion front velocity versus distance for a 10% hydrogen-air mixture at 500 K with and without venting, HTCF Facility

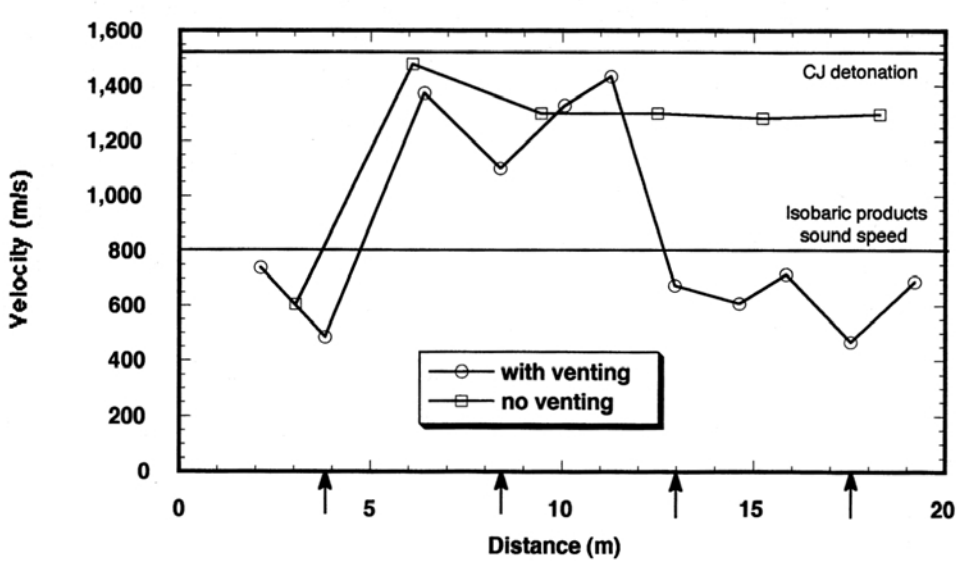

Figure 5.2.2.3-5 Comparison of the combustion front velocity versus distance for a 15% hydrogen-air mixture at 500 K with and without venting, HTCF Facility

5.2.2.4 He-air turbulence tests and modelling

In Reference [5.43] the 12-m tube was modified to allow inert tests in a shock tube mode, where a 3-m-long section can be pressurized (Figure 5.2.2.4-1). After bursting of the membrane, a shock wave travels in the remaining 9-m-long part, which is initially at low pressure (e.g., 1 bar) and contains circular rings as obstacles. The shock wave loses velocity and pressure amplitude by partial reflection and turbulence generation. The measured pressure signals at different locations can then be compared with numerical simulations using different turbulence models. These data allow us to verify the turbulence modelling under inert conditions without interference from combustion process, which is exemplarily shown for the COM3D-code in Section 5.3.3.

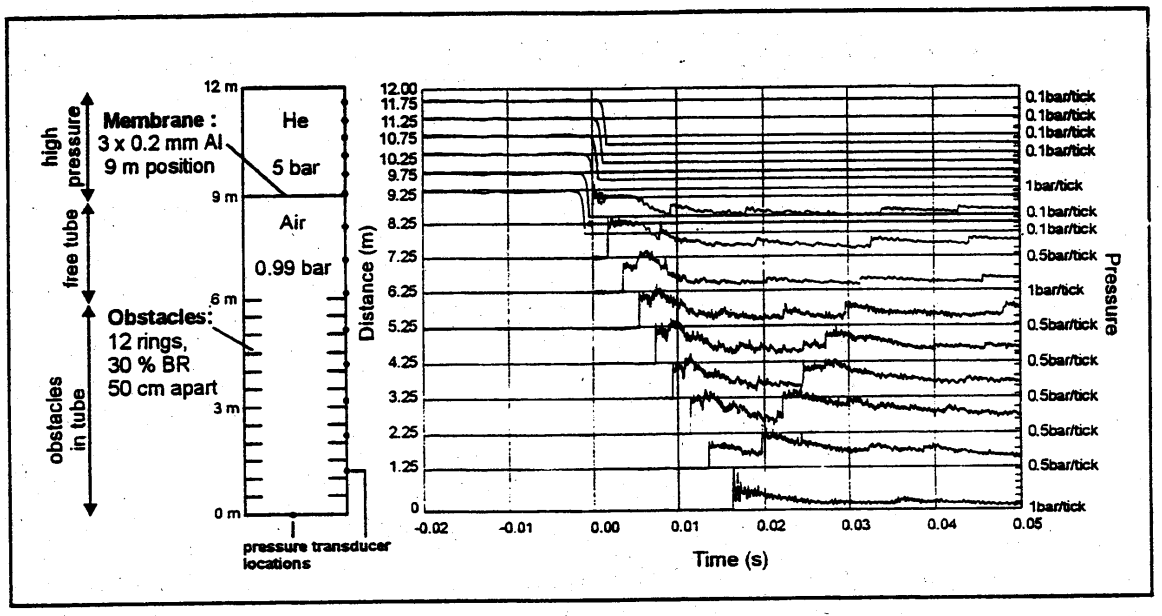

Figure 5.2.2.4-1 Inert shock tube experiments in FZK "12-m tube". The measured pressure data contain information about turbulence generation and dissipation without combustion.

5.2.3 Experiments in Large-scale and Complex Geometries[*]

5.2.3.1 Preliminary remarks

The explosion tubes, described in the previous sections, are very suitable for a first validation of computational tools for several reasons. The scale of the applied test facilities is relatively small (usually up to a volume of 1 m^3), which facilitates a very detailed investigation of the respective combustion phenomenon by means of a conventional measurement technique, with a high resolution in time and in space or optical measurement techniques. The geometries of these facilities are, in most cases, very simple (e.g., periodic obstacles in a tube) and can, therefore, be easily modelled at a very detailed level. In order to apply the numerical codes for the simulation of propagating flame fronts in realistic geometries, they have to be validated with experiments that have been performed in facilities with a scale of several magnitudes larger compared with the scale of a small-scale explosion-tube. In Figure 5.2.3.1-1, the sizes

[*] Contributed by A. Eder and Dr. M. Heitsch

Table 5.2.3.1: Recent experiments in complex and large-scale geometries

Test Facility	Country/ Operator	Geometry	Mixture	Instrumentation	Test Parameters
MuSCET	Germany, TU-Munich	286×286 mm, $L = 6.7$m	9%-16% Hydrogen	LIPF, LDV, schlieren, pressure gauges, thermocouples, photodiodes	Visualization, flame-acceleration due to obstacles
L.VIEW	Italy/ University of Pisa, TU-Munich	670×670 mm, $L = 3.2$ m	8.5%-10% Hydrogen	Video, LDV, schlieren, pressure gauges, thermocouples, volume fraction	Vizualisation, ignition and opening location, jet ignition, turbulence
AECL Interconnected Vessels	Canada/ AECL	$V_{sphere} = 2.3m^3$, $V_{cyl.} = 10.7m^3$	6-20 vol % H_2	pressure gauges	Jet ignition, independent hydrogen conc. in sphere and cylinder
LSVCTF	Canada/ AECL	$10 \times 4 \times 3m, V = 120m^3$	$8 - 14\% H_2$, Steam	Pressure gauges	Vented Combustion with different ventareas
HTCF	USA/ BNL	ID 273 mm, $L = 21.3$ m	H_2-Air-(Steam)	Photodiodes, smoked foils, fast response thermocouples and piezoelectric pressure transducers	Effect of mixtures's composition and high initial temperature on mixture's sensitivity to detonation and DDT, as well as effect of venting on DDT
Battelle Model Containment BMC	Germany/ Battelle	$D = 10$ m, $H = 10$ m, $V = 40 - 200$ m^3	7-14% Hydrogen, 0-50% Steam, (CO2)	Pressure gauges, thermocouples, IR-diodes, volume fraction, (Hot wire turbulence)	Slow and fast combustion, vented combustion, jet ignition, realistic obstacles
DN-400	Germany/ Battelle	Diameter 0.4m, $L = 8$ m, $V = 1$ m^3	8.5-17% Hydrogen, 0-40% Steam	Pressure gauges, thermocouples, IR-diodes, volume fraction, hot wire turbulence	Scaling to BMC, realistic obstacles
PHDR	Germany/ FZK	Typical L=10m,$V = 535m^3$	8-12% Hydrogen, 34-30% Steam	Pressure gauges, thermocouples, volume fraction	Scaling to BMC
NUPEC Large Scale	Japan/ NUPEC	Diameter 8m, $V = 270m^3$	8-15% Hydrogen, 0-60% Steam	Pressure gauges, thermocouples, volume fraction, video	Ignition location, spray, elevated initial pressure, transient behaviour
RUT Facility	Russia/ Kurchatov Inst.	Channel: $L = 34.6$ m, $W = 2.5$ m, $H = 2.3$ m, "Canyon:" $L = 10.55$ m, $H = 6.3$ m, $W = 2.5$ m, $V = 480$ m^3	$H_2 - Air - H_2O$-Mixtures	Photodiodes, Pressure-Gauges	Influence of mixtures sensitivity to detonation and DDT

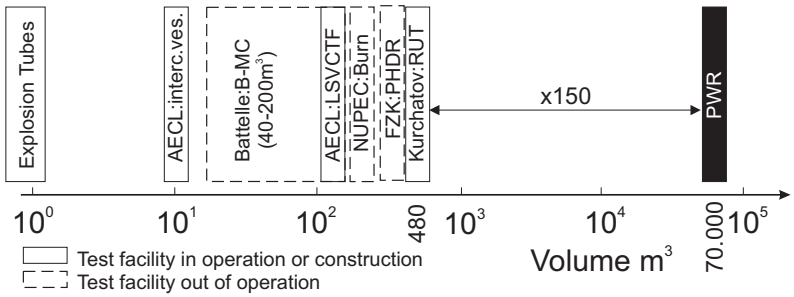

Figure 5.2.3.1-1 Scale of large-scale test facilities

of several large-scale facilities, presented among others in this section, in comparison to the size of a PWR containment are shown.

It is not possible to model realistic geometries with a full level of detail because of the enormeous requirement of computer memory. On the other hand, each grid-iron or tube in a room has, possibly, a significant influence on the propagation speed of a flame and, therefore, on the resulting pressure load on the containment structure. Nevertheless, the influence of these geometries has to be taken into account. Hence additional experiments are presented in this section, which focus on the influence of complex and realistic geometries for a containment in different scaled test facilities.

Table 5.2.3.1-1 summarizes the main parameters of the test series, which were conducted at different test facilities. A short summary of the investigated combustion phenomena, as well as the applied instrumentation, is described in this table, in order to give a general idea of which experiments should be used for a specific code validation.

5.2.3.2 Recent experiments applicable to code validation

The influence of obstacles, typical for a reactor containment (tubes, grid-irons, and doors) on the flame propagation was examined in the MuSCET Facility [5.56, 5.57] at the Technische Universität München (Figure 5.2.3.2-1). This explosion tube is equipped with a window section with an optical access for the application of optical measurement techniques (schlieren and laser-induced predissociation fluorescence (LIPF) for the investigation of the flame propagation and flame shape, laser Doppler velocimetry (LDV) for the determination of the flow velocity of the expansion flow and the turbulence-quantities). The investigated obstacles (see Figure 5.2.3.2-2) are classified into 3 categories: tubes (single tubes and tube-bundles, BR 7.5% to − 17%); grid-irons (BR 25%); and a door-opening (BR 85%).

The maximum pressure for several obstacle configurations at different hydrogen concentrations is plotted in Figure 5.2.3.2-3. The maximum pressure rise of the three obstacle categories can be summarized as follows:

- Because of the low blockage ratio of the tube obstacles, the influence on the flame velocity is low (see below). Therefore, the pressure rise for all investigated tube-shaped obstacles is low, and the differences between the tube obstacle can be neglected.
- At the grid-type obstacles, a big difference was found depending on the angle of the grid blades. With the grid blades having an angle of 45^o to the main axis of the tube, the change of the flow

direction leads to an increased turbulence intensity. This results in a higher pressure rise compared with that in the rectangular grid-iron. It is of interest to note that because of buoyancy effects the blades of the 45^o grid iron are almost rectangular to the surface of lean hydrogen-air flames.

- The highest pressure was measured in the case of the highest blocking obstacle with a blockage ratio of 85%. With this obstacle configuration, a jet was formed, leading to a strong increase of the flow velocity and the intensity of the turbulence .

The maximum measured flame velocities for different types of tube-shaped obstacles, different types of grids, and the highly blocking obstacle are shown in Figure 5.2.3.2-3. The principle behaviour of the maximum flame velocity can be directly compared to the pressure measurements shown in Figure 5.2.3.2-4.

By means of the optical measurement techniques, the flame structure in the area near the orifice could be visualized in order to identify the important physical effects responsible for FA. The investigations were performed by means of the high-speed schlieren technique as well as the laser-induced predissociation fluorescence (see References [5.58 – 5.63]). Examples of schlieren images of the flame propagation inside the empty tube without obstacles are shown in Figure 5.2.3.2-5. At low hydrogen concentrations, the flame propagation is dominated by the influence of gravity. At 9 vol % H_2, the flame merely burns at the upper part of the tube and does not propagate to the bottom of the facility. Even at 12 vol %, the gravitational effect can still be clearly identified. At the highest investigated concentration of 16 vol % ,the burning velocity dominates the gravitational effect, which leads to a spherical flame front.

The visualization of the flame propagation shows a considerable difference in the flame structure, depending on the hydrogen concentration. These differences can be explained by the instability effects that occur at hydrogen-air flames, e.g., the Rayleigh-Taylor instability or the Darrieus-Landau instability.

Nevertheless, the structure of a 9 vol % hydrogen-air flame is not as smooth as it appears to be in the schlieren images. The application of the laser-induced predissociation fluorescence (see Figure 5.2.3.2-6) identified a distributed reaction zone. Because of the instability effects (see Chapter 2), the combustion process is completely quenched at the negatively curved areas and enhanced at the positively curved cusps.

The L.VIEW Facility [5.64 – 5.68] offers the opportunity to perform medium-scaled deflagration tests with complete optical access from 2 directions simultaneously (from the front and the top side by means of a mirror placed above the test facility). The apparatus consists of a regular test section with the inner dimensions of 677 mm $\times 677$ mm $\times 3200$ mm, divided into 2 chambers, which simulate 2 connected rooms, e.g., by a door or a window. The first chamber has a length of 1050 mm and is separated from the second chamber by a wall with a central round orifice (see Figure 5.2.3.2-7). The blockage ratio of the orifice can be varied from 96% up to 99.6% in order to investigate the influence of blockage ratios on the flame propagation. The second chamber is equipped with a weak rupture disk to the ambient atmosphere with the dimension 300 mm $\times$ 300 mm at the end flange.

The conventional instrumentation consists of 7 high-speed piezo-capacitive pressure transducers and 7 thermocouples. The visualization of the flame propagation is performed by means of a standard video camera with a frame rate of 25 Hz as well as a high-speed video camera with a maximum frame rate of $40\,000$ Hz. In addition, the velocity of the expansion flow can be measured without inertia and non-intrusively for the horizontal and the vertical component with a two-component LDV system.

A representative example of the flame propagation can be seen in Figures 5.2.3.2-8 and 5.2.3.2-9. In the experiments, areas of direct ignition in the second chamber, ignition after a certain delay time, or even total flame extinction without ignition in the second chamber at all were observed, depending on the hydrogen concentration and the blockage ratio of the obstacle.

In the case of a direct ignition in the second chamber, the measured burning velocity can be compared with the velocity that is calculated with a turbulent burning correlation (e.g., Koroll et al. [5.69], Peters [5.70], Beauvais [5.71]). Because of the high turbulence intensities, which were measured in front of the flame in the middle of the second chamber, the product of the Karlovitz flame stretch factor K and the Lewis number Le exceeds the value of 0.3. Therefore, local flame quenching effects during the flame propagation in the second chamber have to be expected, as described in Abdel-Gayed and Bradley [5.72].

The integral length scale, which is an essential quantity either for the classification of the combustion process according to Borghi (see Chapter 2) or the calculation of the turbulent burning velocities (see above) could not be measured at the L.View Facility. Literature data (e.g., Lindstedt and Sakthitharan [5.73]) reveal that the integral length scale can be determined to have a value of 0.125 times the hydraulic diameter of the chamber behind a plate having a blockage ratio of 50% for combustion processes of stoichiometric methane-air flames. In Figure 5.2.3.2-10, the measured turbulent burning velocity in the second chamber is plotted versus the hydrogen concentration of the initial mixture as well as the calculated burning velocity (according to Beauvais [5.71]).

Measurements of the flame-structure during the combustion process in the second chamber by means of the laser-induced predissociation fluorescence were performed in a comparable small-scale facility at the Technische Universität München (PuFlaG Facility, [5.64]). These measurements showed that in case of a direct ignition the combustion is initiated from several ignition kernels. At a later stage, the leading flame contour, which was observed during the combustion in the first chamber, is replaced by a volumetric reaction. This corresponds to the classification of different combustion regimes as suggested by Borghi. As it can be seen in Figure 5.2.3.2-11, the combustion in the second chamber in this case is located within the regime of the "well-stirred reactor", which corresponds to the experimentally observed volumetric reaction, where similar conditions exist over a large volume.

In case of an ignition after a delay, burned gas is blown into the second chamber where it is mixed with the unburned gas. The ignition occurs with a delay of up to 1 s after the flame in the first chamber has reached the orifice. It could be observed that the flame has approximately a constant velocity over the entire length of the second chamber and that the flame velocity does not vary significantly over the cross-section of the chamber (flat shape of the flame, see example in Chapter 2), although the gas-mixture is highly inhomogeneous.

This can be explained by the transport from the first into the second chamber together with the burned gas. Once mixed with the unburned gas, these free radicals decrease the chemical induction time and, consequently, increase the burning velocity. As a result, the flame velocity reaches a high value, although the flow velocity and, thus the turbulence before the ignition is rather low (see Figure 5.2.3.2-12).

In Figure 5.2.3.2-13, the maximum pressure in the second chamber is shown as a function of the hydrogen concentration and the ignition delay. It can be seen that the direct ignition in the second chamber causes the highest pressure rise in the second chamber. This is explained by the fact that during the longer ignition delay, more exhaust gas is blown into the second chamber, which leads to a leaner mixture. Moreover, it was observed that the burning velocity is a decreasing function of the ignition delay. In case

of a longer ignition delay, a higher amount of radicals is recombined, which results in a lower radical concentration before the igntion.

The flame quenching at high turbulence intensities has been studied in detail by various authors. According to Abdel Gayed and Bradley [5.72], turbulent flame quenching occurs when the product of the Karlovitz flame stretch factor K and the Lewis number Le exceeds a value of 1.5. In case of quenching that is due to a turbulent jet, this value has to be modified to fit the conditions that have to be expected during the flame propagation between to rooms connected by an opening. This value was determined to be $K \cdot Le = 0.9$; see Figure 5.2.3.2-14.

The maximum design pressure of the L.View Facility did not allow one to perform experiments with hydrogen concentrations of more than 11 vol %. However, an increased hydrogen concentration leads to an increased laminar burning velocity that reduces the probability of flame-quenching. Small-scale experiments at the Technische Universität München (PuFlaG Facility, see above) showed that higher hydrogen concentrations lead again to a direct ignition in the second chamber (Figure 5.2.3.2-15). Because of the smaller dimension of the PuFlag Facility (diameter 80 mm), the flame quenching takes place at lower hydrogen concentrations. The reason for this can be found in the smaller integral length scale that is an important parameter for the occurrence of quenching effects.

The total extinction of the flame depends on both the initial mixture and the blockage ratio of the central orifice. A critical hydrogen concentration, at which no ignition in the second chamber occurs, was determined to be 11 vol % for an orifice diameter of 70 mm, and 9 vol % for an orifice diameter of 52 mm.

The burning of near-flammability limit hydrogen-air mixtures in interconnected vessels was examined in a Large-scale Interconnected Vessels Facility at AECL, Whiteshell Laboratories [5.74]. Figure 5.2.3.2-16 shows a schematic of the experimental apparatus. It consists of a 6-m-high and 1.5-m-diameter cylindrical vessel (volume = 10.7 m^3) and a 2.3-m-diameter sphere (volume = 6.3 m^3). The 2 vessels are joined together by a 2.7-m-long pipe with an inside diameter of 0.45 m. The entire system is rated for a pressure of 10 MPa. To vary the size of the opening between the 2 vessels, orifices of different hole diameters (30 cm and 15 cm) were mounted between the pipe and the cylinder. The hydrogen concentration was independently varied from 6 to 20 vol % in the sphere and 0 to 20 vol % in the cylinder. The initial pressures in the vessels were atmospheric. The gas mixture in the sphere was ignited at the centre by an electric spark. The facility was equipped with a gas sampling and analysis system allowing gases from various locations in the 2 vessels to be sampled and analyzed.

Upon ignition, the expanding flame kernel propagated through the pipe and subsequently emerged into the cylinder, igniting the gas mixture. Results showed that, depending on the size of the orifice, the combustible mixture in the downstream vessel was not always ignited by the flame jet emerging from the upstream vessel. These critical conditions for 8 to 14 vol % H_2 in the sphere are illustrated in Figure 5.2.3.2-17. This figure shows that for 10 vol % H_2 in the sphere, complete burning was achieved for all H_2 concentrations higher than 14 vol % in the cylinder. Since 10 vol % H_2-air mixture is above the downward flammability limit, the mixture in the sphere should be completely burned. However, for H_2 concentration in the cylinder between 8 and 12 vol %, unburned hydrogen was observed in both vessels. It is reasonable to speculate that for all these cases, the hydrogen in the sphere was completely burned, but the flame emerging from the connecting pipe failed to ignite the gas in the cylinder. The hydrogen detected in the sphere was caused by the back flow of the gas from the cylinder after the steam in the sphere had condensed. This result implies that the turbulence induced by the vent flow is capable of

causing total extinction of the flame emerging from a 15-cm-diameter hole. Since the flow velocity at the orifice depends on the opening area and the mixture composition in the upstream vessel, the critical conditions (in terms of H_2 concentration in the cylinder) should also depend on these parameters. For extinction of the 12 vol % and 14 vol % H_2 flames as they emerge from the orifice, the H_2 vol % in the cylinder needs to be less than about 10 vol % and 8 vol % H_2 respectively. It should be pointed out that no flame extinction was observed for 8 vol % H_2-air mixtures. We speculate that since the burning rate of a 8 vol % H_2-air mixture and the resulting vent flow velocity were very low, the turbulence in the vicinity of the orifice was probably not sufficient to cause a total extinction of the flame. As a result, burning may have occurred in both vessels.

The Large-scale Vented Combustion Test Facility (LSVCTF) is located at the Whiteshell Laboratories in Pinawa, Manitoba, Canada. Figure 5.2.3.2-18 shows a cutaway schematic of the facility. The facility is a 10 m long, 4 m wide, and 3 m high rectangular enclosure with an internal volume of $120\ m^3$. It is constructed of 1.25-cm-thick steel plates welded to a rigid framework of steel I-beams. The entire structure is anchored to a 1-m-thick concrete pad. Two roller-mounted movable end walls are provided to open the vessel for internal modifications or to move in bulky experimental equipment, when needed. The combustion chamber, including the end walls, is electrically trace-heated and heavily insulated to maintain temperatures in excess of 100^oC for extended periods of time. The entire combustion chamber is enclosed in an insulated metal Quonset, which houses the gas analysis and hydraulic fan systems on one side and all the process piping on the other side. Venting occurs through openings in the end walls. The end walls are covered with removable rectangular steel plates bolted to the end-wall structure. Hydraulic fans in the combustion chamber are used for mixing and to generate turbulence during ignition and combustion. The test chamber is instrumented for pre-test gas analysis, pressure transients, flame tracking, and vent velocity. The facility is located in a fenced area and is remotely operated.

The LSVCTF has been used to perform a wide variety of experiments. Some of these are

- unobstructed vented combustion experiments in 30, 60, or $120\ m^3$ volumes to evaluate the effects of scale,
- turbulent vented combustion experiments to study the effects of initial turbulence,
- flame propagation studies between interconnected compartments, and
- catalytic recombiner testing for hydrogen mitigation applications in large enclosures.

Figures 5.2.3.2-19 and 5.2.3.2-20 show some results obtained from the Large-scale Vented Combustion Test Program. Results in both figures are from experiments performed in the $120\ m^3$ geometry ([5.75], [5.76]). Figure 5.2.3.2-19 shows the variation in peak pressure with increasing vent size. As the vent area increases, the peak pressure caused by the combustion decreases. Figure 5.2.3.2-20 shows the variation in peak pressure with increasing steam concentration. As the steam concentration in the H_2-air-steam mixture increases, the peak pressure decreases.

The experiments performed at the Brookhaven National Laboratory (BNL) in the High-Temperature Combustion Facility (HTCF) showed that venting has a significant influence on both, the maximum flame speed and the transition to detonation. For a detailed description refer to Section 5.2.2.

The most comprehensive experimental program was conducted at the Battelle Model Containment ([5.77 – 5.81]). A view of this facility is given in Figure 5.2.3.2-21. More than 100 combustion

experiments were conducted in the BMC with the aim to study combustion under realistic severe accident conditions in a scaled-down volume. Tests are available from single-room arrangements with $40\ \mathrm{m}^3$ up to five-room selections with about $200\ \mathrm{m}^3$. In any case, a venting opening from the test section to the environment was included to restrict the combustion pressure rise to about 2 bar. The combustion phenomena studied in detail are ignition, slow combustion, acceleration, and jet ignition, as well as diluent impact (steam and CO_2) and obstacles. An example for the obstacle set-up is shown in Figure 5.2.3.2-22. Here, generic obstacles such as cylinders and rows of pipes with different blockage ratios were investigated apart from jets through openings of different diameters. In a simplified way the measured flame speed increases by a row of pipes in the flame path as illustrated in Figure 5.2.3.2-23. These data may be useful for model validation if larger obstacles or equipment are modelled explicitly by a code.

In order to look at scaling phenomena, the test facility DN-400 [5.82] was built. In this facility (Figure 5.2.3.2-24) that has only $1\ \mathrm{m}^3$ of volume, scaled identical obstacles were investigated and detailed measurements including turbulent fluctuations were conducted. The tests revealed a considerable scaling effect when the resulting flame speeds were compared with similar findings from the Battelle Model Containment, as shown in Figure 5.2.3.2-25. This strong effect of the test volume size on the combustion progress was identified to be mainly due to the much stronger wall effects and the missing buoyant influence in the early phase of combustion in the small facility and appeared to be challenging to applied combustion models.

A scaling to larger volume was achieved by using parts of the outdated PHDR [5.83] containment for combustion experiments (Figure 5.2.3.2-26). In this almost empty set of compartments with a volume of about $550\ \mathrm{m}^3$, tests with gas compositions typical of severe accidents including steam as a diluent were conducted. The data obtained can be used to validate combustion models in comparison with the experiments from the Battelle Model Containment.

Quite a different test facility has been operated in Japan. The NUPEC Large-scale Combustion Test Facility [5.84] is shown in Figure 5.2.3.2-27. With a volume of about $270\ \mathrm{m}^3$, it is rather big and is designed as a closed volume in contrast to the Battelle Model Containment and PHDR (vented combustion). With the numerous internal structures to represent large containment equipment such as steam generators and the connecting pipes between them, complex flame progress patterns can develop. This, together with the strong flame acceleration in the ring-like thick pipes (with internal orifices for additional flame acceleration), creates challenging situations to be simulated by combustion models. An example of possible flame branching following ignition near the bottom of one of the vertical cylinders is given in Figure 5.2.3.2-28. Very soon after ignition, the flame splits according to the available openings. Usually inside the horizontal ring-like pipes, a considerable increase of the flame speeds to several hundreds metres per second takes place coupled with local overpressures in the remainder of the test facility. As these last only short time and the test facility is completely closed the resulting long-term pressure build-up is dominated by the combustion in the main sphere. This is illustrated for different gas compositions in Figure 5.2.3.2-29.

The RUT Facility (Kurchatov Institute, Russia) was designed to investigate FA phenomena and the transition to detonations of various hydrogen-air-steam mixtures in a very large volume ($480\ \mathrm{m}^3$). It consists of a flame-acceleration section with periodic obstacles, followed by a "canyon". This facility is, therefore, very adequate for the scaling of experiments, performed in small-scale explosion tubes. The geometry of this test facility, together with the position of the instrumentation, is shown in Figure 5.2.3.2-30. For a description of representative experiments refer to Chapter 3 of this report.

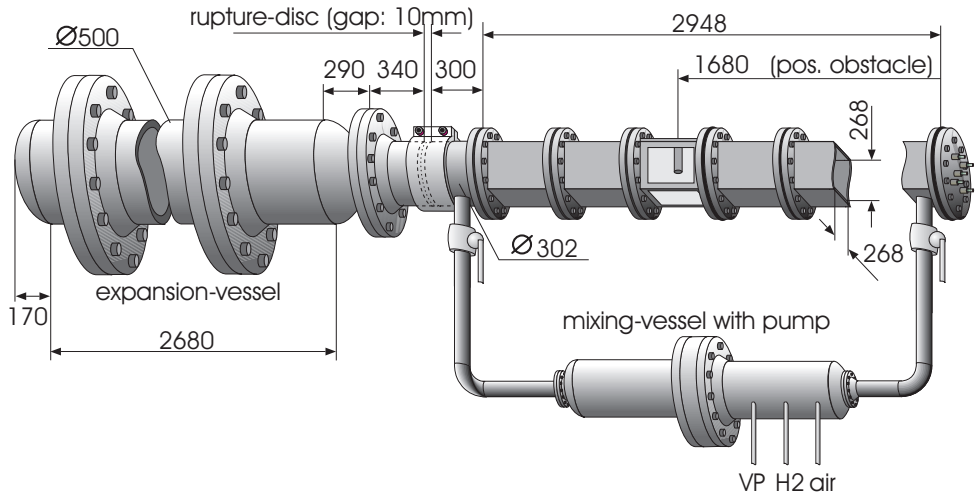

Figure 5.2.3.2-1 Geometry of the MuSCET Facility

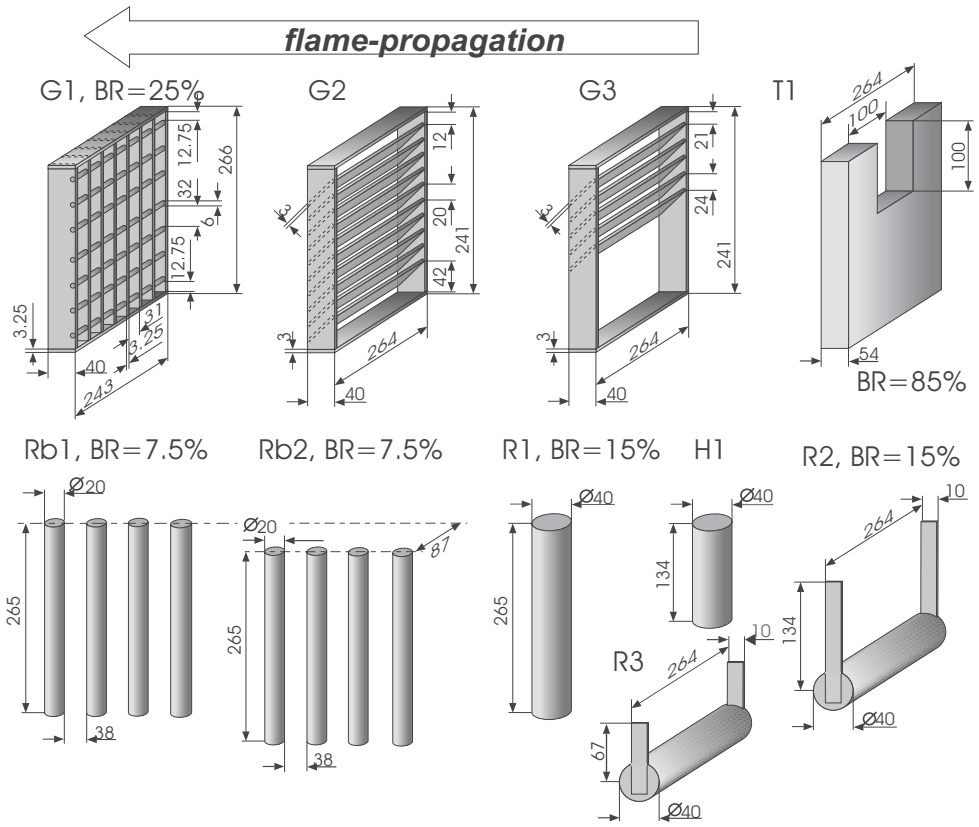

Figure 5.2.3.2-2 Containment typical obstacles investigated in the MuSCET Facility

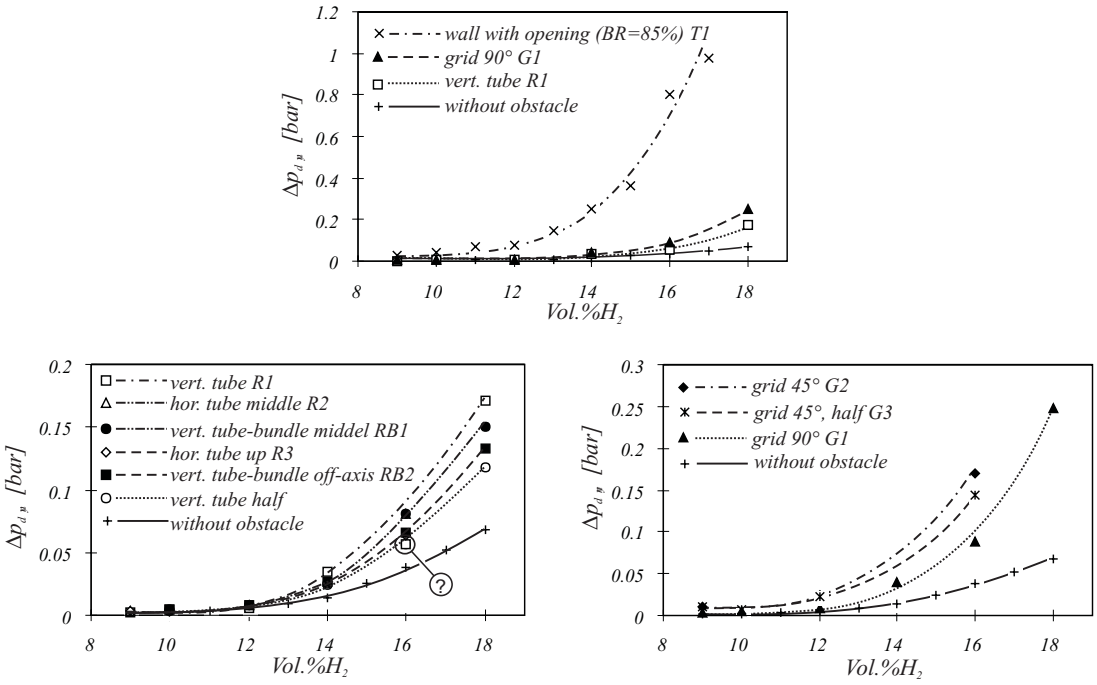

Figure 5.2.3.2-3 Maximum pressure rise for several obstacles of the MuSCET Facility

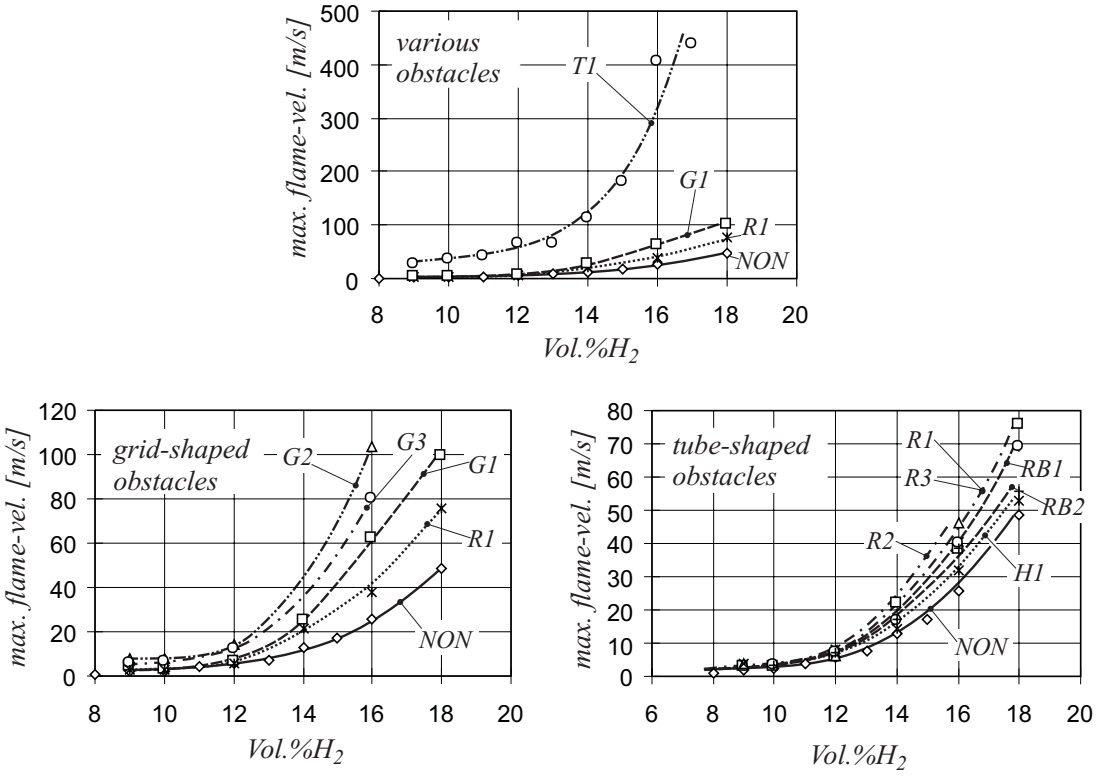

Figure 5.2.3.2-4 Maximum flame velocity behind various obstacles of the MuSCET Facility

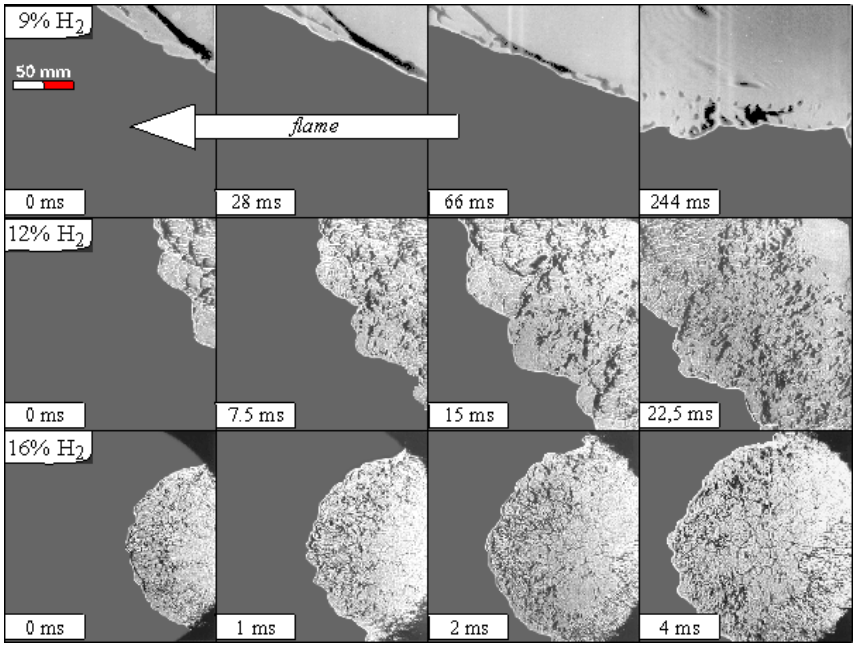

Figure 5.2.3.2-5 Schlieren images of propagating hydrogen-air flames without obstacles, MuSCET Facility

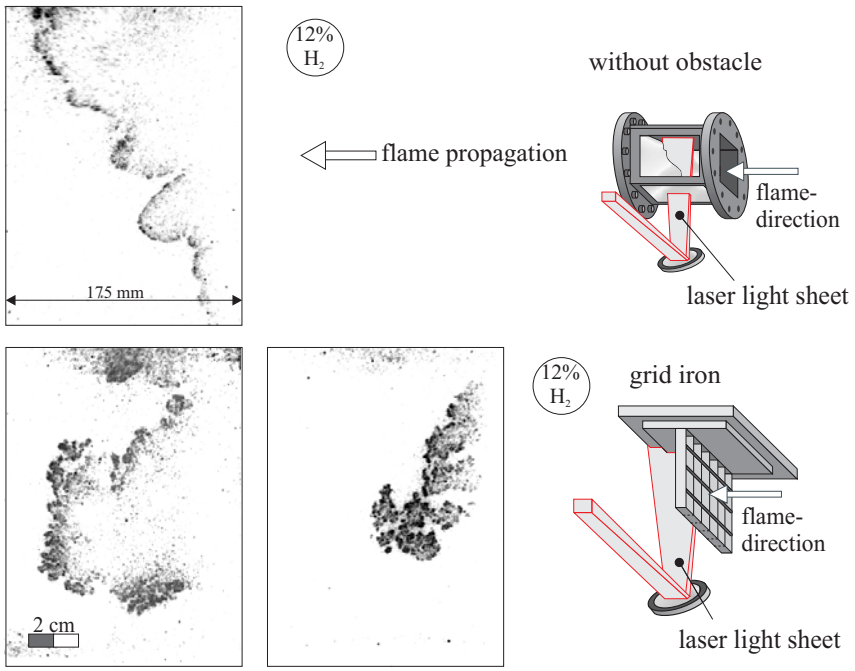

Figure 5.2.3.2-6 LIPF images of propagating hydrogen-air flames with and without being influenced by an obstacle, MuSCET Facility

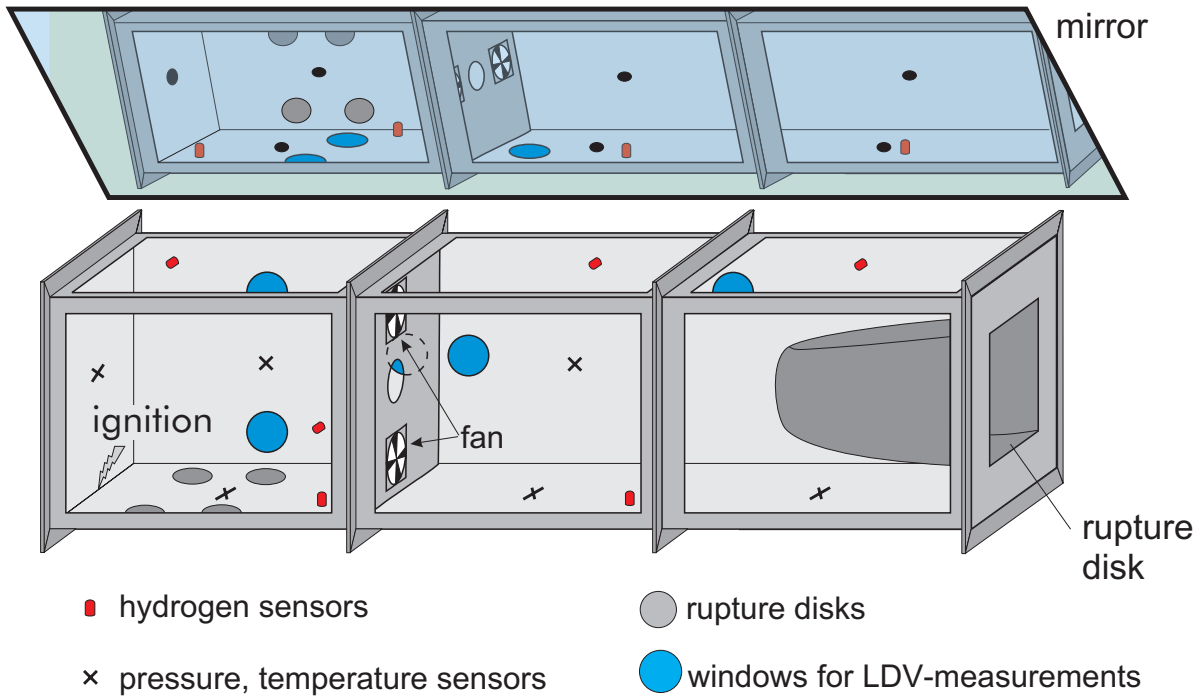

Figure 5.2.3.2-7 L.View Test Facility, University of Pisa

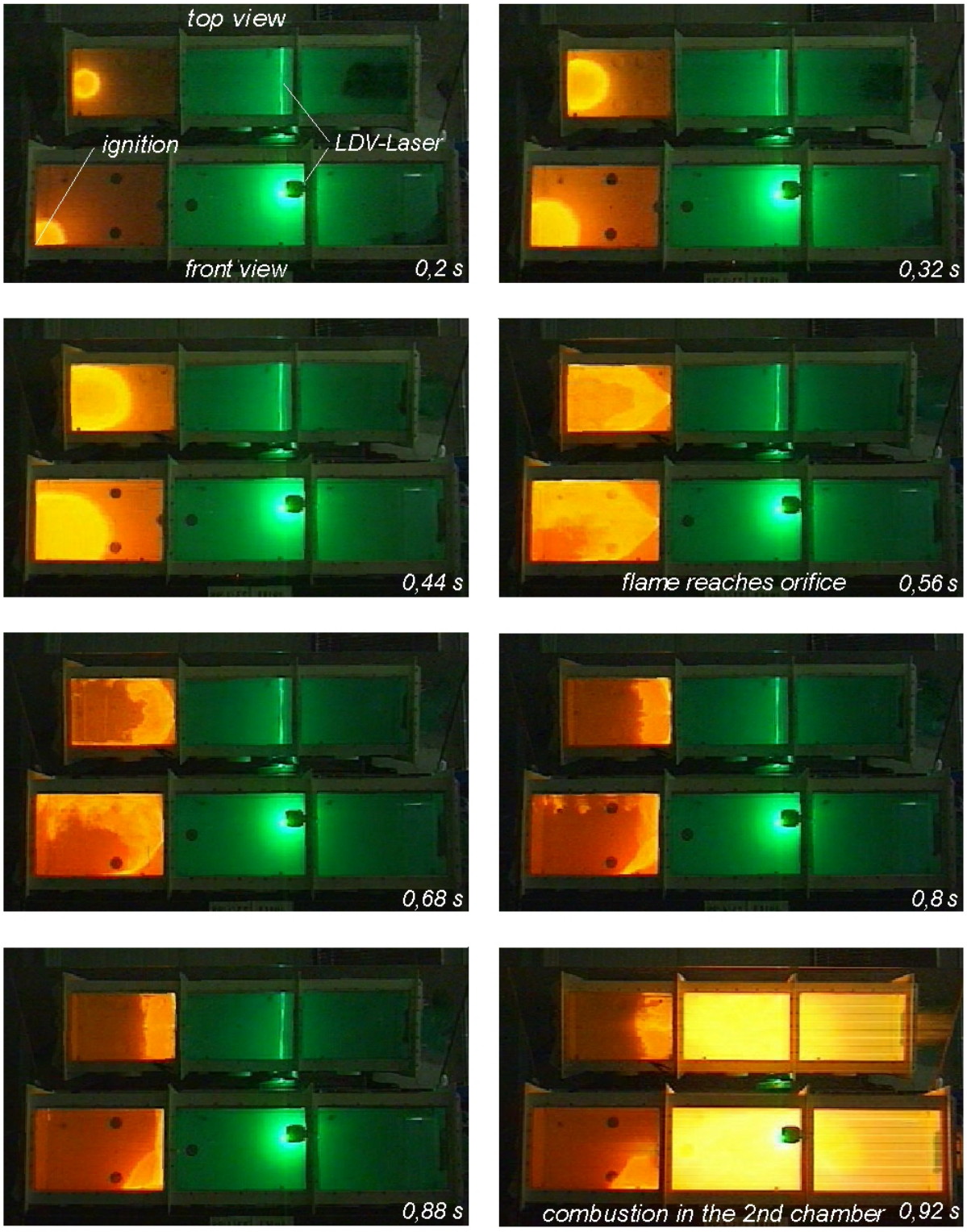

Figure 5.2.3.2-8 Example of a hydrogen combustion process in the L.VIEW Facility with a hydrogen concentration of 10.5 vol % and an orifice diameter of 70 mm

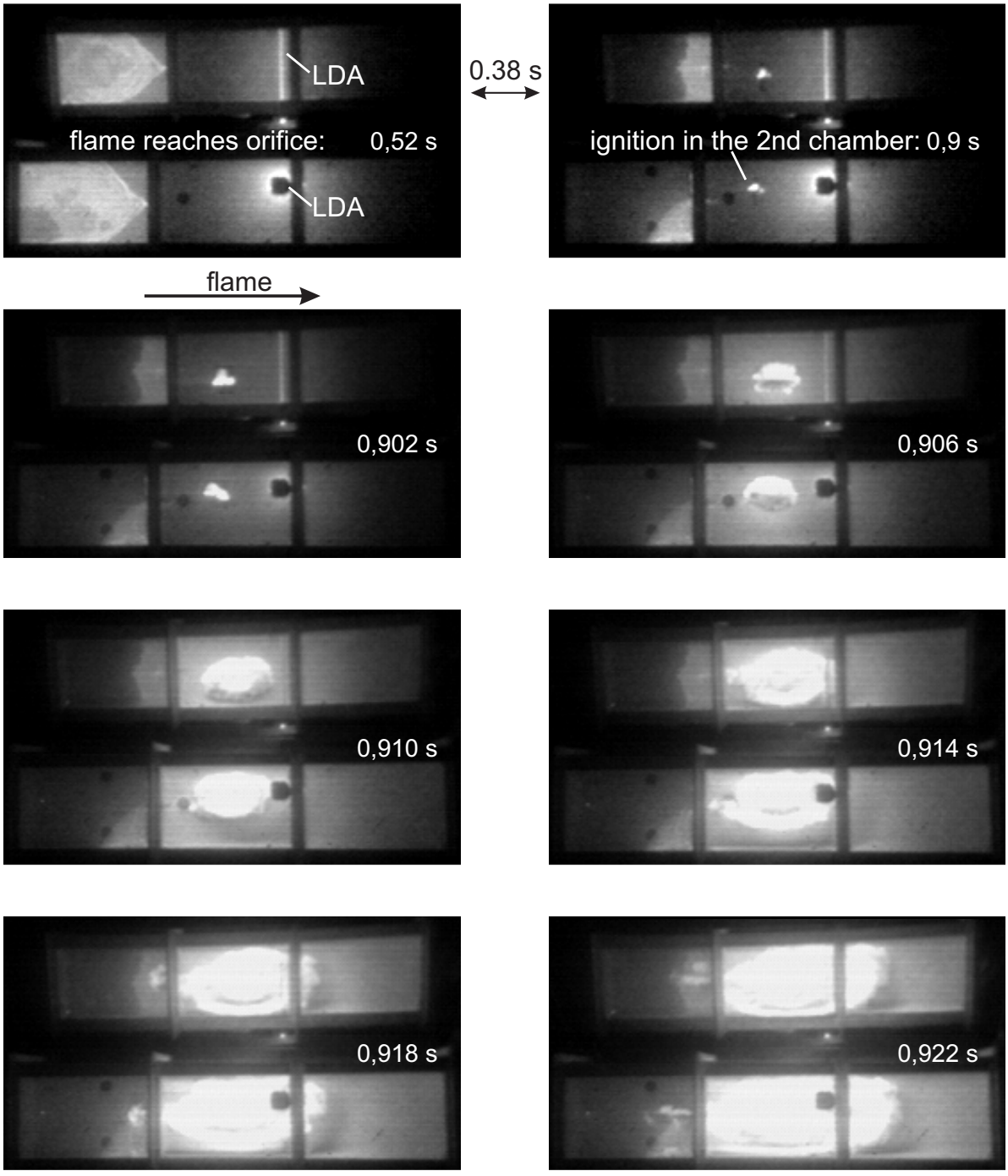

Figure 5.2.3.2-9 Ignition process of the test shown in Figure 5.2.3.2-8 with high temporal resolution

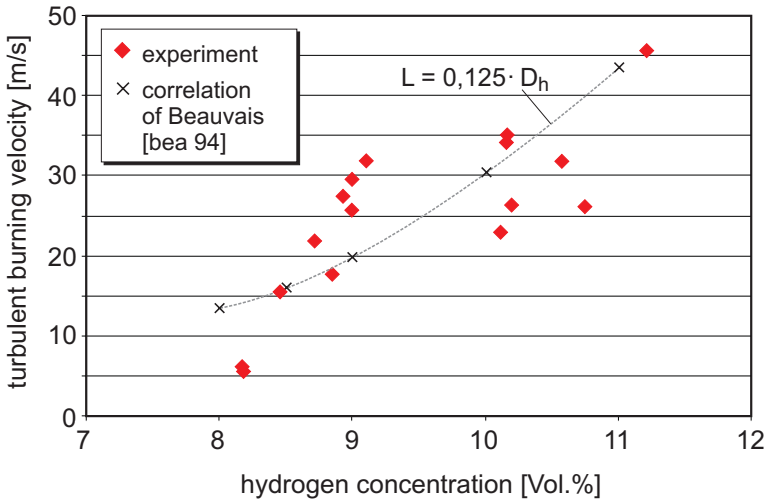

Figure 5.2.3.2-10 Calculated and measured turbulent burning velocity in the L.View Facility for direct ignition

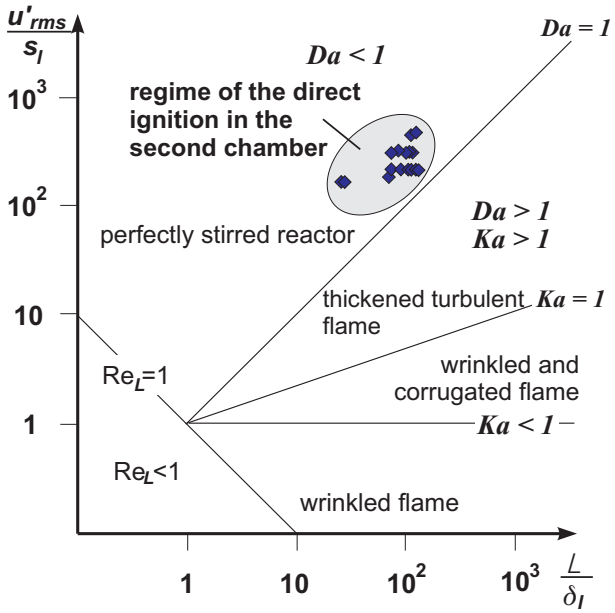

Figure 5.2.3.2-11 Regime of direct ignition in the second chamber

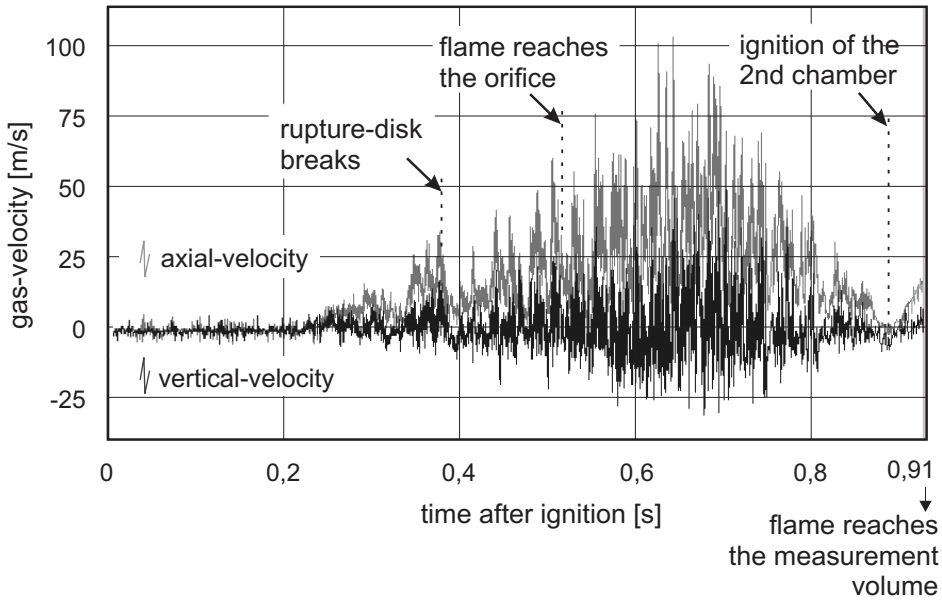

Figure 5.2.3.2-12 Flow velocity measured in the middle of the second chamber in the L.View Facility

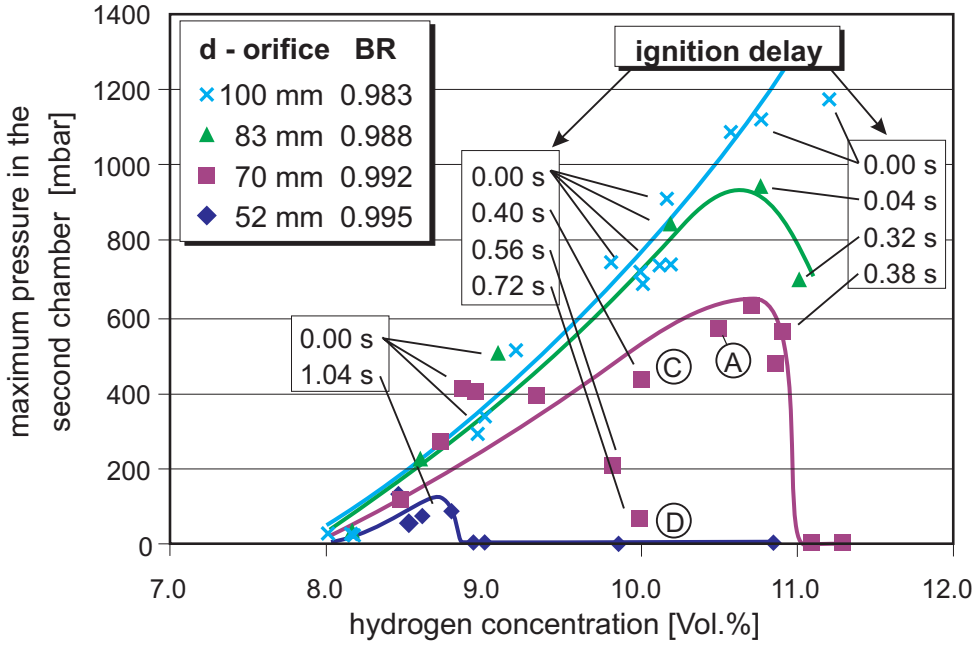

Figure 5.2.3.2-13 Maximum pressure in the second chamber in a dependence on ignition delay

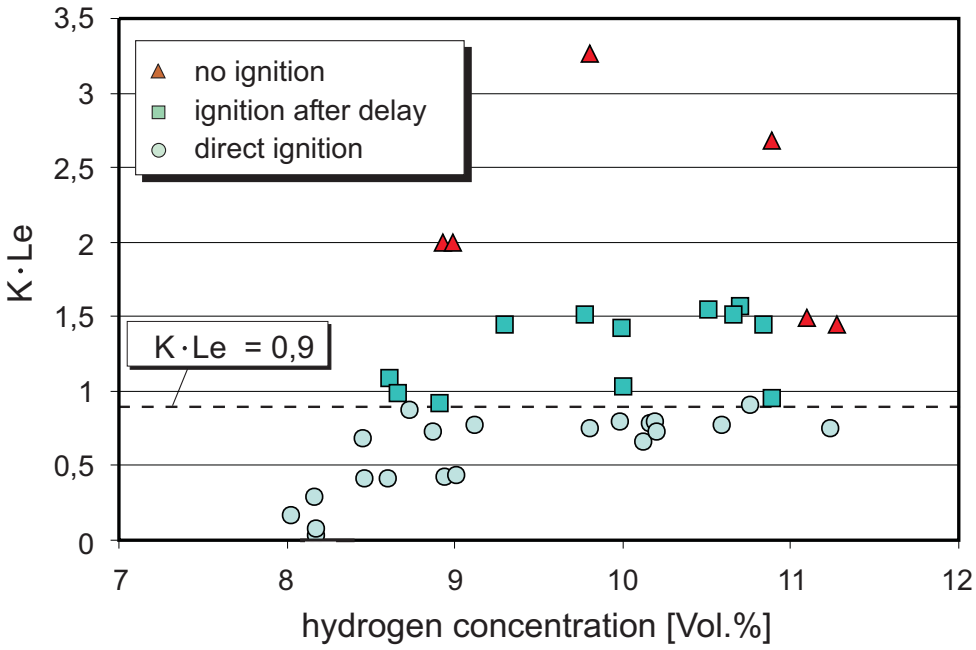

Figure 5.2.3.2-14 Quenching criterion for jet ignition

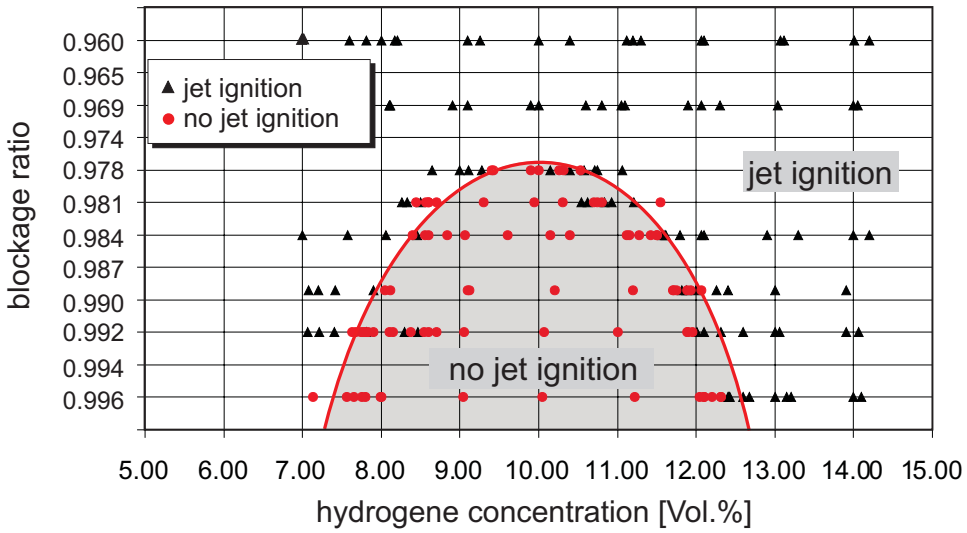

Figure 5.2.3.2-15 Flame-quenching as a function of blockage ratio, PuFlaG Facility

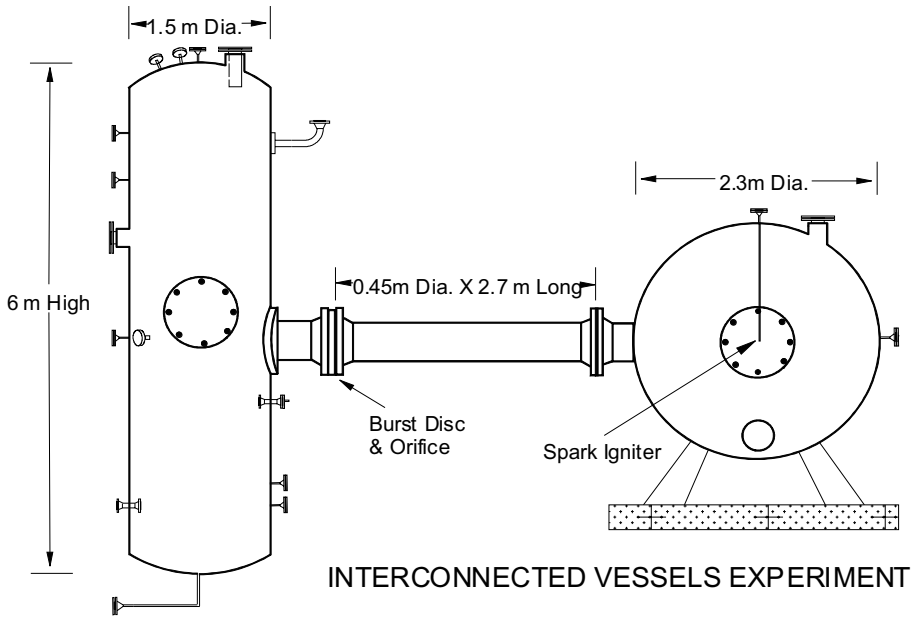

Figure 5.2.3.2-16 Schematic of the Large-scale Interconnected Vessels Facility showing burst disc holder and spark igniter locations, AECL's Whiteshell Laboratories

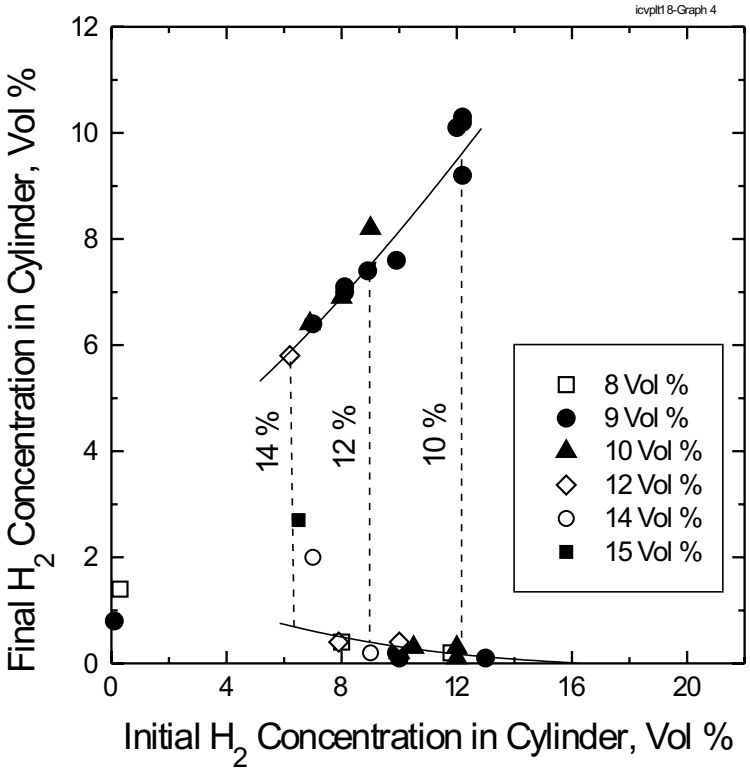

Figure 5.2.3.2-17 Final hydrogen concentration in cylinder versus initial hydrogen concentration in the cylinder for 8, 10, 12, and 14 vol % initial hydrogen concentration in the sphere with 15-cm orifice in the connecting pipe.

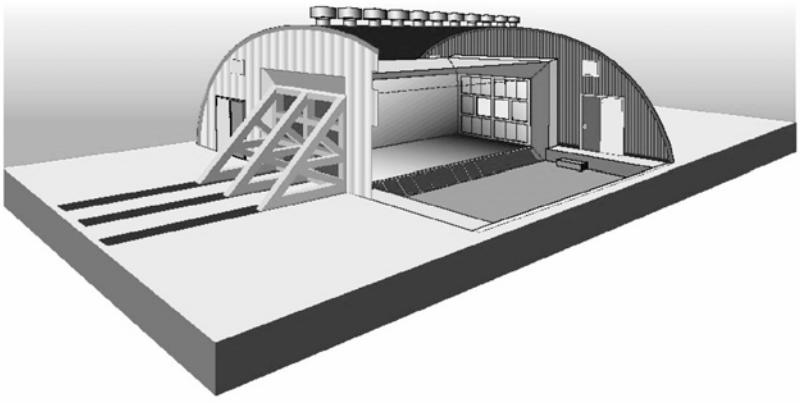

Figure 5.2.3.2-18 Cutaway schematic of the large-scale Vented Combustion Test Facility at theWhiteshell Laboratories, AECL

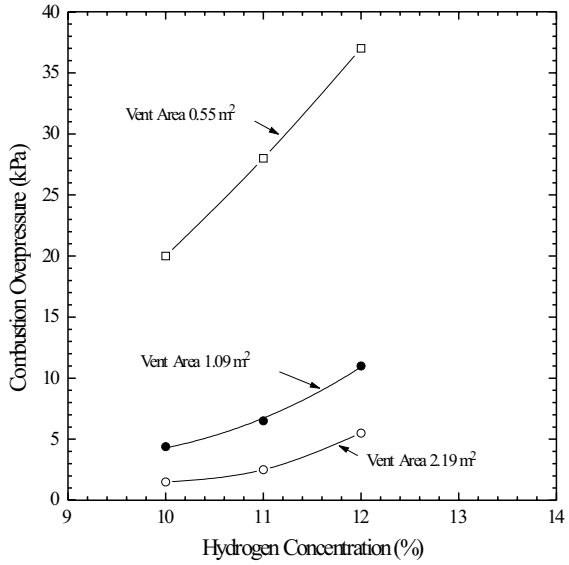

Figure 5.2.3.2-19 Variation of peak pressure as a function of hydrogen concentration for varying vent areas. Results of $120\ \mathrm{m}^3$ test chamber geometry at 25^oC

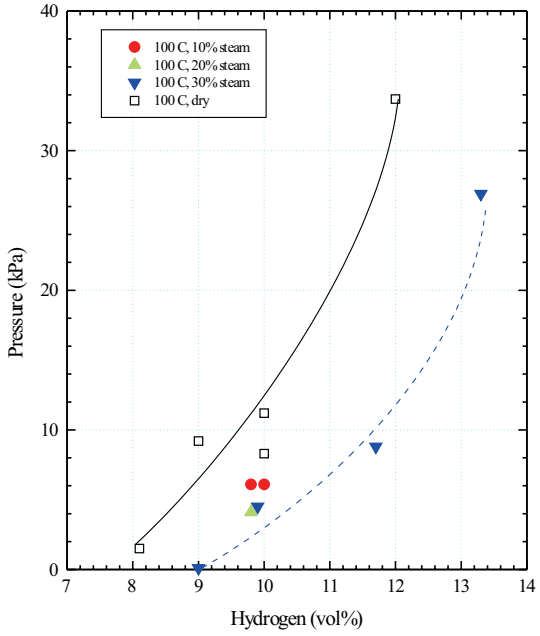

Figure 5.2.3.2-20 Variation of peak pressure as a function of hydrogen concentration for varying steam concentrations. Results of $120\ \mathrm{m}^3$ test chamber geometry, at 25^oC, with $0.55\ \mathrm{m}^2$ vent.

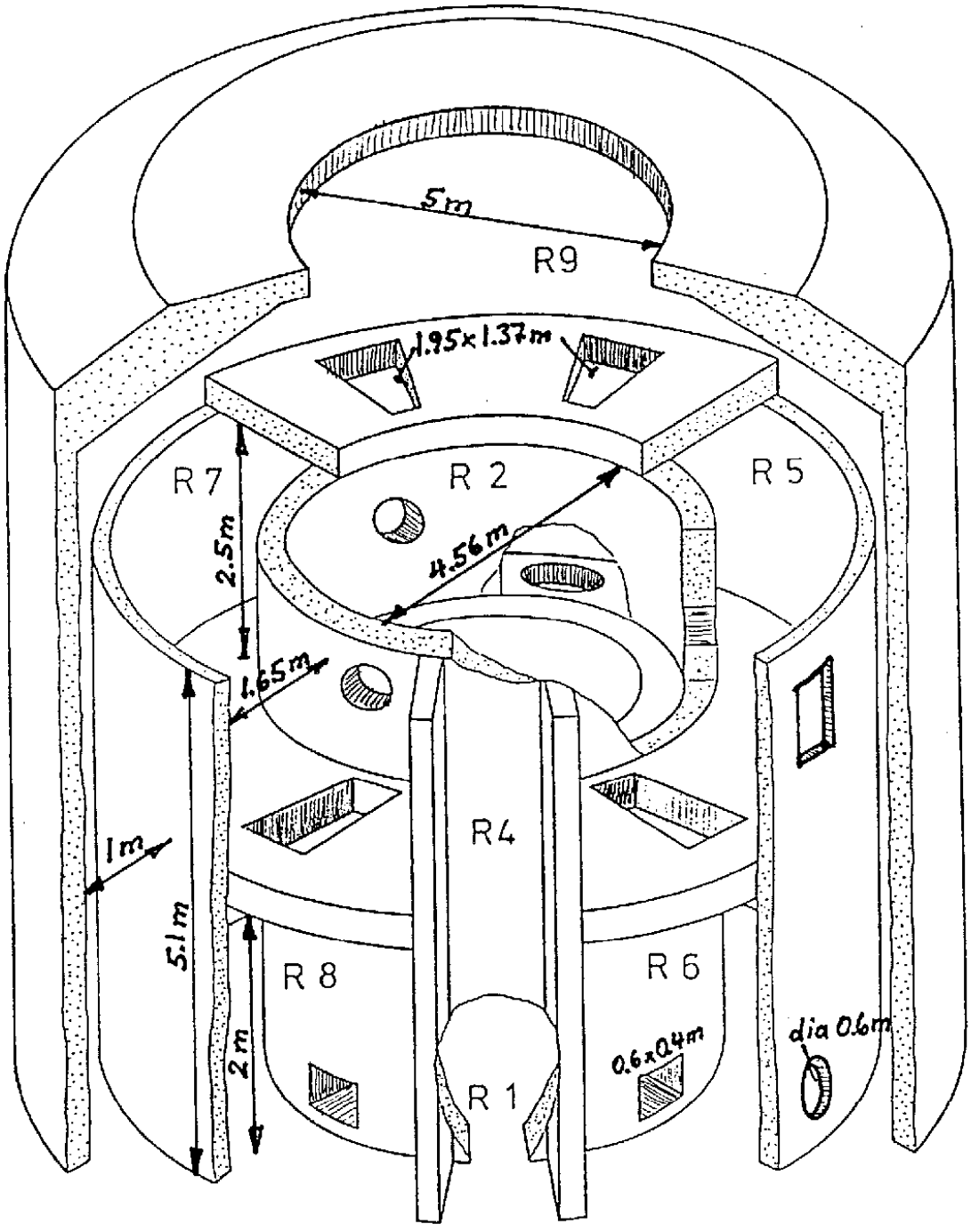

Figure 5.2.3.2-21 View of the Battelle Model Containment

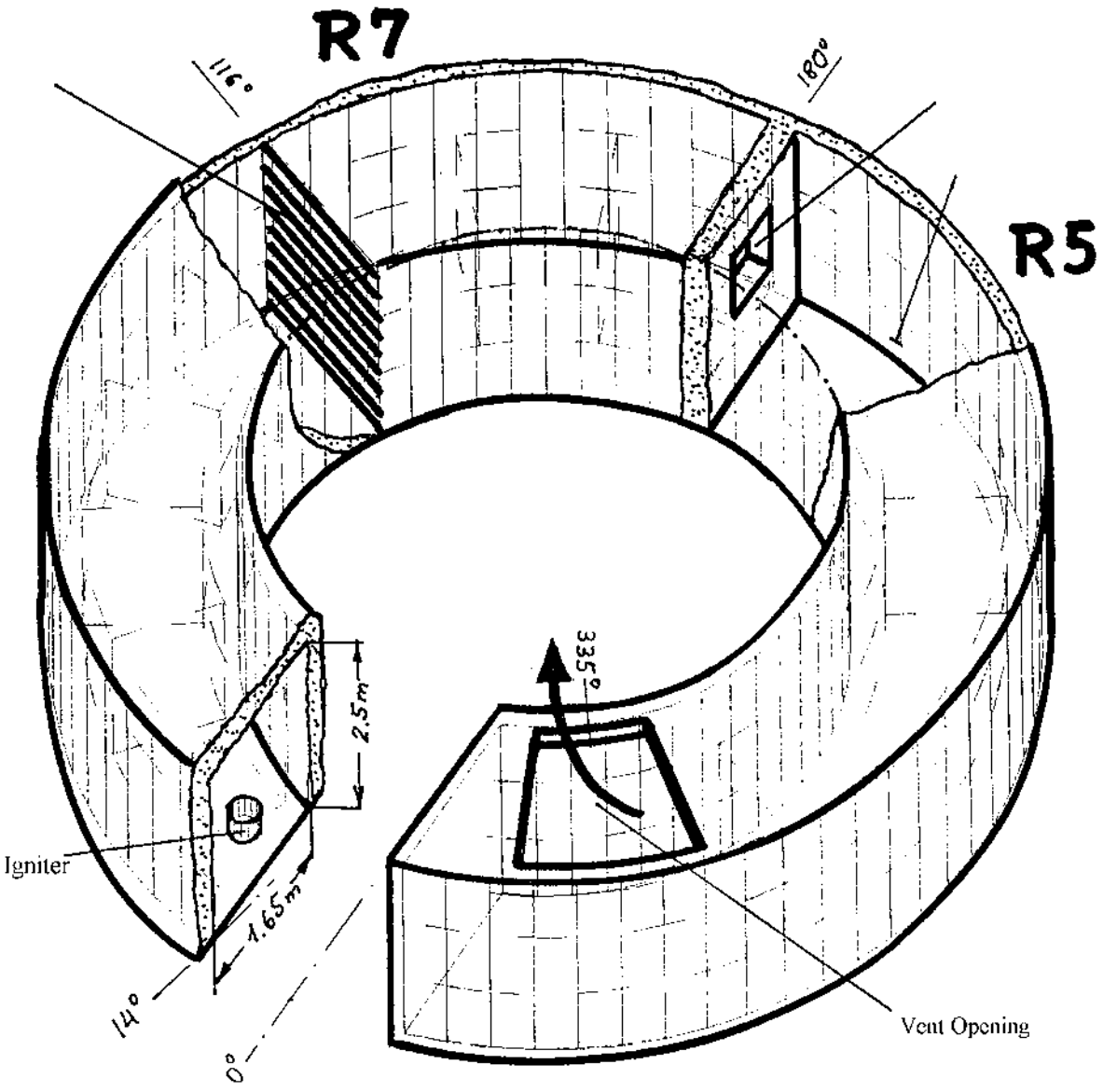

Figure 5.2.3.2-22 Two-compartment arrangement for the investigation of generic obstacles

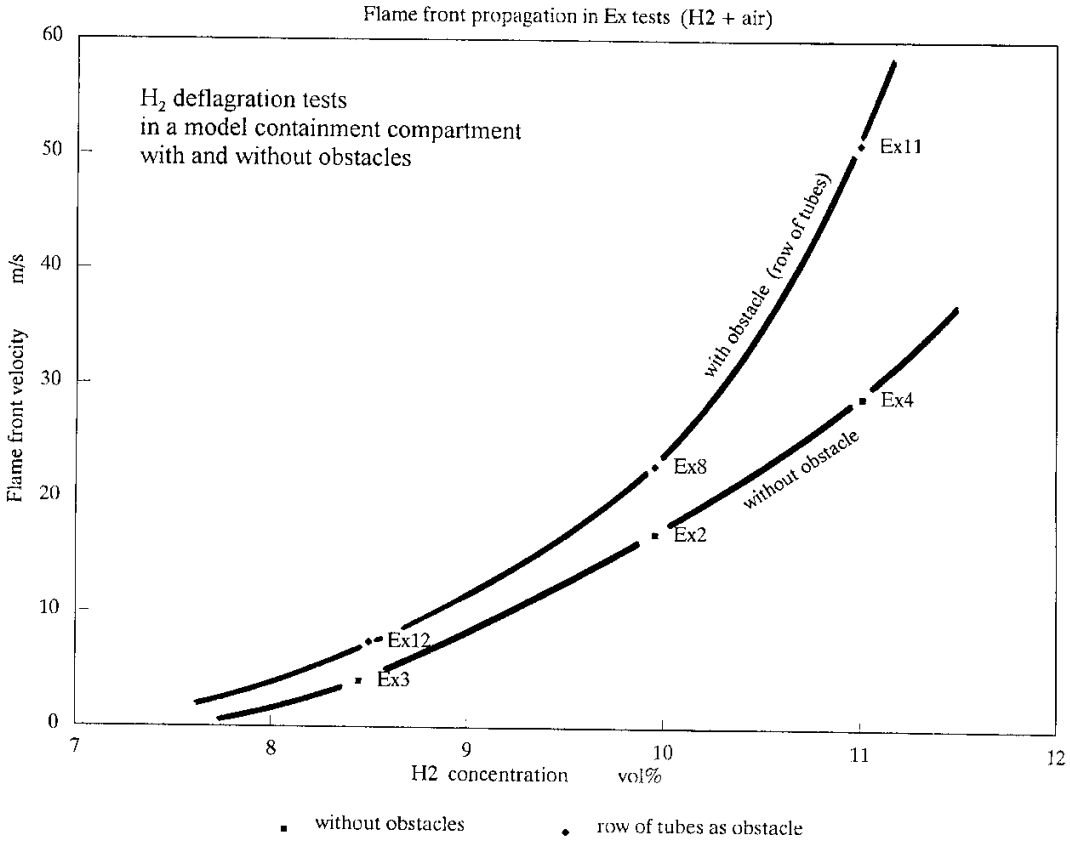

Figure 5.2.3.2-23 Impact of obstacles on the flame-front velocity in the Battelle Model Containment

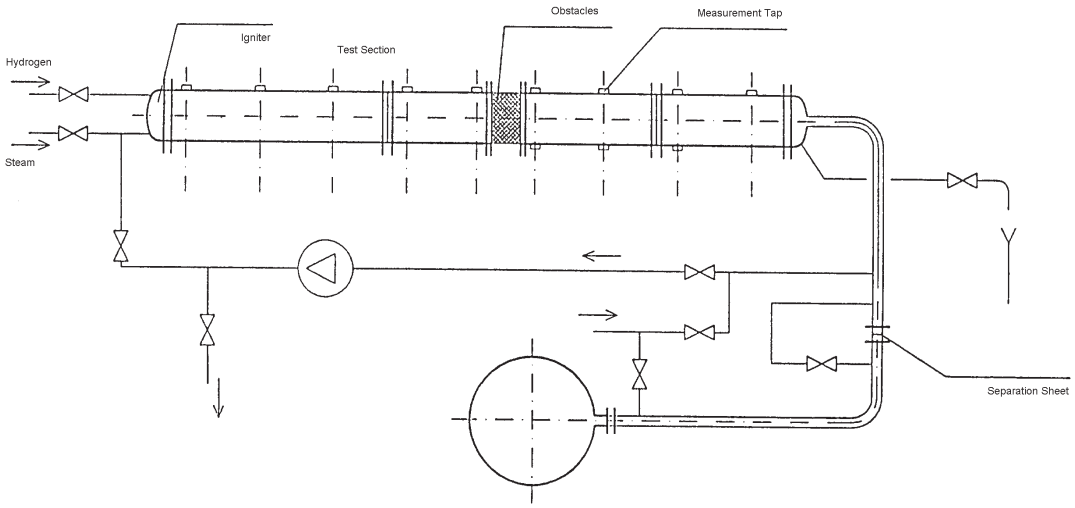

Figure 5.2.3.2-24 Test facility DN-400 for scaling from the Battelle Model Containment

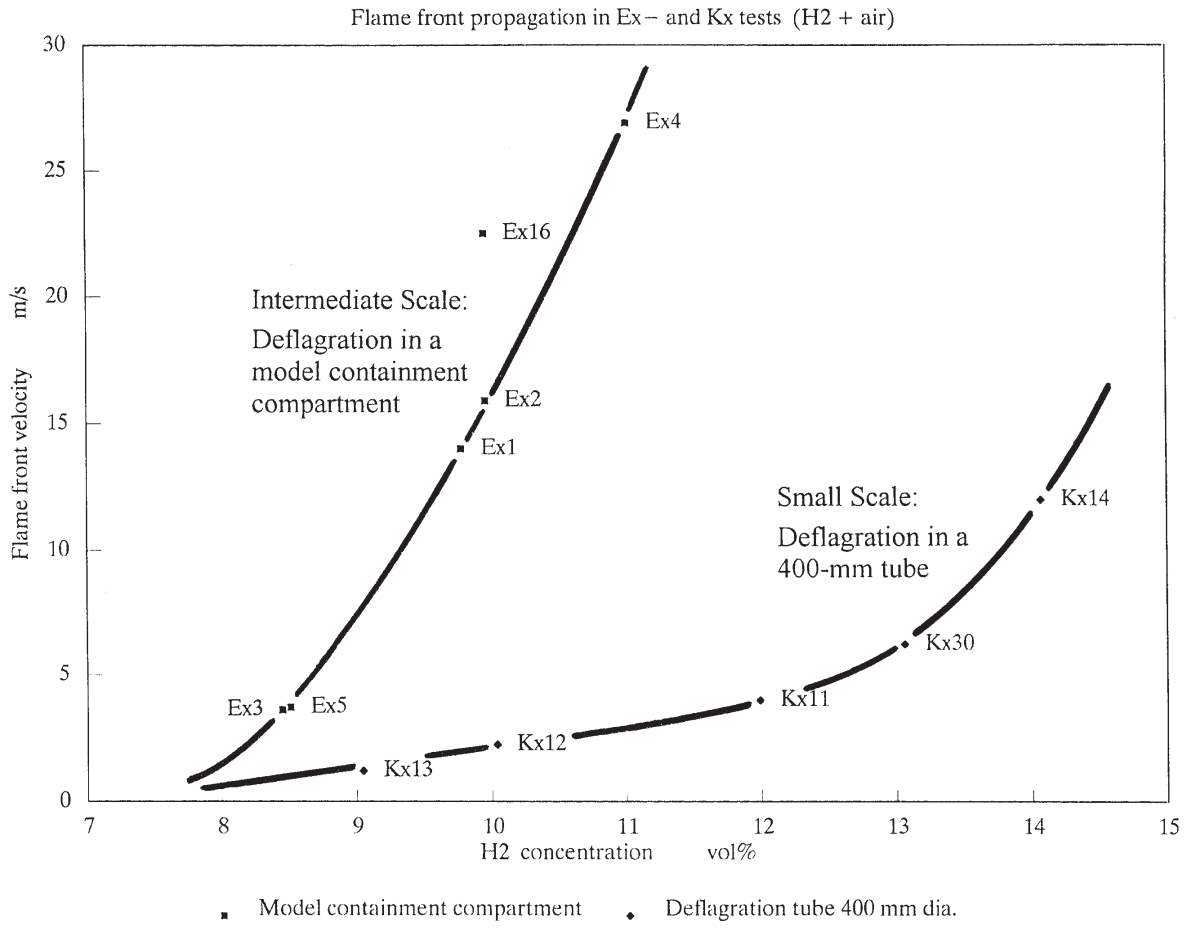

Figure 5.2.3.2-25 Impact of linear scale of the test facility on the flame propagation

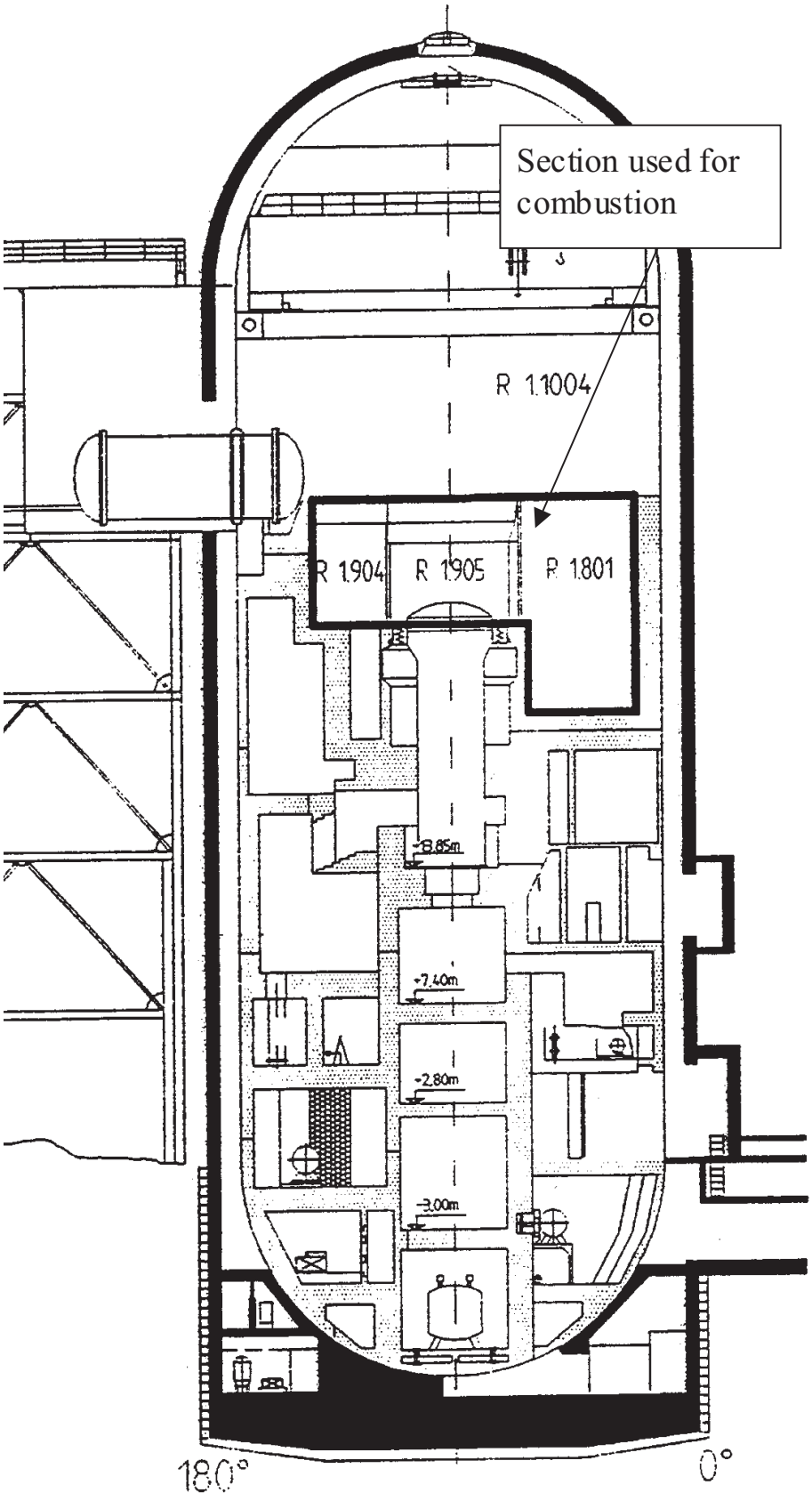

Figure 5.2.3.2-26 Hydrogen combustion experiments in the HDR

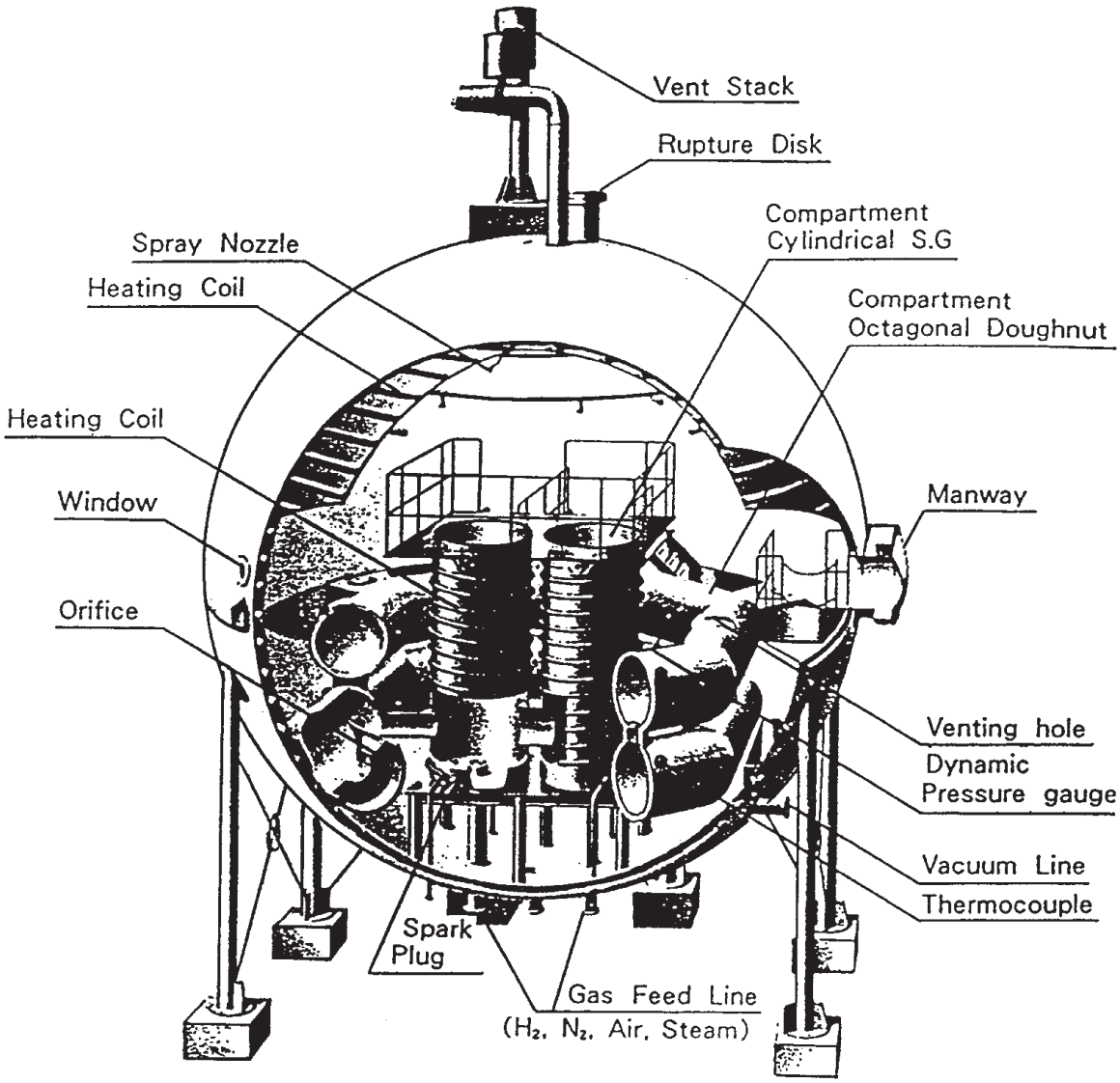

Figure 5.2.3.2-27 NUPEC's Large-Scale Combustion Test Facility

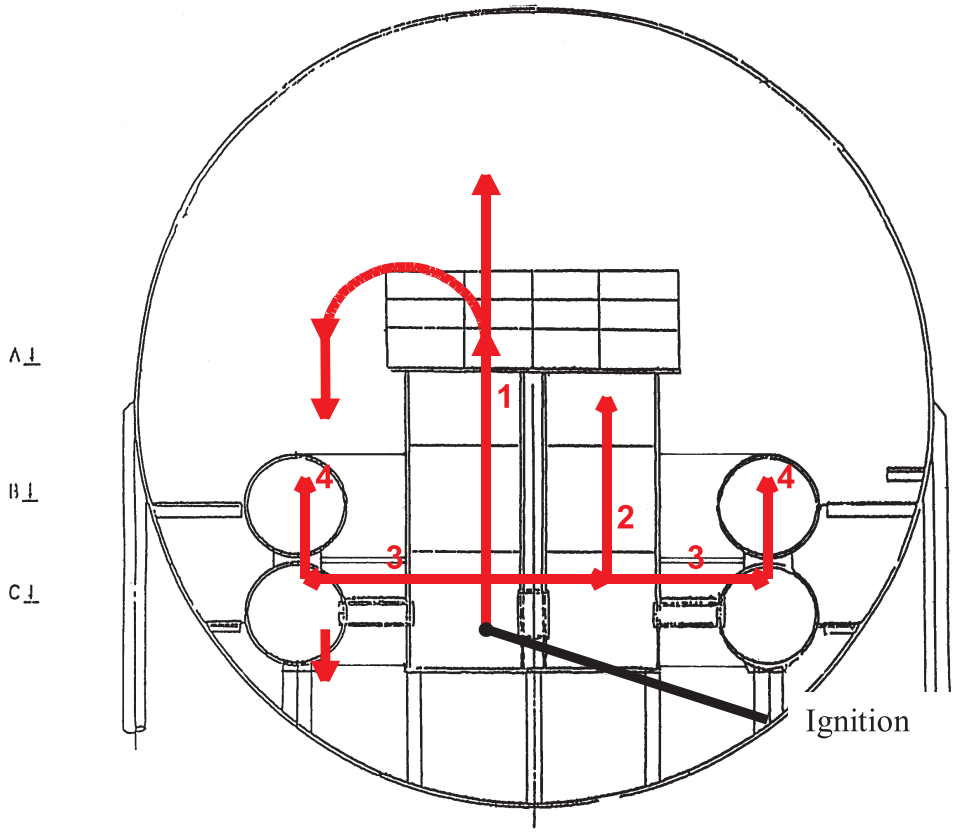

Figure 5.2.3.2-28 Principle flame branching for the steam generator, bottom ignition

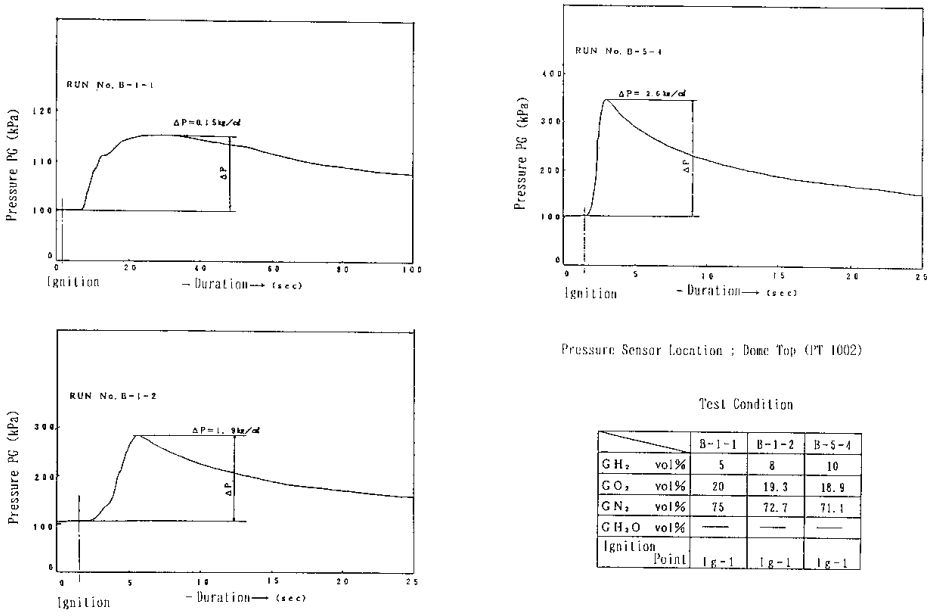

	B-1-1	B-1-2	B-5-4
GH_2 vol%	5	8	10
GO_2 vol%	20	19.3	18.9
GN_2 vol%	75	72.7	71.1
GH_2O vol%	—	—	—
Ignition Point	Ig-1	Ig-1	Ig-1

Figure 5.2.3.2-29 Pressure histories for different gas compositions

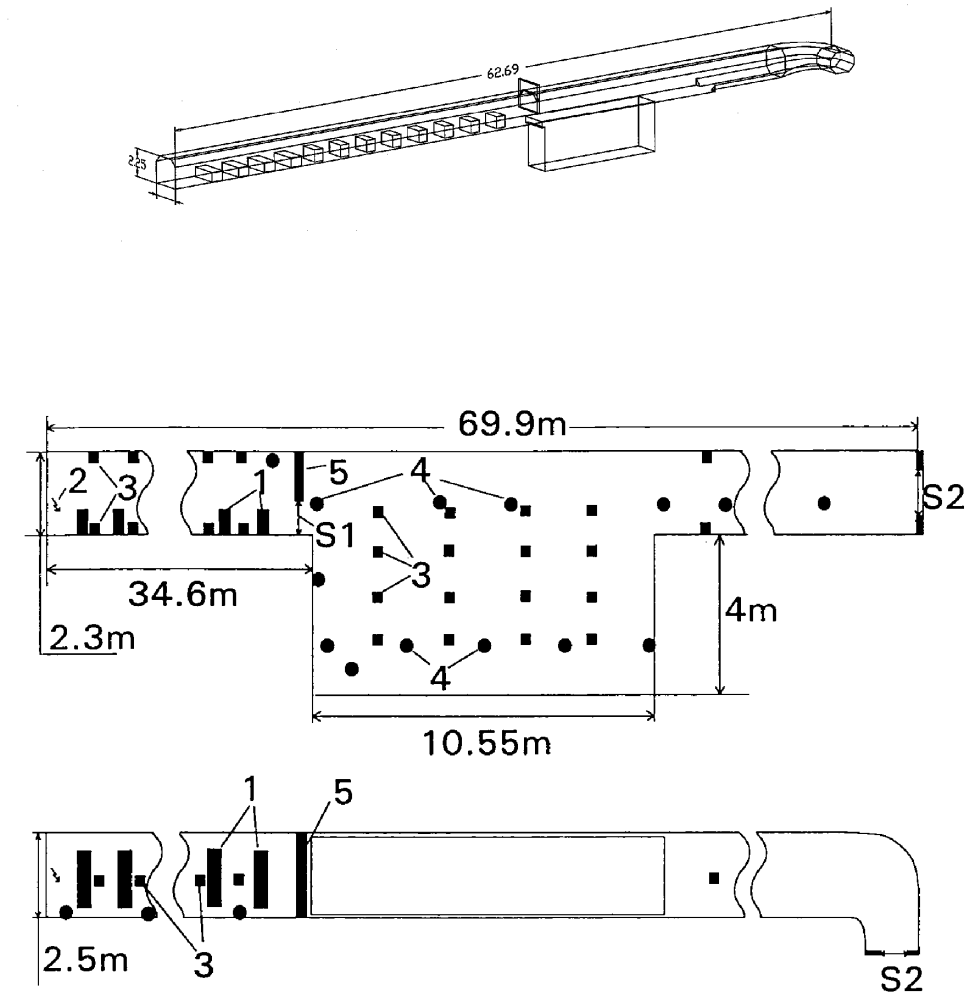

Figure 5.2.3.2-30 RUT Facility, Kurchatov Institute

5.3 Model Hierarchies Used in Practical Applications

5.3.1 Combustion in Containment System Codes (Lumped Parameter)[*]

5.3.1.1 Introduction

System codes are codes that are designed to describe the complexity of processes in a nuclear containment under accident conditions. The main physical phenomena of the multi-component multi-phase mixtures to model are

- releases of gases and water (steam), mixing of species;
- heat transfer, mainly heat losses to solid structures by convection and condensation;
- particle transport of water droplets, aerosols, and melt fragments; and
- chemical reactions, including fires and gas combustion.

These processes proceed in a more or less complex way (depending on the containment type and design and large geometry) over long time periods (typically in the order of days). Process times can be very different and can range from seconds for combustion to always-present for heat losses to structures.

In order to cover most or all of the processes mentioned, related code systems use a simplified mathematical approach. They subdivide a given geometry into zones, which can be linked to other zones by flow connections. Each zone may have sources or sinks of mass and energy. These codes can solve the following parameters:

- energy conservation of the system composed of zones. The kinetic energy transported by gas flows is very low and, therefore, not estimated.
- mass conservation in all zones. Mass changes caused by flows between zones are included.
- momentum balance between zones under the assumption that the momentum of a flow dissipates totally when entering a zone. This assumption is made because physical compartments of the containment and, hence, the model zones are usually large in volume ($100 \text{ to } 1000 \text{ m}^3$). With low speeds (1 to 10 m/s), it is unlikely that a flow continues through a zone. Therefore, momentum conservation in zones is not considered.

Apart from the standard lumped-parameter concept, the MELCOR code [5.85] (see Table 5.4.0-1) offers the possibility to solve for a momentum conservation. This feature is not included in the combustion model and will be discussed briefly.

A more complex combustion model – a flame-front combustion model – is implemented in the COCOSYS code [5.86] (see Table 5.4.0-1). The discussion of this model will also be used to illustrate the lumped-parameter concept in general.

[*] Contributed by Dr. M. Heitsch

Common to all lumped-parameter codes is that all nodes and flow connections have to be described individually. Therefore, models that have more than 200 to 250 nodes and more than 400 flow connections appear to be the upper limit of what a user can handle. The omission of the momentum conservation leads to a system of ordinary differential equations that can be solved implicitly and allows relatively large time steps.

5.3.1.2 The MELCOR Combustion Model

MELCOR is a fully integrated, engineering-level control volume computer code whose primary purpose is to model the progression of accidents in LWR NPPs. The relevant section of the user manual describes best the features of the combustion model [5.85]:

"The Burn (BUR) package models the combustion of gases in control volumes. These models consider the effects of burning on a global basis without modeling the actual reaction kinetics or tracking the actual flame front propagation. The models in the BUR package are based on the deflagration models in the HECTR 1.5 code. The only significant modifications made were to provide more direct user control of the models through the implementation of sensitivity coefficients and to include optional model parameters that are used to override the nominal parameters in control volumes in which direct containment heating (DCH) is occurring.

Deflagrations are ignited if the mole fraction composition in a control volume satisfies a form of LeChatelier's formula. Tests for sufficient H_2 and O_2 are performed, as well as an inerting test for the presence of excessive diluents (H_2O and CO_2). Deflagrations are propagated into adjoining control volumes after a user-specified fraction of the total burning time in the control volume has passed. Additional tests for the H_2 and CO mole fractions in those volumes need to be satisfied and a non-zero area for a gas flow path has to exist. There is, however, no test for checking valves.

The combustion rate is determined by the flame speed, the volume characteristic dimension, and the combustion completeness. The flame speed and combustion completeness can each be input as constant values, or they may be calculated from either user-specified control functions or the default HECTR correlations. The latter are derived from experimental data and depend on combustible and diluent gas concentrations.

For user convenience, the BUR package also prints messages to warn the user when the detonability criteria are satisfied in a control volume. However, only deflagrations are modeled; detonations are merely flagged and no other action is taken unless deflagration criteria are satisfied."

In summary, this combustion model adds sources of mass and energy to the respective control volumes but does not solve differential equations. For each control volume, a burning time is evaluated from the characteristic dimension (user input) and a flame speed (either user specified or calculated). These flame speeds may be uncertain.

The ignition limits checked include carbon monoxide and are adopted to mixtures in a containment under accident conditions.

5.3.1.3 The COCOSYS Combustion Model

By the very nature of MELCOR being a control volume code, it cannot simulate some aspects of combustion such as the following:

- The cold gas compression ahead of the reacting zone and hot gas expansion behind it are not modelled. Instead, a homogeneous mixture is used.
- Branching of a flame is not possible with this type of control volume code. Flame branching would only be possible with multiple nodes, properly defined. The potential difference introduced by this simplification is, in part, a function of analyst's nodalization of the problem.

In order to get a more predictable combustion model, a flame-front model according to Figure 5.3.1.3-1 has been implemented in COCOSYS. The model, named DECOR [5.87], [5.88], is characterized as follows:

- For those zones, which are subject to combustion, an unburned and a burned part are defined and are separated by a flame front.
- It is one-dimensional model with averaged conditions normal to the flame front.
- Combustion is possible in three predefined directions.
- Full pressure relief is assumed between the unburned and the burned parts on both sides of the flame front.

In principal, on both sides of the flame front, mass and energy balances are set up and the momentum exchange with other nodes, according to pressure and height differences, is calculated. Then both parts are linked together by the chemical reaction over the flame discontinuity. The chemical reaction inside the flame results in a displacement of the front, driven by a burning velocity derived from experiments.

The general lumped-parameter differential equations are first applied to both node parts linked by the flame, and then additional equations for the coupling between both are added. In an open thermodynamic system with a variable volume size, the following energy equation holds:

$$dQ = dU + dW \tag{5.3.1}$$

or with the definition of enthalpy ($I = U + pV$)

$$dQ = dI - pdV - vdp + pdV \text{ with } dW = pdV\ . \tag{5.3.2}$$

Time dependent, it writes

$$\frac{dQ}{dt} = \frac{dI}{dt} - V\frac{dp}{dt} = \frac{d(M_i)}{dt} - V\frac{dp}{dt}\ . \tag{5.3.3}$$

The code distinguishes between steam-saturated and steam-superheated conditions. The model derivation is similar; therefore, only the more common superheated situation is considered and presented. In a single node, we have ($k = 1..l$) species. Unlike the saturated conditions, no liquid water is available but

steam is included. To this node there are (j=1..q) entering flows and (j=1..p) leaving flows. The energy balance around the zone (or part of a zone in Figure 5.3.1.3-1) can be written as

$$\sum_{k=1}^{l}\left[\sum_{j=1}^{q} G_{kj}^{e} I_{kj}^{e} - \sum_{j=1}^{p} G_{kj}^{a} I_{kji}^{a}\right] + \frac{dQ^{e}}{dt} - \frac{dQ^{a}}{dt} = \sum_{k=1}^{l}\frac{d}{dt}(M_k I_k) - \sum_{k=1}^{l} V_k \frac{dp_k}{dt} \; . \tag{5.3.4}$$

On the left side of the equation we have the sum of the energy flows involving mass transport entering or leaving the node and of heat without mass transport entering or leaving the node. These flows lead to an increase of the inner energy expressed on the right side. The left side of Equation (5.3.4) shall be

$$H_1 = \sum_{k=1}^{l}\left[\sum_{j=1}^{q} G_{kj}^{e} I_{kj}^{e} - \sum_{j=1}^{p} G_{kj}^{a} I_{kji}^{a}\right] + \frac{dQ^{e}}{dt} - \frac{dQ^{a}}{dt} \tag{5.3.5}$$

and the right-most term can be modified to

$$\sum_{k=1}^{l} V_k \frac{dp_k}{dt} = V \sum_{k=1}^{l} \frac{dp_k(T, \mathrm{v}_k)}{dt} = V \sum_{k=1}^{l}\left[\left(\frac{\partial p_k}{\partial T}\right)_{\mathrm{v}_k} \frac{dT}{dt} + \left(\frac{\partial p_k}{\partial \mathrm{v}_k}\right) \frac{d\mathrm{v}_k}{dt}\right] \; . \tag{5.3.6}$$

The gradient of the enthalpy can be written as

$$\frac{dI_k(T, p_k)}{dt} = \left(\frac{\partial I_k}{\partial T}\right)_{p_k} \frac{dT}{dt} + \left(\frac{\partial I_k}{\partial p_k}\right)_{T} \frac{dp_k}{dt} \; , \tag{5.3.7}$$

and the specific volume

$$\frac{dv_k}{dt} = \frac{d\left(\frac{V}{m_k}\right)}{dt} = \frac{1}{M_k}\frac{dV}{dt} - \frac{V}{M_k^2}\frac{dM_k}{dt} \; . \tag{5.3.8}$$

Equations (5.3.6) to (5.3.8) merged into Equation (5.3.4) yield

$$\begin{aligned} H_1 = & \left\{\sum_{k=1}^{l} M_k \left[\left(\frac{\partial I_k}{dT}\right)_{p_k} + \left(\frac{\partial I_k}{\partial p_k}\right)_{T}\left(\frac{\partial p_k}{\partial T}\right)_{\mathrm{v}_k}\right] - V\left(\frac{\partial p_k}{dT}\right)_{\mathrm{v}_k}\right\}\frac{dT}{dt} \\ & + \sum_{k=1}^{l}\left\{I_k + \left[\frac{V}{M_k} - \left(\frac{\partial I_k}{\partial p_k}\right)_{T}\right]\left(\frac{\partial p_k}{\partial \mathrm{v}_k}\right)_{T}\frac{V}{M_k}\right\}\frac{dM_k}{dt} \\ & - \left[\sum_{k=1}^{l}\left(\frac{\partial I_k}{\partial p_k}\right)_{T}\left(\frac{\partial p_k}{\partial \mathrm{v}_k}\right)_{T} - \frac{V}{M_k}\left(\frac{\partial p_k}{\partial \mathrm{v}_k}\right)_{T}\right]\frac{dV}{dt} \; . \end{aligned} \tag{5.3.9}$$

Mass balances can be set up for $k = 1..l$ non-condensable species and steam entering ($j = 1..q$) or leaving ($j = 1..p$) the zone under consideration

$$\frac{dM_k}{dt} = \sum_{j=1}^{q} G_{K_j}^{e} - \sum_{j=1}^{p} G_{k_j}^{a} = G_k \; . \tag{5.3.10}$$

Mass flows between nodes are derived from a momentum balance. The standard equation of an incompressible flow is

$$\dot{G}_j = \frac{A_j}{I_j}\left[\left(p_{j_s} - p_{j_t}\right) + W_j - K_j G_j \mid G_j \mid\right] \tag{5.3.11}$$

where s indicates the source zone and t the target zone in case of a positive flow. The kinetic part is neglected. The static pressure head driving the flow in the simplest case is

$$w_j = \rho_j g\left(h_{j_s} - h_{j_t}\right) \; . \tag{5.3.12}$$

The density is averaged between both zones:

$$\rho_j = \frac{1}{2}\left(\rho_{j_s} + \rho_{j_t}\right). \tag{5.3.13}$$

The flow resistance is given by

$$K_j = \left(\zeta_0 + \zeta_A\right)\frac{1}{2\rho_j A_j^2}. \tag{5.3.14}$$

The form factor ζ_0 is user input and can be different for both flow directions. ζ_A is the loss coefficient of a pipe flow either in a laminar or in a turbulent flow regime that is decided by the code. After transformation of the preceding equations, a relation of the temperature gradient in the node can be found.

$$\frac{dT}{dt} = \frac{H_1 - H_2 - H_3 - H_5\frac{dV}{dt}}{H_4} \tag{5.3.15}$$

with Equation (5.3.5):

$$H_1 = \sum_{k=1}^{l}\left[\sum_{j=1}^{q} G_{kj}^{e} I_{kj}^{e} - \sum_{j=1}^{p} G_{kj}^{a} I_{kji}^{a}\right] + \frac{dQ^e}{dt} - \frac{dQ^a}{dt},$$

$$H_2 = \sum_{k=1}^{l} G_k I_k, \tag{5.3.16}$$

$$H_3 = \sum_{k=1}^{l}\left\{\left[\frac{V}{M_k} - \left(\frac{\partial I_k}{\partial p_k}\right)_T\right]\left(\frac{\partial p_k}{\partial \mathrm{v}_k}\right)_T \frac{V}{M_k}\right\} G_k, \tag{5.3.17}$$

$$H_4 = \sum_{k=1}^{l} M_k\left[\left(\frac{\partial I_k}{dT}\right)_{p_k} + \left(\frac{\partial I_k}{\partial p_k}\right)_T\left(\frac{\partial p_k}{\partial T}\right)_{\mathrm{v}_k}\right] - V\left(\frac{\partial p_k}{dT}\right)_{\mathrm{v}_k}, \tag{5.3.18}$$

$$H_5 = \sum_{k=1}^{l}\left[\left(\frac{\partial I_k}{\partial p_k}\right)_T - \frac{V}{M_k}\right]\left(\frac{\partial p_k}{\partial \mathrm{v}_k}\right)_T \tag{5.3.19}$$

Now with Equations (5.3.10), (5.3.11) and (5.3.15) mass and energy conservation in each node is available and can be applied to the combustion problem. Equation (5.3.15) contains the volume change over time as a free parameter. For two flame-front-coupled nodes (Figure 5.3.1.3-1), there is the following relation for the change in volume:

$$\left(\frac{dV}{dt}\right)^U = \left(\frac{dV}{dt}\right)^B. \tag{5.3.20}$$

The purpose of the deflagration model is primarily to describe combustion initiated by deliberate ignition, that means by ignition sources, which ignite a given mixture as early as possible. This allows one to assume full pressure relief on both sides of the flame and leads to

$$\left(\frac{dp}{dt}\right)^U = \left(\frac{dp}{dt}\right)^B. \tag{5.3.21}$$

Under superheated steam conditions (steam-saturated conditions are dealt with as well, but are not detailed here) the total pressure gradient can be written as

$$\left(\frac{dp}{dt}\right) = \sum_{k=1}^{l}\frac{dp_k}{dt} = \sum_{k=1}^{l}\left(\frac{\partial p_k}{\partial T}\right)_{\mathrm{v}_k}\frac{dT}{dt} + \left(\frac{\partial p_k}{\partial \mathrm{v}_k}\right)_T\frac{d\mathrm{v}_k}{dt}. \tag{5.3.22}$$

The specific volume can be expressed as

$$\frac{dv_k}{dt} = \frac{1}{M_k}\left(\frac{dV}{dt} - \frac{V}{M_k}\frac{dM_k}{dt}\right) . \tag{5.3.23}$$

Equation (5.3.23) integrated into Equation (5.3.22) yields

$$\frac{dp}{dt} = A\frac{dT}{dt} + B - C\frac{dV}{dt} \tag{5.3.24}$$

with

$$A = \sum_{k=1}^{l}\left(\frac{dp_k}{dT}\right)_{\mathrm{v}_k} \tag{5.3.25}$$

$$B = -V\sum_{k=1}^{l}\frac{G_k}{M_k^2}\left(\frac{\partial p_k}{\partial \mathrm{v}_k}\right)_T \tag{5.3.26}$$

$$C = -\sum_{k=1}^{l}\frac{1}{M_k}\left(\frac{\partial p_k}{\partial \mathrm{v}_k}\right)_T . \tag{5.3.27}$$

Equation (5.3.24) can be written down for the burned (B) and unburned (U) zone parts and together with Equation (5.3.15), (5.3.20) and (5.3.21) a system of three linear equations arises:

$$\begin{aligned} H_4^B\,\frac{dT^B}{dt} + H_5^B\,\frac{dV^B}{dt} &= H_1^B - H_2^B - H_3^B \\ H_4^U\,\frac{dT^U}{dt} - H_5^U\,\frac{dV^B}{dt} &= H_1^U - H_2^U - H_3^U \\ -A^B\,\frac{dT^B}{dt} + A^U\,\frac{dT^U}{dt} + \left(C^U + C^B\right)\frac{dV^B}{dt} &= B^B - B^U . \end{aligned} \tag{5.3.28}$$

This system of linear equations can be solved for the unknowns . The constants H_1 through H_5 and A, B, C on both sides of the flame front are known by the convective mass and energy exchange with other nodes and heat sources available. Which source terms the chemical reaction adds will be discussed next. Together with the mass balance equations for k species (Equation (5.3.10)), the flows between nodes (Equation (5.3.11)) and the equations from Equation (5.3.29) in case of combustion in a node or Equation (5.3.15) if no combustion is running, a coupled system of ordinary differential equations exists to describe the time-dependent behaviour of the total compartment model. COCOSYS automatically switches between Equation (5.3.15) and Equation (5.3.29) and re-organizes the Jacobi matrix if combustion in any zones starts or ends. The coupled system of equations is implicitly solved, thus allowing relatively large time steps. A more convenient quantity can be derived from the volume growth on the burned side:

$$\frac{dV^B}{dt} = \frac{dL_F}{dt}A_N\ n. \tag{5.3.29}$$

Equation (5.3.29) defines an average flame-front position from the growth of the volume on the burned side of the flame by multiplying with the cross-section of the node normal to the flame (see also Figure 5.3.1.3-2). The amount of volume burned per time is expressed as

$$\frac{dV^{BR}}{dt} = SfA_N . \tag{5.3.30}$$

S is the actual burning velocity (laminar or turbulent) according to local conditions ahead of the flame. f is a stretching factor which takes care of the folding and stretching of the flame and is related to the normal cross-section. The factor f also absorbs phenomena of the physics not included in the model and general uncertainties; these need to be determined from experiments. The burning velocity is correlated from experiments. So far, most of the application of the combustion model has been done with a correlation from Reference [5.89]. It reads

$$\frac{S_T}{S_L} = \left[1 + B\left(\frac{\mathrm{u}'}{S_L}\right)^2\right]^{1/2} + \left[1 - exp\left(\frac{-u'}{S_L}\right)\right]\frac{(\varepsilon - 1)}{\sqrt{3}},\ \varepsilon = \frac{\rho^U}{\rho^B},\ B = 16\ . \tag{5.3.31}$$

Other options for this correlation can be found in Reference [5.87]. The chemical reactions are modelled as simplified one-step reactions. They include the reaction

$$2H_2 + O_2 \rightarrow 2H_2O + 119.8MJ\ \ and\ \ 2CO + O_2 \rightarrow 2CO_2 + 10.1MJ\ . \tag{5.3.32}$$

Source terms caused by combustion can be found in the equations of the zone parts on both sides of the flame for mass and energy. They are summarized for the hydrogen reaction in Table 5.3.1.3-1.

The specification of the source terms includes the possibility of incomplete combustion ($M^R_{H_2}$), which was observed during many experiments and is dependent on the hydrogen mole fraction ($< 10\%$) available as correlation. Further modules, necessary to run the model presented, are

- The deflagration limits in all zones of the containment model must be constantly checked to either start or stop combustion. During a running combustion that is due to the ongoing flow exchange processes, the limits may no longer be fulfilled and combustion stops.
- The combustion model allows a more realistic flame branching into other zones if the flame front crosses open flow connections. This is illustrated in Figure 5.3.1.3-3. This figure depicts a representation with two burning axes and shows that additional input to characterize the connections between zones is now necessary. A flame can only propagate, if the flame front comes close to the respective connection.
- The folding of a flame and local pressure differences usually lead to a somewhat earlier flame propagation to another zone than the flame-front position would allow. An empiric mechanism is built in to accomplish this.

Table 5.3.1.3-1 Source terms with the combustion of hydrogen

	Mass per Time	Energy per Time
	Zone Part B (Burned Side)	
Contribution to (Species k)	$\sum_{j=1}^{q} G_{k_j}^{e}$, Entering the zone part	$\sum_{j=1}^{q} G_{k_j}^{e} i_{k_j}^{e}$
Hydrogen ($C_{Mol} = 7.936$)	$\frac{dV^{BR}}{dt} / V^{U} \left\{ M_{H_2}^{U} - min\left[M_{O_2}^{U}, C_{Mol}\left(M_{H_2}^{U} - M_{H_2}^{R} \right) \right] / C_{Mol} \right\}$	$\frac{dV^{BR}}{dt} / V^{U} M_{H_2}^{U} I_{H_2}^{U}$
Oxygen	$\frac{dV^{BR}}{dt} / V^{U} \mathrm{x} \left\{ M_{O_2}^{U} - min\left[M_{O_2}^{U}, C_{Mol}\left(M_{H_2}^{U} - M_{H_2}^{R} \right) \right] \right\}$	$\frac{dV^{BR}}{dt} / V^{U} M_{O_2}^{U} I_{O_2}^{U}$
Steam	$\frac{dV^{BR}}{dt} / V^{U} \left\{ M_{D}^{U} + \frac{1 + C_{Mol}}{C_{Mol}} \times min\left[M_{O_2}^{U}, C_{Mol}\left(M_{H_2}^{U} - M_{H_2}^{R} \right) \right] \right\}$	$\frac{dV^{BR}}{dt} / V^{U} M_{D}^{U} I_{D}^{U}$
Other species	$\frac{dV^{BR}}{dt} / V^{U} M_{k}^{U}$	$\frac{dV^{BR}}{dt} / V^{U} M_{k}^{U} I_{k}^{U}$
		$\frac{dV^{BR}}{dt} \left(\frac{Q_{com}}{V^{U}} \right) \left(M_{H_2}^{U} - M_{H_2}^{R} \right)$
	Zone Part U (Unburned Side)	
Contribution to (Species k)	$\sum_{j=1}^{p} G_{k_j}^{a}$, leaving the zone part	$\sum_{j=1}^{p} G_{k_j}^{a} I_{k_j}^{a}$
Hydrogen	$\frac{dV^{BR}}{dt} / V^{U} M_{H_2}^{U}$	$\frac{dV^{BR}}{dt} / V^{U} M_{H_2}^{U} I_{H_2}^{U}$
Oxygen	$\frac{dV^{BR}}{dt} / V^{U} M_{O_2}^{U}$	$\frac{dV^{BR}}{dt} / V^{U} M_{O_2}^{U} I_{O_2}^{U}$
Steam	$\frac{dV^{BR}}{dt} / V^{U} M_{D}^{U}$	$\frac{dV^{BR}}{dt} / V^{U} M_{D}^{U} I_{D}^{U}$
Other species	$\frac{dV^{BR}}{dt} / V^{U} M_{k}^{U}$	$\frac{dV^{BR}}{dt} / V^{U} M_{k}^{U} I_{k}^{U}$

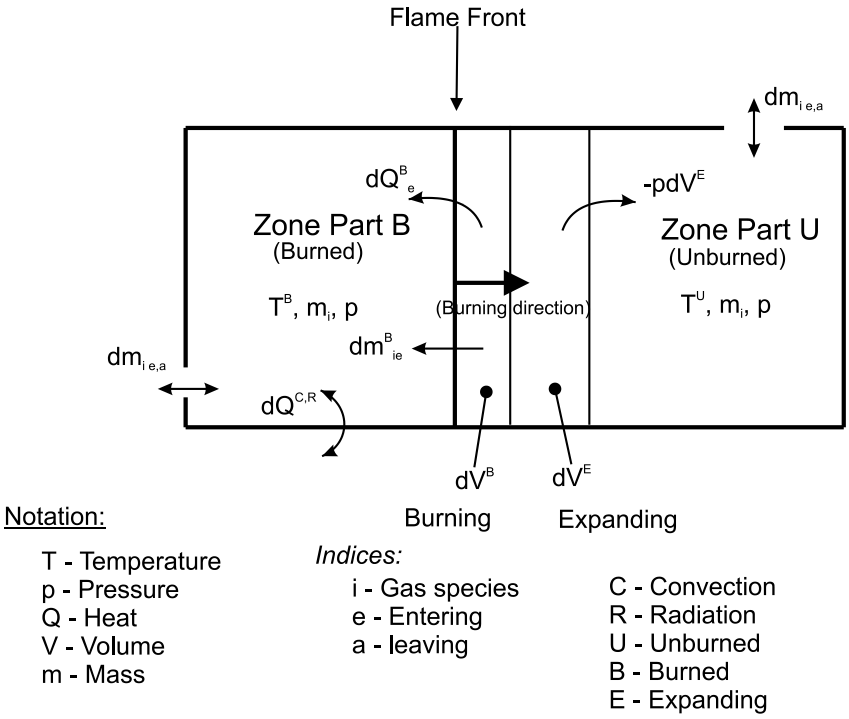

Figure 5.3.1.3-1 Outline of the flame-front model of COCOSYS (DECOR)

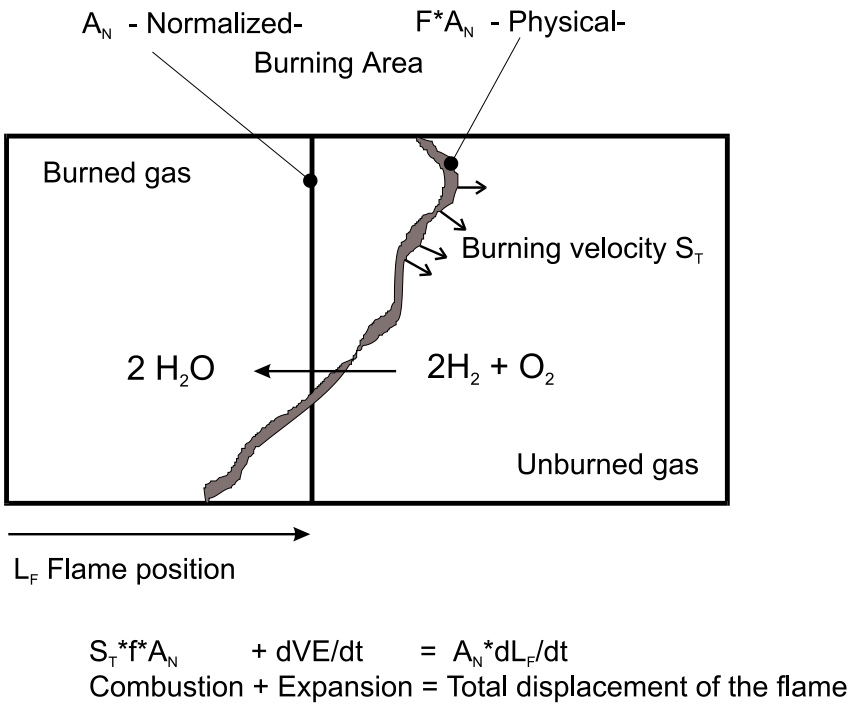

Figure 5.3.1.3-2 Flame-front definition and burning velocity

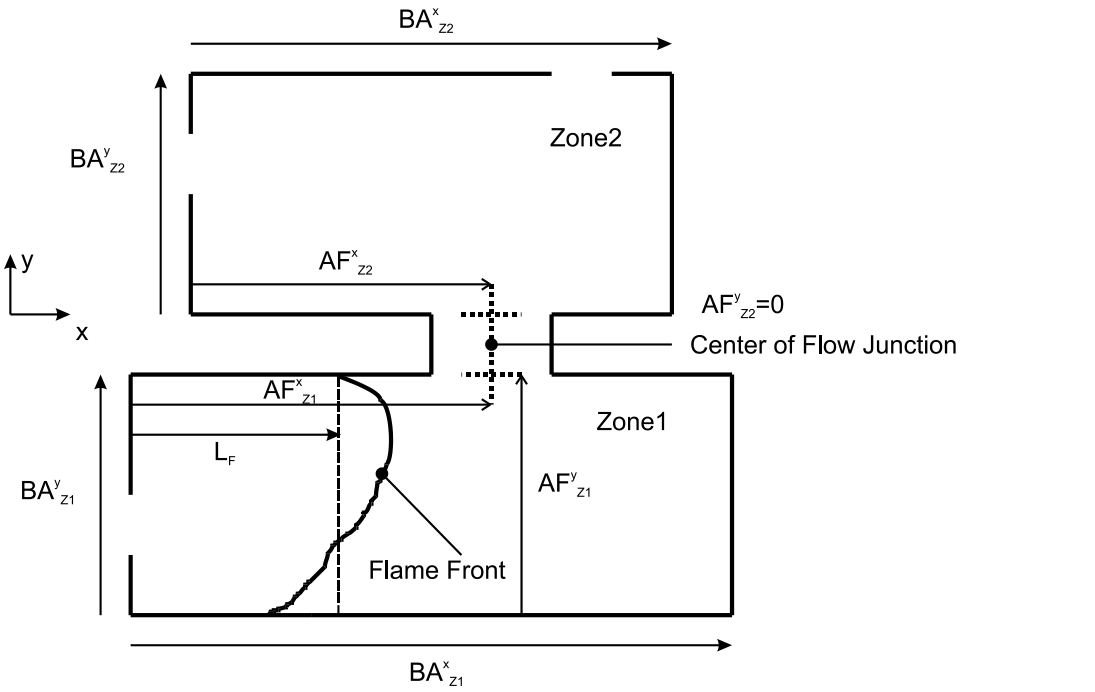

Figure 5.3.1.3-3 Flame branching and burning axes

5.3.1.4 Examples of application

Two applications to experiments illustrate the use of the described combustion model. The first is an experiment conducted at the L.VIEW Test Facility (Figure 5.2.3.2-7). It was conducted using 10.5% of hydrogen in air homogeneously premixed in both compartments. The COCOSYS nodalization can be very simple because the flame fronts moves through the zones, and their subdivision is not important (Figure 5.3.1.4-1). Combustion starts slowly in compartment R1, reaches the circular connection to R2, undergoes strong acceleration in this orifice and burns much faster in R2. Combustion in R2 is approximately 10 times faster than in R1 and ends long before combustion in R1 is completed. This also leads to a short time backflow from R2 to R1 because of the pressure distribution $(p_{R1} > p_{R2})$ and an intensification of the combustion in R1. These effects can well be modelled by the flame-front model DECOR, as can be seen from Figure 5.3.1.4-2. The considerable acceleration through the orifice between R1 and R2 can also be seen from Figure 5.3.1.4-3. The flame-front position versus time in R1 increases much slower than in R2.

The second example is a simulation of complex deflagration in the NUPEC's Large-scale Combustion Test Facility in Japan (Figure 5.2.3.2-27). This test facility permits a number of flame paths and therefore intensive flame branching, as illustrated in Figure 5.2.3.2-28. One test with 10.5% of hydrogen and 30% of steam in the initial mixture (B-2-6) has been analyzed with DECOR [5.90]. The resulting pressure versus time as a comparison between measurement and analysis is depicted in Figure 5.3.1.4-4. According to the fact that the test facility is closed and completely filled with a burnable mixture, dynamic pressure peaks in several locations are superimposed by a constant pressure increase all over the facility.

The one-dimensional combustion model needs the derivation of the flame-stretching factor Equation (5.3.30) from experiments. For this purpose, throughout the validation process of the model, several combustion modes were defined and then stretching factors were determined. The code decides at the beginning of a combustion in a zone, which mode should be applied by checking local mole fractions and the history of the preceding combustion in neighbouring zones. Figure 5.3.1.4-5 gives a summary of the combustion modes available in the code and the values used for the NUPEC tests. The flame-stretching factors depend on the progress of the flame (expressed in the figure by the dimensionless factor x/d) and accelerate the flame depending on their curvature.

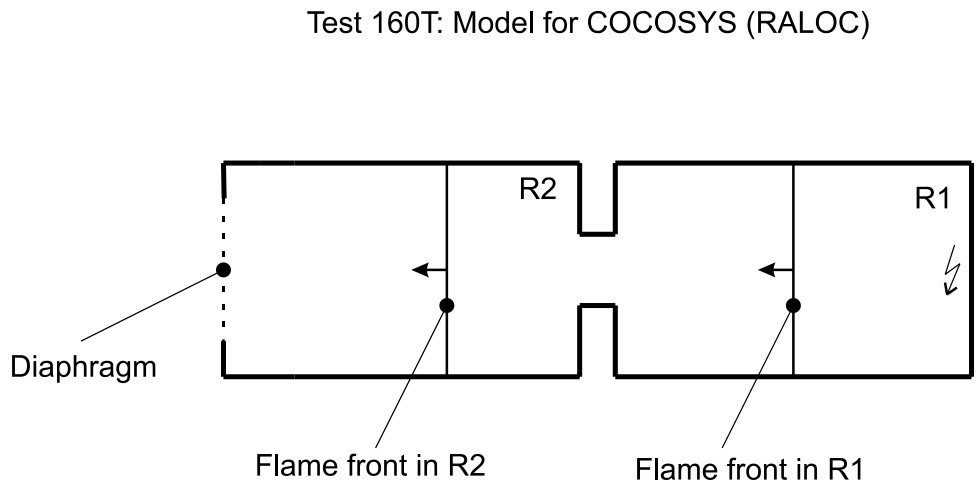

Figure 5.3.1.4-1 Nodalization scheme for the L.VIEW test 160T

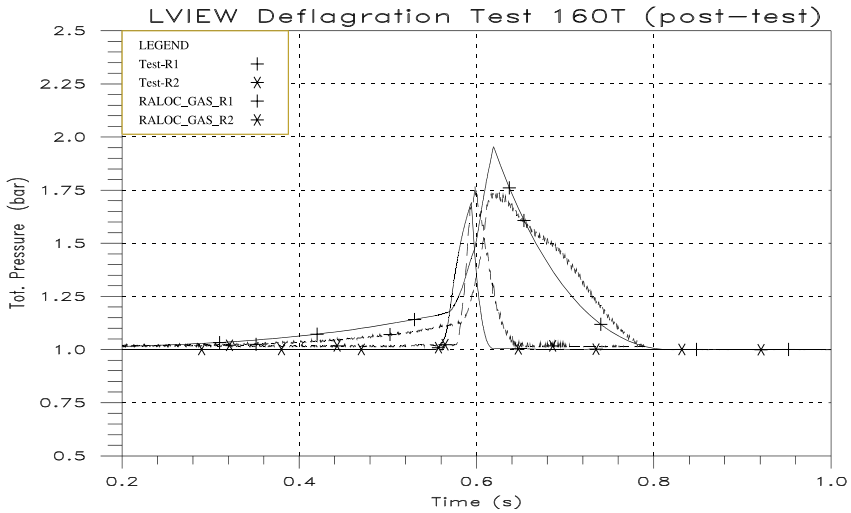

Figure 5.3.1.4-2 Pressure history in the 2 compartments of the L.VIEW test facility with initial conditions of 10.5% hydrogen in air (test values are dotted)

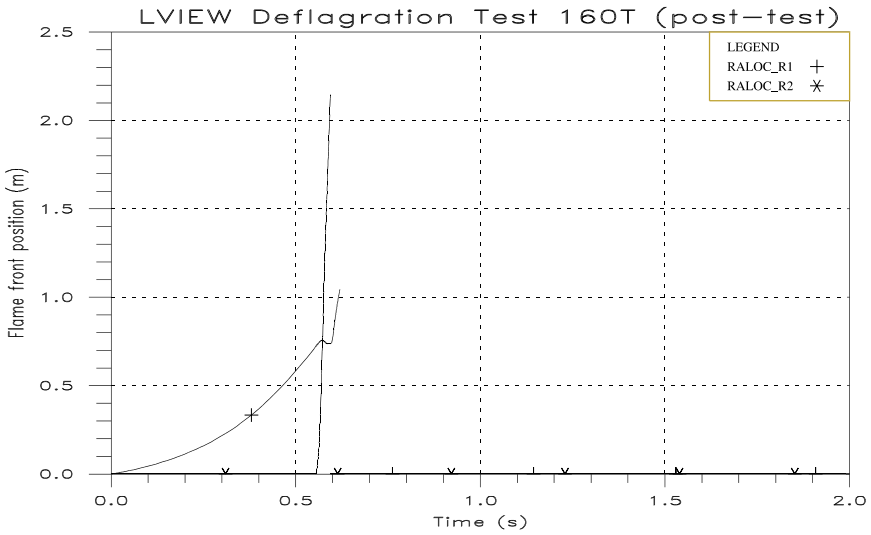

Figure 5.3.1.4-3 Progress of the flame fronts in both test compartments

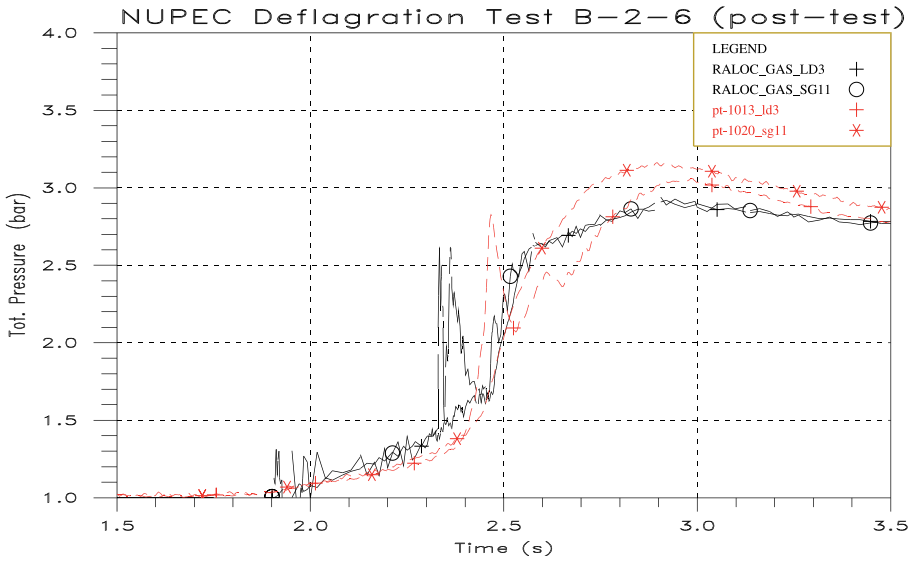

Figure 5.3.1.4-4 Comparison of the pressure buildup of experiment B-2-6 to the COCOSYS simulation

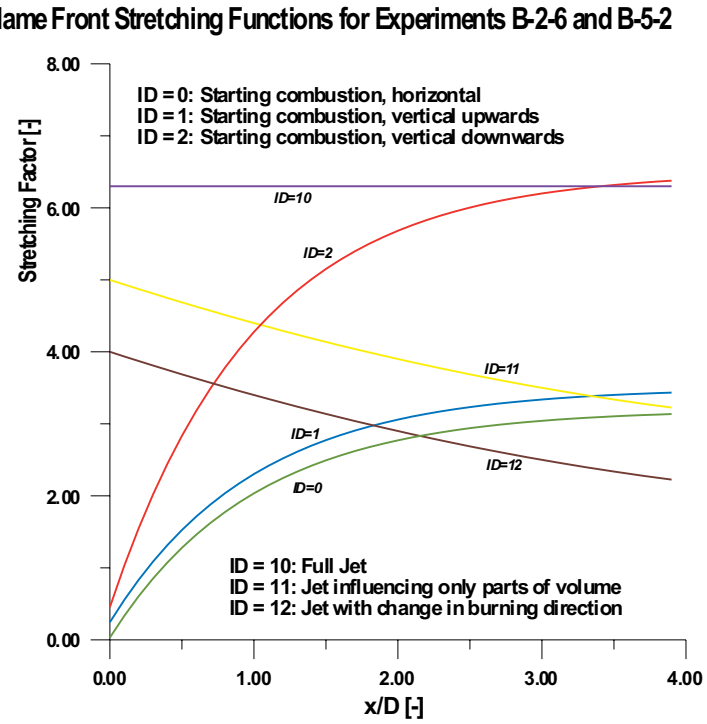

Figure 5.3.1.4-5 Stretching factors for six different combustion modes applicable to the NUPEC large-scale combustion tests (x is the current flame position in a zone, and D is the hydraulic diameter)

5.3.1.5 Coupling to CFD combustion codes

Instead of using the built-in combustion model DECOR in COCOSYS, an interface has been developed to include an external CFD combustion code. By this action, it is expected that the increased capabilities of CFD combustion modelling can be made available to long-term system codes. The interface is characterized by the following features:

- The codes to be involved were developed independently and should retain their individual structure. This eases later inclusion of modified code versions or other codes.
- A message paradigm (PVM - Parallel Virtual Machine [5.91]) is used to provide online data transport between the codes. Additional modules in the codes are needed to send and receive data.
- With respect to a nuclear safety application, the lumped-parameter code is considered as the basic code that runs all the time. If combustible conditions are detected anywhere in the spatial model, the CFD combustion code with actual initial conditions is activated and starts providing combustion data.
- The computational grids of the areas in question have to be created before the coupled run and are not subject to data exchange. They must be consistent.
- The COCOSYS combustion model is only partially used. It gets combustion rates from the CFD code and sends back actual boundary conditions. The combustion rates find access into the source

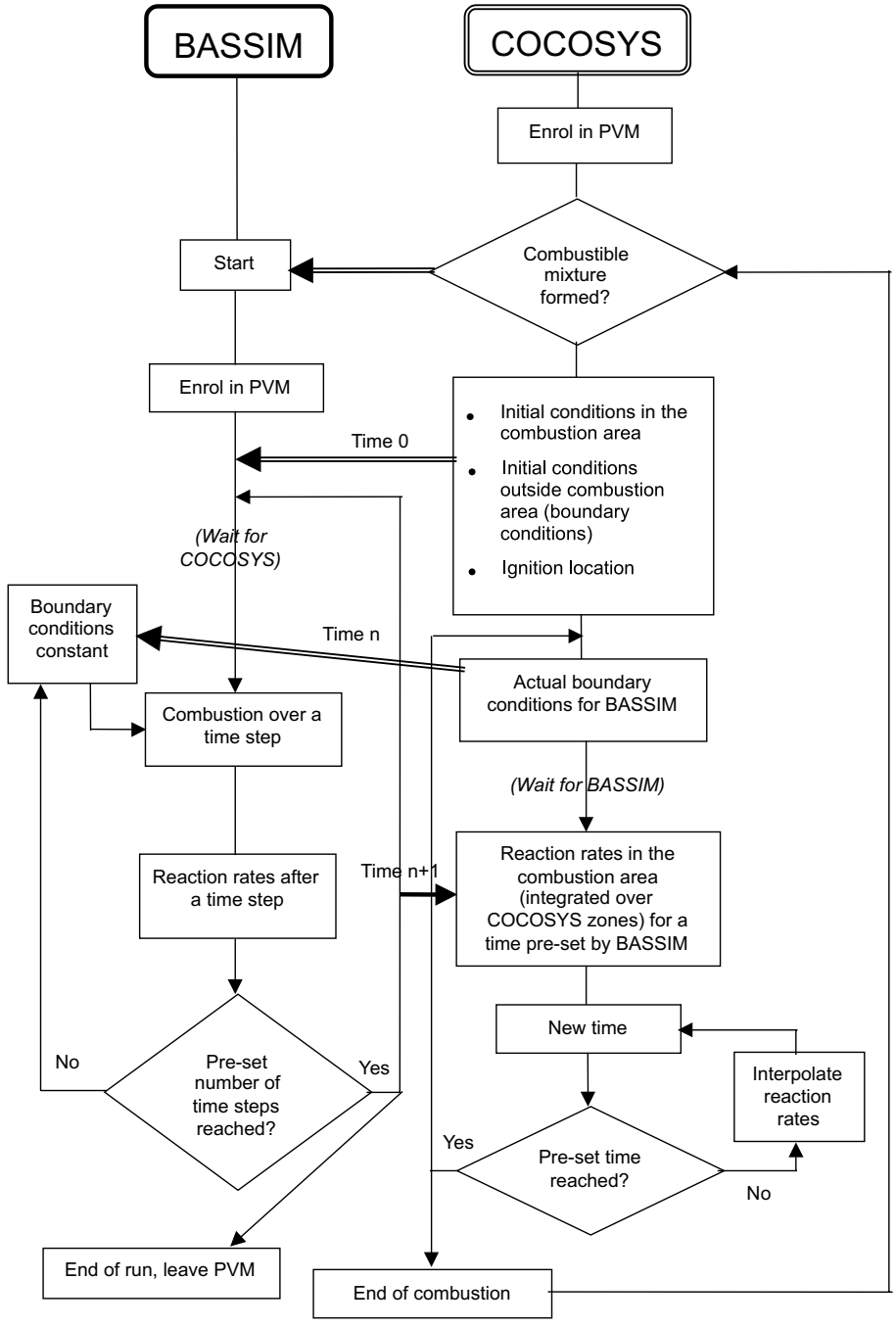

Figure 5.3.1.5-1 Outline of data exchange between a CFD code (here, BASSIM) and the lumped-parameter environment COCOSYS

terms of DECOR (see Table 5.3.1.3-1). It is expected, that the CFD combustion code models only a section of the total system; therefore, it needs the actual conditions at the boundaries.

This type of coupling has been implemented in the CFD combustion code BASSIM and COCOSYS. The principle data flow between these codes is outlined in Figure 5.3.1.5-1. COCOSYS has the general control and spawns also BASSIM as a child process when combustible mixtures have been detected. It is possible to have several child processes, which means there is combustion at different isolated locations. During combustion, the CFD code gets the time control because it is easier to synchronize both codes by steering the lumped-parameter code accordingly. Pressure, temperature, and concentrations in zones surrounding the combustion area (boundary conditions) are held constant during a CFD time step.

Computing times of the CFD code are approximately 10 times higher than for the lumped-parameter code. This code is therefore often in a wait cycle. A different data flow is also available for a coupling when solely gas mixing is of interest.

5.3.1.6 Limitations of combustion models in lumped-parameter codes

Limitations of the lumped-parameter concept in terms of combustion are as follows:

- They cannot provide detailed flow field predictions. All processes that mainly depend on these may be restricted in their results. These can be high-momentum gas-mixing phenomena, combustion, particle flows, and others.
- Therefore, lumped-parameter combustion models are only applicable to slow combustion (FA and DDT criteria not fulfilled) with flame speeds not exceeding $200 \text{ to } 300$ m/s. Whether this is fulfilled may be hard to decide prior to running a simulation. Special care should be taken during the validation process of the model to fix the application limits.
- Combustion as a very fast- and short-term process cannot be described in many details. It is worthwhile simulating combustion with a lumped-parameter code, whenever the impact within a large system like a containment is of interest and to get a first idea of the pressure increase and energy input.

However, there are also merits of the use of lumped-parameter codes in containment accident analyses:

- They are widely used to describe relevant physical processes expected to occur during severe accidents.
- They reflect the interactions between the different processes and are well-suited to perform parameter investigations to identify the impact of uncertainties. This applies mainly to phenomena not fully understood and modelled because the inherent uncertainties do not either justify or even enable the high effort of more detailed (CFD) models.
- They can run over the necessary process times (several days) with the available computer resources.
- Many years of user experience and experimental validation have been spent to get mature code tools.

As a result, a coupling between the simpler lumped-parameter concept and complex CFD codes appears to be very promising. The interface can be arranged that all slow, long-term processes are included in the standard lumped-parameter models and all fast and flow-dependent phenomena into CFD models. The two groups of models have then to communicate online to provide the necessary data exchange (see above).

5.3.2 Combustion in Hybrid CFD/LP-Codes[*]

5.3.2.1 The TONUS code [5.92]

There are two different types of safety analysis codes: (i) multi-compartment lumped-parameter codes such as CONTAIN [5.93], JERICHO [5.94], MAAP [5.95] or RALOC [5.96] and (ii) general-purpose multi-dimensional field codes, such as GASFLOW/HMS [5.97] and GOTHIC/WGOTHIC [5.98] (see Table 5.4.0-1). The advantages of type (i) codes relative to type (ii) codes are simplicity and fast processing; the disadvantages are its limitations for inherently multi-dimensional and unsteady events. The idea of the IPSN TONUS code development is to combine the two modelling approaches in a single system so as to leave the user with the option of either way of modelling. The TONUS code consists of the following features:

- A lumped-parameter model for distribution and slow combustion, comparable with that in JERICHO. Bulk and wall condensation, wall heat transfer and spray models are available, and simplified models for hydrogen combustion using flame velocity correlations are implemented.
- A semi-implicit finite-element low-Mach-number scheme for distribution and slow combustion using the standard zero-Mach-number combustion model [5.99], [5.92]. Turbulence is modelled by the Favre-averaged Navier-Stokes equations and a $k - \varepsilon$ model including buoyancy and weak compressibility effects. Transport equations are discretized by a second-order finite-element method for arbitrary Reynolds number. Both single-step Arrhenius kinetics for laminar and an eddy breakup model for turbulent combustion are available.
- An explicit finite-volume fully compressible scheme for up-to-now detonation simulations. The reactive Euler equations are solved using a second-order upwind finite volume formulation on unstructured grids. Source terms are handled by "operator-splitting" ([5.100], [5.101]).

5.3.2.2 Code construction and structure

The TONUS code is built using the CASTEM 2000 [5.102] system, and its user data manipulating language is called GIBIANE to achieve the flexibility and modularity required in modelling the complex reactor system at hand. The object-oriented structure of this system allows us to build, in a limited amount of time, versatile tools for computing complex flow situations. In particular, CASTEM 2000 encapsulates algorithms in generic data/operation sequences called "procedures", which present to the user a simplified interface with only a limited number of parameters to define. Thus TONUS consists of a set of procedures dedicated to containment modelling.

[*] Contributed by E. Studer

5.3.2.3 Combustion modelling in the lumped-parameter approach

The TONUS lumped-parameter combustion model is derived from work performed for French PSA level 2. This first model has been developed in order to have an estimation of the maximum flame velocity reached in real containment geometry. In this stand-alone model described in Figure 5.3.2.3-1, the following hypotheses have been made:

- Containment geometry is described by interconnected parallelepipedic control volumes for which pressure, temperature, and mixture compositions, that is, the thermalhydraulic conditions are know before ignition (conditions in the unburned gas are not modified during the calculation).
- Combustion in a control volume only depends on the thermalhydraulic conditions described above and on combustion processes in the previously burnt volume (upstream conditions). Acoustics-induced preconditioning of gases far in front of the flame is modelled here by an approximate increase of turbulence intensity u'.

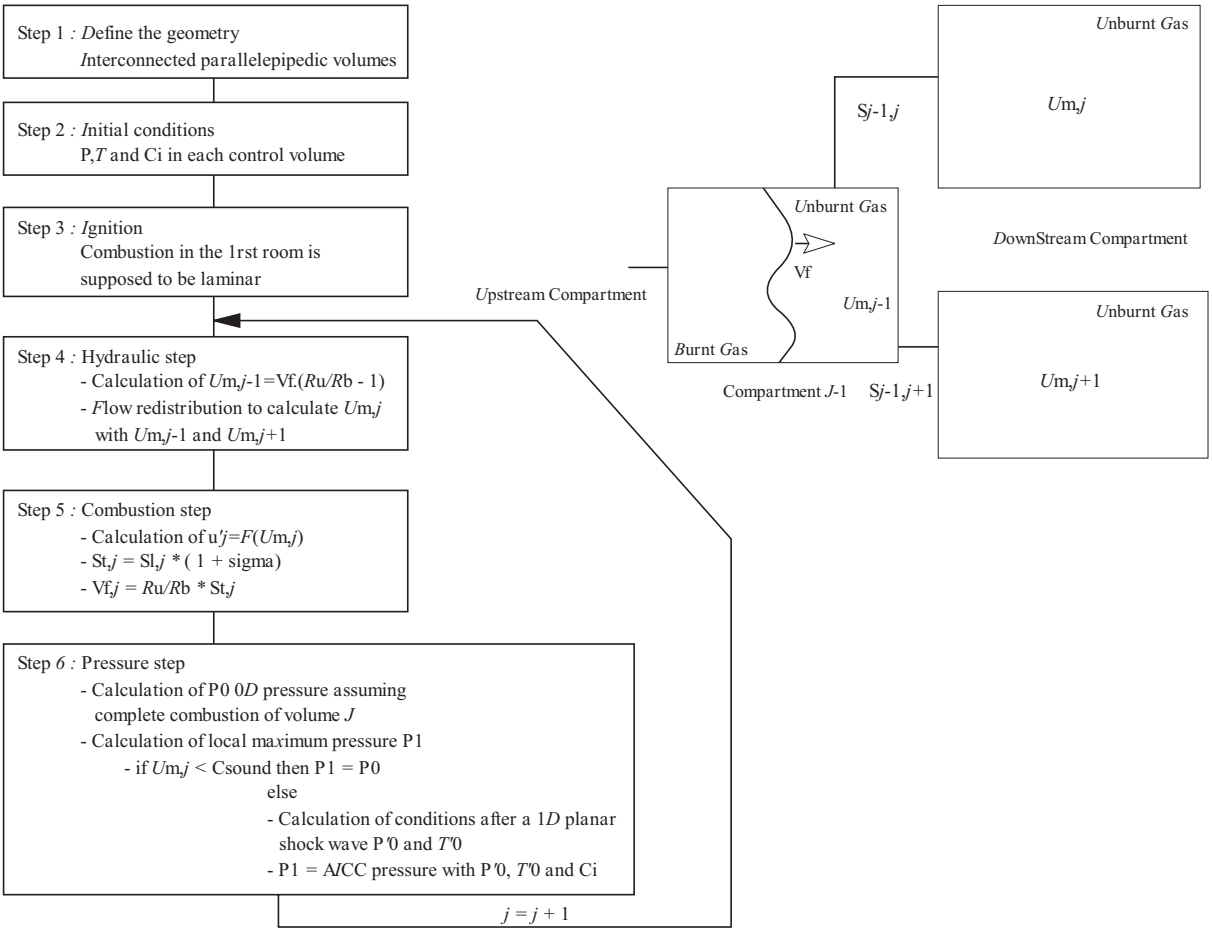

Figure 5.3.2.3-1 Flow chart of the simplified probabilistic safety analysis (PSA) level 2 combustion model

With these preliminaries, the description of combustion is essentially reduced to determining the passage of a turbulent flame speed S_T over the characteristic length L of the control volume, [5.103]. Passage of

flames between control volumes is determined on the basis of additional propagation conditions based on the Shapiro diagram.

Turbulent velocity correlation. Many authors have proposed correlations for turbulent combustion [5.104 – 5.108]. Parameters are mainly laminar flame velocity S_L, expansion ratio ρ_u/ρ_b, the root-mean-square (RMS) fluctuation velocity u', the turbulence integral length scale and adjusted constants. These laws are derived from experimental and theoretical considerations. Three turbulent combustion correlations were compared for a given mixture composition and with different level of turbulence (via u'). Hydrogen-air mixtures at room temperature and pressure were chosen. Explosion tube diameter is supposed to be 6.6 cm with a blockage ratio of 30%. Characteristics of the mixtures are given in Table 5.3.2.3-1 and the results are summarized in Figure 5.3.2.3-2. In the present study, Peters correlation has been chosen:

$$\frac{S_T}{S_L} = 1 + \bar{\sigma} \tag{5.3.33}$$

$$\bar{\sigma}^2 + 0.39\frac{l}{l_F}\ \bar{\sigma} - 0.78\frac{u' \cdot l}{S_L \cdot l_F} = 0 \tag{5.3.34}$$

with S_L: laminar flame velocity (m/s), u': RMS fluctuation velocity (m/s), l: turbulence integral length scale (m), and l_F laminar flame thickness (m).

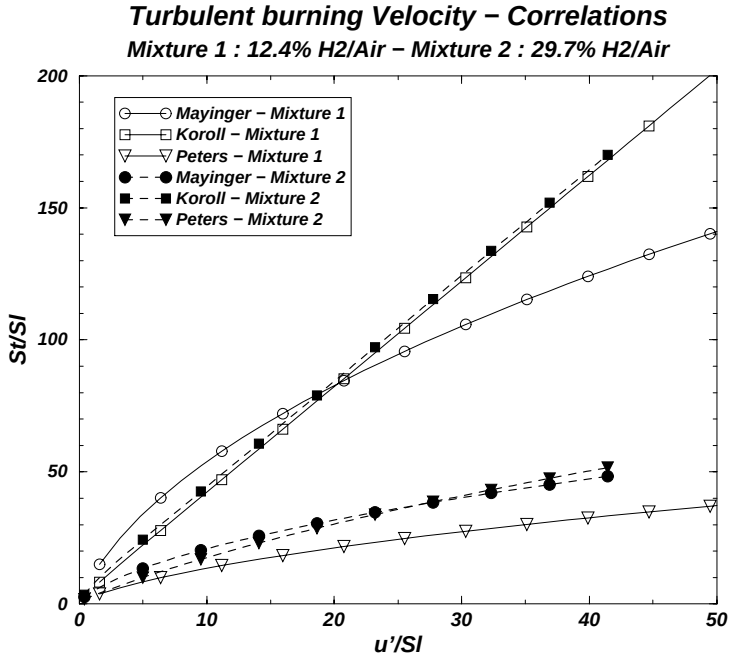

Figure 5.3.2.3-2 Comparison of turbulent flame velocity correlation

It should be emphasized that considerable uncertainties exist even after a turbulent velocity correlation has been selected. Typically, these correlations appear in the form of non-dimensional ratios of S_T/u', so that precise evaluation of S_T still requires an accurate assessment of the turbulent intensity u'.

RMS fluctuation velocity u'. Unfortunately, there is only a minor database for these estimates. In this work, we have used results from the Russian RUT Facility to determine the missing parameters. The

Table 5.3.2.3-1 Mixture characteristics

Characteristics	Mixture 1	Mixture 2
Hydrogen vol %	12.4	29.7
Laminar flame velocity (m/s)	0.62	2.41
Laminar flame thickness (m)	$1.2\ 10^{-4}$	$3.1\ 10^{-5}$
Turbulence integral length scale (m)	$6.4\ 10^{-3}$	$6.4\ 10^{-3}$

RUT Facility has a characteristic geometrical size similar to inner rooms in a real containment, and this model is mainly devoted to a pressure-water reactor (PWR) with pre-stressed concrete containment vessel. The turbulence intensity is defined as a fraction of the fluid velocity U_m.

Validation. The first step concerning validation of this simplified combustion model is verification on selected RUT large-scale turbulent combustion results. As an example, Figure 5.3.2.3-3 gives the flame position versus time calculated in the first channel of the RUT Facility with the model on RUT stm7 test. Blockage ratio is about 30%, and the mixture composition is 17.5 vol % hydrogen diluted by 25.7 vol % of steam at about 100^oC (well-mixed initial conditions).

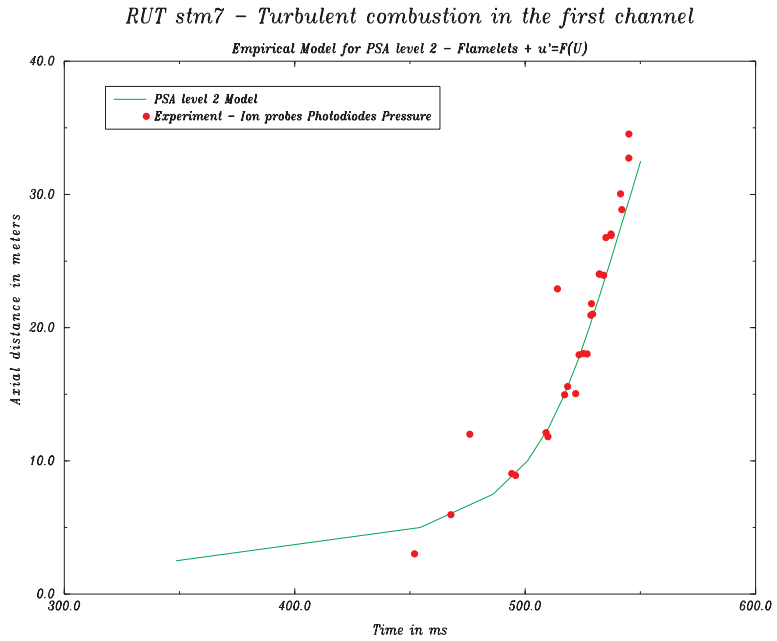

Figure 5.3.2.3-3 Verification of the simplified combustion model.

Other tests such as FLAME experiments were calculated and also some small-scale experiments were performed at AECL (Figure 5.3.2.3-4). Developed correlations give good results if the blockage is between 0.3 and 0.6 and if the ratio between tube diameter and obstacle spacing is between 1 and 2.

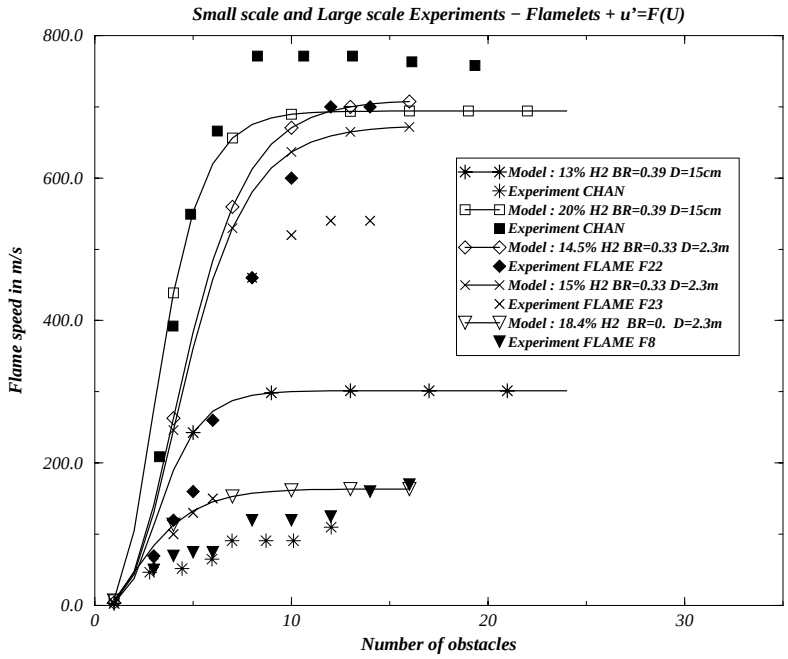

Figure 5.3.2.3-4 Validation against experimental data from AECL [5.109] and from the FLAME facility [5.110]

Effect of mixture gradients has also been computed using an experiment performed in Russia [5.43]. The tube diameter is 17 cm, and, a hydrogen gradient in air has been created via hydrogen diffusion (19.5 vol % near the ignition point and 4.5 vol % at the end of the tube). Results show a good agreement with the experiment and the quenching point is well predicted (Figure 5.3.2.3-5).

Other large-scale verifications were performed regarding the NUPEC large-scale combustion experiments [5.111]. Tests number B1-2 and B1-3 have been simulated (8 vol % and 15 vol % of hydrogen in dry air at initial room pressure and temperature). These verification tests show a good behaviour of our very simplified combustion model in terms of flame-front propagation (Figure 5.3.2.3-6.) and also pressure transient (Figure 5.3.2.3-7). Some additional work is needed to validate the correlation for the turbulent velocity correlation u' in case of small tube diameter. Some preliminary investigations show a large influence of the definition of the turbulent integral length scale.

The model described above was implemented in the TONUS lumped-parameter code only for slow flame regime. In this implementation, the turbulent flame velocity, described above, is calculated in each downstream control volume using the turbulence intensity u' constructed with the junction velocity between the two connected volumes (once at the ignition time). Modifications regarding leading shock wave were not implemented because of the restrictions of lumped-parameter equations (low Mach-number hypothesis). Validation studies of slow flame regime are in progress in the NUPEC large-scale experiments (B1-2 test: 8 vol % in dry air).

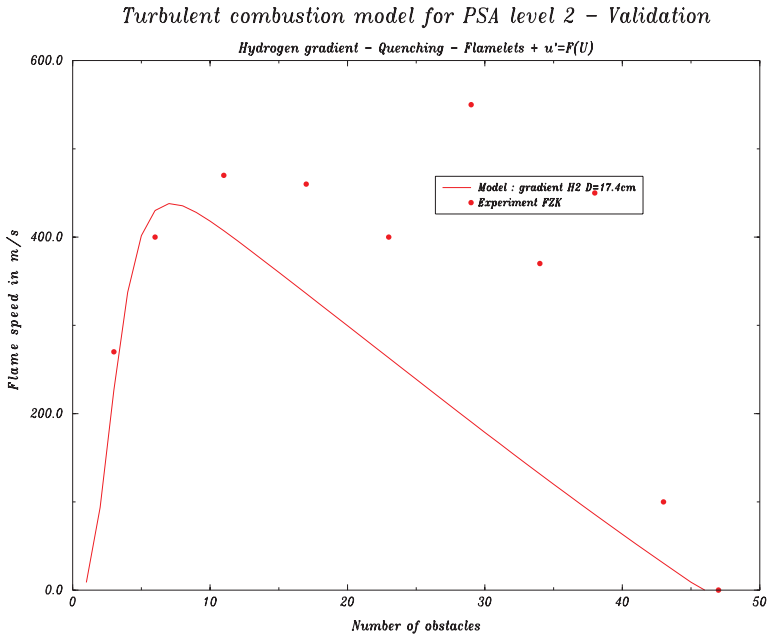

Figure 5.3.2.3-5 Verification of simplified combustion model – Effect of hydrogen gradient

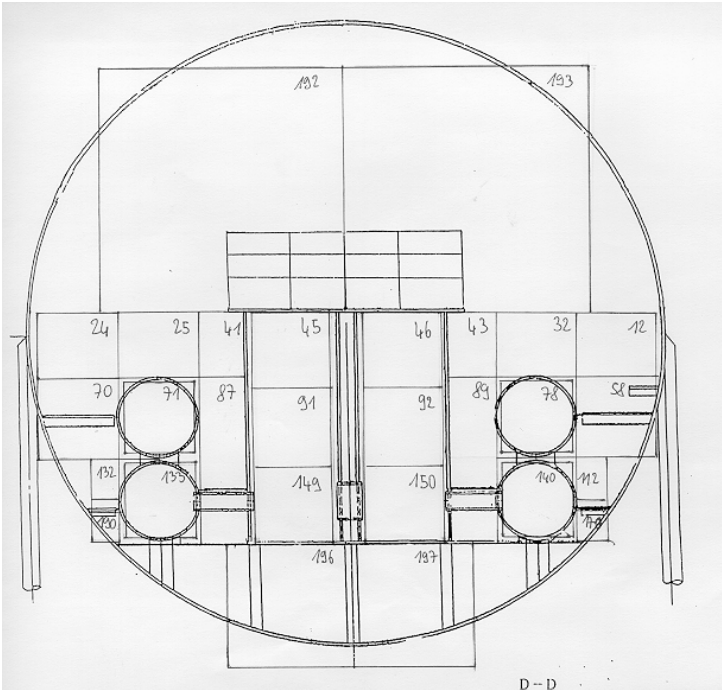

Figure 5.3.2.3-6 Flame arrival time in seconds (experiment B1-2 calculation)

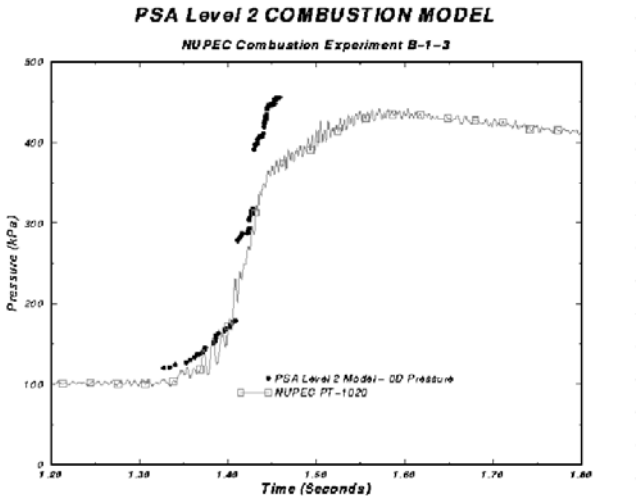

Figure 5.3.2.3-7 Pressure transient – comparison between calculation and experimental results (lumped-parameter pressure P0)

5.3.2.4 Multi-dimensional combustion simulation

Multi-dimensional combustion simulations using the TONUS environment are work that is in progress. An illustration of the TONUS low Mach-number flow solver and eddy breakup turbulent combustion model validation is given in Figures 5.3.2.4-1 and 5.3.2.4-2 [5.112]. This test corresponds to a turbulent combustion in the FZK tube (12 m long, 350 mm diameter). The blockage ratio is 0.3, and the mixture is 10 vol % of hydrogen at room conditions. Verifications are also available for the fully compressible flow solver in the same final report. Others validation and verification studies are not yet available.

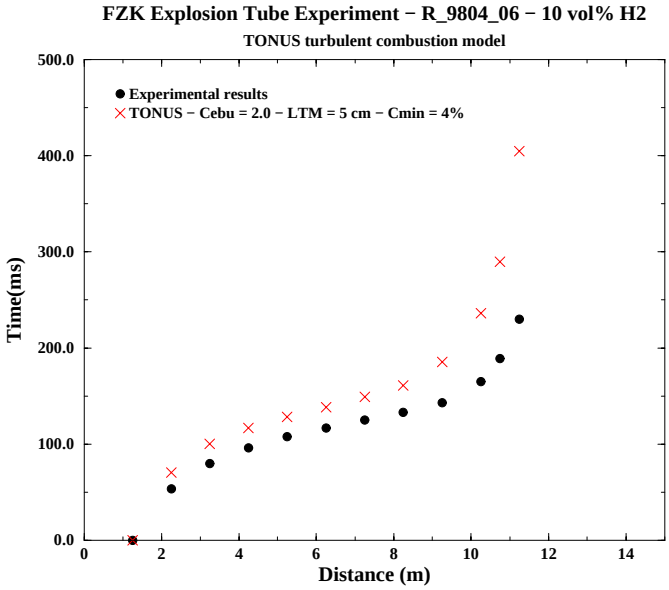

Figure 5.3.2.4-1 Flame position, TONUS calculation

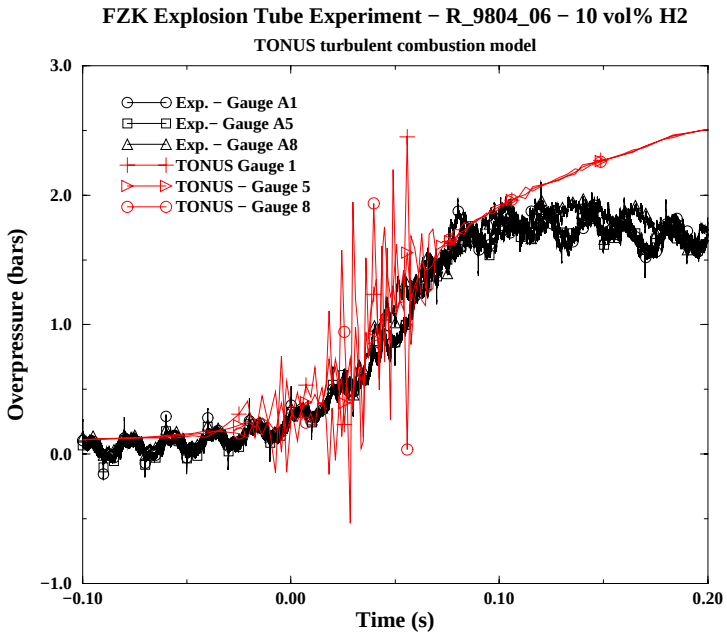

Figure 5.3.2.4-2 Overpressure, TONUS calculation

5.3.2.5 Current implementation of DDT criteria in TONUS

The following two necessary conditions to create a detonation from a fast turbulent flame are currently favoured as DDT criteria implemented in the TONUS code:

Criterion 1. (Data compiled at the Kurchatov Institute in Moscow [5.113]) According to a review of international data related to the onset of DDT and specific experiments conducted at the RUT Facility, this criterion is related to the mixture explosion sensitivity. The DDT condition requires a characteristic system size D to be larger than 7 times the corresponding detonation cell size λ. The length scale D depends on the geometry involved (e.g., in large volumes it should be the size of the room or the size of an hydrogen cloud; in channel geometries, it should be the height or the distance between obstacles).

Criterion 2. (Data compiled at AECL and FZK experiments, [5.109]) A minimum turbulent deflagration velocity, characterized by the lead shock Mach number, appears to be required to create DDT. The proposition by AECL is $Ma > 1.5$ for a limited range of mixtures. More generally, FZK proposes $Ma = f(H_2)$ for general hydrogen concentrations and with an empirical fitted function f(.). This approach is supported by the RUT Facility experiments. This criterion is related to an older approach based on the minimum running distance. These two necessary conditions will be used to create a single condition for the onset of a detonation in the TONUS code. The methodology is first to compute where criterion 1 is reached before ignition of the mixture and then, during combustion, to evaluate the location where criterion 2 is reached. DDT is likely to occur wherever both criteria are met simultaneously. To calculate the 2 criteria, the follwing data are needed in the lumped-parameter and in the multi-dimensional approach:

Detonation cell size evaluation. Different alternatives have been considered: (i) computation of induction lengths from a Zeldovic-von Neumann-Döring (ZND) model and correlation to cell size following

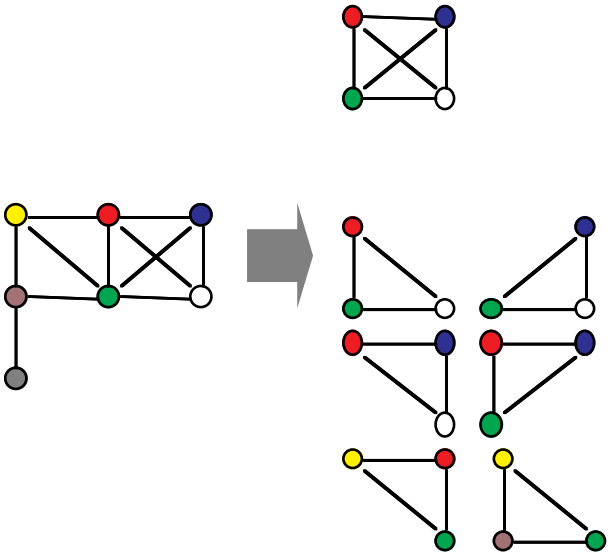

Figure 5.3.2.5-1 Extraction of a sub-graph representing the relevant connected control volumes in a lumped-parameter approach for DDT criteria evaluation

Reference [5.114], and (ii) polynomial interpolation between experimental data. Because the first option requires an expensive detailed chemistry model, we employed the second option for the first implementation. An Arrhenius law ($= A \cdot exp(-E_a/R \cdot T)$ was chosen as an approximate formula, and the free parameters A, E_a/R were fitted on experimental results available in the open literature [5.115 – 5.117] (For details see the final report [5.118]).

Local Mach-number evaluation. Computation of the local sound speeds is straightforward in both the lumped-parameter and multi-dimensional approaches. While the latter also provides the characteristic flow velocity as a field variable, an ad hoc approximation must be invoked in the former. We have chosen to assess the fluid velocity in a cell by the atmospheric junction velocity. Others choices should be examined during applications.

Geometrical size D. The geometrical size D is a characteristic length of a reactive mixture cloud, and in well-mixed conditions it corresponds to the room size. In the calculations, it has been chosen to use the detonation cell size variable to determine the size of the cloud. According to minimum and maximum system dimensions, isovalues of detonation cell sizes have been chosen by the user. In groups of cells in which the detonation cell size is smaller, the Nth isovalues are determined. Using these subgrids, the geometrical size D can be estimated as the smallest distance between the barycentre and border, volume over border area etc. There are still open questions on this subject to determine the right geometrical dimension. Sensitivity studies should be performed for each possible choice. In the lumped-parameter approach, when a cloud has been identified (detonation cell size lower than the Nth isovalue) a graph is constructed and then, we have to extract all the complete graphs with a dimension greater than 3 (all possible connections). An example is given in Figure 5.3.2.5-1. A revised methodology will be implemented according to the conclusions of this report especially concerning the geometrical characteristic length size D. Regarding lumped-parameter approach, a proposal is given in Chapter 6.

*5.3.3 Combustion in CFD Codes Using the Eddy Dissipation/ Eddy Breakup Concept (EDC/EBU)**

5.3.3.1 Introduction

This section presents an example for turbulent combustion simulation using an eddy dissipation concept, as described in Chapter 4.3, by means of the COM3D code (see Table 5.4.0-1). This code was selected for this purpose because of its current active application to full-scale 3D reactor containment problems (2 million cells). The development of the COM3D code was started at the Kurchatov Institute [5.119] and was continued at FZK ([5.120], [5.121]). The sections that follow describe the code models and their validation by experimental results on different scales.

5.3.3.2 Code Description

The structure, the essential components, and the underlying physical models of the COM3D code are shown in Figure 5.3.3.2-1, and the models equations are summarized in Figures 5.3.3.2-2 and 5.3.3.2-3.

- The gas dynamic model includes the Favre-averaged conservation laws of total mass, momentum, energy, and species mass.
- The turbulence modelling offers the choice between two different treatments
  - standard $k - \varepsilon$, and
  - RNG $k - \varepsilon$ [5.122] (renormalization group theory)

  The RNG model, compared with the standard $k - \varepsilon$-model, provides more accurate predictions for flows with rapid distortions and large eddys.
- The thermodynamic model distinguishes four gas components (H_2, O_2, N_2, H_2O).
- The chemistry model describes the reaction rate with medium and high turbulence intensity. This allows one to treat thickened turbulent flames ($Da > 1$) and a quasi-homogeneous reaction regime ($Da < 1$). If the chemical reaction is the faster step, the rate is governed by the turbulent dissipation or the decay of eddies (eddy dissipation model). Otherwise, a corresponding Arrhenius equation is used to model the chemical reaction rate.
- To solve these equations numerically, a TVD [5.123] (total variation diminishing) procedure is used. The equations are solved on a 3D Eulerian carthesian grid.

It is crucial to verify the different models implemented in the COM3D code in a systematic step-by-step procedure. Different individual models were tested on increasingly complex problems.

*Contributed by Dr. W. Breitung

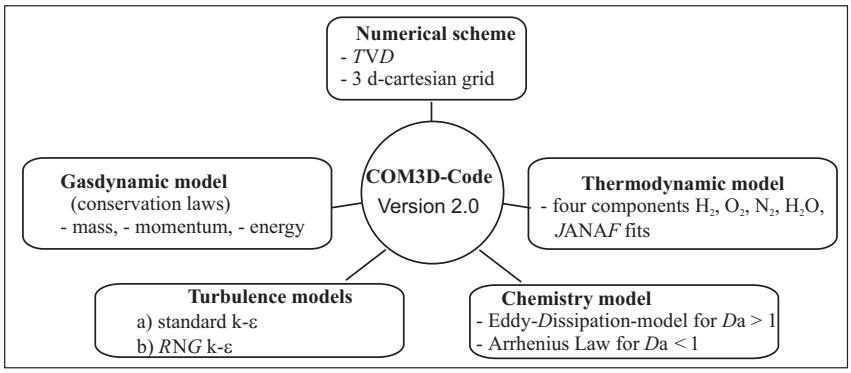

Figure 5.3.3.2-1 Structure and models of the COM3D code

Hydrodynamic equations

The set of conservation laws for mass, momentum, energy and species reads as

$$(\rho)_t + (\rho u_j)_{x_j} = 0,$$

$$(\rho u_j)_t + (\rho u_i u_j)_{x_j} = \rho g_i - p_{x_i} + M_{ij,x_j}, \quad i = 1,2,3$$

$$(\rho e)_t + ((\rho e + p)u_j)_{x_j} =$$

$$\rho g_j u_j + u_i M_{ij,x_j} + (\frac{\mu_{tur}}{C_h}(e - \frac{1}{2}u_i u_i + \frac{p}{\rho})_{x_j})_{x_j} + B + \rho\epsilon,$$

$$(\rho f_\alpha)_t + (\rho f_\alpha u_j)_{x_j} = \overline{\dot{w}}_\alpha + (\frac{\mu_{tur}}{C_{f_\alpha}} f_{\alpha,x_j})_{x_j},$$

here

$$e = \sum_{\alpha=1}^{N} \frac{f_\alpha}{\mu_\alpha}\left(h_\alpha + \Delta h_\alpha^0 - RT\right) + \frac{1}{2}u_j u_j, \quad f_\alpha = \frac{\rho_\alpha}{\rho},$$

$$M_{ij} = -\frac{2}{3}\delta_{ij}(\rho k + \mu_{tur} u_{r,x_r}) + \mu_{tur}(u_{i,x_j} + u_{j,x_i}).$$

Closure of the equation depends on the knowledge of the following variables: μ_{tur}, k, ε, (theory of turbulence) and $\overline{\dot{w}}_\alpha$ (combustion model).

Figure 5.3.3.2-2 Hydrodynamic equations of the COM3D code

Figure 5.3.3.2-3 Standard $k-\varepsilon$, $RNG-k-\varepsilon$, and reaction model, as implemented in the COM3D code

5.3.3.3 Code validation

The forward facing step problem. The supersonic flow through a 2D duct with a forward-facing step was analyzed. This numerical test problem has been investigated by many authors using various codes and different numerical methods. The correct solution is well-known. This high-velocity problem provides a good test for both the ability of the COM3D code to solve the Euler equations numerically and for the correctness of the thermodynamic data (JANAF-fits). Figure 5.3.3.3-1 shows a corresponding result. The calculated stagnation pressure, angle of bow shock, shear layer position, and downstream shock pattern are in good correspondence with the known numerical solutions. The total variation diminishing (TVD) scheme used in the COM3D code preserves shock fronts very well.

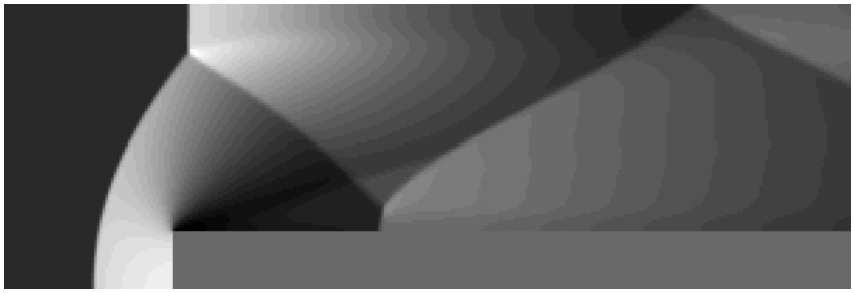

Figure 5.3.3.3-1 COM3D verification on a hydrodynamic test problem. Supersonic flow through a duct containing a forward-facing step: N_2**,** $M = 3$**,** $p_0 = 1$ **bar,** $T_0 = 298$ **K. The computational grid is** 100×300 **cells. Good agreement is observed with the known solutions.**

He-air turbulence test. The 12-m FZK tube was used for inert tests in a shock tube mode. The tube is divided by a membrane in two parts (Figure 5.3.3.3-2). The 3-m-long section can be pressurized, and the bursting of the membrane creates a shock wave travelling into the adjacent low-pressure section (e.g., at 1 bar), which contains circular orifices as obstacles. The velocity and pressure amplitude of the shock wave decrease by partial reflection and turbulence generation. Then, the measured pressure signals at different locations can be compared with numerical simulations based on different turbulence models. This allows the verification of the turbulence models under inert conditions, without disturbances by a combustion process. Using three different levels of turbulence modelling – without turbulence, with $k - \varepsilon$, with RNG $k - \varepsilon$ – the experiment on turbulence generation and dissipation in inert He-air was simulated with COM3D. An uniform 3D cartesian grid with 1-cm mesh spacing, which results in a total of 390 000, cells, was used for the calculation. Figure 5.3.3.3-3 compares a measured pressure signals with the COM3D calculations without turbulence model and the RNG $k - \varepsilon$ model. The calculation without the turbulence model shows considerable deviations from the measured pressure data. Including a $k - \varepsilon$ or RNG $k - \varepsilon$ model provides a better agreement with the experiment. The calculation matches the measured pressure associated with the incoming wave very well. The differences between the $k - \varepsilon$ and RNG $k - \varepsilon$ models were only minor; thus $k - \varepsilon$ appears sufficient for the investigated problem.

Reactive flow tests in different scales. The 12-m tube was modified to allow turbulent combustion tests on a medium scale (Figure 5.3.3.3-4). In the whole tube, equally spaced ring-shaped obstacles are installed to block a certain ratio of the flow path. The eddy break up combustion model of the COM3D code contains a reaction rate constant c_f, which must be obtained empirically from experimental results. A large series of calculations for turbulent combustion experiments with different H_2 concentrations and blockage ratios confirmed a value of $c_f = 6 \pm 1$ for a great variety of experiments. A comparison between measured and calculated pressure is displayed in Figure 5.3.3.3-5 for a test with 15% H_2 and

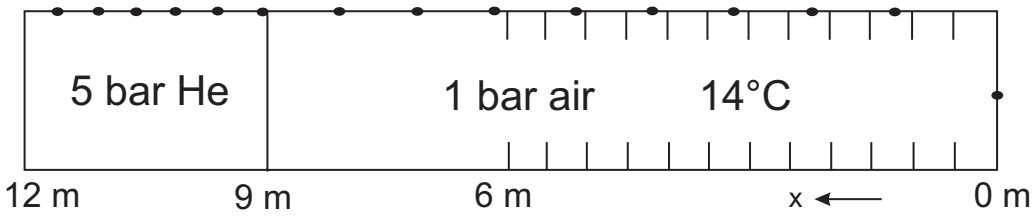

Figure 5.3.3.3-2 Shock tube configuration of FZK 12-m tube

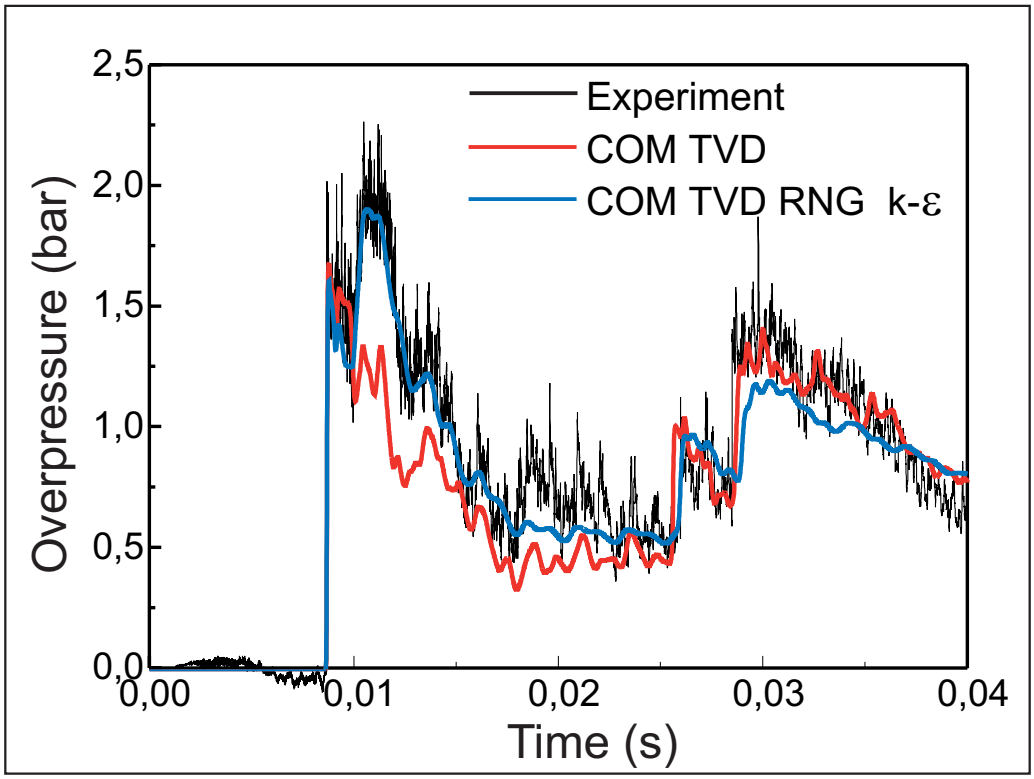

Figure 5.3.3.3-3 Comparison between measured and calculated pressure in inert shock tube test ($x = 4.25$ m)

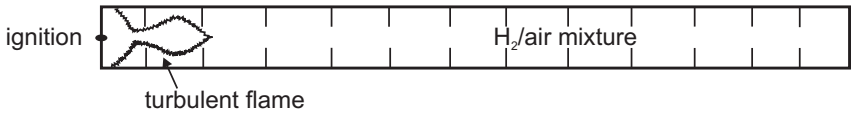

Figure 5.3.3.3-4 Schematic view of 12-m FZK tube equipped with obstacles

30% blockage ratio. It shows good agreement with the data for the integral combustion development and local pressure loads [5.124].

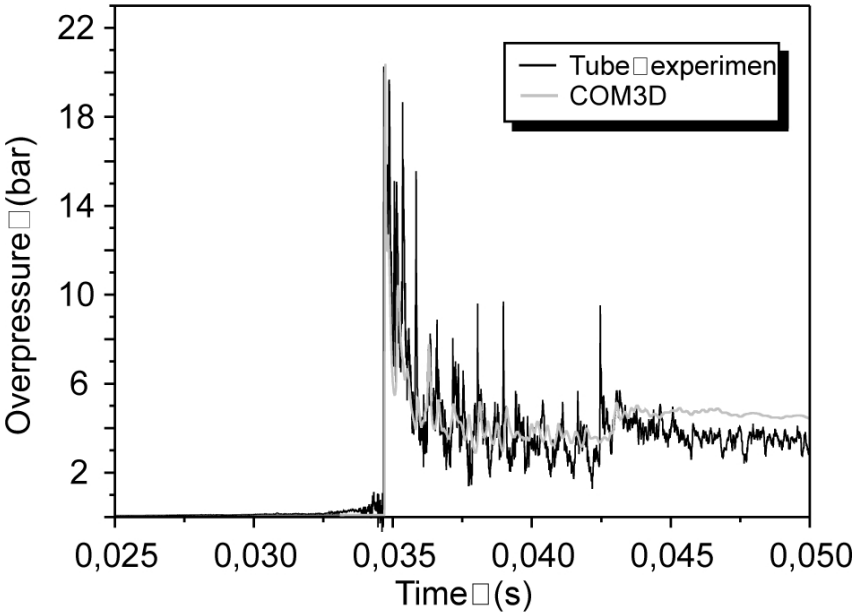

Figure 5.3.3.3-5 Comparison of calculated and measured pressure signals for tube experiments

Large-scale experiments performed in the RUT Facility [5.125] yielded further data for confirmation of the combustion model. The RUT Facility is depicted in Figure 5.2.3.2-30 . The whole facility has a lenght of about 60 m and a cross-section area of $5.25\ \mathrm{m}^2$ in the channel part. Figure 5.3.3.3-6 shows as an example the good agreement between measured and calculated data. A c_f-value of 6 was used as in the medium-scale calculation. All major peaks in the experimental data can be identified in the calculation, showing that the simulation captures properly the essential wave propagation phenomena in the complex 3D enclosure.

Conclusions. Using the COM3D code as an example, this section showed the major steps necessary for the development of a verified CFD program for reactive flow. A 3D code was developed for simulating fast turbulent combustion in H_2-air-steam mixtures. The exploited models (numerical, gas dynamic, thermodynamic, turbulence, chemical kinetics) were validated on medium and large test problems and experiments. The COM3D code may be considered as a verified tool for sufficiently accurate simulations of fast turbulence combustion on a full reactor scale. An example of a reactor application will be given in Chapter 6.

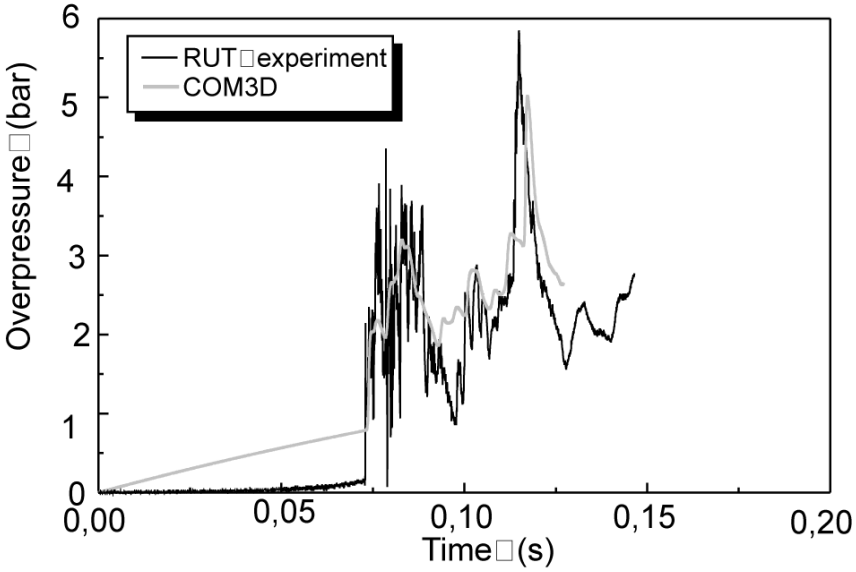

Figure 5.3.3.3-6 Comparison of calculated and measured pressure signals for RUT Facility experiment

5.3.4 Application of the eddy breakup model to a complex geometry[*]

The NUPEC Large-scale Test Facility (Figure 5.2.3.2-27) offers interesting features to be used for combustion model validation. It was built to be similar in design to a nuclear containment, and it models the major components of a nuclear containment in its interior. These components are hollow and are open for gas flow and flame passage but act also as obstacles for flows around them.

For CFX-4.2 ([5.126], see Table 5.4.0-1) a block structured grid was created, with the aim to include all relevant components. Figure 5.3.4-1 shows a view of the inner of the sphere and reveals the two steam generator cylinders surrounded by two ring-like pipes (“doughnuts”). Figure 5.3.4-2 shows a view of the outer shell cut off. This picture shows that all inner parts of the test facility are interconnected by small pipes. From the cylinders, two pipes enable flows to the lower doughnuts. After a circular turn of 90^o, two pipes branch the flow to the upper doughnuts. From there, again after a 90^o turn, connections to the outer sphere exist.

The grid consists currently of about 52 000 cells, and this number can be considered as a minimum. Respective investigations have not yet been conducted to characterize the influence of the combustion process. Figure 5.3.4-3 gives two examples of the grid related to internals of the test facility. On the right side of Figure 5.3.4-3 the upper part of the upper doughnut has been removed. This reveals that in the doughnuts additional orifices are installed in order to provoke continued flame acceleration.

The combustion model used is the eddy breakup approach with Damköhler cut-off to model flame quenching. The reaction then rate reads as follows:

$$R = -\rho \frac{\varepsilon}{k} \, C_R C_A M_{lim} \tag{5.3.35}$$

[*] Contributed by Dr. M. Heitsch

with

$$C_R = 23.6 \left(\frac{\mu\varepsilon}{\rho k^2} \right)^{\frac{1}{4}}, \tag{5.3.36}$$

$$C_a = 1.0 \; if \; D \geq D_{ie}$$
$$C_a = 0.0 \; if \; D < D_{ie} \; . \tag{5.3.37}$$

D_{ie} is a threshold Damköhler number below which the chemical reaction is suppressed to simulate local quenching.

$$M_{lim} = min \left(m_F, \frac{m_O}{I}, B\frac{m_P}{1+I} \right) \; . \tag{5.3.38}$$

The m_F, m_O, and m_P are the mass fractions of fuel, oxidizer, and products respectively. The stoichiometric coefficient of the chemical reaction is denoted by i. The Damköhler number is defined by the following form:

$$D = \frac{\tau_t}{\tau_{CH}} \tag{5.3.39}$$

with the turbulent time scale defined as

$$\tau_t = \frac{k}{\varepsilon} \tag{5.3.40}$$

and the chemical induction time (after Schott and Kinsey [5.127]) given by

$$\tau_{CH} = A_{CH} e^{\frac{T_A}{T}} \left(\rho m_F\right)^a \left(\rho m_O\right)^b \; . \tag{5.3.41}$$

A_{CH} is a constant, T_A an activation temperature, and a and b are exponents for the fuel and oxygen density respectively. The constants from Equations (5.3.37), (5.3.38) and (5.3.41) are distinct for the hydrogen-oxygen reaction but depend also on the scale of the test facility. In Reference [5.128] detailed investigations on different scales and test facilities were conducted to fix the constants. With this support, the following constants are set:

$$D_{ie} = 5, A_{CH} = 2.25 * 10^{-11}, T_A = 9132, a = 0, b = -1, B = 1 \; . \tag{5.3.42}$$

Test B-2-6 from the NUPEC experimental program has been simulated. The same deflagration experiment has also been analyzed, as described in Reference [5.90]. The initial mixture is composed of 10.5% hydrogen, 12.5% oxygen, 30% steam, and the rest is nitrogen. Ignition takes place in the left steam generator close to the bottom, and the combustion progress is most of the time asymmetric. First, a flame expands upwards through the steam generator cylinder into the outer sphere of the test facility. Very soon, the flame front also branches through the available connection pipes into the outer lower doughnuts. In Figure 5.3.4-4 at two different times, the progress of the deflagration is shown. Shaded contours of temperature are used to illustrate the flame propagation. The upper part (at 0.9 s) spots the moment when on the left side of the test facility the lower doughnut is reached, and in the right steam generator cylinder the flame progressed less . Later, at 1.305 s (lower part of the figure), hot gases tend to leave from the upper doughnut into the sphere. This means, that (invisible in the figure) through the available connection pipes the upper doughnut is already reached by a flame. However, in the lower doughnut, combustion has not reached the right section because no elevated temperatures can be seen there.

Figure 5.3.4-5 is a comparison of the pressure history in the left steam generator and in the upper doughnut, a comparison of measured values with simulated values. In the early phase, the modelled combustion

is faster than the measured combustion. This is why the laminar initial phase has not been modelled and from the beginning a full turbulent combustion is assumed. Later, the simulation overestimates the buildup of total pressure in the test facility. This may be true to the complete consumption of all the fuel, what is inherently involved in the eddy breakup model by default. Radiative losses from the hot steam may also play a certain role and may lower the pressure but have not yet been included. It should be stressed that the presented simulation intentionally did not modify basic model constants in order to get a better agreement with measured data. Instead, this analysis demonstrates the capabilities of the combustion model and its implementation in the CFX model available for a blind simulation,for example, in a nuclear containment.

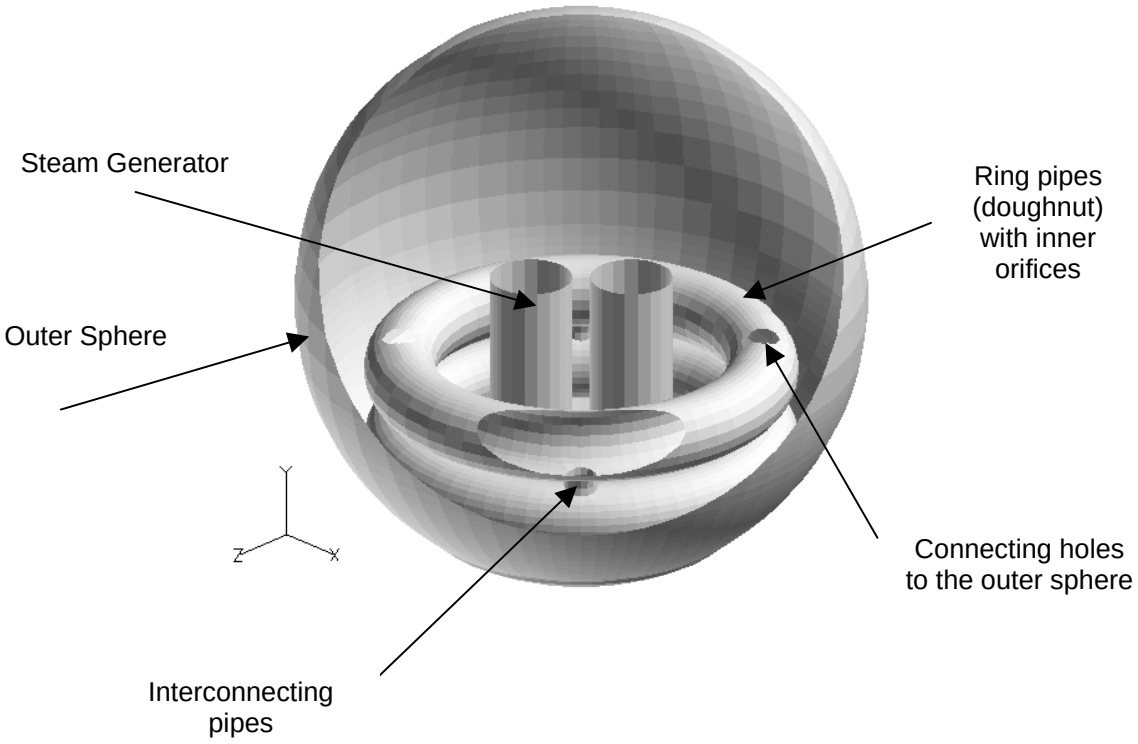

Figure 5.3.4-1 Cutaway view through the CFX model of the NUPEC Large-scale Test Facility

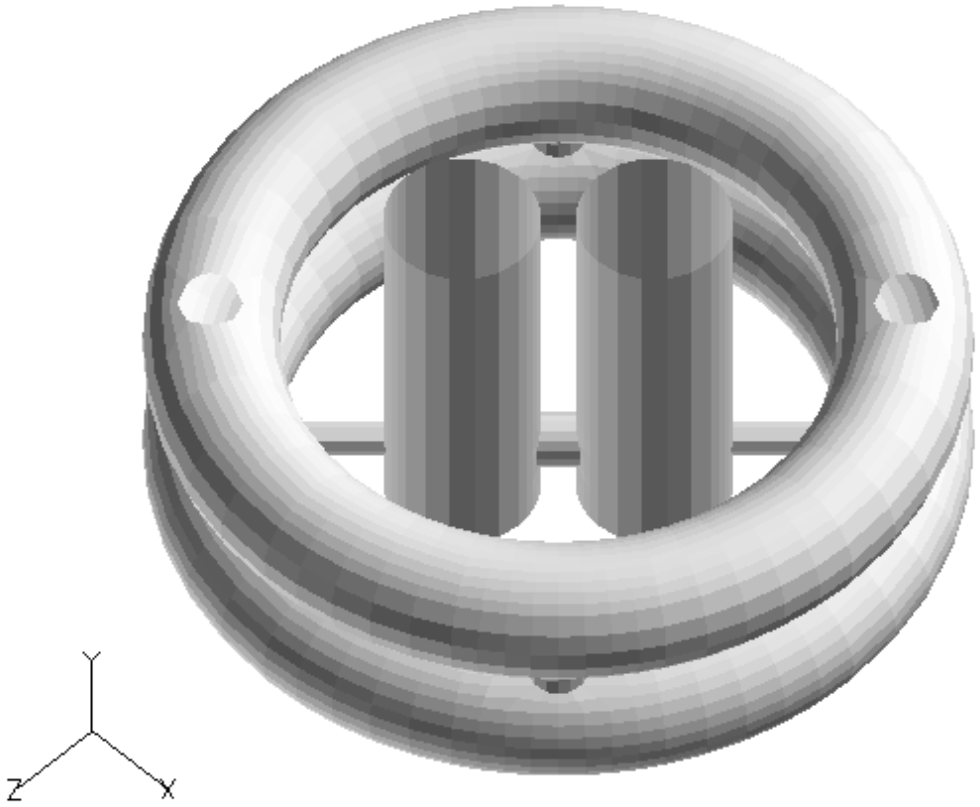

Figure 5.3.4-2 Perspective view of the modelled internals with interconnecting pipes

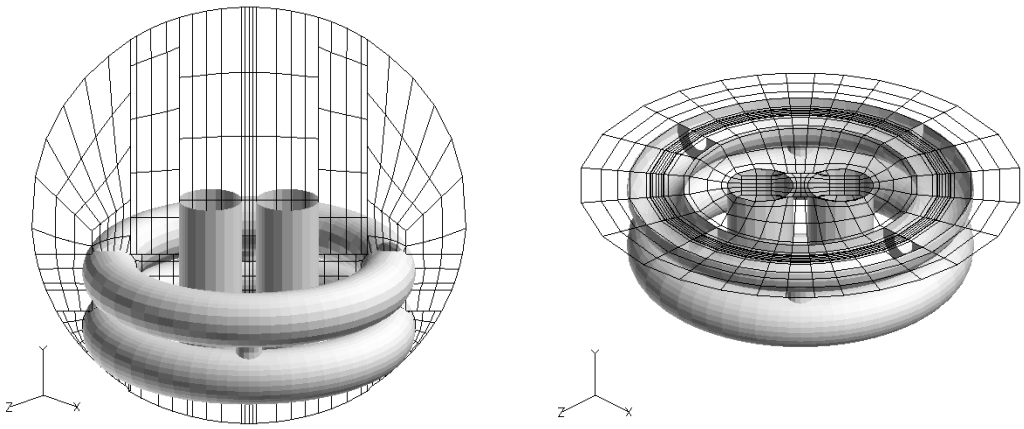

Figure 5.3.4-3 Examples of the grid used

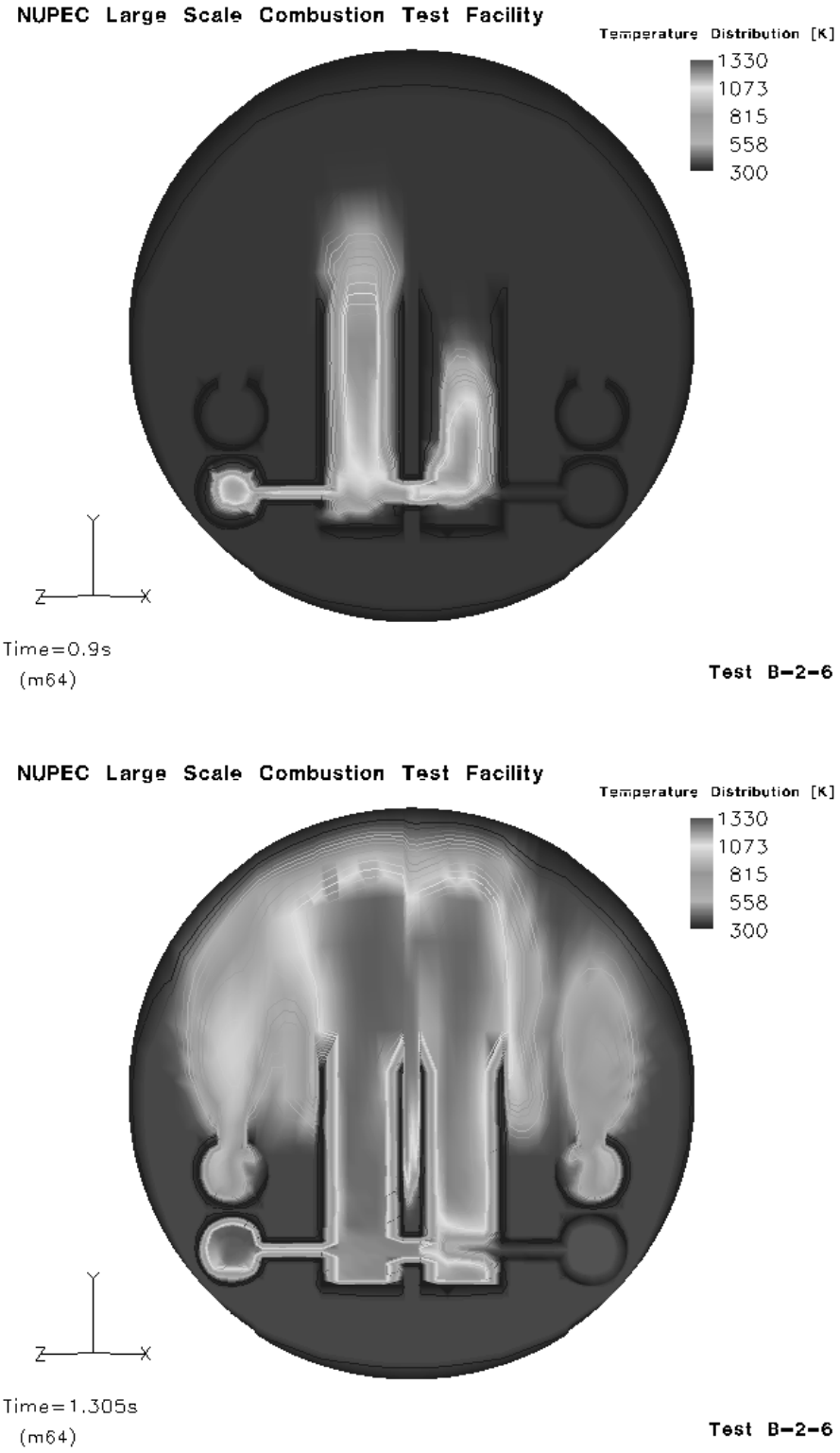

Figure 5.3.4-4 Shaded contours of temperature to characterize the flame progress at two different times

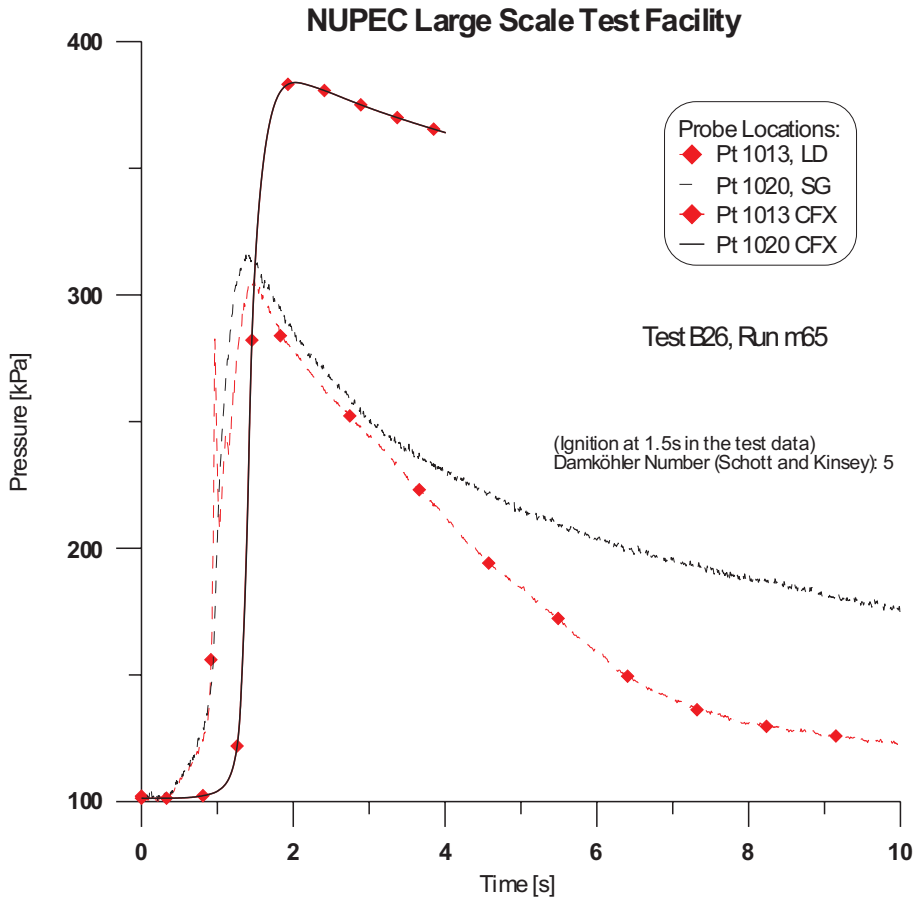

Figure 5.3.4-5 Pressure increase as comparison between measurement (dotted) and simulation

5.3.5 Combustion in CFD Codes Using a Probability Density Function (PDF)[*]

5.3.5.1 Introduction

A calculation method for combustion systems of interest comprises a number of essential components. These include the conservation equations, numerical solution methods, turbulence models, and combustion models. In order to focus the attention on the development of a model for the premixed hydrogen-air combustion process, it is convenient to implement the model into a commercial CFD code. The present contribution describes the implementation of a PDF combustion model into the commercial codes CFX and CFX-TASCflow from AEA Technology plc. (see Table 5.4.0-1). The basic development of the reported model is described by Durst and Mayinger [5.129] and Durst [5.130, 5.131], and follows along the lines of Pope [5.132], Bray [5.133] and Borghi [5.134].

The main assumption of the model is that the thermodynamic state of the system can be related to one single progress variable

$$c = \frac{Y_{H_2O}}{Y_{H_2O,\infty}} \,, \tag{5.3.43}$$

taken to be the mass fraction of water as the reaction product, normalized by the final water mass fraction

[*] Contributed by A. Eder

at the end of the combustion reaction. Further, it is assumed that the chemical rections are in equilibrium, which leads to deterministic relations between the mass fractions of the involved species. The chemical conversion rates of the involved species can generally be expressed depending on the thermodynamic state and composition of the involved mixture and an Arrhenius-type rate factor.

Together with the former of the above assumptions, which relates any thermodynamic quantity to the reaction progress, the latter assumption enables us to relate the chemical conversion rates of the individual species to the reaction progress c. The production rate of c itself is defined correspondingly to Equation (5.3.43):

$$w_c = \frac{w_{H_2O}}{Y_{H_2O,\infty}} \, , \tag{5.3.44}$$

with w_{H_2O} as the chemical production rate of water is treated in the same way. The resulting balance equation for the reaction progress variable reads

$$\frac{\partial}{\partial t}(\rho c) + \frac{\partial}{\partial x_i}(\rho u_i c) = \frac{\partial}{\partial x_i}\left(\Gamma_{H_2O}\frac{\partial c}{\partial x_i}\right) + w_c(c) \, . \tag{5.3.45}$$

The chemical closure problem arises from the well-known difficulty of resolving the length and time scales involved in a turbulent flow with the spatial resolution of the numerical grid and appropriate time steps, resulting from limitations both in computer memory and calculation time. Consequently, turbulent flows in engineering applications are treated by suitably averaging the corresponding balance equations (time–/Reynolds–, ensemble–, density-weighted/Favre-averages). In the above balance equation for the reaction progress, this leaves us with an average of the reaction rate, which, because of the high non-linearity of the exact term (involving an exponential function in the Arrhenius rate factor), cannot be expressed in terms of the average of the reaction progress, i.e.,

$$\overline{w}_c(c) \neq w_c(\overline{c}) \, . \tag{5.3.46}$$

In fact, as many authors point out, this approach can lead to errors of several orders of magnitude. Therefore, the turbulent reaction rate $\overline{w}_c$ must be accounted for by an appropriate turbulent combustion model.

The approach reported in the present contribution is based on a relation known from experimental investigations. If the instantaneous values of a turbulently fluctuating quantity φ and the corresponding probability density function (PDF) $P(\varphi)$ can be determined, then the mean value can be calculated as

$$\overline{\varphi} = \int_{-\infty}^{+\infty} \varphi P(\varphi) \, d\varphi \, . \tag{5.3.47}$$

In our case of the turbulent reaction rate this leads to

$$\overline{w}_c(\mathbf{x}, t) = \int_0^1 w_c(c) P(c; \mathbf{x}, t) \, dc \, , \tag{5.3.48}$$

where we have extended the dependencies in order to indicate that we are intererested in solutions in the whole calculation domain rather than only at one single measuring location. Contrary to the situation of an experiment where both the expressions that are integrated result from measurements, we are left with the task of still having to relate the second term to the (mean) flow. The present contribution simply assumes a generic shape for $P(c)$ with specific shapes constituted by not too many parameters, which,

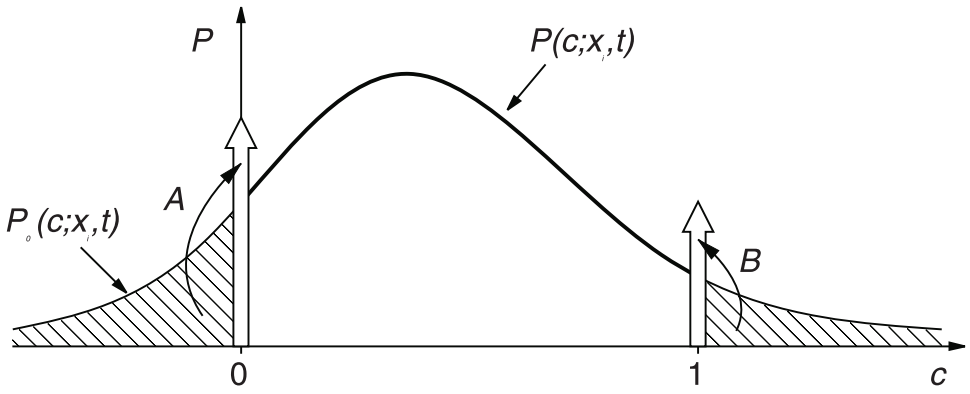

Figure 5.3.5.1-1 Gaussian PDF clipped to $0 \leq c \leq 1$

in turn, can be determined from the flow field. As, in general, these parameters will vary with the flow field, this gives $P(c; \mathbf{x}, t)$. The mean value can then be determined by numerically equating the above integral. Similar to Lockwood and Naguib (cf. [5.135]), we chose a Gaussian distribution for the shape of the PDF, clipped to the region of definiton of the progress variable (Figure 5.3.5.1-1), in order for the PDF to meet the required normalization condition

$$\int_1^0 P(c)\, dc = 1 \,. \tag{5.3.49}$$

A Gaussian distribution is given by

$$P(c) = \frac{1}{\sigma\sqrt{2\pi}} e^{-\frac{1}{2}\left(\frac{c-\mu}{\sigma}\right)^2} , \tag{5.3.50}$$

with the two parameters μ and σ determining the specific shape. The relation to the mean flow is achieved by taking into account that the first and second (central) moments of the distribution of the reaction progress c; that is, mean $\overline{c}$ and variance $\overline{c'^2}$ are defined in connection with the PDF:

$$\overline{c} = \int cP(c)\, dc \tag{5.3.51}$$

and

$$\overline{c'^2} = \int (c - \overline{c})^2 P(c)\, dc \,. \tag{5.3.52}$$

Provided that, in addition to the mean reaction progress $\overline{c}(\mathbf{x}, t)$, which is one of the flow variables anyway, $\overline{c'^2}(\mathbf{x}, t)$ is also known from the solution of the flow field; the two equations above determine μ and σ appropriately, so that $P(c; \mathbf{x}, t)$, required in Equation (5.3.48), is defined. Therefore, the solution of an additional balance equation for $\overline{c'^2}$ is required. This equation can be derived from the balance equations for c and $\overline{c}$.

In order to speed up the calculation procedure, the combustion model makes use of the fact that the region of definition of c is restricted between 0 and 1 and that $\overline{c'^2}$ is bounded, too:

$$0 \leq \overline{c'^2} \leq \overline{c}(1 - \overline{c}) \,. \tag{5.3.53}$$

Therefore, $P(c;\mathbf{x},t)$ can be tabulated as $P(c;\overline{c},\overline{c'^2})$ beforehand, so that the calculation of $P(c)$ during the flow solution is replaced by a simple lookup table procedure.

Regarding the instantaneous reaction rate $w_c(c)$ we have, so far, deliberately remained vague, as it leads us to some demanding difficulties regarding the combustion model. Our first assumption was that one reaction progress variable is sufficient to adequately describe the state of the reaction. Consequently, we can take into account no more than one chemical reaction. We are therefore talking about what in chemical reaction kinetics is known as a one-step global reaction scheme.

The implied difficulties arise as we try to find quantitative data for reaction parameters required in the Arrhenius rate factor such as activation energies and frequency factors. A global reaction scheme can only serve as an approximation of, in fact, a far more complex reaction scheme involving maybe hundreds of elementary reaction steps. Only few contributions in the literature actually state values for these parameters by fitting the results of a calculation with a one-step scheme to some experimental or numerical set-up of greater complexity. Naturally, the results found in this way are not only influenced by the chosen reaction scheme and initial conditions as would be required in our case, but also by varying boundary conditions and even the type of combustion, i.e., premixed versus diffusion flames.

We have, therefore, chosen to determine $w_c(c)$ from the simulation of a simple model flame (one-dimensional, laminar, adiabtic, propagating freely at steady state) taking into account detailed chemical kinetics. For such set-ups, programs such as PREMIX (Kee et al. [5.136]) from the CHEMKIN (Kee et al. [5.137]) suite of codes or INSFLA (c.f. Maas [5.138], Maas and Warnatz [5.139]) exist. These codes account for finite rate chemical kinetics and exact molecular transport mechanisms. Starting from a initialization, the profiles of all involved species over the flame front can be calculated for a flame, propagating in a premixed H_2 in air mixture. From this result the required information regarding w_c can be extracted for discrete water mass fractions, relating w_c to c to give $w_c(c)$.

5.3.5.2 Code validation

Test geometry. The applied PDF combustion model has been validated with measurements performed in explosion tubes of different scale. In this section, an exemplary code validation for a round explosion tube, closed at both ends – ··PHD-Tube, Technische Universität München·· ([5.41,5.71,5.112,5.140 – 5.142]), inner diameter 66 mm, length 6.5 m – is shown. This tube is filled with turbulence-promoting obstacles over a length of 3 m, starting from the ignition spot (round obstacles with a blockage ratio of 60% and a spacing of 185 mm, $l/d \approx 2.8$), in order to accelerate the flame rapidly. The mesh for the explosion tube used by the numerical simulation is based on a block-structured topology. Figure 5.3.5.2-1 shows the mesh of the explosion tube, used for this test calculation. This mesh consists of about 6700 control volumes. In order to avoid degenerated cells in the centre of the tube, a butterfly topology has been used; that is, a H-grid topology in the centre of the mesh is connected to a surrounded O-grid topology (see Figure 5.3.5.2-1). Because of the symmetry of the investigated problem only one half of the tube is considered. A further reduction is not possible because bouyancy effects have to be taken into account for the investigated combustion regime (13 vol % H_2). In the region where the mixture is ignited, the grid is refined. Since the obstacles are placed only in the first half of the tube, a coarser grid resolution is used behind the last obstacle.

Boundary conditions and initialization. At the walls, slip conditions are defined for the momentum equation. The use of slip boundary conditions is valid in the considered combustion processes because the expansion flow passing through the obstacles placed in the tubes dominates the turbulence production.

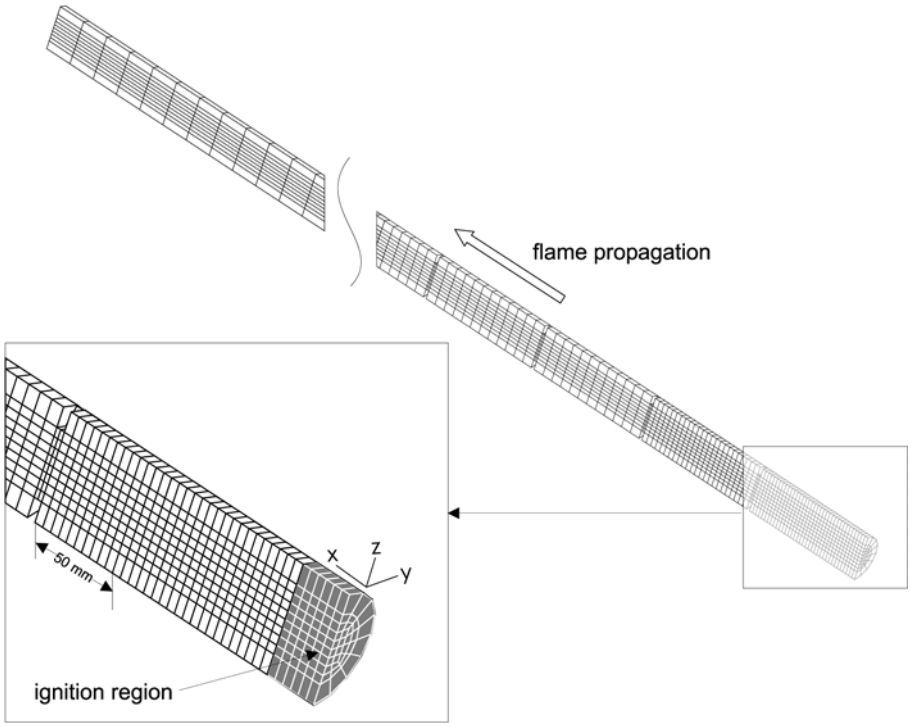

Figure 5.3.5.2-1 Mesh for the PHD tube

Therefore, shear stress at the walls serving as a turbulence promotor can be neglected. Concerning the energy equation, an adiabatic boundary condition is set. Test calculations revealed that the use of a constant ambient wall temperature, which is suggested by Ardey [5.56], has no significant influence on the combustion simulation.

It is often suggested that when combustion simulations in closed facilities are being done that an ignition model be used (e.g. [5.130]) in order to get a good approximation of the startup process, and to overcome the problem of the initialization of an existing flame front and the flow field involved. Further in the verification process and the comparison with experimental data, the ignition process has been found to be insignificant for the investigated geometries. For the initialization of the combustion process, a preburnt area in the ignition region (see Figure 5.3.5.2-1) is defined. In this region the value for the reaction process is set to $\tilde{c} = 1.0$ (fully burnt) and the temperature to the corresponding value.

Numerical control. In principle, the time resolution should be chosen in a way that it is possible to resolve the occuring pressure waves. With respect to the grid resolution, the time step should be of the magnitude

$$\Delta t < \frac{\Delta x}{a_0}\,, \tag{5.3.54}$$

where a_0 is the speed of sound in front of the flame (unburnt gas). In combustion simulations pressure waves occur, which possibly propagate much faster than the speed of sound a_0. The time step has to be adjusted to take into account the expected propagation speed of the pressure wave and the flame front. This is an absolute necessity if the numerical solution of the flow field is calculated explicitly for reasons of the stability of the solution process. In the case of an implicitly calculated flow field, the time step can be set higher with the consequence that pressure waves are not clearly resolved. In the performed

combustion simulations, the time step has been chosen to be $\Delta t = 2 \cdot 10^{-5}$s.

Comparison of calculation and experiment. A comparison between the flame propagation measured in the experiments and the calculation revealed a significant difference, which is shown in Figure 5.3.5.2-3. The calculated flame speed is considerably slower compared with the measurement. The difference can be explained by the flame propagation: The maximum measured flame speed is of the magnitude of 600 m/s. By the fact that this is a supersonic propagation related to the initial mixture, a direct interaction of the flame front and the induced pressure wave is taking place. In the case of the 13 vol % H_2 in air combustion process in the explosion tube, it was observed that after the ignition process and the passing of the first obstacles, the flame front is coupled to the pressure wave because of the strong acceleration of the flame in this region. In Figure 5.3.5.2-2 the described coupling is shown at a position of $x = 2.25$ m. After passing the last obstacle, the flame decelerates and a decoupling of the pressure wave occurs. This behaviour can be seen in the lower picture of Figure 5.3.5.2-2 where the flame front and the pressure distribution are shown over time at the position $x = 4.25$ m, which is located in the second half of the tube.

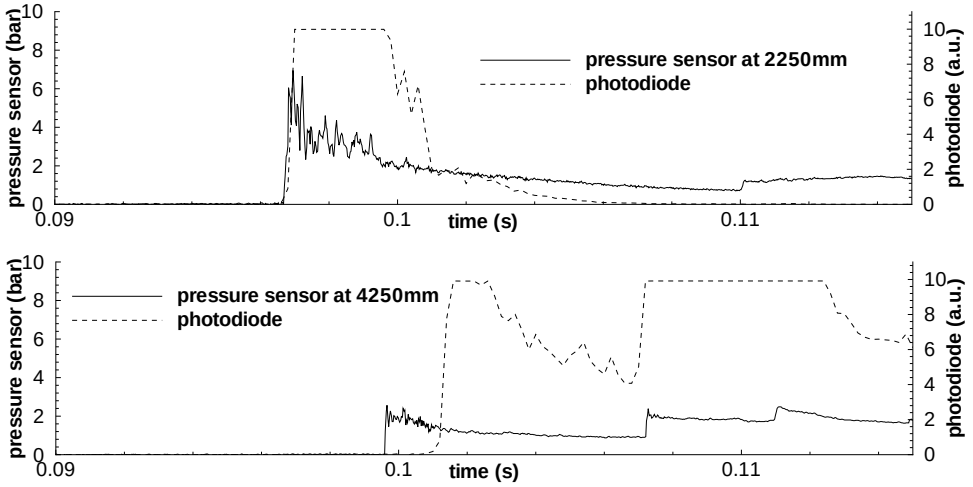

Figure 5.3.5.2-2 Flame-front and pressure-wave interaction in the PHD-tube (13 vol % H_2 in air combustion process)

The coupling of the flame front and the pressure wave has the consequence that the flame is burning into a mixture with a thermodynamic state, which is different from the initial conditions of $T_0 = 293.0$ K and $p_0 \approx 1$ atm. In this case the combustion takes place in an area that is due to the compressing effect of the shock wave characterized by a higher pressure and enthalpy level, which causes significant higher reaction rates. For the initialization with a higher pressure and enthalpy level, a pressure of $p_0 = 6$ bar and a temperature of $T_0 = 488$ K have been chosen. The pressure level is extracted from the measurements and the temperature is calculated by assuming an isentropic change of the thermodynamic state. This leads to an increase of the reaction rate in the range of about an order of magnitude. It has to be emphasized that the change of the reaction rate $w_{H_2O}(c)$ has of course a strong influence on the PDF reaction rates.

Because the consideration of changes of the enthalpy and pressure level during one calculation is not yet implemented in the presented PDF model, the following approach is applied: In order to improve the numerical simulation in the part of the tube where the flame is accelerated to its maximum speed, the

calculation is performed with a PDF reaction rate based on the actually occuring pressure and temperature level. It has to be emphasized that the definition of these levels is a very rough approximation but is appropriate enough to prove the assumptions. Of course, this strategy will lead to an overestimation of the reaction rate during the startup process and the end of the combustion process but will be a good approximation if the flame front is coupled to the pressure wave.

In Figure 5.3.5.2-3 the calculated flame propagation based on the modified PDF reaction rates is shown. It can be seen that within the startup process the flame speed is overestimated. This originates on the one hand because of the initialization and on the other hand because of the earlier described overestimation of the reaction rate in this region. Comparing the region from 1 m to 3 m distance from the ignition point, a good agreement between the calculation and the experiment can be seen. The maximum flame speed is well predicted with the calculation. In this region, the assumption of the coupling of the flame front and the pressure wave is valid. After passing the last obstacle (at $x = 3$ m) the calculated PDF reaction rate overestimates the real reaction rate and, therefore, the flame speed is not predicted accurately. The simulation was performed up to the time when the flame front reached the end of the tube.

For the comparison of the pressure distribution over the time of the calculation and the experiment, the position $x = 2.25$ m is chosen. As can be seen in Figure 5.3.5.2-4 the pressure level and distribution behind the maximum peak is well predicted. But the calculation is not able to predict the maximum pressure peak because the chosen resolution in time (time step size of $\Delta t = 2 \cdot 10^{-5}$ s) and space ($\Delta x \approx 0.04$ m) is not accurate enough.

In Figure 5.3.5.2-5 the flame front and the concerning turbulence field are depicted in the range of 2.5 m $\leq x \leq 3.0$ m of the PHD tube during the combustion process. It can be seen that because of the propagation of the flame front with a velocity faster than the speed of sound of the initial mixture, the turbulence field is induced together with the arrival of the flame front.

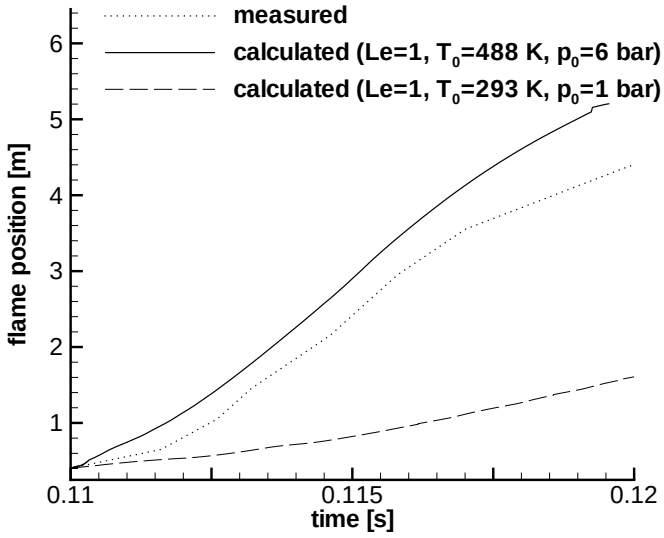

Figure 5.3.5.2-3 Comparison of experimentally determined data with numerical calculations of the flame propagation in the PHD tube for a 13 vol%-H_2 in air mixture

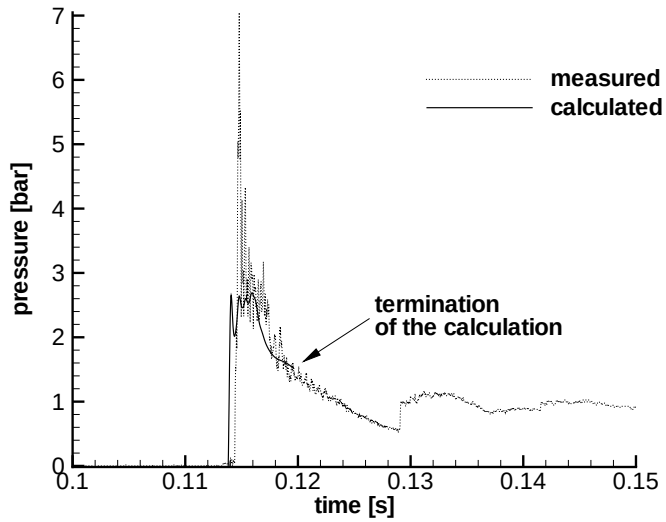

Figure 5.3.5.2-4 Comparison of the pressure distribution between experiment and calculation

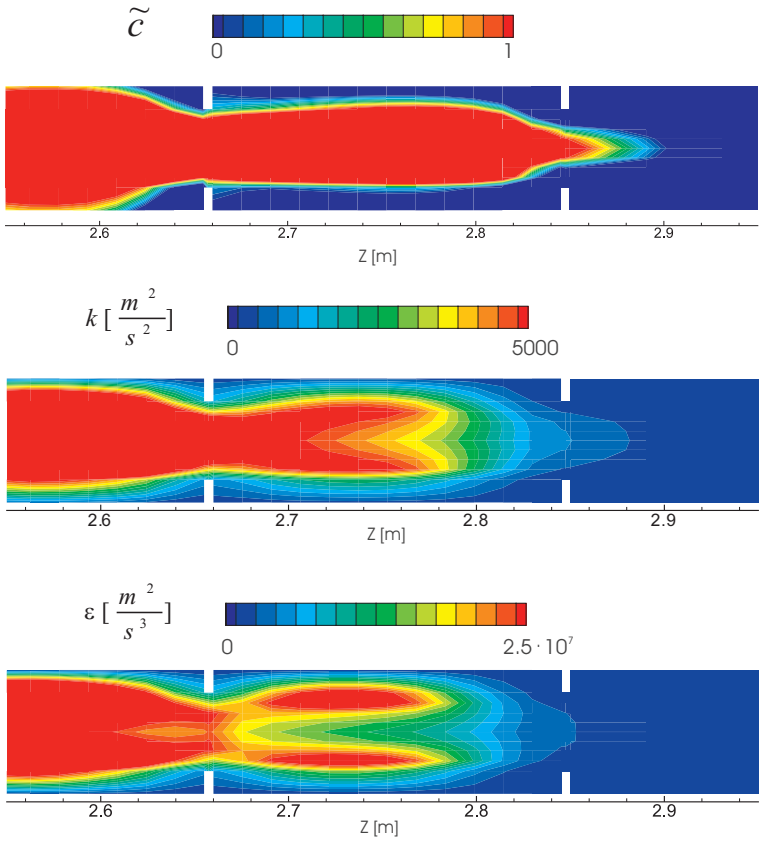

Figure 5.3.5.2-5 Flame-front and the turbulence field during the combustion process in the PHD tube (13 vol % H_2 in air)

5.3.6 Model Clusters with Specialized Tools for Specific Tasks[*]

5.3.6.1 High-performance computing capabilities

Numerical simulations of reacting flows in complex geometries (e.g., associated with hot jet ignition, flame acceleration, or explosion phenomena) have shown that significant computer resources are necessary, to resolve different time and length scales of the physical processes involved [5.143 – 5.146]. Therefore, new versions of reactive Navier-Stokes and Euler flow solvers have been developed for high-performance computing (HPC) with parallel processing capabilities, including pre- and post-processing with an advanced visualization based on tools such as PATRAN, AVS, etc. In order to investigate the capabilities of HPC, a computer complex consisting of several supercomputers (CRAY-T90/T3E/J90) with parallel vector processing (PVP) and massively parallel processing (MPP) was established at the Research Center Jülich (FZJ); the computer complex is integrated into a connecting high-speed network (gigaring). Depending on the specific computer platform with shared or distributed memory, different parallelization concepts of reactive field codes have been realized, especially in the massively parallel mode. Effective parallelization routines are available for load balancing, synchronization, and communication of the allocated processors, e.g., see [5.147] and [5.148].

In order to cover a wide range of combustion modes, several field codes are applied at this computing cluster, each being specific for describing a particular phenomenon:

- the *CFX code* from AEA Technology Ltd. with an implemented eddy dissipation concept for the simulation of hydrogen deflagrations within complex geometries;
- the *AIXCO-2D* code with a flamelet concept for the simulation of a DDT process ahead of the flame with shock wave reflection and auto-ignition processes;
- the *DET-2D* code with a global reaction model for the simulation of stable detonation processes in hydrogen-air mixtures; and
- the *IFSAS-2/3D* code with an induction time model for describing both, shock ignition and detonations of single- and multi-phase flows as well as fluid-structure calculations.

For a detailed description and classification of these codes, refer to the references listed in Table 5.4.0-1.

More recently, first standard versions of reactive field codes have been established on massively parallel supercomputers with promising test results, as follows: First, the reactive Navier-Stokes flow solver code CFX-5 with combustion modelling was ported to the T3E using domain decomposition and PVM (parallel virtual machine) tools ([5.149], [5.150]). Second, the reactive Navier-Stokes flow solver code AIXCO with the flamelet concept was restructured on the T3E using multi-block grids and MPI tools (message passing interface). Third, the reactive Euler solver code DET with high-speed combustion modelling was optimized on the T3E using HPF tools (high-performance FORTRAN). These new parallel code versions showed in tests cases for slow, fast, and rapid flames a proper performance, quite good speed, and scaling with increasing number of processor nodes and grid sizes, [5.151]. For example, Figure 5.3.6.1-1 displays the measured performance of the DET code for parallel processing on the T3E with nearly linear speeding up to 100 processor nodes. In this test case 500 000 cells were used for a fine grid resolution of a detonation wave propagating over obstacles in a channel.

[*] Contributed by Dr. W. Rehm, Research Center Jülich/Forschungszentrum Jülich (FZJ), Germany

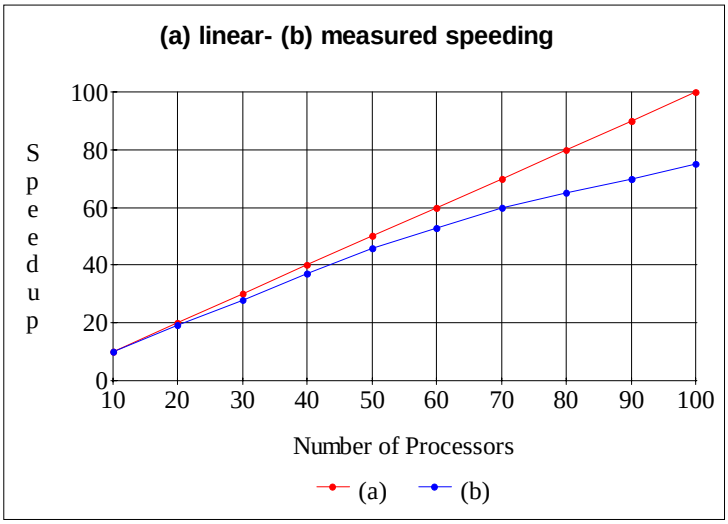

Figure 5.3.6.1-1 Parallel performance of the reactive Euler solver DET-2D/HPF on the CRAY-T3E for a detonation test case in a channel with obstacles using 500000 cells

5.3.6.2 Specific studies and sample-of-proof tests

The complexity of explosion phenomena may involve many combustion processes ranging from deflagrations to detonations, producing static or dynamic loadings on the safety enclosure, which depend on the mixture sensitivity and the geometrical configuration. For the safety analysis of accidental consequences, special numerical models have been accomplished for specific studies related to DDT phenomena, introducing high-performance computations with parallel processing. The modern field code cluster (MFCC) used comprises special reactive Navier-Stokes solvers as well as reactive Euler solvers, which were tested in combination on coarse- and fine-grid levels. As a sample of proof tests, benchmark calulations were performed for integral large-scale explosion tests of the RRC in Moscow (RUT Facility, see Figure 5.2.3.2-30) and for detailed small-scale laboratory tests of the Shock Wave Laboratory in Aachen, ([5.51], [5.152]). For the RUT Test Facility, the following specific post-test analyses were produced for combustion modes in hydrogen-air mixtures in the range 10-15-20 vol % H_2 [5.118]:

- Deflagration mode: turbulent flame acceleration over obstacles with flame velocities in the range 250-500-1000 m/s;
- Transition mode: DDT with shock wave focusing and auto-ignition conditions for mild and strong limits between 850 and 1200 K;
- Detonation mode: Ignition with detonation propagation and resulting pressure and impulse history in different positions up to 50 to 75 bar.

Flame acceleration. Three-dimensional simulations were performed using the CFX code for the flame acceleration over repeated obstacle arrays (35 m x 2.25 m x 2.5 m) with the flame propagation into the cavity (10.55 m x 2.5 m x 6.25 m) and into the outlet channel (25 m x 2.25 m x 2.5 m), whereby the

RUT-23 test was modelled with 11 vol % H_2 in air and 30% to 60% BR. The turbulent combustion model (RNG/EDC) was fine-tuned concerning the empirical constants in the reaction parameters of the source term. Examples of pressure and temperature contours are shown in Figure 5.3.6.2-1 for a simplified 2D simulation. These CFX results were compared with the AIXCO-2D results, which are based on the flamelet model with flame tracking and an empirical burning law. Both codes are in good qualitative agreement and agree quantitatively quite well with the measurements, concerning the flame velocity in the first channel and the pressure-time history in the cavity (e.g., see Figure 5.3.6.2-2). The mean grid resolution was of the order of 10 cm (flame quenching and re-ignition were not simulated in these tests).

DDT conditions. Based on the above reference cases, conditions for defagration- to-detonation transition were analyzed in more sensitive hydrogen-air mixtures. For this purpose, the code AIXCO-2D was adapted to the RUT-22 test with 14 vol % H_2 in air and 60% BR. In the numerical simulation, the flame propagated as a deflagration with about 800 m/s from the channel into the cavity. A transition from deflagration to detonation can occur by shock wave focusing and auto-ignition in the unburnt gas ahead of the flame (i.e., in preconditioned fresh gas pockets). The numerical results showed that the calculated shock reflection temperatures approach the auto-ignition conditions with increasing mixture sensitivity or grid resolution. For this reason, separate grid refinement studies were performed applying the IFSAS code and using adaptive mesh refinement with a maximum resolution in the cavity of the order of 1 mm. In this way, it is in principle possible to resolve DDT processes as far as shock wave focusing with auto-ignition and detonation propagation for various initial and boundary conditions are concerned. Typical test results are shown in Figure 5.3.6.2-3 for shock wave collision in the corner of the cavity and initiation of detonation in a 15 vol % H_2-air mixture, assuming a sustainable propagation.

Gas dynamic effects. In paramter and sensitivity studies, the gas dynamic effects on auto-ignition conditions were analyzed, using the parallel code DET with fine grid resolution in the cavity and the outlet channel of the order of 1 cm. The inlet conditions were specified at the end of the acceleration channel entering into the cavity and were varied in a wide range for the inlet parameters: pressure, velocity, and temperature. These test results reveal that high reflected shock pressures between 30 and 40 bar (factor 5) are necessary to reach auto-ignition temperatures between 850 and 1200 K in a 15 vol % H_2-air mixture. Figure 5.3.6.2-4 shows the reflected shock wave temperatures versus time in two corners of the cavity. The parameter is the inlet velocity of the burnt gas with 7.5 bar and 1000 K for an unburnt gas at 1 bar. The sequential combination of the parallel AIXCO code (Navier-Stokes solver) with the parallel DET code (Euler solver) via an interface allows the numerical simulation of DDT conditions for flame acceleration, shock ignition, or hot jet ignition at different model levels with grid refinement. In sensitivity studies with the parallel DET code, it was observed that the cavity can burn out rapidly by DDT and that a supersonic flame enters into the outlet channel. In addition, multiple ignitions can occur in the cavity. It was found that a DDT near a corner produces higher pressures but lower impulses compared with a DDT far from a corner in the cavity and vice-versa (turbulent mixing triggering DDT was not taken into account in these studies).

Ignition aspects. An important aspect for the onset of detonation concerns the sufficient resolution of the shock wave collision in correlation with the ignition process for detonation formation in H_2-air mixtures at ambient conditions. Strong and mild ignition processes were observed in shock tubes, whereby measured ignition delay times are not consistent with theoretical predictions in the low-temperature regime. The measured ignition delay times can be used for fitting reaction kinetic data. In a first step, a global reaction model with induction delay was implemented in the parallel Euler code DET with modified Arrhenius parameters and validated with shock tube experiments, performed at SWL-Aachen. Ignition delay times were measured in a 15% hydrogen-air mixture in a quadratic shock tube (5.4 cm x

6.4 m), using a plane end wall with a narrow gap (e.g., similar to the RUT geometry on a small scale). The numerical simulation was performed with a fine grid resolution of the order of 0.5 mm and resulted in a reasonable qualitative and quantitative agreement with the measurements for strong ignition behind the normal reflected shock. The CJ detonation velocity was about 1550 m/s. Characteristic numerical schlieren pictures (i.e., density gradients) for the DDT experiment are shown in Figure 5.3.6.2-5. The comparison of measured and calculated pressure transients is presented in Figure 5.3.6.2-6.

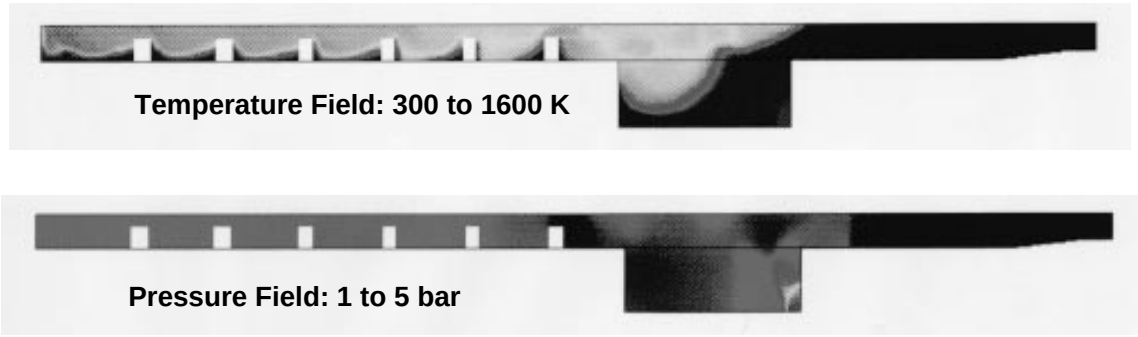

Figure 5.3.6.2-1 CFX temperature and pressure contours of the RUT-23 deflagration test with 11% hydrogen in air at NTP and BR = 60% at about 1 s

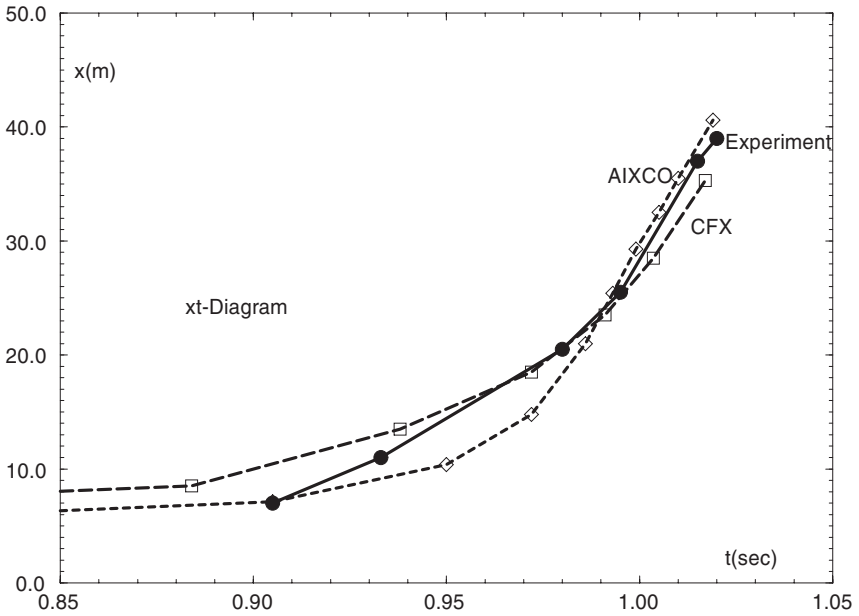

Figure 5.3.6.2-2 Comparison of experimental and numerical results with the codes CFX and AIXCO for RUT-23 deflagration test with 11% hydrogen in air at NTP and BR = 60%

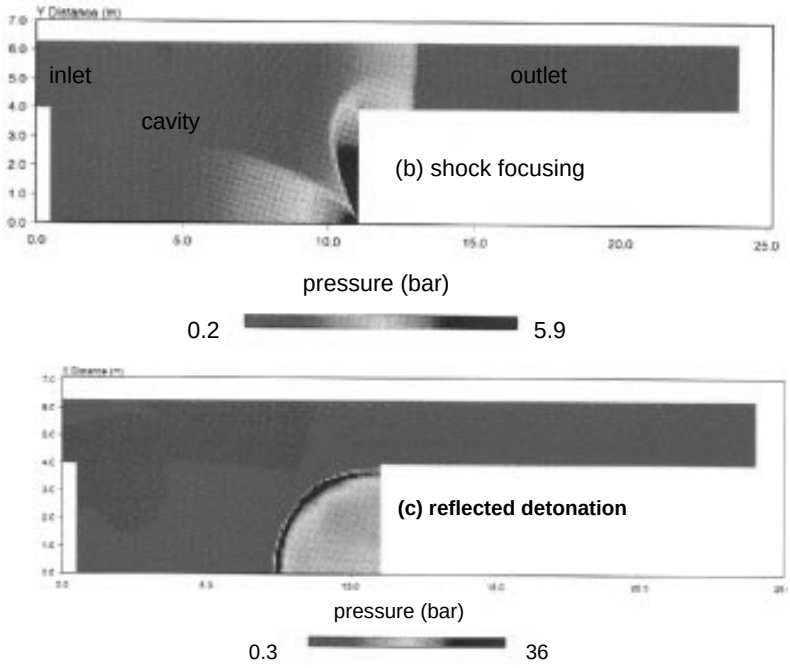

Figure 5.3.6.2-3 Pressure contours of the IFSAS code for transition from deflagration-to-detonation by shock wave focusing with auto-ignition in the RUT cavity (15% hydrogen)

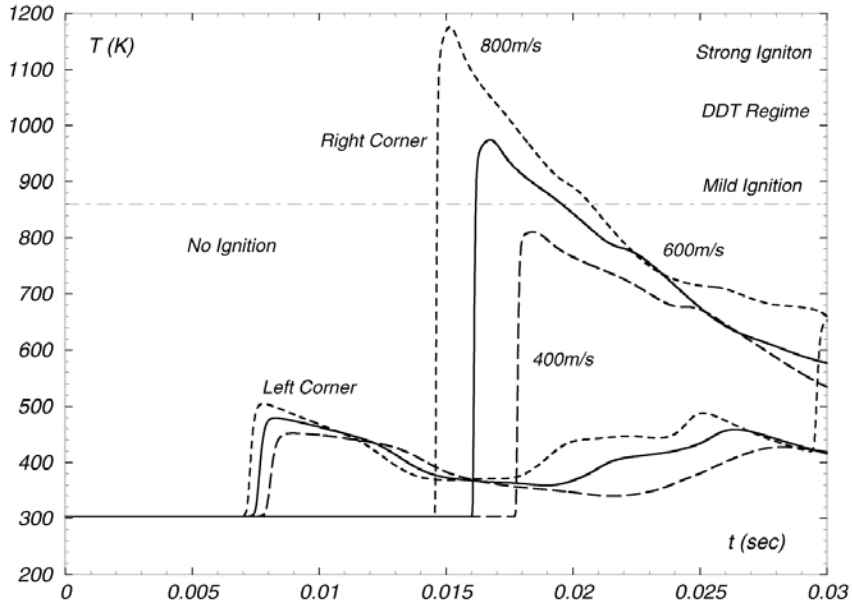

Figure 5.3.6.2-4 Parameter study of the parallel DET code for DDT conditions by shock wave focusing for mild and strong ignition temperatures in two corners of the the RUT cavity (15% H_2-air at NTP for p(in) = 7.5 bar, T(in) = 1000 K) and v(in) as parameter

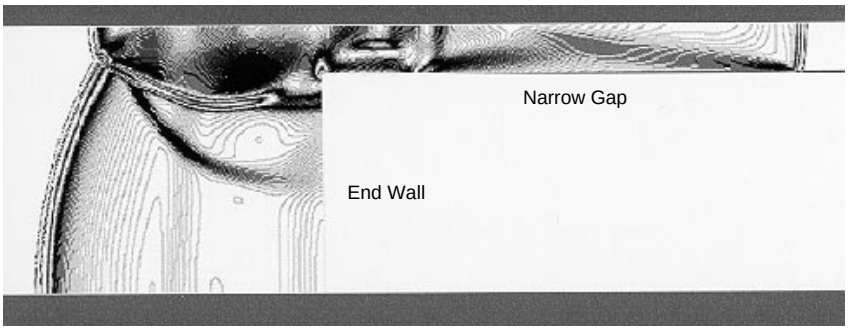

Figure 5.3.6.2-5 Numerical schlieren picture of the parallel DET code for DDT experiments in a quadratic shock tube with a narrow gap performed at SWL (15% H_2)

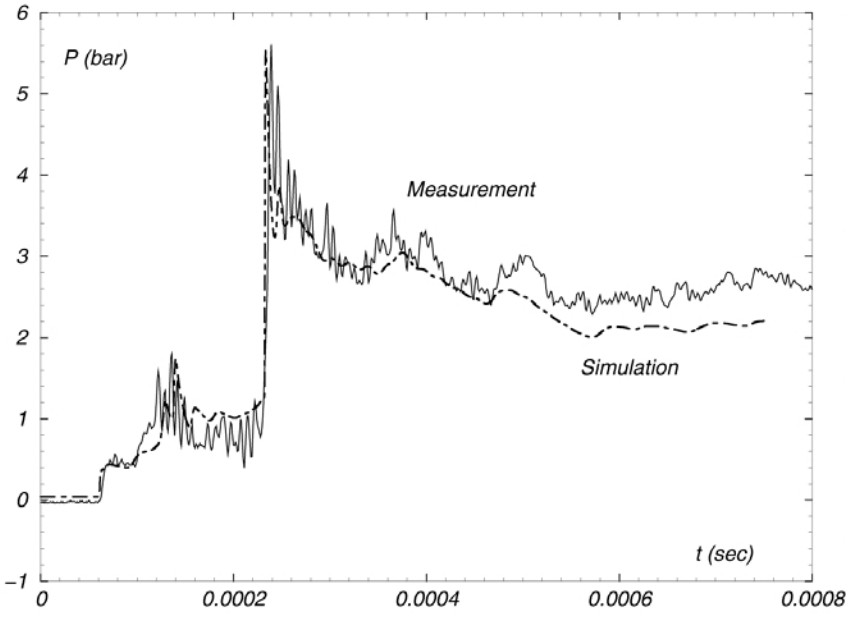

Figure 5.3.6.2-6 Comparison of experimental and numerical pressure transients for strong ignition and detonation formation with the parallel DET code (15% H_2)

5.4 Summary

This chapter has compiled both an overview of available experiments on FA and DDT, which are applicable for code validation, and the validation of the various codes with different levels of complexity.

The experiments presented addressed shock-focusing, flame acceleration, and transition to detonation in obstructed areas, and flame propagation in complex and large-scale geometries with various levels of detail in the instrumentation - all these parameters depend mainly on the size of the facility. At the small-scale facilities, it is possible to investigate the flame propagation highly resolved with different types of transducers or to visualize the flame propagation itself by means of sophisticated optical measurement techniques. A disadvantage of small-scale combustion experiments is the influence of relatively high heat losses and possible boundary layer influences on the combustion process. These influences decrease with increasing scale of the facility. On the other hand, large-scale tests generally do not allow the application of modern optical diagnostic techniques to characterize flow fields or reaction progress. Large-scale experiments usually employ conventional instrumentation such as pressure transducers, photo diodes, thermocouples, and ionization gauges, which provide local information at different points of the test facility. The investigated gas mixtures consisted mainly of dry hydrogen-air or hydrogen-air-steam mixtures. Moreover, the influence of diluents on the combustion process was investigated in some experiments, e.g., CO_2 in the test series conducted in the Battelle Model Containment [5.77 – 5.82].

Our main knowledge of flame acceleration and transition to detonation is based on experimental results from test facilities with volumes in the range of $0.01\ \mathrm{m}^3$ (explosion tubes) up to about $500\ \mathrm{m}^3$ (RUT Facility, Kurchatov Institute) in hydrogen-air-mixtures with and without steam as well as temperatures between ambient and 100^o C. Concerning an accident scenario, elevated initial pressures up to 3 bar are expected. Here, the database is still very poor because only few experiments [5.153] have been conducted.

It appears that the database available today on flame acceleration, local ignition, detonation onset, and shock-focusing contains a wide range of examples covering all relevant major processes. Nevertheless, there are still some unsolved topics as far as re-ignition, quenching, elevated initial pressure, and, in particular, scaling are concerned.

The model validation performed up to date with the described database may be summarized as follows: In the area of flame acceleration lumped-parameter (LP) and CFD approaches have been pursued. The LP class of tools allows rough but quick assessments of possible flame acceleration phenomena in a large number of accident sequences.

In the CFD class of tools, model validation has concentrated on flamelet models, eddy breakup (EBU) and statistical probability density function (PDF) type of combustion models, implemented in Reynolds-averaged Navier-Stokes codes for the simulation of various turbulent combustion regimes. It could be shown that the EBU approach is able to provide reasonable agreement with experimental data, if either free model constants are benchmarked on experiments with different scales [5.128], or a theoretical extension is implemented in the code [5.120], which leads to a model without any free constants.

The validation of the presumed PDF approach [5.129 – 5.131] without any free model constants showed promising results as it could be realized for small- and medium-scale turbulent combustion experiments. A further improvement of both numerical methods and model optimization will allow the application to large-scale problems within a reasonable running time.

Compared to FA, the prediction of DDT events is generally in a much less-advanced stage although the principal mechanisms are mostly understood. It is necessary to discriminate DDT on reflection from the more complicated case of DDT near a turbulent flame brush. Today, CFD tools allow us to reproduce DDT in reflection in small-scale 3D geometries or in medium-scale 2D configurations. It appears that one- or few-step chemistry models are sufficient to reproduce the occurrence and timing of the local explosion and the succeeding detonation propagation. Simulation of DDT in or near a turbulent flame brush is a more complicated problem that still requires substantial development in theoretical models, numerical techniques, and computational resources.

Table 5.4.0-1 List of codes. This list shall only give an exemplary overview of typical codes which are currently applied for the simulation of turbulent combustion or detonations. A very comprehensive list of multi-purpose field codes can be found on the World Wide Web under the URL: http:\\www.cfd-online.com

Code	Reference	Note
Lumped-Parameter Codes		
COCOSYS/(RALOC)	GRS, Germany	
MELCOR	USNRC, USA	
CONTAIN	Sandia National Laboratories, USA	
JERICHO	IPSN, France	
Muphi-Burn	NUPEC, Japan	
Hybrid CFD-Lumped-Parameter Codes		
GOTHIC	Numerical Applications Inc.	
TONUS	CEA, France	
CFD Codes		
FLACS	Christian Michelsen Research	
AutoReaGas	TNO and Century Dynamics Ltd.	
CFX	AEA Technology Ltd., UK	
CFX-TASCflow	AEA Technology Ltd., UK	
EXSIM	Aalborg University Esbjerg, DK	
Fluent	Fluent Inc., USA	
IFSAS	Combustion Dynamics Ltd., Canada	Flow-solver and Fluid-structure interaction
COM3D	Kurchatov Institute, Russia / FZK, Germany	
COMET	ICCM GmbH, Germany	
FIRE	AVL List GmbH, Austria	
Bassim	Battelle IT, Germany	
Gasflow	FZK, Germany	
AIXCO-2D	RWTH-Aachen, Germany	explicit Na-St. solver
DET-2D/3D	FZK and FZJ, Germany	explicit Euler solver
STAR-CD	Computational Dynamics Ltd., UK	
ACE+	CFD Research Corporation, USA	
GLACIER, Banff	Reaction Engineering Int., USA	
PHOENICS	Cham Ltd., UK	

5.5 Nomenclature

a	Sound speed in unburnt mixture
a_0	Sound speed in front of the flame
b, c	Constants
c	Heat capacity
c	Reaction progress
$\tilde{c}$	Reaction process
c_F	Reaction rate constant
d	Tube diameter
d_i, d_0	Diameters of orifice and obstacle
d/λ	DDT limit criterion
f	Stretching factor
i	Specific enthalpy
p_0	Initial pressure of unburned hydrogen-air mixture
k	Constant
k	Turbulent kinetic energy
l	Turbulence integral length scale
l_F	Laminar flame thickness
m_F	Mass fraction of fuel
m_O	Mass fraction of oxidizer
m_P	Mass fraction of products
p	Pressure
s	Step between obstacles
s/δ	Relative step between obstacles
t	Time
u,	Turbulent fluctuating velocity
u'	Turbulence intensity
u_m	Fluid Velocity
u_n	Normal flame velocity
u_v	Visible flame velocity
v	Specific volume
w_{H_2O}	Chance of the reaction rate
x	Running distance
A	Area
A, B, C	Constants
BR	$= 1 - (d_i/d_0)^2 = 1 - F_i/F_0$ – blockage ratio
C	Mole Fraction
D	Diameter
D_{ie}	Threshold Damköhler number

F	Covered area
F/s_f	Ratio of relector covered area to cross-section of the test channel
F_i, F_0	Areas of orifice and obstacle
FF	Flame front
FF_i	Flame front inside
G	Mass flow
$H_{1..5}$	Constants
I	Enthalphy
K	Karlovitz flame stretch factor
L	Flame-front position
L	Integral Length Scale
L	Total length of a channel
L/D	Length-diameter ratio
L_e	Lewis number
L_r	Length of reflector
L_{obs}	Length of obstructed part of a channel
L_{obs}/s	Density (compactness) of obstacles
M, m	Mass
M	Mach number
M_{min}	Minimum Mach number
M_t	Mach number corresponding to the appearance of the self-ignition
M_{tr}	Mach number corresponding to the transient regime of self-ignition
P	Pressure
P_1	Initial pressure
P_4	Maximum pressure reached
Q	Heat
R	Radius of curvature
R_e	Reynolds number
S	Burning velocity
S_L	Laminar flame velocity
T	Temperature
T_0	Initial temperature of unburned hydrogen-air mixture
T_A	Activation temperature
U	Inner energy
V	Volume
W	Volume displacement work
γ	Specific heat
δ	$= d_0$ – tube diameter flame thickness
ϵ	Density radio
ε	Dissipation rate

λ	Detonation cell width
ρ	Density
ρ_b	Density of combustion products
ρ_u	Density of the unburnt mixture
σ	Expansion ratio after burning
η	Dynamic viscosity
τ	Time of existence of zones of increased temperature
τ_i	Ignition delay time
τ_{CH}	Chemical induction time
τ_t	Turbulent time scale
ν	Kinematic viscosity
Θ	Time of chemical reactions
$\%\mathrm{H_2}$	Volume fraction of hydrogen in mixture
$\%\mathrm{H_2O}$	Volume fraction of water steam in mixture
$\%\mathrm{N_2}$	Volume fraction of nitrogen in mixture
$\%\mathrm{CO_2}$	Volume fraction of carbon dioxide in mixture

5.6 References

[5.1] A. Borisov, B. Gelfand and G. Skatchkov, Current topics in shock waves: Ignition of gaseous combustible mixtures in focused shock waves. In: *17th International Symposium on Shock Waves*. American Institute of Physics, New York, 1990, 696–701.

[5.2] B. Gelfand, S. Medvedev and S. Tsiganov, Three cases of shock waves focusing in combustible media. In: *18th International Symposium on Shock Waves*. (K. Takayama, (editor)), Vol. 2. Springer Verlag, 1992, 837–842.

[5.3] B. Gelfand, S. Khomik, S. Medvedev, A. Polenov and W. Breitung, Selfignition of combustible mixture behind shock waves reflected at non-flat surfaces at high initial pressure. In: *20th International Symposium on Shock Waves*, California Institute of Technology, Pasadena, CA, USA. 1995, 251.

[5.4] S. Medvedev, A. Polenov, B. Gelfand and S. Khomik, Experimental evidences on peak temperature at shock wave focusing. In: *20th International Symposium on Shock Waves*, California Institute of Technology, Pasadena, CA, USA. 1995, 131–132.

[5.5] C. K. Chan, Collision of a shock wave with obstacles in combustible mixture. Comb. & Flame, Vol. 100, 1995, 341–348.

[5.6] C. K. Chan, D. Lau, P.A. Thibault and J.D. Penrose, Ignition and detonation initiation by shock focussing. In: *AIP Conf. Proc.: Current topics in shock waves*. (Y. M. Kim, (editor)), American Institute of Physics, New York, USA. 1990, 696–701.

[5.7] A.A. Borisov, B. E. Gelfand and G. I. Skatchkov, Selfignition of gaseous mixtures by focusing of reflected shock waves. Chimicheskaya phisika, Vol. 7, 1988, 1387–1392.

[5.8] C. K. Chan, A. Guerro and D. Mc-Cooeye, Shock induced transition to detonation. In: *Paper at 2nd Canadian / German workshop*, 1993.

[5.9] O. V. Achasov, S. A. Labuda, O.G. Penzijakov and R. M. Puskin, Shock waves initiation of detonation in semiclosed cavity. Chimicheskaya phisika, Vol. 12, 1993, 714–716.

[5.10] M. Rose, P. Roth and U. Uphoff, Ignition of reactive gas by focusing of shock wave. In: *16th ICDERS*, Krakow, Poland. 1997, 554–556.

[5.11] V. Yu. Gidaspov, I. A. Ivanov and I. A. Krinkov, Numerical modeling of detonation in focusing channel. Mathematical modeling, Vol. 4, 1992, 85–88.

[5.12] B. E. Gelfand and W. Breitung, Detonation ignition characteristics of H_2 + Air mixtures under conditions of shock focusing. Inst. of Chemical Physics, RAS & Inst. Neutronenforschung und Reaktortechnik, FZK, , 1993.

[5.13] B. E. Gelfand and W. Breitung, Complete experimental investigation of shock wave focusing phenomena in H_2 + Air mixtures with additives. Inst. of Chemical Physics, RAS & Inst. Neutronenforschung und Reaktortechnik, FZK, , 1994.

[5.14] B. E. Gelfand, S. V. Khomik, S. P. Medvedev, A. N. Polenov, A. M. Bartenev, W. Breitung and A. Veser, Investigation of hydrogen +air fast flame propagation in tubes with multidimensional endplates. In: *Proc. Intl. Symp. on hazard, prevention and mitigation of industrial explosions*, Vol. 2, Safety Cons. Eng., Schaumburgh Ill., USA. 1998, 434 – 456. see also:

Abstracts of Intern. Colloq.: Advances in experimentation / computation of detonation, ENAS Publ., 1998, p. 65.

[5.15] B. E. Gelfand, A. N. Polenov, S. P. Medvedev, S. W. Khomik, A. M. Bartenev and H. Groenig, The selfignition of homogeneous gaseous mixtures near nonflat surfaces. Dokl. RAS, Vol. 359, 1998, 490–493.

[5.16] M. Rose, P. Roth and U. Uphoff, AMR calculation of ignition and detonation formation in reactive gas by shock wave focusing. In: *Abstracts of Intern. Colloq.: Advances in experimentation / computation of detonation*. ENAS Publ., 1998, 17–18.

[5.17] A. M. Bartenev, B. E. Gelfand, S. P. Medvedev, , A. N. Polenov, S. W. Khomik, H. Groenig and H. Olivier, Numerical modeling of ignition and detonation under focusing conditions. In: *Abstracts of Intern. Colloq.: Advances in experimentation / computation of detonation*. ENAS Publ., 1998, 26–27.

[5.18] B. E. Gelfand and W. Breitung, DDT experiments with focusing of H_2 + Air blast waves. Inst. of Chemical Physics, RAS & Inst. Neutronenforschung und Reaktortechnik, FZK, , 1998.

[5.19] G. Ciccarelli, Critical tube diameter measurements in high-temperature hydrogen-air mixtures. FIN L-1924, , 1998.

[5.20] B. E. Gelfand, O. Popov, S. P. Medvedev and S. W. Khomik, The features of hydrogen+oxygen mixture selfignition at high pressure. Dokl. RAS, Vol. 349, 1996, 482–485.

[5.21] B. E. Gelfand, O. Popov and S. W. Khomik, Selfignition of hydrogen-air mixtures at high pressure. Dokl. RAS, Vol. 330, 1993, 457–459.

[5.22] R. Blumental, K. Fieweger, G. Adomeit, B. E. Gelfand and K. Komp, Self-ignition of hydrogen + air mixtures at high pressure and low temperature. In: *20th International Symposium on Shock Waves*, CalTech, Pasadena, CA, USA. 1995, 175–176. See also, Shock Waves, 1996, vol.2, World Sci., p. 935-940.

[5.23] B. Gelfand, O. Popov, A. Kusharin, G. Agafonov and W. Breitung, High-temperature self-ignition and detonation of hydrogen+air mixtures with NO_x additives. In: *Proc. 15th ICDERS*, Boulder, Colorado, USA. 1995, 473–475.

[5.24] B.E. Gelfand, O. E. Popov, S. P. Medvedev, S. V. Khomik, A. Yu. Kusharin and G. L. Agafonov, Self-ignition of hydrogen-oxygen mixtures at high pressure. In: *CD-ROM Proc. 21st Inti. Symp. on Shock Waves*, 1997, paper 2400.

[5.25] B.E. Gelfand and W. Breitung, Measurement of hydrogen-air ignition length under severe accident conditions. In: *Proceed. Engl.-Germ. Symp. on combustion*, 1993, 419–420.

[5.26] R. Blumental, K. Fieweger and G. Adomeit, Self-ignition of hydrogen+air mixtures. In: *Paper at 11th World Hydrogen Energy Conference*, 1996.

[5.27] R. Blumental, K. Fieweger, K. Komp and G. Adomeit, Gas dynamic features of self-ignition of non-diluted fuel / air mixtures at high pressure. Comb. Sci. and Technol., Vol. 113/114, 1997, 137–166.

[5.28] J. Lu, A. K. Gupta, A. A. Pouring and E. L. Veating, A preliminary study of chemically enhanced auto-ignition in an internal combustion engine. In: *Proc 14th ICDERS*, Vol. 1, Coimbra, Portugal. 1993, 1–10.

[5.29] A. V. Eremin, V. Yu. Velikodny and V. S. Ziborov, Nonequilibrium of H2 / O2 mixtures in the weak wave front. In: *Proc 16th ICDERS*, Crakow, Poland. 1997, 597.

[5.30] C. Viguier, D. Desbordes, L. F. Figuera Da Silva and L. Guerrad, Oblique shock wave induced supersonic combustion and oblique detonation in H2 / air and H2 / O2 mixtures. In: *2-nd Intern. meeting: properties of reactive fluids and their application to propulsion*, ENSMA, France. 1996.

[5.31] B. E. Gelfand and W. Breitung, Measurement of H2 + Air ignition length under severe accident conditions. Inst. of Chemical Physics, RAS & Inst. Neutronenforschung und Reaktortechnik, FZK, , 1992.

[5.32] B. E. Gelfand and W. Breitung, Investigation of spontaneous detonation ignition under non-uniform pressure and temperature conditions. Inst. of Chemical Physics, RAS & Inst. Neutronenforschung und Reaktortechnik, FZK, , 1993.

[5.33] B. E. Gelfand and W. Breitung, Measurements and prediction of detonation of H2 + H2O +Air mixtures with accident relevant additives (CO, CO2, NOx). Inst. of Chemical Physics, RAS & Inst. Neutronenforschung und Reaktortechnik, FZK, , 1994.

[5.34] B. E. Gelfand and W. Breitung, Suppression of explosive phenomena by CO2 admixing. Inst. of Chemical Physics, RAS & Inst. Neutronenforschung und Reaktortechnik, FZK, , 1996.

[5.35] C. Viguier, L. F. Figuera Da Silva, D. Desbordes and B. Deshaies, Onset of oblique detonation waves. In: *26th Intl. Symp. on Combustion*. The Combustion Inst., Pittsburgh, USA, 1996, 3023– 3031.

[5.36] D. L. Baulch, C. J. Cobos, R. A. Cox R.A., C. Esser, P. Frank, Th. Just, J. A. Kerr, M. J. Pillig, J. Troe, R. W. Walker and J. Warnatz, Evaluated kinetic data for combustion modelling. J. Phys. Chem. Ref. Data, Vol. 21, 1992, 411–736.

[5.37] H. G. Wagner, personal communication. 1997.

[5.38] G. Ciccarelli, J. L. Boccio, T. Ginsburg, C. Finfrock, L. Gerlach, K. Sato and A. M. Kinoshita, High-temperature hydrogen+air+steam detonation experiments in the BNL small - scale development apparatus. BNL-NUREG-52414, NUREG/CR - 6213, , 1994.

[5.39] R. J. Kerr, CHEMKIN - II: A fortran chemical kinetic package for analysis of gas-phase chemical kinetics. Sandia Nat. Lab. Report: SAND 89-8001, , 1989.

[5.40] F. Mayinger, G. Strube and R. Beauvais, Derzeitiger Wissenstand über den Verlauf der Grenze für den Deflagrations-Detonations-Übergang (DDT) im Dreistoff-Diagramm [Current knowledge about deflagration to detonation transition (DDT) in the trenary mixture diagram]. TU München, Abschlussbericht, BMU-SR-403, , 1988.

[5.41] F. Mayinger and N. Brehm, Grenze für den Übergang von der Deflagration in die Detonation (DDT) in H_2-Luft-Wasserdampf–Gemischen [Limit for the transition from deflagration to detonation (DDT) in H_2-air-steam mixtures]. TU München, Abschlussbericht, BMFT 150 0712 4, , 1988.

[5.42] J. H. S. Lee, R. Knystautas and A. Freiman, High speed turbulent deflagration and transition to detonation in H_2 + Air mixtures. Comb. & Flame, Vol. 56, 1984, 227–239.

[5.43] W. Breitung, P. Royl and A. Veser, Results of hydrogen behaviour and mitigation in severe PWR accidents. FZTU Karlsruhe, Report 5914, , 1997.

[5.44] F. Mayinger and G. Strube, Struktur und Brenngeschwindigkeiten hochturbulenter Wasserstoff-flammen [Structure and burning velocity of highly turbulent hydrogen-air flames]. TU München, Abschlussbericht, BMTF-GRS-150 0769, , 1990.

[5.45] F. Mayinger and N. Brehm, Zündgrenzen von Wasserstoff in aerosolhaltiger Atmosphäre [Ignition limits of hydrogen in an aerosol atmosphere]. TU München , Abschlussbericht , BMTF-GRS-15006150, , 1987.

[5.46] B. E. Gelfand and W. Breitung, Laminar and turbulent flame propagation in H_2 / Air / Steam mixtures at accident relevant pressure and temperature conditions. Inst. of Chemical Physics, RAS & Inst. Neutronenforschung und Reaktortechnik, FZK, , 1995.

[5.47] R. Beauvais, F. Mayinger and G. Strube, Severe accident in a light water reactor influence at elevated initial temperature on H_2 combustion. In: *2nd ASME-JSME conference*, Vol. 1, 1993, 425–433.

[5.48] R. K. Kumar and E. M. Bowles, Flame acceleration in H_2 / air / steam mixtures in the presence of repeated obstacles in a closed volume. In: *CEC-Workshop "Hydrogen behaviour and mitigation in water-cooled nuclear power reactors"*. European Commission, Brussels, Belgium, 1992, 129–140.

[5.49] R. K. Kumar, Combustion of H_2 / Air / steam mixtures in presence of repeated obstacles in a confined volume. Comb. Sci. and Technol., Vol. 126, 1997, 23–52.

[5.50] B. E. Gelfand and W. Breitung, Investigation of H_2 + Air fast flame propagation and DDT in tube with multidimensional endplates. Inst. of Chemical Physics, RAS & Inst. Neutronenforschung und Reaktortechnik, FZK, , 1997.

[5.51] S. B. Dorofeev, V. P. Sidorov and A. B. Dvoinishnikov, DDT in large confined volumes of lean H_2 + Air mixtures. Comb. & Flame, Vol. 104, 1996, 95–110.

[5.52] C. K. Chan and W. A. Dewitt, DDT in end gases. In: *26th Intl. Symp. on Combustion*. The Combustion Inst., Pittsburgh, USA, 1996, 2679–2684.

[5.53] G. Ciccarelli, J. L. Boccio and T. Ginsberg, The influence of initial temperature on flame acceleration and DDT. In: *26th Intl. Symp. on Combustion*. The Combustion Inst., Pittsburgh, USA, 1996, 2973–2979.

[5.54] G. Ciccarelli, J. L. Boccio, T. Ginsberg, C. Finfrock, L. Gerlach, H. Tagawa and A. Malliakos, The effect of initial temperature on flame acceleration and DDT phenomenon. NUREG/CR-6509, BNL-NUREG-52515, , 1998.

[5.55] G. Ciccarelli, J. L. Boccio, T. Ginsberg, C. Finfrock, L. Gerlach, H. Tagawa and A. Malliakos, The effect of lateral venting on DDT in hydrogen - air - steam mixtures at various initial temperatures. NUREG/CR-6524, BNL-NUREG-52518, , 1998.

[5.56] N. Ardey, *Struktur und Beschleunigung turbulenter Wasserstoff-Luft-Flammen in Räumen mit Hindernissen [Structure and acceleration of turbulent hydrogen-air flames in obtacle obstructed rooms]*. PhD thesis, Technische Universität München, 1998.

[5.57] N. Ardey and F. Mayinger, Einfluß Containment-typischer Strömungshindernisse auf die Ausbreitung trubulenter Wasserstoff-Luft-Flammen [Influence of containment typical obstacles on the propagation of turbulent hydrogen-air flames]. Abschlußbericht zum Forschungsvorhaben BMFT, Nr. 150 0957, TU München, , 1998.

[5.58] A. Eder and M. Jordan, Application and Potentials of Optical Measurement Techniques for the Investigation of Transient Combustion Phenomena. In: *Applied Optical Measurement Techniques*. (D. Mewes and M. Lehner, (editors)). Springer-Verlag, Heidelberg, 1999.

[5.59] F. Mayinger, (editor), *Optical Measurement Techniques*. Springer-Verlag, Heidelberg, 1994.

[5.60] A. Eder, M. Jordan and F. Mayinger, Einfluß von hindernis-induzierter Turbulenz auf die Beschleunigung von H2- und CH4-Luftflammen in geschlossenen Behältern [Influence of turbulence due to obstacles on the acceleration of H2- and CH4-air flames in closes vessles]. In: *Proc. der 6. Fachtagung Lasermethoden in der Strömungsmeßtechnik der GALA e.V.* GALA, 1998. ISBN: 3-8265-4287-8.

[5.61] A. Eder, B. Edlinger, M. Jordan and F. Mayinger, Investigation of Transient Flame Development using a Combination of Advanced Optical Measurement Techniques. In: *Proc. of the 8th Int. Symp. on Flow Visualisation*, Sorrento, Italy. 1998.

[5.62] M. Jordan, R. Tauscher and F. Mayinger, New Challenges in Thermo-Fluiddynamic Research by Advanced Optical Techniques. In: *Proc. of the 15th UIT National Heat Transfer Conference*, Torino, Italy. 1997.

[5.63] C. Gerlach, A. Eder, M. Jordan, N. Ardey and F. Mayinger, Advances in Understanding Flame Acceleration for the Improving of Combustion Efficiency. In: *Energy Conservation Through Heat Transfer Enhancement of Heat Exchangers*, Cesme, Turkey. Nato Advanced Study Institute, 1998.

[5.64] M. Jordan, *Ignition and Combustion of premixed turbulent jets (in German)*. PhD thesis, Technische Universität München, 1999.

[5.65] M. Jordan, N. Ardey and F. Mayinger, Effect of the molecular and turbulent transport on flame acceleration within confinements. In: *Proc. of the 11th Int. Heat Transfer Conference*, Kjongju, Korea. 1997.

[5.66] I.S. Zaslonko, V.P. Karpov, S.M. Frolov, M. Jordan, A. Eder and F. Mayinger, Flame-Jet Ignition of Fuel Air Mixtures. Experimental Findings and Modeling. In: *Proc. of the 16th Int. Conl. on the Dynamics of Explosions and Reactive Systems (ICDERS-16)*, Heidelberg, Germany. 1999.

[5.67] M. Jordan, A. Eder, B. Edlinger and F. Mayinger, Turbulent Quenching and Acceleration of Flames by Highly Blocking Obstacles. FISA Symposium 1999, to be published.

[5.68] M. Jordan, N. Ardey, C. Gerlach and F. Mayinger, Quenching Effects at Jet-Ignition of Lean Hydrogen- and Methane-Air Mixtures. In: *Proceedings of the 10th Int. Symp. on Transport Phenomena in Thermal Science and Process Engineering*, Vol. 1, Kyoto, Japan. 1997, 19–24.

[5.69] G. W. Koroll, R. K. Kumar and E. M. Bowles, Burning velocities of hydrogen-air mixtures. Combustion and Flame, Vol. 94, 1993, 330–340.

[5.70] N. Peters, Cours sur la combustion turbulent. Institut de l'Ecole Normale Superieure, Paris, 1997.

[5.71] R. Beauvais, *Brennverhalten vorgemischter, turbulenter Wasserstoff-Luft-Flammen in einem Explosionsrohr [Compustion properties of premixed, turbulent hydrogen-air flames in an explosion tube]*. PhD thesis, Technische Universität München, 1994.

[5.72] R.G. Abdel-Gayed and D. Bradley, Combustion Regimes and the Straining of Turbulent Premixed Flames. Combustion and Flame, Vol. 76, 1989, 213–218.

[5.73] R. P. Lindstedt and V. Sakthitharan, Time Resolved Velocity and Turbulence Measurements in Turbulent Gaseous Explosions. Combustion and Flame, Vol. 114, 1998, 469–483.

[5.74] D.R. Greig and C.K. Chan, Burning of Near-Flammability H2-air Mixtures in Interconnected Vessels. AECL report, COG-97-474, , 1998.

[5.75] R.K. Kumar, J. Loesel-Sitar, W.A. Dewit, E.M. Bowles and B. Thomas, Experiments in the Large-Scale Vented Combustion Test Facility: Series S01-Quiescent Vented Combustion Tests with Central Ignition in Hydrogen-Air Mixtures in the Full- Volume Geometry. AECL, COG-96-578, , 1997.

[5.76] J. Loesel-Sitar, W.A. Dewit, E.M. Bowles and B. Thomas, Experiments in the Large- Scale Vented Combustion Test Facility: Series S03-Vented Combustion Tests at $100^{o}C$ in Hydrogen-Air-Steam Mixtures in the Full-Volume Geometry. AECL report, COG-99-135, , 1999.

[5.77] T. Kanzleiter, Hydrogen Igniter Experiments Performed in the Model Containment Utilities Program. Battelle Institute, Final Report No. BF-V67.503-01, , 1992.

[5.78] T. Kanzleiter, Hydrogen Igniter Experiments Performed in the Model Containment Hx Tests. Battelle Institute, Final Report No. BleV-R66.985-01, , 1992.

[5.79] T. Kanzleiter, Experiments on the Efficacy of Hydrogen Mitigation Methods within a Multi-Compartment Containment Geometry. Battelle Institute, Final Report No. BleV-R67.036-01, , 1991.

[5.80] T. Kanzleiter and J Tenschert, Experiments on Hydrogen Deflagrations in Compartments with Obstacles. Battelle Ingenieurtechnik GmbH, Final Report No. BF-R68.145-01, , 1995/1997.

[5.81] T. Kanzleiter, DIVA - Versuche zur H2-Deflagration in einer Inertgas-verdünnten Sicherheitsbehülter-Atmosphäre [DIVA - H2-deflagration experiments in a containment, diluted with inert gas]. Battelle Ingenieurtechnik GmbH, Final Report No. BF-V 68.338-1, , 1996.

[5.82] J. Tenschert, Wasserstoff-Deflagrations-Experimente in einer kleinmaßstäblichen Versuchsanlage DN400 [Hydrogen deflagration experiments in the small-scale test facility DN400]. Battelle Ingenieurtechnik GmbH, Reports BF-R68.145-302, BF-R68.145-303, BF-R68.145-304, , 1995.

[5.83] L. Valencia, Wasserstoffdeflagrationsversuche in großer 3-Raumgeometrie im HDR-Containment [Hydrogen deflagration experiments in the large-scale 3D HDR containment]. In: *Jahrestagung Kerntechnik*, Karlsruhe. 1992.

[5.84] T. Hashimoto, K. Inagaki and J. Ogata, Large-Scale hydrogen Combustion Test at NUPEC. In: *Proceedings of the International (5 countries) Cooperative Exchange Meeting on Hydrogen in Reactor Safety*, Toronto, Canada. 1997.

[5.85] MELCOR 1.8.4, User's Guide. USNRC, Office of Nuclear Regulatory Research, NUREG/CR-6119, Rev.1, 1998.

[5.86] COCOSYS V1.1, Program Reference Manual. GRS, , 1999.

[5.87] M. Heitsch, Das Verbrennungsmodell DECOR für das Programmsystem RALOC mod4 [The combustion model DECOR for the RALOC mod4 code]. GRS-A-2292, , 1995.

[5.88] M. Heitsch, A Model of Vented Hydrogen Deflagrations in a Containment. Nuclear Technology, Vol. 114, 1996, 68–76.

[5.89] G.W. Koroll, R.K. Kumar and E.M. Bowles, Burning Velocities of Hydrogen-Air Mixtures, Combustion and Flame. Combustion and Flame, Vol. 94, 1993.

[5.90] M. Heitsch, Begleitung und Analyse großmaßstäblicher Wasserstoff- Verbrennungsversuche im Rahmen der Zusammenarbeit mit NUPEC (MITI) Japan [Analysis of large-scale deflagration experiments within the scope of cooperation with NUPEC (MITI) Japan]. GRS-A-2397, , 1996.

[5.91] A. Geist et al., PVM User's Guide and Reference Manual. RNL/TM-12187, Oak Ridge National Laboratory, , 1994.

[5.92] H. Paillre et al., Development of hydrogen distribution and combustion models for the multi-dimensional/lumped parameter TONUS code. 1997. Proc. 8th NURETH Conf., Kyoto, JAPAN.

[5.93] K.K. Murata et al., Users Manual for CONTAIN 1.1 : A Computer Code for Severe Nuclear Reactor Accident Containment Analysis. Sandia National Laboratories SAND87-2309, NRC Report NUREG/CR-2309, 1989.

[5.94] J. Gauvain and J.P. LHériteau, JERICHO, a code for computation of containment thermal hydraulic behaviour during a severe accident in a NPP. 1989. Proc. Int. Conf. NURETH 4, 909-914, Karlsruhe, Germany, October 10-13.

[5.95] M. Plys et al., MAAP4 model and validation status. 1993. Proc. 2nd Int. Conf on Nuclear Engineering, San Francisco, USA, March 21-24.

[5.96] H. Jahn et al., Description of the RALOC/FIPLOC family - Part 2 : Physical modeling of thermal hydraulics and integration methods. GRS Report, GRS-A-1426, 1988.

[5.97] J. R. Travis, HMS: a computer program for transient three dimensional fluid flows with chemical reactions and fuel sprays. NRC Report, NUREG/CR-4020, 1984.

[5.98] T. L. Georges et al., Containment Analysis with GOTHIC. 1991. Proc. 27th Nat. Heat Transfer Conf., Minneapolis, Minnesota, USA.

[5.99] A. Majda and J. Sethian, The Derivation and Numerical Solution of the Equations for Zero Mach Number Combustion. Combustion Science and Technology, Vol. 42, 1985, 185–205.

[5.100] A. Beccantini et al., Upwind flux splitting schemes for the 1D Euler equation : Application to shock tube and blast wave model problem. CEA internal report, 1997.

[5.101] A. Beccantini et al., A two-dimensional high order unstructured grid solver for unsteady shock propagation problems. CEA internal report, 1998.

[5.102] P. Verpeaux et al., A Modern approach of computer codes for structural analysis. 1989. Proc. of the 10th Conf. On structural Mechanics in Reactor Technology, Anaheim, USA.

[5.103] C.K. Chan, J. Loesel-Sitar, R. Beauvais and F. Mayinger, Modeling maximum flame speed. Nuclear Engineering and Design, Vol. 166, 1998, 463–470.

[5.104] G. E. Andrews, D. Bradley and S. B. Lwakabamba, Turbulence and turbulent flame propagation: A critical Appraisal. Combustion & Flame, Vol. 24, 1975, 285–304.

[5.105] F. Mayinger, R. Beauvais, G. Strube and N. Ardey, Einfluss der Temperatur auf die Grenzen für den Übergang zur Detonation in Wasserstoff/Luft/Wasserdampf-Gemischen AND Einfluss der Strömungsstruktur auf die Ausbreitung von Wasserstoff-Luft Flammen [Influence of Temperature on the Transition to Detonation in Hydrogen/Air/Steam Mixtures AND Influence of the Fluid Flow on the Propagation of Hydrogen-Air Flames]. 1995. BMFT 1 500 824 and BMFT RS 1500 810.

[5.106] G.W. Koroll, R.K. Kumar and E.M. Bowles, Burning velocities of hydrogen-air mixtures. Combustion & Flame, Vol. 94, 1993, 330–340.

[5.107] L.S. Kozachenko and I.L. Kuznezov, Burning velocity in a turbulent stream of a homogeneous mixture. Combustion, Explosions, Shock waves, Vol. 1, 1965, 22ff.

[5.108] N. Peters, New developments in the theory of premixed turbulent combustion. 1997. Cours sur la combustion turbulente, Institut de lEcole Normale Suprieure, Paris, FRANCE.

[5.109] C.K. Chan, Flame acceleration and transition to detonation experiments at AECL. 1995. Hydrogen combustion working group meeting, Tokyo, JAPAN.

[5.110] M. P. Sherman, S. R. Tieszen and W. H. Benedick, FLAME Facility. 1975. NUREG CR-5275.

[5.111] T. Hirose, H. Ogasawara (NUPEC) and J. Ogata (MHI), Large scale hydrogen combustion test. 1995. Hydrogen combustion Working group Meeting, Tokyo, JAPAN.

[5.112] B. Edlinger, C. Poruba, A. Eder, F. Mayinger, U. Bielert, A. Veser, A. Kotchourko, W. Breitung, P. Royl, W. Scholtyssek, H. Wilkening, T. Huld, M. Movahed, F. Dabbene and E. Studer, Multi-dimensional simulation of hydrogen distribution and combustion in severe accident. EU contract FI4S-CT-95-0001, Final Report (to be published), 1999.

[5.113] S.B. Dorofeev, A.S. Kotchourko, A.A. Efimenko and B.B. Chaivanov, Evaluation of hydrogen explosion hazard. Nuclear Engineering and Design, Vol. 148, 1994, 305–316.

[5.114] J. E. Shepherd, Chemical kinetics of hydrogen-air-diluent detonations. Progress in Astronautics and Aeronautics, Vol. 106, 1986, 263–293.

[5.115] G. Ciccarelli et al., High temperature hydrogen-air-steam detonation experiments in the BNL Small-Scale Development Apparatus. BNL-NUREG-52414, , 1994. NUREG CR-6213.

[5.116] J.H.S. Lee, R. Knystautas, C. Guirao, W.B. Benedick, J.E. Shepherd and P. A. Freiman, H2-Air Detonations. 1982. SAND82-1864C.

[5.117] D. W. Stamps, Detonation cell widths in hydrogen-air-diluent mixtures. 1990. SAND90-2251C.

[5.118] W. Breitung, I. Coe, H. Grönig, L. He, R. Klein, H. Olivier, W. Rehm, E. Studer and B. Wang, *Models and Criteria for Prediction of Deflagration-to-Detonation Transition (DDT) in Hydrogen-Air-Steam Systems under Severe Accident Conditions*. Projekt FI4S-CT96-0025 - Final Report. European Commission, Brussels, 1999.

[5.119] S.B. Dorofeev, A. Kotchourko, A. Lelakin, A. Baitin and A. Efimenko, Development of numerical programs for 3d reactive flow simulation in complex containment geometry. Turbulence Modeling. Final report for FZK, Kurchatov Institute Moscow, , 1994.

[5.120] A. Kotchourko, W. Breitung and A. Veser, Reactive Flow Simulations in Complex 3d Geometries using the COM3D Code. In: *Jahrestagung Kerntechnik*, Karlsruhe, Germany. May 18-20 1999, 173.

[5.121] A. Veser, A. Kotchourko and W. Breitung, Experiments on Turbulent Combustion and COM3D Verification. ibid, .

[5.122] V. Yakhot and S.A. Orszag, Renormalization group analysis of turbulence. I.Basic theory. J.sci. Comput., Vol. 1(3), 1986.

[5.123] A. Harten, High resolution schemes for hyperbolic conservation laws. J.Comput. Phys., Vol. 49, 1983, 357–393.

[5.124] A. Kotchourko, W. Breitung, A. Veser and S.B. Dorofeev, Tube experiments and numerical simulation on turbulent hydrogen-air combustion. In: *21st Symp. (Int.) on Shock Waves*, Great Keppel Island, Australia. 1997.

[5.125] W. Breitung, S.B. Dorofeev, A.A. Efimenko, A.S. Kotchourko, R. Redlinger and V.P. Sidorov, Large-scale confined hydrogen-air detonation experiments and their numerical simulation. In: *20th Symp. (Int.) on Shock Waves*, Pasadena, CA, USA. 1996.

[5.126] AEA Technology Ltd., Oxfordshire, United Kingdom, *CFX4.2, Solver Manual*, 1997.

[5.127] G.L. Schott and J.L. Kinsey, Kinetic studies of hydroxyl radicals in shock waves, II. Induction times in the hydrogen-oxygen reaction. J. Chem. Phys., Vol. 29, 1958, 1177–1182.

[5.128] K. Fischer et al., Verification and further development of a predictive multidimensional model for hydrogen deflagration in a multiple compartment LWR-containment. Final report BF-R68.121, Battelle, Eschborn, Germany, , 1996.

[5.129] B. Durst and F. Mayinger, Einfluß Containment-typischer Strömungshindernisse auf die Ausbreitung von Wasserstoff-Luft-Flammen – Band II: Lokale Strömungsmessungen und dreidimensionale Modellierung der turbulenten Verbrennung [Influence of containment typical obstacles on the propagation of turbulent hydrogen-air flames – vol II: measurement of flow velocity and modelling of turbulent combustion]. Abschlußbericht zum Forschungsvorhaben BMFT, Nr. 150 0957, TU München, 1999.

[5.130] B. Durst. PhD thesis, Technische Universität München, 1999. To be published.

[5.131] B. Durst, N. Ardey and F. Mayinger, Interaction of Turbulent Deflagrations with Representative Flow Obstacles. In: *Proceedings of the OECD/NEA/CSNI Workshop On the Implementation of Hydrogen Mitigation Techniques*, Winnipeg, Manitoba. 1996, 433–447.

[5.132] S. B. Pope, The Statistical Theory of Flames. Phil. Trans. R. Soc. London, Vol. A 291, 1979, 529–568.

[5.133] K. N. C. Bray, Turbulent Flows with Premixed Reactants. In: *Turbulent Reacting Flows*. (P. A. Libby and F. A. Williams, (editors)), Topics in Applied Physics, chapter 4, 115–183. Springer Verlag, Berlin, Heidelberg, 1980.

[5.134] R. Borghi, Turbulent Combustion Modelling. Prog. in Energy and Combust. Sci., Vol. 14, 1988, 245–292.

[5.135] F. C. Lockwood and A. S. Naguib, The Prediction of Fluctuations in the Properties of Free, Round-Jet, Turbulent, Diffusion Flames. Combust. and Flame, Vol. 24, 1975, 109–124.

[5.136] R. J. Kee, J. F. Grcar, M. D. Smooke and J. A. Miller, A FORTRAN Program for Modeling Steady Laminar One-Dimensional Premixed Flames. Sandia National Laboratory, Technical Report SAND85-8240, 1985.

[5.137] R. J. Kee, F. M. Rupley and J. A. Miller, CHEMKIN-II: A FORTRAN Chemical Kinetics Package for the Analysis of Gas-Phase Chemical Kinetics. Sandia National Laboratory, Technical Report SAND89-8009, 1989.

[5.138] U. Maas, *Mathematische Modellierung instationärer Verbrennungsprozesse unter Verwendung detailierter Reaktionsmechanismen [Mathematical modelling of transient combustion processes using detail reaction mechanisms]*. PhD thesis, Universität Heidelberg, 1988.

[5.139] U. Maas and J. Warnatz, Ignition Processes in Hydrogen-Oxygen Mixtures. Combust. and Flame, Vol. 74, 1988, 53.

[5.140] A. Eder, B. Edlinger and F. Mayinger, Einfluß Containment-typischer Strömungshindernisse auf die Ausbreitung von Wasserstoff-Luft-Flammen, Vol.III,Maßstabseffekte und Anlaufvorgänge [Influence of containment typical obstacles on the propagation of turbulent hydrogen-air flames – vol III: Scaling and run-up effects]. TU München, Abschlussbericht, BMFT 1500957, , 1998.

[5.141] A. Eder, C. Gerlach and F. Mayinger, Determination of Quantitative Criteria for the Transition from Deflagration to Detonation in H2/Air/H2O-Mixtures. In: *Proceedings of the 22nd International Symposium on Shock-Waves*, London, UK. 1999.

[5.142] A. Eder, C. Gerlach and F. Mayinger, Experimental Observation of Fast Deflagrations and Transition to Detonations in Hydrogen-Air-Mixtures. In: *Proceedings of the Symposium on Energy Engineering in the 21st Century, to be published*, Hong Kong. 2000.

[5.143] W. Rehm, M. Heitsch, W. Jahn and F. Semler, Numerical Investigations of Gas Mixing and Deflagration-to-Detonation Effects Using Multi-Dim. Computational Fluid Dynamic Tools. In: *3rd Int. CFX Users Conference*. AEA Harwell, UK, 1997, 393–413.

[5.144] W. Rehm, R. Klein, N. Peters, P. Thibault and C. Chan, Effects of DDT on Hydrogen Explosion Loads in Large Scale Enclosures. Pilot Project Final Report, Contract No. FI3S-CT92-0003, Brussels, Aug. 25, '95, 1995.

[5.145] W. Rehm, P. Royl, F. Fineschi, M. Heitsch, K. Reinders and W. Breitung, Combustion Phenomena in Nuclear Reactor Containments. In: *FISA-95 Symposium, EC Research on Severe Accidents*. European Commission, 1996, 330–357. ISBN 92-827-6980-1.

[5.146] R. Klein, W. Breitung, W. Rehm, H. Olivier, L. He, P. Armand and M. Ang, Models and Criteria for Prediction of Deflagration-to-Detonation Transition (DDT) in Hydrogen-Air-Steam Systems under Severe Accident Conditions. In: *FISA-97 Symposium, EC Research on Severe Accidents*. European Commission, 1997.

[5.147] F. Hoßfeld, E. Maehle and E.W. Mayr, PASA '96, Parallel Systems and Algorithms. In: *Proc. of the 4th Workshop*. Research Center Jülich, Germany, 1996, 393–413.

[5.148] M. Gerndt, Compilers for Parallel Computers. In: *Proc. of the Sixth Workshop*, Vol. 21. Research Center Jülich, Germany, 1996.

[5.149] F. Unger, Port of the CFX-5 to the CRAY System at FZJ. AEA Technology Otterfing, Germany, Technical Report, 1998.

[5.150] M. Kuntz and W. Rehm, Combustion Modelling in CFX-5. In: *CFX User Conference, Friedrichshafen*. AEA-Technology, 1999.

[5.151] W. Rehm, M. Gerndt, W. Jahn, F. Semler and I. Jones, CFD Simulation of Deflagration-Detonation Processes Using Vector- and Parallel Computing Systems. Journal for Applied Mathematical Modelling, Vol. 22, 1998, 811–822.

[5.152] B. Wang, M. Weber and H. Olivier, Ignition Phenomena and Detonation Formation in H2-Air and H2-Air-Steam Mixtures. RWTH-SWL, Aachen, Germany, , 1998.

[5.153] A. Veser, W. Breitung and G. Engel, Hydrogen combustion experiments. Projekt Nukleare Sicherheitsforschung, Jahresbericht 1997, 1998, 82. Report FZKA-6126.

6. APPLICATIONS TO REACTOR CONTAINMENT ANALYSIS*

6.1. Introduction**

Since the Three Mile Island accident, there has been a great deal of interest regarding the problem of hydrogen production, distribution, and combustion in LWRs. Regarding reactor safety analyses or studies, hydrogen combustion can involve wide time scales (between milliseconds in case of a detonation and several seconds in case of a slow deflagration) and pressures (between 4 and 30 times the initial pressure or more, depending on the reflections of the shock waves). These two parameters characterize the main combustion consequences of importance to reactor safety, i.e., pressure load and impulse (integral of pressure over time). In some cases, the temperature increase can also be of concern for the behaviour of equipment or the integrity of the containment, but, usually, this parameter presents no serious threat because the flame front travels comparatively fast because of propagation in structures. Depending on time and natural frequency scales, the effect of a combustion process inside containment can be divided in two main categories: static and dynamic loading. According to combustion propagation, this effect can be local (inside a compartment) or global (for the whole containment).

All the combustion modes are potentially possible for the same accident scenarios. The process of combustion during a severe accident is an ignition by a weak source, an electric spark, for example. Starting at low speed near the ignition point, the flame can be strongly accelerated by turbulence, and thus the flame speed can reach levels well above those of the speed of sound with complex systems of pressure waves. This combustion or acceleration process depends on many parameters, such as concentrations of reactants and diluents, presence and nature of ignition source, geometry, initial thermalhydraulics (temperature, pressure, and turbulence, etc.), and operating system effects (spray, venting, etc.).

First of all, to ensure the adequacy of developed criteria with the reactor safety requirements, the range of influencing parameters has to be specified for various severe accident scenarios and different geometry. Guidelines should be defined to apply the developed criteria to reactor scale.

6.1.1 General Data for Criteria Application

The aim of this introduction is to summarize some general data related to our present knowledge of hydrogen behaviour in actual NPPs. This task has been done in order to avoid plant-specific considerations, especially for the guidelines to apply foreseen macro-criteria on FA and DDT, and also to be sure that the developed criteria are available for the whole range of severe accident scenarios and geometry configurations.

For safety reasons, the goal has to be a minimization of severe accident scenario occurrences dealing with accidental combustion and strong FA, which could jeopardize the containment integrity. The main parameters influencing the development of such a combustion process can be summarized in the areas of mixture concentration (including initial thermodynamics conditions) and geometrical configuration.

---

* Dr. W. Breitung is the lead author of Chapter 6.

** E. Studer contributed Sections 6.1 through 6.3.

Present criteria developed for FA and DDT entail these two different informations connected to mixture composition and geometrical configuration.

6.1.1.1 Mixture composition

Mixture composition is strongly affected by the initial thermalhydraulic conditions, i.e., the initial temperature and degree of initial turbulence. Initial temperature is of interest because the sensitivity of a given mixture increases with higher temperature (reaction rate, detonation cell size, less-efficient turbulence quenching). Concerning turbulence, the main effect can be considered as a balance between initial turbulence and flame-induced turbulence and mixing. The initial pressure is normally not relevant to the behaviour of a flame front, but it can be of importance for the value of absolute pressure obtained during a combustion process.

For mixture composition, the following parameters should be considered: mean values and gradients for combustible gases (hydrogen or carbon monoxide or both) and diluents (steam or carbon dioxide or both) and oxidant concentration. Any indication of gradients between a possible ignition position and the end of the combustion path is also important because in terms of negative combustible gradients, the combustion may be quenched during propagation. For this case, the effect should only be local (inside a compartment) and not global (for the whole containment). Consequently, the way to jeopardize the containment may be different: possible missiles created by a local explosion compared to global pressure loading of the containment.

Regarding the generation of combustible gases, many severe accident scenarios could be divided in 6 different phases; each scenario can only involve two or three phases or parts of these phases:

- Phase 1 : hydrogen release during in-vessel clad oxidation (main short-term source of hydrogen);
- Phase 2 : from molten pool formation to vessel lower head failure;
- Phase 3 : reflooding of degraded core;
- Phase 4 : long-term behaviour without core-concrete interaction;
- Phase 5 : short-term core-concrete interaction; and
- Phase 6 : long-term core-concrete interaction.

For each phase, the gaseous composition in the containment must be known in order to estimate or calculate the behaviour of potential combustion phenomena. Aside from the above 6 phases of hydrogen generation, the initial steam release phase prior to the hydrogen production can also have an important influence on the combustion regime because it affects the long-term distribution of heat sources and sinks, and hence the convection flows.

The mixture composition or the occurrence of ignition can also be influenced by the following system boundary conditions:

- pre-inertization in the containment as in some BWR power plants,
- recombiner mitigation devices as in a Belgian large dry PWR power plant,

- igniters as in some US nuclear power plants, and

- operating systems (spray, venting, etc).

In the following lumped-parameter application, scenarios related to phase 2 and recombiners will be examined.

6.1.1.2 Geometry

The geometry of a combustion volume is the most important and the most complex parameter for FA. Especially, in case of real situations, geometry of a single combustion compartment and arrangement of a multi-compartment combustion process are of main importance. The three main parameters can be summarized as size of obstacles, distance between 2 obstacles, and degree of confinement (all geometrical discontinuities on the combustion path). In actual NPP geometry, data such as blockage ratio or spacing of obstacles cannot always be defined because of their complexity. The main characteristics of such geometry are the very irregular arrangements compared to well-defined experimental conditions. Long channels such as explosion tubes or those used in the RUT [6.1] or FLAME [6.2] facilities can be regarded as quasi-one-dimensional, but real geometry leads to two- or three-dimensional combustion processes. The main parameter in this case is the expansion flow created in the unburned mixture, which strongly depends on the degree of confinement. At the present time, experimental programs are not designed to get an appropriate model in all needed scenarios of this complex phenomenon.

6.2. Illustration of Combustion Calculation at Reactor-relevant Scale with Lumped-parameter Approach [6.3]

Concerning the lumped- parameter approach, the whole methodology described in Chapter 5 could be applied on a simplified test case. The geometry chosen is that of a prototypic French 900 MWe PWR. The severe accident scenario is assumed to be a 2-inch small-break cold-leg loss-of-coolant accident (LOCA) with safety injection and spray failure. Containment transient has been calculated using the lumped-parameter code RALOC mod4.0 [6.4] using about 85 nodes in the gas phase of the containment. No mitigation measures are taken into account in this calculation, and hydrogen production during in-vessel core degradation is maximized. Hydrogen and steam distribution at the time of vessel failure is shown in the Figure 6.2-1.

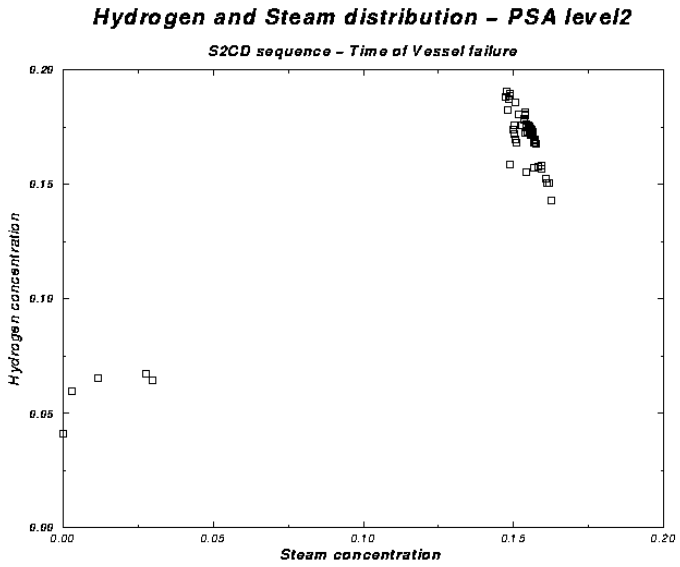

Figure 6.2-1 Hydrogen and steam concentration in each control volume at vessel failure time (2-inch-diameter LOCA)

Each point represents one gas node in the containment atmosphere. The mixture is quite homogeneous in the whole containment: hydrogen concentration is between 14 and 18 vol % and steam is around 14 to 16 vol %. Some rooms show special behaviour because they are poorly influenced by the main convection loops (basemat and in-core instrumentation room located in the lower part of the containment).

This hydrogen distribution has been used as an initial condition in the probabilistic safety analysis (PSA) 2 simplified combustion model. The geometry has been modified to ensure that the restrictions of the model are verified: this means, for example, that channel regions such as the annular region have been subdivided to create an arrangement of cubic volumes. The containment is now subdivided into about 500 rooms, with more than 1000 atmospheric junctions. Concerning modelling, an additional parameter has been introduced to enhance the vertical flame propagation of upward direction versus horizontal or downward direction. This is done by using a simple parameter K (>1) to weight each atmospheric junction: K is applied to upward vertical junction, 1.0 to horizontal junction, and 1/K to downward propagation. Concerning ignition, studies have shown that potential ignition locations are located in the lower part of the containment (between –3.5 and 4.65 m). Three test cases have been simulated with our model:

- Case 1: ignition in the annular region (level 0.0 m) loop number one (all the rooms involving components of the first reactor primary circuit loop) with K = 1.0;

- Case 2: same as case 1, but K = 5.0; and

- Case 3: ignition in the residual heat removal system exchanger room (level –3.5 m) with K = 1.

Results are given in Figure 6.2-2 in terms of flame velocity V_F in metres per second for the 3 test cases and for loop number one (the mixture in room number R448 is non-flammable). Geometry has been averaged on the initial geometrical arrangement used for distribution calculation.

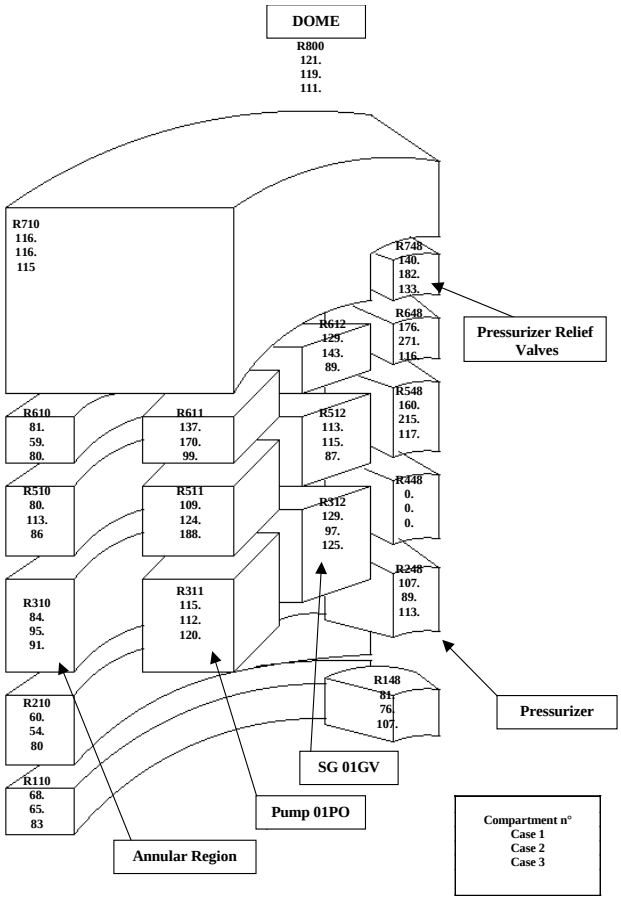

Figure 6.2-2 Turbulent combustion velocity in each control volume (2-inch-diameter LOCA at vessel failure time)

In the dome region, the flame velocity is less than 120 m/s. Combustion velocity is slow in the lower part of the containment. Acceleration can be seen in the steam generator, pump or pressurizer rooms (mainly for the second test case where the vertical upward combustion is enhanced). This implies, for example, that the dome region burns before the lower part of the containment is ignited. Maximum flame velocity is about 270 m/s in the upper part of the pressurizer rooms. If one looks at the other loops, the results are the same, and a maximum flame velocity of 430 m/s is calculated in the upper part of the pump region on loop number 3. One important phenomenon, which is not modelled in the present combustion process, is the occurrence of multiple ignition in a single room if the combustion process arrives from 2 or 3 different room connections at the same time.

Our simplified modelling for this hydrogen distribution test case (which can represent an upper bound for hydrogen distribution) does not predict any dynamic effect on the containment (fast turbulent deflagration, DDT or stable detonation) although the hydrogen mixture is very sensitive. Large open sections between volumes in a French 900 MWe PWR reduce the FA process. This study has only been performed to have an estimation of the FA process in a real containment geometry. These conclusions must be treated as preliminary because of the simplification in the modelling and the lack of knowledge concerning flame propagation in real 3D geometry.

6.3 Lumped-parameter Approach

This section is dedicated to application of criteria developed in Chapter 3 (criteria for FA and DDT). The example given here is related to the lumped-parameter approach for containment thermalhydraulics calculations. Examples for multi-dimensional CFD tools are given in the next section. Lumped-parameter nodalization is important because in many countries and for several years, lumped-parameter codes are often used for hydrogen risk analyses in the containment. Thus the database for hydrogen distribution covers a wide spectrum of postulated severe accident scenarios.

The criteria developed in Chapter 3 are expressed in terms of necessary conditions. They can be applied to select in a large number of possible scenarios that are important for FA or DDT. Then for these scenarios, detailed distribution and combustion calculations should be performed with detailed modelling (CFD models) in order to quantify loads to the third barrier (containment) and then structural mechanics behaviour.

6.3.1 Criteria

The following 3 criteria were developed in Chapter 3:

- the necessary condition for detonation propagation (criterion 1),
- the necessary condition for DDT (criterion 2) and
- the necessary condition for flame acceleration (criterion 3)

In the present study, criteria 1 and 2 will be aggregated and expressed in the following application by the L/λ criterion.

Criterion 2 is divided in 2 parts:

- requirements for DDT in terms of fast flame, critical flame, or shock Mach number. This part will not be studied because one needs to calculate the propagation of turbulent flames in a lumped-parameter approach. Therefore, simplified models like the one described in the previous section can be used. The present study aims only to use distribution results for estimating the potential for FA or DDT.
- onset of DDT: the 7λ criterion. Regarding the lumped-parameter approach, this criterion is expressed in terms of size of a room or block of rooms. The key point is to define this geometrical size, and some possible rules are given in Chapter 3. This criterion should not be applied in case of strong hydrogen gradients (near the break if the release velocity is high compared with the convection velocity).

Criterion 3 is expressed in Chapter 3 by two different critical values depending on $\beta(Le-1)$. To avoid uncertainties in the value of activation energy E_a, it has been proposed to use a temperature-dependent σ-value $\sigma^*(T_u)$ despite the preceding critical values (Figure 3.2.3-1). This is considered valid for a hydrogen-air-steam mixture without any others diluents, which is the foreseen mixture encountered in the containment during a severe accident scenario. It has been chosen to express criteria by the 2 manners, and to compare the results in the following application. This criterion is expressed by the σ-criterion in the following application.

6.3.2 Values Used to Calculate the Criteria

Regarding lumped-parameter calculations, the following variables are calculated in each control volume at each time step: total pressure *P*, gas temperature *T*, gas composition (mass or volume fractions of each gaseous species).

Geometrical data affect the total free volume of the cell V_{li}, the height H_i, the sump area S_{pi}, the total wall area S_{wi} and the area of gaseous flow path between « cells » S_{ij} (Figure 6.3.2-1).

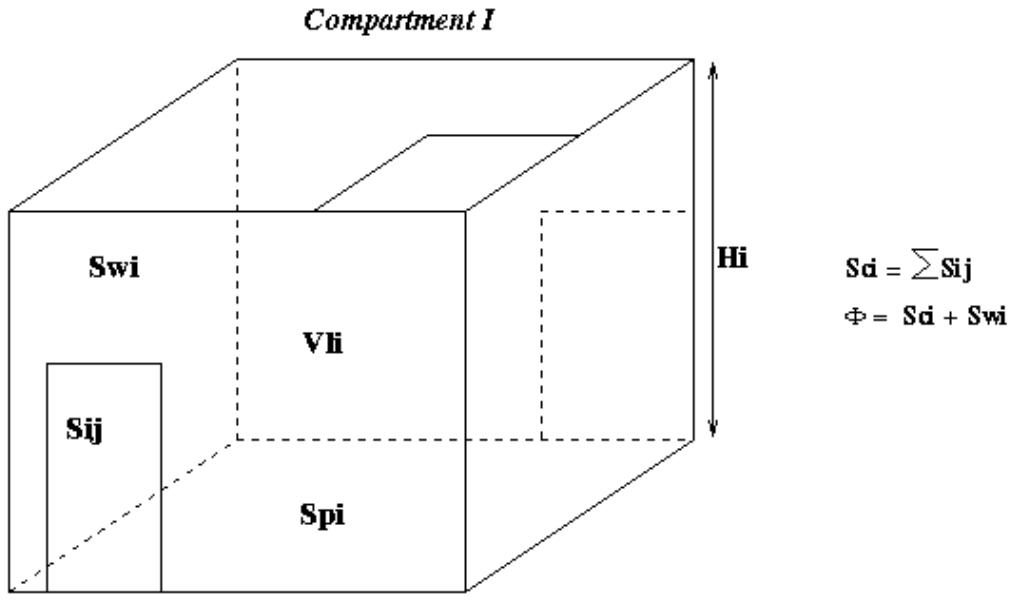

Figure 6.3.2-1 Compartment geometrical parameters in lumped-parameter approach

6.3.2.1 Detonation cell size

A correlation proposed by S. Dorofeev, (see Appendix D of this report) can be used to determine the λ criterion. The detonation cell size is the result of the fitted function depending on initial pressure, temperature, steam, and hydrogen concentrations.

6.3.2.2 Characteristic size L of the room

The following guidelines have been derived in Chapter 3:

- For a cubic single room, *L* corresponds to the height of the room,
- For a single room where the width (*W*) is smaller than the length (*D*) and the height (*H*):
  $L = (D + H)/2$
- For two connected rooms: $L = L_1 + \alpha \times L_2$ where $\alpha = (1 - BR)^{1/2}$; BR represents the blockage ratio between the two rooms; this means the open area versus the total area. If the BR is smaller than a

critical value (0.1 for example), the two interconnected rooms are considered as a single one using the preceding formula to determine *L*.

- For a system of interconnected rooms, $L = L_1 + \alpha_2 \times L_2 + \alpha_3 \times L_3 ... \alpha_i$ are calculated using the preceding definition. If it is difficult to define a BR in a real containment, then alternative definitions such as $(L_1 \times S_{1i}/V_1)^{1/2}$ or $(6 \times S_{1i}/(S_{wi} + S_{ci}))^{1/2}$ may be used.

The preceding rules have a clear definition with cubic volumes, comparable sizes, and small connecting flow paths. Unfortunately, in a large dry French-type PWR, the "room" volumes are not always cubic, the atmospheric junction areas are very large, and two interconnected volumes can have very different characteristic sizes.

There are different ways of calculating the characteristic size *L*. The first one is to look at the drawings of the NPP containment and to define a characteristic length scale for each room as long as it is possible to define a room. Then, rules defined above can be applied. A second possibility is to use a nodalization scheme (control volumes) built for a lumped-parameter analysis of hydrogen distribution with a lumped-parameter code. Using this second approach, the rules defined above lead to unrealistic characteristic length mainly because in the nodalization the control volumes are not always "rooms" but free volumes with large openings. Because of this fact, a special set of rules has been developed for a 900 MWe French PWR (see Appendix F). Sensitivity studies of the different nodalization schemes of the same containment have not been performed.

6.3.2.3 Other mixture characteristics

Others parameters of mixture characteristics are necessary to express the σ criteria. These are

- σ: density ratio between fresh (ρ_u) and burnt (ρ_b)gases;

- T_b: temperature of the burnt gases;

- $Le = \lambda/(\rho \times C_p \times D)$: Lewis number with λ the thermal conductivity, ρ the density, C_p the heat capacity of the gaseous mixture (at initial temperature), and *D* the diffusion coefficient of the limiting gaseous species;

- $\beta = E_a(T_b - T_u) / (R \times T_b^2)$: Zel'dovich number with E_a/R the reduced activation energy.

Fourth-order polynomial regressions are used to calculate the heat capacity $C_p(T)$ of each chemical species. To simplify, T_b is calculated assuming a complete combustion at constant pressure. The mixtures studied are relatively lean equivalent hydrogen-air mixtures (dry conditions) and the reduced activation temperature is taken from $E_a/R = 9800$ K as suggested in Chapter 3. Thermal conductivities and diffusion coefficients are calculated with the TRANFIT program in the CHEMKIN II code package [6.5] (polynomial regression versus temperature). Comparison between these calculated values and the values given in References [6.6], leads to the following results (Table 6.3.2.3-1).

Table 6.3.2.3-1 Verification of mixture characteristics

[H_2] dry conditions	σ*	β*	Le*	β(Le-1)*	σ	β	Le	β (Le-1)
9 vol %	3.31	6.86	0.344	-4.5	3.26	6.77	0.377	-4.2
10 vol %	3.54	6.56	0.352	-4.3	3.48	6.48	0.383	-4.0
11 vol %	3.77	6.28	0.360	-4.0	3.71	6.21	0.389	-3.8
15 vol %	4.63	5.35	0.394	-3.2	4.55	5.29	0.411	-3.1

* according to [6.6]

The values have some differences between 3% and 7% for β(Le-1) and lower than 2% for σ but not so important, and this could be included in the uncertainties.

6.3.3 Illustration

6.3.3.1 Geometrical considerations

The chosen geometry corresponds to a French 900 MWe pressurized reactor with a large dry containment. The total volume is about 50 000 m^3 and the lumped-parameter nodalization uses 85 different compartments to describe the whole free volume.

With these "complex" definitions, the characteristic size of each compartment is given in Figure 6.3.3.1-1. In this calculation 85 nodes are considered with a free volume varying between 100 m^3 and 15 000 m^3 (upper dome region).

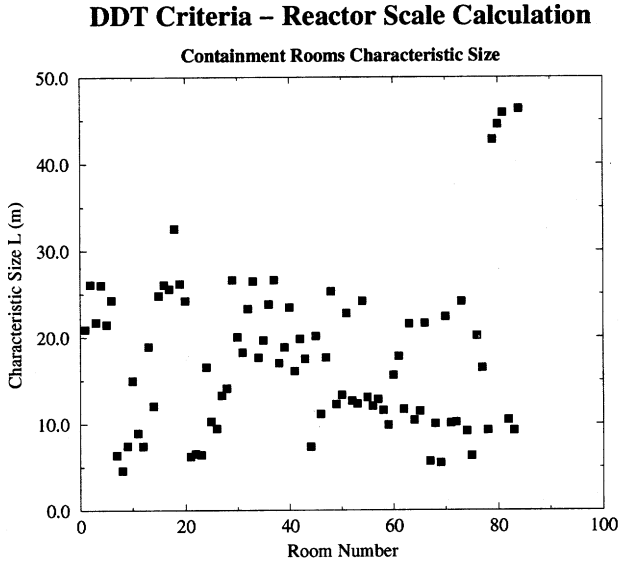

Figure 6.3.3.1-1 Containment characteristic length *L*

These calculated characteristic lengths vary from 5 m (small confined room in the lower part of the containment) and about 45 m (dome region) where all the ”volumes” are open. This last length is quite the maximum length scale available in the containment (bottom of the pool and top of the dome), and this length scale can be used to validate the aggregation rules defined in Appendix F.

6.3.3.2 Severe accident scenario

In all the possible scenarios regarding PSA, it was decided to select two situations. The choice we made implies a scenario and also a selected time during the whole scenario. One can notice that the criteria could be directly implemented in the lumped-parameter code, and thus it will be useful to follow the value of the criteria during the whole scenario. In this current application, a post-processing methodology was chosen, and the criteria will only be evaluated at selected times during the scenario. The selected situations are as follows:

- Case 1: high hydrogen concentration (vol %) and low steam concentration. This corresponds to a small break (2-inch diameter) in the cold leg with failure of both the safety injection (SI) and the spray system. The selected time corresponds to just before the failure of the vessel’s lower head. This scenario has slow in-vessel kinetics, and this means a large hydrogen production (more than 100% of the active part of the cladding), the release rate is also slow.

- Case 2: the preceding scenario is an unmitigated severe accident scenario, and now the same scenario as that used in case 1 is used but hydrogen mitigation countermeasures (catalytic recombiners) have been implemented in the calculation. The equivalent of 28 FR90-1500 (Siemens type) recombiners has been distributed in the containment geometry. The selected time is the time of maximum hydrogen concentration.

These 2 test cases have been calculated with the RALOC mod 4.0 Cycl AF lumped-parameter code. To illustrate the calculation, Figure 6.3.3.2-1 presents the total mass of hydrogen in the containment until the vessel’s lower head failure, and Figure 6.3.3.2-2 compares the hydrogen and steam distribution in each control volume at the selected time.

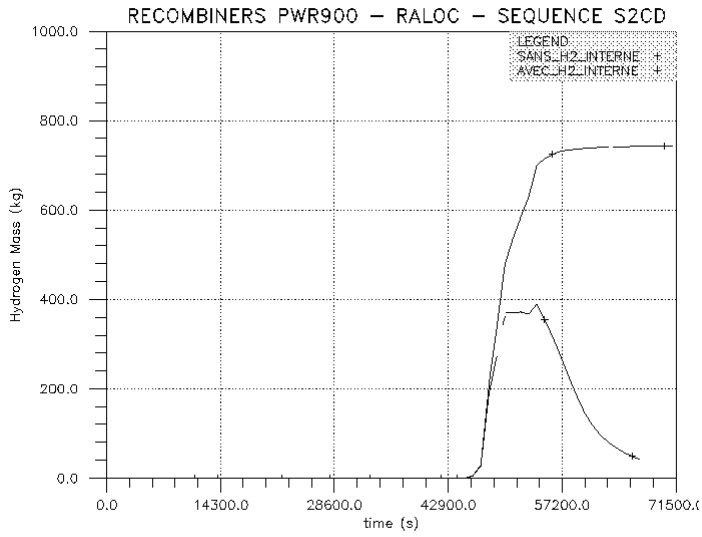

Figure 6.3.3.2-1 Severe accident scenario – hydrogen released mass

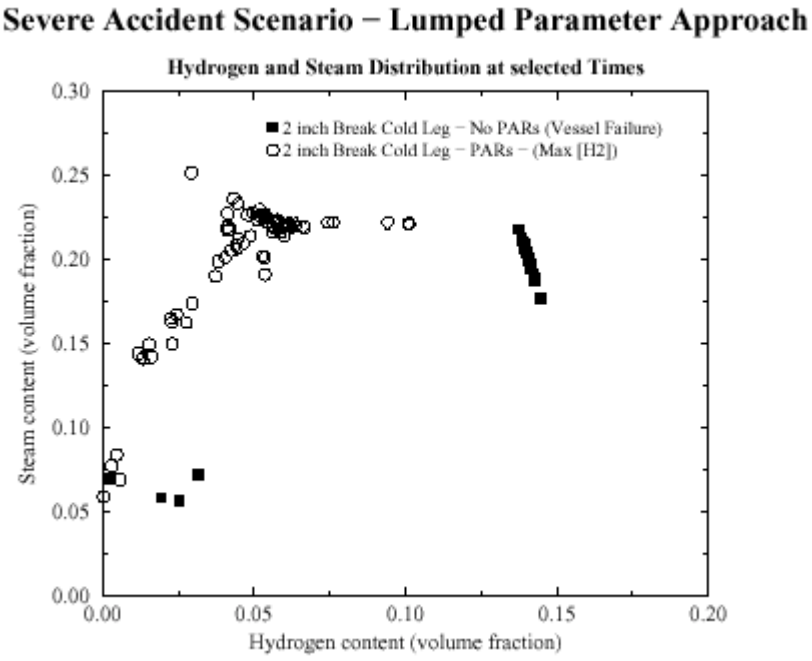

Figure 6.3.3.2-2 Severe accident scenario – hydrogen and steam distribution

These two test cases must be considered as an illustration of initial conditions for criteria application and not as results for all the possible scenarios involved in a level 2 PSA. Higher hydrogen release rates are expected during in-vessel core reflooding, for example.

6.3.3.3 Applications

6.3.3.3.1 The σ criterion

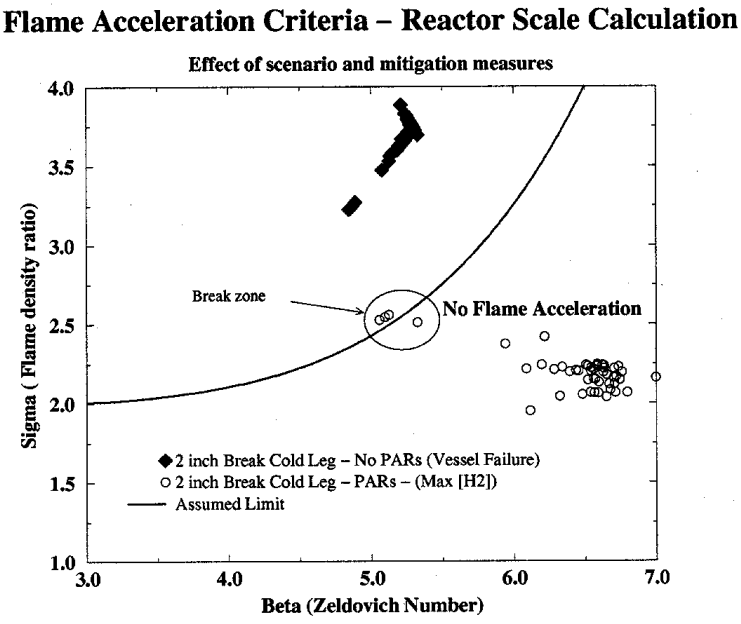

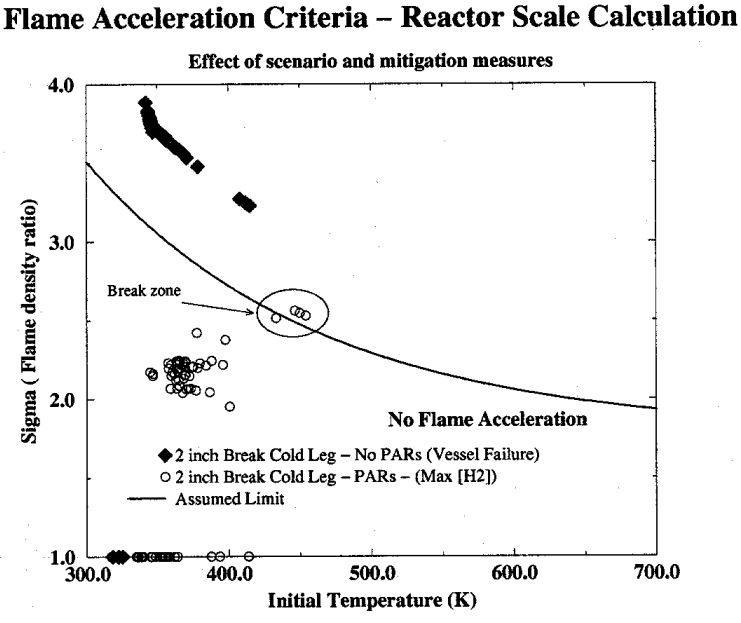

Figure 6.3.3.3.1-1 σ criterion application

The σ−criterion has been expressed relating to Zel'dovich number β and initial temperature T_u, the results are the same. For the first scenario, most of the containment rooms are above the assumed

limit; thus, this scenario cannot be excluded according to FA potential (Figure 6.3.3.3.1-1). In the second one, (use of passive autocatalytic recombiners, PARs), because of hydrogen risk counter-measures most of the rooms that are below the limit except three or four rooms located near the break (in the break plume) and are close to the assumed limit. This situation has a very short time period regarding the whole scenario, and one can conclude that this scenario has a small probabilistic contribution to FA risk.

6.3.3.3.2. The L/λ criterion

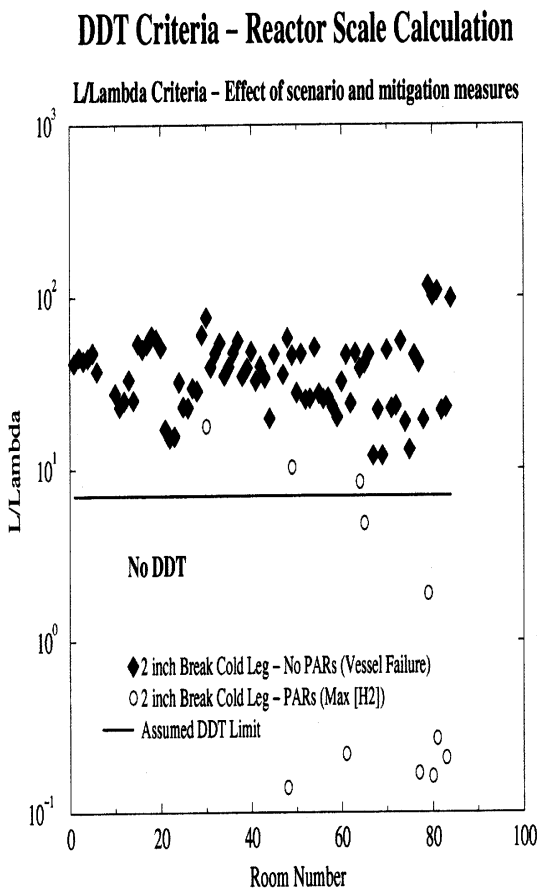

Figure 6.3.3.3.2-1 L/λ criterion application

For the first scenario, all the volumes are above the assumed limit (except non-flammable regions). This scenario is very sensitive to DDT because it was already sensitive to FA. Regarding fast transient phenomena associated to combustion process, this scenario represents one of the worst cases.

In the second scenario, the criterion is fulfilled in 3 rooms near the break (the neglected points have detonation cell sizes greater than 2 m because of very low equivalent ratio). For these 3 rooms, the criterion is perhaps not directly applicable because of too large hydrogen gradients (Figure 6.3.3.3.2-1). Nevertheless, this scenario is less sensitive to DDT as it also was for FA. According to a certain

level of flame acceleration needed for DDT occurrence, one can conclude that in this scenario, DDT is not expected to occur.

6.3.3.4 Uncertainties and conclusions

Regarding uncertainties, many potential sources are listed in Chapter 3. The largest uncertainty seems to be on the detonation cell size value, but in the present study a decrease by a factor of 1.5 or 2 of the detonation cell sizes does not change the conclusions. For some scenarios, the mixture and the geometrical characteristics are far from the assumed limits, so the conclusions are clear and they can or cannot be excluded in terms of FA and DDT risk analyses. Regarding applications, characteristic length L is very difficult to estimate especially with large openings. For the scenario where the representative points are closer to the limits, one has to look carefully at uncertainties and also at time duration. The preceding criteria are necessary conditions; thus in a conservative approach the first step could be a strict application of the proposed criteria before a more detailed analysis is performed. Results of FA criterion can be used to make this deeper analysis on DDT criterion, for example.

The preceding applications are just an illustration of how to apply the proposed criteria in a lumped-parameter approach. General conclusions cannot be extrapolated without a systematic and probabilistic analysis of the possible scenario for a given type of NPP. Expert judgment is mainly needed to build the characteristic length L and to carefully look at the results, but, in a first step, fast running tools can be built to select the most sensitive scenarios before starting a more detailed analysis on combustion behaviour. Such tools can be used to implement the proposed criteria in a PSA approach.

6.4 Application of FA and DDT Criteria in CFD Codes*

In the analysis of hydrogen behaviour in severe accidents, a chain of interconnected physical processes has to be modelled in a systematic way to arrive at mechanistic and unambigious results for containment loads. Flame acceleration and DDT processes in a severe accident represent just two possible phenomena out of a large event tree. To clearly define the possible applications and limitations of the criteria described in Chapter 3 (σ- and λ-criteria) it is necessary to first describe the general structure of a complete self-consistent hydrogen analysis.

6.4.1 Methodology for Hydrogen Analysis

The modelling of hydrogen behaviour in severe accidents with CFD (and LP) codes requires information for a series of interconnected steps (Figure 6.4.1-1).

6.4.1.1 Plant design

The starting point of any analysis is, of course, selection of the plant. This apparently trivial point is included explicitly into the general analysis procedure because the plant design has many important implications for later stages of the CFD analysis. For instance, the core size and type of reactor (PWR or BWR) will determine the maximum possible hydrogen source term, the free containment volume will influence hydrogen concentrations, and the distribution of steel and concrete masses, as well as surfaces, will affect the equally important steam concentrations.

The geometrical containment design, moreover, defines the mathematical boundary conditions for the solution of the 3D fluid-flow equations of the CFD model. The generation of a computational 3D grid for a complex reactor containment is a very demanding task, in terms of best-possible geometry representation and judgment about the effects of always necessary geometry simplifications. In fact, the experience in Germany with CFD modelling of three different plant designs has shown that a large part of the total analysis work is concerned with the 3D grid generation and corresponding quality control.

6.4.1.2 Hydrogen mitigation system

For a given plant, the next important question for the hydrogen analysis concerns the mitigation system under consideration. For the components of this mitigation system, verified CFD models must exist to predict their efficiency and effects on hydrogen-relevant parameters in the further progression of the accident. The GASFLOW code has, for example, models for spark igniters, and many Siemens as well as NIS recombiners, which were validated on different test series, many of them performed in the Battelle Model Containment (BMC) [6.7,6.8]. If, for example, spark igniters and catalytic recombiners are choosen for the hydrogen mitigation approach, the number and location of each of these modules must be defined within the grid resolution of the CFD containment model.

* Contributed by Dr. W. Breitung

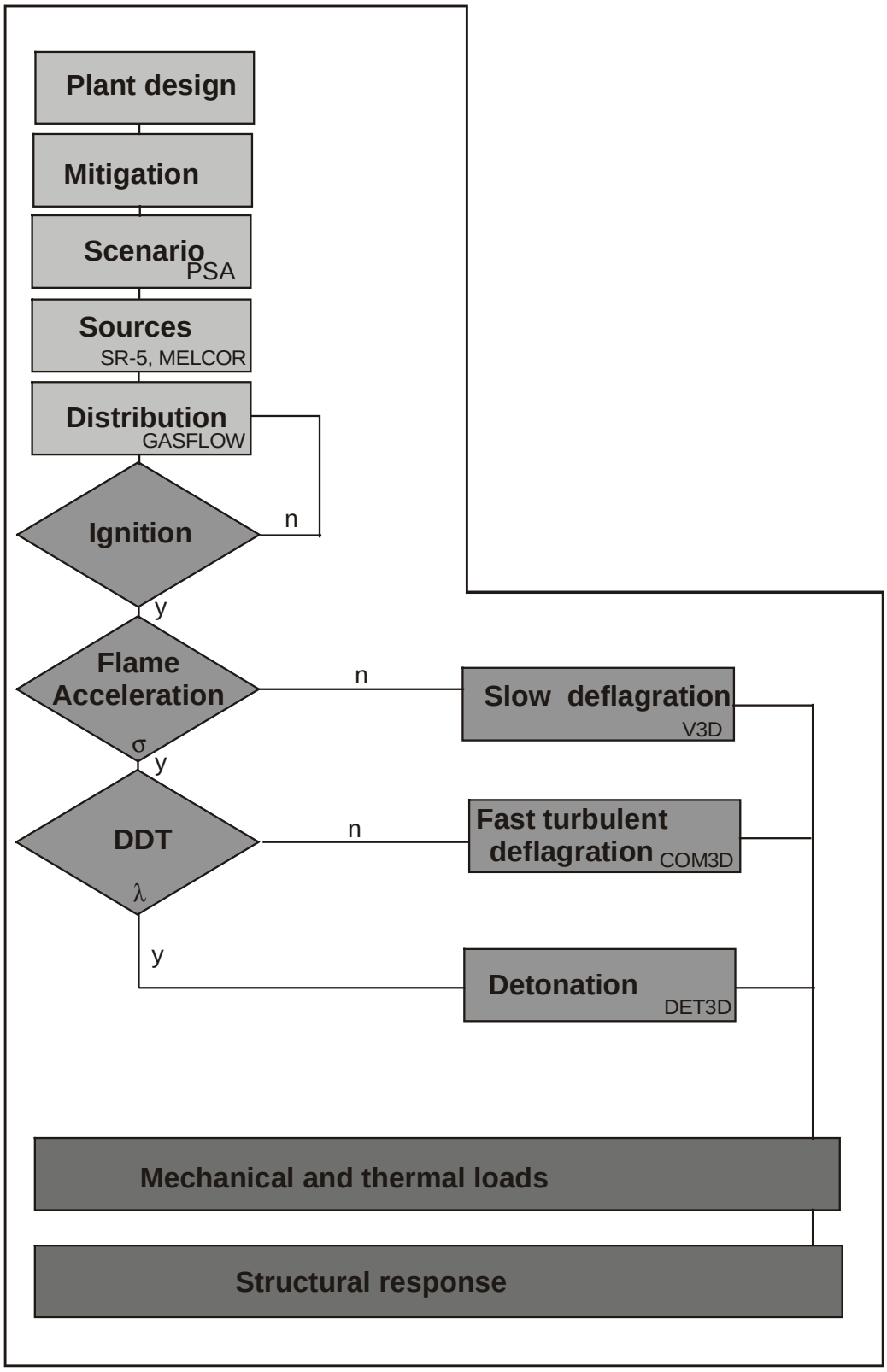

Figure 6.4.1-1 Outline of a complete self-consistent procedure for hydrogen analysis in severe accident research

6.4.1.3 Accident scenario

For a given plant and mitigation system, the next question is what type of severe accidents are physically possible within this installation, and which sequences should be covered in the analysis as representative cases.

Severe accidents require that all safety injection systems fail for an extended period of time (hours). All theoretically possible accident sequences can be grouped into relatively few accident categories, mainly different LOCAs and transients. It is not possible, nor necessary, to analyze all sequences with respect to their hydrogen risk.

In Germany, several criteria were formulated to select from the wide range of severe accidents a subset that covers the whole spectrum of possible requirements for hydrogen mitigation systems. In other words, looking from the perspective of system performance, the question is what are the most serious conditions mitigation systems that could be encountered in core-melt accidents, and which group of selected accidents produces these maximum requirements.

From this point of view, the selected hydrogen scenarios should include the major accident classes (LOCAs and transients), cover detrimental properties of the H_2-steam source (large integral H_2 mass and release rate), and adverse containment conditions (e.g., low steam concentration at the beginning of H_2 release). Each accident will fulfil some of these criteria. Based on these and other considerations, five representative hydrogen scenarios were proposed for PWRs in Germany [6.9]:

1. surge-line LOCA;

2. small-break LOCA, 50 cm^2, without secondary cooldown (heat sink) and including reactor pressure vessel (RPV) failure;

3. station blackout with depressurization of primary circuit and flooding of the core after recovery of the electric grid (no RPV failure).

4. loss of feedwater with primary-system depressurization and

5. steam generator tube rupture with open secondary circuit (bypass scenario).

These five selected hydrogen scenarios generate together a wide spectrum of conceivable adverse conditions for hydrogen control. Most other accident scenarios should be covered by these cases with respect to the hydrogen risk because they are not expected to generate new situations that are more difficult to control. On the other hand, the restriction of the analysis to only one or two hydrogen scenarios will leave questions open about the efficiency of the investigated mitigation approach for severe accidents in general.

6.4.1.4 Hydrogen and steam sources

After definition of the relevant hydrogen scenarios, the next question is what hydrogen and steam-water sources must be expected for these cases. For fully consistent CFD calculations, the mass, momentum, and energy of these species are needed for the whole duration of the accident simulation. In addition, the location of the release must be specified.

In many cases, it will only be possible to derive complete H_2-steam sources by combining parametric code calculations with best estimates for still uncertain hydrogen production processes.

In general, the H_2 and steam mass sources are best predicted for the early in-vessel phase although different code calculations for the same scenario still can vary significantly in the predicted timing of the gas generation. The uncertainties further increase with accident progression because the initial and boundary conditions for the metal oxidation reactions (temperatures, surfaces) as well as the physical phenomena become more and more unknown.

Only parametric models currently exist for the late in-vessel phase, which is dominated by debris and pool behaviour. For prediction of H_2 generation, the time-dependent temperature, Zr, steam, and interface distributions are required.

No applicable predictive models are currently available for hydrogen and steam production from

- oxidation of U-Zr-O melts,
- reflood of an overheated dry core,
- failure of the RPV,
- ex-vessel steam-metal interactions (benign and energetic modes).

The only late process with reasonably verified models is the core-concrete interaction, which also can contribute significant amounts of CO.

Finally, it should not be overlooked that a good database for **steam** release is also important because the fast combustion modes that have the highest potential for containment damage are sensitive not only to the hydrogen but also to the steam concentration.

6.4.1.5 Hydrogen distribution

With known hydrogen and steam sources, the next task is to calculate their transport, distribution, and mixing with the air in the containment. The outcome from this step of the analysis should be temperature, pressure, and composition of the H_2-air-steam atmosphere as function of time and location.

A large number of interconnected physical processes and thermo-physical properties must be modelled with high spatial resolution to obtain gas compositions within precision limits that allow meaningful simulations of hydrogen combustion processes. Reasonable research targets are prediction of hydrogen concentrations within a few absolute percent (e.g., $12 \pm 2\%$ H_2), of steam concentrations within 5 absolute percent (e.g., $12 \pm 5\%$ H_2) and spatial resolutions ≤ 1 m^3 per computational cell. The most important modelling subjects are

- 3D compressible fluid flow,
- convective heat transfer between gas and structure,
- radiative heat transfer (with high steam concentrations and temperatures),
- condensation and vaporization of water,
- heat conduction within structures,
- turbulence modelling and,
- mitigation devices (recombiners, igniters).

One code that has been developed to treat the hydrogen distribution task with 3D CFD methods is GASFLOW [6.7,6.8]; another one is TONUS developed by CEA.

6.4.1.6 Ignition

For typical severe accident sequences in large plants, flammable mixtures will be generally predicted by the distribution analysis for certain time and space regions. To start a combustion process and to generate any potential risk to the containment, an ignition event is necessary. At this stage of the analysis, time and location of the first ignition leading to stable flame propagation must be predicted.

Ignition sources can be classified into random and deliberate (igniters). When igniters are included in the analysis, location and time of the ignition event will be determined by the evolution and expansion of the H_2-air-steam cloud in the containment. With correctly designed igniter systems, ignition will occur shortly after hydrogen release has begun in a region with low hydrogen concentration.

Without deliberate ignition, the location and time of the ignition event is not predictable in a deterministic way. A number of potential ignition sources can exist in a severe accident environment, as, for example, electric equipment, bursting pipes, and core-melt particles. In this case, the consequences of random ignition must be analyzed. An exception that allows a mechanistic calculation would be self-ignition of the hot H_2-steam mixture near the break location.

In any case, an ignition must be either predicted mechanistically (self-ignition or igniters) or it must be postulated with respect to time and location. The inclusion of igniters can be viewed as a possibility to control the ignition event in such a way that it occurs under the apparently most favourable conditions, that is early in the accident before large hydrogen masses could accumulate in the containment. From the point of risk reduction, this approach to mitigate hydrogen by design seems better than an uncontrolled random ignition that may come too late.

The reliable prediction of the ignition event is important because it defines the end of the non-reactive phase of the accident and the beginning of the reactive phase, which can create the potential for containment damage.

6.4.1.7 Flame acceleration

After ignition the flame starts initially as a slow quasi-laminar premixed H_2-air-steam deflagration. It will preferentially propagate along the hydrogen concentration gradient towards the richer or dryer mixtures and into regions with high turbulence generation. This effect and also the self-induced turbulence from the expansion flow of the burned mixture behind the flame can induce a transition from slow laminar to fast turbulent deflagration.

The dominant influencing parameters for FA are the mixture composition, turbulence generation, confinement, and length scale. The σ-criterion, described in Chapter 3, can be used for conservative estimates of the FA potential. If the criterion is not fulfilled, a slow quasi-laminar deflagration must be expected, which should be modelled with an appropriate numerical tool (e.g., V3D at FZK). If the σ-criterion predicts FA, the question arises as to whether the mixture under consideration could also undergo a transition to detonation.

6.4.1.8 Deflagration to detonation transition

For this branching point, the λ-criterion—described in Chapter 3—was developed to check for a certain minimum scale of the reactive cloud relative to its average detonation cell size. If the scale should be insufficient, a fast turbulent combustion must be modelled, for which, for example, the COM3D code was developed at FZK and the TONUS code at CEA. Otherwise, a detonation simulation is appropriate, e.g., with DET3D (FZK) or TONUS (CEA).

The three discussed transition criteria for

- ignition (inert to flammable),
- flame acceleration (slow to fast deflagration), and
- detonation onset (deflagration to detonation),

can be used to select the most probable combustion mode and the corresponding numerical models and codes. These criteria are useful and currently also necessary because the direct numerical simulation of the transition processes themselves is still in its infancy, mainly because of the much smaller length scales that need to be resolved. Mechanistic modelling of the ignition event requires, for example, resolution of the ignition kernel with detailed chemistry treatment; the flame acceleration process would require resolution of the laminar to turbulent transition; and for detonation onset, the resolution of the initial hot spots with strong ignition would be necessary.

It is important to note that the evaluation of the three transition criteria only requires information about the composition and geometrical size of the combustible mixture generated during a severe accident. This information is available from the preceding step of the analysis, namely the 3D distribution analysis. Therefore the 3 criteria can already be evaluated “on-line“ during the distribution calculation to check where and when different risk situations develop during the accident progression, namely

1. occurrence of flammable mixtures,
2. potential for flame acceleration to fast “sonic” flame speeds, and

3. possibility of detonation onset.

The criteria can hence give early indications of the maximum possible mechanical loads to the containment, without actually entering the reactive flow simulation. This offers an easy way to check and optimize the effectiveness of the mitigation measures introduced at the beginning of the analysis. If, for example, the exclusion of local detonations of a given size or energy content is a necessary requirement for the mitigation approach, the mitigation measures should be modified until the λ -criterion is fulfilled accordingly, including a reasonable safety factor to cover uncertainties from other steps in the analysis, e.g., hydrogen release rate or total mass.

In summary, the use of the described criteria offers two important functions for the analysis of hydrogen behaviour:

1. early estimates of the potential combustion regime and corresponding containment loads without the need for combustion calculations, and

2. branching from the distribution calculation into the appropriate tool for simulation of the detailed combustion process and the generated time and space-dependent containment loads.

6.4.1.9 Mechanical and thermal loads

The further flow of the analysis is straightforward. The thermal and mechanical loads of the respective combustion process (slow deflagration, fast deflagration, or detonation) are evaluated from the 3D simulation by storing temperature and pressure histories at different containment locations. Which of these two load categories prevails is mainly determined by the time of first ignition. Early ignition leads to low-pressure amplitudes but high local thermal loads. Late ignition of an accumulated hydrogen-steam-air cloud can result in transient high-pressure loads but negligeable temperature increase in the solid structures. In both cases, the same total combustion energy is released but on largely different time scales (hours versus seconds).

6.4.1.10 Structural response

The calculated loads serve as input for the last step in the analysis, which is to determine the structural response. Thermal loads from standing diffusion flames should not lead to loss of containment integrity by failure of sensitive structural components, as, for example, electrical feedthroughs or seals of hatches. Moreover, equipment needed to terminate the accident should not be disabled directly by a high-temperature environment or indirectly by electric cable damage.

The mechanical loads from fast flames can include pressure waves, impulses, and possibly impacts from combustion-generated missiles. If fast combustion modes cannot be excluded with the chosen mitigation system, the outer containment shell represents the last barrier against radioactive release. A thorough investigation of the local dynamic structural response should then be undertaken to demonstrate containment integrity, which is the ultimate goal of the whole hydrogen analysis.

The investigation of the ultimate containment integrity under severe accident loads is complicated by the fact that a containment building consists of many different components with largely different mechanical and thermal responses. The spectrum ranges from thick concrete structures to elastic gasket in the equipment or personal hatches. Temperatures, pressure, and radiation loads in severe

accidents can also create complex synergy effects on the response of containment components, as was, for example, shown for elastic gasket materials [6.10].

6.4.2 Implementation of Transition Criteria

For a mechanistic 3D CFD analysis of hydrogen behaviour in severe accidents, it is very informative to implement the above-described transition criteria for ignition, flame acceleration, and detonation onset into the code used for simulation of the mixing and transport processes. This section gives a short description of the approach used in the GASFLOW code [6.7,6.8].

The ignition criterion will not be discussed further in detail because the present report concentrates on fast combustion regimes. Currently, the following very simple criteria are evaluated to determine

a. flammability of the mixture: $x_{H2} > 5$ vol % and $x_{O2} > 5$ vol %; and

b. self-ignition: $x_{H2} > 5\%$, $x_{O2} > 5\%$, $T > 800$ K.

Additional work is underway to more precisely quantify the effect of spark energy, length, and duration on the ignition event in H_2-air-steam mixtures of accident-relevant temperatures and pressures.

6.4.2.1 σ-criterion

FZK has recently implemented the σ-criterion into the GASFLOW code to judge the possibility of a slow flame becoming turbulent and accelerating to high speeds. To include nitrogen-enriched mixtures that are generated by the burning process, a four-dimensional table of σ-values was calculated using the STANJAN-code [6.5], with the dependent variables of hydrogen, steam and oxygen volume fractions and temperatures. It is not necessary to vary the initial pressure because σ is independent of p_o. An example of this database is given in Figure 6.4.2.1-1 for H_2-air-steam mixtures at 373 K in the form of a σ-contour plot. The computations were performed using the STANJAN code [6.5]. The physically relevant σ-range is, of course, defined by the flammability limit. At 373 K the critical σ-value is 2.9±0.1 for lean mixtures and 3.75 ± 0.25 for rich mixtures (light gray region). Flame acceleration is possible for larger σ-values (dark gray region).

For evaluation of the acceleration potential the following σ-index is defined in GASFLOW:

$$\sigma_{index} = \frac{\sigma(\overline{x}_{H2}, \overline{x}_{H2O}\, \overline{x}_{O2}, T)}{\sigma_{critical}\,(\overline{x}_{H2}, \overline{x}_{O2}, T)} \qquad (6.1)$$

where the nominator is the expansion ratio of the average mixture in the specified compartment. The x_{H2}, x_{H2O} and x_{O2} are the average hydrogen, steam and oxygen concentrations in the specified compartment, respectively. The denominator is the critical expansion ratio of the average mixture. The idea in this approach is that when the σ-index is <1, flame acceleration is excluded, whereas for $\sigma_{index} > 1$, there is potential for flame acceleration. [6.11]

The expansion ratio of the average mixture in Equation. (6.1) is evaluated by quadratic extrapolation from the computed σ-table. The critical expansion ratio is evaluated by interpolation from the data given in Chapter 3, which are listed in Table 6.4.2.1-1 as used in GASFLOW. Note that $\sigma_{critical}$ is

independent of the steam concentration because the effect of dilutents (in all tests with He, Ar, N_2, H_2O, and CO_2) could be condensed into one common value for $\sigma_{critical}$.

Table 6.4.2.1-1 List of critical σ-values used in the GASFLOW model as function of temperature for lean and rich H_2-air-steam mixtures.

Temperature (K)	$\sigma_{critical}$	
	$x_{H2} < 2\ x_{O2}$	$x_{H2} > 2\ x_{O2}$
300	3.75	3.75
400	2.80	3.75
500	2.25	3.75
650	2.10	3.75

In summary the calculation of the σ-index includes the following steps in the CFD distribution calculation:

1. definition of the control volume, which should as much as possible agree with physical room boundaries; (The definition of a free largely unconfined control zone leads to unphysical and overly conservative results.)

2. calculation of the average mixture composition in this room; (Since the current database for derivation of the σ-criterion is almost exclusively based on homogeneous mixtures, transient time periods with strong mixture gradients in the considered compartment require additional investigations.)

3. calculation of the expansion ratio $\overline{\sigma}$ for the average mixture using a σ (x_{H2}, x_{H2O}, x_{O2}, T)-table to cover H_2-air-steam-N_2 mixtures in general;

4. calculation of the critical expansion ratio $\sigma_{critical}$ according to Table 6.4.2.1-1; and

5. evaluation of $\sigma_{index} = \overline{\sigma} / \sigma_{critical}$.

6.4.2.2 The λ-criterion

The described λ-criterion was implemented into the 3D field code GASFLOW as follows.

Step 1: Characteristic cloud dimension D

The characteristic dimension $D_n(t)$ of the H_2-air-steam cloud in room number n, which evolves from the source location is calculated from

$$D_n(t) = V_n(t)^{⅓} \quad (6.2)$$

$$V_n(t) = \Sigma_i \Delta V_{i,n}(t) \ . \quad (6.3)$$

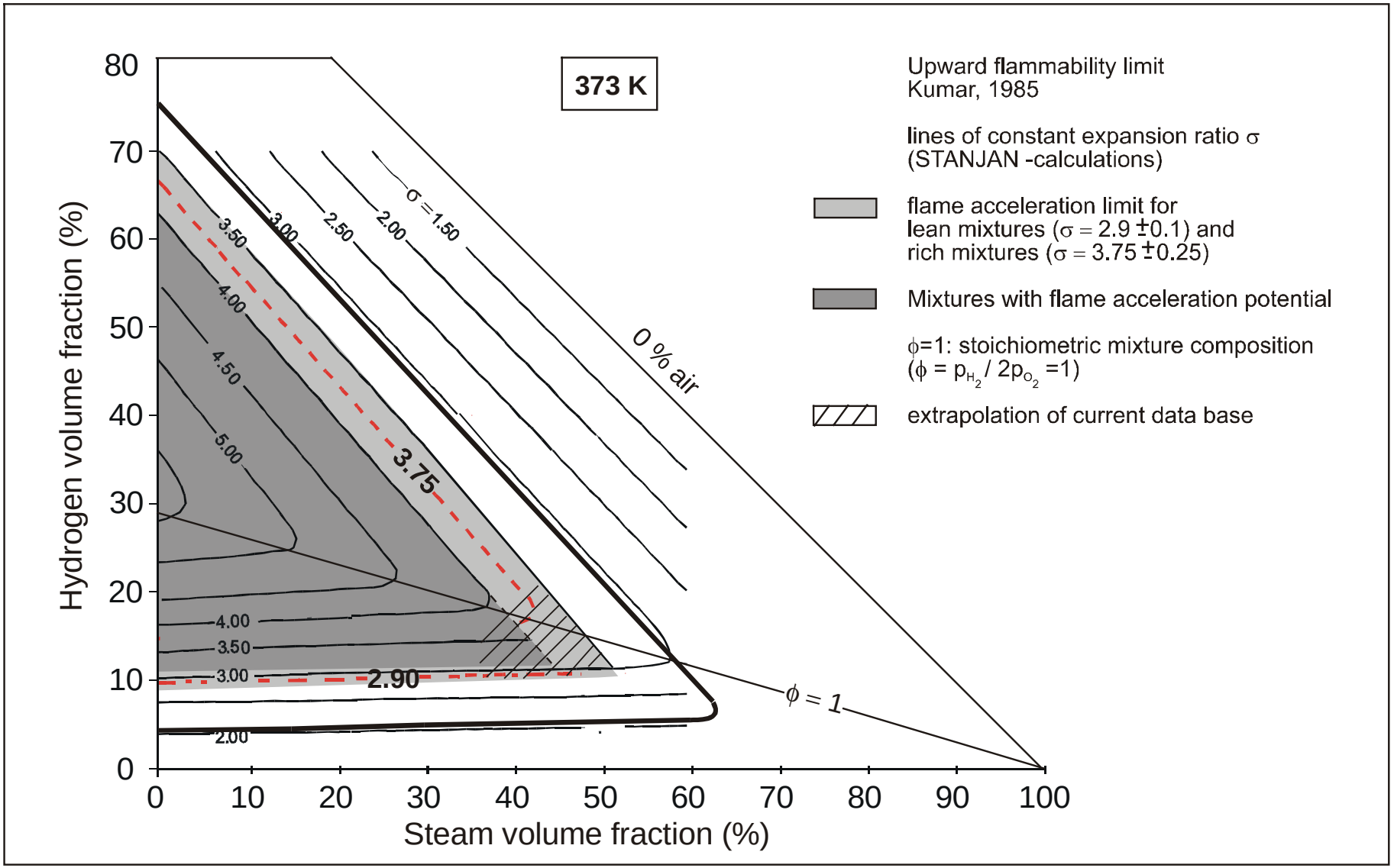

Figure 6.4.2.1-1 Expansion ratio and flame acceleration limits of hydrogen-air-steam mixtures at 373 K. [6.12]

where $\Delta V_{i,n}$ are those computational cells in containment room *n*, which contain a burnable mixture at time *t*. In case of a dry H_2-air mixture, these are the grid cells containing between 4% and 75% H_2, the lower and upper flammability limits, respectively. To identify highly transient hydrogen release phases that can lead to enriched clouds embedded in a large cloud of low hydrogen concentration, the lower integration limit of 4% H_2 can also be raised to 8% and 16% respectively.

Step 2: Average detonation cell width λ

The average composition of the H_2-air-steam cloud in room n at time *t* is

$$\left[\overline{x}_{H2}(t)\right]_n = \left(\Sigma x_{H2,i} \cdot \Delta V_i\right)_n / V_n \qquad (6.4)$$

$$\left[\overline{x}_{H2O}(t)\right]_n = \left(\Sigma x_{H2O,i} \cdot \Delta V_i\right)_n / V_n \qquad (6.5)$$

where x_{H2i}·(t) = hydrogen volume fraction in cell i of the H_2-air-steam cloud in room n, and

x_{H2Oi}(t) = corresponding steam volume fraction.

This average composition is used to calculate the average equivalence ratio ϕ_n of the cloud, which in case of H_2-air-steam mixtures is

$$\phi_n = 2.3866\,\overline{x}_{H2,n} / (1 - \overline{x}_{H2,n} - \overline{x}_{H2O,n}) \ . \qquad (6.6)$$

The average detonation cell width λ_n of the cloud mixture in room n can now be evaluated from measured or calculated data for λ_n (ϕ, x_{H2O}). The average composition and detonation cell size of the cloud is used here as measure for the detonation sensitivity because this evaluation method gave also good agreement with the 7λ-correlation in the RUT tests with dynamic H_2 injection into air.

Step 3: DDT index R

At any given time during the calculation, a DDT index *R* is evaluated for room n according to

$$R_n(t) = \frac{D_n(t)}{7\lambda_n(t)} \ . \qquad (6.7)$$

If this ratio is less than 1, detonation transition is excluded or highly unlikely. If the ratio R_n is larger than 1, DDT cannot be excluded, according to the criterion.

6.4.3 Examples for CFD Application

The described methodology is first illustrated for a single-room geometry and then applied to a full-scale 3D multi-compartment reactor containment.

6.4.3.1 Singl- room geometry

A single room of the BMC was chosen to show the principal use of the λ-criterion for a simple geometry. At the same time, this example is used to demonstrate the applicability of the λ-criterion for selection of a safe igniter position, which prevents a transition to detonation from an deliberate ignition [6.13].

Hydrogen is injected into the closed room of the BMC (Figure. 6.4.3.1-1). The room contains initially dry air at 1 bar pressure and 300 K. The vertical H_2 jet enters the room at the centre of the floor, the H_2 gas being at the same initial conditions (1 bar, 300 K, 21.6 g/s H_2, velocity 1.0 m/s). Two cases will be discussed: a calculation with early ignition ($R < 1$) and a calculation with late ignition ($R > 1$).

6.4.3.1.1 Early ignition

A GASFLOW analysis was performed with a glow plug igniter in the upper corner of the BMC room (Figure 6.4.3.1.1-1). This high location should cause an early ignition because buoyancy forces support the hydrogen transport into this direction.

The cloud dimension grows monotonically with time. At 12 s, the flammable edge of the H_2 air cloud reaches the igniter, which initiates a burn. The flame attaches to the source, reducing the cloud diameter of unburned gas to one or two computational cells. The hydrogen inventory in the room drops rapidly in response the burn. The DDT index *R* initially shows large values when only few cells above the release location are filled with a rich H_2 mixture. *R* then decreases quickly, and it is well below 1 at the time of ignition, so that no DDT potential could have existed. The fluctuations in *R* during the burn are due to the relatively rich but small standing diffusion flame. This diffusion flame does not represent a DDT threat.

6.4.3.1.2 Late ignition

The second calculation involved an igniter at the worst-possible location, namely at the lowest and farthest position form the source (Figure 6.4.3.1.2-1). Hydrogen reaches this point only after the room is completely filled by the H_2-air cloud. At ignition time the cloud dimension *D* is equal to the third root of the room volume [$(41\ m^3)^{1/3} = 3.44$ m]. The calculated DDT index is well above 1. Almost 800 g of hydrogen burns after ignition, about 3 times more than in the early ignition case.

The DDT criterion predicts that in this late ignition case the deflagration could well develop into a local detonation [$R(t_{ign}) \approx 10$]. At the time of ignition, the hydrogen concentration at the ceiling had reached 40%, a highly sensitive H_2-air mixture.

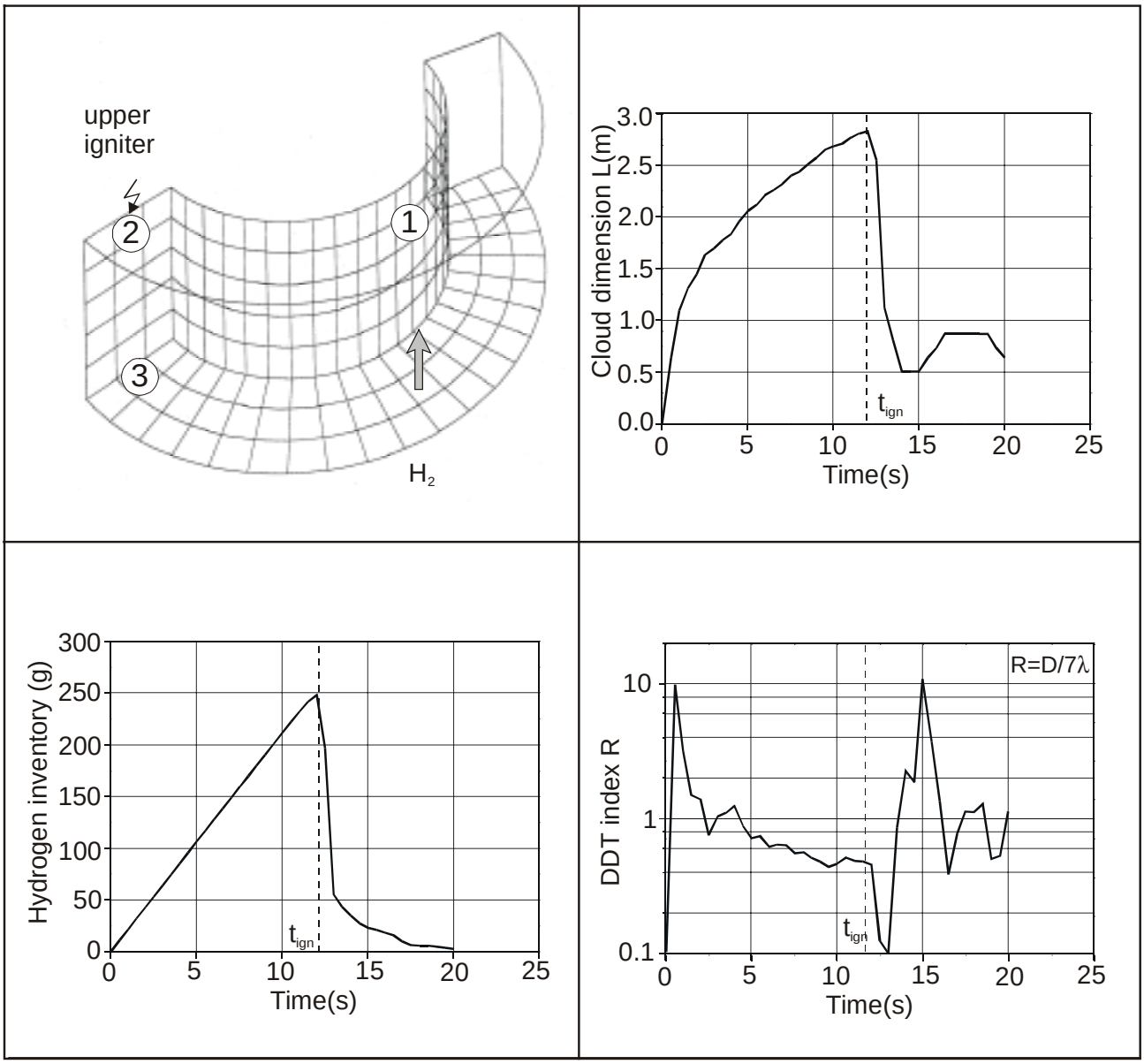

Figure 6.4.3.1-1 Application of λ-criterion to single-room geometry, and results for H_2 injection with igniter in upper corner. Early ignition occurs with DDT index < 1.

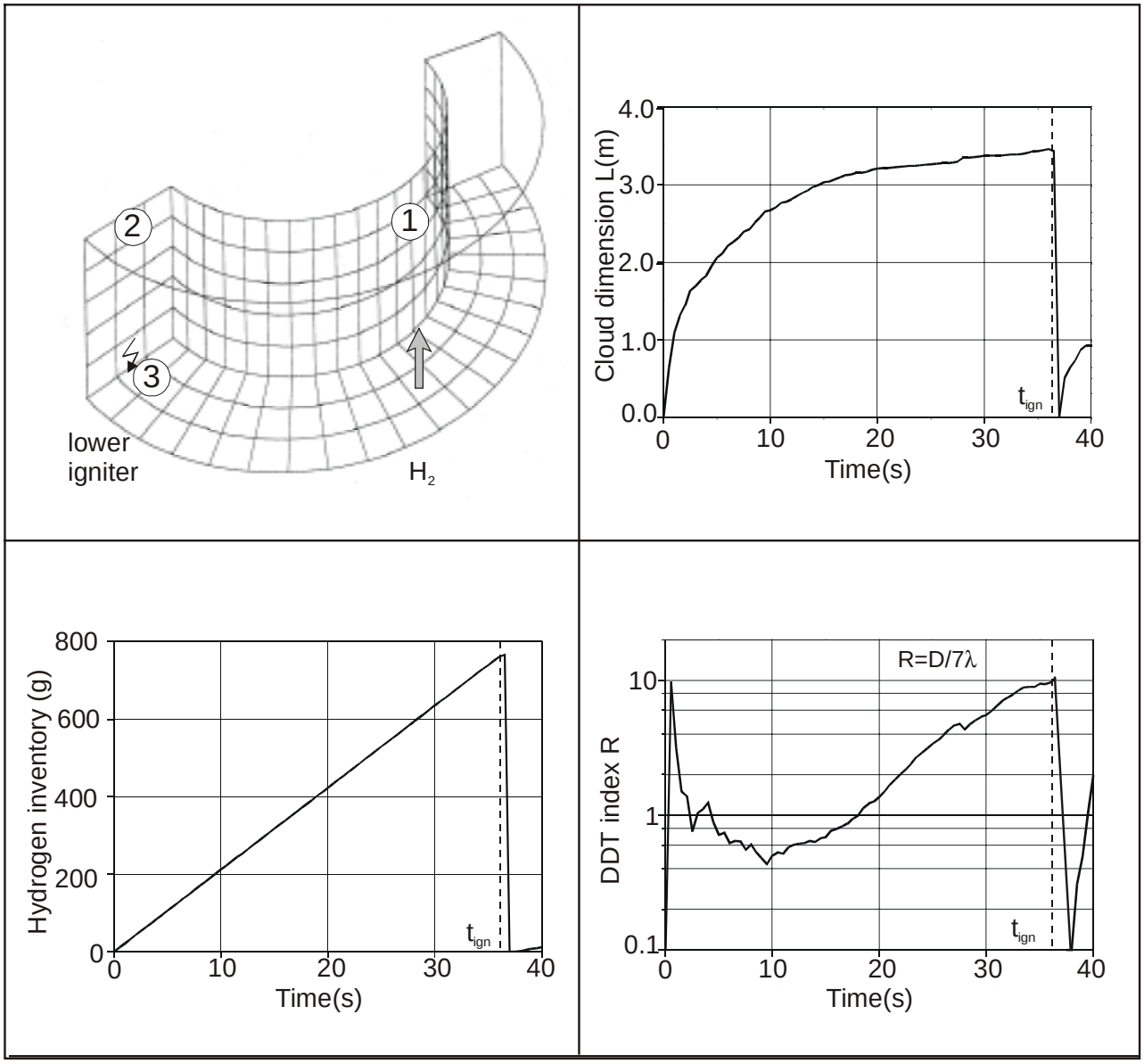

Figure 6.4.3.1.2-1 Application of λ-criterion to single-room geometry and results for H_2 injection with igniter in lower corner. Late ignition occurs with DDT index > 1.

6.4.3.2 Reactor containment

The example given in this section for a full-scale 3D reactor containment application follows the general methodology described in Section 6.4.1 and is summarized in Figure 6.4.3.2-1. The analysis includes the distribution simulation and the evaluation of the σ- and λ-criteria using the GASFLOW code. The calculations were part of a joint study between Siemens and FZK concerning hydrogen mitigation in an EPR design study [6.14].

Plant design: The investigated plant is a PWR with large dry containment, similar to the final design expected for EPR. The free gas volume is about 80 000 m^3. The geometry model contain 139 000 computational cells. A glass model of the 3D containment structure is shown in Figure 6.4.3.2-1.

Mitigation system: For hydrogen mitigation a system of about 50 Siemens recombiners was located in the containment and accordingly modelled in the GASFLOW code. The recombiner model was verified against different test series in the Battelle Model Containment [6.15].

Accident scenario: The investigated accident sequence assumes an unprotected SBLOCA with late reflood of the overheated core. A high reflood rate is assumed so that the burst membrane ruptures, which normally closes the flow path from the primary system to the four internal refuelling water storage tanks' (IRWST) spargers). This event opens four release locations for hydrogen and steam (IRWST release in Figure 6.4.3.2-1), in addition to the break (break release in Figure 6.4.3.2-1).

Hydrogen and steam sources: The hydrogen and steam sources for this long-lasting scenario were calculated with MAAP, using very conservative modelling parameters for this particular study. The results are shown in Figure 6.4.3.2-2 for the time period during which hydrogen was released into the containment. The pre-conditioning phase with pure steam-water release prior to the onset of H_2 generation lasted about 24 500 s. The total hydrogen release amounts to about 700 kg H_2, of which about 160 kg are released through the IRWST. The core reflood is estimated to produce about 400 kg of hydrogen.

Hydrogen distribution: The distribution of the described time-dependent steam and hydrogen sources in the containment were calculated with GASFLOW 2.1. Some results are shown in Figure 6.4.3.2-3 for the break room in which the hydrogen and steam source is located (see Figure 6.4.3.2-1). This room was modelled in GASFLOW by about 2500 computational cells, leading to an average volume per cell of approximately 0.4 m^3. The average steam volume fraction in this room varies between 20% and 40%. The average temperature is about 400 K, whereas the maximum gas temperature reaches more than 1200 K in the immediate vicinity of the break. The average and maximum hydrogen concentrations reach their highest values during the reflood phase (Figure 6.4.3.2-3, top).

Ignition: No ignition by random sources such as, for example, electrical sparks was assumed.

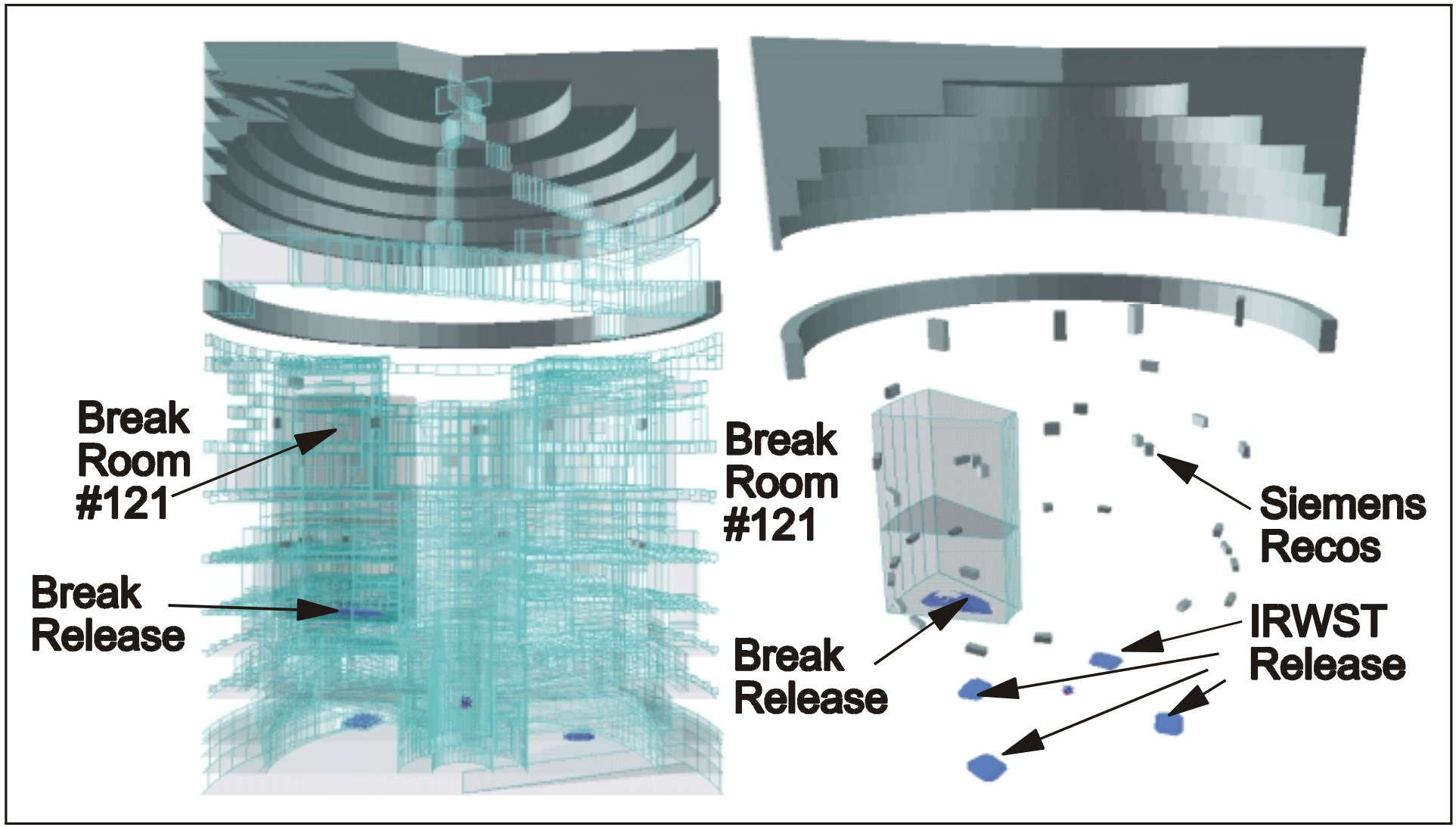

Figure 6.4.3.2-1 GASFLOW geometry model for the EPR design study (80 000 m^3 free gas volume, 139 000 computational cells)

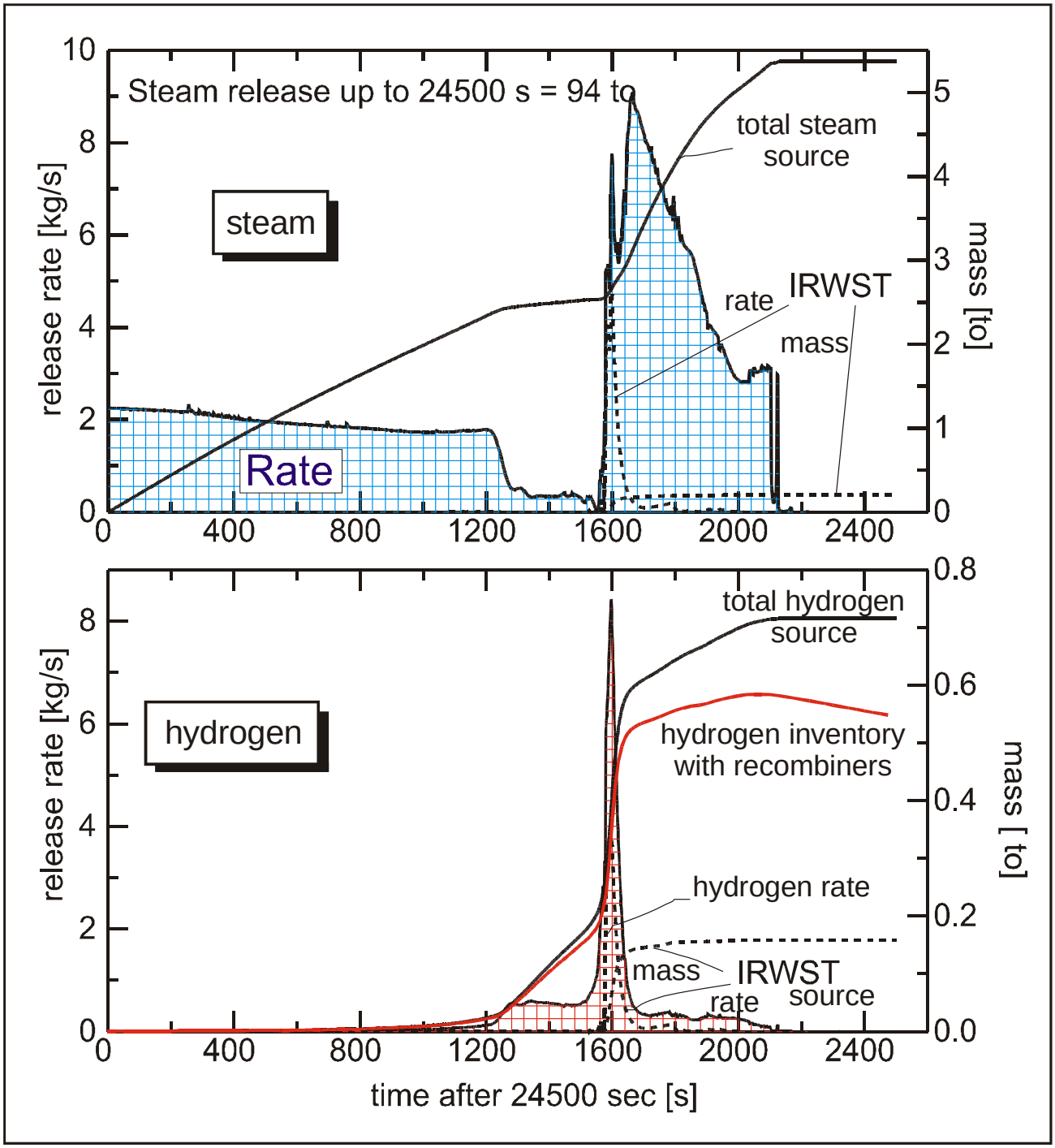

Figure 6.4.3.2-2 Steam and hydrogen sources used for a SBLOCA study of the EPR

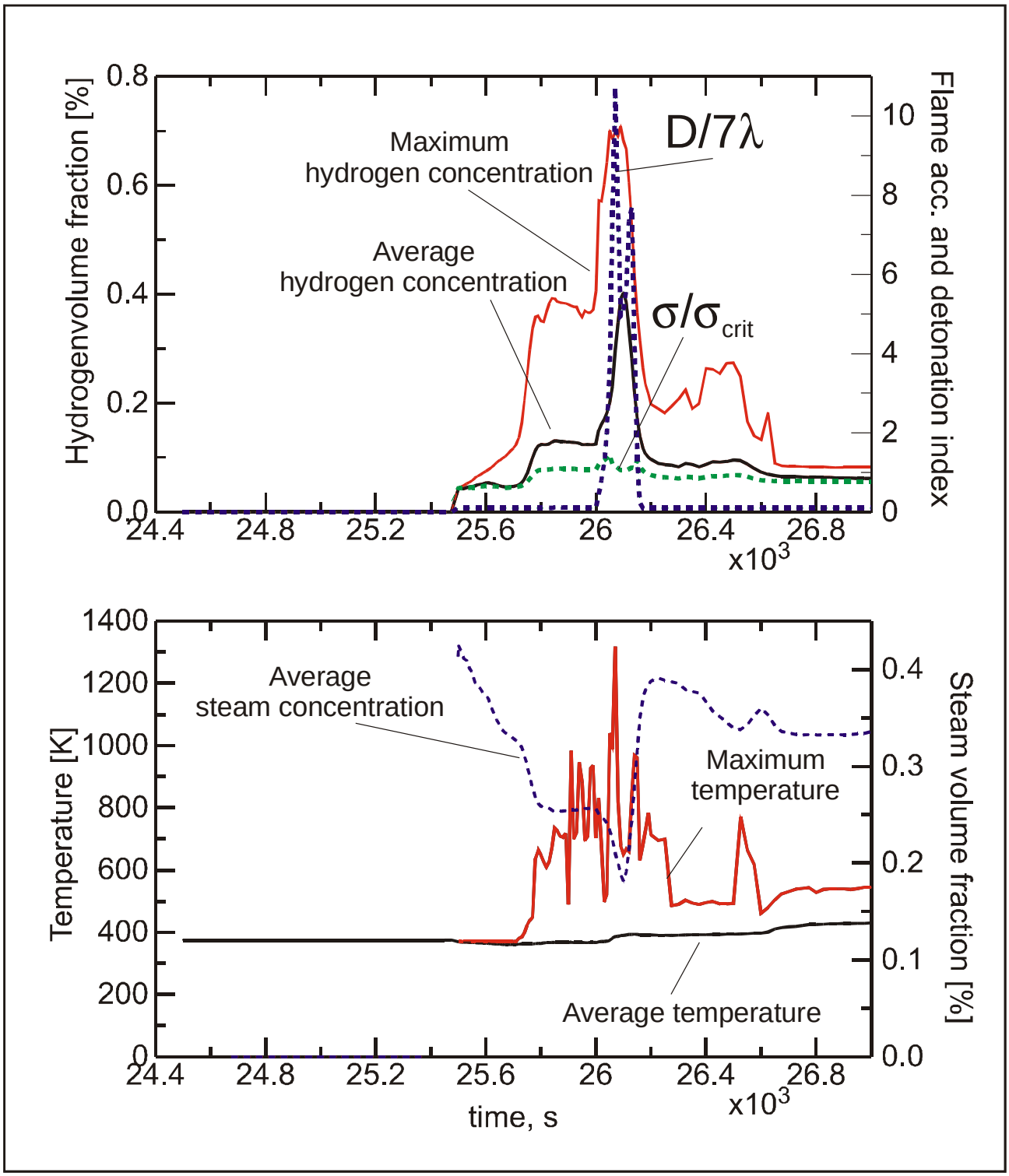

Figure 6.4.3.2-3 GASFLOW results for break room in SBLOCA calculations for EPR design study

Flame acceleration: The flame acceleration index $\sigma/\sigma_{critical}$ was evaluated for different rooms in the containment. The result for the break room is presented in the top graph of Figure 6.4.3.2-3. Values above one are reached shortly before and during the reflood event.

Deflagration-to-detonation transition: The corresponding result for the λ-criterion is also shown in Figure 6.4.3.2-3. DDT possibility exists only during the short reflood phase when, according to the

used MAAP result, a large H_2 release rate combines with a low steam release rate (Figure 6.4.3.2-1). During all other accident phases, D/7λ is much smaller than unity and DDT is excluded.

In summary, the FA and DDT criteria predicted that in the described scenario without ignition, using a quite conservative H_2-steam release function, a potential for complete transition into detonation would only exist for short times during the reflood period.

6.4.4 Example of Containment Section Analysis

This section gives examples for full-scale reactor analysis using the tools described in the previous sections of this report. The first example concerns analysis of a combustion-related topic in a current German power plant, and the second example demonstrates the current abilities in simulating severe accident distribution and combustion processes for the design of a future severe-accident-resistant PWR.
The assessment of combustion loads on equipment (relief valves) to be installed in the annulus section outside the missile protection shield in the containment of BIBLIS-B (KWU design) has been subject to a simulation conducted by the help of the BASSIM code [6.16]. The outer wall of the annulus is the outer-containment steel shell. On the inner side, it is limited by the cylindrical missile protection shield. In a developed manner it has a length of 129.2 m, with a height of about 9.7 m. At intermediate height levels, there are partial subdivisions consisting of catwalks and walls. Larger openings to the dome section of the containment can be found in the area of staircases and four accumulators are placed there. Along the outer-containment steel shell, there is a gap all along the length of the annulus upwards and downwards. Inside the annulus, there are further installations and equipment, which may contribute to flame acceleration. A simplified top view of the annulus and the derived model representation is shown in Figure 6.4.4.-1. The potential locations of the relief valve casings were selected to monitor locations during the runs. A 2.5-dimensional representation of the annulus was chosen in order to save computational resources. This means the grid is two-dimensional with a variable thickness in the third dimension (here the annulus depth) for each cell. Thereby, a locally reduced flow channel width can be modelled. Recently, this approximated approach has been changed in the code to a full 3D representation. In the lower section of Figure 5.2.2.2-5 in Chapter 5 of this report, the developed model of the annulus is depicted. Apart form the pressure accumulators and the staircases, three different zones can be identified. In these zones, six porous regions are modelled to represent different degrees of blockage by obstacles, too small to be explicitly represented in the grid. To account for the increase of turbulence caused by porosity, additional terms are added to the k-ε turbulence model. The resulting grid with 130 x 32 cells is shown in Figure 6.4.4-2. From other experimental validation work it is known that the nodal resolution of the grid chosen is more a minimum to resolve the turbulence formation by obstacles and blockage. Specific investigations on grid convergence, however, have not been done so far. At the outflow areas from the computational domain, independent boundary conditions were set.

According to the German Risk Study, Phase B for a scenario with core-melt in the spatial area of the containment under discussion a hydrogen concentration of 8% combined with 25% of steam (80°C) was identified as what could be expeced. The related system pressure was estimated to be 2.0 bar at the start of combustion. Finally, the existence of a hydrogen mitigation system was assumed and by this the presence of igniters in the annulus. Possible locations are indicated in Figure 6.4.4.-1.
The combustion model in the BASSIM code is the eddy dissipation model of Magnussen combined with the k-ε turbulence model. Prior to this study, the code underwent a number of validation steps with combustion experiments at different test facilities.

Examples of the flame progress through the annulus at different times can be seen in Figure 6.4.4-3. After about 16 s, the flame reaches the right end of the channel. Maximum gas speeds reached are in the range of 45 m/s. The pressure buildup until the end of the simulation is shown in Figure.6.4.4-4. It reaches about 0.5 bar overpressure, compared to the initial value. With 8% of hydrogen, its increase is restricted.

In summary, it can be concluded that, with ignition early taking place, FA and pressure differences over walls remain manageable, although a rather long channel with manifold obstacles is considered.

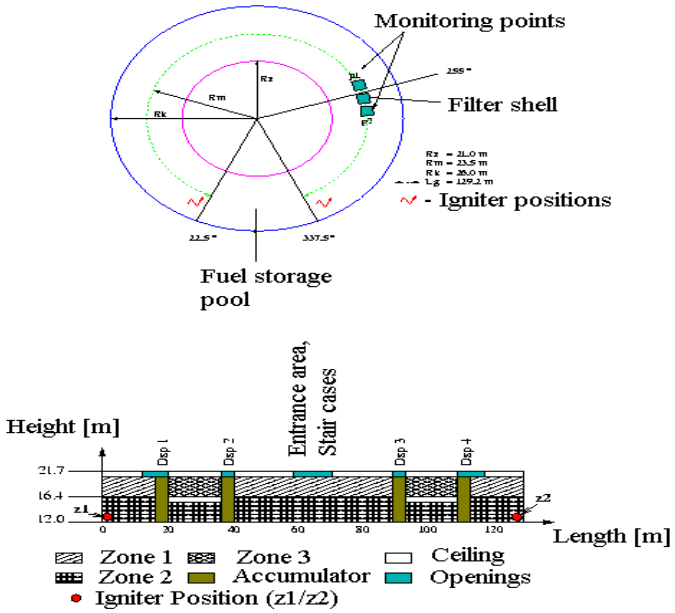

Figure 6.4.4-1 Annulus compartments and derived model

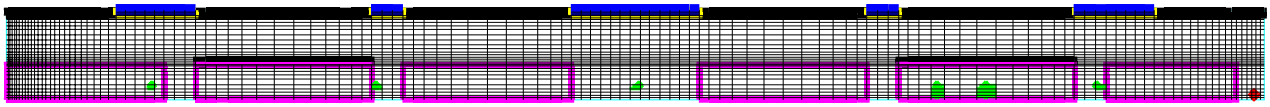

Figure 6.4.4-2 Computational grid

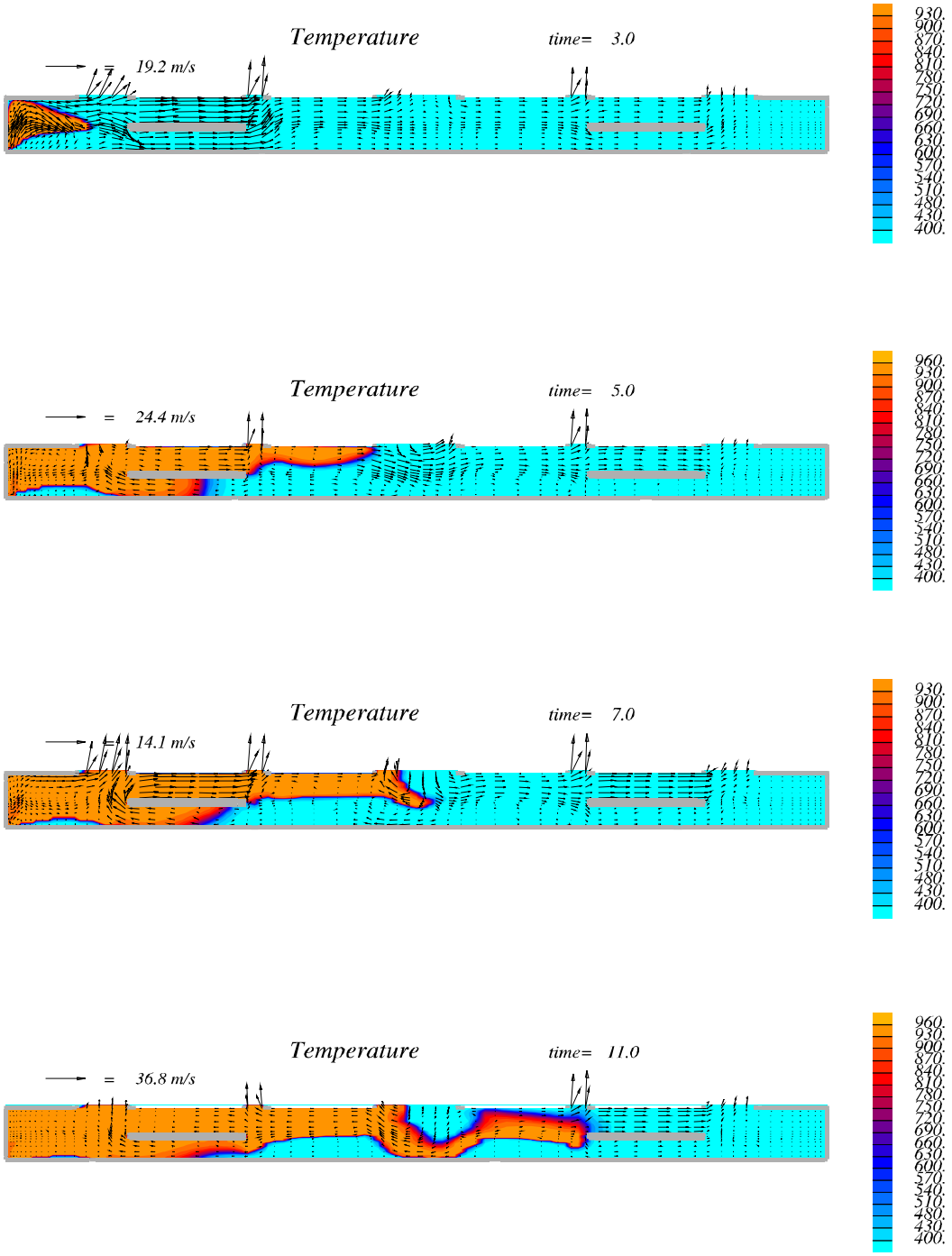

Figure 6.4.4-3 Temperature contours in the annulus at different times of flame progress

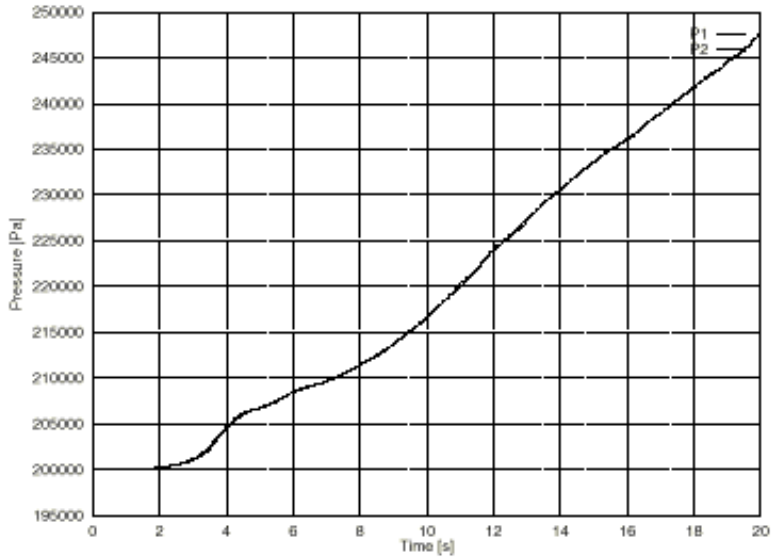

Figure 6.4.4-4 Pressure buildup during the simulation

6.4.5 Applications to Future Plant Analysis

Section 6.4.5 summarizes the calculations of applications that have been done on hydrogen distribution, combustion, and loads for future plant design studies. The central goal of the future plant hydrogen work is to derive hydrogen control systems that fulfil the safety requirements for future LWRs, namely to show that the maximum amount of hydrogen that could be present during a severe accident can be confined without loss of containment integrity. In principle, there are two possibilities for hydrogen management in the future plants. The first one is to increase the strength of the containment design to the maximum possible combustion load. The second, more evolutionary way, is to use an existing containment design and install hydrogen control systems for load reduction, so that the original design load (LOCA) will not be exceeded.

6.4.5.1 Base case

First, a base case analysis without any hydrogen mitigation was performed for a LOOP scenario, to quantify the hydrogen situation in a future plant and to establish a baseline against which the need for and the effectiveness of hydrogen control measures can be compared.

In this dry LOOP scenario with only little steam injection from the IRWST water evaporation, a hydrogen stratification in the containment was predicted, ranging from about 9% to 13% H_2 (Figure 6.4.5.1-1). According to the criterion based on detonation cell size scaling (7λ-rule), a large detonation in the dome could not be excluded. The analysis was made for 90 000m^3 of free containment volume. This base case analysis with a detailed 3D containment model confirmed the development of hydrogen stratification in dry scenarios that were observed in earlier future plant calculations with a coarser computational grid (12 000 cells, [6.17]). The possibility of stratified containment atmospheres, together with the relatively large ratio of Zircaloy mass (core size) to free containment volume in the future plant design, makes additional hydrogen control measures mandatory.

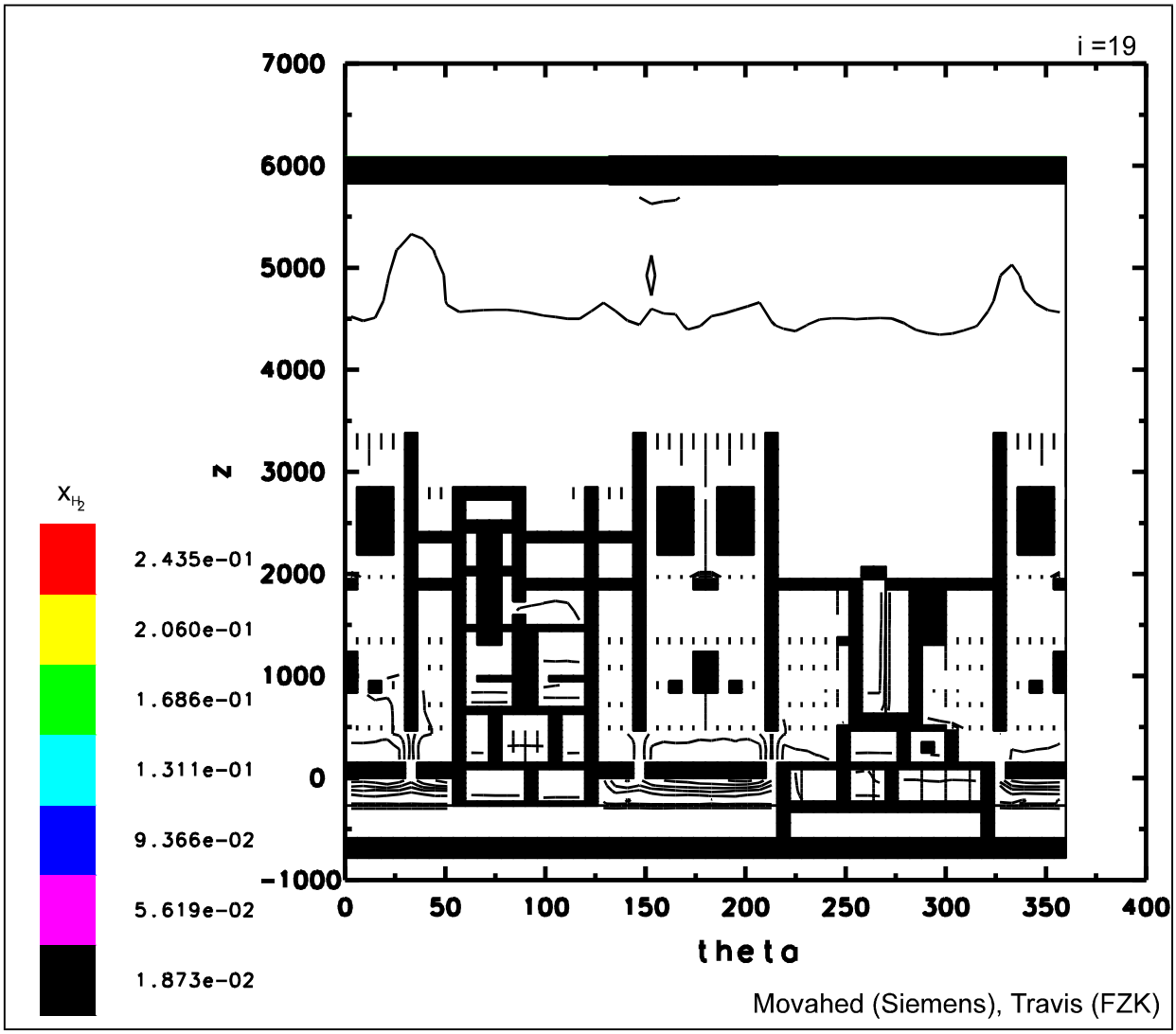

Fig. 6.4.5.1-1 GASFLOW prediction for hydrogen distribution in LOOP scenario, MAAP sources, base case without hydrogen mitigation. The dry release leads to a stratified containment atmosphere (≈ 9% to 13 % H_2).

6.4.5.2 Mitigation with recombiners

6.4.5.2.1 Distribution

The next step in the analysis of hydrogen behaviour was to include 44 catalytic recombiners of the Siemens design. Siemens selected the recombiner positions. The implementation in the GASFLOW model was done jointly by Siemens and FZK. The same hydrogen and steam source was used as before (LOOP scenario, MAAP sources).

The inclusion of this recombiner arrangement led to a decrease of the maximum H_2 inventory in the containment from previously ≈900 kg to about 720 kg hydrogen. This relatively small decrease is due to the fact that the H_2 release during the first heatup of the core is much faster (10 min) than the recombiner removal time (1 to 2 h). The relatively slow-acting recombiners, which remove typically several grams of H_2 per second cannot significantly reduce the high initial release rate in the LOOP scenario (several kilogrames per second). A rapid initial H_2-source occurs in practically all severe accident scenarios because the large chemical heat release of the Zr-steam reaction causes a fast self-accelerating temperature excursion during which initially large surfaces and masses of reaction partners are available.

The investigated 44 recombiners caused a substantial hydrogen reduction on the time scale of hours, but still allowed the accumulation of up to 720 kg of hydrogen in the containment. The next question therefore is what combustion mode and what structural loads after ignition would develop the resulting containment mixture.

6.4.5.2.2 Turbulent combustion

The FA criterion, described in Chapter 3 and Section 5.4, predicts that the mixture present in the upper half of the containment (>11% H_2), would be able to support FA. A COM3D calculation was therefore performed using the stratified H_2 distribution from the GASFLOW calculation as initial conditions (9% to 13% H_2).

The future plant containment model of the COM3D code uses a cubic cartesian grid with 40-cm cell size, a total of 1.1 million computational cells, and about 80 000 m^3 free volume.The turbulent combustion is simulated with the verified extended eddy breakup model described in Section 4.3.3 of the report. The model performed well on different scales (FZK 12-m tube, RUT Facility) and for different H_2-air- steam mixtures. The computation was made on the FZK-INR Cray J-90 using 4 of the 8 vector processors in parallel.

Figure 6.4.5.2.2-1 shows a plot of the H_2 concentration field 0.4 s after ignition on the right-hand side of the containment. The results are quite surprising and are non-trivial. The highest flame speeds (150 m/s) do not occur in regions of highest H_2 concentration, e.g., the dome, but rather in regions with both sufficient hydrogen concentration and turbulence generation, which is below the operating deck, and along the staircases. The highest loads to the outer containment wall (≤8.5 bar) develop on the containment side opposite to the ignition point because two propagating flame fronts meet here, leading to pressure wave superposition (top part of Figure 6.4.5.2.2-2). The right wall near the ignition point is loaded quite uniformly with pressures up to about 4 bar (bottom part of Figure 6.4.5.2.2.-2). Because this pressure rise time is much longer than the typical containment wall period, this represents a quasi-static load to the structure.

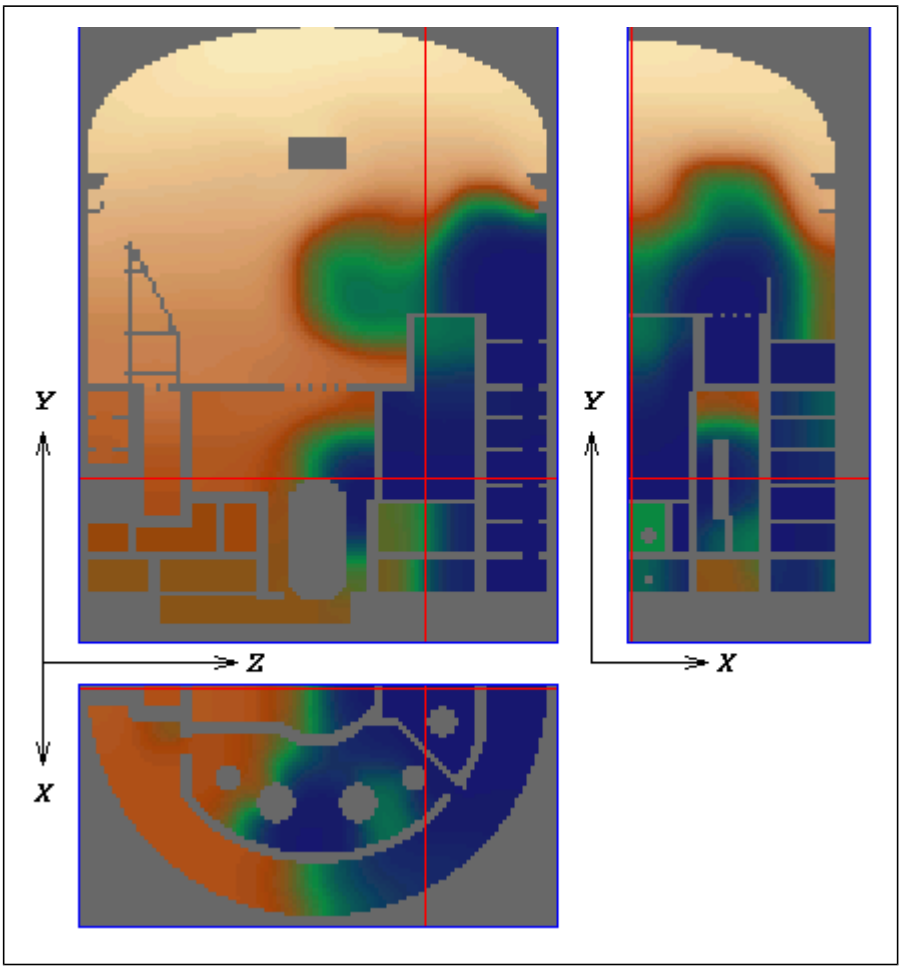

Figure 6.4.5.2.2-1 Simulation of turbulent combustion in the future plant with the COM3D code, 1.1 million computational cells, parallel computation on the FZK-INR Cray J90. The highest flame velocities (150 m/s) develop in regions where both sufficient hydrogen concentration and turbulence generation exist. Initial conditions from GASFLOW calculation, LOOP scenario, 44 recombiners.

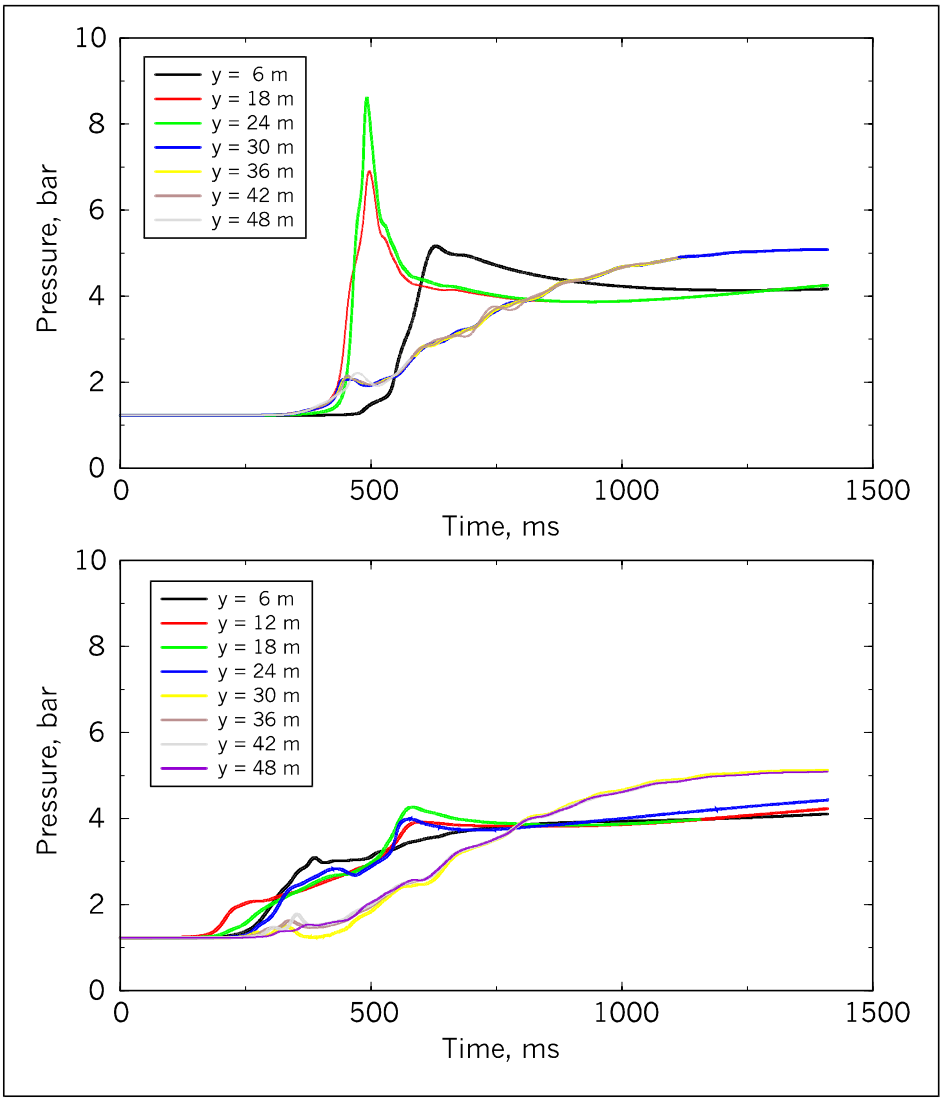

Figure 6.4.5.2.2-2 Containment loads from fast turbulent combustion in future plant, 3D COM3D calculation, initial gas distribution from GASFLOW, LOOP scenario, 44 recombiners installed. Top: pressure on the left containment wall, opposite from ignition point. Bottom: pressures on right containment wall near ignition point.

The characteristic loading times of the left and right containment wall are quite different, about 50 ms and 300 ms, respectively. When compared to the typical natural response times T_{cont} of a dry PWR concrete containment [6.18], the first case represents a dynamic load, ($T_{load}/T_{cont} << 1$), and the second case a load regime that is in the transition from dynamic to quasi-static ($T_{load} / T_{cont} \approx 1$). In the first domain, the deformation is proportional to the wave impulse, whereas in the quasi-static domain it is proportional to the peak pressure reached.

6.4.5.2.2 Local detonation

Application of the previously outlined DDT criterion to the calculated hydrogen distribution leads to the result that the mixture in the dome is sufficiently sensitive and large enough to support a detonation, provided a local FA would take place. The loads from such an event were estimated by a calculation using the detonation code DET3D, developed at FZK (Figure 6.4.5.2.3-1). The same computational grid as in the COM3D calculation was used. The origin of the detonation was assumed near the crane support on the left-hand side of the building where some turbulence-generating structures are located. This scenario should result in an upper limit for fast local combustion loads, which could be possible with the hydrogen inventory in the containment under the present conditions (LOOP, MAAP sources, GASFLOW distribution, 44 recombiners). A linear H_2 gradient from 7% to 13% was assumed, leading to a total H_2 mass of 690 kg in the containment. The initial temperature was 320 K, and the initial pressure 1.23 bar. Figure 6.4.5.2.3-2 shows the predicted pressure loads at different points along the upper edge of the containment cylinder (1 to 7). Ignition is initiated at point 1. In points 2, 3, and 4 basically side-on pressures are generated, whereas in points 5, 6, and 7 higher reflected pressures appear. Because of the short loading times of typically 10 ms, these loads clearly fall into the impulsive regime, where the building deformation is proportional to the wave impulse. The calculated impulses in the detonation wave range from about 5 to 20 kPa.

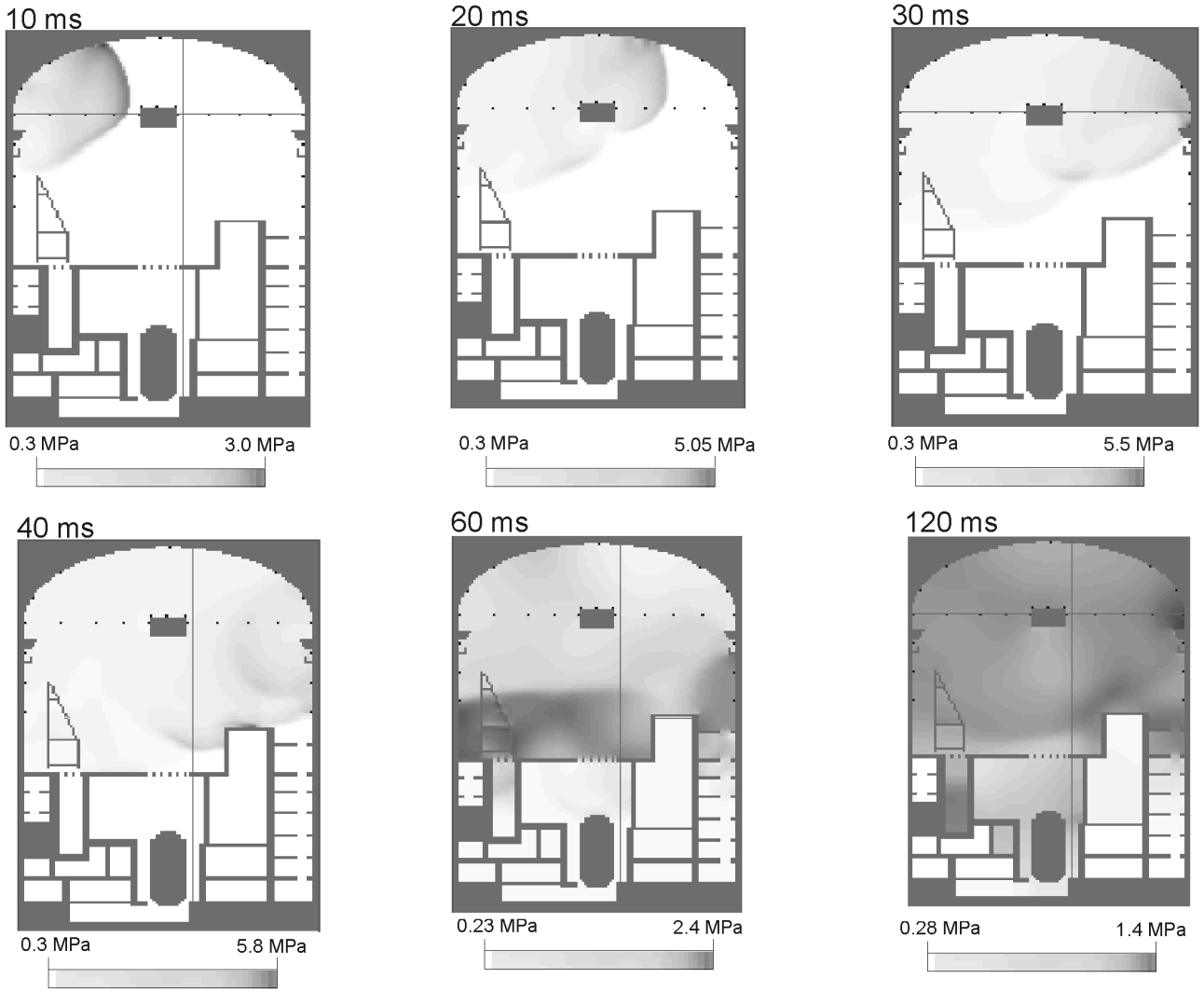

Figure 6.4.5.2.3-1 Simulation of a local detonation in the containment dome

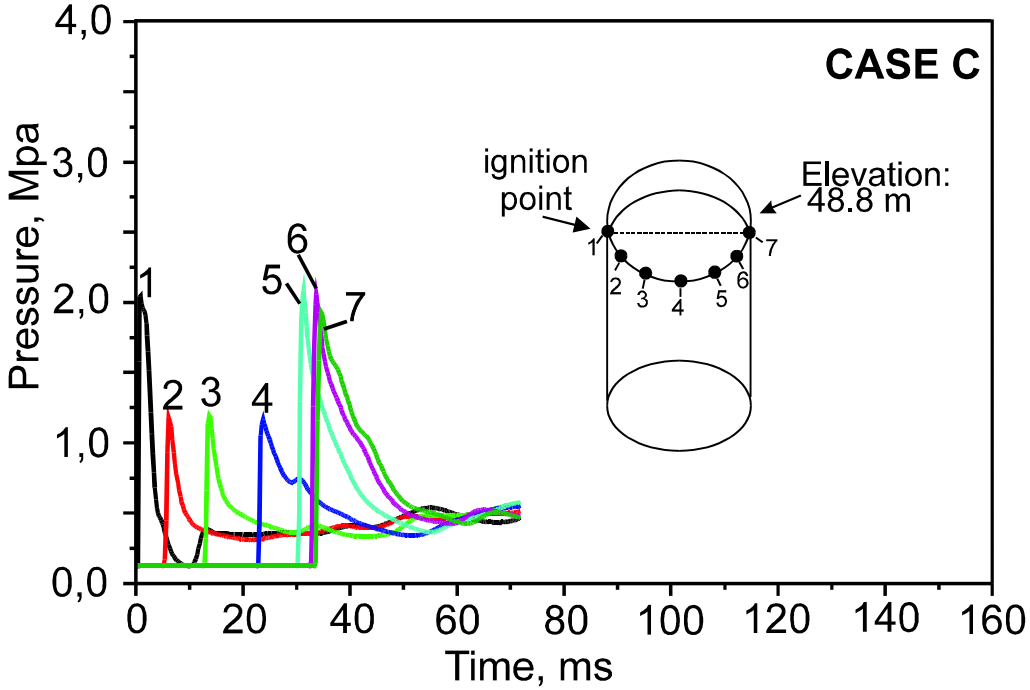

Figure 6.4.5.2.3.-2 Calculated pressures from a local detonation in the containment dome. Total H_2 inventory in the building 690 kg H_2, vertical H_2 gradient from 7% to 13% H_2, initial pressure 1.23 bar, initial temperature 47°C, LOOP scenario with 44 recombiners .

6.4.5.2.4 Results

The described calculations have shown that mitigation with recombiners alone still allows accumulation of up to roughly 700 kg H_2 in the containment and that combustion of this hydrogen mass could lead to significant dynamic loads. Although these loads may not endanger the containment integrity in the undisturbed areas, they would certainly require extensive analysis of containment integrity in regions around penetrations. Moreover, these dynamic loads could have severe consequences for safety systems that are needed for further management of an accident. Especially vulnerable are the structurally weak recombiner boxes and the spray system.

A general conclusion from these investigations is that early deliberate ignition in severe accidents, e.g., by igniters, appears necessary for further reduction of the maximum possible hydrogen inventory and of the corresponding pressure loads. Recombiner systems alone will not allow one to fulfil the new safety recommendations for future plants at least for dry LOOP scenarios. Therefore, an analysis with recombiners and igniters was performed.

6.4.5.3 Mitigation with recombiners and igniters

In addition to the 44 recombiners, one igniter was installed at each of the four IRWST exits from which the hydrogen-steam mixture would emerge in dry scenarios. Again, the MAAP sources for the LOOP scenario with reflood were used as input to the GASFLOW code.

In the simulation, the first ignition occurred at a hydrogen inventory of 110 kg in the building. Thereafter a continuous burn was predicted, with one large standing flame at each IRWST exit (Figure 6.4.5.3-1). The evaluation of the 7λ-criterion, as it is implemented in GASFLOW, showed that at no time was there a possibility of a DDT occurring and that a safe implementation of igniters is possible for the LOOP scenario. The early ignition, with most of the hydrogen still in the IRWST as a non-flammable mixture, reduced the maximum combustion pressure effectively to insignificant values.

The use of igniters basically transforms the previously large containment pressure load to a thermal load. The combustion energy is not released in a short event (seconds), but rather over a long time period (several thousand seconds). The thermal power of the diffusion flames can be quite high (1kg H_2/s ≡ 120 MW). Experimental investigations at the Russian Academy of Sciences on the stability limits of H_2-air-steam diffusion flames, [6.19] have shown that the flame length will be in the range of 20 to 200 times the fuel gas exit diameter, depending on the Froude number and gas competitions. The flame length is governed by the exit velocity of the fuel gas (plume or jet).

Because of the potentially large thermal power and geometrical extension, the thermal effects of standing diffusion flames should be investigated in future work. The results can then be used to avoid thermal overloads to safety systems (igniters, recombiners, spray, liner) by design modifications, if necessary .

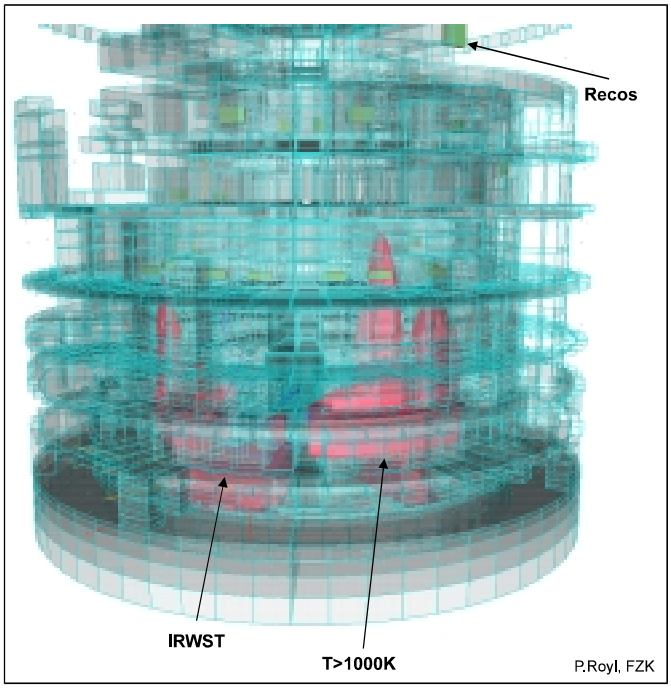

Figure 6.4.5.3-1: GASFLOW analysis of LOOP sequences with 44 recombiners and 4 igniters at the IRWST exits. Low hydrogen inventories, low-pressure loads, and standing flames are predicted.

6.4.5.3 Conclusions

Theoretical tools for the analysis of distribution and combustion process in severe accidents were used to investigate the effectiveness of different options for future plant hydrogen mitigation systems. The problems analyzed in Sections 6.4.3.2 and 6,4.5 for example., lead to different outcomes. In the first case, only a short time window for fast deflagration was detected from the criteria. In the second case, a long-term combustion potential was predicted, and the analysis was conducted through the possible chain of combustion regimes up to detonation propagation. The goal of future reactor containment analyses is to fulfil new safety requirements for future reactors, which require control of the maximum amount of hydrogen that can accumulate in the containment building during a low-pressure scenario. Although a mitigation system consisting only of recombiners would be attractive for acceptance and cost reasons, the magnitude of the still-possible combustion loads makes the installation of additional deliberate ignition sources highly desirable. The calculations, done so far, have shown that igniters can be safely positioned and that they reduce the pressure loads very effectively. The described analysis tools allow us to exam relative merits of different mitigation schemes.

6.5 REFERENCES

[6.1] S.B. Dorofeev, A.S. Kochucko, A.A. Efimenko and B.B. Chaivanov Evaluation of Hydrogen Explosion Hazard, Nuclear Engineering and Design, Vol. 148, 1994 305-316.

[6.2] M.P. Sherman, S.R. Tieszen and W.H. Benedick, The Effect of Obstacles and Transvers Venting on Flame Acceleration and Transition to Detonation for Hydrogen-Air Mixtures at Large Scale, NUREG CR-5275, FLAME Facility.

[6.3] R. Klein et al. (to be published) Contract FI4S-CT-96-0026, Models and Criteria for Prediction of DDT in Hydrogen/Air/Steam Systems under Severe Accident Conditions.

[6.4] *AE,* W. Klein-Hessling, S. Arndt, M. Heitsch and B. Huttermann, GRS internal Report GRS-A-2308, *RALOC* mod4.0 cycl.

[6.5] W.C. Reynolds, The Element Potential Method for Chemical Equilibrium Analysis : Implementation in the Interactive Program *STANJAN,* Dept of Mechanical Engineering Stanford Universtiy, Palo Alto, CA, 1986.

[6.6] S. Dorofeev et al, Effect of Scale and Mixture Properties on Behaviour of Turbulent Flames in Obstructed Areas, .IAE-6127/3 or FZKA-6268, 1999.

[6.7] J.R. Travis, P. Royl, R. Redlinger, G.A. Necker, J.W. Spore, K.L. Lam, T.L. Wilson, B.D. Nichols and C. Müller, "GASFLOW-II: A Three-Dimensional Finite-Volume Fluid-Dynamics Code for Calculating the Transport, Mixing, and Combustion of Flammable Gases and Aerosols in Geometrically Complex Domains, Vol.1, Theory and Computational Model, Reports FZKA-5994, LA-13357-MS, 1998.

[6.8] J.R. Travis, P. Royl, R. Redlinger, G.A. Necker, J.W. Spore, K.L. Lam, T.L. Wilson, B.D. Nichols and C. Müller, "GASFLOW-II: A Three-Dimensional Finite-Volume Fluid-Dynamics Code for Calculating the Transport, Mixing, and Combustion of Flammable Gases and Aerosols in Geometrically Complex Domains, Vol. 2, User's Manual, Reports FZKA-5994, LA-13357-MS, 1998.

[6.9] J. Rohde and W. Breitung, Selection of Representative Accident Sequences for Design and Evaluation of H_2-control Measures in PWR-containments, 141st Session of RSK Light Water Reactor Committee, January 30, 1997.

[6.10] P. Vanini, P. Becue, A. Orden Martinez, G. Forasassi and E. Pinno, Benchmark on Containment Penetration Sealing Areas Behaviour, FISA-97 Symposium on EU Research on Severe Accidents, Luxembourg, Nov. 17-19, 1997, 303.

[6.11] W. Breitung and S.B. Dorofeev, Criteria for Deflagration-to-Detonation Transition (DDT) in Nuclear Containment Analysis, SMiRT-15 Post-Conference Seminar on Containment of Nuclear Reactors, Seoul, Korea, August 23-24, 1999.

[6.12] R.K. Kumar, Flammability Limits of Hydrogen-Oxigen-Diluent Mixtures, Journal of Fire Siciences, Vol.3, 1985.

[6.13] W. Breitung, S.B. Dorofeev and J.R. Travis, A Mechanistic Approach to Safe Ignitor

Implementation for Hydrogen Mitigation, Proc. of the OECD/NEA/CSNI Workshop on the Implementation of Hydrogen Mitigation Techniques, Winnipeg, Manitoba, May 13-15, 1996, AECL Report, AECL-11762; CSNI Report, NEA/CSNI/R(96)8; March 1997, 199-218.

[6.14] M. Movahed, H. Petzold, J.R. Travis, P. Royl and G. Necker, private communication, July 1999.

[6.15] P. Royl, W. Breitung, J.R. Travis, H. Wilkening and L. Seyffarth, "Simulation of Hydrogen Transport with Mitigation Using the 3D Field Code GASFLOW", 2nd Int. Conf. on Advanced Reactor Safety, Orlando, FL, USA, June 1-4, 1997.

[6.16] K., Fischer, A. Kneer and A.K., Rastogi, Berechnung von, H_2- Deflagrationslasten auf Entlastungsfiltergehäuse im SB-Ringraum [Calculation of H_2 Deflagration Loads to the Vent Filter Casing in the Annular Compartment of a Containment] , Final report BF-V68.391, Eschborn, 1997.

[6.17] R. Hüper (Ed), Projekt Nukleare Sicherheitsforschung, Jahresbericht 1995, [Project of Nuclear Safety Research, Yearly Report 1995]; Report FZKA 5780, August 1996, 14.

[6.18] E.Studer and M. Petit, Use of RUT Large Scale Combustion Test Results for Reactor Applications", SMIRT-14, Lyon, France, August 17-22, 1997.

[6.19] B.E. Gelfand, S.P. Medvedev and B.E. Popov, Flame Stabilization and Flammability Limits of H_2+air+steam (fog) Mixtures, Final report to FZK, contract 15/20089955/INR, December 1998

7. SUMMARY AND ISSUES [*]

7.1 Summary

This report concerns the key issue of hydrogen combustion behaviour that may occur as a result of severe accidents in NPPs. Chapter 1 gives an overview of the hydrogen combustion issue in relation to NPP safety. Mechanical (pressure) and thermal loads from hydrogen combustion are one mechanism that can result in the failure of the outermost containment structure of an NPP. The estimation of these loads and the evaluation of the potential hazards associated with various accident scenarios have been the subject of extensive investigation over the last two decades. There are many issues, but the one that is most difficult to evaluate is to determine what type of combustion will occur: slow flames, fast flames, or detonations.

Because of the non-linear feedback between fluid motion and flame propagation, determination of the boundaries separating various flame regimes is not just a matter of conducting a few experiments on selected mixtures. Not only is the mixture composition important, but experimentation has demonstrated that initial conditions, geometrical configuration, and—most importantly—the physical size or scale of the apparatus is crucial in determining the outcome of a combustion experiment. The most difficult behaviour to predict, and one of the most significant for evaluating potential hazards, is the occurrence of detonation as the result of the FA processes. As described in Chapter 2, the basic elements of FA and DDT have been understood for many years. What has been missing up until now are quantitative predictions of the criteria for FA and transition-to-detonation.

This report describes the significant advances in the understanding of FA and DDT that have been made in the last decade (1990-1999). Focused programs of experimental research—described in Chapters 3, 5, Appendices A, B, C and D, and also numerical simulation (Chapters 4 and 5)—have enabled the identification of criteria for boundaries of fast flame and detonation regimes in hydrogen-air-steam mixtures of interest to reactor safety. These criteria enable a more refined evaluation of explosion regimes than was previously possible for severe accidents in NPPs (see Chapter 6).

The significant factors in improving our understanding of FA and DDT are

1. systematic large-scale experimentation on FA and DDT using hydrogen-air-steam mixtures;

2. measurement of hydrogen-air-steam mixture properties such as detonation cell width and flame speed at elevated temperatures (100°C to 377°C) and pressures (up to 3 bar);

3. using fundamental models of flames and detonations to identify relevant non-dimensional parameters that were used to correlate experimental data;

4. multi-dimensional (3D) field-equation modelling of species transport, flame, and detonation propagation; and

5. spatially resolved visualization of chemical species during transient flame propagation.

However, it is important to note that despite these advances in our understanding of FA and DDT, our knowledge of FA and DDT is largely empirical. The current state of the art in computation is such that even with research tools, numerical simulation is unable to provide a truly predictive capability

[*] Professor Joseph E. Shepherd is the lead author of Chapter 7.

for DDT. What we are able to do is to provide a framework of ideas that can be used with existing engineering simulations to screen accident scenarios for situations in which FA and DDT may be possible. This framework is limited in the sense that many situations arise in which we cannot rule out the possibility of FA and DDT, but we have no means to predict whether these will actually occur. If the criteria are not satisfied, then FA and DDT are extremely unlikely in those cases, but exceptions are always possible in marginal situations.

7.1.1 Framework for Evaluating FA and DDT

First, it is important to note that only empirical necessary conditions for FA and DDT can be supplied at the present time. This limitation is due to the complexity of the processes involved, the limited database of experimental results, the lack of a theoretical foundation, and the inability to run end-to-end numerical simulations from first principles. These conditions have been culled from experiments conducted to date and are the subject of ongoing research.

1. Detonations can only be created indirectly by the processes of low-speed flame ignition, FA, and transition-to-detonation. The "direct initiation" pathways are highly unlikely because of the large amount of concentrated energy, which is required for direct initiation. Therefore, it is anticipated that in all but the most exceptional cases, FA is a prerequisite condition for DDT to occur.

2. In order for FA to occur, a sufficiently large expansion ratio $\sigma = \rho_u/\rho_b$ must exist between the burned and unburned gas. A critical magnitude can be computed based only on the properties of the mixture within the containment. There are two cases, one for lean and one for rich hydrogen mixtures. Chapter 3 discusses the experimental evidence and boundaries for these cases in detail, and Figure 7.1.1-1 plots the values of the expansion ratio for one set of thermodynamic conditions.

3. Even if the expansion ratio is sufficiently large, the flame must accelerate to sufficiently high velocities—approximately equal to the speed of sound in the burned gas—before the conditions for detonation initiation can be reached. This means that flame propagation through obstructions, channels, or interconnected rooms must occur in order to produce the fluid motions required for flame folding and stretching.

4. Once the necessary conditions for detonation onset are set up, then detonation may only occur if the physical size of the containment compartment or region is sufficiently large compared with a length that characterizes the reactivity of the mixture. The usual choice of the reactivity length scale is the detonation cell size λ. Measurements of the detonation cell width (Appendix D, Tables D.1-1 and -2) and correlation functions (Figure 7.1.1-2) are available for estimating cell size as a function of mixture composition and thermodynamic conditions.

5. Characteristic Size Evaluation

   Results of numerous FA and DDT experiments (described in Chapter 3) have demonstrated that the physical dimension, L, of the compartment or experiment has to be greater than some multiple of the cell width in order for DDT to be possible. These lead to the necessary criteria for DDT

$$L \geq \alpha\lambda$$

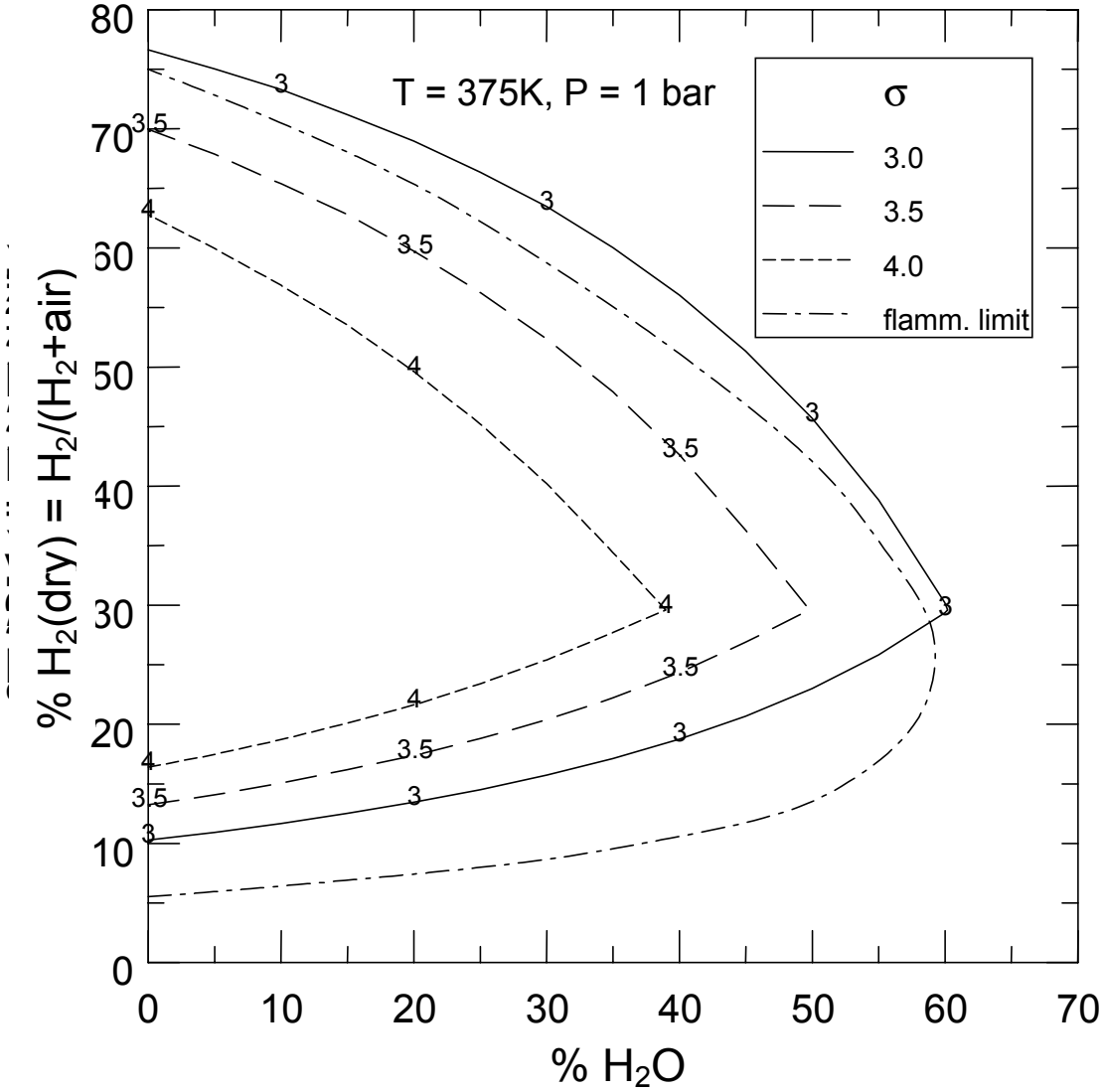

Figure 7.1.1-1 Expansion ratio σ as a function of hydrogen and steam concentration for a mixture at 375 K and 1 bar. The results shown are illustrative of the general situation; computations should be performed directly for mixtures at other temperatures and pressures

where the value of the constant α depends on the particular geometric configuration. For example, in the case of a long channel with obstructions, the minimum value of $\alpha = 1$ when L is the transverse dimension of the smallest cross-section in the channel. For large compartments or clouds, the minimum value of α is about 7 when L refers to the largest transverse extent of the cloud. In the case of turbulent jets, α is between 14 and 24 when L refers to the exit diameter of the jet. For interconnected rooms or channels with various blockage ratios, formulas for computing the effective value of L are suggested in Chapter 3.

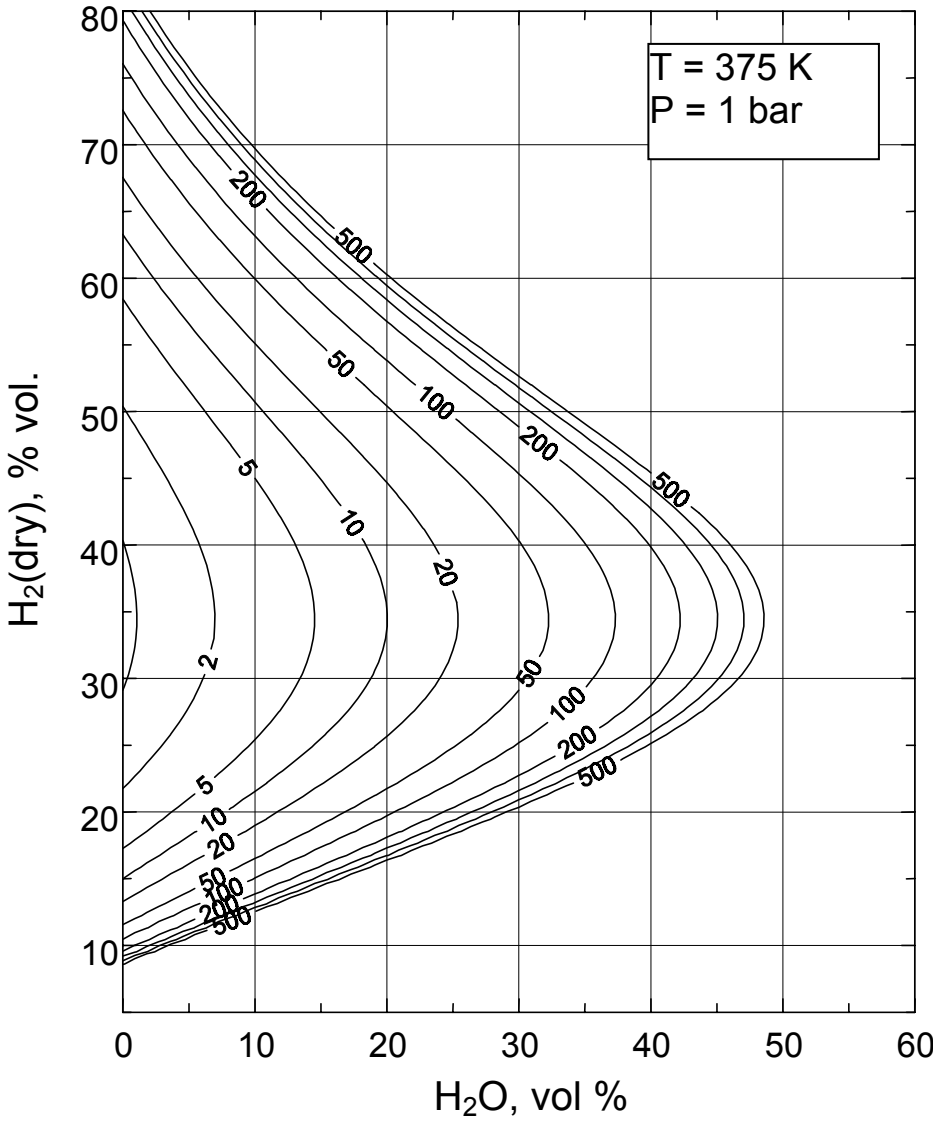

Figure 7.1.1-2 Detonation cell width λ (cm) as a function of hydrogen and steam concentration for a mixture at 375 K and 1 bar. The results shown are illustrative of the general situation, the correlation should be evaluated directly for mixtures at other temperatures and pressures

6. Combustion Regimes

The results of the previous considerations enable the construction of a combustion regime map for a particular set of thermodynamic conditions. The key parameters in this map are the amounts of hydrogen and steam in the mixture. Figure 7.1.1-3 illustrates that within the flammable regime, there is a narrow region of mixtures for which only slow flames are possible. Inside of this region, fast flames can appear once the expansion ratio is greater than the minimum values described in Chapter 3 and given in Figure 7.1.1-1. The application of the cell width of Figure 7.1.1-2 is shown for two characteristic rooms or compartment sizes, 1 and 10 m. Within the boundaries shown, DDT will be possible. It is extremely important to note that the boundaries

between combustion regimes are not simply fixed concentration values, such as some minimum hydrogen concentration as used in the past, but are a function of hydrogen and steam concentrations and also, the thermodynamic state. Not shown in the illustration, but apparent in the data, is a strong dependence of detonation cell width on initial temperature.

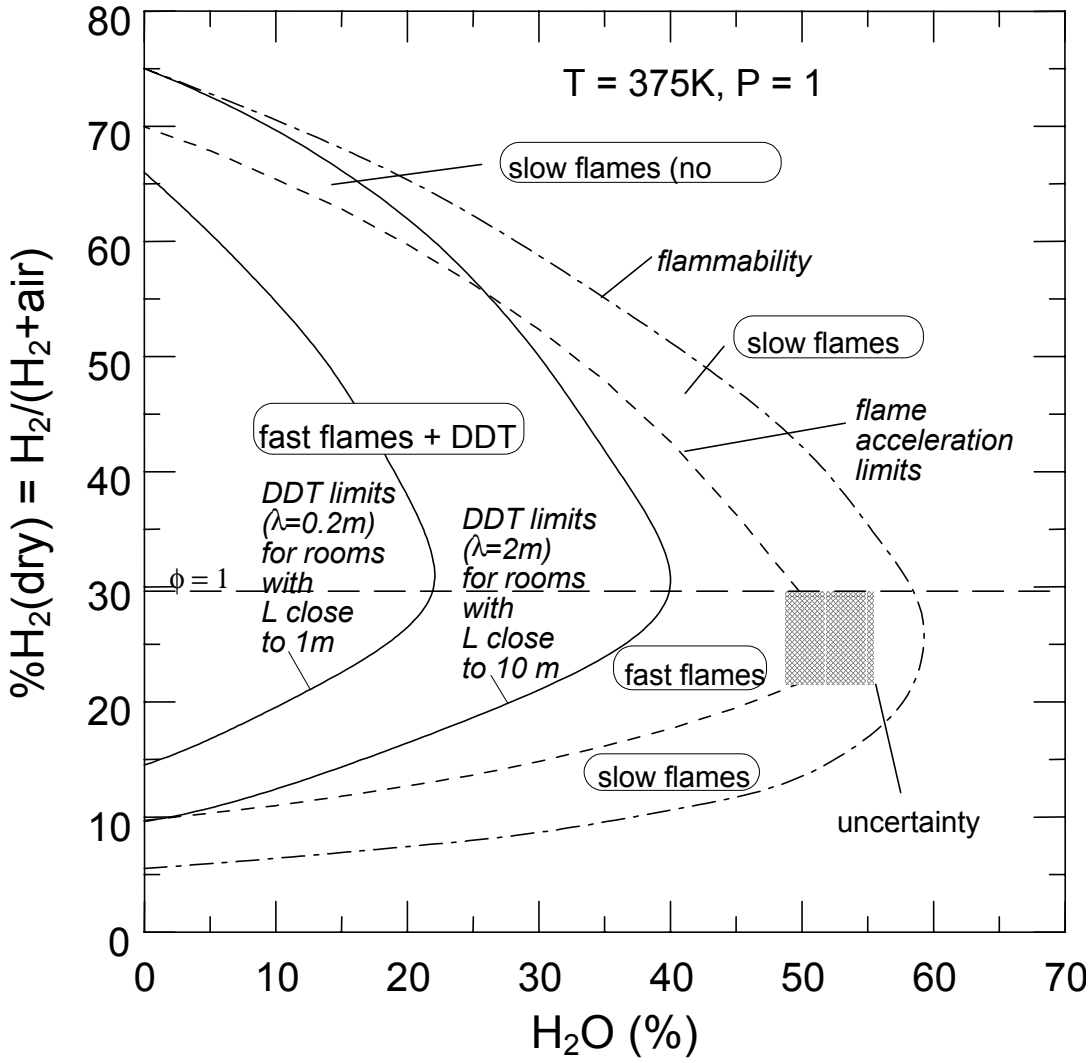

Figure 7.1.1-3 Combustion regimes possible in a hydrogen-air steam mixture at 375 K and 1 bar initial pressure. The DDT limits are based on a criteria of $L/\lambda = 5$

7. Evaluating Accident Scenarios

In order to evaluate the hazard of FA and DDT, a sequential process is suggested in Figure 7.1.1-4. The first steps are to use risk assessment methodology to define a set of accident sequences of interest, and then evaluate the hydrogen and steam source terms

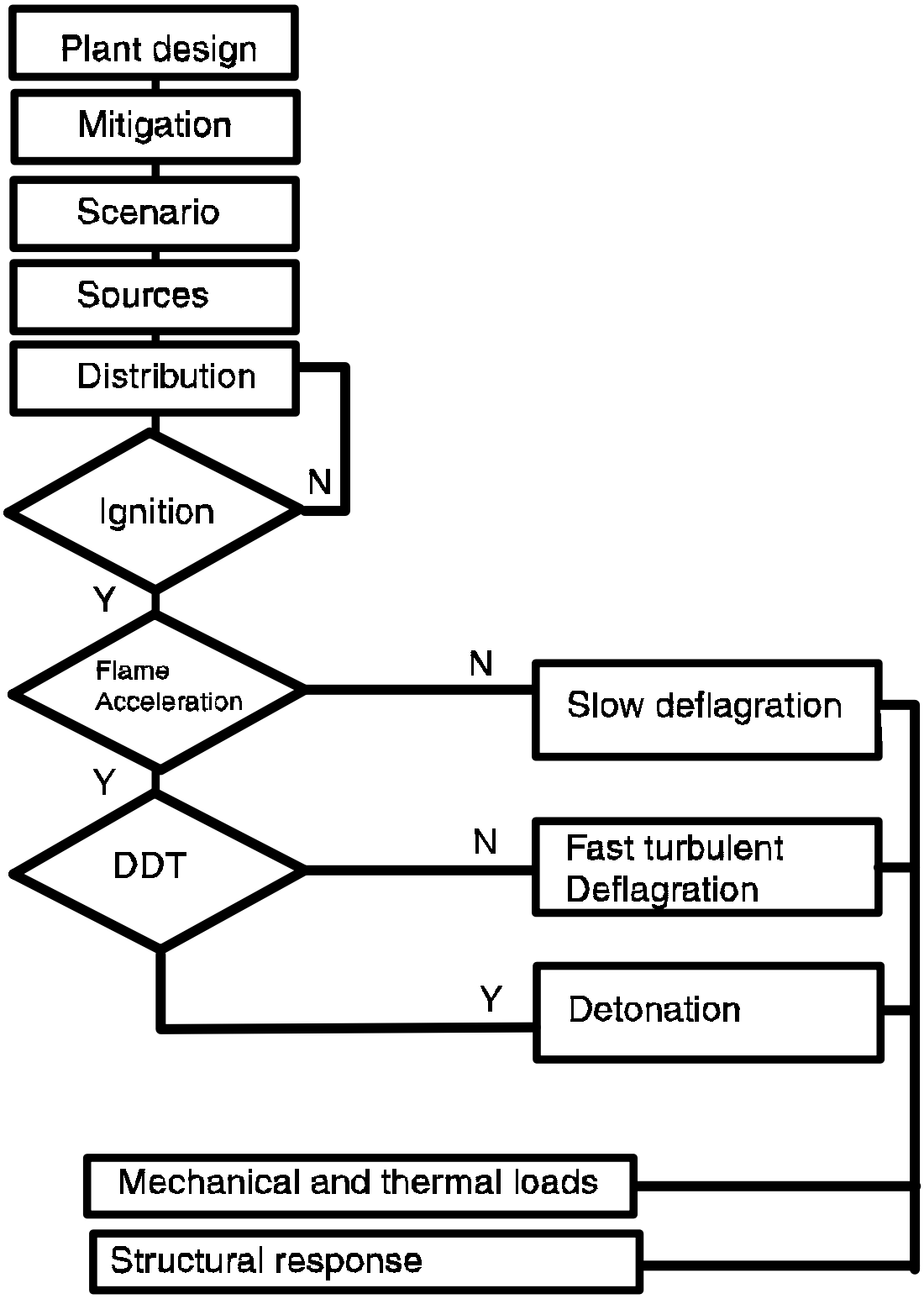

Figure 7.1.1-4 Steps in evaluating flame acceleration and deflagration-to-detonation transition hazards for severe accidents in nuclear power plants

using a system-level simulation of the postulated accident and release scenario. Once the source terms are defined, then some estimate of hydrogen distribution and mixing is needed along with predictions for the containment thermodynamic state, i.e., pressure and temperature. The framework developed above can then be applied compartment by compartment at each point in time to determine detonation and FA indices that provide a quantitative measure of the possibility of these events. In some cases, despite using mitigation schemes, some significant FA or DDT hazard may exist during some part of the transient. In those cases, closer investigation with numerical simulations of flames or detonations may be needed in order to determine whether localized fast flames or detonations pose a threat to containment integrity.

7.2 Issues

7.2.1 Combustion Modelling Appropriate to FA and DDT Events

There is a significant lack of numerical tools available to safety analysts for running approximate simulations of FA and DDT events. The existing lumped-parameter models that have been heavily used to date in reactor safety are completely inappropriate for modelling high-speed flows of any kind. Simulation of turbulent flow (without combustion) in 3D transient situations is a still-developing field without the additional complexity of combustion. In fact, at the present time, there is no single numerical method or simulation tool that can cover the entire range of phenomena in FA and DDT. Numerical models for low-speed (laminar) flames, high-speed (turbulent) flames, and detonations are distinct and, at present, there are no practical methods for running an end-to-end simulation with the goal of predicting DDT. Even at the research level, the only technique available is direct numerical simulation, albeit with a simplified chemical and transport model, and the resolution requirements of this technique make this approach impossible to apply to NPPs. This is one of the reasons why an empirical approach to FA and DDT has been so extensively explored in the last decade and will continue to be used for the foreseeable future (see the discussion of Chapter 4 on resolution requirements for numerical simulations).

An important challenge for the future is to develop approximate but reliable methods for simulating both FA and detonation in such a fashion that the simulation can be run within a single software framework. One goal would be to simply eliminate the substantial human effort that is currently required in order to transfer results between simulations and do a hand evaluation of flow fields. A more ambitious goal is to develop reliable combustion models that can be used to model DDT without the judgment and intervention of the simulator.

Progress is now being made in modelling turbulent combustion through using variations on the eddy breakup model and flame-front tracking models with empirical turbulent flame speed correlations. Although confidence is being gained in the ability of these techniques to reproduce certain features of medium- and large-scale experiments, at the core these models are empirical. Additional work is needed to validate computation results against experiments at different scales in order to gain confidence in using these methods at an NPP scale.

Further improvement in the simulation of fast turbulent deflagration will depend foremost on progress in turbulence modelling for transient flows. A current trend is to shift away from isotropic 2-equation models towards non-isotropic LES models. For chemical reaction rates, the situation is less clear. In some combustion regimes, multi-dimensional β-PDF approaches appear promising, provided fast numerical integration schemes can be found for the required multi-dimensional integrals. Future work should also address better spatial resolution or the development of sub-grid models or both for representation of unresolved structures. These models need to represent the sub-grid-scale effects on momentum balance (drag), turbulence generation, and combustion rate.

7.2.2 First-principles Modelling of DDT

At present, DDT has been modelled in a near-first-principles fashion only by research codes simulating small spatial regions of sensitive fuel-oxygen mixtures with very simplified chemical models. Because of the wide range of possible outcomes and also the sensitivity to initial and boundary conditions, it is not clear whether individual simulations would be useful for engineering evaluations of NPP safety. However, continued development of first-principles research-grade simulation tools will be very valuable in gaining insight into the mechanisms and physical-chemical parameters that are important in characterizing DDT. In particular, further exploration of the critical gradient or SWACER mechanisms is needed with detailed chemistry and multi-dimensional situations.

7.2.3 Loads and Structural Response

Ultimately, the structural response to the loads created by the combustion event is the most important measure of risk to the containment integrity. First, although it is known that the loads from fast flames can be severe, it is not clear how these compare with detonations or a DDT event. Second, work to date indicates that one must consider the details of the structural response in order to determine what is the most threatening combustion mode for a particular structure. Finally, there are at least as many uncertainties in modelling the failure of complex structures as there are in CFD and combustion modelling.

7.2.4 Experiments

7.2.4.1 FA and DDT criteria

DDT conditions are only necessary criteria and as such provide bounds that are most useful in evaluating when DDT will not occur. Combining criteria should make the boundaries sharper but at the present time, it is not possible to eliminate the essential feature of only being able to specify necessary conditions. Individual criteria also have uncertainties and in some cases are also overly bounding. Cell size uncertainty and uncertainties related to extrapolation and interpolation between distant values must be taken into account.

7.2.4.2 Minimum tube diameter

In the case of short channels or rooms, the $d/\lambda \geq 1$ criterion for detonation is probably overly restrictive as a necessary condition.

7.2.4.3 The 7-λ Criterion

Defining the physical length scale can be ambiguous in many cases. In the case of large volumes (L > 10 to 15 m), there is considerable uncertainty about cell widths greater than 2 m. No measurements are available in this regime, and no detonations have ever been observed in mixtures with cell width greater than 2 m.

7.2.4.4 Non-uniform mixtures

There are 3 issues regarding non-uniform mixtures: first, the difference in sensitivity between the mixtures as expressed by a variation in chemical length (lambda) between the most- and least-sensitive portions; second, the variation in energy content between the most-sensitive and least-sensitive mixtures; and third, how to define the characteristic physical size of a non-uniform cloud. All factors need to be taken into account, but a useful estimate of the appropriate chemical length is the cell size corresponding to the average mixture. For a non-uniform mixture within a well-defined room, the 7-λ criteria can be applied directly using the physical dimensions of the room. For a non-uniform cloud within a large volume, there are several proposals (one is discussed in Chapter 3) of how to compute the appropriate length scale. Another issue is how to determine the effective expansion ratio in a non-uniform cloud. In general, FA in non-uniform mixtures has not been investigated sufficiently to draw firm conclusions at the present time. One area of particular uncertainty is the role of the gradient dimensions and the need to investigate more realistic gradients in the hydrogen concentration.

7.2.4.5 Detonation initiation by shock focusing

It is unclear how to apply the existing data (see Appendix C) on shock focusing obtained in 50- to 350-mm-diameter shock tubes to NPP-scale situations. Shock tubes have a limited test time, and the tube walls provide confinement that will probably not be present in an NPP containment building. Although a wide range of hydrogen concentrations has been investigated, it is unclear whether the observed Mach number thresholds are independent of scale or whether the Mach number ranges investigated to date are realistic to expect in NPP severe accident conditions. Other experiments on FA and DDT show a very strong influence of system size on combustion behaviour, for example, the DDT criteria of a minimum length scale as compared to the detonation cell width. Shock focusing is now a well-established mechanism of creating critical conditions for detonation onset and will occur whenever shocks interact with concave corners. A systematic effort is needed to identify non-dimensional scaling parameters in shock-focusing experiments and to correlate these to the observed behaviour. Based on our previous experience with cell size scaling, it seems clear that it will be necessary to extend the experimental database to much larger scales before these results can be applied directly to safety analyses for NPPs.

7.2.4.6 Shock tube experiments and kinetic modelling

Detailed chemical reaction networks and modelling of flames and detonations on this basis have a role in estimating parameters such as flame speed and detonation cell width. However, there is scant data at high pressures and low temperatures with which to calibrate detailed reaction network models. The limited data that are available (see Chapter 5, Appendices A and B) suggest that there is an up to 3-order-of-magnitude discrepancy between computed and measured induction times at temperatures below 1200 K, an important regime in reactor safety applications. The direction of this discrepancy is such that computations predict much more benign conditions (longer induction times than the actual values) than may exist in practice. This may result in serious underestimation of the severity of an explosion hazard in these cases. A greater effort is needed, both in refining the experimental measurements and in investigating the reaction mechanism failures, before reaction mechanisms can be used with confidence in this regime.

7.2.4.7 Mixtures including CO and CO_2

Up to now, most of the experimental effort has been concentrated on hydrogen-air-steam mixtures. This has been appropriate since the accident scenarios predict that steam and hydrogen are the major constituents released from the primary system into the containment atmosphere. However, in some accident scenarios, significant amounts of carbon monoxide (CO) and dioxide (CO_2) may also be generated in the containment. Although some data are available (see Appendices B and C) on dilution with these components, the interaction with H_2 and H_2O has not been carefully investigated. There is a need to systematically measure parameters such as laminar and turbulent flame speed, transition limits, and detonation cell width.

7.2.4.8 Buoyancy

For lean mixtures of hydrogen, there is significant deformation of the flame and induced fluid flow resulting from the action of gravity on the hot products within the flame. This is one of the key mechanisms for accelerating very lean flames in large compartments. Lean flames generally have expansion ratios less than the critical value observed for FA in a channel geometry. For marginal situations (near the FA limit), it will be important to evaluate the influence of buoyancy at physical sizes appropriate to NPP applications. The issue of scaling is particularly crucial since the time available for buoyancy to act will vary with both physical size and hydrogen concentration. It is unclear at this time whether scale model experiments will suffice or whether large-scale experimentation is needed. An additional complexity for lean mixtures is the creation of flame instabilities (cellular structure) and the unusual influence of flame stretch in this regime; see the next subsection.

7.2.4.9 Lean hydrogen-air flame behavior

Lean hydrogen-air mixtures have Lewis numbers less than unity and negative Markstein numbers. This means that flame speed initially increases rather than decreases with positive straining motion (flame stretch) in the flow. This makes the application of standard turbulent flame speed and quenching criteria suspect in these flows. Turbulent flame speeds for lean hydrogen-air mixtures have been measured; however, the correct treatment of these data is unclear since there is no theoretical basis for treating phenomena such as quenching in these cases. There is a need for both more measurements on turbulent flame speed and quenching limits as well as an improved theoretical treatment.

7.3 Application to Safety Assessments in NPPs

There are a number of issues in applying the proposed framework to NPP safety assessment. Many of these issues are connected with reducing the uncertainty in mechanistic analysis of hydrogen behaviour.

7.3.1 Length Scales

A key issue in applying the 7-λ criterion is in determining the appropriate length scales associated with the physical compartments within the containment volume. There is a particular difficulty in evaluating this issue in conjunction with using the lumped-parameter models, which are often employed by utilities and safety agencies to screen accident sequences for potential hydrogen explosion hazards.

The lumped-parameter models can use an artificial subdivision of the physical volumes into logical volumes for the purposes of convenience in the computation. It is not obvious how to correctly ascribe a scaling length to these subvolumes in order to apply the 7-λ criteria to the results of lumped-

parameter simulations. Results of model computations (discussed in Chapter 6) indicate that although a reasonable range of length scales is obtained through a simple set of rules, the sensitivity of the results to other choices of subdivision has not been examined.

7.3.2 Source Terms

Initial conditions and distribution computations play an important role in evaluating FA and DDT potential. Although hydrogen and steam sources are highly plant- and scenario-dependent, there is a general need for better understanding of hydrogen and steam generation from certain in- and ex-vessel phenomena (in PWRs). These phenomena include fast transient sources such as reflood of an overheated core; steam explosions; hydrogen generation through steel oxidation; B4C behaviour during core-melt; and the oxidation of Zr-Ur-Oxide conglomerate; effect of fuel irradiation, and vessel failure. Core-concrete interaction can, in addition to hydrogen, also contribute important amounts of CO and CO_2. There is little information available today on flame acceleration and DDT in H_2-CO-air-steam-CO_2 mixtures.

7.3.3 Lumped-parameter Models

It is commonly assumed that lumped-parameter approaches are adequate in simulating the initial phase of the accident that determines the distribution of hydrogen and steam prior to ignition. However, there are particular cases in which this may fail. One such case occurs when large control volumes (100 to 1000 m^3) are employed that average out or mask local concentrations that may actually exist. Another case is when significant natural convection loops exist within large compartments or simultaneous inflow and outflow occur within the same opening to a compartment. Finally, since lumped-parameter codes do not conserve momentum, any situation in which the fluid momentum is significant will not be correctly computed. Examples include the prediction of peak pressure from slow flames in complex geometries. In such cases, it may be necessary to take an approach based on computational fluid dynamics (CFD), simulating the solution of the field equations of mass, momentum, and energy conservation on a fine spatial mesh.

7.3.4 Computational Fluid Dynamics

CFD is playing an increasingly important role in simulations of hydrogen distribution, FA, DDT, and detonation propagation. Modelling of turbulence and turbulent combustion is a major research area that is receiving intense study from many researchers, and all CFD codes will benefit from these efforts. For nuclear safety applications, future work is especially important with respect to improved treatment of the water phase (spray, film behaviour), modelling of radiation heat transfer, and development of improved numerical solution methods (massive parallel processing). Finally, it is important that the results of CFD simulations be carefully validated against experiments, examining both the dependence on submodels and the effects of mesh size. Several new experimental facilities are currently under construction in Western Europe that will provide the high-resolution data necessary for further validation of CFD models. A particular concern when validating CFD codes is demonstrating convergence in the face of necessarily coarse spatial meshes that are used when modelling NPP containments.

7.3.5 Ignition Predictions and Effectiveness of Mitigation Techniques

An important part of accident simulations is the prediction of the time and location of the first (and eventually subsequent) ignition of the reactive containment mixture. There is a need to develop improved criteria for ignition by spark-plug igniters as a function of spark parameters, criteria for

self-ignition by high temperatures, and a treatment of other random ignition sources (electrical sparks, hot surfaces, hot particles). The influence of high γ-radiation levels on the ignition process should also be better understood.

7.3.6 Analysis Strategies

The analysis of accident sequences and potential explosion hazards always involves evaluating complex phenomena in the face of considerable uncertainties. Often because of these uncertainties, the results of analysis are not clear-cut. In some cases, it may be necessary to use CFD or experimentation in order to sharpen the limits and provide sufficient as well as necessary conditions. As an example, if detonation cannot be completely ruled out in a particular portion of a containment, CFD simulations can be used to estimate structural loads. Computation structural simulation can then be used to see whether these loads actually pose a threat to the integrity of the containment.

LIST OF AUTHORS

Dr. Wolfgang Breitung	(**Chairperson**)
Dr. Wolfgang Breitung	(FZK, IKET, Germany)
Dr. Calvin K. Chan	(AECL, Canada)
Dr. Sergei B. Dorofeev	(Kurchatov Institute, Russian Federation)
Mr. Andreas Eder	(Technical University of Munich, Germany)
Professor Boris E. Gelfand	(Russian Academy of Sciences, Russian Federation)
Dr. Matthias Heitsch	(GRS, Germany)
Professor Dr.-Ing. Rupert Klein	(Free University of Berlin, Germany)
Dr. Asimios Malliakos	(US Nuclear Regulatory Commission, United States)
Professor Joseph E. Shepherd	(California Institute of Technology, United States)
Mr. Etienne Studer	(IPSN, France)
Dr. Paul Thibault	(Combustion Dynamics Ltd., Canada)

Secretariat:

Dr. Jacques Royen	(OECD/NEA)

LIST OF ACRONYMS

Acronym	Definition
3D	THREE DIMENSIONAL
AECL	ATOMIC ENERGY OF CANADA LIMITED
AICC	ADIABATIC ISOCHORIC COMPLETE COMBUSTION
BML	BRAY-MOSS-LIBBY (MODEL)
BMC	BATTELLE MODEL CONTAINMENT
BNL	BROOKHAVEN NATIONAL LABORATORY
BR	BLOCKAGE RATIO
CEA	COMMISSARIAT À L'ÉNERGIE ATOMIQUE
CFD	COMPUTATIONAL FLUID DYNAMICS
CFL	COURANT, FRIEDRICHS, LEVY
CJ	CHAPMAN JOUGUET (VELOCITY)
CSNI	COMMITTEE ON THE SAFETY OF NUCLEAR INSTALLATIONS (NEA)
CSP	COMPUTATIONAL SINGULAR PERTURBATION
DCH	DIRECT CONTAINMENT HEATING
DDT	DEFLAGRATION-TO-DETONATION TRANSITION
DNS	DIRECT NUMERICAL SIMULATION
DPEA	DÉPARTEMENT DE PRÉVENTION ET D'ÉTUDE DES ACCIDENTS (FRANCE)
EBU	EDDY BREAKUP (CONCEPT)
EDC	EDDY DISSIPATION CONCEPT
EPR	EUROPEAN PRESSURIZED REACTOR
FA	FLAME ACCELERATION
FCT	FLUX-CORRECTED TRANSPORT
FZJ	FORSCHUNGSZENTRUM JÜLICH
FZK	FORSCHUNGSZENTRUM KARLSRUHE
GRS	GESELLSCHAFT FÜR ANLAGEN- UND REAKTORSICHERHEIT
HPC	HIGH-PERFORMANCE COMPUTING
HPC	HIGH-PRESSURE CHAMBER
HPF	HIGH-PERFORMANCE FORTRAN
HTCF	HIGH-TEMPERATURE COMBUSTION FACILITY
HPS	HIGH-PRESSURE SECTION
ICDERS	INTERNATIONAL CONGRESS ON THE DYNAMICS OF EXPLOSIVES AND REACTIVE SYSTEMS
IKET	INSTITUT FÜR KERN- UND ENERGIETECHNIK
ILDM	INTRINSIC LOWER DIMENSIONAL MANIFOLD
IRWST	IN-CONTAINMENT REFUELLING WATER STORAGE TANK
IPSN	INSTITUT DE PROTECTION ET DE SÛRETÉ NUCLÉAIRE (FRANCE)
ISW	INCIDENT SHOCK WAVE
LAT	LEHRSTUHL A FÜR THERMODYNAMIK
LES	LARGE EDDY SIMULATION
LBLOCA	LARGE-BREAK LOSS-OF-COOLANT ACCIDENT
LIPF	LASER-INDUCED PREDISSOCIATON FLUORESCENCE
LOCA	LOSS-OF-COOLANT ACCIDENT
LPC	LOW-PRESSURE CHAMBER
LPS	LOW-PRESSURE SECTION
LWR	LIGHT-WATER REACTOR

MFCC	**MODERN FIELD CODE CLUSTER**
MITI	**MINISTRY OF INTERNATIONAL TRADE AND INDUSTRY (JAPAN)**
MPI	**MESSAGE PASSING INTERFACE**
MPP	**MASSIVE PARALLEL PROCESSING**
NEA	**NUCLEAR ENERGY AGENCY (OECD)**
NIS	**NUKLEAR INGENIEUR SERVICE (GERMANY)**
NPP	**NUCLEAR POWER PLANT**
ODE	**ORDINARY DIFFERENTIAL EQUATION**
OECD	**ORGANISATION FOR ECONOMIC CO-OPERATION AND DEVELOPMENT**
PAR	**PASSIVE AUTOCATALYTIC RECOMBINER**
PDF	**PROBABILITY DENSITY FUNCTION**
PSA	**PROBABILISTIC SAFETY ANALYSIS**
PVM	**PARALLEL VIRTUAL MACHINE**
PVP	**PARALLEL VECTOR PROCESSING**
PWR	**PRESSURIZED-WATER REACTOR**
QC	**QUASI-STEADY COMPLEX**
RMS	**ROOT MEAN SQUARE**
RNG	**RENORMALIZATION GROUP THEORY**
RNS	**REYNOLDS-AVERAGED NAVIER-STOKES**
RPV	**REACTOR PRESSURE VESSEL**
RSW	**REFLECTED SHOCK WAVE**
RUT	**FACILITY AT THE KURCHATOV INSTITUTE**
RW	**REFLECTED WAVE**
RWTH	**RHEINISCH WESTFÄLISCHE TECHNISCHE HOCHSCHULE AACHEN**
SEAC	**SERVICE D'ÉTUDES SUR LES ACCIDENTS (FRANCE)**
SEW	**SECONDARY EXPLOSION WAVE**
SI	**SAFETY INJECTION**
SIMPLE	**SEMI-IMPLICIT METHOD FOR PRESSURE-LINKED EQUATIONS**
SBLOCA	**SMALL-BREAK LOSS-OF-COOLANT ACCIDENT**
SNL	**SANDIA NATIONAL LABORATORIES**
SOAR	**STATE-OF-THE-ART REPORT**
SWACER	**SHOCK WAVE AMPLIFICATION BY COHERENT ENERGY RELEASE**
TVD	**TOTAL VARIATION DIMINISHING**
USNRC	**UNITED STATES NUCLEAR REGULATORY COMMISSION**
ZND	**ZELDOVIC-VON NEUMANN-DÖRING (CORRELATION)**

Writing Group of the state-of-the-art report on *Flame Acceleration and Deflagration-to-Detonation Transition in Nuclear Safety* at the group's final meeting at FZK, Karlsruhe, August 5 and 6, 1999

Front row (from left): Dr. Jacques Royen (Secretary), Dr. Asimios Malliakos, Dr. Calvin K. Chan, Professor Boris E. Gelfand, and Dr. Wolfgang Breitung (Chairperson);

Second row (from left): Dr. Matthias Heitsch, Mr. Etienne Studer, Professor Joseph E. Shepherd, Mr. Andreas Eder, and Dr. Sergei B. Dorofeev.

Absent from the photo are Dr. Paul Thibault and Professor Dr.-Ing. Rupert Klein.

APPENDIX A: LAMINAR AND TURBULENT FLAME PROPAGATION IN HYDROGEN–AIR–STEAM MIXTURES*

A.1 Laminar Burning Velocities of Hydrogen-Air and Hydrogen- Air - Steam Mixtures

A.1.1 Background

Methods of measuring flame velocity can be divided into 2 groups: stationary-flame and free-flame propagation methods. More detailed classification of the methods is shown in Table A.1.1-1 [A1,A.2] .

One of the important disadvantages of a simple tube burner is the parabolic velocity profile for unburned gas. Moreover, the apparent burning velocity varies over the defined surface (schlieren, shadow or luminous) and a mean value is obtained.

The most crucial disadvantage of the burner method is flame unsuitability in lean hydrogen-air mixtures (15% H_2 or less). A usual symmetrical cone is absent in such mixtures, and the flame has a polyhedral structure. It consists of several luminous reaction zones separated by dark regions. Another example of flame instability is the breakup of the flame cone top. Table A.1.1-2 summarizes the discrepancies between the burning velocity data obtained by different methods for hydrogen-air premixed flames at atmospheric pressure and room temperature [A.1,A.2]. Laminar burning velocity data for hydrogen-air mixtures are shown in Figure A.1.1-1. The nozzle burner data of Liu and MacFarlane [A.3] differ markedly from both the spherical bomb data and the Bunsen burner data. Such results may be reasonably explained by the influence of flame stretch. Liu and MacFarlane [A.3] used a very small nozzle (3 mm), and this is why they obtained a higher value for burning velocity.

The burning velocity, S_u , can be calculated from the measured flame speed $S_b = dr_f /dt$ by employing the following equation:

$$S_u = S_b / \sigma \quad , \qquad (A.1)$$

where σ is the expansion ratio for constant pressure burning. This value may be determined by thermodynamic computations of the adiabatic burning temperature T_b with regard to a change of the gas density in combustion:

$$\sigma = \rho_0 / \rho_b = (n_b T_b) / (n_0 T_0) \quad . \qquad (A.2)$$

Here, r_0 and $\mathbf{r_b}$ are the density of unburned and burned gas, T_0 is the initial temperature of the gaseous mixture, and n_0 and n_b are the moles of unburned and burned gases respectively.

The values of adiabatic flame temperatures and moles of burned gases can be calculated by using available thermodynamic data JANAF. Adiabatic flame temperature T_b and expansion ratio $\boldsymbol{s}$ for hydrogen-air-steam mixture (f = 0.39) are shown in Table A.1.1-3.

---

*Professor Boris E. Gelfand is the lead author of Appendix A.

T_0(K)	T_b(K)			s		
	0% H_2O	10% H_2O	20% H_2O	0% H_2O	10% H_2O	20% H_2O
293	1393	-	-	4.42	-	-
323	1418	1293	1175	4.08	3.75	3.43
373	1459	1335	1217	3.64	3.35	3.08
393	1476	1352	1234	3.49	3.22	2.96
423	1501	1378	1259	3.30	3.05	2.81
473	1544	1420	1302	3.04	2.81	2.60
523	1586	1463	1345	2.82	2.62	2.43

If the initial pressure p_0 varies from 1 to 10 bar, T_b and s remain practically unchanged. This is due to the insignificant dissociation of combustion products at given temperatures of lean hydrogen-air-steam mixtures. Examples of radius-flame registrations and photographs of hydrogen-air-steam flames will be shown below along with experimental data.

A.1.2 Results of Laminar Burning Velocity Measurements in Lean H_2-Air and H_2-Air-Steam Mixtures at Room and at Elevated Temperatures

The influence of initial pressure is illustrated in Figure A.1.2-1. Solid lines correspond to our numerical predictions. Solid circles and triangles denote pressure-time and flame radius-time methods of burning velocity measurements. Experimental data obtained by Andrews and Bradley [A.4] and by Shebeko et al. [A.5] are also shown. Andrews and Bradley [A.4] used double-kernel and single-kernel methods with schlieren photography; Shebeko et al. [A.5] used p-t procedure without photography. It is interesting to note that the relative deviation of experimental and theoretical data is greater for 10% H_2-air mixture than for 20% H_2-air mixture. Moreover, the deviation increases with pressure. Numerical simulation predicts the negative pressure exponent for 10% H_2-air mixture, but p-t measurements do not corroborate this relationship.

A.1.3 Temperature and Pressure Influence on Burning Velocity

Burning velocities, measured by the flame radius-time method, are shown in Figure A.1.3-1. The measurements was performed for hydrogen-air-steam mixtures at two initial pressures of 3 and 5 bar. Experimental results are in good agreement with theoretical results. This fact has substantially facilitated the solution of the pressure exponent determination problem.

A.1.3.1 *Pressure and temperature exponents*

A power law dependence of the following form

$$S_u = S_{u0} (T/T_0)^a (P/P_0)^b \quad \text{(A.3)}$$

is often used for burning velocity approximation. *a* is referred to as temperature exponent (or temperature index) and *b* as pressure exponent (or pressure index). T_0 and P_0 are initial values of pressure and temperature, $S_{u0} = S_u$ at $T = T_0$ and $P = P_0$.

Measured and predicted burning velocities of hydrogen-air mixtures in the range 0.5 to 10 bar at room temperature are shown in Figure A.1.2-1. The data indicate that the values of pressure exponent are negative for hydrogen-air mixtures with a hydrogen percentage of less than 15% by volume. In a similar manner, pressure exponents *b* for hydrogen-air-steam mixtures (f = 0.39) are also negative. However, the value of *b* depends upon steam concentration and initial pressure. Figure A.1.3-2 shows the influence of pressure on laminar burning velocity for hydrogen-air-steam mixtures ($\phi = 0.39$) at 393 K. As is evident from the graph, burning velocity decreases gradually with a rise of pressure. To illustrate the rate of change of the burning velocity with pressure, we plotted the relative burning velocity S_u / S_{u0} as a function of initial pressure, where percent of steam was a parameter. Pressure exponents were calculated in the range of interest (3 to 5 bar) . The values of pressure exponents are indicated near the curves.

The influence of temperature on the burning velocity is illustrated in Figure A.1.3-3 (a, b, c). In Figure A.1.3-3a, we have plotted the dependence of S_u on initial pressure for H_2-air mixture ($\phi = 0.26$) at 298 K, 373 K, and 473 K. Experimental data are in good agreement with the results of the calculations. In Figure A.1.3-3b, burning velocities are plotted as a function of initial temperature at two pressures, 1 and 4 bar. Burning velocity is seen to increase with temperature. Temperature exponent *a* is shown as a function of hydrogen concentration in the range from 10% H_2 to 70% H_2. Temperature exponent is equal to 1.6 at 42% H_2 and it rises significantly at 10% H_2, where it is equal to 3.2. The data on the influence of steam concentration on laminar burning velocity of hydrogen–air-steam mixtures are given in Reference [A.6].

A.1.4 Turbulent Combustion Rates in Hydrogen-Air and Hydrogen-Air-Steam Mixtures

Essential experimental results of References [A.1, A.2, A.7] are presented below. Figure A.1.4-1 shows the measured turbulent combustion rates S_T of a lean hydrogen-air mixture ($\phi = 0.26$) as a function of the turbulent intensity in the pressure range from 1 to 5 bar. For comparison, laminar burning velocity S_u for the mixture is about 17 cm/s at 1 bar and 8 cm/s at 5 bar. As it seen from Figure A.1.4-1, in the case of turbulent combustion, the pressure dependence is absent.

Turbulent consumption rates S_T measured for hydrogen-air-steam mixtures are shown in Figures A.1.4-2 and A.1.4-3. Three hydrogen-air compositions were chosen—namely, 8% H_2, 10% H_2 and 14% H_2—and were diluted with steam as shown in the legends of the figures. The limiting steam concentrations and limiting turbulence intensity were found for elevated temperatures in the range 393 to 400 K at atmospheric pressure. The influence of initial pressure was investigated by comparison of experimental data at 1 bar and 3 bar, as shown in Figure A.1.4-3. An extinction regime was observed in turbulent flames of hydrogen-air-steam near-limit mixtures. Turbulent flame covers a small part of the experimental vessel. Pressure rise does not exceed 0.1 to 0.15 bar. Three examples of pressure-time curves at an extinction limit in the case of 10% steam dilution are shown in Figure A.1.4-4.

A.1.5 Flammability Limits for Lean Hydrogen–Air–Steam Mixtures

The flammable range of H_2-air-steam mixtures is illustrated in Figure A.1.5-1a. Shown here are the experimental results both for upward and downward (only Kumar's data [A.8]) flame propagation. Results of measurements of limit hydrogen concentrations for the most-lean composition are slightly different, whereas considerable distinctions are observed in the region of the "nose" of the flammability curve. Most likely, the discrepancy between experimental findings involves the use of various energy

deposits of ignition sources. For ignition source, energy is equal 1 to 2 J [A.1,A.2] and 40 J (Kumar), and the measurements are in a good agreement. According to Figure A.1.5-1a, turbulent extinction limits lie between upward and downward laminar combustion limits.

The influence of initial temperature T_0 [A.1-A.3] and steam dilution on the limit hydrogen concentrations $(H_2)_{lim}$ at different fixed initial pressure is given in Figure A.1.5-1 (b, c), respectively. With a rise of T_0, $(H_2)_{lim}$ decreases, approximately, on the value 0.45% (vol) for every 100 K, and this value practically does not change up to 7 bar. With steam dilution up to 50% (vol), $(H_2)_{lim}$ increases on the value 0.34% (vol) for every 10% H_2O (vol) at initial pressures of 1 bar and 7 bar.

The effect of the extent to which the residence time (of up to 2 h)—i.e., time interval between the moment of acquiring the desirable temperature by the hydrogen–air mixture and initiation of spark ignition—and, consequently, the existence of pre-ignition reactions that may influence the value of the flammability limits was investigated [A.3]. In the temperature range up to 473 K, the limits were not affected by the length of the residence time. However at T > 473 K, the flammability limits—especially the rich limit—narrowed with an increase in the temperature and were very significantly affected by the length of the residence time before spark ignition. This means that the time of exposure of the mixture to elevated temperature before initiation of ignition should be taken into consideration and should be reported together with obtained values of the limits. It was suggested [A.13] that the drop in the value of the rich limit and increase in the value of the lean limit with the increase of the residence time were caused by relatively low-temperature catalytic reactions on the stainless steel surface of the test tube.

A.2 References

[A.1] Laminar and Turbulent Flame Propagation in H_2 + Air + Steam Mixtures at Accident Relevant Pressure at Temperature Conditions, IChPh RAS at INR FZK Research Report, 1995.

[A.2] Laminar and Turbulent Flame Propagation in H_2 + Air + CO_2 Mixtures at Accident Relevant Pressure at Temperature Conditions, IChPh RAS at INR FZK Research Report, 1996.

[A.3] D. Liu and R. MacFarlane, Laminar Burning Velocities of H_2 – Air and H_2 –Air –Steam Flames, Combustion and Flame, Vol. 49, 1983, 59-71.

[A.4] G. Andrews and D. Bradley, Determination of Burning Velocities : A Critical Review. Comb. Flame Limits of H_2 – O_2- Diluent Mixtures, Journal of Fire Sciences, Vol. 3, 1985, 242-262.

[A.5] Shebeko et al.

[A.6] B.W. Marshall, Hydrogen–Air–Steam Flammability Limits and Combustion Characteristics in the FITS Vessel, NUREG Report, CR –3468, 1986.

[A.7] S. Heimel, Effect of Initial Mixture Temperature on Burning Velocity of Hydrogen-Air Mixtures with Preheating and Simulated Preburning, NASA TN- 3833, 1956.

[A.8] T. Iijima and T. Takeno, Effects of Temperature and Pressure on Burning Velocity, Combustion and Flame, Vol. 65, 1986, 35-43.

[A.9] C.K. Wu and C.K. Low, On the Determination of Laminar Flame Speeds from Stretched Flames, Proc. of 20th Symp. (International) on Combustion, Combustion Institute, Pittsburgh, 1984, 1941-1949.

[A.10] I . Wierzba and B.B. Ale, Effects of Temperature and Time of Exposure on the Flammability Limits of Hydrogen–Air Mixtures, International Journal of Hydrogen Energy, Vol. 23, 1998, 1197.

[A.11] D.R . Dowdy, D.B. Smith and S.C. Taylor, The Use of Expanding Spherical Flames to Determine Burning Velocities and Stretch Effects in Hydrogen–Air Mixtures, Proc. of 23rd Symp. (International) on Combustion, Combustion Institute, Pittsburgh, 1990, 325- 331.

[A.12] M. Berman and J.C. Cummings, Hydrogen Behavior in Light–Water Reactors, Nuclear Safety, Vol. 25, 1984, 61-70.

[A.13] G.W. Koroll and S.R . Mulpuru, The Effect of Dilution with Steam on The Burning Velocity and Structure of Premixed Hydrogen Flames, Proc. of 21st Symp. (International) on Combustion, Combustion Institute, Pittsburgh, 1986, 1811-1819.

Table A.1.1-1 Experimental methods for burning velocities determination

Table A.1.1. Experimental Methods for Burning Velocities Determination

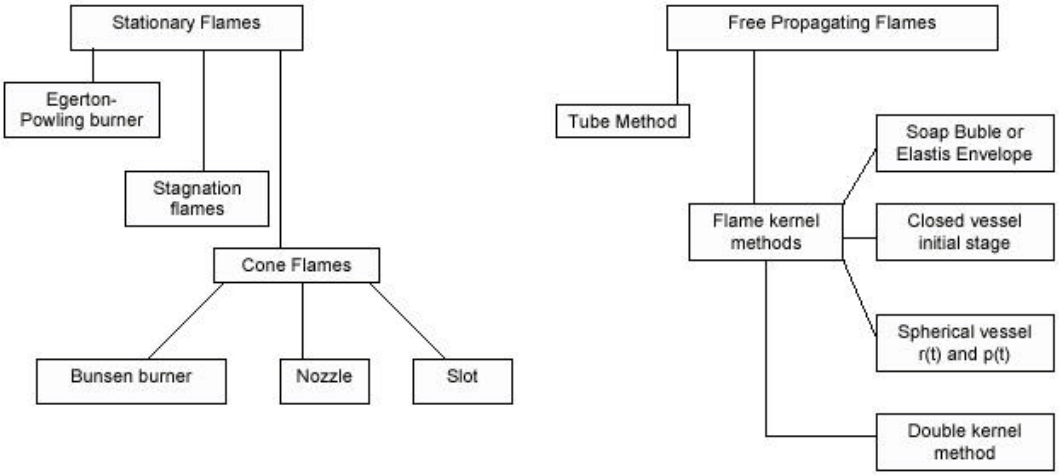

Table A.1.1-2 Hydrogen-air laminar burning velocities (cm/s) at atmospheric pressure and room temperature

Table A.1.2 Hydrogen - Air laminar burning velocities (cm/s) at atmospheric pressure and room temperature

Author	Year	Method	%H2	S_u^o	S_u^{max}
Michelson	1889	B	15.3-74.6	217[1]	281
Jahn	1934	B	30-75	187	267
Bartholome	1949	N	40-51.2		320
Kozachenko	1954	B	20-70	233[3]	287
Manton & Milliken	1956	S	30-70	232	300
Fine	1956	B	28-62	193	304
Heimel	1956	B	28-57	206	297
Grumer et al.	1959	S	48-67.1		
Gunther & Janisch	1972	N[4]	15-70	282	355
Andrews & Bradley	1973	D	10-70		336
Liu & MacFarlane	1983	N	20.6-64		356
Takahashi	1983	N	29.6-64		308[6]
Wu & Law	1984	N	22.7-70		332[5]
Wu & Law	1984	N	29.6-62.7		308[6]
Iijima & Takeno	1986	S	17.4-62.7	238[2]	298
Dowdy et al.	1990	S	9-68	213[7]	285[7]
Koroll et al.	1993	D	8-70		346
Koroll et al.	1993	N	30-70		330

B - Bunsen burner
N - Nozzle burner
S - Spherical vessel method
D - Double kernel method

[1] interpolation according to formula

$S_u = 37.1 + 18x + 3100(x-0.16)(0.71-x)$ cm/s at x=0.296

[2] interpolation according to formula

$S_u = 2.98 - (\phi - 1.7)^2 + 0.32(\phi - 1.7)^3$ m/s

[3] average of two values (224 and 241 cm/s)

[4] button-shaped flame, 4 mm nozzle

[5] 5 mm nozzle; [6] 7 mm nozzle

[7] extrapolation to infinite flame radius

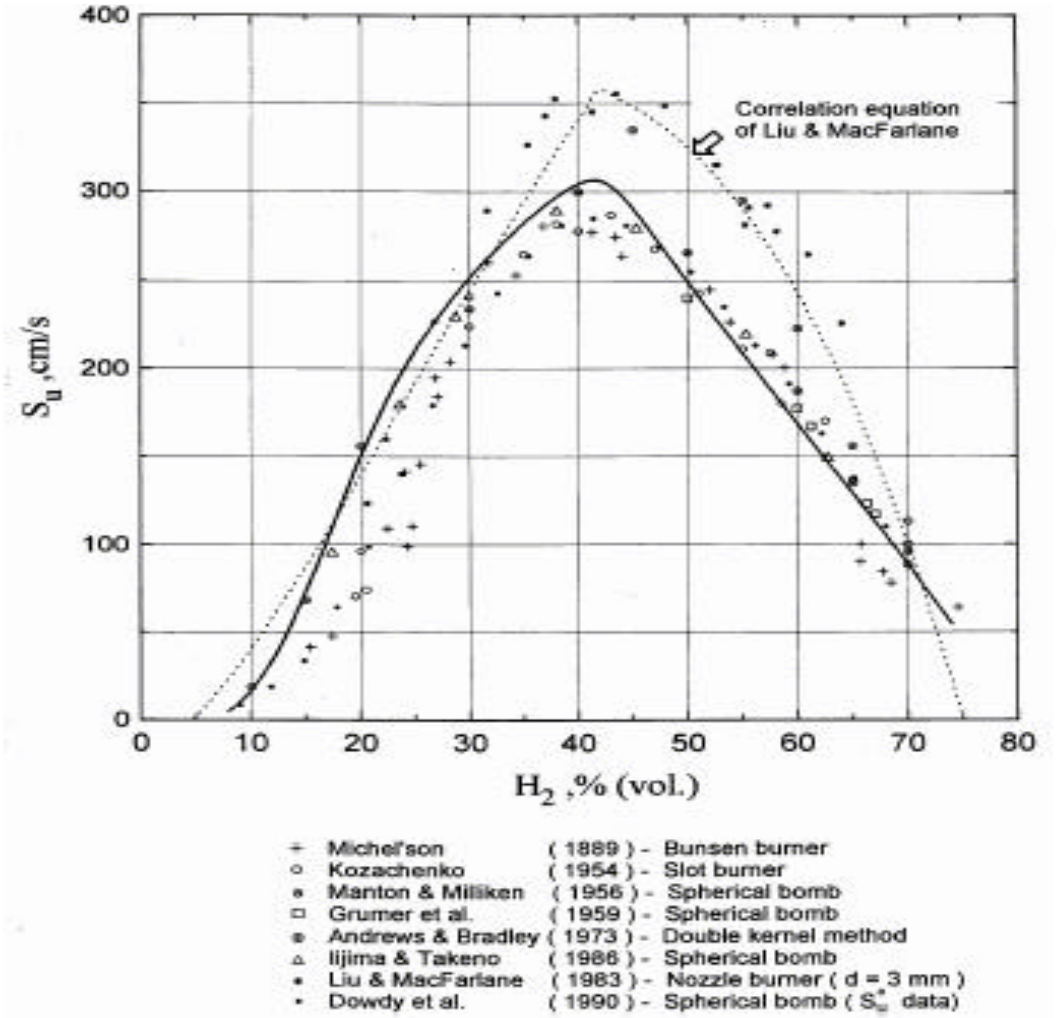

Figure A.1.1. Laminar burning velocity of hydrogen/air mixtures at room temperature and atmospheric pressure measured by various methods. Solid line: computed values for spherical flame propagation; dotted line: correlation equation of Liu and MacFarlane.

Figure A.1.1-1 Laminar burning velocity of hydrogen air mixtures at room temperature and atmoshpheric measured by various methods. Solid line computed values for spherical flame propagation; dotted line correlation equation of Liu and MacFarlane.

Figure A.1.2-1 Dependence of the laminar burning velocity S_T on initial pressure P_0 for lean hydrogen-air mixtures at 298 K. Solid lines: calculations; points: experimental data.

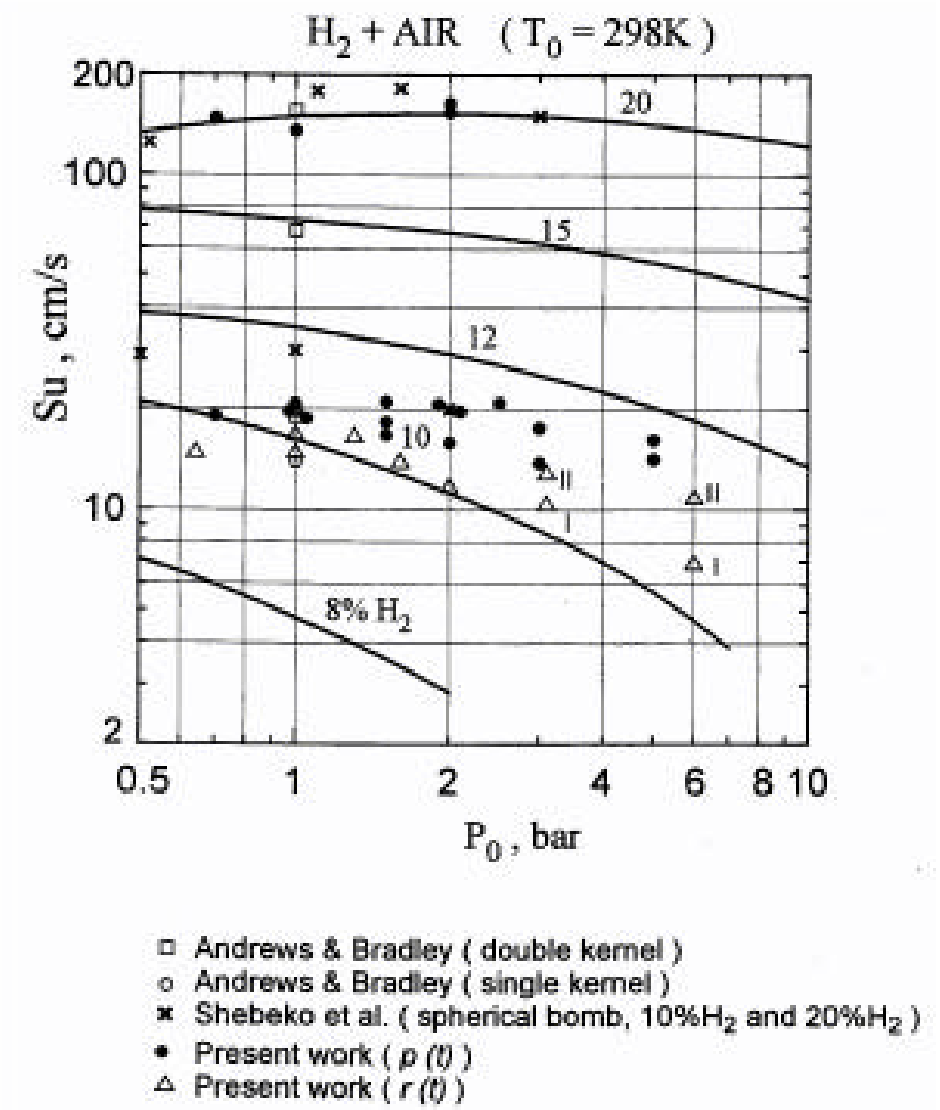

Figure A.1.2. Dependence of the laminar burning velocity S_u on initial pressure P_0 for lean hydrogen/air mixtures at 298K. Solid lines: calculations; points: experimental data.

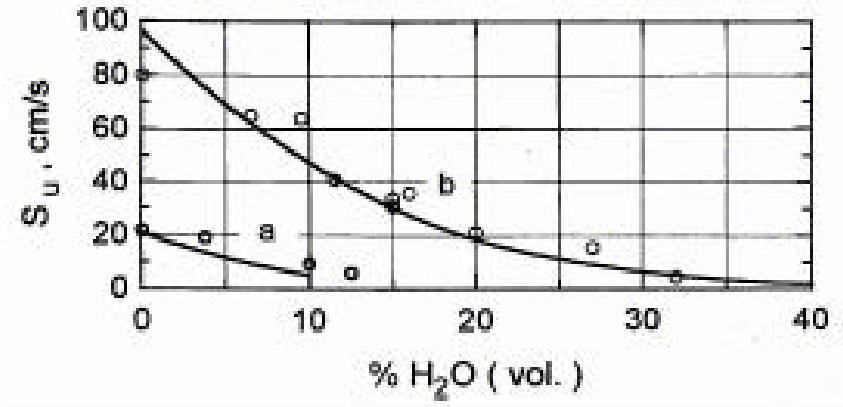

Figure A.1.3. Comparison between measured (points) and calculated (solid lines) laminar burning velocities for hydrogen-air-steam mixtures.
(a) $-T_0$=393K, P_0=5bar, ϕ=0.26; (b) $-T_0$=393K, P_0=3bar, ϕ=0.39

Figure A.1.3-1 Comparison between measured (points) and calculated (solid lines) laminar burning velocities for hydrogen-air-steam mixutes.

(a) $-T_0$ = 393 K, P_0 = 5 bar, f = 0.26; (b) $-T_0$ = 393 K, P_0 = 3 bar, f = 0.39

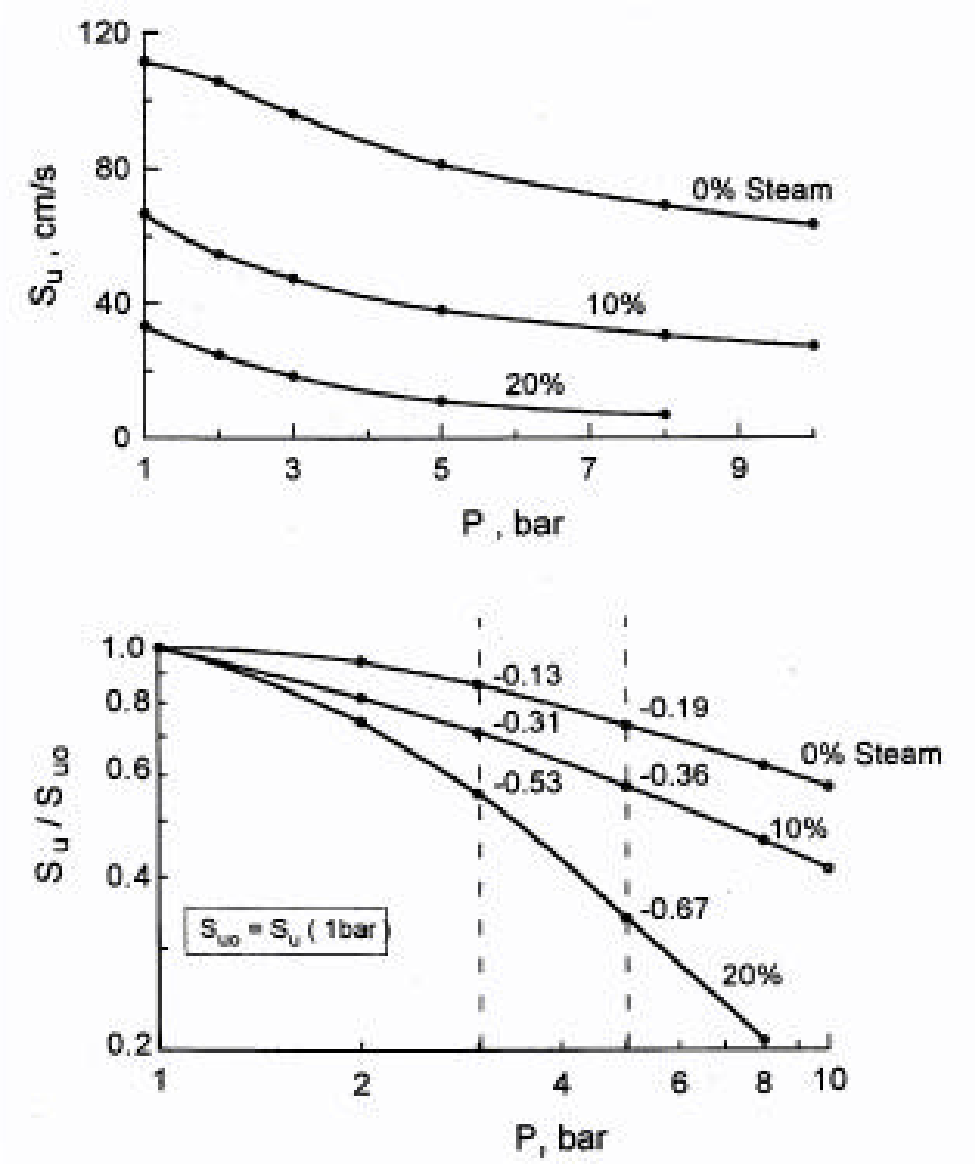

Figure A.1.4. Effect of pressure on the laminar burning velocity of hydrogen-air-steam mixtures (ϕ=0.39) at 393K. Numbers on curves indicate pressure exponent.

Figure A.1.3-2 Effect of pressure on the laminar burning velocity of hydrogen-air-steam mixtures (f = 0.39) at 393 K. Numbers on curves indicate pressure exponent.

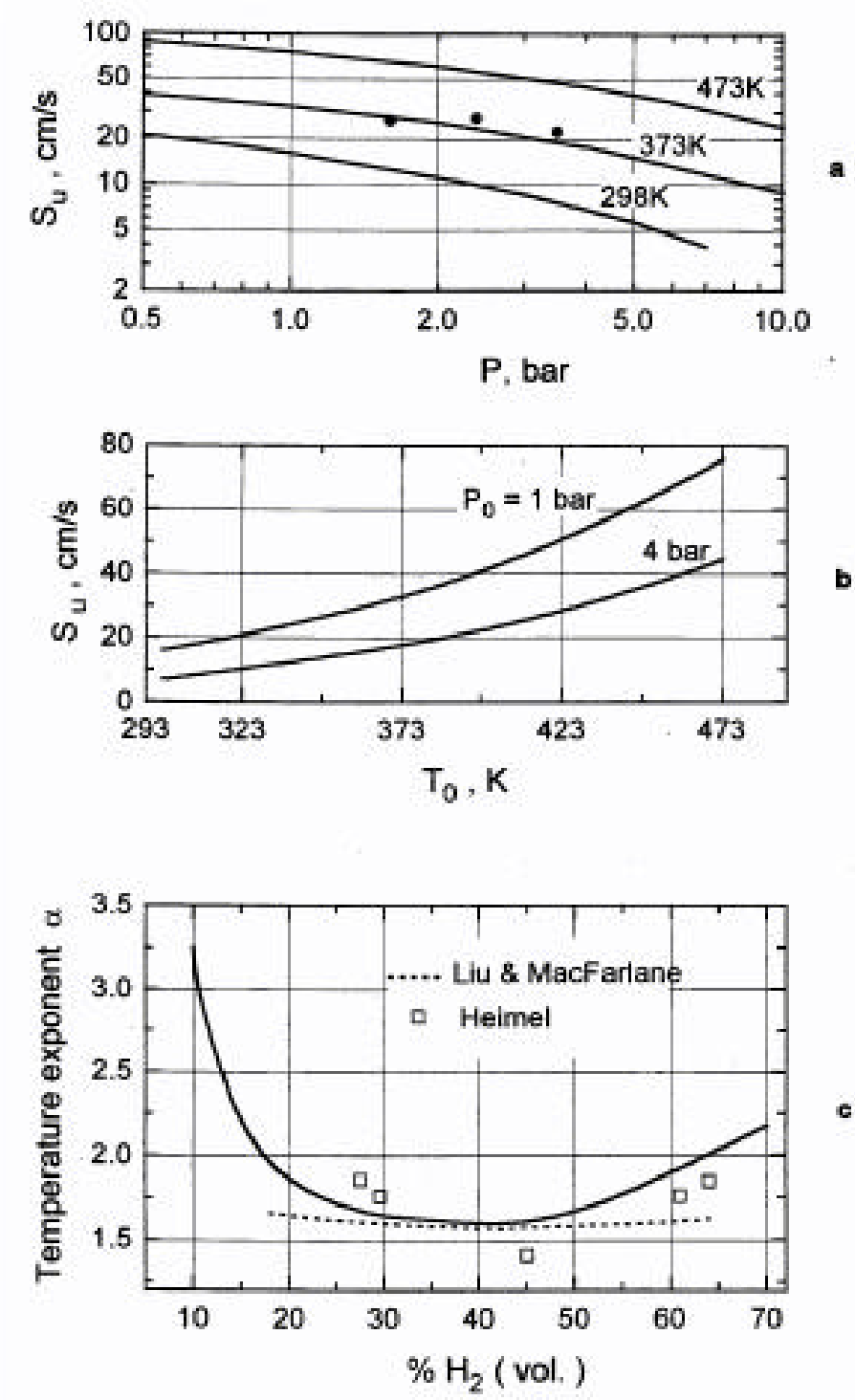

Figure A.1.5. Laminar burning velocity as a function of pressure (a) and temperature (b) for 10% H_2 - air mixture (ϕ = 0.26). (c) - Comparison between theoretical and experimental data for temperature exponent α in H_2 - air mixtures at 29% and 1 bar.

Figure A.1.3-3 Laminar burning velocity as a function of pressure (a) and temperature (b) for 10% H_2-air mixture (f = 0.26. (c) Comparison between theoreticla and experimental data for temperature exponent a in H_2-air mixtures at 29% and 1 bar.

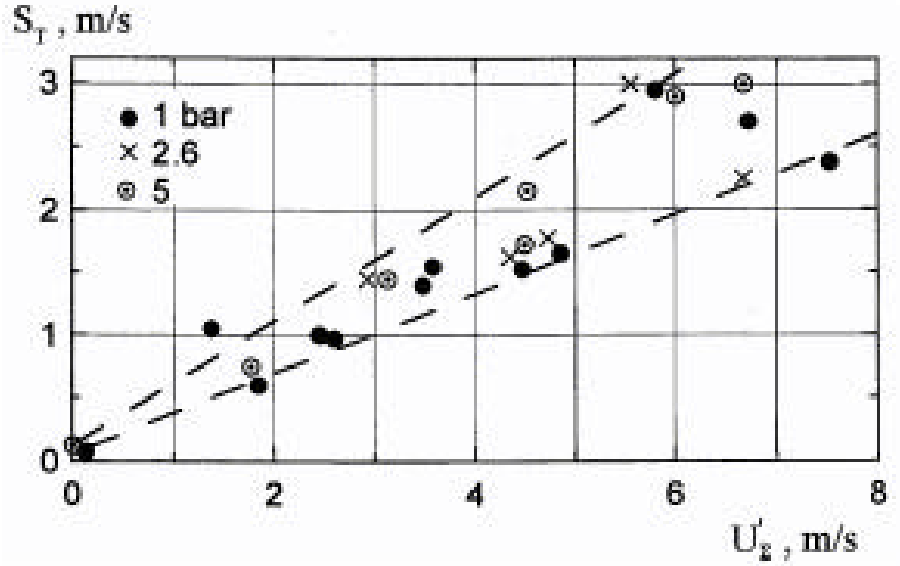

Figure A.1.6. Turbulent. consumption rate S_T for H_2- air mixture (ϕ = 0.26) at 298K.

Figure A.1.4-1 Turbulent consumption rate S_T for H_2 -air mixture (f = 0.26) at 298 K.

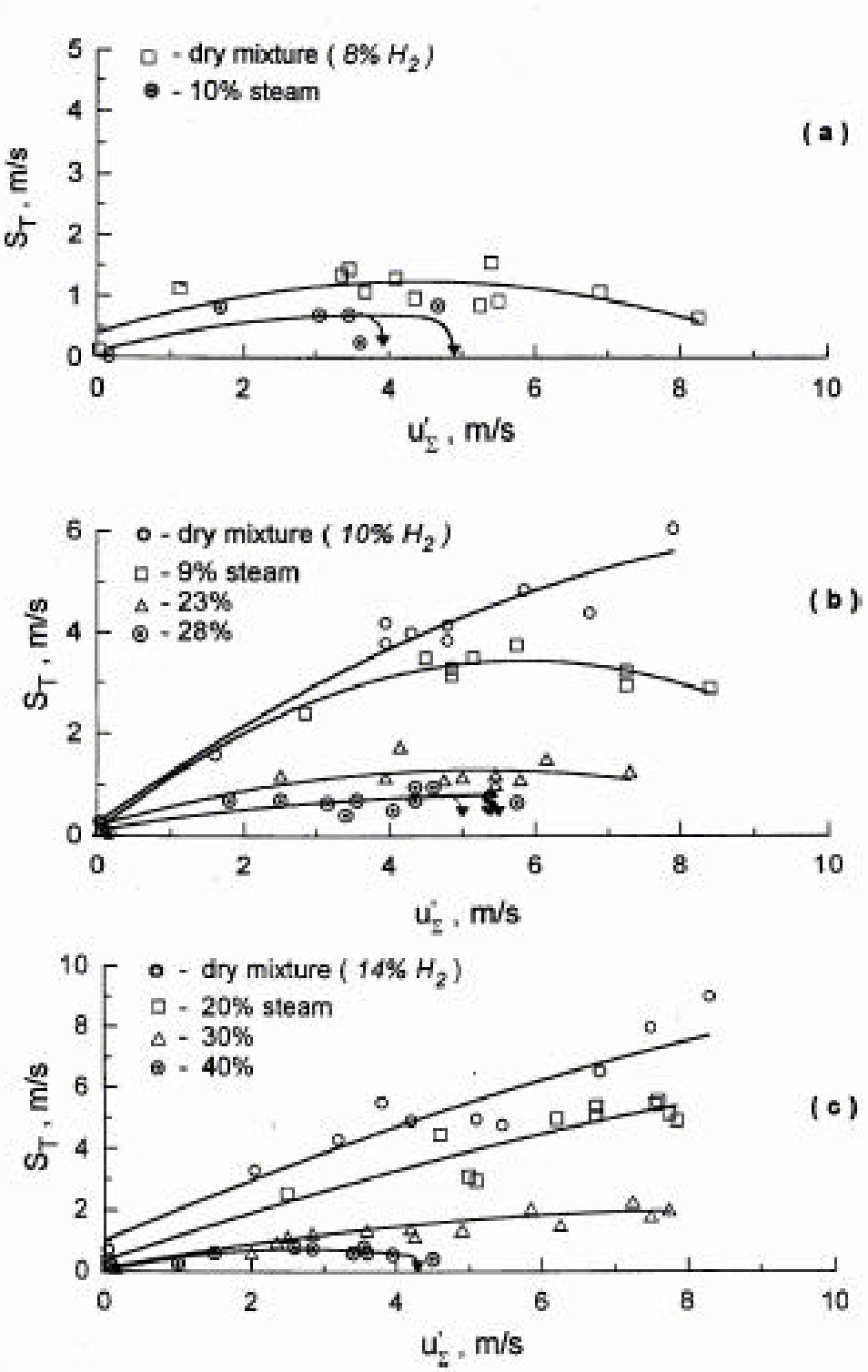

Figure A.1.7. Influence of turbulence intensity on the turbulent consumption rate S_T for hydrogen-air-steam mixtures at temperatures 393 - 400K and atmospheric pressure a) ϕ = 0.207; b) ϕ = 0.26; c) ϕ = 0.39.

Figure A.1.4-2 Influence of turbulence intensity on the turbulent consumption ratio S_T for hydrogen-air-steam mixtures at temperatures 398 - 400 K and atmospheric pressure a) f = 0.207; b) f = 0.26; c) f = 0.39.

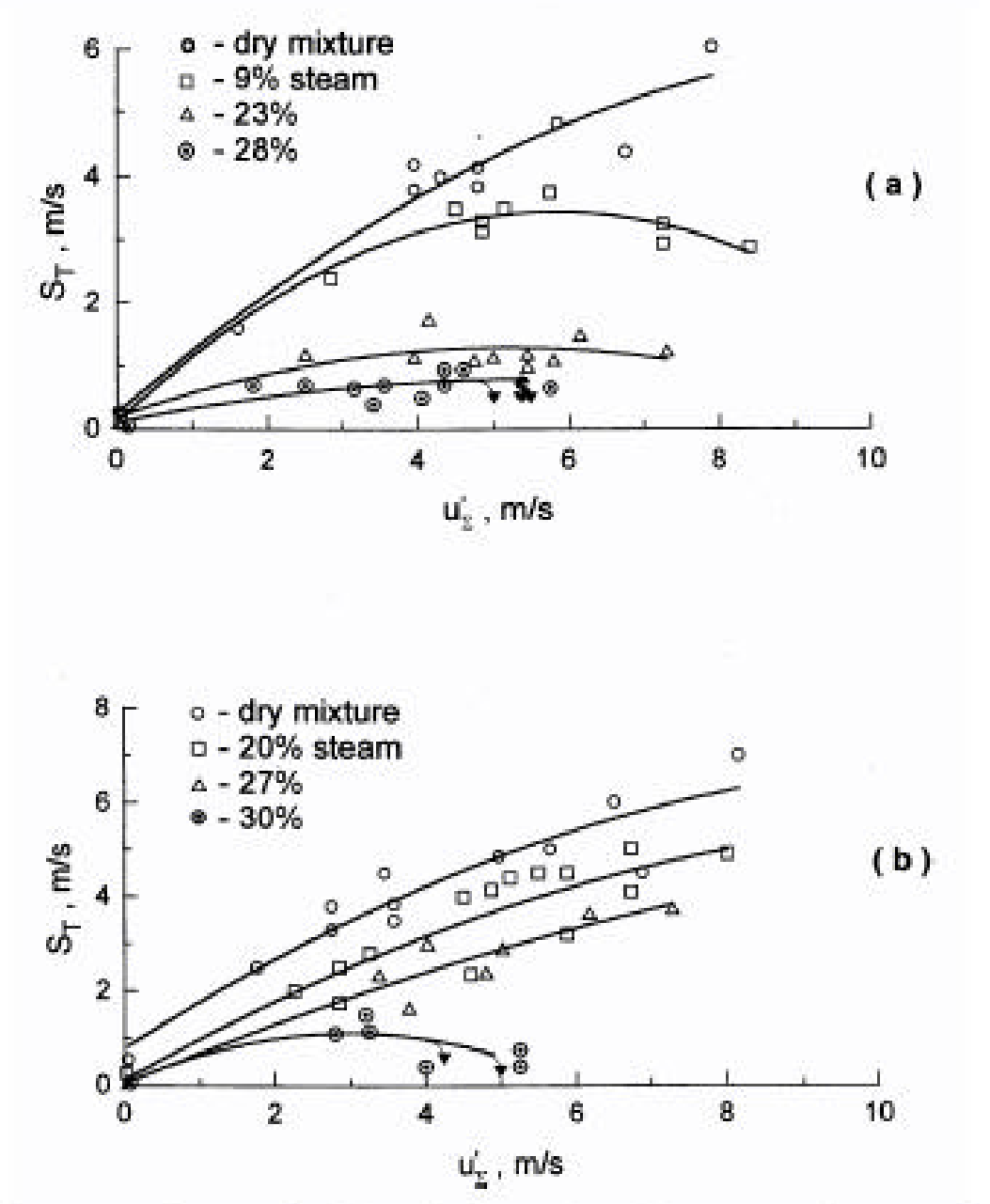

Figure A.1.8. Influence of turbulence intensity on the turbulent consumption rate S_T for hydrogen-air-steam mixtures ($\phi = 0.26$) at temperatures 393 - 400K. a) P_0=1 bar; b)P_0=3 bar.

Figure A.1.4-3 Influence of turbulence intensity on the turbulent consumption rate S_T for hydrogen-air-steam mixutes (f = 0.26) at temperatures 393 - 400 K. a) P_0 = 1 bar; b) P_0 = 3 bar.

Figure A.1.4-4 Pressure-time curves at an extinction limit for turbulent flames in hydrogen-air-steam mixtures (f = 0.2; 10% H_2O; P_0 = l bar; T_0 = 398 K).

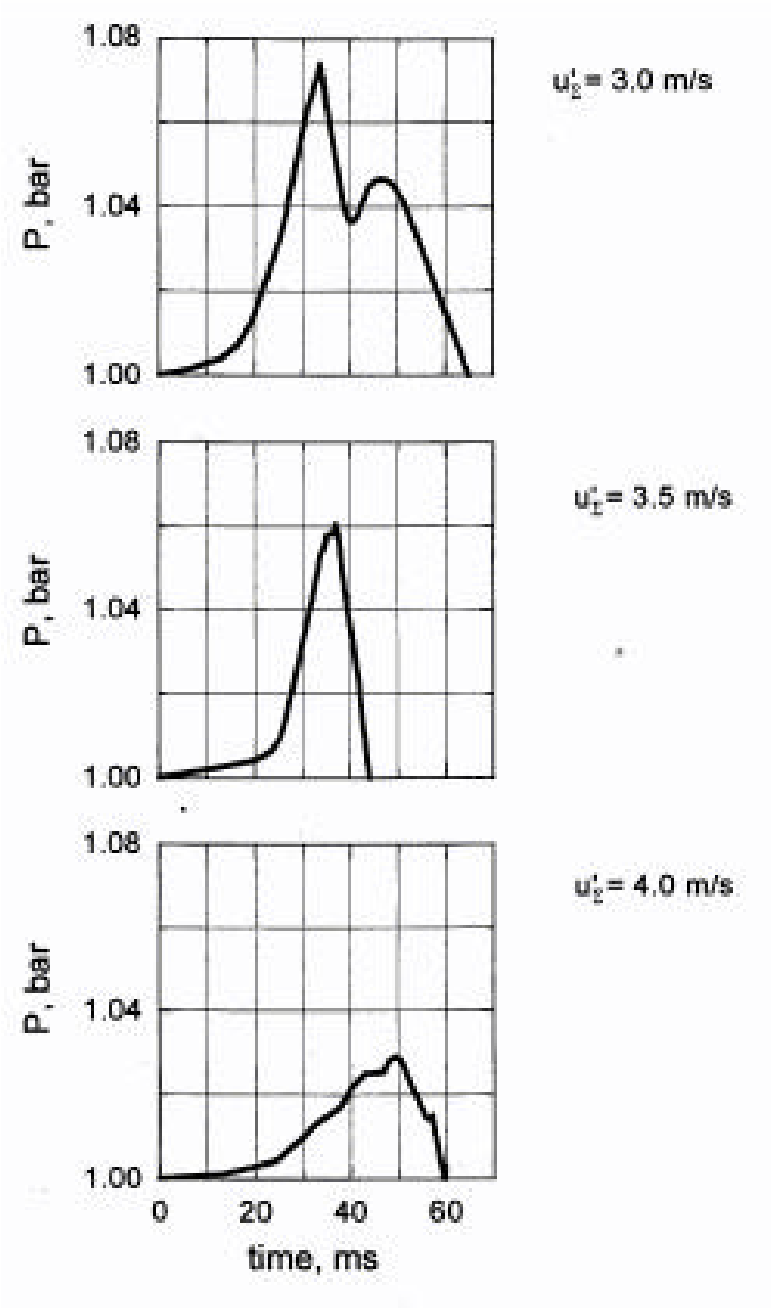

Figure A.1.9. Pressure-time curves at an extinction limit for turbulent flames in hydrogen-air-steam mixtures (ϕ = 0.2; 10% H_2O; P_0=1 bar; T_0=398K).

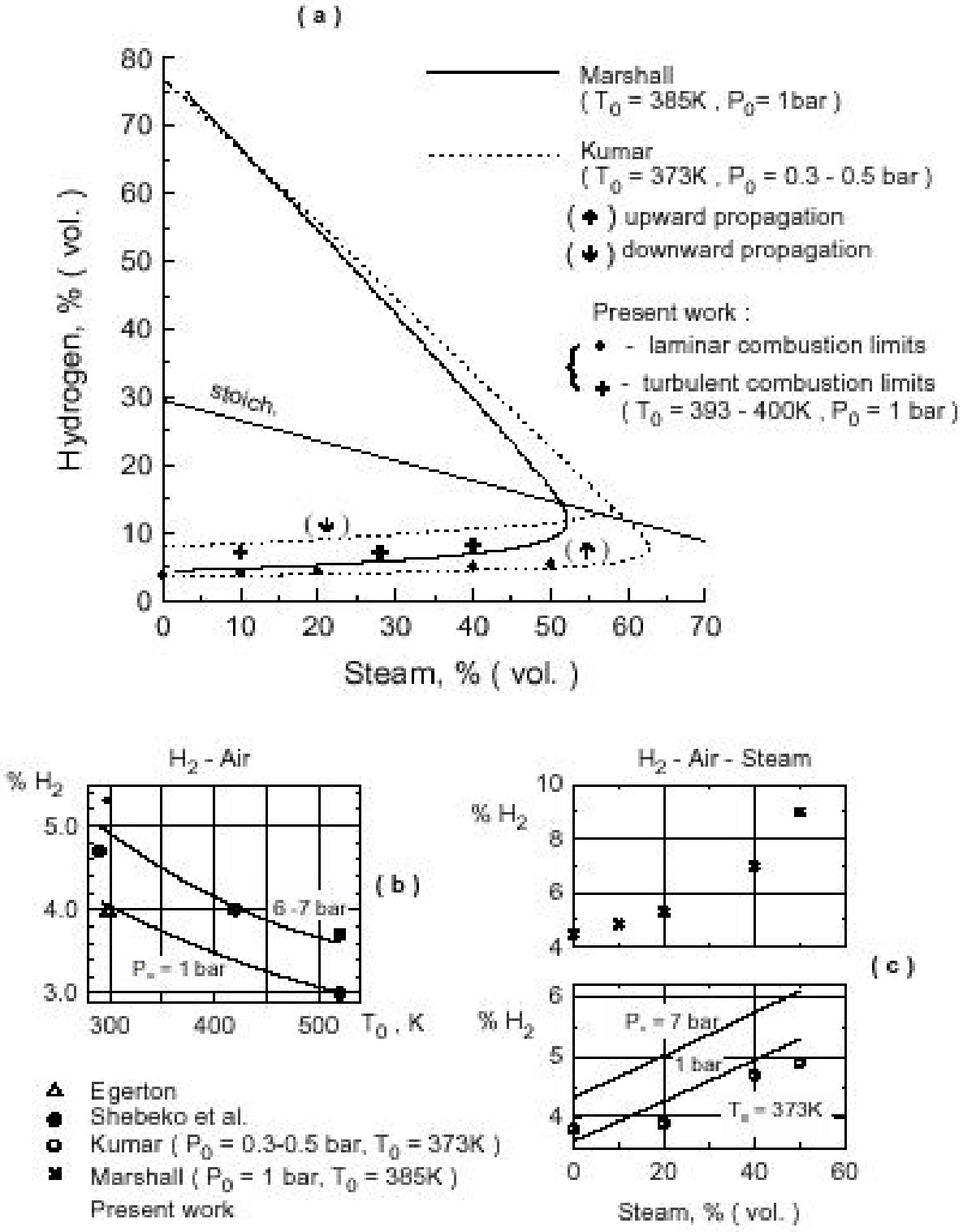

Fig. A 1.10. Flammability limits in H_2-air-steam mixtures (a) and dependence of limit hydrogen concentration on initial pressure and temperature in the lean H_2-air (b) and H_2-air-steam mixtures (c).

Figure A.1.5-1 Flammability limits in H_2-air-steam mixtures (a) and dependence of limit hydrogen concentration on initial pressure and temperature in the lean H_2-air (b) and H_2-air-steam mixutes (c).

APPENDIX B: LAMINAR AND TURBULENT FLAME PROPAGATION IN HYDROGEN-AIR–CARBON DIOXIDE MIXTURES AND DETONABILITY OF HYDROGEN-CONTAINING GASEOUS MIXTURES*

B.1 Laminar and Turbulent Flames in H_2-Air-CO_2 Mixtures

Appendix B presents experimental data and numerical predictions on burning velocities in lean hydrogen-air-carbon dioxide premixed flames at pressures ranging from 1 to 5 bar . The effect of pressure on the laminar and turbulent combustion has been studied using the spherical bomb method.

B.2 Laminar Premixed Flames

Research on laminar flame propagation in H_2-air-CO_2 mixtures is motivated by its applications in suppression of the explosion. In this investigation, the constant-volume bomb technique is used to determine the effect of CO_2 dilution on burning velocities and flammability limits in ternary mixtures of hydrogen, air, and carbon dioxide. Data on the laminar burning velocities may by used in computer codes for the calculation of dynamic pressures generated by turbulent flames. Moreover, we want to verify the possibility of numerical predictions of the laminar burning velocities at normal and elevated pressure and temperature conditions using the model of spherical flame propagation.

Data on the burning velocities of more reactive H_2-air-CO_2 mixtures were obtained using the method of a mathematical processing of pressure-time records [B.1, B.2].Listed in Table B.2-1 are some characteristic data on the laminar burning velocities in hydrogen-air mixtures diluted with carbon dioxide.. As can be seen from the table, a significant reduction in the burning velocity results when the CO_2 dilution takes place. The pressure influence on the burning velocity is weak.

B.3 Comparison Between Measured and Computed Data on Laminar Burning Velocities

B.3.1 Effect of Dilution with CO_2

Shown in Figure B.3.1-1 are the experimental data on the burning velocities measured in a spherical bomb by p(t) and r(t) methods for the lean H_2-air mixtures (ϕ = 0.39, 0.26, and 0.21) diluted with different amounts of CO_2. Mixture compositions are written here as

$$xCO_2 + (100 - x)\,[yH_2 + (1 - y)\,\text{air}],\ \phi = 2.38\,y / (1 - y)\ ,$$

where xCO_2 is the percentage CO_2, and y is the mole fraction of H_2 in an undiluted H_2-air mixture.

Numerical results are shown by solid lines. On the lower portion of the Figure B.3.1-1, the influence. of a dilution with CO_2 is illustrated in the form of the relative burning velocity S_u / S_{uo}, where S_{uo} is the burning velocity for undiluted mixtures (x = 0), and the equivalence ratio f is a parameter. This parameter varies from ϕ = 1 (stoichiometric mixtures) to ϕ = 0.21.

---

* Professor Boris E. Gelfand is the lead author of Appendix B.

As is evident from the graphs, the burning velocity depends on the values of f and f decreasing with a dilution. The relative value of the burning velocity decreases slower in the case of stoichiometric mixtures. Measured burning velocities are in close agreement with predicted ones.

B.3.2 *Effect of Pressure*

Figure B.3.2-1 shows the influence of initial pressure on the burning velocity in lean H_2-air-CO_2 mixtures (ϕ = 0.39 and 0.26) at two initial temperatures, 298 K and 393 K. According to the predicted results, the laminar burning velocity tends to diminish with a rise in pressure. This effect is similar to that in H_2-air-H_2O mixtures .The results show that the pressure exponent is negative at the overall range of pressure and temperature investigated here. Table B.3.2-1 lists the pressure exponents for lean hydrogen-air mixtures diluted with different amounts of carbon dioxide.

It can be seen in Table B.3.2-1 that the pressure exponent does not depend on temperature at the range of pressure from 1 to 3 bar and that it decreases with pressure rise. In the range of pressure 3 to 5 bar, the pressure exponent for the H_2-air mixtures (ϕ = 0.39) diluted with 20% CO_2 at 298 K (-0.72) is higher in absolute value than that at 393 K (- 0.59). Similar behaviour may be observed for the leaner mixture (ϕ = 0.26) diluted with 5% CO_2.

B. 3. 3 *Effect of Temperature*

Temperature dependence of the burning velocity in H_2-air-CO_2 mixtures at the range between 298 K and 473 K is illustrated in Figure B.3.3-1. We calculated the burning velocities at 1, 3, and 5 bars of initial pressure for H_2-air mixtures (ϕ = 0.39) diluted with 10% CO_2 and 20% CO_2 and for H_2-air mixtures (ϕ = 0.26) diluted with 5% CO_2. As is evident from the graphs, the burning velocity increases gradually with temperature. This dependence may be described by a power function $S_u = S_{uo}(T / T_o) \alpha$, where α is referred to as temperature exponent. T_o = 298 K is the standard temperature, and S_{uo} is the burning velocity at 298 K.

As can be seen (Table B.3.3-1), the temperature exponent depends on the mixture composition. It is higher for the mixtures with a low reactivity (ϕ = 0.26). The temperature exponent depends only slightly on pressure. Figure B.3.3-1shows the experimental data obtained by the method of pressure-time records in the explosion bomb at 3 and 5 bar. The influence of temperature on the burning velocity is similar to that obtained by computer simulation, but the measured burning velocities are higher than the computed burning velocities. The reason is that the influence of surface disturbances increases with pressure. In the model, the flame surface is accepted to be both smooth and spherical.

B.4 Turbulent Flames in H_2-Air-CO_2 Mixtures

The turbulent combustion rates of hydrogen-air and hydrogen-air-steam mixtures at the range of pressure and temperature relevant to the accident conditions have been investigated.. Experiments were conducted in a 2.5-L near-spherical explosion bomb. Turbulence was produced by four identical fans with rotational speeds up to 6000 rpm. The turbulent intensity ($U'\Sigma$) ranged up to about 10 m/s and was measured by a thermoanemometer . Non-homogenity of the turbulent intensity did not exceed 20%. During the flame propagation, pressure was measured with a high-sensitivity piezoelectric transducer mounted in the bomb wall. Shown in Figure B.4-1 are the experimental data on the dependence of the turbulent combustion rates S_T as a function of the turbulent intensity $U\iota S$ measured for hydrogen-air mixtures (ϕ = 0.39) diluted with various amounts of carbon dioxide up to 36% by volume. The influence of initial pressure is investigated by comparison of experimental data at 1 and 5 bar. These data are obtained at room temperature.

Figure B.4-2 shows the turbulent combustion rates S_T measured in the lean hydrogen-air-carbon dioxide mixtures (ϕ = 0.26 and ϕ = 0.21) as a function of the turbulent intensity $U¢s$ at atmospheric and elevated 3 bar pressure at room temperature. For comparison, the results of measurements of S_T in undiluted hydrogen-air mixtures at the same equivalence ratios ϕ = 0.26 and ϕ = 0.21 are plotted.

As would be expected , the turbulent combustion rates S_T far exceed the laminar burning velocities for the same mixtures. For the mixtures diluted with CO_2, the dependence of the turbulent combustion rate on the turbulence intensity has a maximum.

According to the experimental data presented in Figures B.4-1 and B.4-2, the variation of initial pressure from 1 to 5 bar does not affect the turbulent combustion rate. The turbulent combustion rates behave in a similar way in hydrogen-air, hydrogen-air-steam, and hydrogen-air-carbon dioxide mixtures.

B. 5 Flammability Limits of H_2-Air-CO_2 Mixtures

Practical considerations of safety require knowledge of the flammability limits for H_2-air-CO_2 mixtures. As mentioned earlier, there is a lack of data for mixtures of H_2-air-CO_2 at elevated pressures. Most of the experimental work reported in literature has been conducted at room temperature and at atmospheric pressure. In the case of elevated pressure-temperature conditions, experimental data exhibit a great deal of scatter for high inert component fractions.

Effect of pressure on the flammability limits of hydrogen-air-carbon dioxide mixtures is studied using the bomb method for the flammability determination. The maximum percentage of hydrogen at a given percentage of carbon dioxide in a hydrogen-air-carbon dioxide mixture, for which ignition by a sufficiently powerful source (about 1 to 2 J) did not cause a noticeable increase in pressure, was used as the practical definition of the limit. Such an approach has been used for hydrogen-oxygen-steam mixtures at various pressures.

Figure B.5-1 shows the experimental data measured in the spherical bomb of 4.2 L with central ignition at two initial pressures of 1 and 5 bar at 298 K . Ignition energy is equal to about 2 J. These data are presented on the domain (%CO_2) ÷ (% H_2) and are compared with the experimental data on the flammability limits by Coward and Jones [B.3] .Maximum pressures on combustion are shown in Tables B.5-1 and B.5-2.

It is apparent that the pressure rise from 1 bar to 5 bar diminishes the flammability of H_2-air-CO_2 mixtures in the vicinity of the quenching point. The lean branch of the flammability curve measured here coincides with the data obtained by Coward and Jones [B.3] . Measured limiting percentage of CO_2 is equal 57.6% by volume at atmospheric pressure and 51.2% at 5 bar.

B.6 Detonability of Hydrogen-containing Mixtures with CO_2, H_2O, and N_2 Additives

Detonation limits exist in tubes because of interaction between the flow in the reaction zone and tube walls. In a tube that is smaller in diameter than a certain limiting value (limiting tube diameter - D*) self-sustaining detonation becomes impossible. The computation of D* for detonation in hydrogen-contained air mixtures is described in Reference [B.4]. These results were compared with available data and experimental results in tubes of 24 mm and 41 mm inner diameter .The agreement between the calculated and the measured value of D* was good. Therefore, the same method and detailed kinetic scheme were used for limits of detonability in H_2-CO-air mixtures and multi-component H_2-CO-CO_2-H_2O-air systems relevant to accident scenario in a pressured-water reactor (PWR) .A distinguishing feature of the multi-component H_2–CO–CO_2–H_2O-air system is two different combustible gases, namely, H_2 and CO_2 in mixture. It is reasonable to display experimental and theoretical results for such a system with the help of a percent H_2 and a percent CO_2 diagram.

Shown in Figures B.6-1 (a) and (b) are examples of computation of detonability curves for H_2–air –CO_2 and H_2-air–H_2O mixtures in a tube of 41 mm diameter . A triangular domain is formed as a result of this computation . A inner part of this domain corresponds to detonable mixtures. The results of limiting concentration measurements at initial pressure p_0 = 1 bar and temperature T_0 = 298 K and 373 K for H_2-air–CO_2 mixture are plotted on the graph by open and solid squares .The increase of initial temperature tends to enlargement of the detonability area . The mitigation effect of steam is less than that of carbon dioxide. The influence of the tube's diameter on the detonability is conveniently illustrated in a diagram. Figure B.6-2 shows the limiting concentrations of H_2 and H_2O (the rest being air) for tubes of 10 mm, 41 mm and 300 mm inner diameter and at initial temperature 373 K. Kumar's experimental data [B.5] plotted (as a dotted line) for the flammability limits of the same mixtures shown relevant downward flame propagation.

Shown in Tables B.6-1 to B.6-3 are the concentrations of hydrogen and additive (CO_2 or N_2) in characteristic points of detonability diagrams. The points *A* and *B* correspond to lean (lower) and rich (upper) limits for non-diluted mixtures. The point *C* corresponds the *nose * of the detonability domain. The narrowing of the region of detonability in the case of dilution with nitrogen is accounted for in Figure B.6-3 by an upper branch. A lower branch of detonability curve does not change at dilution with N_2 up to 50% N_2.

The flammability limits can coincide with the detonability limits predicted for mixtures with large amounts of hydrogen. This coincidence is likely if tube diameter is great. In narrow channels the detonability area is narrower than the flammability area.

Specific features of detonability of mixtures with two-component fuel were verified by use H_2+ Air + CO + CO_2 systems . Figure B.6-4 shows the detonability diagram for that case. Percentage of CO_2 diluent is used as a parameter and percentage of air is known from material balance. The detonability domain at given tube diameter has the form of a * peninsula * with size dependent on amount of diluent in the mixture . Experimental points [B.4, B.13] are plotted on the diagram for case of undiluted mixture (solid circles) and for the variant of dilution by 10% CO_2 (solid squares). Calculated and measured data at p_0 = 1 bar and T_0 = 298 K show a reasonable agreement .The additional combustible gas (carbon monoxide) decreases the limiting concentration of hydrogen in the mixture proportionally the carbon monoxide concentration. This proportionality exists at small additions of CO to hydrogen. An additional set of the experimental data about limiting conditions of detonation propagation in tubes of different size is presented in Tables B.6-4 to B.6-7.

B.7 Ignition Limits of H_2 + Air + CO_2 and H_2 + Air + H_2O Mixtures by a Hot Gas Jet

The ignition limits of hydrogen–air mixtures diluted with steam or carbon dioxide have been studied as a function of mixture composition [B.14]. Ignition was produced by a hot transient jet emerging from the downstream end of a shock tube and entering a combustion chamber. The spurted gas was heated by a reflected shock wave between 750 K and 2800 K. The ejection velocity was subsonic. With an initial jet at 2600 K, the ignition area of H_2-air-CO_2 mixtures was larger than that of the H_2-air-H_2O mixtures. The ignition area was located inside the flammability range of these systems for rich mixtures. On the contrary, ignition limits and flammability limits were almost similar for lean mixtures.

B.8 References

[B.1] Laminar and Turbulent Flame Propagation in H_2 + Air + Steam Mixtures at Accident Relevant Pressure @ Temperature Conditions, ICh Ph RAS at INR FZK Research Report, 1995.

[B.2] Laminar and Turbulent Flame Propagation in H_2 + Air + CO_2 Mixtures at Accident Relevant Pressure @ Temperature Conditions, IChPh RAS at INR FZK Research Report, 1996.

[B.3] Coward and Jones

[B.4] B. Lewis and G. Elbe, Combustion, Flames and Explosions in Gases, 3rd ed., Academic Press, 1987, 739 p.

[B.5] G.L .Agafonov, O.E. Popov, A.Yu. Kusharin and B.E. Gelfand, Detonability of H_2 / CO / CO_2 / AIR mixtures, Combustion Science and Technology, Vol 135, 85–96, 1998.

[B.6] R.K. Kumar, Flammability limits of $H_2 – O_2$ – Diluent Mixtures, Journal of Fire Sciences, Vol 3, 1985, 245-262.

[B.7] G. Ciccarelli , J.L. Boccio, T. Ginsburg , C. Finfrock, L. Gerlach, K. Sato and A.M. Kinoshita, High-Temperature Hydrogen + Air + Steam Detonation Experiments in the BNL Small-scale Development Apparatus, BNL-NUREG-52414, NUREG /CR-6213, 1994.

[B.8] G. Ciccarelli , T. Ginsberg , J.L. Boccio , C. Finfrock , L.Gerlach and H. Tagawa, Detonation Sell Size Measurements of High Temperature H_2 + Air + Steam Mixtures, BNL-NUREG-52482, NUREG/CR–6391, 1997.

[B.9] S.R . Tieszen , M.P. Sherman , W.D. Benedick and J.E. Shepherd, Detonation Sell Size Measurements in H_2 + Air + Steam Mixtures, Progress in Astronautics and Aeronautics, AIAA Inc., NY, Vol 106, 1986, 205.

[B.10] Evaluation of H_2-Contained Mixtures Detonability, Report of IchPh RAS at INR FZK, 1996.

[B .11] W. Jost and H.Gg .Wagner, Influence of Various Parameters on Initiation, Stability and Limits of Detonation, AFOSR-78-35871979; AFOSR-79-0117A , 1981; AFOSR-TR-69-09, 1969.

[B.12] S.R . Tieszen, P.S . Martin, W.B. Benedick and M. Berman, Detonability of H_2- Air –Diluent Mixtures, NUREG/CR-4905, SAND–85-1263, 1986.

[B. 13] D.W. Stamps, W.B. Benedick and S.R. Tieszen, Hydrogen-Air–Diluent Detonation Study for Nuclear Reactor Safety Analyses, NUREG/CR-5525 SAND–89-2398, 1991.

[B.14] Detonability of Hydrogen-Containing Mixtures Under Conditions Relevant to PWR Accident Scenarios, ICh Ph RAS at INR FZK Research Report,1994.

[B.15] N. Djebaili, R Lisbet, C. Paillard and G. Dupre, Comparison Between Ignition of H_2–Air– O_2 and H_2–Air-H_2O Mixtures by a Hot Gas Jet, Shock waves @ Marseille, 2 , Proc. 19th ISSW (ed. R.Brun and L. Dumitrescu),1995, 149-154.

Table B.2-1 Laminar burning velocities in lean H_2-air-CO_2 mixtures

f	%H_2	%CO_2	S_u (cm / s)		
			1 bar	3 bar	5 bar
0.21	8	-	3.3		
0.21	7.6	5.0	2.1		
0.21	7.2	10	2.0		
0.26	10	-	20.2		
0.26	9.5	5	9.9		
0.26	9.0	10	6.5		
0.26	8.2	17.8	4.3	4.1	3.5
0.39	14	-	54		
0.39	12.6	10	30		
0.39	11.2	20	15		
0.39	9.8	29.7	3.3	3.7	3.4
0.59	17	15	69		

Table B.3.2–1 Pressure exponents for lean H_2-Air-CO_2 mixtures

Pressure range, bar	f = 0.39; 10% CO_2		f = 0.39; 20% CO_2		f = 0.26; 5% CO_2	
	298 K	393 K	298 K	393 K	298 K	393 K
1 - 3	-0.32	-0.30	-0.46	-0.42	-0.46	-0.44
3 - 5	-0.43	-0.43	-0.72	-0.59	-1.1	-0.59

Table B. 3.3-1 Temperature exponents for lean H_2-air-CO_2 mixtures

Temperature	**f = 0.39; 10% CO_2**			**f = 0.39; 20% CO_2**			**f = 0.26; 5% CO_2**		
range, K	1 bar	3 bar	5 bar	1 bar	3 bar	5 bar	1 bar	3 bar	5 bar
298 - 473	2.8	2.9	2.9	3.1	3.1	3.2	3.6	3.6	4.1

Table B.5-1 Relative pressure rise in H_2-air-CO_2 mixtures at T_o = 298 K and P_o = 1 bar

H_2 , %	5.0	5.3	6.0	6.55	7.2	8.0	8.9	10.9	15.0
CO_2 , %	33.2	50.0	53.4	55.2	56.4	57.6	57.6	55.6	52.0
$(P_e / P_o)_{exp}$	1.04	1.04	1.02	1.02	1.02	1.03	1.03	1.07	1.07

Table B.5–2 Relative pressure rise in H_2-air-CO_2 mixtures at T_o = 298 K and P_o = 5 bar

H_2 , %	5.45	6.55	8.0	8.95	15.0
CO_2 , %	46.4	50.4	51.2	50.4	44.8
$(P_e / P_o)_{exp}$	1.01	1.02	1.01	1.10	1.71

Table B.6-1 Percentage of H_2 and $C0_2$ (or N_2) in the characteristic points of the detonability diagrams in hydrogen-air-diluent mixtures at 298 K

Initial pressure, bar	**A, $\%H_2$**	**B, $\%H_2$**	**C, CO_2**	**C, $\%N_2$**
Tube diameter d = 2 cm				
1	18.0	57.8	113	35.0
3	18.8	60.0	13.3	35.0
5	18.2	61.6	15.2	36.9
Tube diameter d = 100 cm				
1	12.7	73.8	29.2	56.9
3	12.0	75.7	32.7	57.7
5	11.7	76.7	34.4	60.2

Table B.6-2 Percentage of H_2 and $C0_2$ (or N_2) in the characteristic points of the detonability diagrams in hydrogen-air-diluent mixtures at 400 K

Initial pressure, bar	A, $\%H_2$	B, $\%H_2$	C, CO_2	C, $\%N_2$
Tube diameter d = 2 cm				
1 3 5	14.3 16.1 16.0	64.4 65.7 67.1	160 173 19.2	46.3 44 1 44.8
Tube diameter d = 100 cm				
1 3 5	10.4 10.2 9.8	78.8 80.5 81.5	347 38.3 40.1	65.0 65.6 66.8

Table B.6-3 Percentage of H_2 and $C0_2$ (or N_2) in the characteristic points of the detonability diagrams in hydrogen-air-diluent mixtures at 500 K

Initial pressure, bar	A, $\%H_2$	B, $\%H_2$	C, CO_2	C, $\%N_2$
Tube diameter d = 2 cm				
1 3 5	10.9 13.1 13.6	70.0 71.5 72.5	21.7 22.1 23.8	56.2 567 53.6
Tube diameter d = 100 cm				
1 3 5	7.9 7.9 7.8	837 84.6 85.5	41 3 45.0 46.8	73 4 72.3 73.2

Table B.6-4 Near-detonability limit mixtures in tube Æ 100 mm [B.6]

Test [1]	$\%H_2$	$\%H_2O$	T [K]	Regime
312	30.27	24.77	500	DH
223	30.01	30.01	500	SH
314	29.92	19.96	300	DH
316	29.92	24.95	300	SH
148	16	-	300	DH
255	15	-	300	SH
284	12.04	-	500	DH
288	11.58	-	500	DH
348	9	-	650	DH
375	9	-	650	SH

DH – double-head detonation, **SH** – single-head detonation

Table B.6-5 Near-detonability limit mixtures in tube Æ 273 mm [B.7]

Test [1]	% H_2	% H_2O	T [K]	Regime
308	29.37	50	650	SH
310	17.26	30	650	DH
385	18.21	20	400	SH
389	9.86	15	650	SH
327	7.02	-	650	DH
317	7.39	-	650	SH
302	6.24	-	650	SH
110	9.9	-	500	DH
25	14.31	-	300	DH
232	13.83	-	300	DH
233	13.48	-	300	DH

DH – double-head detonation , **SH** – single-head detonation

Table B.6-6 LDL and RDL in H_2 + air mixtures

D	LDL	RDL	Ref.	Lab.
mm	% H_2	% H_2	-	-
100	15	-	[B.6]	BNL
273	13.5	-	[B.7]	BNL
430	13.5	70	[B.8]	SNL
300	13.5	70	[B.8]	Mc Gill
41	19	-	[B.9]	IchPh @ FZK
26	15	61	[B.0]	GU

Table B.6-7 LDL and RDL in SNL tests [B.6, B.7]

D	T	LDL	RDL	Ref.
Mm	[K]	% H_2	% H_2	-
430	293	13.5	70	[B.8, B.11]
430	373	13	-	[B.8, B.11]
430	293	11.6	74.9	[B.12]
430	373	9.4	76.9	[B.12]

LDL- lean detonability limit, **RDL** – rich detonability limit

BNL – Brookhaven National Laboratory (USA), **SNL** – Sandia National Laboratory (USA), **McGill** – McGill University (Canada) , **I ChPCh** – Institute of Chemical Physics RAS (Russian Federation) , **GU** – Göttingen university (Germany), **FZK** – Research Center Karlsruhe (Germany)

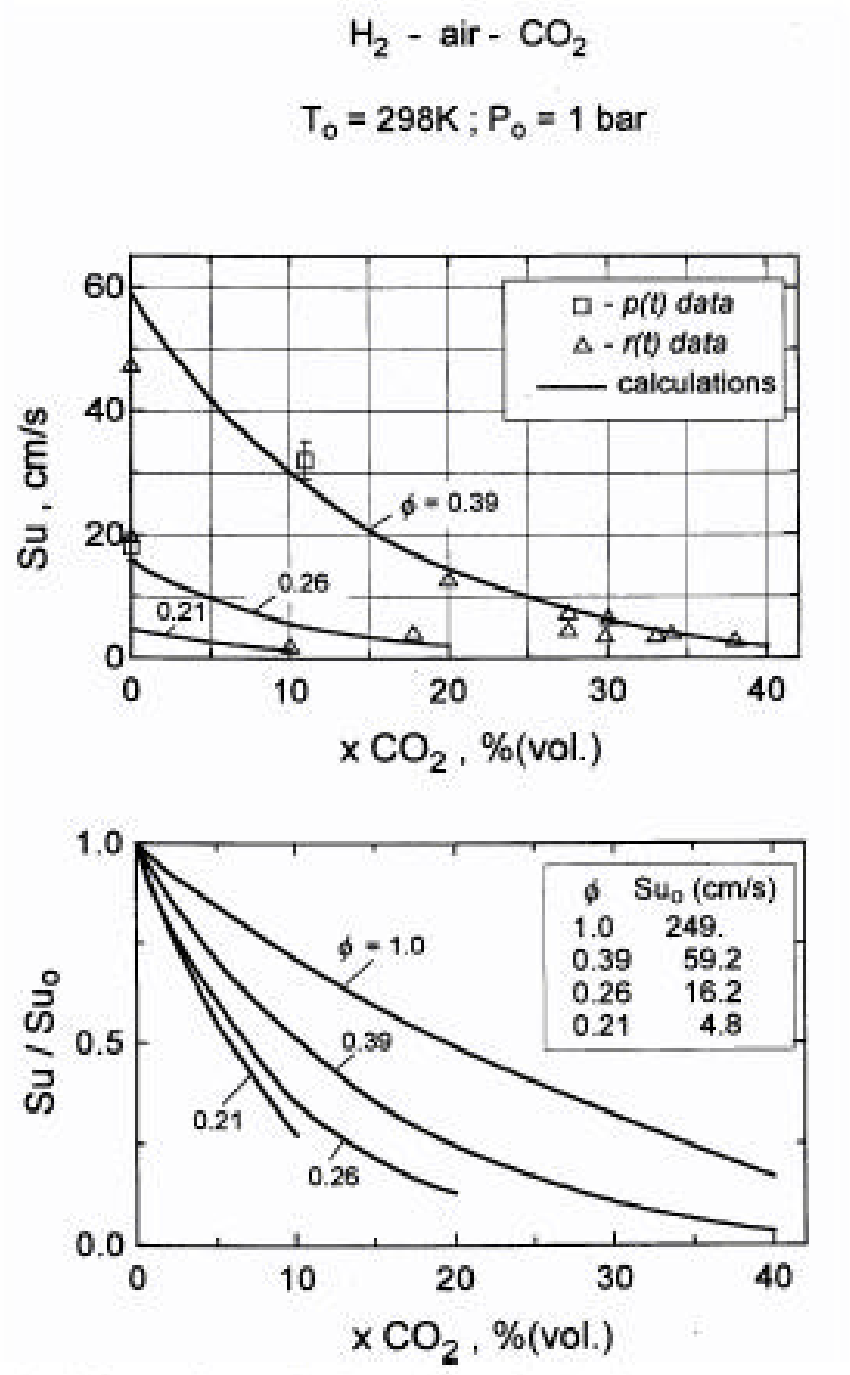

Figure A.2.1. The influence of CO_2 – dilution on the burning velocity

Figure B.3.1-1 The influence of CO_2 dilution on the burning velocity

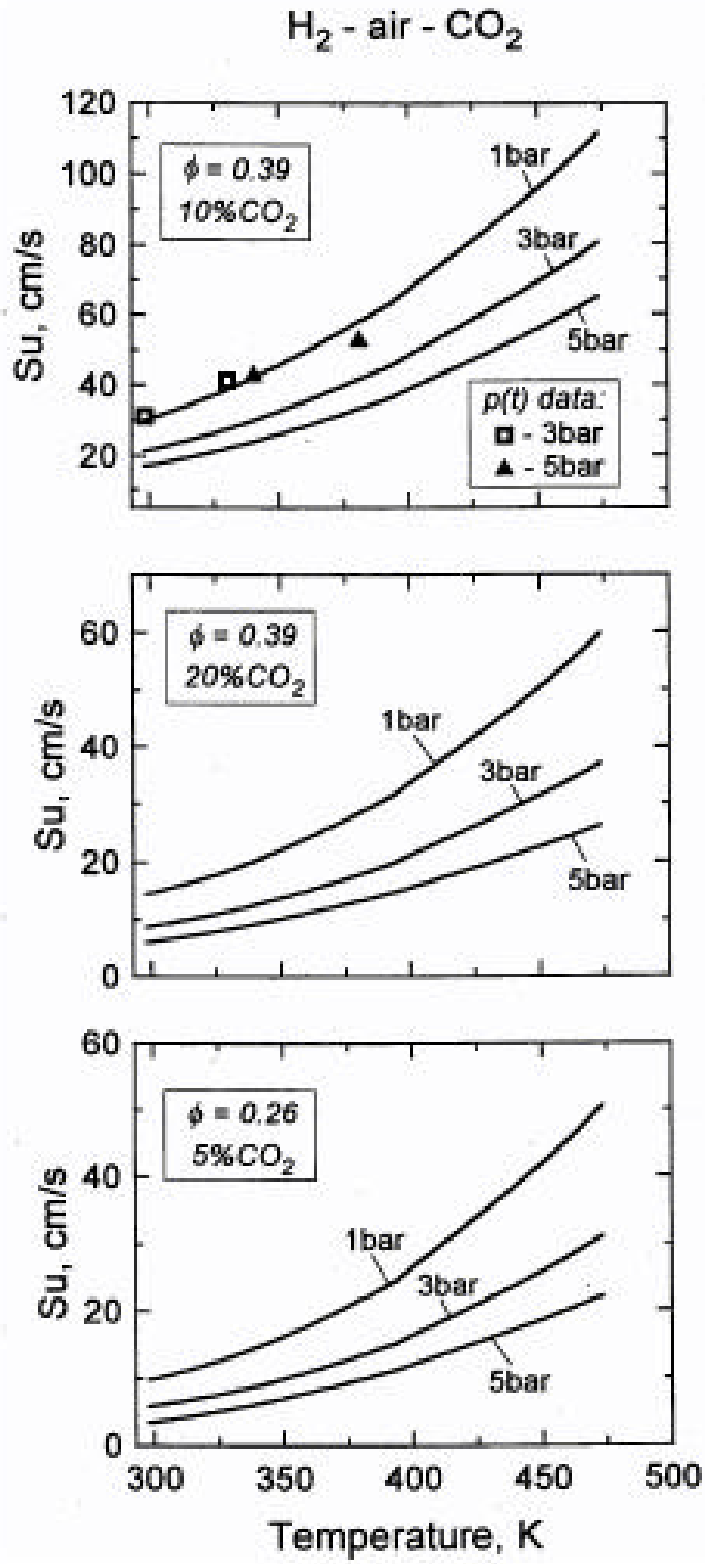

Figure A.2.3. The influence of temperature on the burning velocities in the H_2-air-CO_2 mixtures.

Figu
mixt

Figure B.3.3-1 The influence of temperature on the burning velocities in the H_2-air-CO_2 mixtures

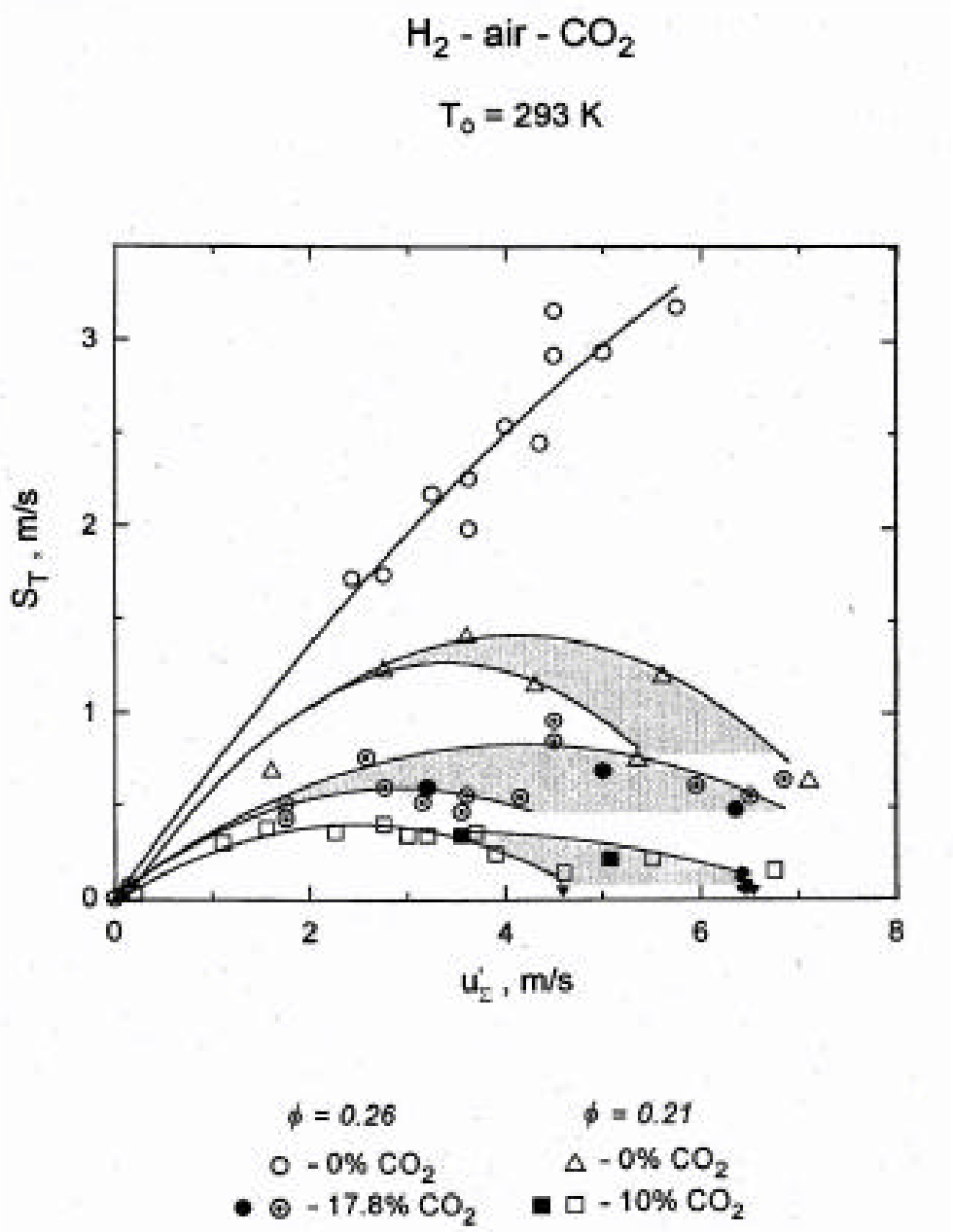

Figure A.2.4. Influence of turbulence intensity on the turbulent combustion rate S_T in the lean H_2-air-CO_2 mixtures. Open points: P_0=1 bar; solid points; P_0=3 bar.

Figure B.4-2 Influence of turbulence intensity of the turbulent combustion rate S_T in the lean H_2-air-CO_2 mixtures. Open points: P_0 = 1 bar; solid points; P_0 = 3 bar.

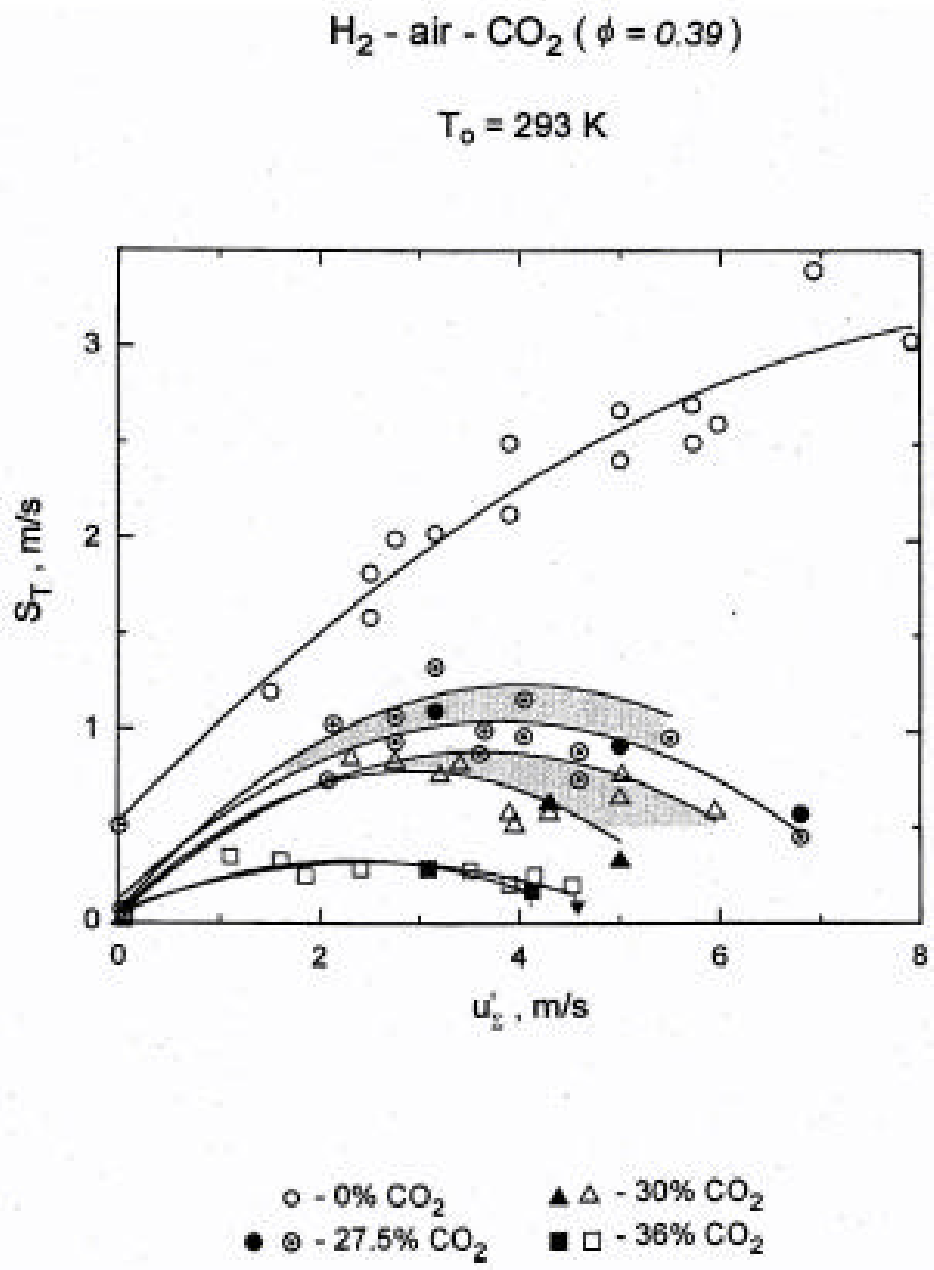

Figure A.2.5. Influence of turbulence intensity on the turbulent combustion rate S_T in the lean H_2-air-CO_2 mixtures. Open points: P_0=1 bar; solid points; P_0=5 bar.

Figure B.4-1 Influence of turbulence intensity on the turbulent combustion rate S_T in the lean H_2-air-CO mixtures. Open points: P_0 = 1 bar; solid points: P_0 = 5 bar.

Figure B.5-1 The influence of initial pressure on the flammability limits in H_2-air-CO_2 mixtures

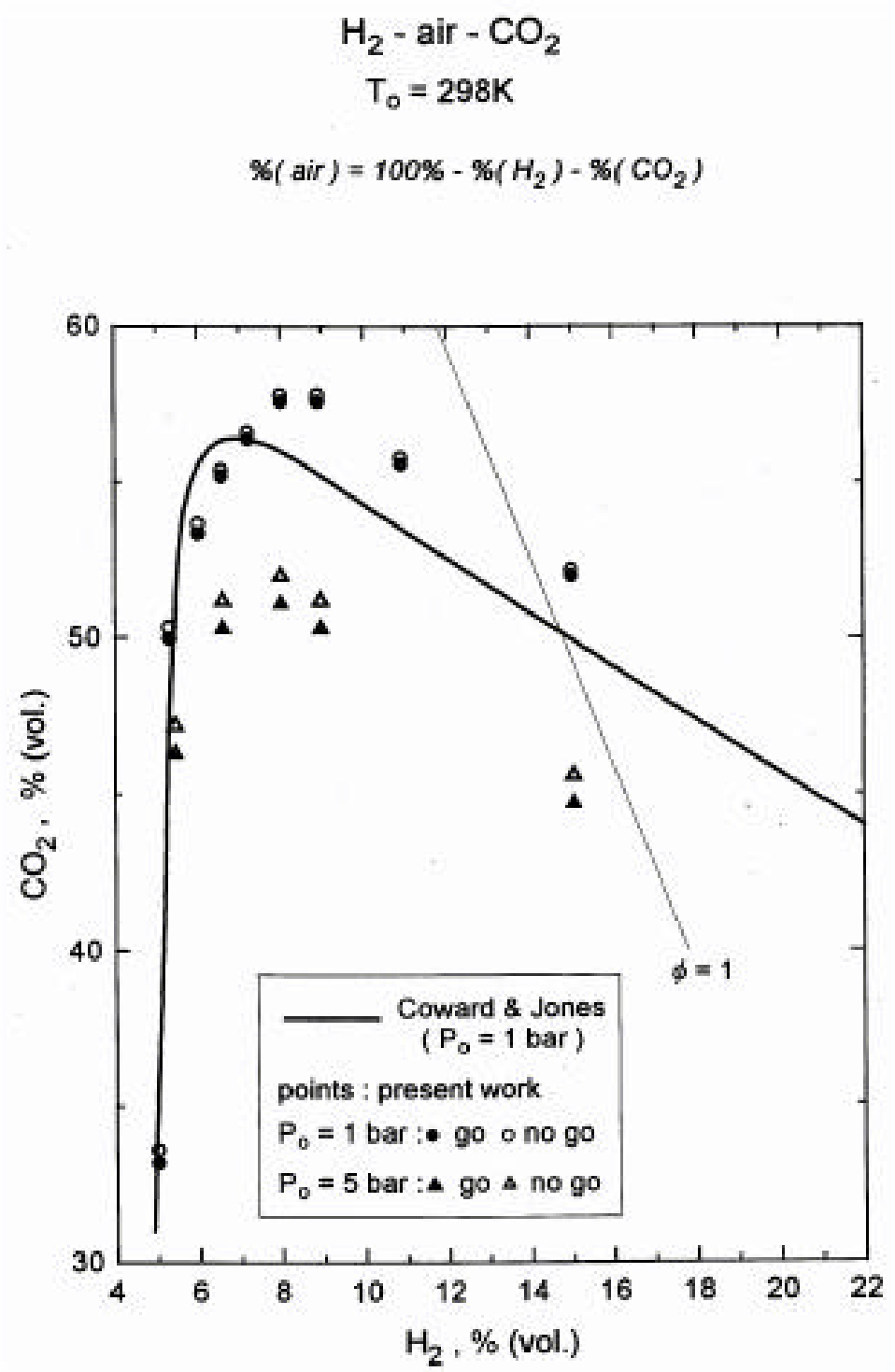

Figure A.2.6. The influence of initial pressure on the flammability limits in H_2-air-CO_2 mixtures.

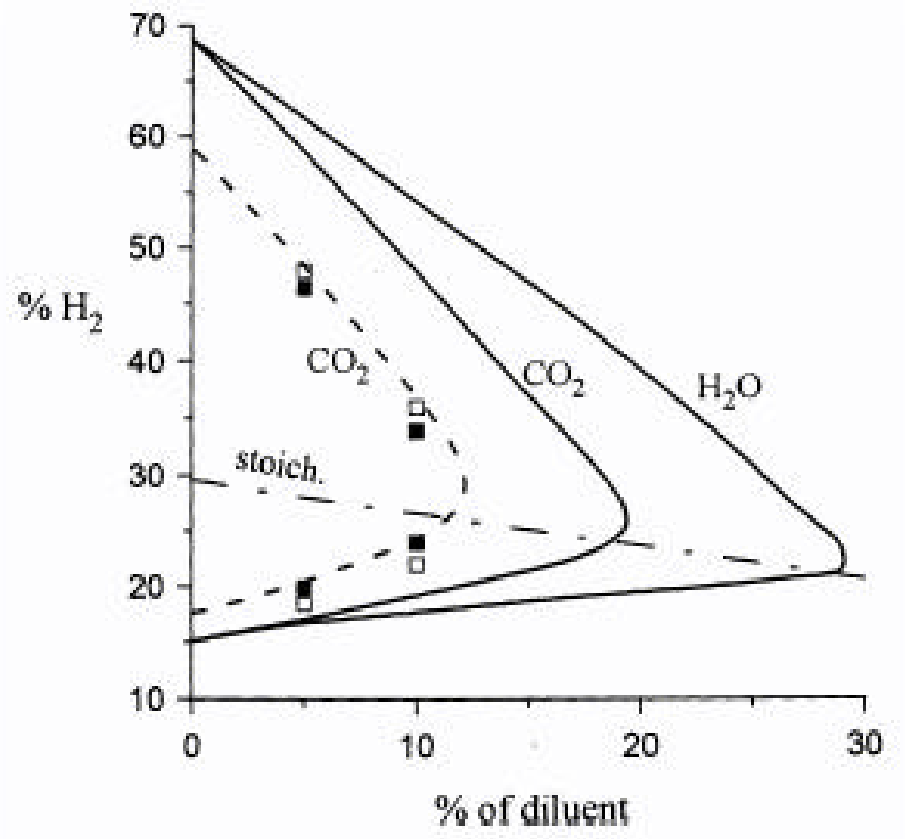

Figure A.2.7(a). Detonability diagram for H_2 + Air +CO_2 and H_2 + Air + H_2O mixtures at fixed tube diameter 41 mm.

Solid lines: T_0=373K; ρ_{air}=41.6mole/m^3.

Broken lines : T_0 = 298 K , P_0 = 1 bar.

Points: ■ - go , □ - no go.

Figure B.6-1a Detonability diagram for H_2 + air + CO_2 and H_2 + air + H_2O mixtures at fixed tube diameter 41 mm

Solid lines: T_0 = 373 K; r_{air} = 41.6 mole/m^3.

Broken lines: T_0 = 298 K; P_0 =1 bar.

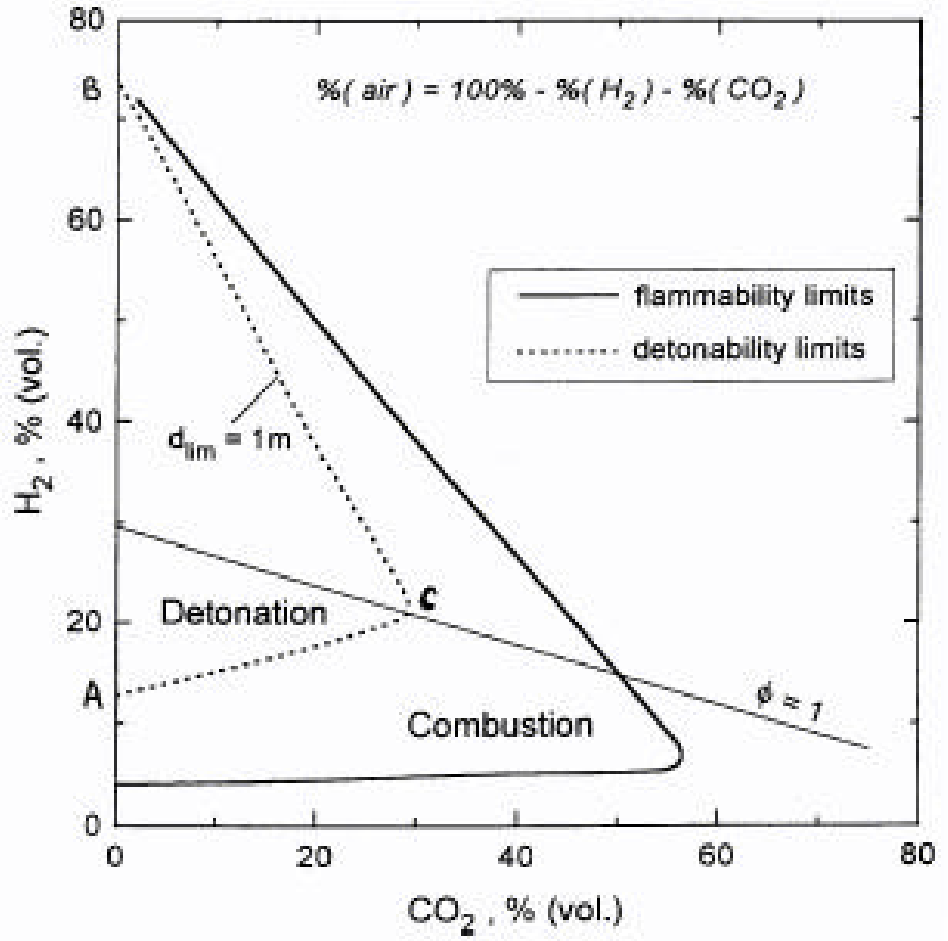

Figure A.2.7(b). Effect of CO_2 on suppression of detonation and deflagration in H_2 + Air mixtures.

Figure B.6-1b Effect of CO_2 on suppression of detonation and deflagration in H_2 + air mixtures

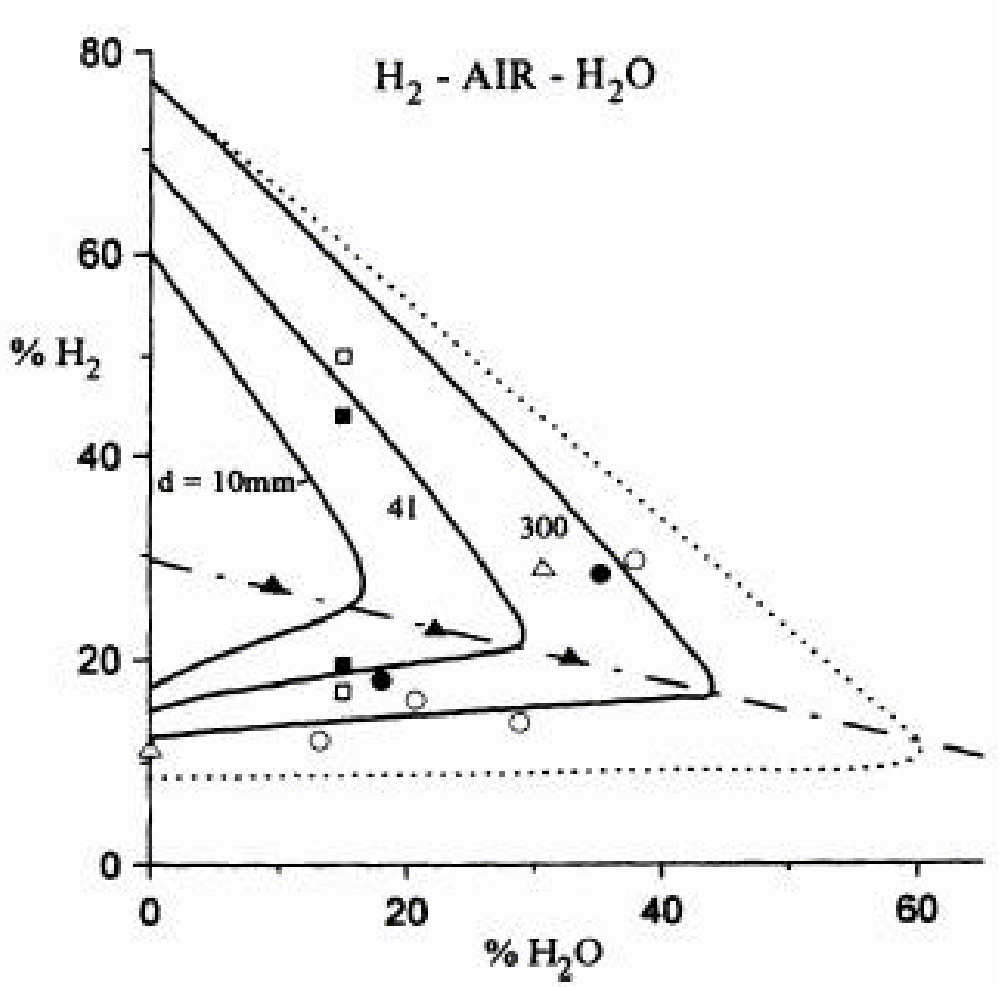

Figure A.2.8. Detonability diagram (solid lines) for H_2 + Air + H_2O mixtures. Calculations for different tube diameters: T_0 = 373 K : ρ_{air} = 41.6 mole/m^3 .

Points : measurements for d = 41 mm ; ■ - go , □ - no go.

Dotted line : experimental data for downward flame propagation limits at sub-atmospheric pressure P_0 = (0.2 ÷ 0.5) bar.

NUREX - 6213 (d=100 mm) ▲ - go △ - no go

NUREG - 6391 (d=270 mm) ● - go ○ - no go

Figure B.6-2 Detonability diagram (solid lines) for H_2 + air + H_2O mixtures. Calculations for different tube diameters: T_0 = 373 K; r_{air} = 41.6 mole/m^3.
Points: measurements for d = 41 mm;
Dotted line: experimental data for downward flame propogation limits at sub-atmospheric pressure P_0 = (0.2 ¸ 0.5) bar.
NUREX = 6213 (d = 100 mm)
NUREG = 6391 (d = 270 mm)

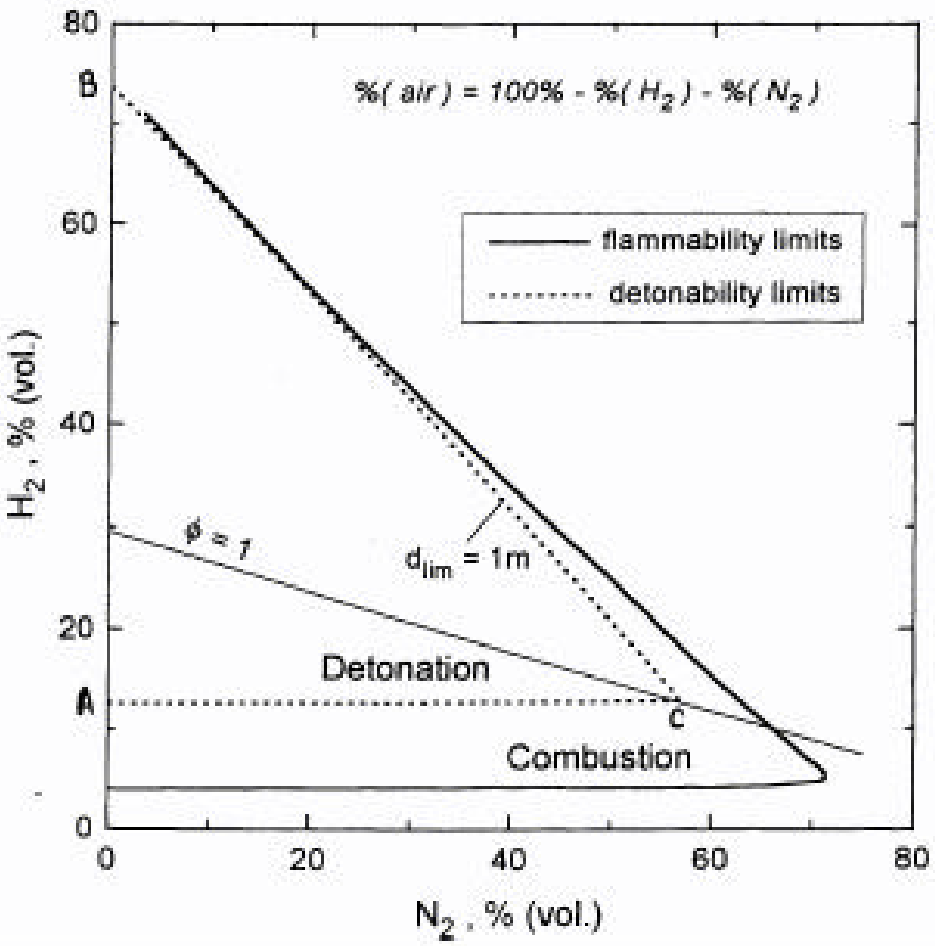

Figure A.2.9. Effect of N_2 on suppression of detonation and deflagration in H_2 + Air mixtures.

Figure B.6-3 Effect of N_2 on suppression of detonation and deflagration in H_2 + air mixtures

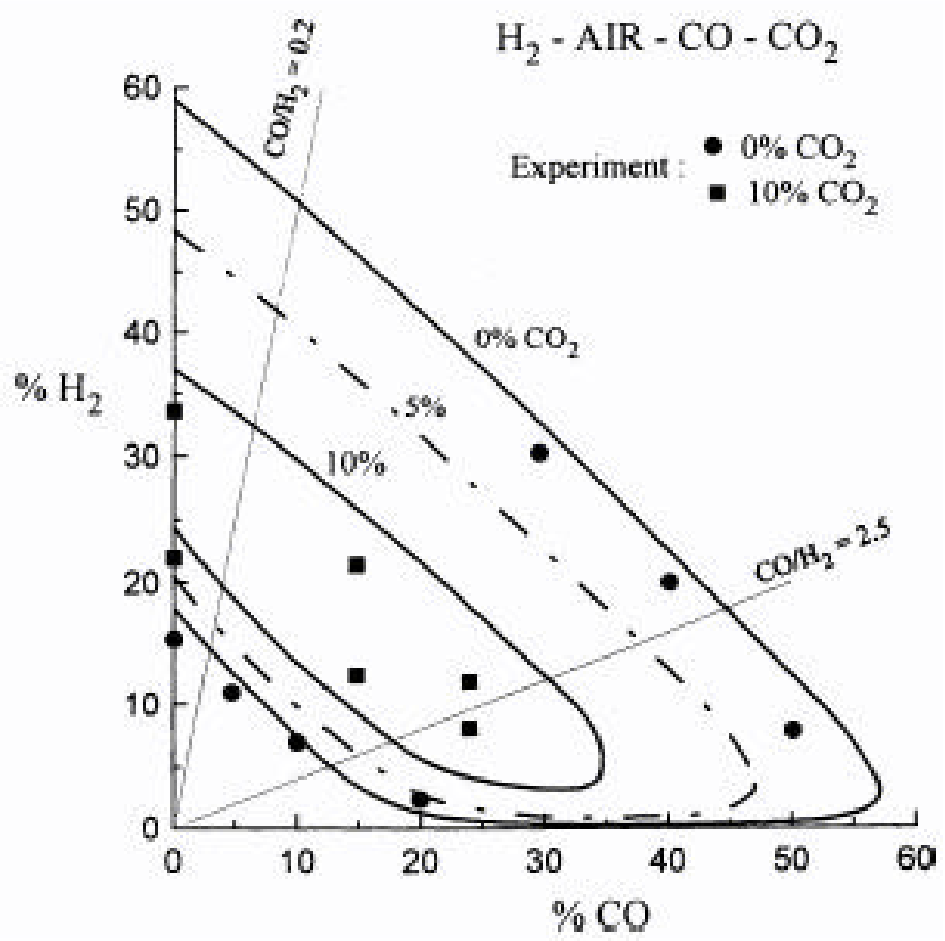

Figure A.2.10. Detonability diagram for H_2 + Air + CO + CO_2 mixtures with two-component fuel at fixed tube diameter 41 mm. Comparison of calculated and measured data at T_0 = 298 K, P_0 = 1 bar .

Figure B.6-4 Detonability diagram for H_2 + air + CO + CO_2 mixtures with two-component fuel at fixed tube diameter 41 mm. Comparison of calculated and measured data at T_0 = 298 K, P_0 = 1 bar.

APPENDIX C: THE TYPICAL REFLECTORS AND CRITICAL CONDITIONS OF DIFFERENT EXPLOSION PHENOMENA NEAR NON-FLAT REFLECTING SURFACES

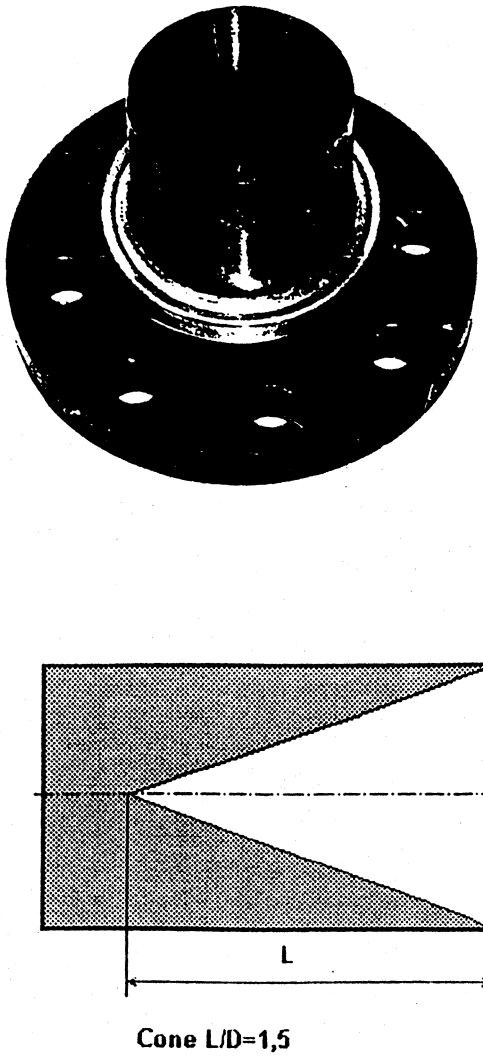

Figure C.3.1(a) Photograph and chart of the conical reflector with L/D = 1.5

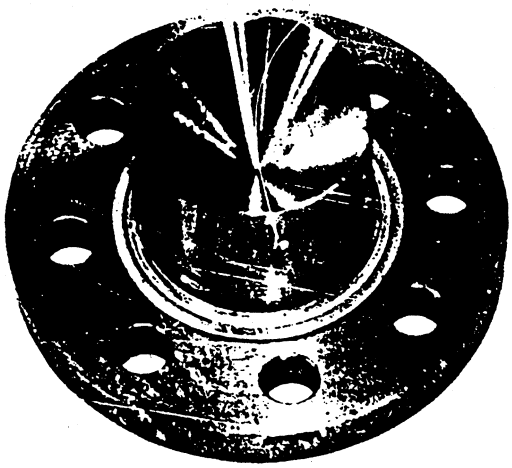

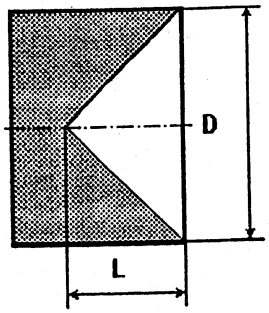

Cone L/D=0,5

Figure C.3.1(b) Photograph and chart of the conical reflector with L/D = 0.5

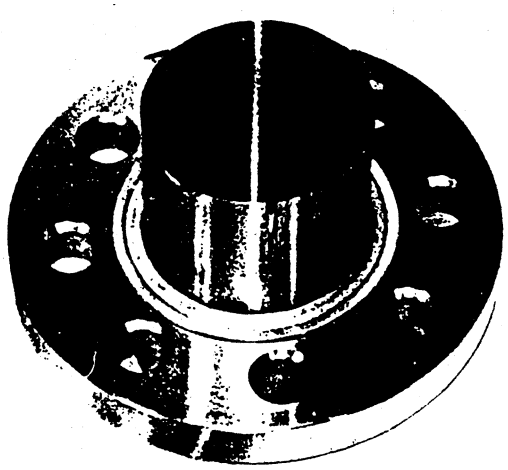

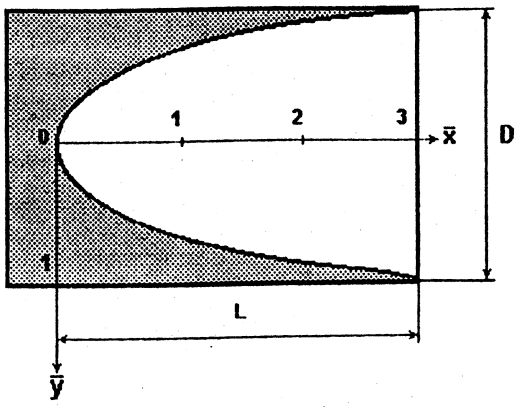

Figure C.3.1(c) Photograph and chart of the parabolic reflector with L/D = 1.5

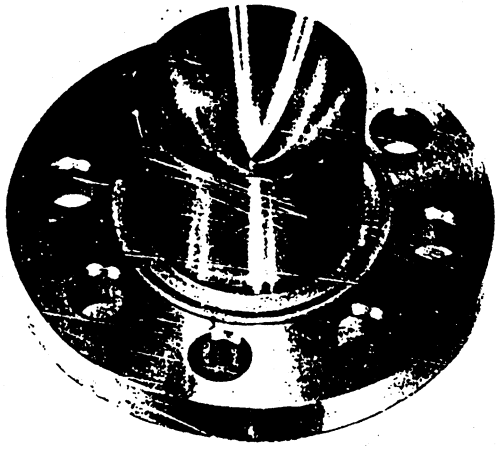

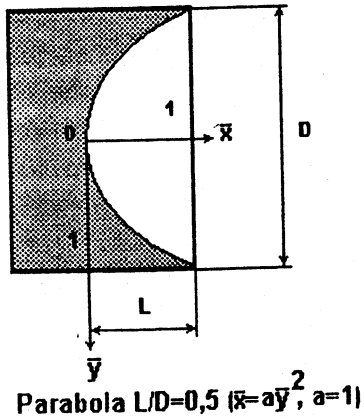

Figure C.3.1(d) Photograph and chart of the parabolic reflector with L/D = 0.5

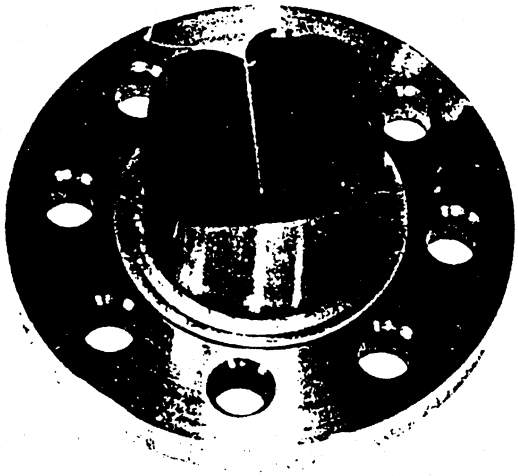

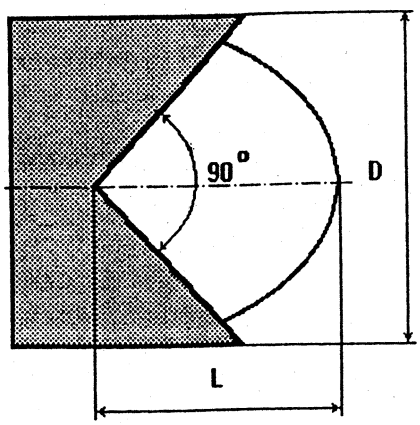

Pyramid L/D=0,7

Figure C.3.1(e) Photograph and chart of the pyramidal reflector with L/D = 0.7

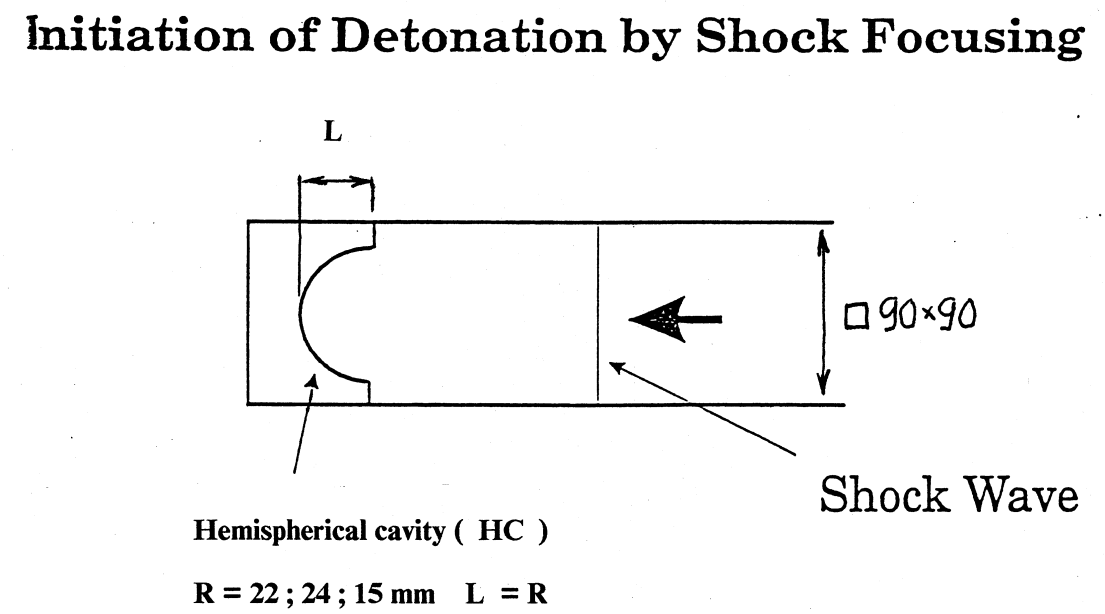

Figure C.3.1 (f) The chart of spherical reflector in [8]

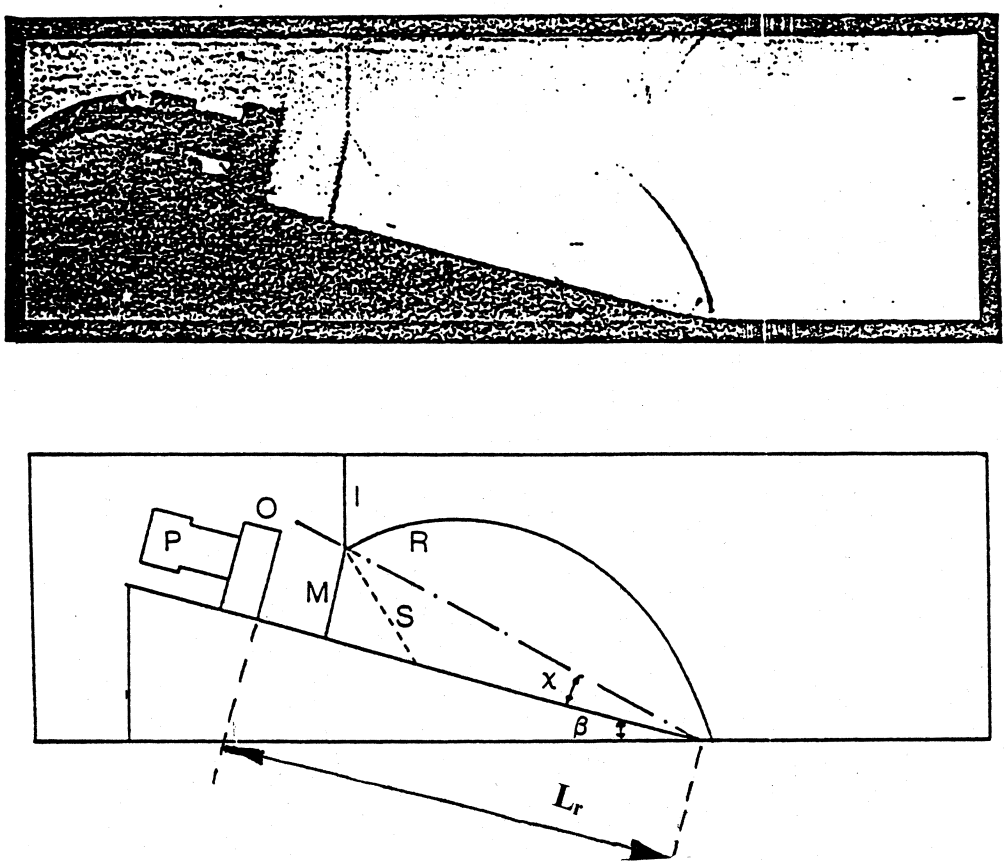

Figure C.3.2 The chart of wedge reflector in [6, 8].

I – incident shock, M – Mach steam, R – reflected shock, S – slip line, O – obstacle,

P – pressure gauge, $\beta = 0^0, 15^0, 30^0, 45^0$, $L_r = 12.7 \div 60$mm

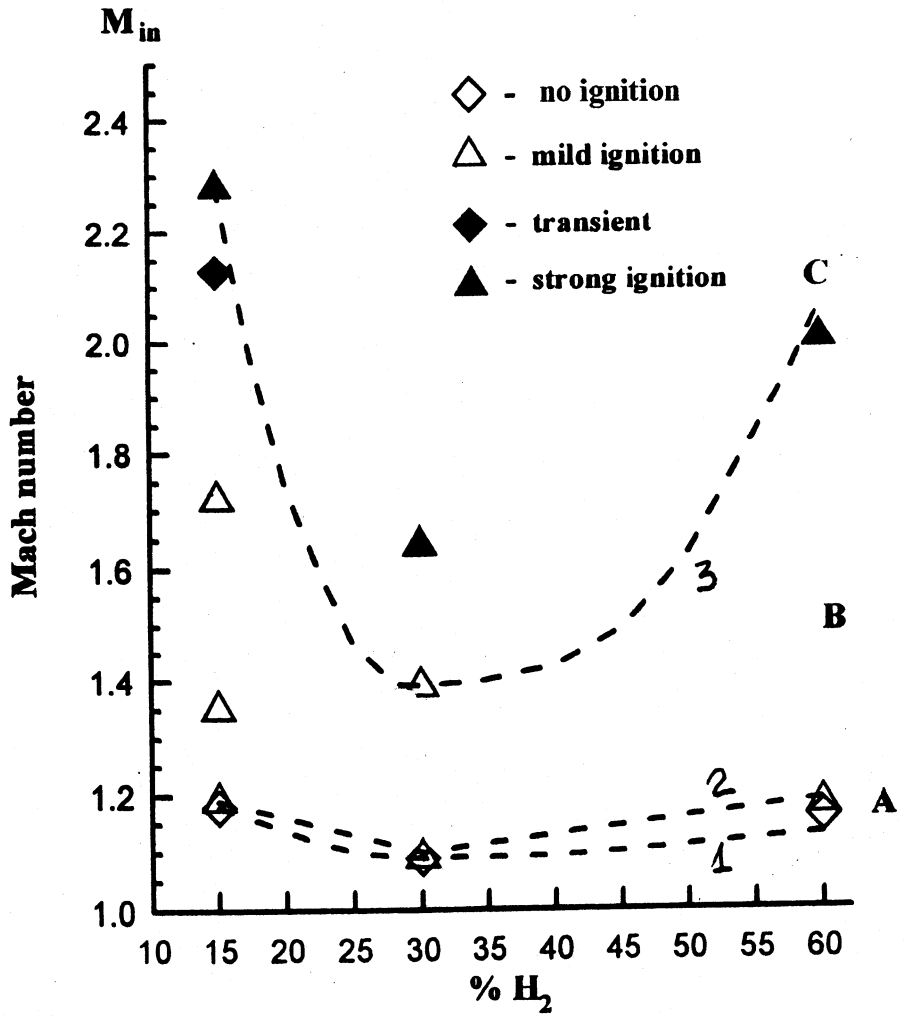

Figure C.3.3(a) The incident shock Mach numbers corresponding various modes of the selfignition vs. hydrogen-air mixture composition. Reflector Parabola L/D = 1.5. The curves 1, 2, 3 and regions A, B, C correspond to Figure 16 for the reflector Cone L/D = 1.5.

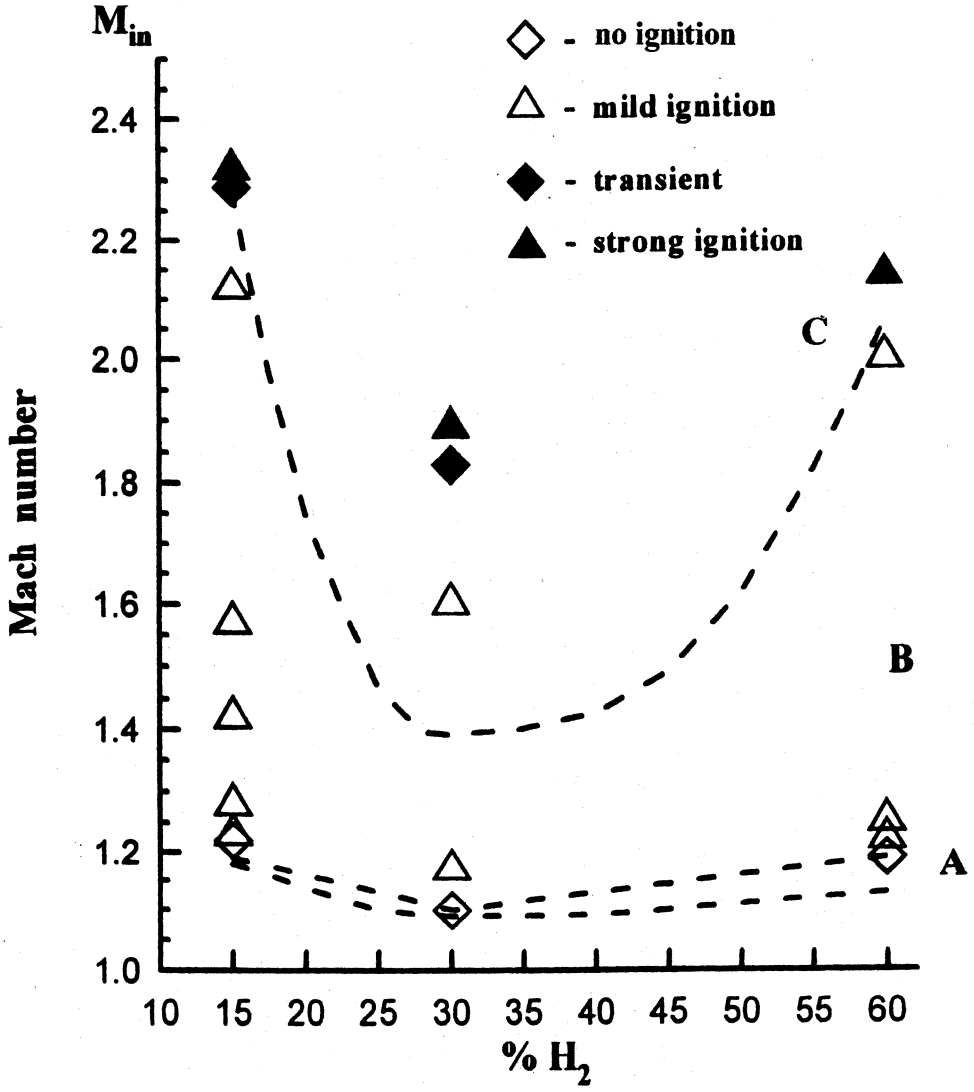

Figure C.3.3(b) The incident shock Mach numbers corresponding various modes of the self-ignition vs. hydrogen-air mixture composition. Reflector Cone L/D = 0.5. The curves 1, 2, 3 and regions A, B, C correspond to Figure 16 for the reflector Cone L/D = 1.5.

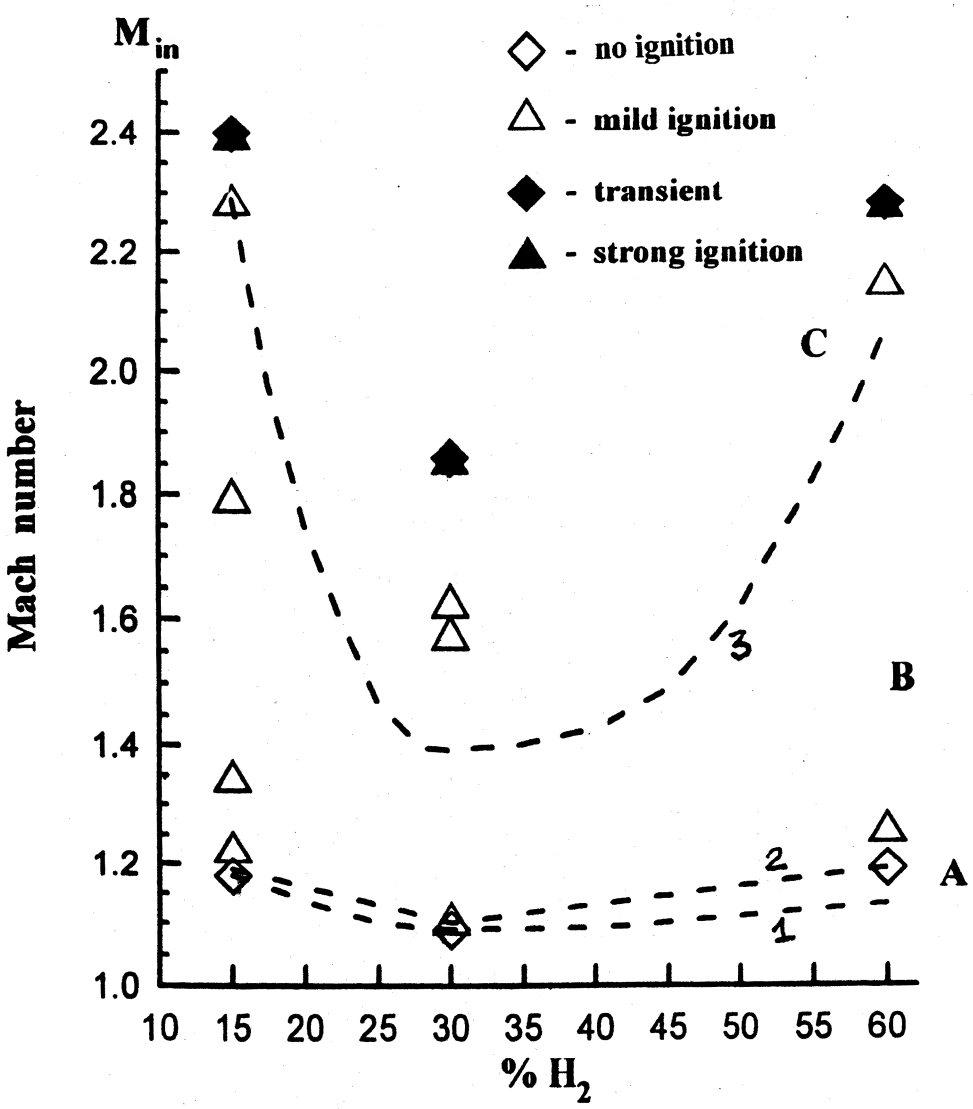

Figure C.3.3(c) The incident shock Mach numbers corresponding various modes of the self-ignition vs. hydrogen-air mixture composition. Reflector Parabola L/D = 0.5. The curves 1, 2, 3 and regions A, B, C correspond to Figure 16 for the reflector Cone L/D = 1.5.

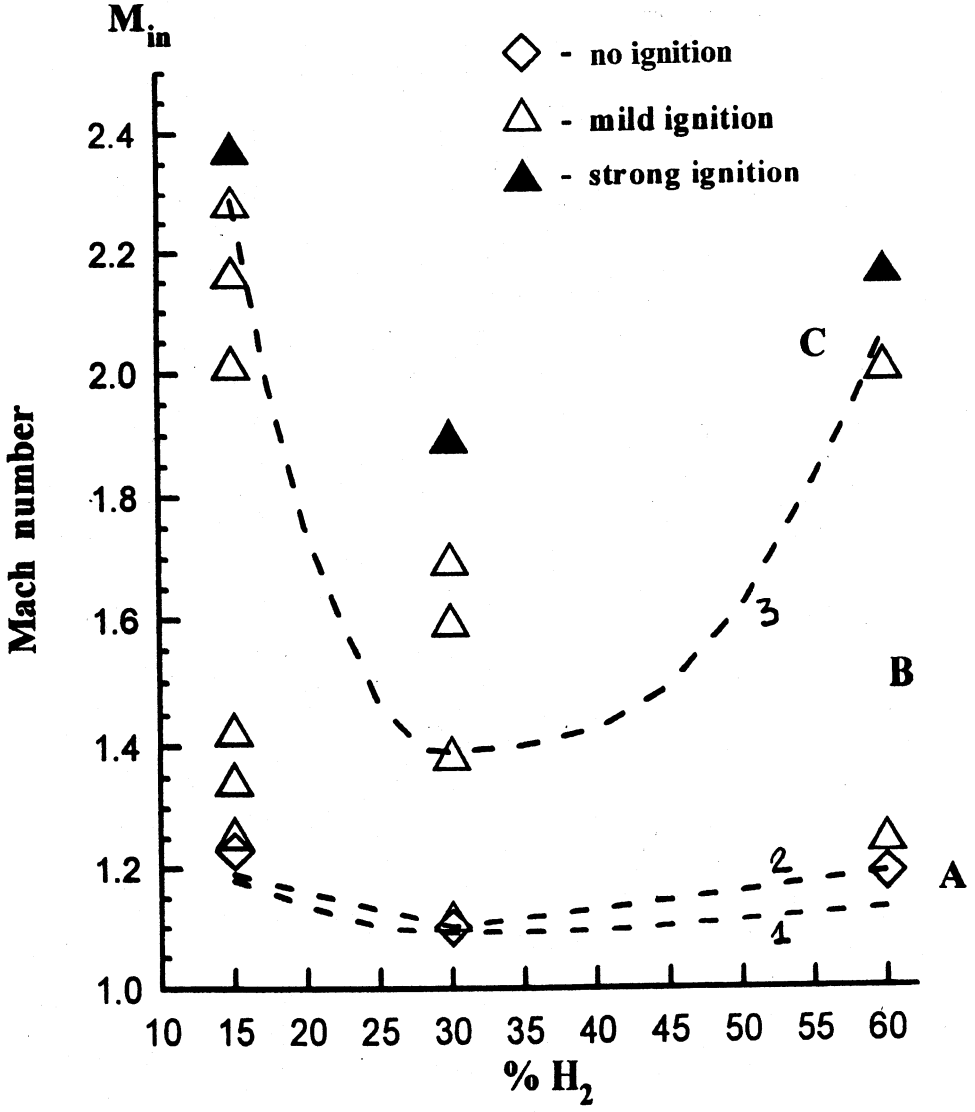

Figure C.3.3(d) The incident shock Mach numbers corresponding various modes of the self-ignition vs. hydrogen-air mixture composition. Reflector Pyramid L/D = 0.5. The curves 1, 2, 3 and regions A, B, C correspond to Figure 16 for the reflector Cone L/D = 1.5.

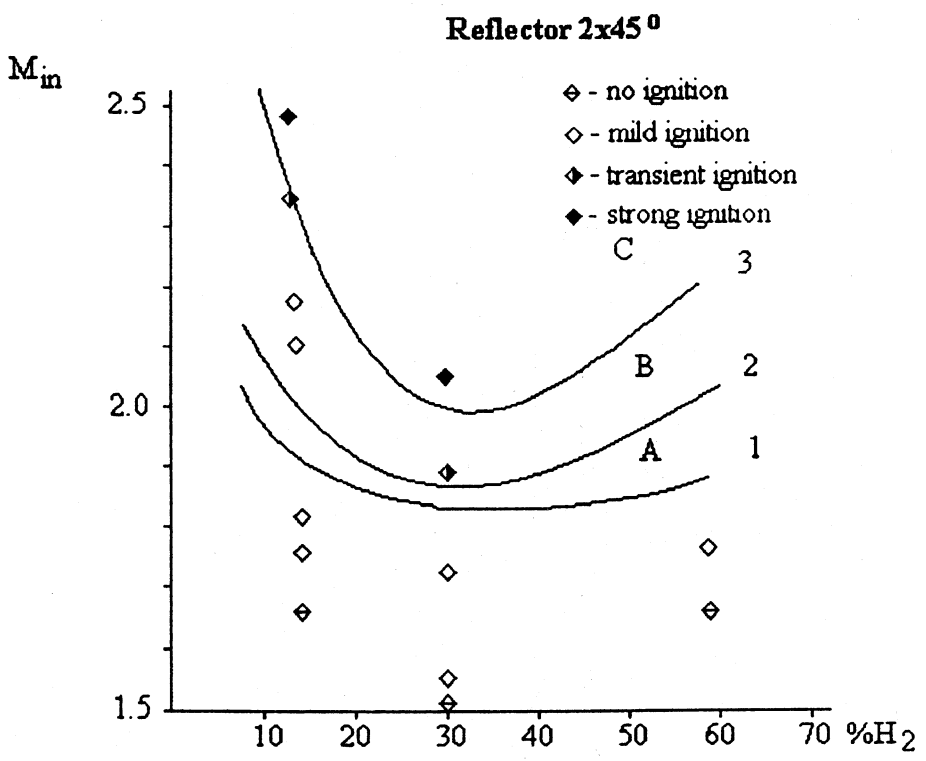

Figure C . 3 . 4(a) The critical incident shock Mach number vs. the H_2-air mixture composition, reflector 2 x 45^0. The regions A, B and C, and the curves 1, 2 and 3 correspond to Figure 22 for reflector R17.

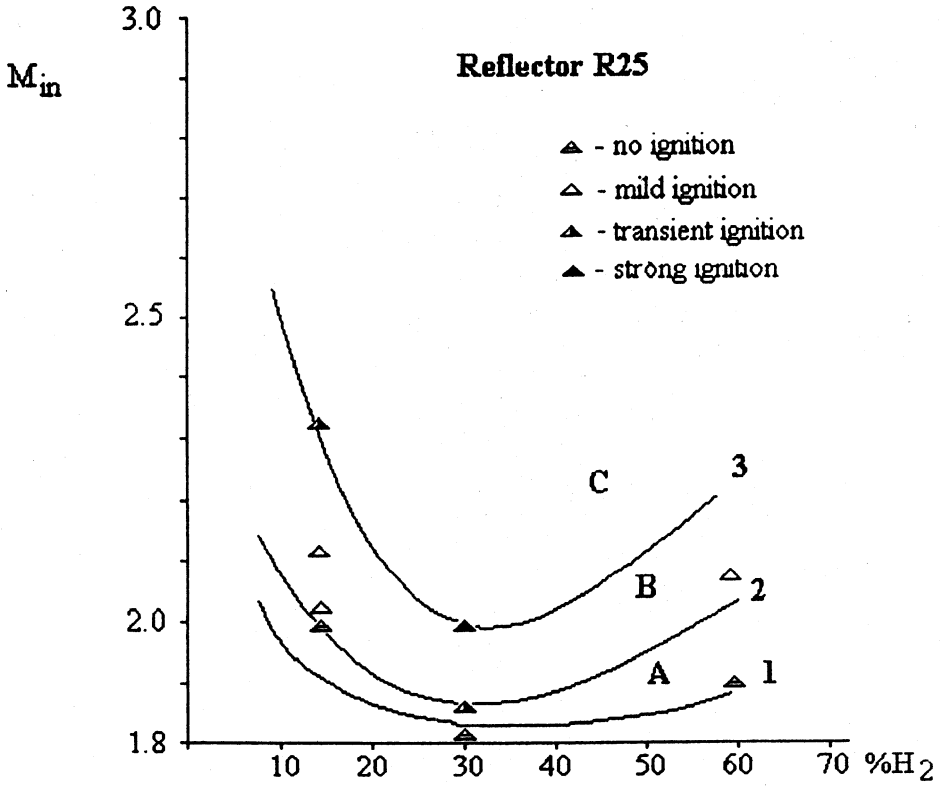

Figure C . 3 . 4(a) The critical incident shock Mach number vs. the H_2-air mixture composition, reflector R25. The regions A, B and C, and the curves 1, 2 and 3 correspond to Figure 22 for reflector R17.

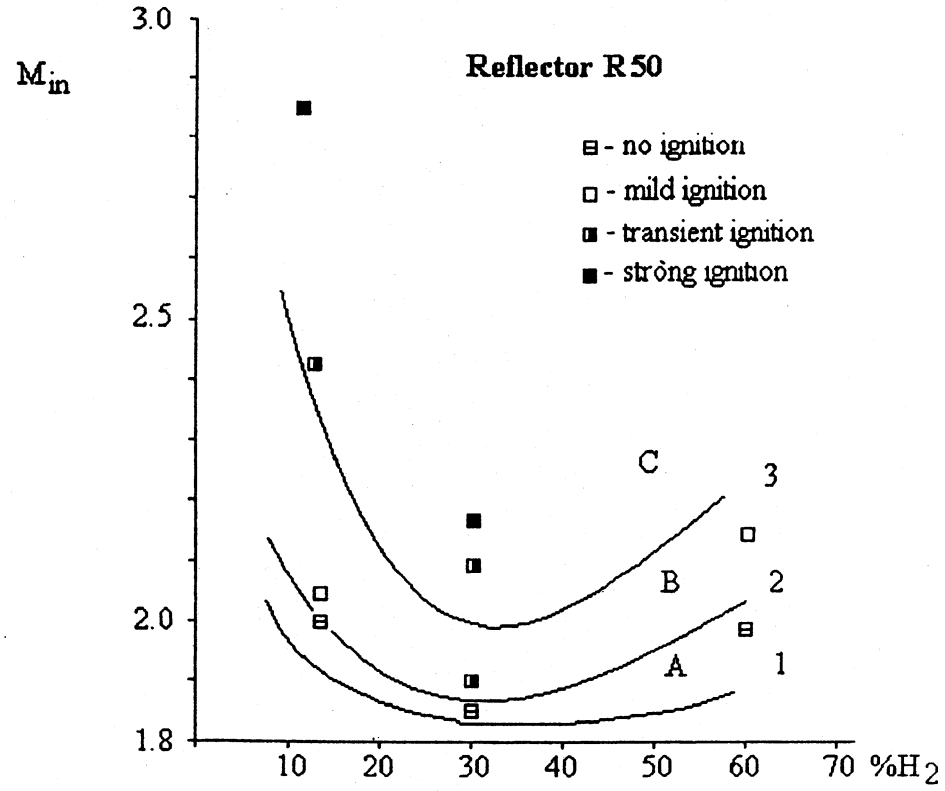

Figure C .3.4(a) The critical incident shock Mach number vs. the H_2-air mixture composition, reflector R50. The regions A, B and C, and the curves 1, 2 and 3 correspond to Figure 22 for reflector R17.

APPENDIX D: DETONATION CELL SIZE DATA*

D.1 Experimental Data

Hydrogen-air-steam mixtures at elevated initial temperatures and pressures are typical compositions for severe accident conditions in a nuclear containment building. Most of the detonation cell size data for these mixtures are given in References [D.1 to D.7], and are collected in detonation database [D.8], which is also available on the Web at the URL **http://www.galcit.caltech.edu/~jeshep/detn_db/html**. For the system under consideration, the detonation cell size is a function of four main variables: hydrogen concentration, steam concentration, initial temperature, and pressure. Experimental data for detonation cell size for hydrogen-air-steam mixtures at normal initial pressure are presented in Tables D.1-1 and D.1-2. Some data are given in Figures D.1-1 to D.1-4. Considerable data spread for the same initial conditions can be found in these tables and figures; it reflects the accuracy of the cell size measurements. Some values for the same initial conditions differ by a factor of 3, but this is an extreme deviation. The general impression is that the accuracy of the data is within a factor of 2 or so.

Experimental data on the cell size are available only for some particular compositions and initial conditions. These measurements do not permit direct estimation of the cell size for arbitrary compositions and initial conditions typical of severe accidents. Analytical or numerical tools are necessary that can give reliable values of detonation cell sizes for accident analyses. Different approaches have been used to develop the methods for estimation of the cell size data.

One of the approaches was based on fitting of experimental data by an analytical function [D.9]. If the accuracy of such an approximation falls within the range of experimental data, a corresponding analytical function can be used for interpolation of the detonation cell size data. It is clear that such a fit can be used only within the range of experimental data. Extrapolation of the fitted function beyond the range of measurements cannot give reliable values. One of the analytical functions giving the least deviation among other simple expressions is given in Section D.2.

Another approach was based on analysis of a correlation of reaction zone widths calculated from chemical kinetic models with experimental detonation cell sizes [D.10]. This approach allows estimations of detonation cell sizes for mixture compositions that differ from hydrogen-air-steam mixtures. Examples are mixtures with reduced oxygen content (compared with that in air), and multi-component mixtures such as H_2-O_2-N_2-H_2O-CO_2. Both of the above examples can be important for safety analyses, but no experimental data are available, and simple interpolation methods cannot be used. A short description of this approach and its limitations are given in Section D.3.

* Dr. Sergei B. Dorofeev is the lead author for Appendix D.

Table D.1-1 Detonation cell size data for hydrogen-air-steam mixtures at normal initial pressure. Data for spin detonations are also given, assuming $\lambda = \pi d$.

H_2 (dry) (vol %)	T (K)	H_20, (vol %)	λ (cm)	Ref.	H_2 (dry) (vol %)	T (K)	H_20 (vol %)	λ (cm)	Ref.
Data for T ≈ 300 K					**Data for elevated temperatures**				
11.65	296	0.00	135.2	D.2	9.42	375	0.00	135.0	D.2
12.00	300	0.00	135.2	D.2	10.40	375	0.00	135.2	D.2
12.34	300	0.00	135.2	D.2	11.30	375	0.00	135.2	D.2
13.48	300	0.00	42.4	D.4	12.48	376	0.00	30.5	D.2
13.58	300	0.00	121.5	D.1	13.14	373	0.00	44.4	D.2
13.78	300	0.00	119.6	D.1	14.88	370	0.00	15.0	D.2
13.78	300	0.00	61.9	D.1	17.87	375	0.00	3.8	D.2
13.83	300	0.00	42.4	D.4	20.00	370	0.00	2.4	D.2
13.98	300	0.00	63.6	D.1	29.64	375	0.00	0.7	D.2
13.98	300	0.00	56.3	D.1	29.75	371	0.00	2.0	D.2
14.21	300	0.00	46.6	D.1	45.91	374	0.00	1.4	D.2
14.31	300	0.00	42.4	D.4	56.10	374	0.00	3.7	D.2
14.54	300	0.00	33.6	D.1	76.00	375	0.00	135.2	D.2
14.57	300	0.00	41.5	D.1	76.98	375	0.00	135.2	D.2
14.89	300	0.00	24.8	D.4	29.78	375	5.00	2.0	D.2
14.93	300	0.00	18.7	D.4	20.12	375	9.10	18.4	D.2
14.99	300	0.00	33.8	D.1	63.97	375	9.80	61.0	D.2
15.00	300	0.00	25.0	D.4	17.23	376	9.90	47.0	D.2
15.08	300	0.00	30.4	D.1	45.74	375	10.50	4.2	D.2
15.30	300	0.00	29.9	D.1	29.75	375	11.50	2.8	D.2
15.36	300	0.00	30.6	D.1	30.67	375	14.90	4.5	D.2
15.36	300	0.00	26.2	D.1	30.60	374	15.00	5.0	D.2
15.50	300	0.00	26.0	D.4	45.67	376	19.80	29.0	D.2
15.55	300	0.00	35.6	D.1	26.07	375	20.10	25.0	D.2
16.00	300	0.00	24.5	D.5	30.16	376	20.10	16.5	D.2
16.20	300	0.00	23.0	D.4	21.91	375	20.30	100.0	D.2
16.50	300	0.00	18.3	D.5	28.10	375	29.90	127.0	D.2
17.00	300	0.00	13.0	D.4	30.01	375	29.90	65.0	D.2
17.00	300	0.00	16.2	D.5	38.96	375	29.90	50.0	D.2
17.22	300	0.00	9.5	D.4	29.67	375	35.40	135.2	D.2
17.24	297	0.00	7.6	D.2	29.57	375	37.00	135.2	D.2
17.29	300	0.00	9.3	D.4	29.75	375	38.80	135.2	D.2
17.36	300	0.00	14.0	D.5	17.81	400	10.00	30.5	D.4
17.50	300	0.00	12.4	D.5	30.00	400	10.00	1.7	D.4
17.50	300	0.00	8.9	D.4	30.00	400	10.00	1.5	D.4
18.00	300	0.00	11.1	D.5	18.21	400	20.00	84.8	D.4
18.60	300	0.00	8.9	D.5	30.00	400	20.00	17.0	D.4
19.00	300	0.00	8.0	D.5	29.88	400	25.00	16.2	D.4
19.20	300	0.00	7.6	D.5	30.23	400	25.00	21.4	D.4
19.91	300	0.00	2.7	D.4	9.90	500	0.00	42.4	D.4

Table D.1-1 (continued)

H_2 (dry) (vol %)	T (K)	H_20 (vol %)	λ (cm)	Ref.	H_2 (dry) (vol %)	T (K)	H_20 (vol %)	λ (cm)	Ref.
Data for T ≈ 300 K					**Data for elevated temperatures**				
20.00	300	0.00	5.5	D.5	10.87	500	0.00	42.9	D.4
20.00	300	0.00	4.0	D.4	11.16	500	0.00	19.6	D.4
20.13	300	0.00	5.1	D.5	12.50	500	0.00	9.8	D.4
21.00	300	0.00	4.4	D.5	12.93	500	0.00	12.0	D.4
22.00	300	0.00	3.1	D.5	13.96	500	0.00	8.0	D.4
22.73	300	0.00	2.6	D.5	13.96	500	0.00	6.5	D.4
23.00	300	0.00	2.6	D.5	14.61	500	0.00	5.2	D.4
23.96	300	0.00	2.2	D.5	16.00	500	0.00	2.9	D.4
24.00	300	0.00	2.1	D.5	16.00	500	0.00	2.3	D.4
24.11	300	0.00	1.1	D.4	17.43	500	0.00	2.0	D.4
25.00	300	0.00	1.8	D.5	17.59	500	0.00	1.5	D.4
25.00	300	0.00	1.2	D.4	21.96	500	0.00	0.8	D.4
25.16	300	0.00	1.9	D.5	29.58	500	0.00	0.6	D.4
26.00	300	0.00	1.7	D.5	29.98	500	0.00	0.9	D.4
27.00	300	0.00	1.6	D.5	29.98	500	0.00	0.6	D.4
27.44	300	0.00	1.6	D.5	50.00	500	0.00	1.8	D.4
28.00	300	0.00	1.6	D.5	50.00	500	0.00	1.1	D.4
28.53	300	0.00	1.6	D.5	50.30	500	0.00	1.0	D.4
29.00	300	0.00	1.5	D.5	30.00	500	10.00	1.3	D.4
29.17	282	0.00	1.5	D.2	30.00	500	10.00	1.2	D.4
29.46	302	0.00	1.1	D.2	30.00	500	20.00	5.6	D.4
29.57	300	0.00	1.6	D.5	30.00	500	20.00	5.3	D.4
29.60	300	0.00	1.5	D.5	30.30	500	30.00	28.6	D.4
29.67	300	0.00	0.8	D.4	30.00	601	30.00	17.0	D.4
30.00	300	0.00	1.5	D.5	6.24	650	0.00	84.8	D.4
30.00	300	0.00	0.9	D.4	7.02	650	0.00	42.4	D.4
30.12	300	0.00	0.9	D.4	7.39	650	0.00	84.8	D.4
30.54	300	0.00	1.3	D.4	7.51	650	0.00	23.0	D.4
30.54	300	0.00	2.1	D.4	7.83	650	0.00	21.3	D.4
32.00	300	0.00	1.6	D.5	8.77	650	0.00	9.4	D.4
34.00	300	0.00	1.7	D.5	8.83	650	0.00	7.4	D.4
36.00	300	0.00	1.9	D.5	9.58	650	0.00	4.6	D.4
38.00	300	0.00	2.2	D.5	9.90	650	0.00	8.0	D.4
40.00	300	0.00	2.3	D.5	9.90	650	0.00	8.0	D.4
40.00	300	0.00	0.9	D.4	9.94	650	0.00	4.8	D.4
42.00	300	0.00	2.7	D.5	10.83	650	0.00	4.0	D.4
44.00	300	0.00	3.1	D.5	10.87	650	0.00	3.7	D.4
46.00	300	0.00	3.7	D.5	10.87	650	0.00	3.6	D.4
48.00	300	0.00	4.2	D.5	11.42	650	0.00	3.0	D.4
50.00	300	0.00	5.0	D.5	11.88	650	0.00	3.2	D.4
50.00	300	0.00	2.6	D.4	11.88	650	0.00	3.3	D.4

Table D.1-1 (concluded)

H_2 (dry) (vol %)	T (K)	H_20 (vol %)	λ (cm)	Ref.	H_2 (dry) (vol %)	T (K)	H_20 (vol %)	λ (cm)	Ref.
Data for T ≈ 300 K					**Data for elevated temperatures**				
51.36	300	0.00	1.8	D.4	12.00	650	0.00	3.3	D.4
52.00	300	0.00	5.5	D.5	14.28	650	0.00	1.7	D.4
54.00	300	0.00	7.9	D.5	15.00	650	0.00	1.8	D.4
54.50	300	0.00	4.6	D.4	15.03	650	0.00	1.7	D.4
55.00	300	0.00	9.5	D.5	17.48	650	0.00	1.2	D.4
56.00	300	0.00	10.0	D.5	17.50	650	0.00	1.9	D.4
58.00	300	0.00	14.2	D.5	30.00	650	0.00	0.4	D.4
58.00	300	0.00	8.0	D.4	30.29	650	0.00	0.5	D.4
58.00	300	0.00	7.8	D.4	50.00	650	0.00	1.0	D.4
60.00	300	0.00	18.9	D.5	50.00	650	0.00	1.0	D.4
70.46	300	0.00	135.2	D.2	50.00	650	0.00	1.1	D.4
73.08	300	0.00	135.2	D.2	9.85	650	7.50	42.9	D.4
75.00	299	0.00	135.2	D.2	17.55	650	10.00	3.3	D.4
30.54	298	3.10	1.3	D.2	30.00	650	10.00	0.8	D.4
29.53	311	0.00	0.9	D.2	9.86	650	15.00	84.8	D.4
					17.63	650	20.00	9.1	D.4
					30.00	650	20.00	2.3	D.4
					30.00	650	20.00	2.2	D.4
					18.06	650	25.00	27.5	D.4
					30.00	650	25.00	2.6	D.4
					17.26	650	30.00	42.4	D.4
					29.46	650	30.00	7.5	D.4
					30.00	650	30.00	7.3	D.4
					30.00	650	30.00	6.2	D.4
					30.00	650	30.00	6.5	D.4
					30.00	650	30.00	5.7	D.4
					28.64	650	35.00	17.5	D.4
					29.43	650	40.00	50.3	D.4
					29.37	650	50.00	84.8	D.4

Table D.1-2 Detonation cell size data for hydrogen-air-steam mixtures at sub-atmospheric and elevated initial pressures

H_2 (dry) (vol %)	T (K)	P (MPa)	H_20 (vol %)	λ (cm)	Ref.	H_2 (dry) (vol %)	T (K)	P (MPa)	H_20 (vol %)	λ (cm)	Ref.
30.00	300	0.003	0.00	2.3	D.6	15.00	373	0.146	0.00	17.0	D.2
30.00	300	0.007	0.00	13.0	D.6	17.36	373	0.149	0.00	6.3	D.2
30.00	300	0.008	0.00	14.0	D.6	17.36	373	0.164	10.00	53.0	D.2
30.00	300	0.01	0.00	11.0	D.6	20.13	373	0.168	10.00	23.0	D.2
30.00	300	0.0105	0.00	7.8	D.6	20.40	373	0.153	0.00	2.4	D.2
30.00	300	0.0115	0.00	6.4	D.6	20.40	373	0.169	10.00	21.0	D.2
30.00	300	0.012	0.00	6.3	D.6	20.67	373	0.154	0.00	2.3	D.2
30.00	300	0.013	0.00	4.7	D.6	20.67	373	0.169	10.00	20.0	D.2
30.00	300	0.02	0.00	4.1	D.6	21.45	373	0.155	0.00	1.8	D.2
30.00	300	0.023	0.00	3.4	D.6	22.73	373	0.156	0.00	1.3	D.2
30.00	300	0.025	0.00	3.2	D.6	25.16	373	0.159	0.00	0.9	D.2
30.00	300	0.035	0.00	2.1	D.6	25.16	373	0.175	10.00	5.3	D.2
30.00	300	0.05	0.00	2.0	D.6	25.63	373	0.192	20.00	22.0	D.2
30.00	300	0.07	0.00	1.8	D.6	27.44	373	0.162	0.00	0.6	D.2
30.00	300	0.1	0.00	1.6	D.6	27.44	373	0.211	30.00	35.0	D.2
17.29	303	0.010	0.00	25.0	D.2	29.59	373	0.165	0.00	0.5	D.2
14.39	293	0.114	0.00	40.0	D.2	29.59	373	0.180	0.00	0.5	D.2
17.50	293	0.118	0.00	11.0	D.2	29.59	373	0.200	10.00	3.0	D.2
19.05	293	0.119	0.00	3.8	D.2	29.59	373	0.225	20.00	9.5	D.2
24.44	293	0.124	0.00	1.2	D.2	29.59	373	0.255	30.00	28.0	D.2
28.10	293	0.128	0.00	1.0	D.2	29.59	373	0.255	30.00	32.0	D.2
43.06	293	0.143	0.00	1.3	D.2	29.69	373	0.165	0.00	0.5	D.2
29.63	296	0.025	0.00	2.4	D.2	37.04	373	0.174	0.00	0.6	D.2
16.72	296	0.026	0.00	45.0	D.2	45.66	373	0.185	0.00	1.1	D.2
29.19	296	0.051	0.00	1.5	D.2	45.66	373	0.204	10.00	4.0	D.2
17.04	296	0.015	0.00	21.5	D.2	45.66	373	0.223	20.00	13.0	D.2
29.02	297	0.151	0.00	0.8	D.2	55.76	373	0.198	0.00	2.0	D.2
17.01	297	0.051	0.00	15.7	D.2	29.60	375	0.215	29.60	25.0	D.2
17.44	299	0.026	0.00	26.0	D.2	9.30	650	0.240	0.00	8.5	D.4
17.13	301	0.264	0.00	10.0	D.2	17.78	650	0.200	20.00	10.7	D.4
12.50	373	0.143	0.00	42.0	D.2	17.91	650	0.150	20.00	10.3	D.4
13.45	373	0.144	0.00	32.0	D.2	30.13	650	0.150	30.00	4.5	D.4
13.77	373	0.145	0.00	29.0	D.2	30.22	650	0.200	30.00	3.7	D.4

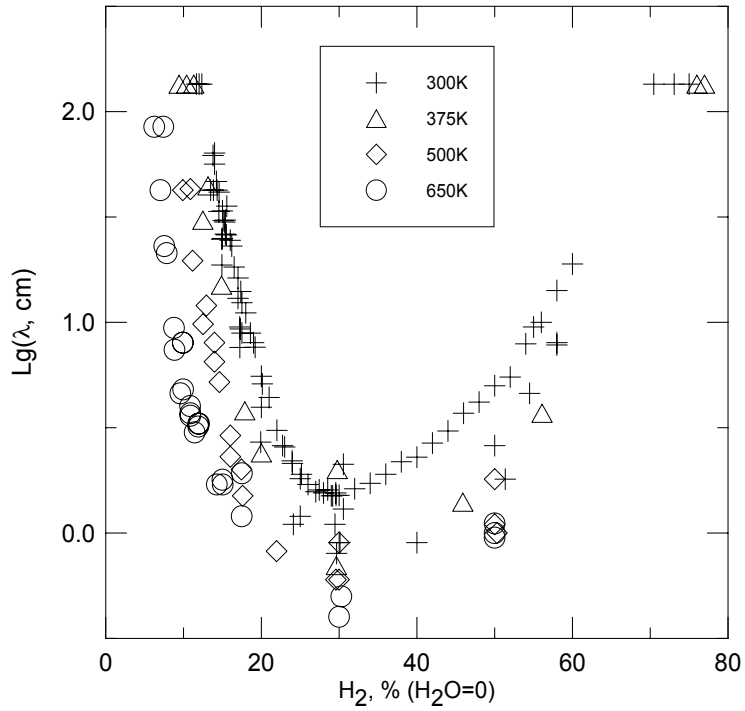

Figure D.1-1 Experimental data on detonation cell width versus hydrogen concentration at different initial temperatures for mixtures without steam

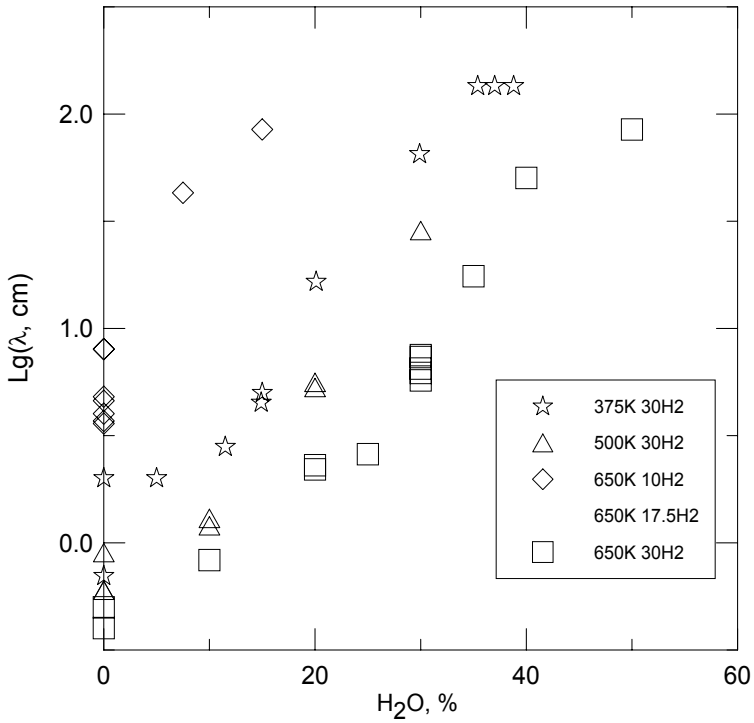

Figure D.1-2 Experimental data on detonation cell width versus steam concentration at different initial temperatures and dry hydrogen concentrations

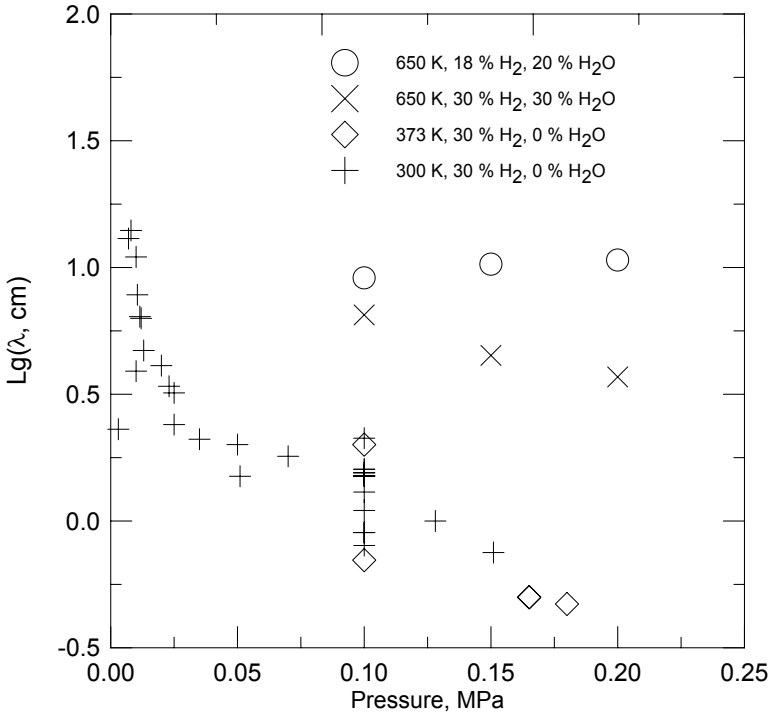

Figure D.1-3 Experimental data on detonation cell width versus initial pressure at different initial temperatures, dry hydrogen, and steam concentrations

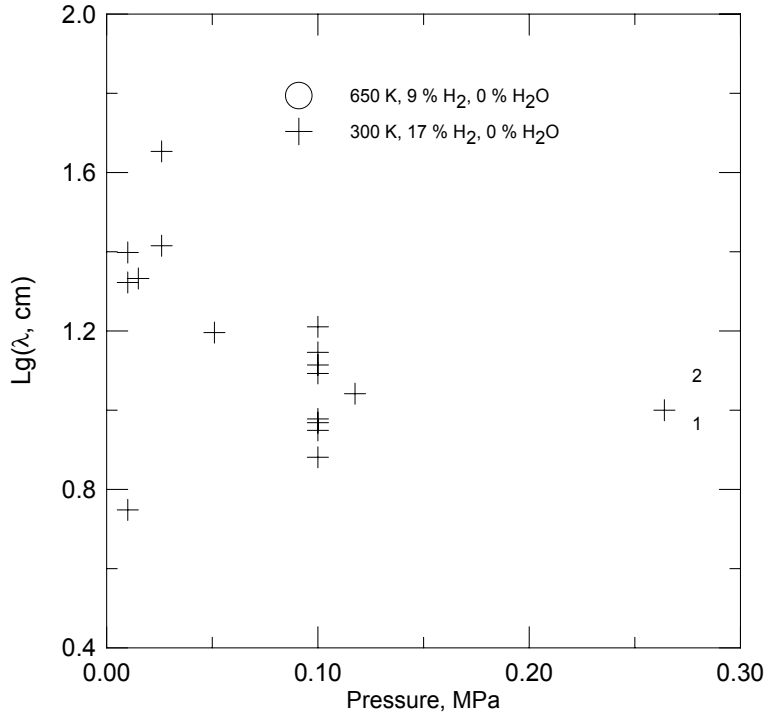

Figure D.1-4 Experimental data on detonation cell width versus initial pressure at different initial temperatures and dry hydrogen concentrations without steam

D.2 Data Interpolation with Analytical Functions

Different analytical functions $\lambda([H_2], [H_2O], T, p)$ were applied to fit experimental data [D.9]. One of the functions giving the least deviation among other simple expressions is given here.

Function B67p. Variables: A - dry hydrogen concentration $[H_2]_{dry} = H_2/(H_2+air)$, vol %; B - initial temperature T, K; C - steam concentration, vol %; D - initial pressure, MPa. Cell size λ is in cm.

$$\lg(\lambda) = (a-m+(b/(A-k/B)^f +h\cdot(A-g\cdot B)^2+i\cdot(A-g\cdot B))\cdot(1+d\cdot C+e\cdot B\cdot C^2)\cdot j/B)\cdot$$

$$\cdot(D-c)\cdot(1/(0.1-c)+n\cdot(D-0.1))+m$$

Parameters:
a = -1.13331E+00
b = 4.59807E+01
c = -1.57650E-01
d = 4.65429E-02
e = 3.59620E-07
f = 9.97468E-01
g = -2.66646E-02
h = 8.74995E-04
i = -4.07641E-02
j = 3.31162E+02
k = -4.18215E+02
m = 2.38970E+00
n = -8.42378E+00

The regression mean-square deviation is $\sigma = 1.72128E-01$.

Deviation of experimental data from the fitted function can be calculated as $\lambda_{fit}/\lambda_{exp} = 10^{\sigma}$. The mean standard deviation is about 1.5. The maximum deviation is about 2.6.

Examples of comparison of experimental data with function B67p are given in Figures D.2-1 and D.2-2. A "map" of the cell widths plotted in $[H_2]_{dry}$ - $[H_2O]$ plane for T = 375 K, p = 1 bar* using function B67p, is shown as an example in Figure D.2-3 ($[H_2]_{dry} = [H_2]/([H_2]+[air])$).

---

*1 bar = 100 kPa.

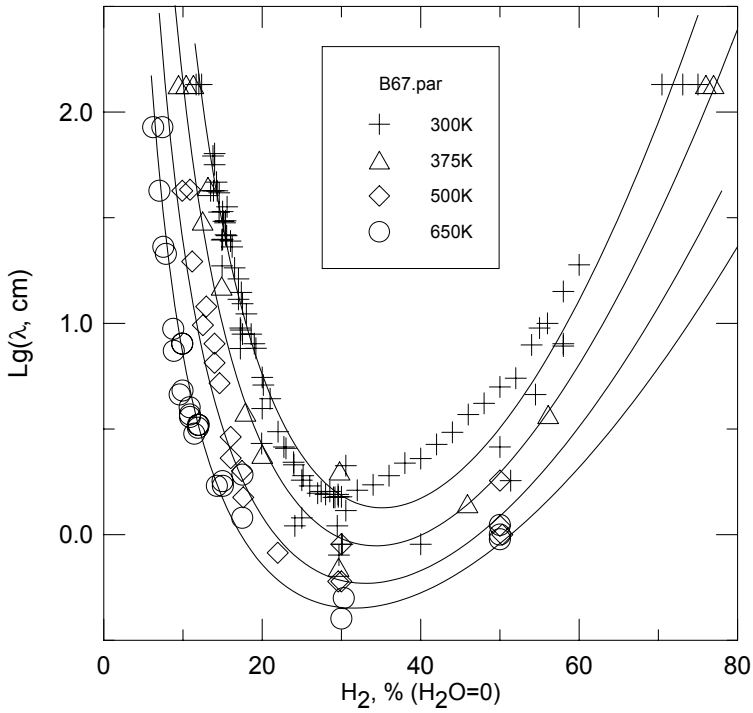

Figure D.2-1 Experimental data and fitting function B67. Cell width versus hydrogen concentration at different initial temperatures for mixtures without steam

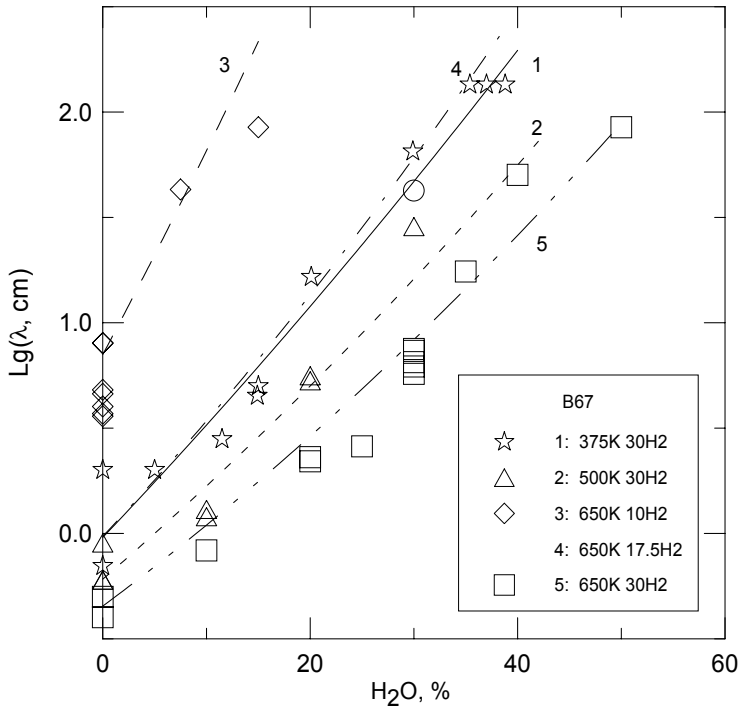

Figure D.2-2 Experimental data and fitting of function B67. Cell width versus steam concentration at different initial temperatures and dry hydrogen concentration

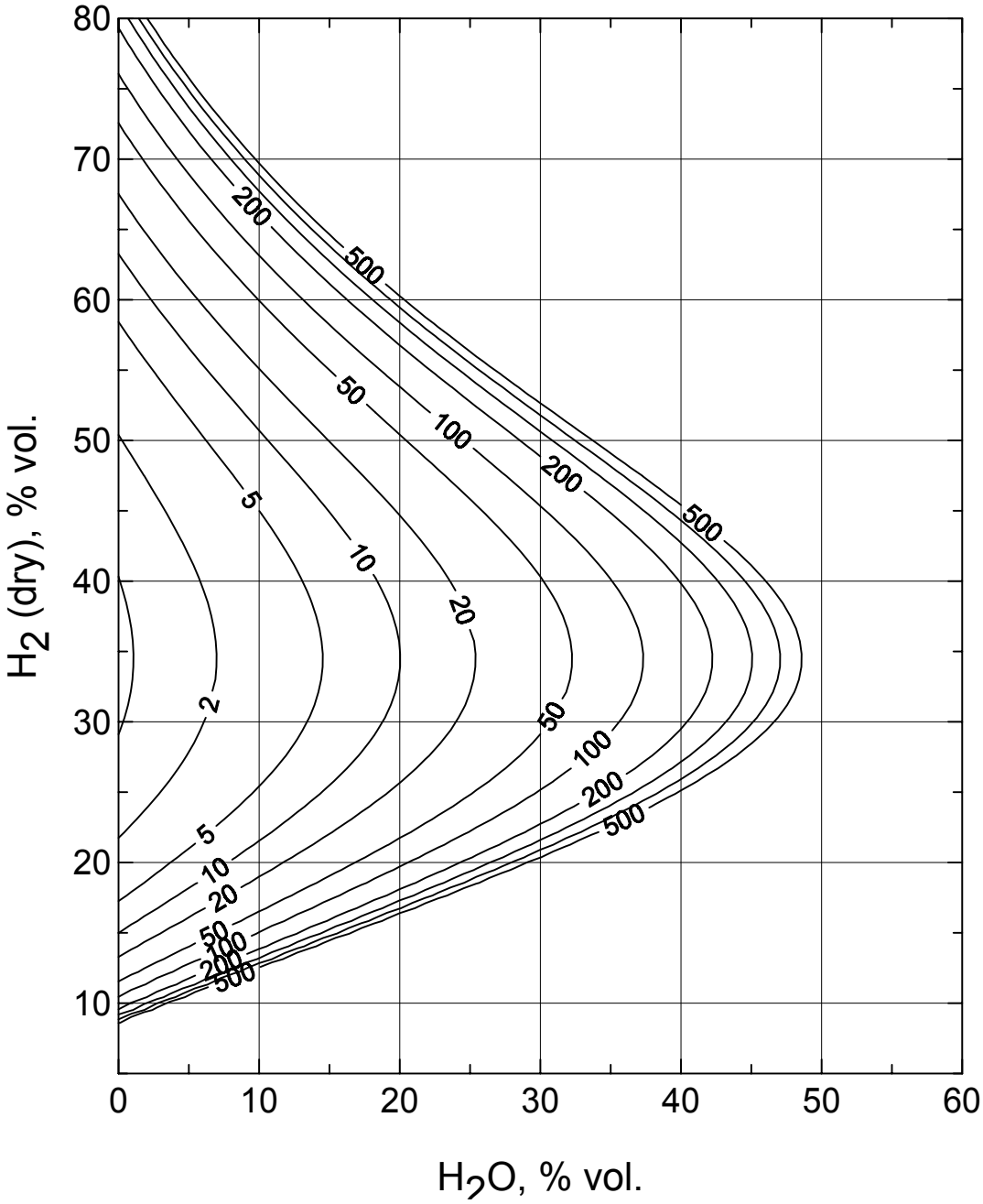

Figure D.2-3 Cell widths (cm) in $[H_2]_{dry}$ - $[H_2O]$ plane. Function B67, T = 375 K, p = 1 bar, ($[H_2]_{dry}$ = $[H_2]/([H_2]+[air])$)

D.3 Generalization of the Zeldovich-von Neumann-Döring (ZND) Correlation

A simple model was proposed in Reference [D.10] to generalize the correlation between characteristic reaction zone widths δ and the cell sizes λ. As typical of ZND correlations, it was assumed that characteristic reaction zone width, δ, can be estimated from a detailed chemical reaction model. It was suggested that parameters influencing the wave stability and regularity of the cellular structure should play a role in a correlation between the detonation cell sizes and reaction zone widths. Two parameters were considered to be of the main importance. The first one – dimensionless activation energy Ea/RT_{ps} – gives a measure of the reaction time sensitivity to changes of the initial reaction conditions (shock strength). The second parameter, T_{vn}/T_0, gives a measure of the chemical energy release compared with the initial thermal energy. Here Ea is effective activation energy, R is gas constant, T_{ps} is representative post-shock temperature, and T_{vn} and T_0 are von Neumann and initial temperatures respectively.

An attempt was made to take into account the multi-dimensional structure of real detonations in this model by choosing representative reaction conditions (or characteristic post-shock temperature T_{ps}) that allow one to correlate reaction zone width $\delta(T_{ps})$ and detonation cell size λ. The CHEMKIN-II code was used for kinetic calculations. An analytical expression was suggested to describe the function of $\lambda/\delta(Ea/RT_{ps}, T_{vn}/T_0)$ in the range of $Ea/RT_{ps} = 3 \div 16$, and $Tvn/T_0 = 1.5 \div 8$. The mean deviation of the calculated values from experimental data was about 50%.

A numerical model was developed [D.10], which permits one to calculate detonation cell sizes from mixture composition and initial temperature and pressure. The corresponding computer code is available on the Web at URL **http://www.iacph.kiae.ru/lichr**.

Compared with the standard ZND models, which are able to give only general trends in the cell size behaviour, the numerical model [D.10] gives more reliable estimates for the cell sizes. In most cases, the deviation is within the scatter of the experimental data. The estimates of λ values, however, should be treated carefully if the stability parameters appear outside the range of variables, where the λ/δ-function was defined. The limitations of kinetic calculations with the CHEMKIN-II code should be also taken into consideration.

Examples of comparison of experimental data with calculations are given in Figures D.3-1 and D.3-2. A “map” of the cell widths plotted in $[H_2]_{dry}$ - $[H_2O]$ plane for T = 375 K, p = 1 bar using this model, is shown as an example in Figure D.3-3 ($[H_2]_{dry} = [H_2]/([H_2]+[air])$).

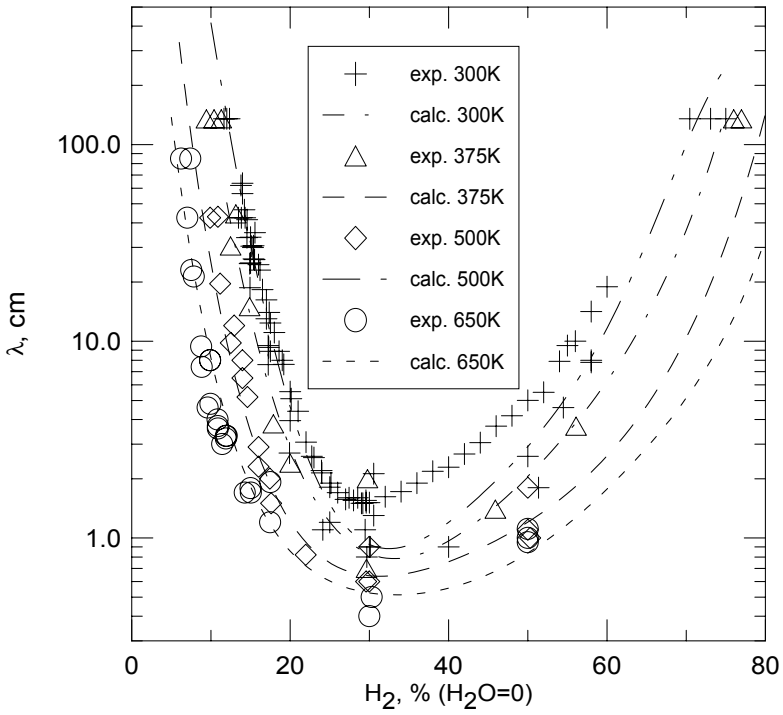

Figure D.3-1 Cell width versus hydrogen concentration at different initial temperatures for hydrogen-air mixtures without steam. Experimental data and calculations.

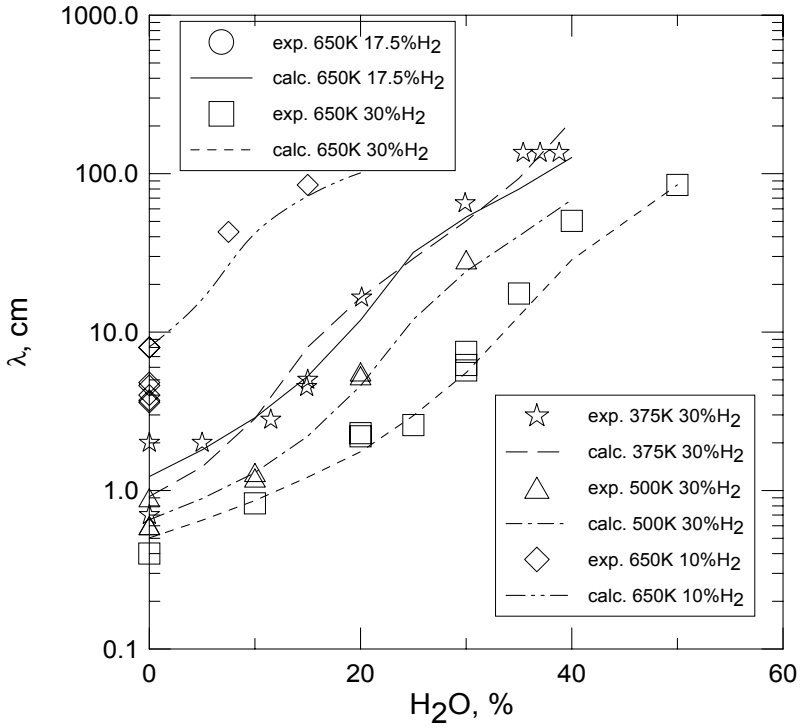

Figure D.3-2 Cell width for hydrogen-air-steam mixtures versus steam concentration at different initial temperatures and dry hydrogen concentrations. Experimental data and calculations.

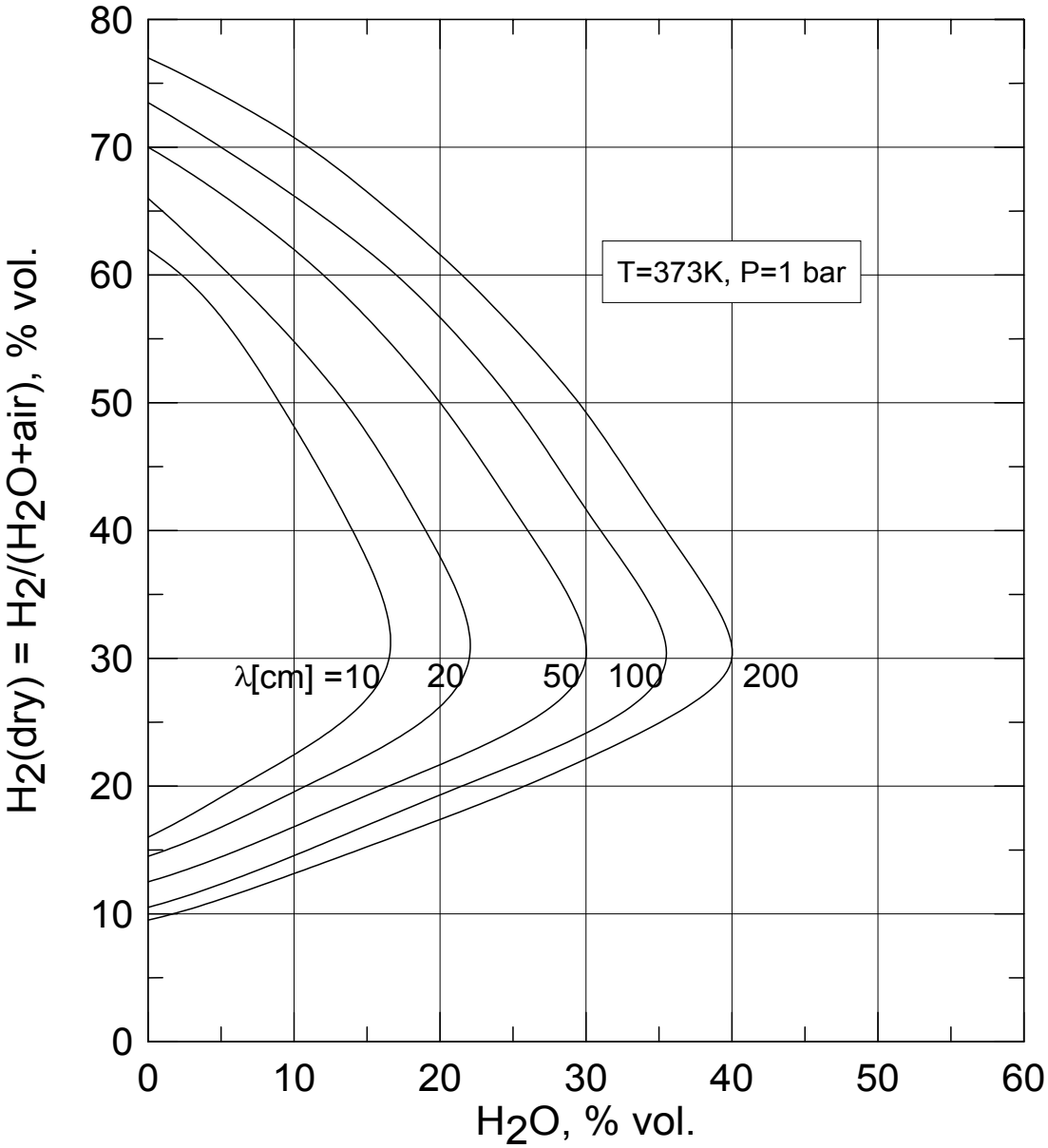

Figure D.3-3 Cell widths (cm) in $[H_2]_{dry}$ - $[H_2O]$ plane. Calculations with model [D.10], T = 373 K, p = 1 bar, ($[H_2]_{dry} = [H_2]/([H_2]+[air])$)

D.4 References

[D.1] C. M. Guirao, R. Knystautas and J. H. Lee, A Summary of Hydrogen-Air Detonations for Reactor Safety, Sandia National Laboratories / McGill University, NUREG/CR-4961, 1989.

[D.2] D. W. Stamps, W. B. Benedick and S. R. Tieszen, Hydrogen-Air-Diluent Detonation Study for Nuclear Reactor Safety Analyses, Sandia National Laboratories Report No SAND89-2398, NUREG/CR-5525, 1991.

[D.3] G. Ciccarelli, T. Ginsberg, C. Finfrock, J. Boccio, C. Economos and M. Kinoshita, Detonation Cell Size Measurements and Predictions in Hydrogen-Air-Steam Mixtures at Elevated Temperatures, *Combusion and Flame,* Vol. 99, 1994, 212-220.

[D.4] G. Ciccarelli, T. Ginsberg, J. Boccio, C. Finfrock, L. Gerlach, H. Tagawa and A. Malliakos, Detonation Cell Size Measurements in High-Temperature Hydrogen-Air-Steam Mixtures at BNL High-Temperature Combustion Facility, Brookhaven National Laboratory Report No NUREG/CR-6391, BNL-NUREG-52482, 1997.

[D.5] C. M. Guirao, R. Knystautas, J. H. Lee, W. Benedick and M. Berman, Hydrogen-Air Detonations, *Ninetinth Symposium (International) on Combustion*, The Combustion Institute, Pittsburgh, 1982, 583-590.

[D.6] D. C. Bull, J. E. Elsworth, P. J. Shuff and E. Metcalfe, Detonation Cell Structures in Fuel/Air Mixtures, *Combusion and Flame,* Vol. 45, 1982, 7-22.

[D.7] S. R. Tieszen, M. P. Sherman, W. B. Benedick, J. E. Shepherd, R. Knystautas and J. H. S. Lee, In *AIAA Progress in Astronautics and Aeronautics* (Bowen, J. R., et al., Eds.), AIAA, New York, Vol. 106, 1986, 205.

[D.8] M. Kaneshige and J. E. Shepherd, Detonation Database, Report FM-97-8, GALCIT, Explosion Dynamics Laboratory, 1997.

[D.9] S. B. Dorofeev, A. A. Efimenko and A. V. Besmelnitsyn. DDT Scaling for Severe Accidents. Detonation Cell Size Data as a Function of Composition and Initial Conditions. Report RRC “Kurchatov Institute” RRC KI 80-05/15, 1997.

[D.10] A. I. Gavrikov, A. A. Efimenko and S. B. Dorofeev. A Model for Detonation Cell Size Predictions from Chemical Kinetics, *Combustion and Flame*, Vol. 120, 2000, 19-33.

APPENDIX E: DDT EXPERIMENTS IN SHOCK TUBE AND OBSTACLE ARRAY GEOMETRYy [*]

E.1 Recent DDT Experiments at FZK

Appendix E presents selected results of recent experiments conducted at FZK [E.1] on three different modes of DDT that are relevant for nuclear safety investigation and risk analysis:

- focusing of pressure and shock waves produced by bursting vessels or pipes,
- focusing of precursor pressure and shock waves generated by an accelerating flame,
- DDT within or near the turbulent flame brush of a flame accelerating in an obstructed and highly confined part of the containment.

E.1.1 Experiment Design

Three test series addressing these different DDT modes were performed in the FZK combustion tube (12 m long, 35 cm ID). The corresponding test configurations are displayed in Figure E.1.1-1:

a. Shock tube with conus

The tube was divided by a membrane into a low-pressure section (LPS, length 9 m) and a high-pressure section (HPS, length 1 or 3 m). The experiments were conducted with a conical reflector at the end of the low-pressure section to focus the pressure wave and to reach self-ignition temperatures (Figure E.1.1-2). The main idea behind this experiment design is the observation that in many tests with fast combustion modes, DDT events are apparently triggered by waves reflected in corners or other converging multi-dimensional parts of the enclosure. The conus is used to produce local hot spots in the combustible gas because hot spots generally develop from the interaction of a pressure wave with a complex multi-dimensional target.

After evacuating both sections, the low-pressure section was filled up to the desired initial pressure with a defined hydrogen-air mixture. The parameters that changed during the experiments were the initial pressure (0.5 to 1.5 bar) and the composition of the hydrogen-air mixture (9% to 30% H_2). The high-pressure section was filled with helium up to membrane failure. To detect DDT processes, pressure transducers, photodiodes, and film thermocouples were located along the tube. Ionization gauges were installed in and near the conus.

b. Partially obstructed shock tube with conus

About half of the tube was equipped with an array of ring obstacles blocking 30% of the flow cross-section (BR = 30%) over a length of 5 to 6 m to accelerate the flame to a high velocity. The tube also contained a conus to focus the precursor shock wave.

The main idea behind this experimental set-up is that after a weak spark ignition, the propagation flame reaches a highly obstructed region in which it can accelerate because of the generation of intense turbulence. This fast flame then emits precursor pressure waves that can propagate through a relatively open region until they are reflected from the enclosure. In most practical cases, the precursor wave will not simply be normally reflected from a flat wall but rather will be focused by two walls

[*] Dr. W. Breitung is the lead author of Appendix E.

(2D wedge) or three walls (3D corner). Such focusing geometries in industrial buildings were simulated in the tube tests by a conical reflector situated at the end of the tube, opposite to the ignition location. The investigated tube geometry contains therefore all characteristic elements of a combustion sequence in a complex nuclear containment. These are

- a combustible gas,
- a weak ignition source,
- a partly blocked region with flow obstacles producing high turbulence levels,
- an open region that permits pressure wave propagation without significant losses, and
- a multi-dimensional reflector as part of the enclosure.

The tube was evacuated and then filled with a defined hydrogen-air mixture (9% to 30% H_2) to the initial pressure (1 bar). The mixture was ignited with a glow plug. Pressure transducers, ionization gauges, photodiodes, and film thermocouples were used to locate possible DDT events.

c. Fully obstructed tube

The combustion tube was equipped with an array of ring obstacles (BR = 60%) over its full length of 12 m. The evacuated tube was filled with a defined hydrogen/air mixture (9% to 20% H_2) up to the initial pressure (0.5 to 2.0 bar) and was then ignited with a glow plug. To observe the combustion processes, pressure transducers, photodiodes, and film thermocouples were located along the tube.

E.1.2 Results of DDT in a Shock Tube with Conus

Three criteria can be used to determine whether a detonation initiation occurred. The first is the velocity of the reflected wave, the second is coupling or decoupling of pressure and light signals, and a third method is to analyze the pressure amplitudes and profiles along the tube. At given times, the pressures at each pressure transducer location can be collected and depicted as function of tube location. The spatial distribution of the pressure gives clear indications about the existence of a deflagration or detonation.

Figure E.1.2-1 shows the x-t diagrams obtained in two experiments with 15% H_2 in air, one leading to a mild ignition without detonation (top) and one leading to DDT (bottom). In the first case, the Mach number of the incident shock wave (ISW) was measured to M = 1.93, and the reflected shock wave (RSW) initially reached 506 m/s, which is close to the speed of a normally reflected inert wave without combustion. The measured trajectories for the flame and the RSW separate soon after the flame-shock complex leaves the conus, well before the expected arrival of the He-contact surface.

Increasing the Mach number only slightly to M = 2.01 results in very different findings. The measured RSW velocity obtains 1333 m/s, which is close to the theoretical CJ detonation speed in the countermoving H_2-air mixture. (wave speed W in laboratory frame is D_{CJ} minus particle velocity u behind the incident shock: $W = D_{CJ} - u$.). In addition, the RSW and the flame front remain coupled until they come close to the contact surface. These are clear indications of a detonative combustion returning from the conus.

The measured pressure profiles along the tube are compared in Figures E.1.2-2 and E.1.2-3 for two other experiments with 15% H_2 in air.

Figure E.1.2-2 is the case with mild ignition. Curves 1, 2, and 3 represent pressures of the ISW, and curves 4, 5, 6 those of the RSW. These reflected pressures are only slightly higher than those measured for the inert case without hydrogen in the LPS [E.1], except that the maximum pressure in the conus reaches almost 40 bars, compared with only 8 bars in the inert case. These values indicate that a local explosion kernel was created in the focus but that it decayed to a slow deflagration outside of the conus.

Figure E.1.2-3 shows the measured pressure profiles for the strong ignition case with DDT. The pressure profiles of the incoming shock are similar to the pressure profiles shown in Figure E.1.2-2, but the reflected pressure profiles closely resemble those of CJ detonations. Note that the initial pressure in the LPS was only 0.45 bar, which indicates that the detonation decayed from an overdriven state towards CJ conditions as it propagated away from the reflector. In addition, the higher RSW velocity and the observed coupling between light and pressure supports the conclusion that DDT occurred in this experiment.

Based on these three indicators -namely reflected wave speed, coupling between light and pressure and magnitude and shape of pressure distribution- the experiments could be grouped clearly into cases with and without DDT.

Figure E.1.2-4 shows a summary plot containing the test results with H_2-air mixtures between 10% and 30%H_2. The dashed lines indicate the critical Mach numbers for the respective mixtures at which the reflected wave velocity suddenly switches from typical inert values (lower line) to detonation-like values (upper line). A very low Mach number was found for stoichiometric H_2-air mixtures, demonstrating that DDT can be easily achieved if such mixtures should be present in a multi-dimensional enclosure and a pressure wave should be generated by a bursting pipe or vessel.

Corresponding experiments in a geometrically similar, but scaled-down laboratory shock tube showed the same general trend for the transition from mild to strong ignition, however at consistantly higher Mach numbers [E.2]. The linear scaling ratio between both facilities was 6.5.

Very good reproducibility of individual tests and consistency of the whole database in terms of ignition modes was observed. The detailed processes in the focusing tests are highly mechanistic and seem to be governed by the temperature-dependent reaction kinetics.

The shown data are useful for development of first numerical models because mainly flow dynamics and reaction kinetics are involved, and not complex turbulent combustion.

E.1.3 Results of DDT in a Partially Obstructed Tube with Conus

One example for a DDT driven by flame-generated precursor waves is presented in Figure E.1.3-1, which shows an enlarged part of the R-t diagram near the conus (9.75 to 12.00 m). The precursor wave from the accelerating flame travels into the conical reflector at 750 m/s, causing a strong self-ignition in the focus.

This ignition is detected simultanesouly by the photodiodes, the ionization gauges, and the pressure transducers. The measured pressures initially exceed the theoretical CJ pressures indicating an overdriven detonation. ($p_{CJ}/p_0 \approx 11.2$ for 16.5% H_2 in air.) The flame front and the RSW remain coupled and travel with a measured velocity of 1360 m/s. Such a velocity is typical for a detonation in the counterflowing gas, indicating that a DDT event has occurred.

All experiments performed in the partly obstructed geometry can be grouped into three regimes:

- At low hydrogen concentrations (≤ 11%) the speed of the propagating flame in the obstructed zone remains much slower than the speed of sound in the unburned gas. The flame emits a set of acoustic waves, and the pressure increases practically uniformly in the tube according to the fraction of gas burned at any given time.

- In the second regime, which occurs for hydrogen concentrations from about 12% to 18% (at p_0 = 1 bar, T_0 = 300 K) a coupled flame/shock complex is emitted from the obstacle section. Because of the flame deceleration in the smooth unobstructed part of the tube, a shock wave proceeds from the flame. The shock is faster than the flame. Depending on the Mach number, the precursor wave can trigger a weak (deflagrative) or a strong (detonative) ignition when it is reflected at the tube end.

- A third regime is observed when the hydrogen concentration exceeds 18%. In this case, the flame and shock complex remain coupled after the complex leaves the obstructed region, at least for the travel distance available in the present test set-up. Flame and shock have the same velocity. The interaction of this complex with the tube end causes only a reflected wave back into combustion products, and contrary to regime (2), no secondary ignition can occur.

DDT from fast flame precursor waves is only possible in the second regime where the shock velocity exceeds the flame speed. The corresponding measured range of hydrogen concentrations (12% to 18%) is not universal; it will generally depend on the tube dimensions and details of the obstacle section (length, blockage ratio). Experiments in a geometrically similar but scaled-down facility of the Russian Academy of Sciences (linear scale 1:6) have identified the same three regimes but at hydrogen concentrations that were several percent higher than in the FZK-tube tests [E.3].

The three described regimes lead to different load mechanisms and load magnitudes. In the first case ($v_{flame} \ll c$), the pressure increases nearly uniformly in the tube. The pressure increase at a given time is proportional to the fraction of burned gas at that time. Shape and size of the reflector have no influence on local pressure loads.

In the second regime ($v_{flame} < v_{shock}$), two effects lead to higher loads compared with the loads in the first regime:

1. directed flow with particle velocities of the order of several 100 m/s, and

2. secondary ignition after reflection in the multi-dimensional target at the tube end.

For low shock velocities, which only trigger a deflagration, the additional loading from the secondary ignition is not substantial. The pressure loads are comparable to those of an inert reflection. However, in case of sufficiently high shock speed, the strong secondary ignition causes very high local pressures because the chemical reaction proceeds from a pre-compressed state.

Compared with the loads in the second regime, the third regime ($v_{flame} = v_{shock}$) produces lower pressures and impulses. The particle velocities of the directed flow increase, but this is more than compensated by the fact that no secondary ignition can result from the reflection process.

In summary, the highest loads were observed inside the 3D reflector in the second regime under DDT conditions. In this case, the flow was directed into the conus pre-compressed unreacted gas, which then ignited rapidly. An overdriven detonation propagates away from the reflector into the rest of the unburned gas.

E.1.4 Results of DDT in a Fully Obstructed Tube

An example of DDT in or near a turbulent flame front is presented in Figure E.1.4-1 for a flame acceleration test with 16.5% H_2 in air. The top figure shows that coupling between the visible light front (flame brush), and the pressure front occurs between the 5.25 m and 6.25 m positions. The pressure amplitudes and shapes change from deflagration to detonation-like in the same region (bottom figure). The detonation-like pressure profile is stable for the rest of the combustion up to the tube end.

The flame velocity measured in this test is depicted in the lower left corner of Figure E.1.4-2 The DDT event seems to cause a locally overdriven detonation, which then relaxes to a stable quasi-detonation with near-CJ velocity (1577 m/s for this mixture).

The other data shown indicate consistently that the transition process requires a flame velocity of about 800 to 900 m/s, which is close to the isobaric speed of sound in the combustion products (sound speed in Figure E.1.4-2).

E.2 References

[E.1] A. Veser, W. Breitung, G. Engel, G. Stern and A. Kotchourko, Deflagration-to-Detonation-Transition Experiments in Shock Tube and Obstacle Array Geometries, Report FZKA-6355, Research Center Karlsruhe, P.O. Box 36 40, 76021 Karlsruhe, 1999.

[E.2] B.E. Gelfand, S.V. Khomik and S.B. Medvedev, Investigation of Hydrogen and Air Fast Flame Propagation and DDT in Tube with Multidimensional Endplates, Research Report No.2, Institute of Chemical Physics, Russian Academy, 1997.

[E.3] B.E. Gelfand, S.V. Khomik and A.N. Polenov, DDT Experiments with Focusing of H_2-Air Blast Waves, Final Report, Institute of Chemical Physics, Russian Academy of Sciences, Moscow, to Forschungszentrum Karlsruhe, 1998.

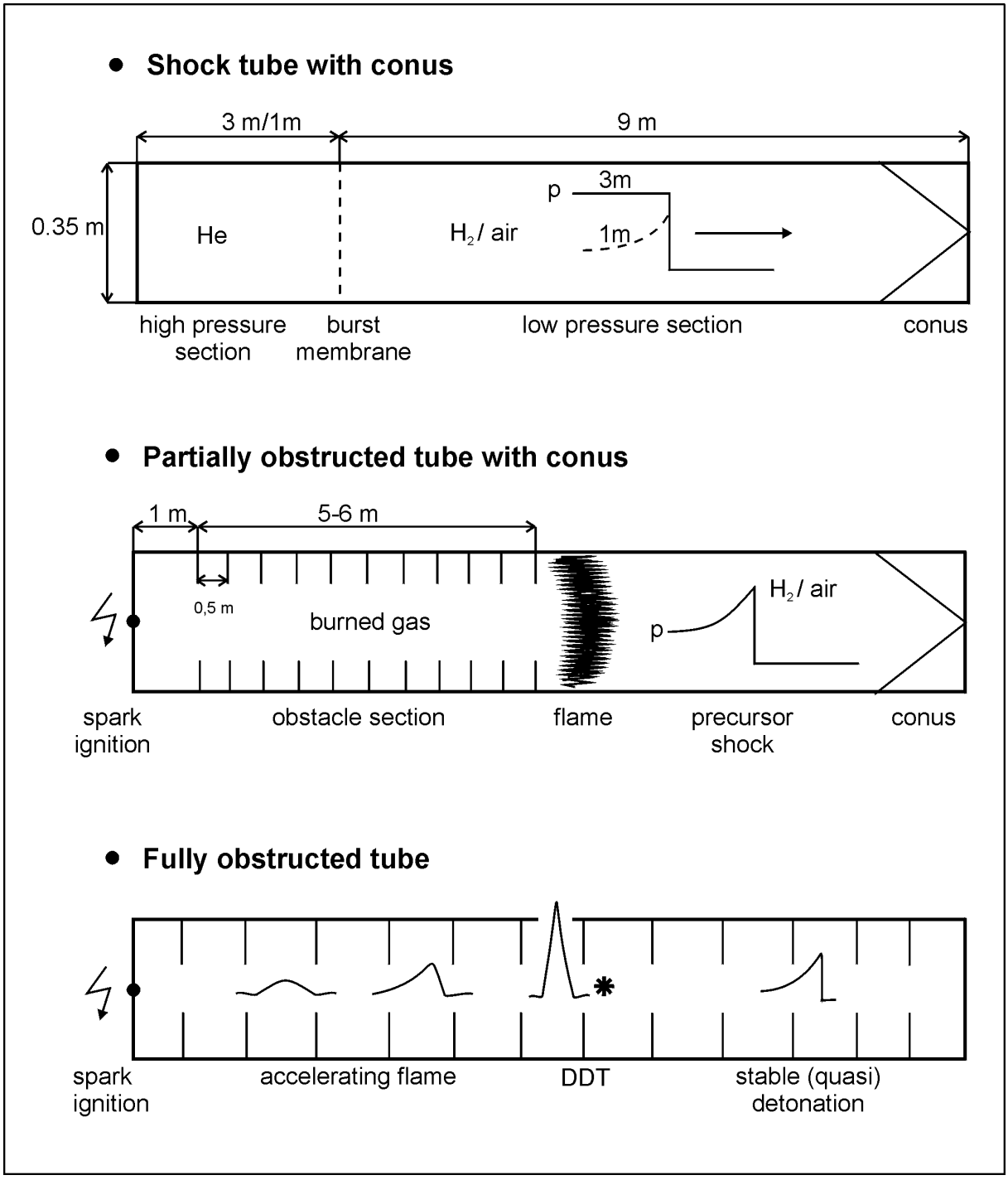

Figure E.1.1.-1 FZK experiments on three different DDT mechanisms using three experimental configurations of the 12 m tube. Pressure transducers, photodiodes, film thermocouples, and ionization gauges were used for instrumentation.

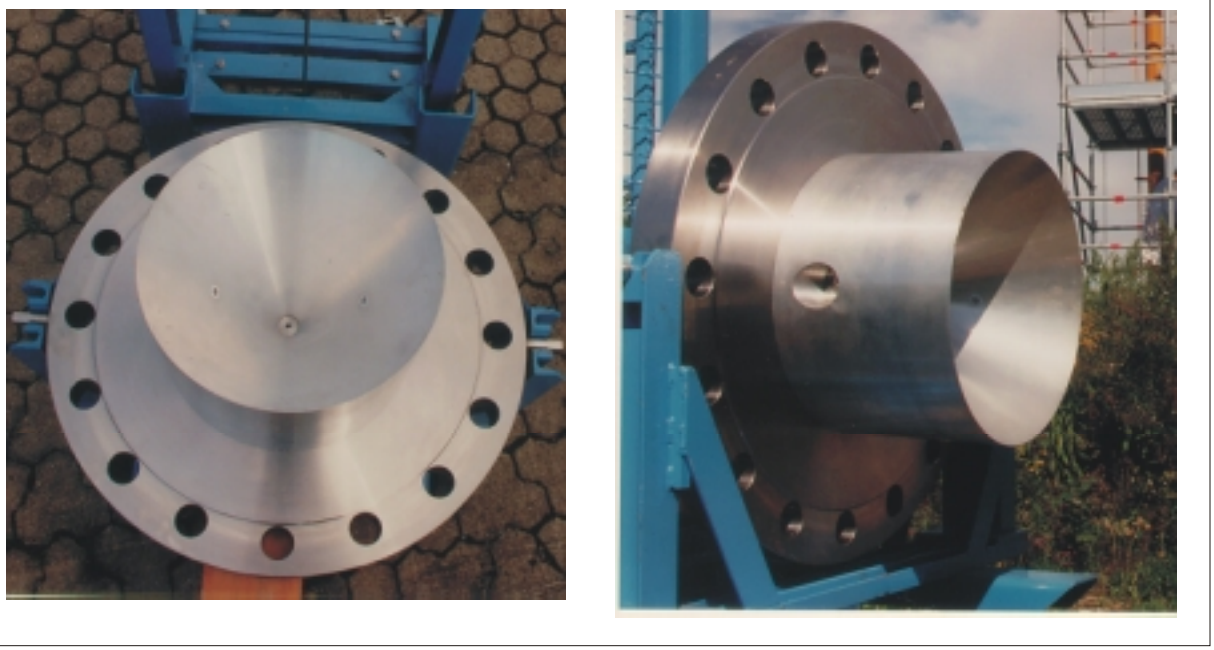

Figure E.1.1.-2 Photographs of the conus used to produce local hot spots for self-ignition of the test gas. The conus diameter, length, and opening angle are 35 cm, 21 cm and 70°, respectively. Three pressure transducers are installed inside the conus.

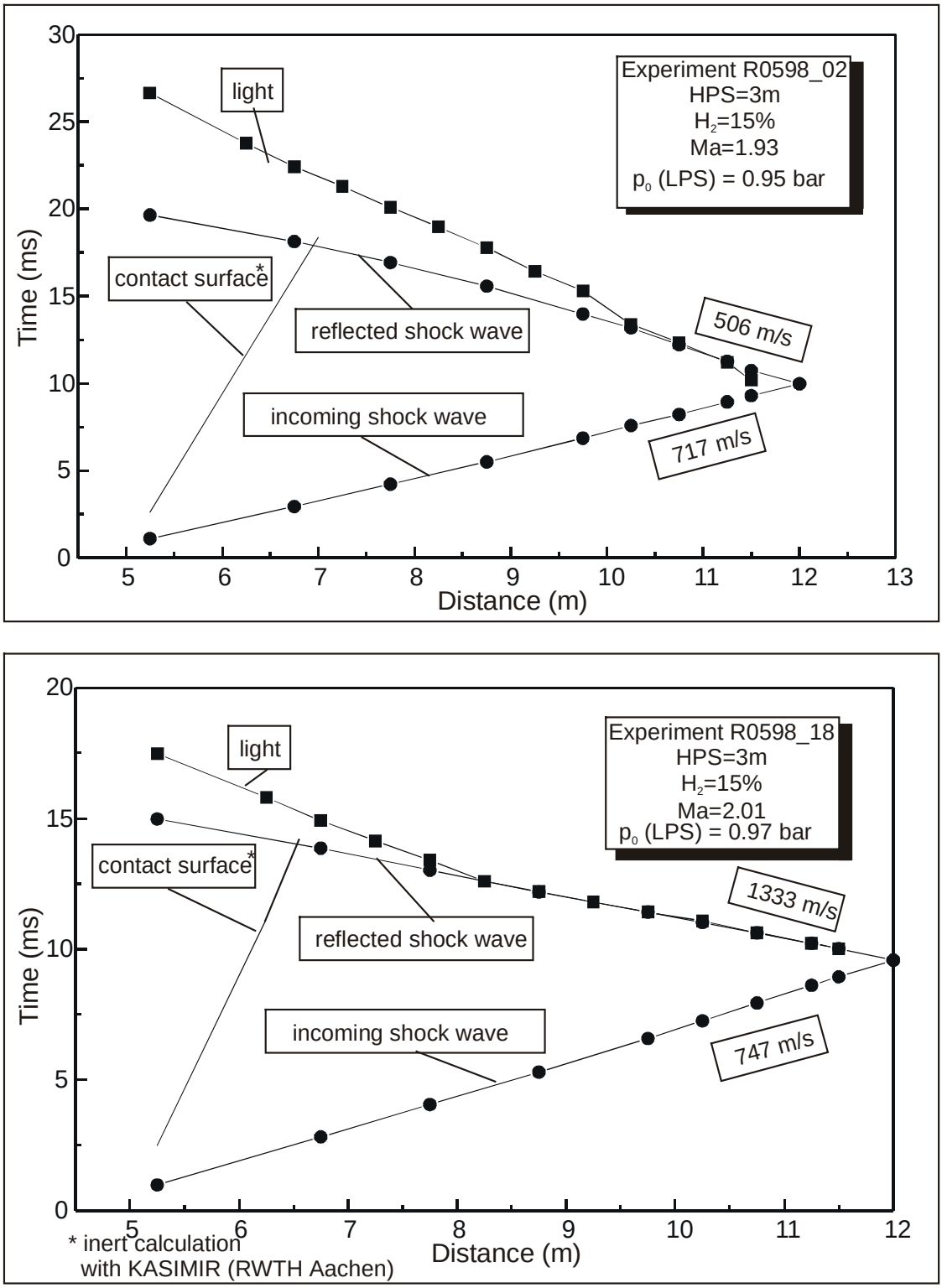

Figure E.1.2-1 Example of measured flame and shock trajectories for 15% hydrogen in air. Upper case leads to weak ignition (decoupling of pressure and flame front); lower case has strong ignition and leads to DDT (stable pressure/flame complex and detonation typical speed of reflected shock wave).

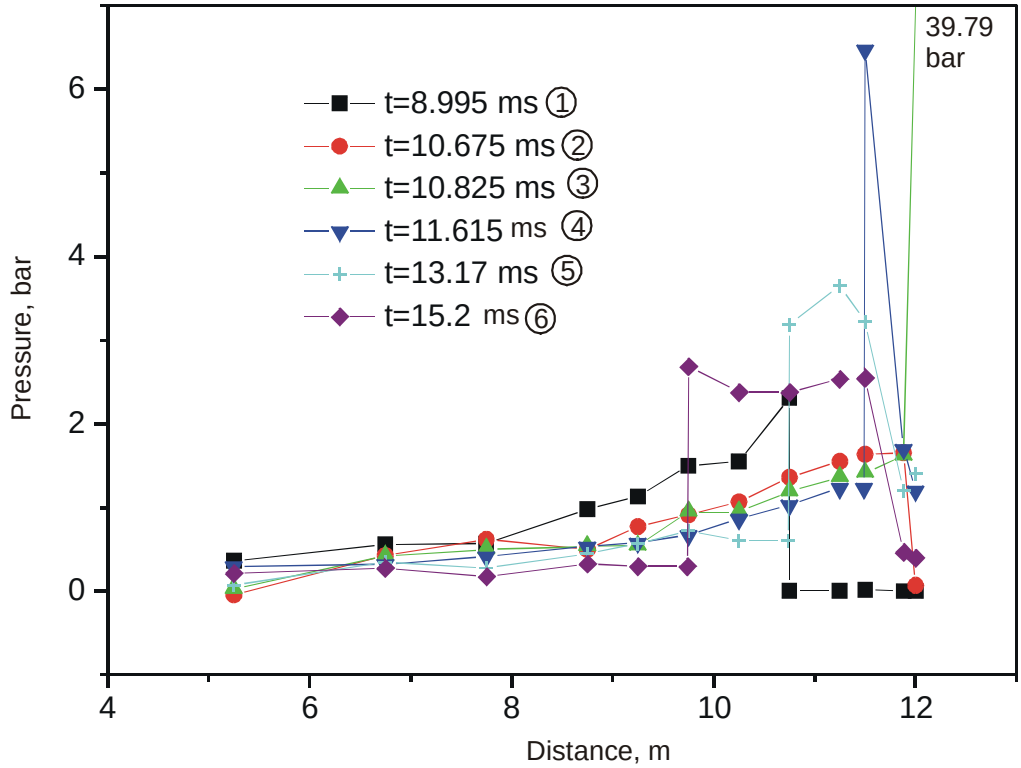

Figure E.1.2-2 Measured pressure profiles along the tube at given times. Initial conditions: 15% hydrogen in air, pressure in LPS 0.7 bar, pressure in HPS 6.7 bar, Ma = 1.77. Measured velocity of reflected shock wave 480 m/s.

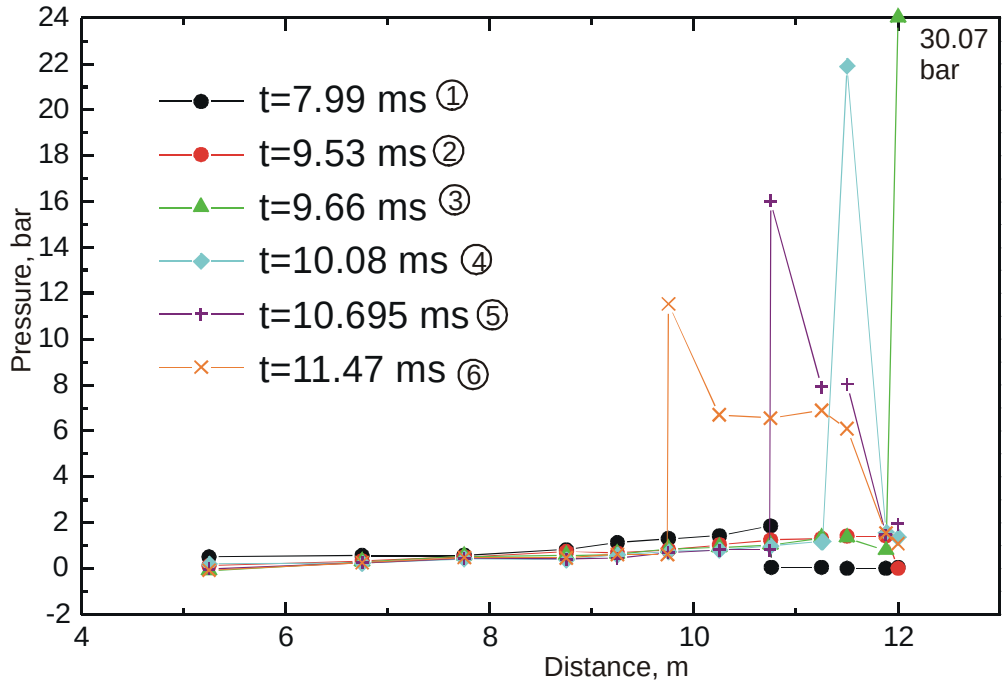

Figure E.1.2-3 Measured pressure profiles along the tube at given times. Initial conditions: 15% hydrogen, pressure in LPS 0.45 bar, pressure in HPS 7.0 bar, Ma = 2.03, velocity of reflected shock wave 1399 m/s

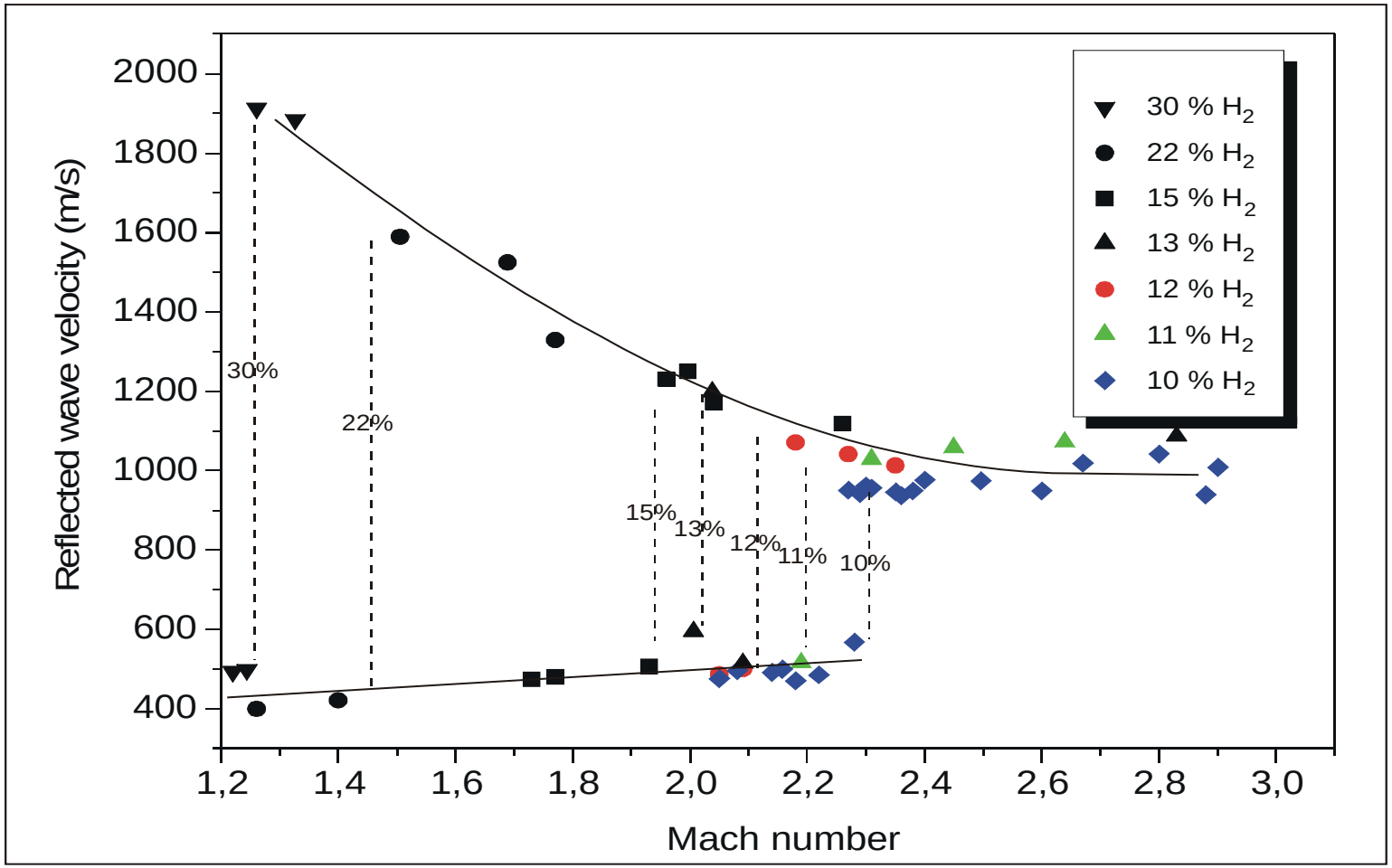

Figure E.1.2-4 Critical Mach numbers for DDT in FZK-tube experiments with shock wave focusing in a conical reflector. The dashed lines indicate the Mach numbers at which a transition occurs from mild ignition (deflagration) to strong ignition (detonation) as a function of the hydrogen concentration in the H_2-air mixture.

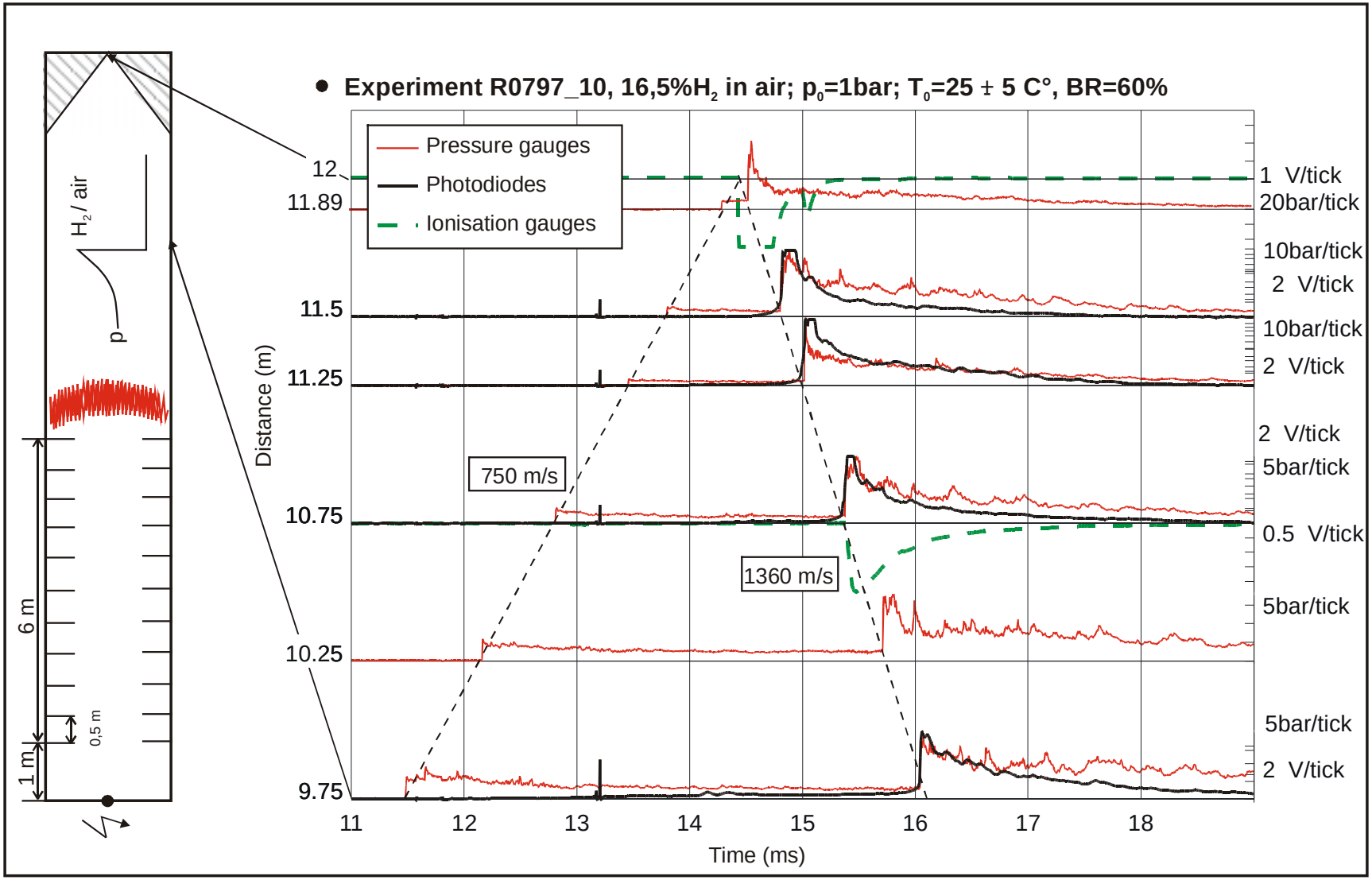

Figure E.1.3-1 Experiment with DDT in the conical reflector induced by focusing of the flame precursor wave

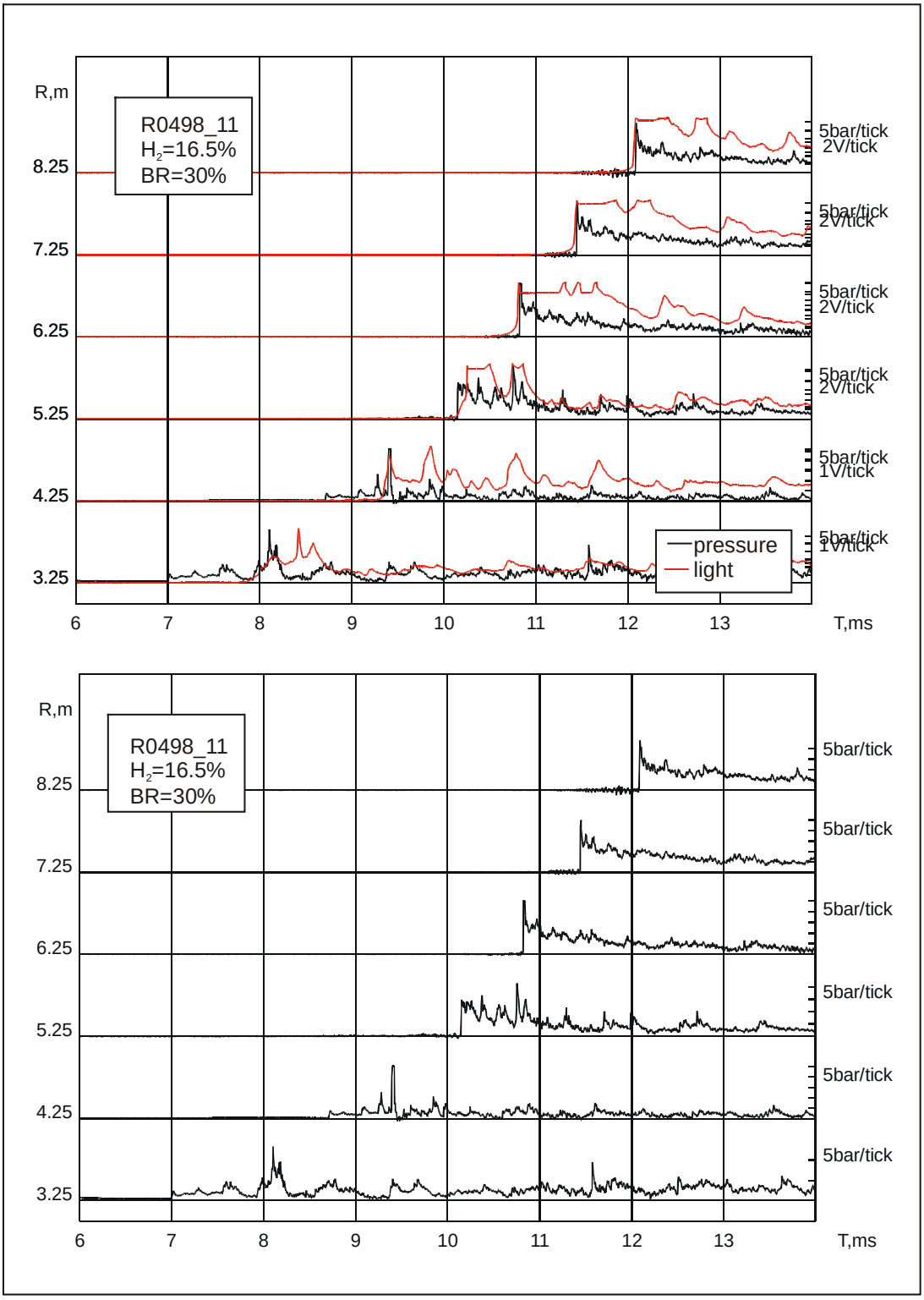

Figure E.1.4-1 Pressure and light signals in an experiment with DDT in or near the turbulent flame brush in the fully obstructed tube. Top: coupling of shock and flame front between the 5.25- and 6.25-m positions. Bottom: change from deflagration to detonation-like pressure amplitudes and shapes.

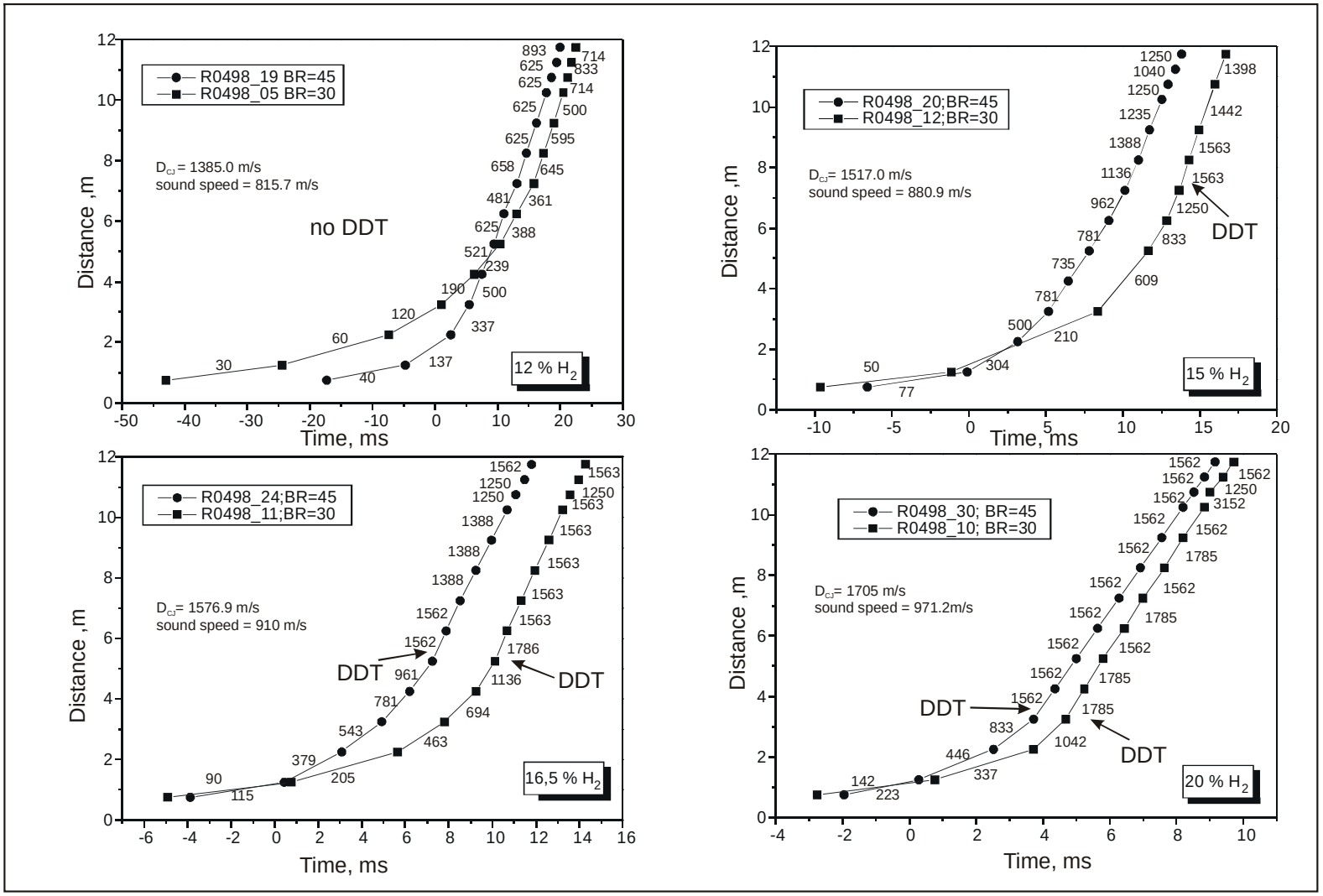

Figure E.1.4-2 Measured local flame speeds in DDT experiments with flames accelerating in a fully obstructed tube geometry. The transition process requires a flame velocity that is close to the isobaric speed of sound in the burnt gas (860 - 1000 m/s).

APPENDIX F: AGGREGATION RULES FOR THE DETERMINATION OF CHARACTERISTIC CONTAINMENT SIZE IN A LUMPED-PARAMETER APPROACH*

F.1 Description of the Rules

A description of the control volumes of a French pressurized-water reactor (PWR) 900 MWe has been used to define the present geometrical parameters. The rooms have four different shapes (Figure F.1-1): most of them can be assumed to be cubic but in the lower part flat and tall volumes are present, and the annular gap is mainly characterized by long rooms.

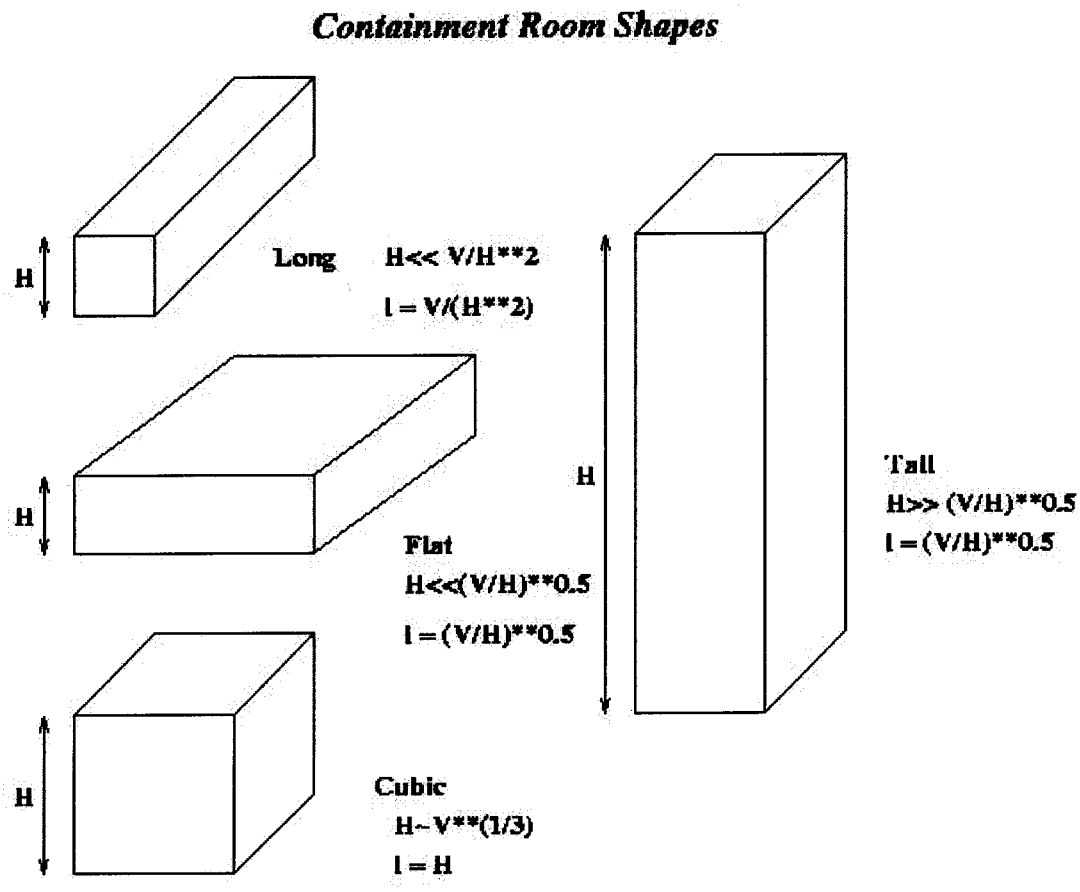

Figure F.1-1: Containment room shapes

Using these shapes, the characteristic length, L, of a single compartment can be defined, as described in Figure F.1-2. Long rooms can have significant size openings, and we have chosen to add a porosity factor, β, to calculate the characteristic size of such a room.

* Mr. Etienne Studer is the lead author for Appendix F.

Compartment Characteristic Size

V: compartment volume
H: compartment height

Shape	Characteristic Size L
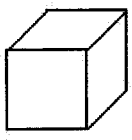	$L = \sqrt[3]{V}$
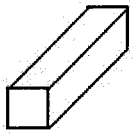	$l = V/(H.H)$ $L = (l+H)/2$
	$l = \sqrt{V/H}$ $L = (l+H)/2$
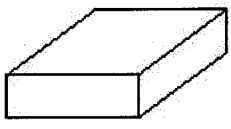	$L = \sqrt{V/H}$

Effect of openings for long and tall shapes:

$\beta = 1. - Sc/(Sc+Sw)$ **and** $L = (H + (H + \beta^2 (l - H)))/2.$

Figure F.1-2: Characteristic room size

According to these hypotheses, the blockage factor, α_i, can be calculated using different junction types (Figure F.1-3). Other formulations can be derived using the assumed shapes and the ϕ parameter, for example. The first step is to propose a formula, and investigation of different formulas can be made during the performance of the sensitivity analysis.

Compartment Junction Rules

V: compartment volume
H: compartment height
s: junction area
Φ: total wall and junction area

Shape	Junction Type	Blockage α
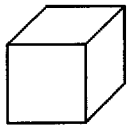	**side**	$\sqrt{\frac{H.s}{V}}$ **or** $\sqrt{\frac{6.s}{\Phi}}$
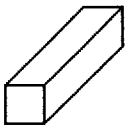	**end** **side**	$\sqrt{\frac{s}{H.H}}$ $\sqrt{\frac{H.s}{V}}$
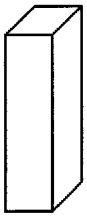	**bottom or top** **side**	$\sqrt{\frac{s}{H.H}}$ $\sqrt{\frac{s}{\sqrt{V}.H}}$
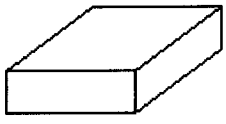	**bottom or top** **side**	$\sqrt{\frac{H.s}{V}}$ $\sqrt{\frac{s}{\sqrt{V}.H}}$

Figure F.1-3: Room blockage parameter

Regarding the system of connected rooms, direct application of the proposed formula (Chapter 3) leads to very large and unrealistic characteristic length L. Thus aggregation rules have been derived for all the possible cases. The bases of these rules are as follows:

- For a single flame path (Figure F.1-4), the proposed formula is used with an upper limit corresponding to a concatenation of the two volumes (a special case is considered when the two connecting rooms have very different characteristic sizes and the contribution depends on the acceleration potential of the flame).

- For a multiple flame path (Figure F.1-4), the contribution is limited by a "limiting" length equal generally to the minimum geometrical size perpendicular to the junction (this reduces the contribution of connected rooms according to multiple flame paths).

Aggregation rules : Definitions

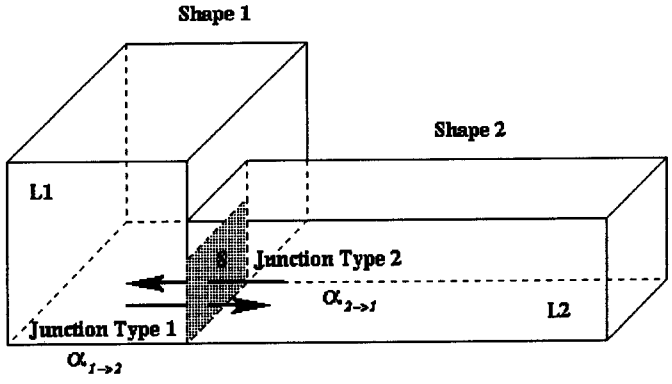

Aggregation rules : Comments

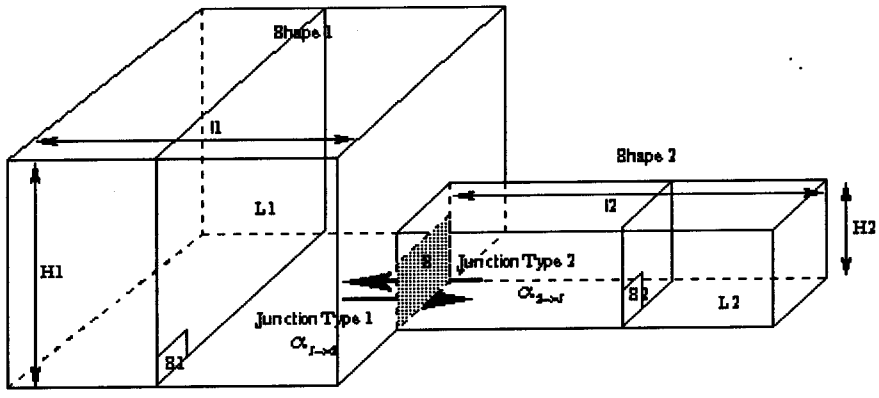

If one single flame path :

If size1 ~ size 2:

$$L(2) = L2 + \alpha_{2\to1}\, L1$$

$$L(1) = L1 + \alpha_{1\to2}\, L2$$

with $\alpha = \min(\alpha, 0.5)$

If size 1 >> size 2:

expansion = slow down

restriction = acceleration

$\beta = S1 / S2$

$$L(1) = L1 + \alpha_{1\to2}\, L2\ \beta$$

$$L(2) = L2 + \alpha_{2\to1} L1 / \beta$$

If multiple flame paths :

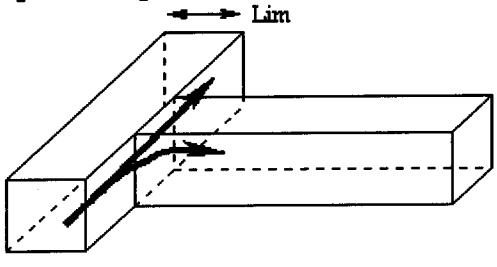

Definition of a limiting Length: Lim

$$L(2) = L2 + \alpha_{2\to1}\, Lim$$

$$L(1) = L1 + \alpha_{1\to2}\, Lim$$

Figure F.1-4: Aggregation definitions and comments

Using these definitions and basic considerations, the following rules (Figure F.1-5) have been used to calculate the characteristic size of a containment room.

Shape 1	Shape 2	Junction Type 1	Junction Type 2	Rules	
		side	side	 L1~L2 L(1) = L1 + α L2 L(2) = L2 + α L1 with α = min (α, 0.5)	L1>>L2 β = H1.H1/(H2.H2) L(1) = L1 +α L2β L(2) = L2 +α L1/β
		side	side	 lmin = min (H1, H2) L(1) = L1 + α lmin	L(2) = L2 + α lmin
			end	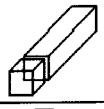 H1~H2 L(1) = L1 + α L2 L(2) = L2 + α L1 with α = min (α, 0.5)	H1>>H2 β = H1.H1/(H2.H2) L(1) = L1 + α L2 β L(2) = L2 + α L1/ β
		side	side	 lmin = min (H1, l2) L(1) = L1 + α lmin	L(2) = L2 + α lmin
			bottom or top	 H1~l2 L(1) = L1 + α L2 L(2) = L2 + α L1 with α = min (α, 0.5)	H1>>l2 β = H1.H1/(l2.l2) L(1) = L1 + α L2 β L(2) = L2 + α L1/ β
		side	side	 lmin = min (H1, H2) L(1) = L1 + α lmin	L(2) = L2 + α lmin
			bottom or top	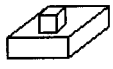 H1~l2 L(1) = L1 + α L2 L(2) = L2 + α L1 with α = min (α, 0.5)	H1>>l2 β = H1.H1/(l2.l2) L(1) = L1 + α L2 β L(2) = L2 + α L1/ β

Shape 1	Shape 2	Junction Type 1	Junction Type 2	Rules	
		side	side	 L(2) = L2 + α H1 L(1) = L1 + α H2	
			end	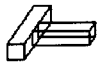 lmin = min (H1,H2) L(2) = L2 + α lmin L(1) = L1 + α lmin	
		end	end	 H1~H2 L(2) = L2 + α L1 L(1) = L1 + α L2 α = min (α, 0.5)	H1>>H2 β = H1.H1/(H2.H2) L(2) = L2 + α L1/ β L(1) = L1 + α L2 β
		side	side	 lmin = min (H1,l2) L(2) = L2 + α lmin L(1) = L1 + α lmin	
			bottom or top	 lmin = min (H1,l2) L(2) = L2 + α lmin L(1) = L1 + α lmin	
		end	bottom or top	 H1~l2 L(2) = L2 + α L1 L(1) = L1 + α L2 α = min (α, 0.5)	H1>>l2 β = H1.H1/(l2.l2) L(2) = L2 + α L1/ β L(1) = L1 + α L2 β
		side	side	 H1~H2 L(2) = L2 + α L1 L(1) = L1 + α L2 α = min (α, 0.5)	H1>>H2 β = H1.l1/(H2.l2) L(2) = L2 + α L1/ β L(1) = L1 + α L2 β
			bottom or top	 L(2) = L2 + α H1 L(1) = L1 + α H2	
		end	side	 l2 is always >> H1	lmin = min (H1,H2) L(2) = L2 + α lmin L(1) = L1 + α lmin

Shape 1	*Shape 2*	*Junction Type 1*	*Junction Type 2*	*Rules*
	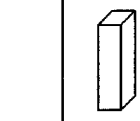	side	side	 L(1)=L1+α l2 L(2)=L2+α l1 α =min(α, 0.5)
		bottom or top	bottom or top	 l1~l2 L(1)=L1+α L2 L(2)=L2+α L1 α =min(α, 0.5) l1>> l2 β =l1.l1/(l2.l2) L(1) = L1 + α L2/β L(2) = L2 + α L1 β
		side	side	 lmin = min (l1,H2) L(1) = L1 + α lmin L(2) = L2 + α lmin
		bottom or top	bottom or top	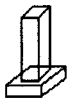 l2 is always >> l1 lmin = min (l1,H2) L(1) = L1 + α lmin L(2) = L2 + α lmin
		side	side	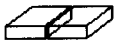 l1~l2 L(1) = L1 + α L2 L(2) = L2 + α L1 α =min (α , 0.5) l1>> l2 β =l1.H1/(l2.H2) L(1) = L1 + α L2/β L(2) = L2 + α L1 β
		bottom or top	bottom or top	 L(1) = L1 + α H2 L(2) = L2 + α H1 α =min (α , 0.5)

Figure F.1-5: Aggregation rules for lumped-parameter approach

LIST OF AUTHORS

Dr. Wolfgang Breitung	(**Chairperson**)
Dr. Wolfgang Breitung	(FZK, IKET, Germany)
Dr. Sergei B. Dorofeev	(Kurchatov Institute, Russian Federation)
Professor Boris E. Gelfand	(Russian Academy of Sciences, Russian Federation)
Mr. Etienne Studer	(IPSN, France)

Secretariat:

Dr. Jacques Royen	(OECD/NEA)

LIST OF ACRONYMS

Acronym	Definition
3D	**THREE DIMENSIONAL**
BR	**BLOCKAGE RATIO**
CJ	**CHAPMAN JOUGUET (VELOCITY)**
CSNI	**COMMITTEE ON THE SAFETY OF NUCLEAR INSTALLATIONS (NEA)**
DDT	**DEFLAGRATION-TO-DETONATION TRANSITION**
DPEA	**DÉPARTEMENT DE PRÉVENTION ET D'ÉTUDE DES ACCIDENTS (FRANCE)**
EBU	**EDDY BREAKUP (CONCEPT)**
EDC	**EDDY DISSIPATION CONCEPT**
EPR	**EUROPEAN PRESSURIZED REACTOR**
FA	**FLAME ACCELERATION**
FZK	**FORSCHUNGSZENTRUM KARLSRUHE**
HPS	**HIGH-PRESSURE SECTION**
ISPN	**INSTITUT DE PROTECTION ET DE SÛRETÉ NUCLÉAIRE (FRANCE)**
ISW	**INCIDENT SHOCK WAVE**
LES	**LARGE EDDY SIMULATION**
LBLOCA	**LARGE-BREAK LOSS-OF-COOLANT ACCIDENT**
LOCA	**LOSS-OF-COOLANT ACCIDENT**
LPS	**LOW-PRESSURE SECTION**
LWR	**LIGHT-WATER REACTOR**
NEA	**NUCLEAR ENERGY AGENCY (OECD)**
NPP	**NUCLEAR POWER PLANT**
PWR	**PRESSURIZED-WATER REACTOR**
RMS	**ROOT MEAN SQUARE**
RPV	**REACTOR PRESSURE VESSEL**
RSW	**REFLECTED SHOCK WAVE**
RW	**REFLECTED WAVE**
RWTH	**RHEINISCH WESTFÄLISCHE TECHNISCHE HOCHSCHULE AACHEN**
SI	**SAFETY INJECTION**
SBLOCA	**SMALL-BREAK LOSS-OF-COOLANT ACCIDENT**
ZND	**ZELDOVIC-VON NEUMANN-DÖRING (correlation)**